NUREG/CR-4794
SAND86-2638

J. A. Wackerly , 8524

Experimental Results of Core-Concrete Interactions Using Molten Steel with Zirconium

Prepared by E. R. Copus, R. E. Blose, J. E. Brockmann,
R. D. Gomez, D. A. Lucero

Sandia National Laboratories

Prepared for
U.S. Nuclear Regulatory Commission

NUREG/CR-4794
SAND86-2638
R3, R4, R7

Experimental Results of Core-Concrete Interactions Using Molten Steel with Zirconium

Manuscript Completed: December 1989
Date Published: July 1990

Prepared by
E. R. Copus, R. E. Blose, J. E. Brockmann,
R. D. Gomez, D. A. Lucero

Sandia National Laboratories
Albuquerque, NM 87185

Prepared for
Division of Systems Research
Office of Nuclear Regulatory Research
U.S. Nuclear Regulatory Commission
Washington, DC 20555
NRC FIN A1218

ABSTRACT

Four inductively sustained experiments, QT-D, QT-E, SURC-3, and SURC-3A, were performed in order to investigate the additional effects of zirconium metal oxidation on core debris-concrete interactions using molten stainless steel as the core debris simulant. The QT-D experiment ablated 18 cm of concrete axially during 50 minutes of interaction on limestone-common sand concrete using a 10 kg charge of 304 stainless steel to which 2 kg of zirconium metal was added subsequent to the onset of erosion. The QT-E experiment ablated 10 cm of limestone-common sand concrete axially and 10 cm radially during 35 minutes of sustained interaction using 50 kg of stainless steel and 10 kg of zirconium. The SURC-3 experiment had a 45 kg charge of stainless steel to which 1.1 kg of zirconium was subsequently added. SURC-3 axially eroded 33 cm of limestone concrete during two hours of interaction. The fourth experiment, SURC-3A, eroded 25 cm of limestone concrete axially and 9 cm radially during 90 minutes of sustained interaction. It utilized 40 kg of stainless steel and 2.2 kg of added zirconium as the charge material. All four experiments showed in a large increase in erosion rate, gas production, and aerosol release following the addition of Zr metal to the melt. In the SURC-3 and SURC-3A tests the measured erosion rates increased from 14 cm/hr to 27 cm/hr, gas release increased from 50 slpm to 100 slpm, and aerosol release increased from .02 g/sec to .04 g/sec. The effluent gas was composed of 80% CO, 10% CO_2, and 2% H_2 before Zr addition and 92% CO, 4% CO_2, 4% H_2 during the Zr interactions which lasted 10-20 minutes. Additional measurements indicated that the melt pool temperature ranged from 1600°C - 1800°C and that the aerosols produced were comprised primarily of Te and Fe oxides.

CONTENTS

PAGE

1. INTRODUCTION....1

2. EXPERIMENTAL RESULTS....3

2.1 QT-D Experiment....3

2.1.1 General....3
2.1.2 Geometry....4
2.1.3 Instrumentation....10
2.1.4 Procedure....20
2.1.5 Data Presentation and Results....20
2.1.6 Posttest Observations and Conclusions....24

2.2 QT-E Experiment....31

2.2.1 General....31
2.2.2 Geometry....32
2.2.3 Instrumentation....33
2.2.4 Procedure....40
2.2.5 Data Presentation and Results....40
2.2.6 Posttest Observations and Conclusions....45

2.3 SURC-3 Experiment....52

2.3.1 General....52
2.3.2 Geometry....53
2.3.3 Instrumentation....81
2.3.4 Procedure....82
2.3.5 Posttest Observations....85
2.3.6 Temperature Data Presentation....88
2.3.7 Flow Data Presentation....104
2.3.8 Aerosol Data Presentation....120
2.3.9 Gas Composition Data Presentation....161
2.3.10 Data Summary and Conclusions....173

2.4 SURC-3A Experiment....179

2.4.1 General....179
2.4.2 Geometry....180
2.4.3 Instrumentation....192
2.4.4 Procedure....193
2.4.5 Posttest Observations....195
2.4.6 Temperature Data Presentation....199
2.4.7 Flow Data Presentation....213
2.4.8 Aerosol Data Presentation....221
2.4.9 Gas Composition Data Presentation....238
2.4.10 Data Summary and Conolusions....250

CONTENTS (concluded)

PAGE

3. COMPARISON AND SUMMARY OF RESULTS.....253

3.1 QT-D Experiment.....253

3.2 QT-E Experiment.....254

3.3 SURC-3 Experiment.....255

3.4 SURC-3A Experiment.....257

3.5 Summary.....260

APPENDIX A - Calorimetric Test Data and Equations.....262
APPENDIX B - Thermistor Bridge Calibration Curve.....272
APPENDIX C - Temperature Data from Boiling Water Calibration, Test QT-E.....274
APPENDIX D - Thermophysical Properties Cast of MgO.....284
APPENDIX E - Zirconium Delivery Section and Crucible Fabrication.....293
APPENDIX F - Thermocouple Data from Test QT-D.....311
APPENDIX G - Thermocouple Data from Test QT-E.....315
APPENDIX H - Thermocouple and Heat Flux Results from Test SURC-3.....323
APPENDIX I - Thermocouple Data from Test SURC-3A.....345
APPENDIX J - Thermocouple Calibration Results, SURC-3 and SURC-3A.....360

REFERENCES.....365

LIST OF FIGURES

FIGURE		PAGE
2.1.1	QT-D Geometry	5
2.1.2	Relative Thermocouple Locations for Test QT-D	11
2.1.3	Thermocouple Placement Map	12
2.1.4	Detail of Thermocouple Arrays	13
2.1.5	Gas Sampling System - Test QT-D	14
2.1.6	Block Diagram of Data Acquisition System	17
2.1.7	QT-D Coil Input Power	19
2.1.8	QT-D Steel Temperature vs. Time	21
2.1.9	Typical Thermocouple Response in QT-D	22
2.1.10	Erosion vs. Time in QT-D	23
2.1.11	QT-D Pool Temperature vs. Time	25
2.1.12	CO/CO_2 Gas Effluent Measurement in QT-D	26
2.1.13	QT-D with Zirconia Reaction in Progress	27
2.1.14	Sectioned QT-D Crucible Posttest	28
2.1.15	Posttest X-ray of QT-D Crucible	29
2.2.1	Overall View of QT-E	32
2.2.2	QT-E Geometry	34
2.2.3	Relative Thermocouple Locations - QT-E	36
2.2.4	QT-E Coil Input Power	41
2.2.5	Initial Steel Temperature vs. Time	42
2.2.6	Typical Axial Thermocouple Response in QT-E	43
2.2.7	Axial Erosion vs. Time for QT-E	44
2.2.8	Typical Radial Thermocouple Response in QT-E	46
2.2.9	Radial Erosion vs. Time for QT-E	47
2.2.10	CO/CO_2 Gas Effluent Measurement in QT-E	48
2.2.11	QT-E with Zr Reaction in Progress	50
2.2.12	Posttest X-ray of QT-E Crucible	51
2.3.1	Test Apparatus, SURC-3 Experiment	54
2.3.2	Relative Thermocouple Locations, SURC-3 Crucible	56
2.3.3	Concrete Thermocouple Array, SURC-3	57
2.3.4	Thermocouple Orientation, Concrete Slug, SURC-3	58
2.3.5	Typical Sidewall Thermocouple Array, SURC-3	59
2.3.6	"1-D" Interaction Crucible, SURC-3	67
2.3.7a	Thermogram (TGA) of K/R Cast 98	69
2.3.7b	Expansion of Thermogram (TGA) of K/R Cast 98 between 360 and 475 C	70
2.3.8	Representative Temperature History of an MgO Sample Exposed to Solar Heat Flux	72
2.3.9	"PROPTY" Thermal Conductivity Prediction for Castible MgO Material	73
2.3.10	Comparison of Experiment Thermal History and Predictions of the "PROPRTY" Code	74
2.3.11	Thermogram (TGA) of Limestone Concrete	76
2.3.12	Coil Power - SURC-3	83

LIST OF FIGURES (continued)

FIGURE		PAGE
2.3.13	Initial Steel Temperature - SURC-3	84
2.3.14	SURC-3 Posttest X-ray	86
2.3.15	SURC-3 Posttest Crucible Section	87
2.3.16	Three Regions of Melt-Concrete Interaction	89
2.3.17	Typical Temperatures Indicated by Thermocouples Embedded in the Concrete Slab	91
2.3.18	SURC-3 Dehydration Front	92
2.3.19	Ablation Event History for the SURC-3 Experiment	93
2.3.20	Comparison of the Location of the 400 K and 1600 K Isotherms	95
2.3.21	Typical Temperatures Indicated by Type C and Type S Thermocouples	96
2.3.22	Peak Melt Temperatures Indicated by Type C and Type S Thermocouples	97
2.3.23	Typical Thermocouple Data Measured by the Sidewall Array Located at Z = 10.0 cm	99
2.3.24	MgO Sidewall Heat Flux History for Z=-24.1 cm, Test SURC-3	101
2.3.25	MgO Sidewall Heat Flux History for Z=10 cm, Test SURC-3	102
2.3.26	MgO Sidewall Heat Flux History for Z=30.1 cm, Test SURC-3	103
2.3.27	Flow Instrumentation Schematic	105
2.3.28	Laboratory Calibration of the ASME Orifice Plate	106
2.3.29	Laboratory Calibration of the LFE	108
2.3.30	Laboratory Calibration of the Turbine Meter	110
2.3.31	Laboratory Calibration of the Rockwell Gas Clocks	111
2.3.32	750 Gas Clock Data - SURC-3	114
2.3.33	Turbine Data (RAW) for SURC-3	116
2.3.34	Turbine Data (Corrected) for SURC-3	117
2.3.35	Orifice Plate Data for SURC-3	118
2.3.36	LFE Data for SURC-3	119
2.3.37	SURC-3 Test Article Schematic	121
2.3.38	SEDS Schematic	122
2.3.39	Crucible Sample Point	123
2.3.40	Flow Diluter Schematic	125
2.3.41	Cascade Cyclone Schematic	126
2.3.42	Filter Sample Box Schematic	127
2.3.43	Impactor Sample Box Schematic	130
2.3.44	Pinhole Diluter Schematic	132
2.3.45	Opacity Meter Schematic	133
2.3.46	Aerosol Pressure Transducer Calibration	134
2.3.47	Aerosol Pressure Transducer Calibration	135
2.3.48	Aerosol Penetration Through a 90° Bend	140
2.3.49	Measured and Predicted Aerosol Penetration	141
2.3.50	Aerosol Data Analysis Technique	144
2.3.51	SURC-3 Opacity Meter	153

LIST OF FIGURES (concluded)

FIGURE		PAGE
2.3.52	SURC-3 Aerosol Mass Source Term	154
2.3.53	Aerosol Size Distribution - Impactor A & B	155
2.3.54	Aerosol Size Distribution - Impactor C & D	156
2.3.55	Aerosol Size Distribution - Impactor E & F	157
2.3.56	Aerosol Size Distribution - Impactor G & H	158
2.3.57	Gas Sampling - SURC-3 Schematic	162
2.3.58	Gas Sampling Nitrogen Cold Trap	163
2.3.59	Grab Sampling Apparatus	164
2.3.60	CO/CO_2 Analyzer and Data Acquisition System	165
2.3.61	Infocon Mass Spectrometer	167
2.3.62	CO/CO_2 Data for Test SURC-3	171
2.4.1	Interaction Crucible, SURC-3A	181
2.4.2	Thermograms of the Limestone Concrete Used in SURC-3A	190
2.4.3	Thermograms of the Limestone Concrete Used in SURC-3A	191
2.4.4	SURC-3A Power History	194
2.4.5	SURC-3A Posttest X-ray	196
2.4.6	SURC-3A Crucible Section	198
2.4.7	Initial Steel Temperature in SURC-3A	200
2.4.8	Typical Axial Thermocouple Response - SURC-3A	201
2.4.9	400 K Isotherm - SURC-3A	202
2.4.10	1600 K Isotherm in SURC-3A	204
2.4.11	Comparison of the Location of the 400 K and 1600 K Isotherms	205
2.4.12	Typical Melt Pool Thermocouple Response in SURC-3A	206
2.4.13	Melt Temperature in SURC-3A	207
2.4.14	Typical Sidewall Thermocouple Response Below the Melt	209
2.4.15	Typical Sidewall Thermocouple Response Adjacent to the Melt	210
2.4.16	Typical Sidewall Thermocouple Response Above the Melt	211
2.4.17	SURC-3A Sidewall Erosion Profile	212
2.4.18	SURC-3A Flow Rate - Turbine	217
2.4.19	SURC-3A Flow Rate - LFD	218
2.4.20	SURC-3A Total Flow - 750 Gas Clock	219
2.4.21	SURC-3A Flow Rate - Orifice Plate	220
2.4.22	SURC-3A Aerosol Instrumentation Schematic	222
2.4.23	SURC-3A Aerosol Concentration - Filter Data	227
2.4.24	SURC-3A Aerosol Concentration - Opacity Meter	228
2.4.25	Aerosol Size Distribution - Impactor A	232
2.4.26	Aerosol Size Distribution - Impactor B	233
2.4.27	Aerosol Size Distribution - Impactor C	234
2.4.28	Aerosol Size Distribution - Cyclone	235
2.4.29	SURC-3A Gas Composition Instrumentation Schematic	239
2.4.30	SURC-3A Gas Composition - CO/CO_2 Monitor	245

LIST OF TABLES

TABLE		PAGE
2.1.1	Chemical Composition of K/R Cast 98 MgO Castible Refractory	6
2.1.2	Engineering Composition of Limestone/Common Sand Concrete	7
2.1.3	Standard Composition of the 304 Stainless Steel Slug	9
2.1.4	Chemical Composition of the Zirconium Metal	9
2.1.5	Thermocouple Locations, Test QT-D	15
2.2.1	Thermocouple Locations, Test QT-E	37
2.3.1	Location of Thermocouples Cast Within the Concrete Slug, SURC-3	60
2.3.2	Location of Thermocouples Installed in the Alumina Tubes Cast into Concrete Slug, SURC-3	62
2.3.3	Location of Thermocouples Cast Within the MgO Sidewall, SURC-3	63
2.3.4	Concrete Specifications	77
2.3.5	Mix Specifications for Limestone Concrete	78
2.3.6	Chemical Composition of Limestone Concrete and Concrete Constituents	79
2.3.7	Comparison of Specified and Actual Size Distributions for the Fine and Coarse Limestone Aggregate	80
2.3.8	Fission Product Simulants Used in the SURC-3 Experiment	81
2.3.9	In-Situ Calibration for SURC-3 Flow Devices	112
2.3.10	Pressure Decay and Leak Rate for SURC-3	112
2.3.11	SEDS Hardware Calibration	128
2.3.12	SEDS Pressure Transducer Hardware	136
2.3.13	Aerosol Sampler Pressure Drops	137
2.3.14	Particle Penetration Through a 90° Bend	139
2.3.15	SURC-3 - Sampling Schedule	143
2.3.16	Orifice Temperatures During SURC-3	147
2.3.17	System and Diluter Pressures	148
2.3.18	Aerosol Filter Data - SURC-3	149
2.3.19	Aerosol Impactor Data - SURC-3	150
2.3.20	Aerosol Filter Concentrations and Mass Source Term	151
2.3.21	Aerosol Data - SURC-3 Impactors Concentration mg/std liter	152
2.3.22	Elemental Analysis of SURC-3 Aerosol (Weight Percent of Element in Sample)	160
2.3.23	Results of GS/MS Analysis on Calibrated Gas	169
2.3.24	Normalized Data - CO/CO_2 Monitor	172
2.3.25	Gas Chromatography Analysis of SURC-3 Grab Samples	174
2.3.26	Mass Spectrometer Data for SURC-3 Test	175

LIST OF TABLES (concluded)

TABLE		PAGE
2.4.1	Location of Thermocouples Cast within the Concrete Slug, SURC-3A	183
2.4.2	Location of the Thermocouples Installed in the Alumina Tubes Cast into the Concrete Slug, SURC-3A	185
2.4.3	Location of Thermocouples Cast Within the Sidewall, SURC-3A	186
2.4.4	Limestone Concrete Compressive Strengths, SURC-3A	188
2.4.5	Fission Product Simulants Used in the SURC-3A Experiment	192
2.4.6	Pressure Decay and Leak Rate for SURC-3A Crucible/Expansion Chamber	213
2.4.7	SURC-3A In-Situ Flow Calibration	214
2.4.8	Flow Controlling Devices Used in SURC-3A Aerosol Collection	223
2.4.9	SURC-3A Sampling Schedule	225
2.4.10	SURC-3A Filter Sample Data	229
2.4.11	Aerosol Impactor Data - SURC-3A	230
2.4.12	Cyclone Data - SURC-3A	236
2.4.13	Elemental Analysis of SURC-3A Filter Data	237
2.4.14	Elemental Analysis of SURC-3A Cyclone Data	238
2.4.15	Normalized Gas Composition Data for SURC-3A -- CO/CO_2 Monitor	244
2.4.16	SURC-3A Gas Composition [Mass Spectrometer --Raw Data]	247
2.4.17	SURC-3A Gas Composition Normalized Mass Spectrometer Data	248
2.4.18	SURC-3A Gas Composition Grab Samples	249
3.1	Summarized Results from Zr-Steel Reactions with Limestone Concrete	261

1. INTRODUCTION

The Ex-Vessel Core Debris Interactions Program is principally an experimental effort which is closely coupled to computer code validation. The charter of the program is to measure, model, and assess the thermal, gas evolution, and aerosol source terms which might occur following a severe nuclear reactor accident. These source terms are the governing phenomena in any realistic post-accident containment integrity analysis or quantitative risk evaluation. A matrix of eight major tests is being conducted along with several smaller scale scoping tests. The major test matrix is designated as the SURC (Sustained Urania-Concrete) test series and the attendant scoping tests are designated as QT (Qualitative Test) experiments.

In addition to extending the data base to include more prototypic debris-concrete interactions, the SURC experiments are designed to provide information necessary to evaluate three important aspects of ex-vessel core debris-concrete interaction models. These are (1) heat transfer mechanisms, (2) gas release and chemistry, and (3) release of aerosols. In order to do this both integral tests which use oxidic UO_2-Zr-O_2 material to simulate core debris as well as separate effects tests using metallic stainless steel to simulate the metallic phase of core debris are conducted as part of the Ex-Vessel Core Debris Interactions Program [Bradley, 1986].

The SURC-3 series of tests (QTD, QTE, SURC-3 and SURC-3A) varied in size from 10 to 50 kg over a 20 cm diameter concrete basemat. They were designed to be separate effects tests which investigated the additional effects of zirconium metal oxidation on sustained core debris-concrete interactions. In these tests, Zr metal was added to molten stainless steel to create melt pools with up to 20% Zr interacting with highly calcareous concrete basemats. The tests were inductively heated in order to sustain the molten attack and lasted as long as four hours. The molten steel charge ablated either limestone concrete which has 35 w/o CO_2 or limestone-common sand concrete which has 22 w/o CO_2 until steady erosion and gas release rates were established. Zirconium metal was then added to the melt pool, and it effects on gas release rates and gas chemistry were observed. Together, QT-D, QT-E, SURC-3 and SURC-3A provide valuable validation and evaluation data for the primary gas release chemistry models used in the CORCON computer code [Cole, 1984]. Particular attention will be drawn to the severity and duration of any coking effects which are predicted to produce extraordinary amounts of carbon monoxide immediately after the zirconium is fully oxidized. At present, the CORCON code calculates that the CO_2 and H_2O released from the concrete will be almost totally reduced by Zr in the melt forming ZrO_2, H_2, and elemental carbon. Virtually no gas

other than hydrogen is predicted to be released during this reduction phase. After nearly all of the Zr metal is oxidized, the residual elemental carbon is expected to react with CO_2 and H_2O to form carbon monoxide. When this occurs, the gas release rate is expected to double the steady state value since two moles of gas are produced from each mole of gas evolved from the concrete. The coking reaction also produces a significant amount of chemical energy. The combination of increased gas production and increased chemical energy resulting from the coking reaction are predicted to result in higher debris temperatures and a substantial aerosol source term. The SURC-3 test series was instrumented especially to test this predicted behavior.

Four tests comprised the SURC-3 series. The first two tests, QT-D and QT-E, were scoping tests performed in open crucibles with limestone-common sand concrete as the basemat material. Instrumentation for these tests was limited to thermocouple arrays within the concrete, semiquantitative gas chemistry analysis, and visual records. The final two tests, SURC-3 and SURC-3A, were complete quantitative tests performed in closed crucibles with limestone concrete as the basemat material. SURC-3 and 3A were fully instrumented and included redundant, well characterized measurements of the melt pool temperature, gas flow rate, gas composition and concrete thermal response as well as a detailed measurement of the aerosol source term. Together the four tests paint a consistent and clear picture describing the phenomena associated with zirconium laden melt pools interacting with limestone-based concretes.

2. EXPERIMENTAL RESULTS

2.1 The QT-D Experiment

2.1.1 General

As part of the Ex-Vessel Core Debris Interaction Program, the QT-D experiment was designed as a scoping test for the SURC experiments. It was designed to achieve three goals: (1) qualitatively determine the extent and nature of interactions resulting from adding zirconium metal to a molten steel pool eroding through concrete, (2) measure melt pool temperatures using a new technique, and (3) obtain information on the composition of gas effluents during Zr metal-concrete interactions.

This test was the first of its kind ever attempted. Up until the execution of QT-D, no data existed pertaining strictly to Zr-core debris-concrete interactions and there was some doubt as to whether or not an effect would be seen. The primary purposes for QT-D were first to determine if a significant difference between steel-concrete interactions and steel-Zr-concrete interactions existed, and, secondly, to determine if the difference lasted long enough to allow gas, aerosol, and temperature measurements to be taken.

Two secondary goals were also set for QT-D. One of these was to test a new measurement technique for obtaining melt pool temperatures. This technique utilizes multiple C-type or S-type thermocouples set in an alumina sheath and cast into the concrete substrate. The stainless steel melt was expected to erode the concrete substrate but not the alumina sheathed thermocouples, thus allowing them to penetrate into the melt pool from below. By using S-type thermocouples, continuous pool temperature measurements could be taken up to 1760°C and C-type thermocouples could potentially measure pool temperatures as high as 2300°C. Another secondary goal of the QT-D test was to measure the composition of effluents coming from Zr-concrete interactions. Large amounts of CO and CO_2 were expected to be produced.

The QT-D test article (Figure 2.1.1) was a right circular cylinder consisting of an MgO (K/R cast-98 MgO castible) annulus with a limestone common-sand concrete slug poured into the base of the annulus. The overall height of the test article was 40 cm. The MgO walls were 5 cm thick, leaving an inside cavity diameter of 20 cm. The limestone-common sand concrete plug filled the bottom 30 cm of the annulus. The stainless steel melt pool material was a solid cylinder of 304 stainless 10 cm in diameter and 15 cm in thickness. Zirconium metal was added to the melt pool in the form of right circular cylinders. Six

cylinders, each with a diameter of 3.3 cm and a length of 6 cm were used. The total weight of Zr metal was 2.0 kg.

The test article was positioned in a copper induction coil with an inside diameter of 41.5 cm and a height of 43 cm. This coil was powered with a 125 kW-variable frequency (800 - 1200 Hz) induction power supply in order to melt and sustain core debris simulant. An MgO coverplate was used over one half of the open crucible in order to reduce radiation heat losses. The QT-D test was run in open air at local atmospheric pressure (.83 atm) and at an ambient temperature of 22°C.

2.1.2 Geometry

Several photographs of the experimental set-up and apparatus are shown in Figures 2.1.1A through 2.1.1C. The major components of the experimental set-up shown in the Figures consist of the interaction crucible, crucible cover, containment crucible, induction coil, video camera, and protective concrete barriers.

Figure 2.1.1B shows a top view photograph of the crucible and coil configuration with the zirconium delivery tube in place. Figure 2.1.1C shows an overhead photograph of the experimental apparatus with a section of the crucible cover and six zirconium cylinders shown in the foreground.

The interaction crucible shown in Figure 2.1.1C is of cylindrical geometry. The purpose of this composite "1-D" crucible is to allow only axial (or one-dimensional) ablation of the concrete slug; thus, all reaction products of the melt/concrete interaction must pass up through the melt, providing data consistent with conditions found at a horizontal surface in a reactor cavity. The sidewalls of the crucible are made of an MgO castible material manufactured by Kaiser Refractions having a trade name of K/R Cast-98. The chemical composition for this material is shown in Table 2.1.1. The dimensions of the annulus were 20.3 cm O.D. x 10.1 cm I.D. x 40.5 cm high. Cast into the base of the annulus was an instrumented limestone/common sand concrete slug. The dimensions of the slug were 10.1 cm O.D. x 15.2 cm thick. This concrete is used because it is typical of that used in the construction of some nuclear power plants. Materials making up this type of carbonaceous concrete are found throughout the United States. The concrete has a melting range of 1423 to 1673 K and liberates quantities of CO_2 gas and H_2O vapor when ablated. The engineering and chemical composition of this concrete are shown in Table 2.1.2.

The interaction crucible was placed inside a thin walled MgO containment crucible manufactured by Lava Crucible-Refractories Co. Thermocouples cast into the interaction crucible were routed

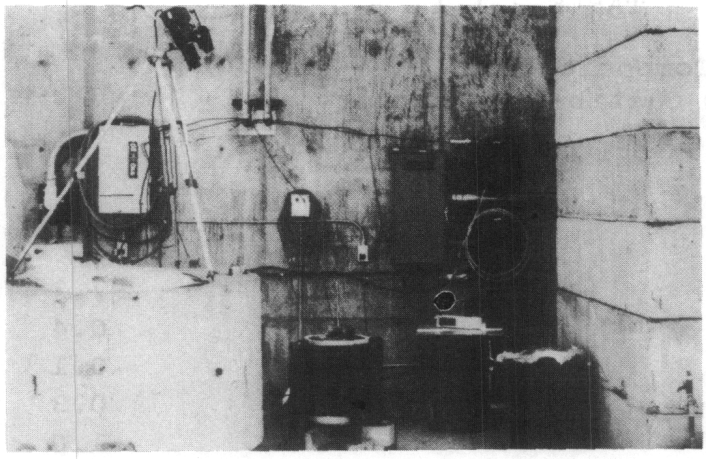

A. Overall View

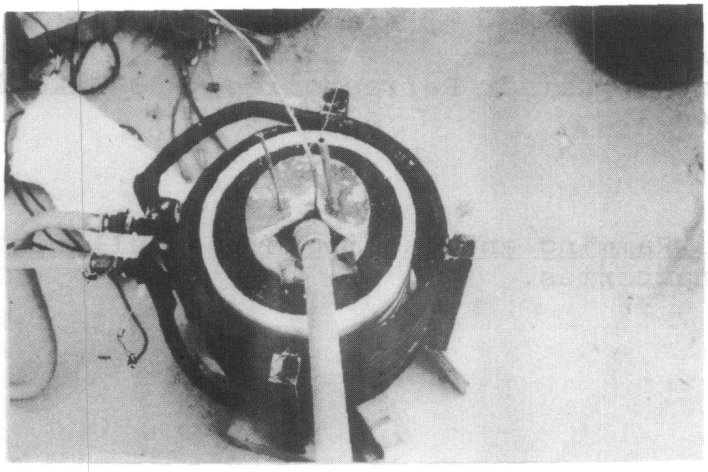

B. Top View with Delivery System

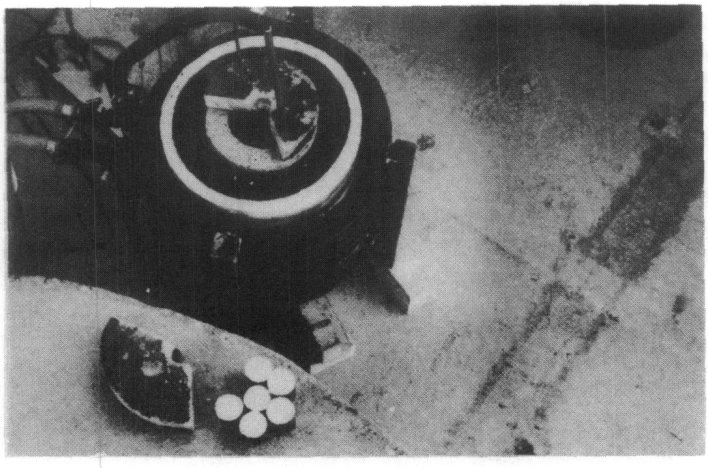

C. Top View with Zr Cylinders

Figure 2.1.1 QT-D Geometry

TABLE 2.1.1

Chemical Composition of K/R-Cast 98*
MgO Castible Refractory

Oxide	Weight %
MgO	97.1
SiO_2	0.4
Al_2O_3	0.1
Fe_2O_3	0.3
CaO	1.0
Cr_2O_3	1.1

* K/R-Cast 98 - a product of Kaiser Refractories, 300 Lakeside Drive, Oakland, CA 94643.

Data obtained from Basic Ramming and Casting Mixes Bulletin Published by Kaiser Refractories.

TABLE 2.1.2

Engineering Composition of Limestone/
Common Sand Concrete

Constituents(b)	Mass	Weight %
Coarse Aggregate (c)	85 kg	30.1
Fine Aggregate (c)	42.3 kg	15.0
Sand	93.2 kg	33.0
Cement	42.7	15.1
Water	10.1	6.8
(a) Air Entraining Agent	22.2 ml	
Water Reducing Agent	29.6 ml	

Chemical Composition of Limestone/Common Sand
Concrete Constituents (a)(b)

Oxide	Type 1 and 2 Cement (%)	Sand (%)	Aggregate(c) (%)	TOTAL %
Fe_2O_3	4.11	2.5	0.33	1.44
Cr_2O_3	0.011	0.042	ND	.01
MnO	0.08	0.02	ND	.03
TiO_2	0.20	0.18	0.05	.20
K_2O	0.54	2.70	0.30	1.22
NaO_2O	0.27	1.74	0.15	.82
CaO	63.5	1.52	45.56	31.2
MgO	1.53	0.34	0.80	.48
SiO_2	20.1	82.8	12.98	35.7
Al_2O_3	4.2	7.24	1.25	3.6
CO_2	ND	ND	40.0	22.0
H_2O	ND	ND	ND	4.8
SO_2	1.0	ND		.2

ND = Not Determined

a) ASTM C-494-71, Standard Specification for Chemical Admixtures for Concrete, American Society for Testing and Materials, Philadelphia, PA.

b) ACTI 211. 1-74, Recommended Practices for normal and Heavy Concrete, American Concrete Institute, Detroit, MI.

c) ASTM 33-74, Standard Specifications for Concrete Aggregates, American Society for Testing and Materials.

through a 7.6 cm diameter hole cored in the base of the containment crucible. The dimensions of this crucible were 37.1 cm O.D. x 1.9 cm I.D. x 49.5 cm high. The void between the interaction crucible and containment crucible was filled with alumina (Al_2O_3) gravel packed to a porosity of 52%. This was done to contain any melt that might flow from the interaction crucible should it be breached by extensive downward or sideward erosion.

A circular cover for the interaction crucible was fabricated from castible MgO and is shown in Figure 2.1.1C. The cover was 20.3 cm in diameter and 5.1 cm thick. The purpose of the cover was to minimize the upward heat loss during the experiment. Two 304 stainless steel tubes were cast into the top of the cover. The tubes had inside diameters of 0.48 and 0.95 cm. These tubes would be typically used for sampling evolved gases and aerosols during the test. However, for this experiment, the tubes were not used. A 120° circular sector was removed from the cover so that realtime video observations could be made throughout the experiment. The cover was placed on the crucible but not sealed to the crucible. A 0.48 cm I.D. 304 stainless steel tube was placed just above the cutout in the cover. This tube was connected to an infrared CO/CO_2 gas monitor.

The melt charge consisted of a solid cylinder of 304 stainless steel having a mass of 10.2 kg. The dimensions of the cylinder were 10.2 cm O.D. x 16.0 cm high. The steel cylinder was placed directly on top of the concrete slug and instrumented with one type K thermocouple installed in the top of the steel cylinder for monitoring the heat up. The specified composition of the 304 stainless cylinder is shown in Table 2.1.3.

Six zirconium cylinders (see Figure 2.1.1C), 99.5% pure, and nominally 6.0 cm long were cut from a 3.3 cm diameter solid round bar 3.0 meters long supplied by Teledyne Wah Chang. The average weight of each cylinder was 0.33 kg. The chemical composition of the zirconium cylinders is shown in Table 2.1.4. The elemental analysis is taken from the top, middle and bottom of the ingot from which the rods were fabricated.

The induction coil used to heat the stainless steel slug and sustain the reaction was of a two lead configuration. The coil had nine turns, a 41.9 cm I.D., and was 43.2 cm high. The coil was placed around the containment crucible and centered vertically with respect to the stainless steel slug.

A galvanized steel tube (Figure 2.1.1B) 3.8 cm I.D. and 2 meters long was used to remotely deliver the zirconium cylinders to the melt at the appropriate time during the experiment.

TABLE 2.1.3

Standard Composition of the
304 Stainless Steel Slug

Element	Weight %
C	.08
Mn	2.0
P	.04
S	.03
Si	1.0
Cr	18.0-20.0
Ni	8.0-11.0
Cu	.5
Mo	.5
Fe	70.-75.

TABLE 2.1.4

Chemical Composition of the Zirconium Metal

	Sample Location on Ingot		
Trace Element	Top (ppm)	Middle (ppm)	Bottom (ppm)
Al	150	135	125
C	150	150	150
Nb	71	76	120
Cr	110	79	62
Fe	1120	1140	1040
H	< 5	9	10
Hf*	0.079%	0.056%	0.055%
N	51	60	57
Ni	< 35	47	85
O	1360	1340	1300
P	10	8	10
Si	48	45	58
Sn	800	600	1100
Ta	<100	<100	<100
Ti	34	27	27
W	< 25	< 25	< 25
Zr*	99.5	99.5	99.5

* Composition given in percent (%) rather than parts per million (ppm).

2.1.3 Instrumentation

A total of 28 data channels were instrumented for the QT-D test. Of these, twenty-two were thermocouples located in the concrete to measure concrete erosion. One additional thermocouple was placed in the stainless steel slug to record the initial heat-up and melt. Two data channels recorded the power being applied to the induction coil and the final three channels recorded the CO/CO_2 content of the gas effluent.

Thermocouple Instrumentation

A total of 22 thermocouples broken into four groups were cast into the concrete slug of the interaction crucible. The relative locations of the thermocouples cast are shown in Figure 2.1.2. Figure 2.1.3 shows a thermocouple placement map defining the nomenclature describing the thermocouple locations with regard to cylindrical coordinates. Table 2.1.5 lists the specific locations of the thermocouples cast into the concrete slug. One array of ten K type thermocouples was located on the axial centerline. Thermocouples in this array were spaced 1 cm apart. These thermocouples had a 0.16 cm diameter, 304 stainless steel, ungrounded sheath. A sketch of the concrete thermocouple arrays is shown in Figure 2.1.4. The sheath of each thermocouple in the axial array was bent at an angle of 90 degrees at a minimum of 10 sheath diameters from the tip. The bent tip of the thermocouple was located in a plane parallel to the concrete surface and thus parallel to the propagating isotherm. This was done to minimize the errors caused by heat conduction down the metal sheaths. Two sets of four K type and one set of C type (Tungsten - 5% Rhenium vs. Tungsten 26% Rhenium) were mounted in alumina tubes and cast into the concrete (see Figure 2.1.5). The alumina tubes were 0.64 cm in diameter and contained four 0.2 cm diameter holes in which the thermocouples were installed. The K type thermocouples installed in two of the alumina tubes were the same as previously described. The C type thermocouples installed in the third tube had a 0.16 cm, ungrounded, tantalum sheath. The four thermocouples in each of the three alumina tubes were cast into the concrete at depths of 1.0, 3.0, 5.0, and 7.0 cm with reference to the surface of the concrete. These alumina tube arrays were cast into the concrete slug on a radius of 3.8 cm from the axis and at 90, 180, and 270 degrees from an arbitrarily chosen 0 degree reference. The K types were installed to measure ablation rate and the C types for measuring melt temperatures.

Gas Composition Instrumentation

Gas sampling for test QT-D was performed using an Infrared Industries (IR) CO/CO_2 monitor. The gas monitoring system consisted of three separate detectors housed in two instruments. The IR 702 gas analyzer consisted of two detectors capable of

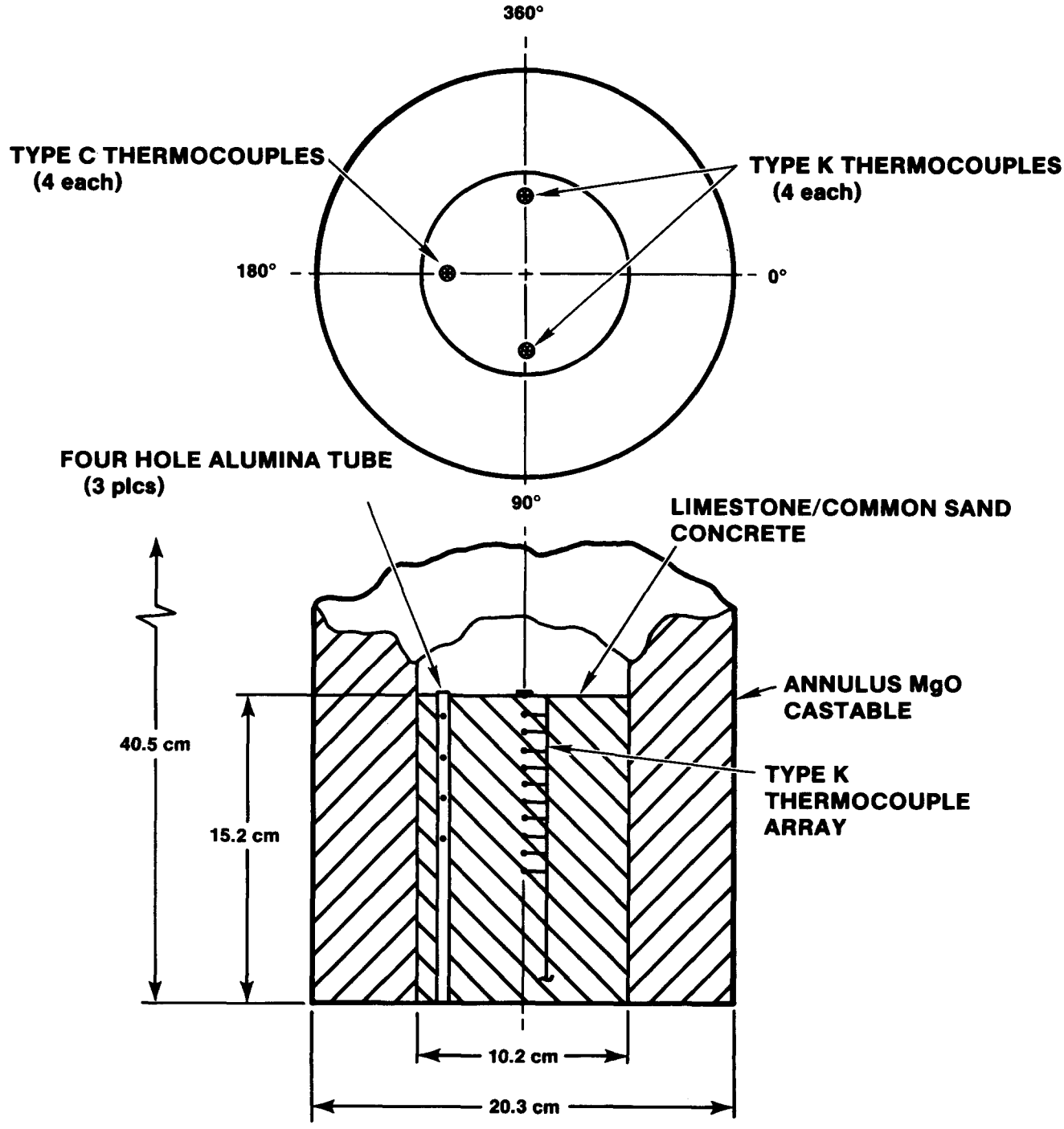

Figure 2.1.2 - Relative Thermocouple Locations for Test QT-D

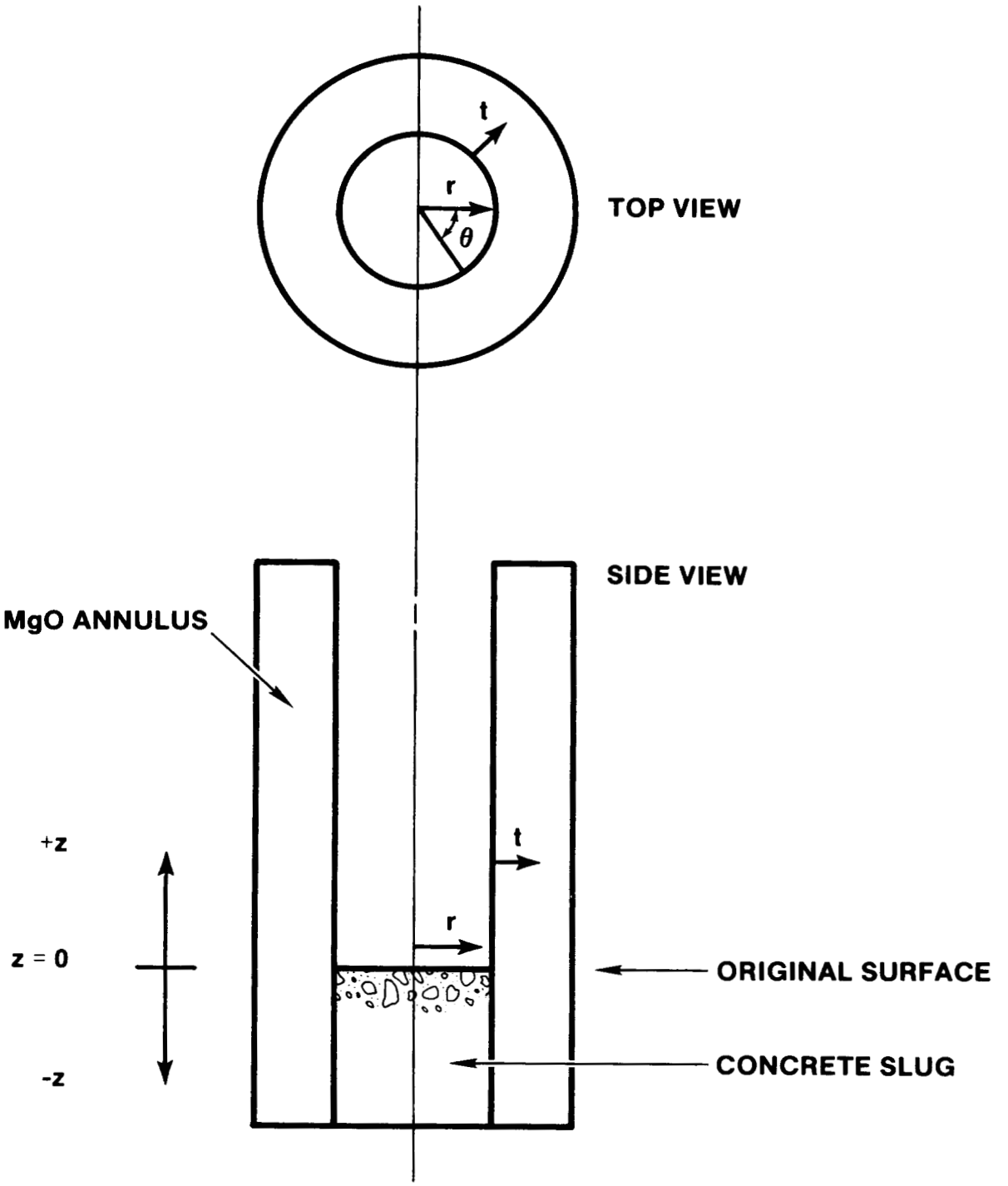

Figure 2.1.3 - Thermocouple Placement Map

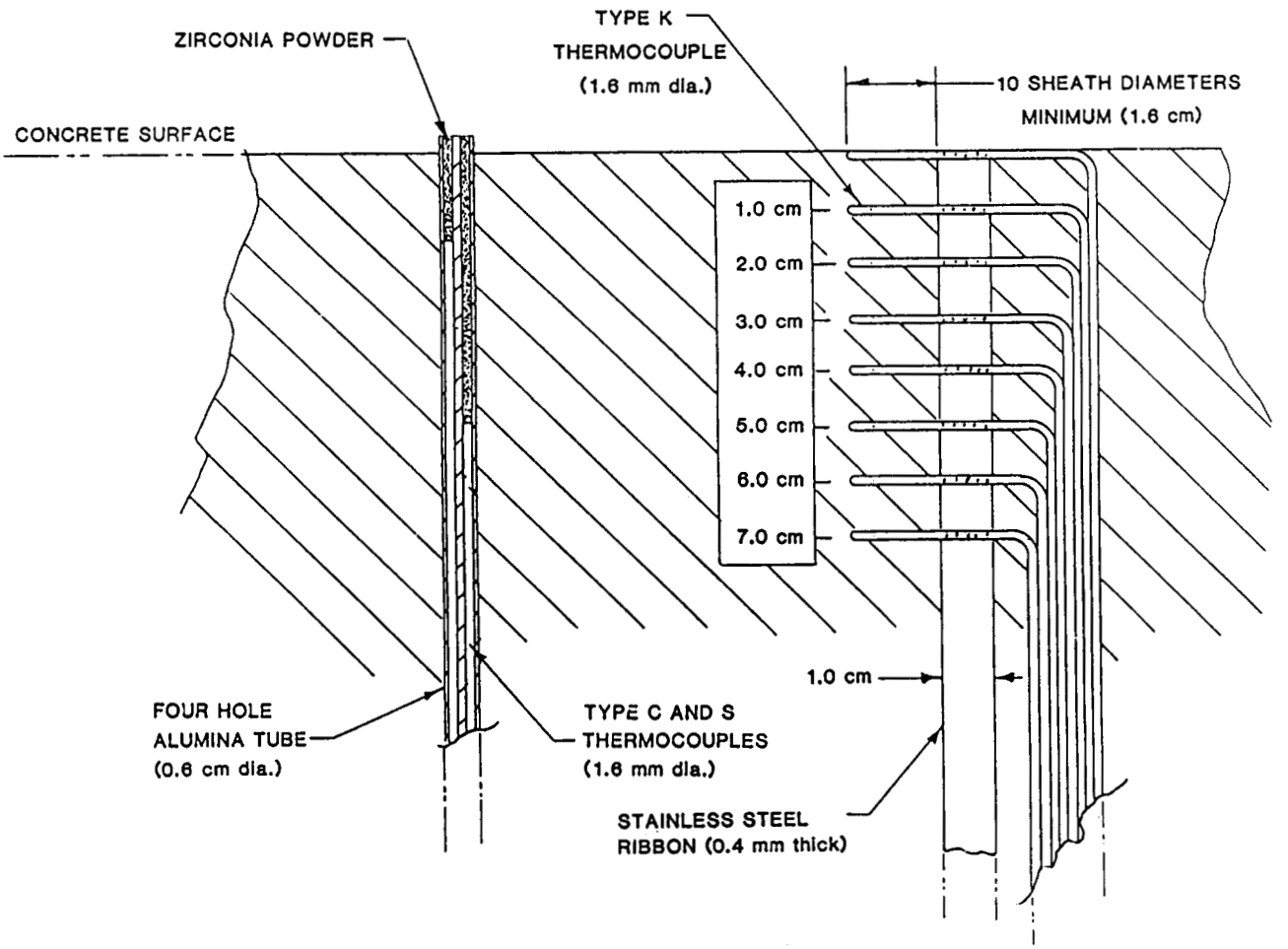

Figure 2.1.4 - Detail of Thermocouple Arrays

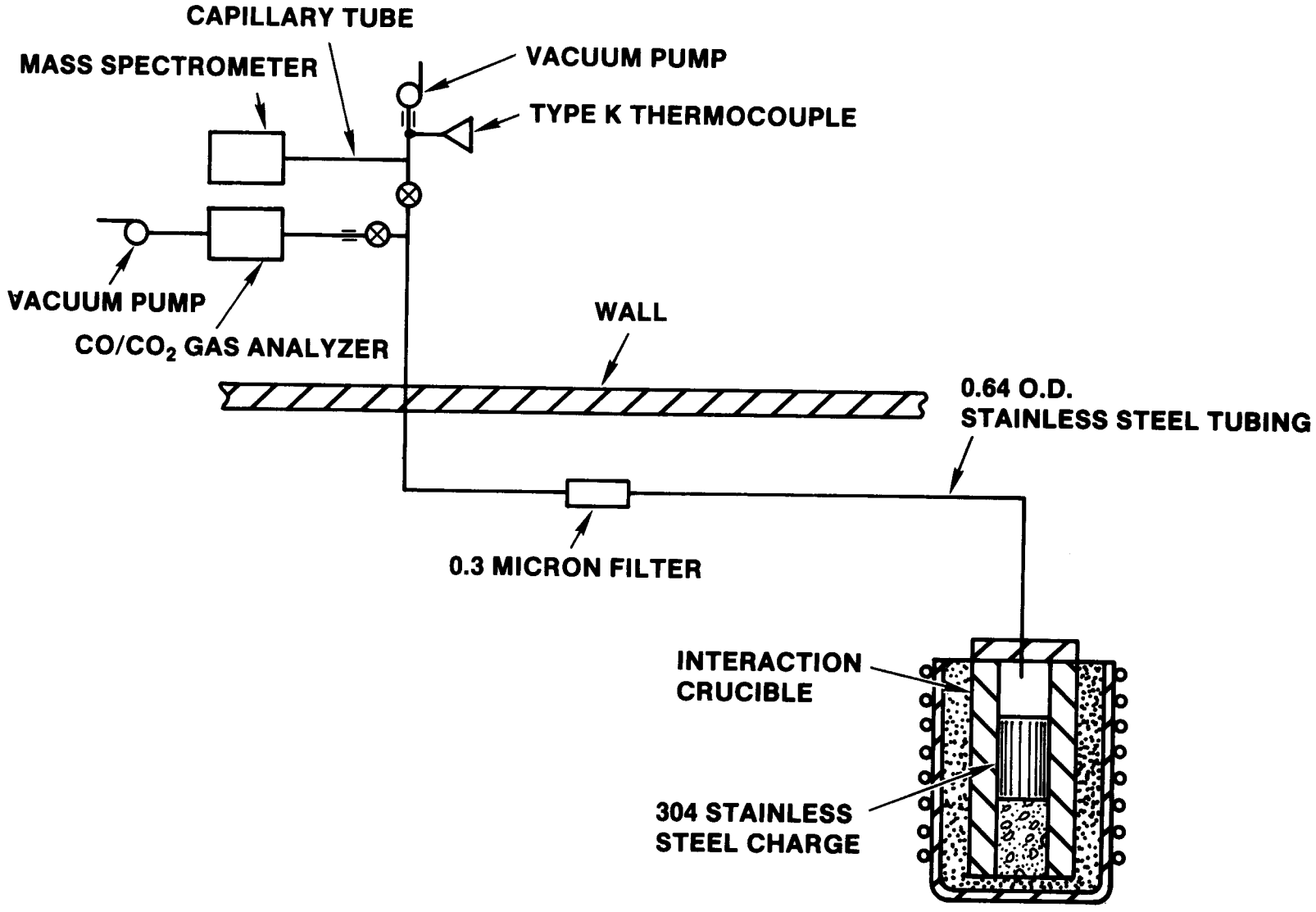

Figure 2.1.5 - Gas Sampling System - Test QT-D

TABLE 2.1.5

Thermocouple Locations, Test QT-D

Thermocouple Identification #	TC Type (C,K,S,T)	r (cm)	t (cm)	θ (deg)	Z (cm)
1	K	0.0		0.0	-0.25
2	K	0.0		0.0	-1.05
3	K	0.0		0.0	-2.15
4	K	0.0		0.0	-3.25
5	K	0.0		0.0	-4.15
6	K	0.0		0.0	-5.15
7	K	0.0		0.0	-6.20
8	K	0.0		0.0	-7.20
9	K	0.0		0.0	-8.20
10	K	0.0		0.0	-9.20
ALUMINA TUBE #1					
A	K	3.8		90	-1.00
B	K	3.8		90	-3.00
C	K	3.8		90	-5.00
D	K	3.8		90	-7.00
ALUMINA TUBE #2					
A	C	3.8		180	-1.00
B	C	3.8		180	-3.00
C	C	3.8		180	-5.00
D	C	3.8		180	-7.00
ALUMINA TUBE #3					
A	K	3.8		270	-1.00
B	K	3.8		270	-1.00
C	K	3.8		270	-1.00
D	K	3.8		270	-1.00

measuring CO in the range of 0 to 2000 ppm and CO_2 from 0 to 20%. A second instrument, an IR 703 analyzer was a single detector capable of measuring CO in the range of 0 to 50%. A schematic of the sampling system is shown in Figure 2.1.5. The sample gas was pulled through a 0.48 cm I.D., 7 meter long stainless steel line, attached to a 0.3 micron HEPA filter at 3 liters/min. The sample port extended vertically into the crucible cavity approximately 8 cm below the cutout in the cover. The HEPA filter removes particles in the gas 0.3 μm and larger. The sample gas was pumped from the test article by an electromechanical pump in the IR 741 CO/CO_2 gas sample conditioner to the IR 702 and IR 703 gas analyzers in series. CO and CO_2 absorbs radiation in the infrared region whereas N_2 and O_2 (the principal components of dry air), do not. Dual beam nondispersive infrared gas analyzers properly limit the range of an infrared source with a spectral filter so the analyzer can be made sensitive to a particular gas. The amount of absorption can be measured, electronically processed, and displayed. This reading is related directly to the gas concentration. The uncertainty in the percent CO and CO_2 detected is less than 2%. A standard pretest and posttest calibration was performed and a comparison showed negligible system drift while maintaining recorded accuracy.

Induction Power Instrumentation

The 10.2 kg of stainless steel was melted and sustained using an Inductotherm 125 kW, 3 kHz induction power supply. Power was delivered to the coils using a pair of No. 16 high current, water cooled, flexible leads. During the melting process, the induction power supply automatically controlled voltage and frequency to deliver the desired power. Maximum efficiency was maintained throughout the experiment without the need to switch capacitors or voltage taps. The power delivered to the crucible coil was measured using a power transducer built by Inductotherm Corporation. The transducer measured coil voltage and current and converted it into a voltage equivalent of the power delivered. This transducer was not manufactured to compensate for the phase angle between the current and voltage and therefore, was calibrated using a calorimetric method. This method is discussed in detail in Appendix A.

In order to determine the amount of power delivered to the molten steel, the power going into heating the coil cooling water had to be considered. The reason for the heating of the cooling water is due to the resistive loss caused by the current in the coil (I^2R loss). This is inevitable in any coil and must be considered in performing an energy balance on the system. The amount of power lost in heating the coil cooling water can be as much as 35% of the power delivered to the coil. The differential temperature of the cooling water was measured at the inlet and exit of each of the coils with two Omega ON-970-44008, 30,000 ohm

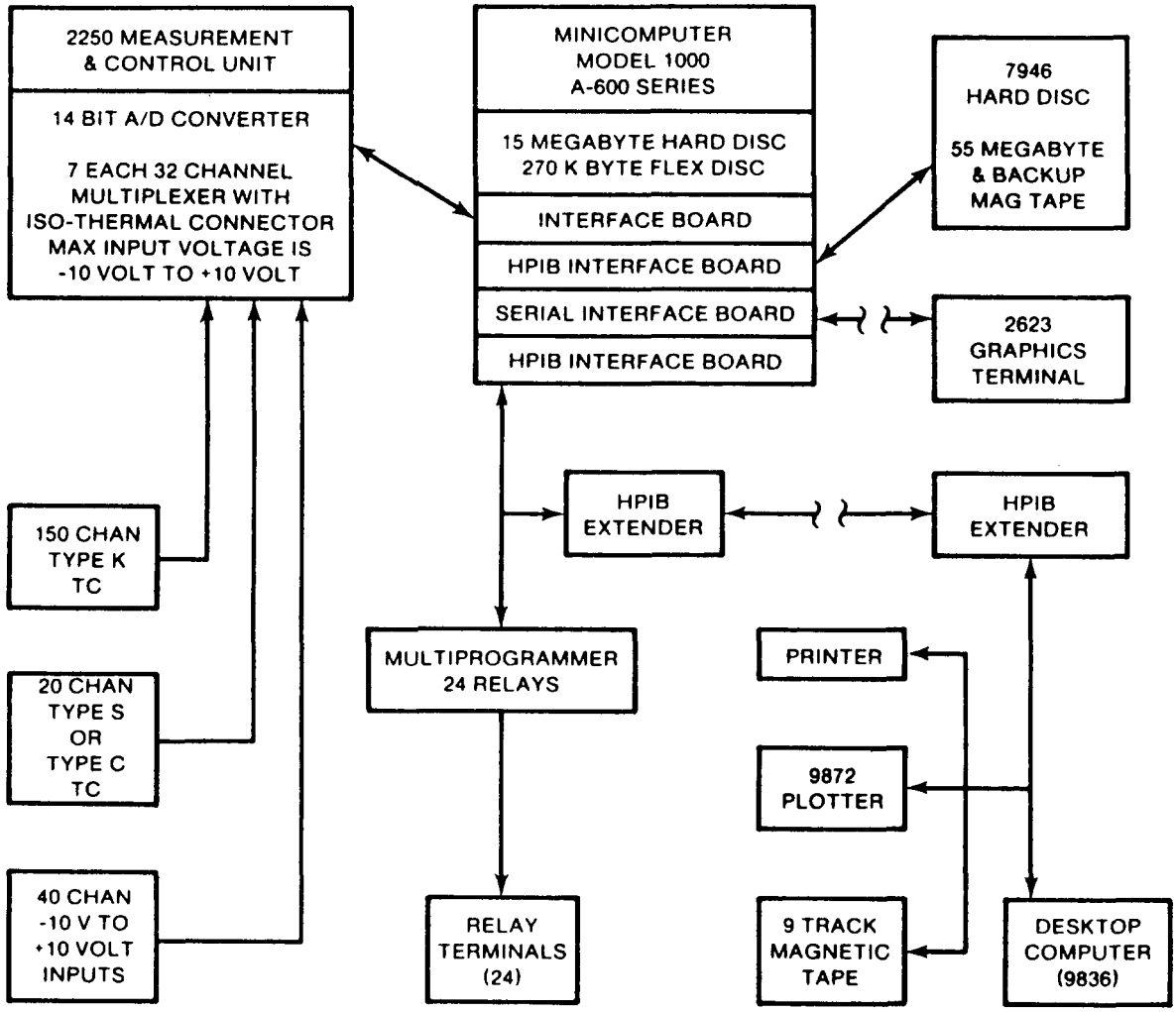

Figure 2.1.6 - Block Diagram of Data Acquisition System Monitor

thermistors arranged in half bridge circuit. The calibration of the bridge is described in detail in Appendix B. The flow of water through the crucible coil was regulated manually with a 19.1 mm diameter ball valve and measured using a Brooks Model 1110 rotameter. A remote control unit located in the control/ instrumentation building was used to control the power to the coils.

All 29 instrument channels were recorded every 10 seconds using an HP 1000 data acquisition system. This system is shown schematically in Figure 2.1.6. Two-hundred-ten channels of data may be acquired during an experiment. Of the 210 channels, 150 are K type thermocouples, 20 are either S or C type thermocouples and the remaining 40 are DC voltage channels. A patch panel routes all the analog data channels from the test location to the Hewlett-Packard Model 2250 Measurement and Control Unit. This unit houses an analog to digital converter capable of multiplexing the 210 data channels. The voltage range of the data acquisition unit is ± 10 volts DC, with a programmable gain to increase sensitivity if the expected signal is small. A Hewlett-Packard Model 1000 series A-600 minicomputer is used to control all remote devices and manipulate the data received from the Measurement and Control Unit. Data may be taken at 1.25 second intervals and are stored on a Hewlett-Packard Model 7946, 15 Megabyte hard disk. A Hewlett-Packard Model 2623 terminal is used to command the minicomputer during test and to display real time data in a tabular format as data acquisition progresses. A desk top terminal Hewlett-Packard Model 9836 is used to display real time data in both graphic and numeric format as well as to provide interrupt control over the minicomputer during a test. A Hewlett-Packard Model 9872 four color plotter and nine track magnetic tape are used for posttest data plotting and transfer.

The measurement accuracy of the 14-bit analog to digital converter is 1.56 microvolts in the most sensitive range and 1.25 millivolts at the highest range (-10 to +10 volts). With the appropriate range setting, the resolution for a K type thermocouple is 1°C, and for a type S or C thermocouple, the resolution is 1.1°C.

Video Monitoring Instrumentation

The experiment was monitored remotely using a Sony Beta Model HVC 2200 video camera connected to a Sony Model SL 2000 portable Beta recorder and Model TT 2000 Tuner/Timer. The real time camera image was displayed on a 19 inch Sony model CVM 1900 color monitor. The image was passed between the video recorder and color monitor via a RG-58 coax cable.

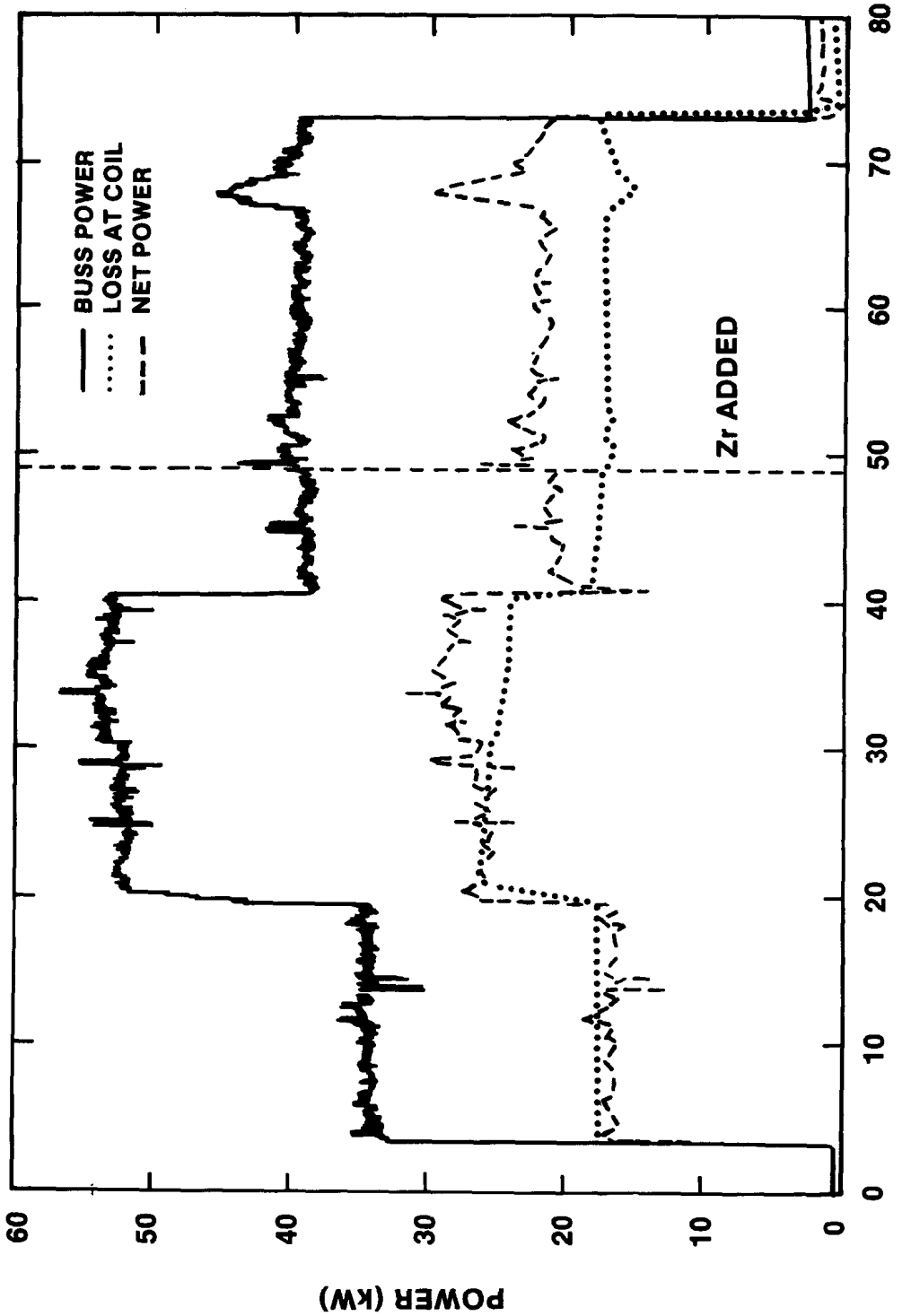

Figure 2.1.7 - QT-D Coil Input Power

2.1.4 Procedure

After initial calibration and pretest checkouts were performed, power was applied to the coil (Figure 2.1.7) at a rate of 35 kW. The pool melt thermocouple (Figure 2.1.8) was monitored to confirm that 15% of the power was being transmitted to the metallic charge. After twenty minutes, the power was increased to 55 kW (8.25 kW net) to overcome increasing heat losses. At time = 30 minutes, the 304 stainless steel charge became molten and concrete attack began. Power was then reduced back to 40 kW to limit concrete attack. Axial thermocouple failures indicated that the melt pool eroded 3 cm of concrete at time = 45 min. Between time = 47 and time = 50 minutes, 6 Zr cylinders, each weighing 335 g, were sequentially dropped into the melt through a 5 cm diameter steel pipe which was canted 45° above the crucible surface. A large bubble of oxidic crust material swelled out of the open half of the crucible immediately after the Zr was added. Erosion slowed considerably when the cold Zr metal was added to the steel melt until time = 63 when a vigorous Zr-Concrete reaction began. This reaction was accompanied by dense aerosol and large flames which expelled hot metal from the crucible. This Zr-steel-concrete interaction continued unabated until the instrumented region (10 cm) of the test article was completely eroded at time = 70 minutes. At time = 75 minutes, the power supply was shut down and the test was terminated.

2.1.5 Data Presentation and Results

Raw data plots for all of the thermocouple instrumentation used in QT-D are presented in Appendix F. Eighteen K-type thermocouples were used to monitor concrete erosion in QT-D. Typical data obtained from four of these thermocouples are shown in Figure 2.1.9. This figure plots temperature as a function of time for centerline thermocouples located 1, 3, 5, and 7 cm deep in the limestone-common sand concrete. These thermocouples failed (exceeded 1600 K) at t=38.5, t=49, t=67, and t=68.5, respectively. A plot of the failure times for all eighteen K-type thermocouples is shown in Figure 2.1.10. This figure presents the failure times for the thermocouple groups (centerline, 90° midradius, and 270° midradius) as a function of their position in the concrete substrate. From this plot, we see that the concrete erosion began at t=30 and proceeded at an average rate of 10 cm/hr until t=48. At that time, the 2.0 kg of Zr was dropped into the melt pool. From t=48 until t=65 the erosion rate averaged 7 cm/hr. At time t=65, the Zr concrete reaction began and the consequent erosion rate for the next few minutes was 100 cm/hr until time t=70 when the instrumented region of the QT-D crucible was completely ablated.

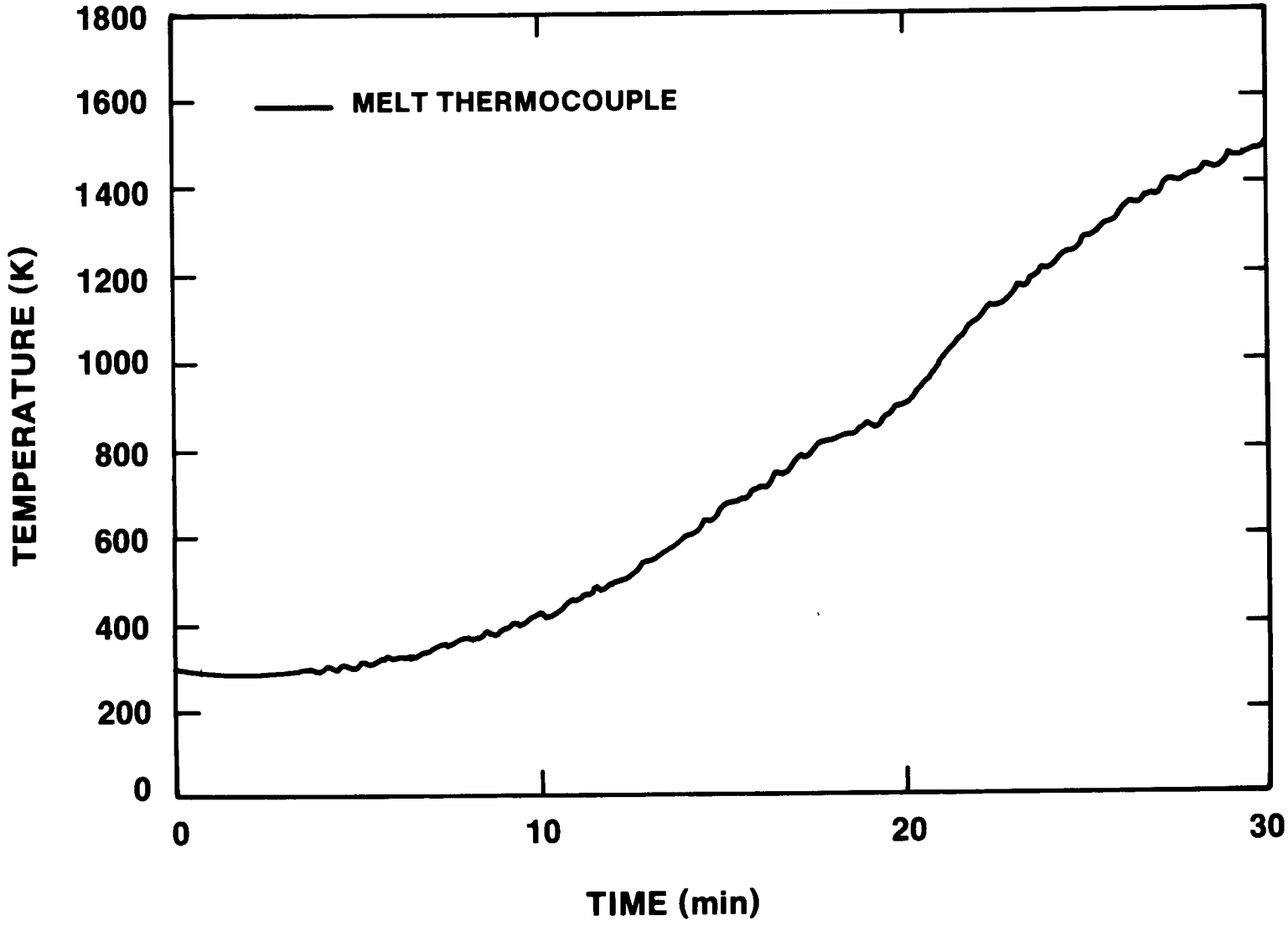

Figure 2.1.8 - QT-D Steel Temperature vs. Time

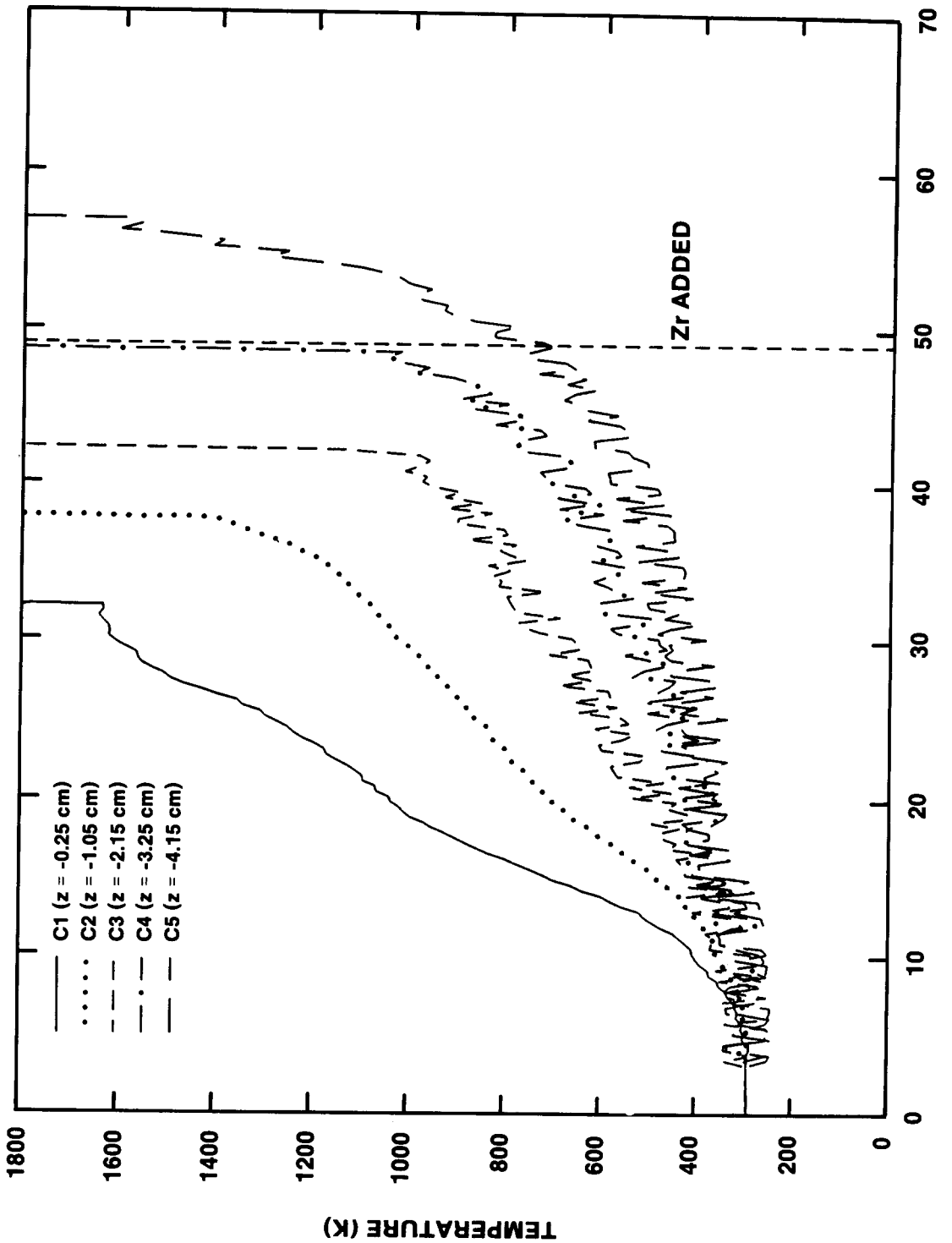

Figure 2.1.9 - Typical Thermocouple Response in QT-D

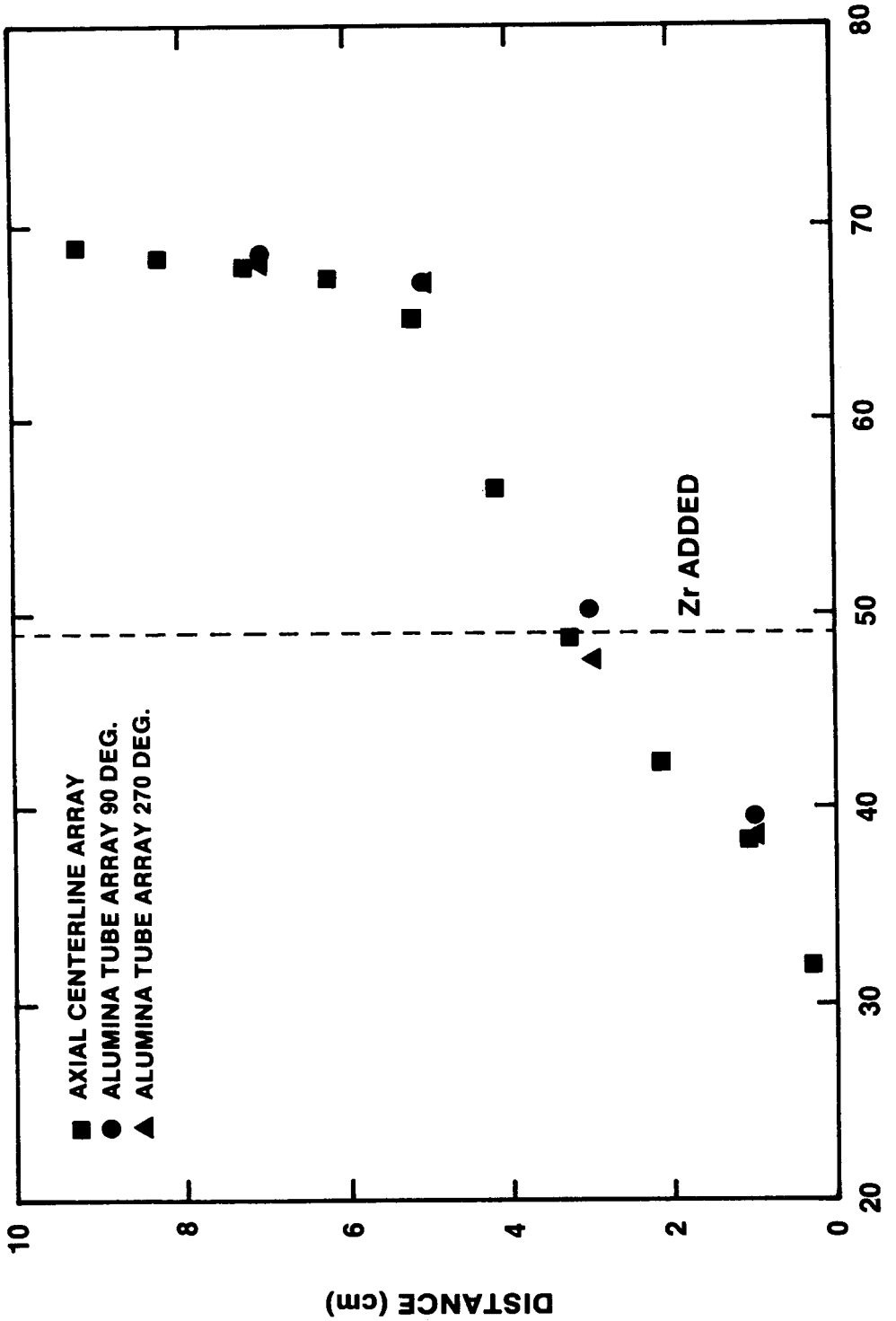

Figure 2.1.10 - Erosion vs. Time in QT-D

Results from the melt pool thermocouples are shown in Figure 2.1.11. These were C-type thermocouples located at 1, 3, 5, and 7 cm depths in the concrete. The first pool thermocouple indicted a maximum pool temperature between 2102 K and 2128 K at time t=57 minutes. The second pool thermocouple failed at time t=64 and registered a maximum pool temperature of 2000 - 2044 K. The third pool temperature measurement ranged from 2072 - 2124 K just before the thermocouple failed at time t=67.5 and the final pool temperature thermocouple failed quickly at time t=69 after registering a maximum pool temperature of 1993 K.

The data from the infrared CO/CO_2 detector are shown in Figure 2.1.12. Five minutes after the power was turned on (t=5 minutes) the CO gas content steadily climbed to greater than 2000 parts per million. At time t=20, the CO_2 registered 2% and CO registered 1%. Approximately 3-5 minutes after the steel had melted (melt at time t=32) the CO_2 gas content rose to an out-of-range value greater than 20% while CO gas content still registered roughly 1%. CO gas production soon increased, however, and peaked at time t=45 at a value of 43%. The Zr metal was introduced at time t=49, at which time CO production dropped to 14%. At time 51, CO peaked again at 35% with CO_2 still higher than 20%. Both gases dropped to near zero concentrations at time t=53 due to blockage of the sample tube by melt debris. For all of the CO/CO_2 measurements, the balance of the gas mixture is assumed to be air, since one half of the QT-D crucible was open to the atmosphere throughout the test. Although aerosols were not measured in QT-D, a significant aerosol source term was produced during the Zr reaction. Figure 2.1.13 shows the exothermic nature of the Zr reaction and the attendant aerosol plume. This reaction started some 13 minutes after the Zr was added and continued for seven minutes.

2.1.6 Posttest Observations and Conclusions

The QT-D crucible was x-rayed and sectioned after the test. Figures 2.1.14 and 2.1.15 show these results. The posttest x-ray (Figure 2.1.15) showed that a total of 11 cm of concrete had been eroded during the experiment. The MgO sidewalls also showed signs of erosion. The initial annulus diameter of 11.5 cm was widened to 12.5 cm during the first four centimeters of concrete attack and then to 14 centimeters for the final 6-7 cm of attack. The steel/Zr slug filled the bottom of the cavity and did not show any voids.

The sectioned crucible (Figure 2.1.14) confirmed the posttest x-ray. The MgO sidewalls were slightly eroded yet still intact and capable of containing the reaction. The walls were covered with an oxide slag material to a depth of 5 mm. Similar oxide crusts were formed immediately above the steel slug and at the top of the interaction cavity.

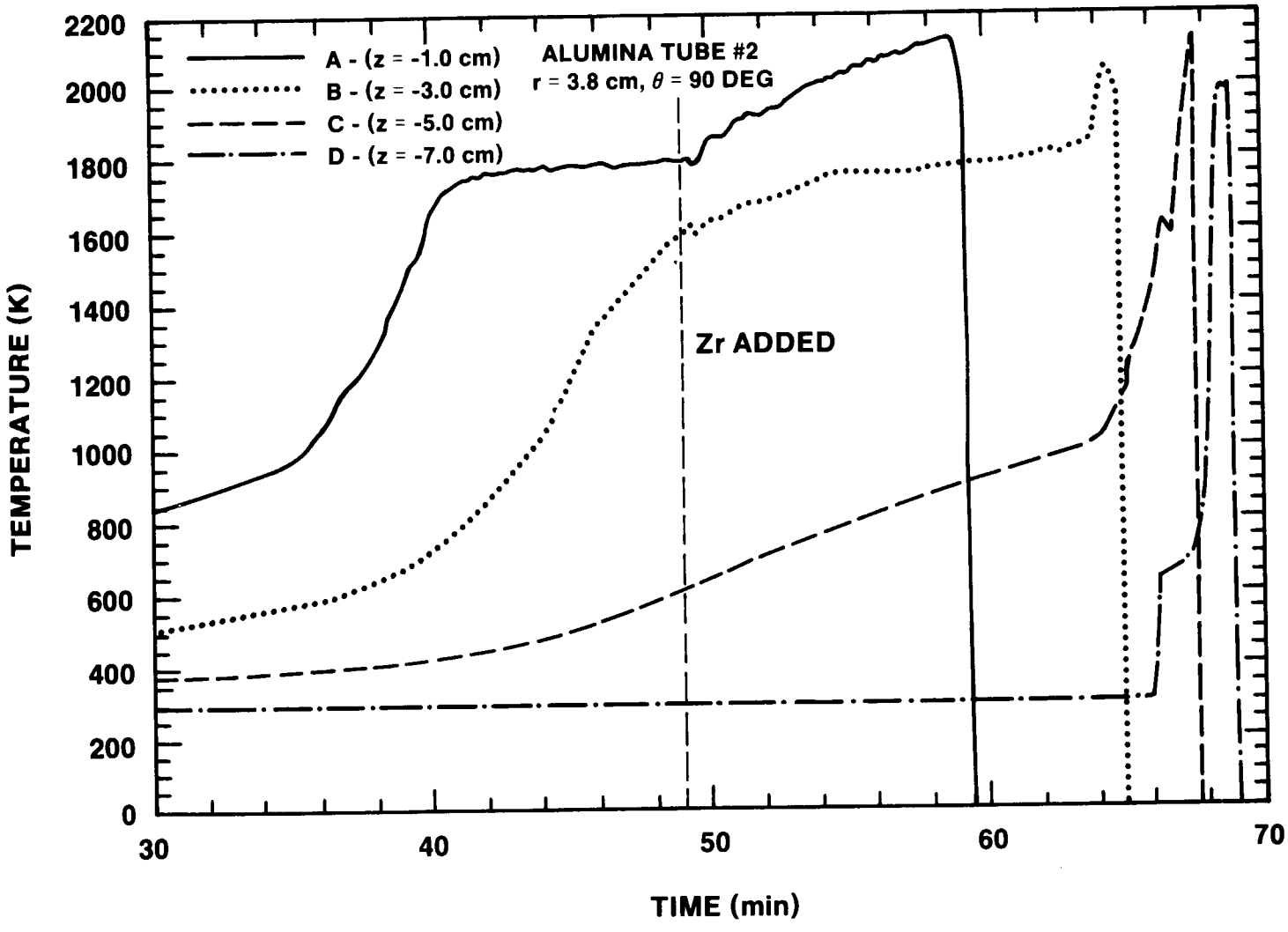

Figure 2.1.11 - QT-D Pool Temperature vs. Time

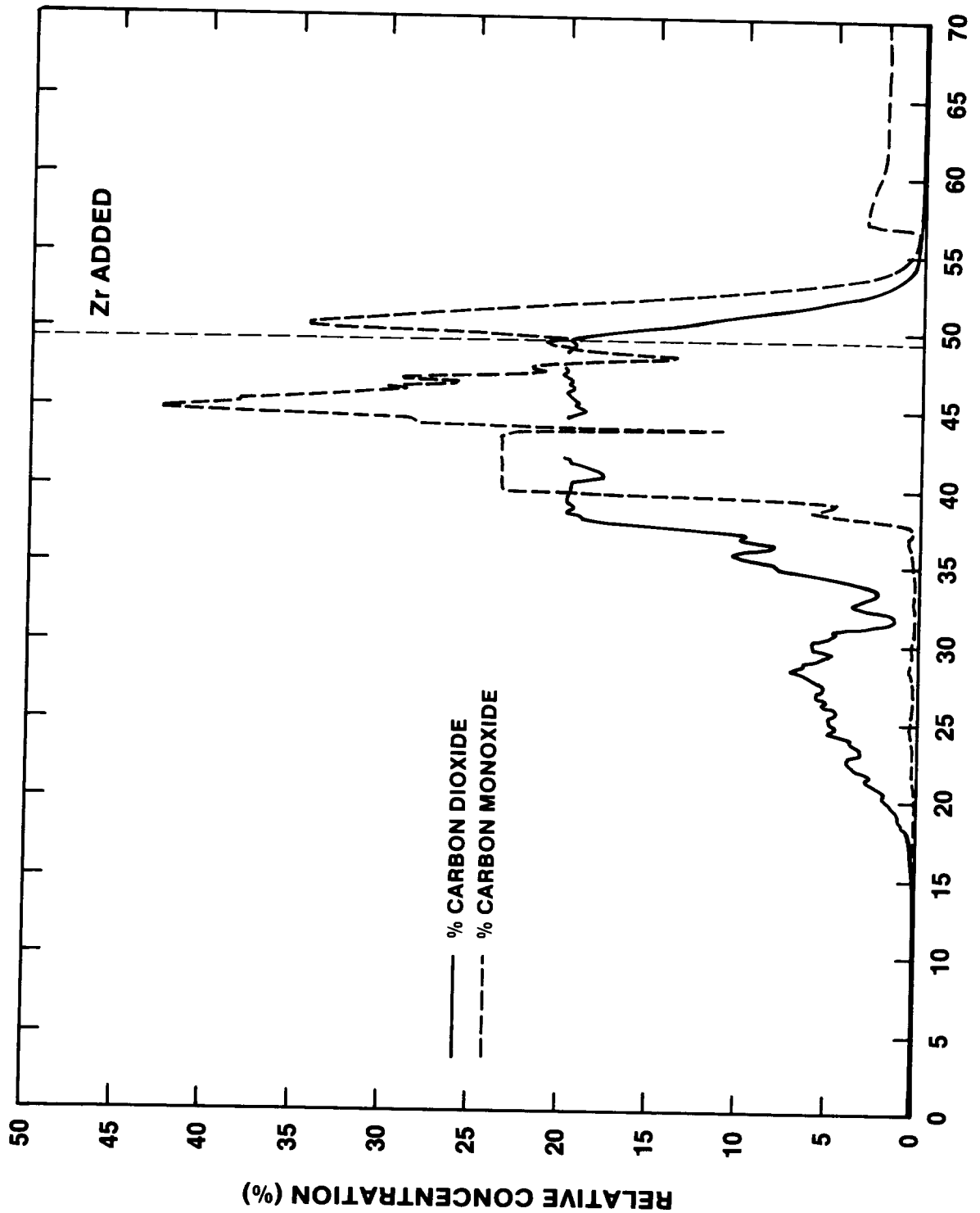

Figure 2.1.12 - CO/CO_2 Gas Effluent Measurement in QT-D

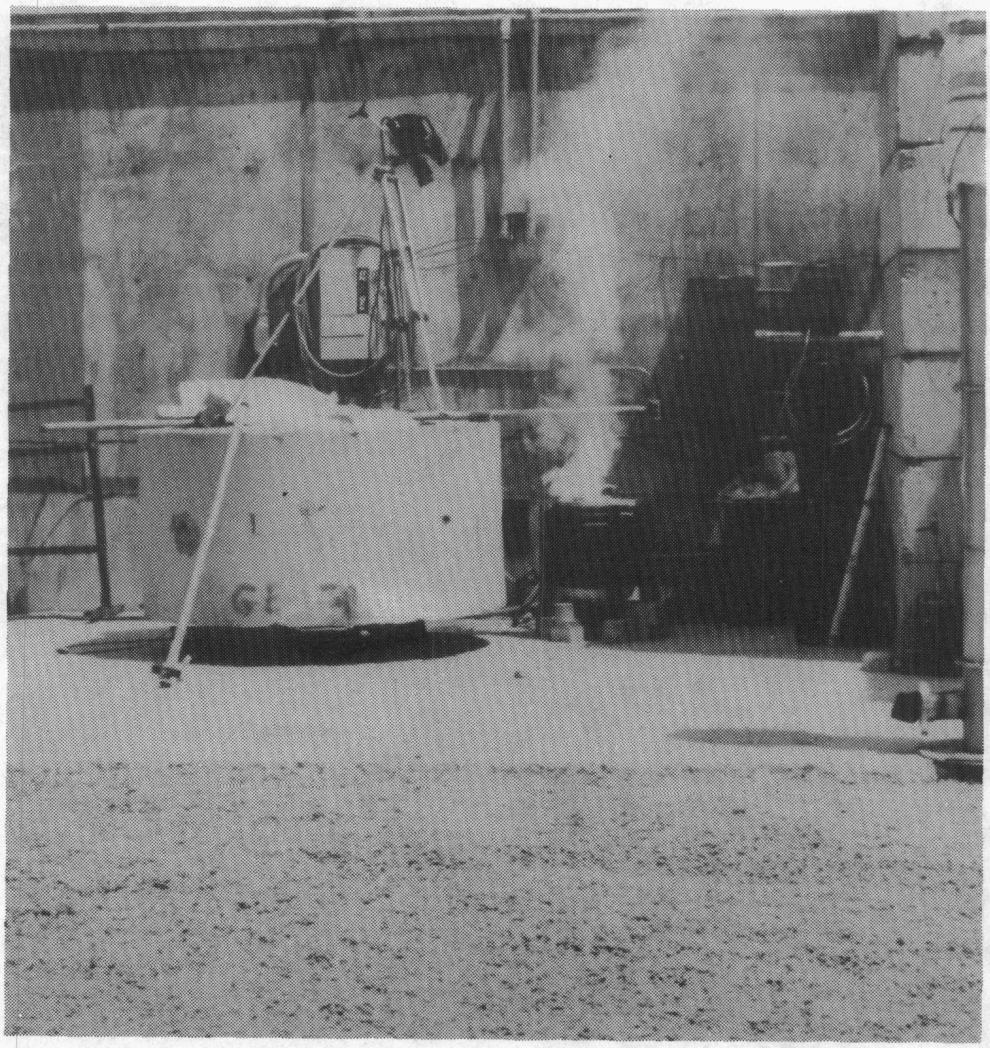

Figure 2.1.13 - QT-D with Zirconia Reaction in Progress

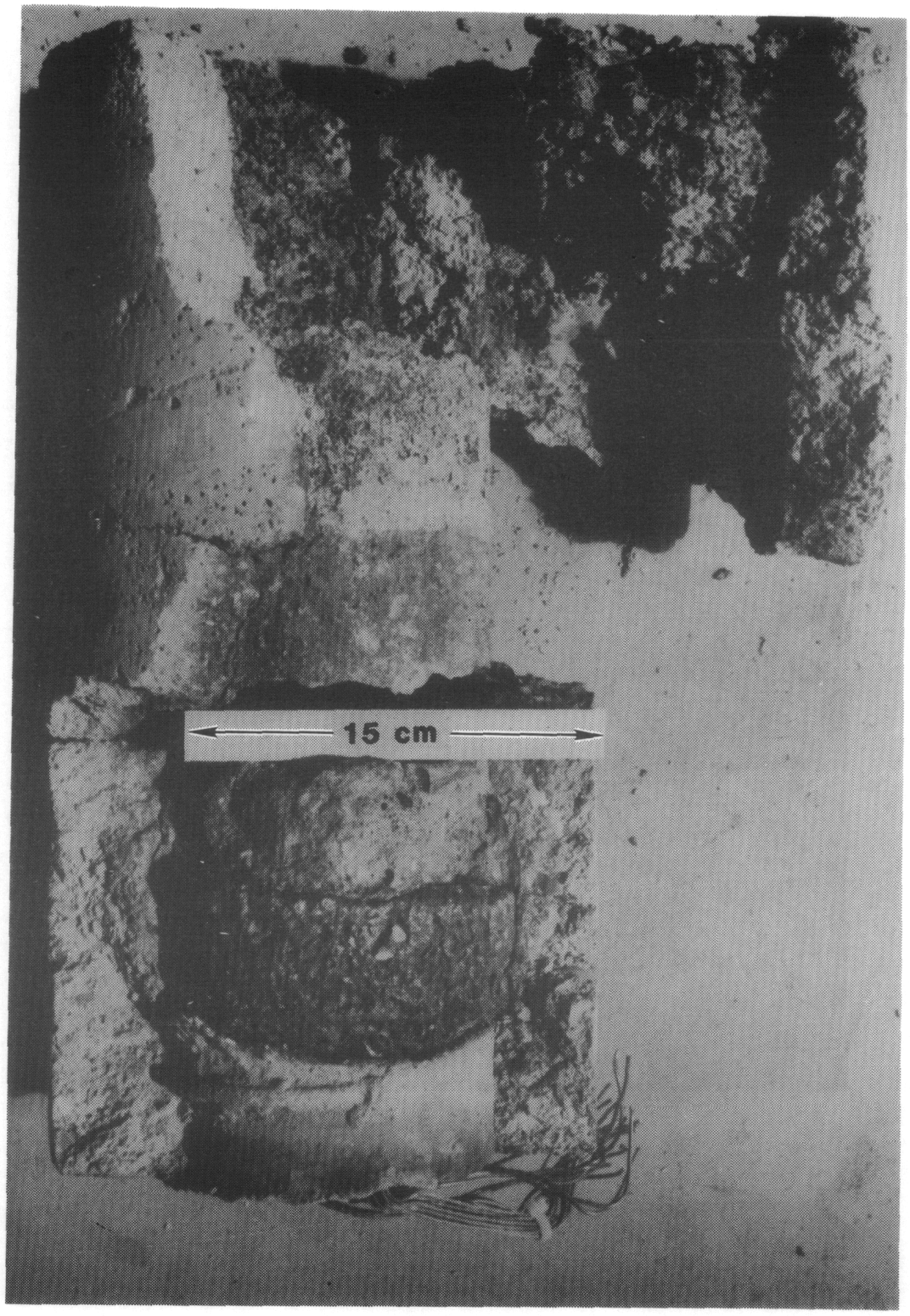

Figure 2.1.14 - Sectioned QT-D Crucible Posttest

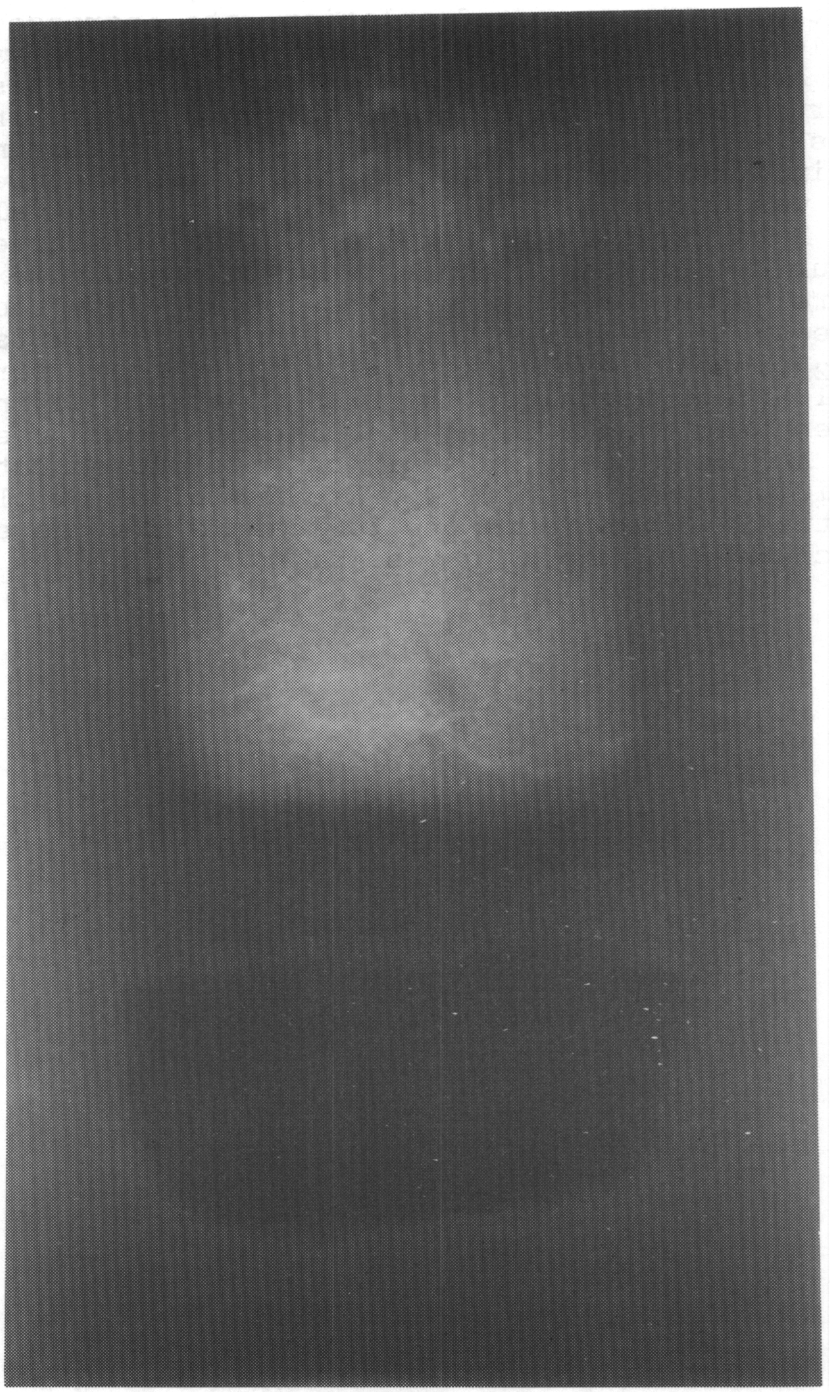

Figure 2.1.15 - Posttest X-ray of QT-D Crucible

Based on the data presentation, on visual observations, and on the posttest observations, the addition of Zr metal to molten steel interacting with concrete definitely results in a significant reaction. The measured ablation rate increased from 10 cm/hr to 100 cm/hr and large amounts of flammable gas with entrained aerosols were observed. This reaction was contained by the MgO crucible and lasted at least ten minutes, indicating that comprehensive gas, aerosol, and temperature measurements would be feasible in future tests. The melt pool temperature measurement technique was successful in obtaining consistent values ranging from 1993 K to 2124 K over a period of twelve minutes with each of the four C-type thermocouples registering the maximum pool temperature value for at least 20 seconds. This technique should also be feasible in future tests. Finally, attempts to measure the CO/CO_2 content in the gas effluent were only partially successful. This technique measured CO at 43% during the period that molten steel was eroding the limestone common sand concrete basemat. At the time of Zr addition, the subsequent reaction caused oxidic crusts to quickly rise and block or plug the gas sampling tube. Future attempts to measure the gas effluent should include a protected gas sampling port and an inert gas purge.

2.2 QT-E Experiment

2.2.1 General

The QT-E experiment was also designed as a scoping test to prepare for the SURC-3 experiments. It was executed for two reasons: (1) to obtain information on a larger scale than the QT-E experiment and (2) to determine the extent and nature of the steel-zirconium-concrete reaction when the crucible was cast entirely with concrete.

The QT-E test used a 50 kg slug of steel and 10 kg of Zr metal as the charge material. This represented a factor of five increase in melt mass over the QT-D experiment, which utilized 10 kg of steel and 2 kg of Zr metal. The geometry in QT-E was meant to be as nearly identical to the SURC-3 geometry as was practicable so as to obtain enough information to finalize the instrumentation strategies for the SURC-3 test and subsequent experiments. In addition, the QT-D experiment was performed in a crucible cast entirely from limestone-common sand concrete instead of the concrete-filled MgO annulus used in QT-D. This would allow us to discern whether or not MgO was a major contributor to the vigorous reaction observed in QT-D and also to measure two-dimensional erosion patterns which result from the steel-zirconium-concrete interaction.

The QT-E test article (Figure 2.2.1) was a right circular cylinder consisting entirely of limestone-common sand concrete. It stood 76.2 cm high and had an outside diameter of 40.6 cm. An internal cavity formed the reservoir for the molten steel charge. This cavity had a depth of 61 cm and a diameter of 20.3 cm. The charge material for QT-E was a 50 kg solid cylinder of 304 stainless steel, which had an outside diameter of 20 cm and a height of 20 cm. Zirconium metal was added to the melt pool in the form of right circular cylinders. Eighteen cylinders, each with a diameter of 3.3 cm and a length of 11.1 cm were used. The total weight of the Zr metal was 20 kg. The test article was positioned in a copper induction coil with an inside diameter of 43 cm and a height of 45 cm. The coil was powered with a 125 kW induction power supply in order to melt and sustain the core debris simulant. An MgO coverplate with a diameter of 45 cm and a thickness of 3 cm was used to reduce radiation losses and to direct the majority of the effluent gas and aerosol through a 2.5 cm diameter sideport. The QT-E test was run in open air at atmospheric pressure and at an ambient temperature of 23°C.

2.2.2 Geometry

A photograph of the experimental apparatus is shown in Figure 2.2.1. The major components of the QT-E test consist of the concrete interaction crucible, alumina cover, melt charge, and induction coil.

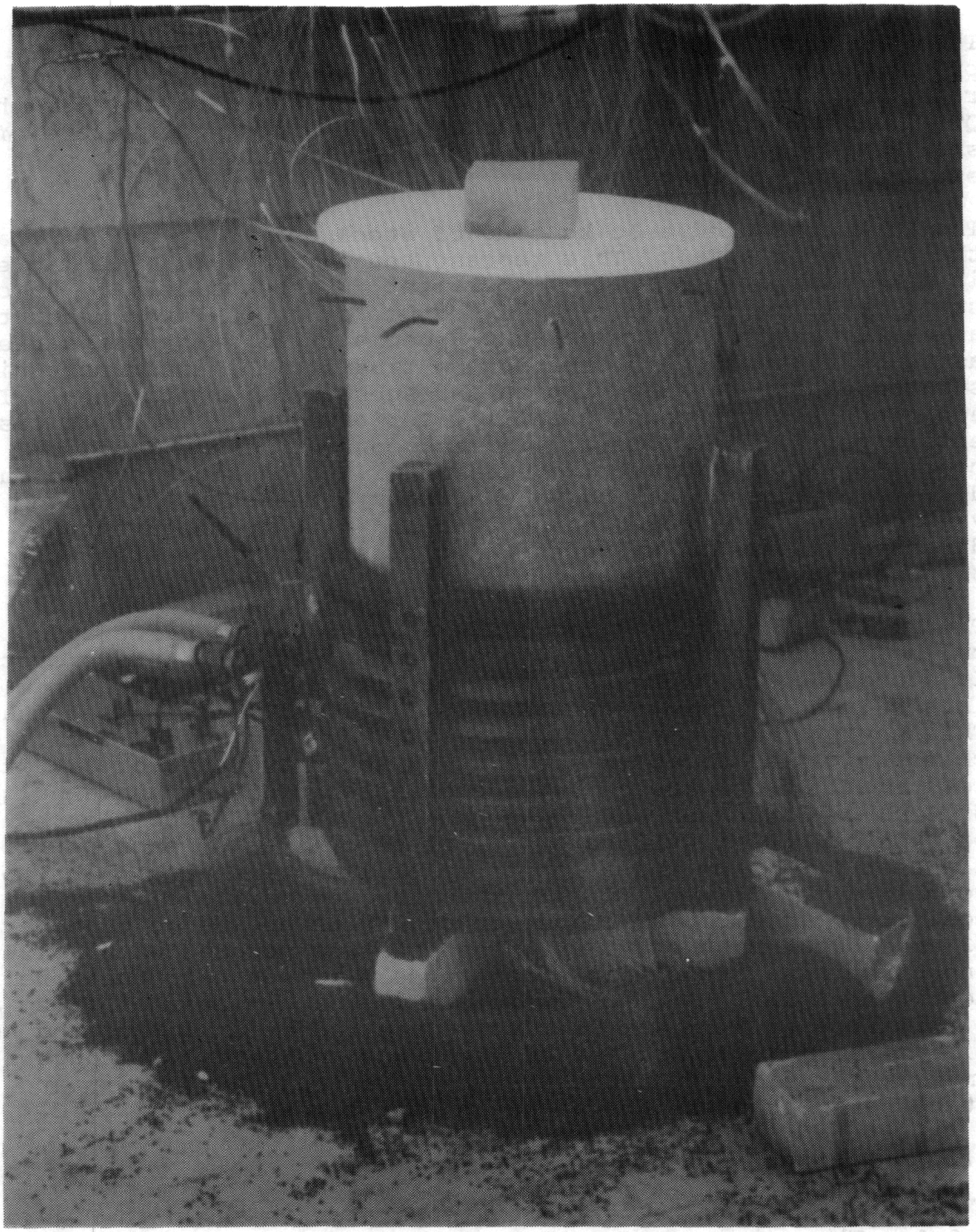

Figure 2.2.1 - Overall View of QT-E

The interaction crucible shown in Figure 2.2.2 is of cylindrical geometry. The sidewalls and base are cast entirely from limestone/common sand concrete. This concrete has been described previously in Section 2.1.2. The engineering and chemical composition have been previously described and can be found in Table 2.1.2. The overall dimensions of the crucible are 40.6 cm O.D. by 76.2 cm high. The cavity dimensions are 20.3 cm I.D. by 61.0 cm deep. Based on these dimensions, sidewall and base are 10.2 and 15.2 cm thick, respectively. Two 304 stainless steel tubes 0.48 cm I.D. were cast into the sidewall of the crucible adjacent to each other approximately 3 cm below the top of the crucible. These tubes were used for gas sampling during the test. The outside diameter of the crucible was laminated with two layers, 2.4 mm thick, of 207 MPa tensile strength fiberglass cloth. This was done to help seal the crucible and provide structural integrity during the experiment.

An alumina disk 45.7 cm in diameter and 0.48 cm thick was used to cover the top of the crucible to retain the reaction products and minimize the upward heat losses.

The melt charge consisted of a solid cylinder of 304 stainless steel having a mass of 50 kg. The dimensions of the cylinder was 20.3 cm in diameter by 19.9 cm high. The stainless cylinder was placed directly into the cavity of the concrete test article. Two K type thermocouples were installed into the top of the cylinder for monitoring the steel temperature. The standard composition of the 304 stainless cylinder has been previously presented in Table 2.1.3.

Sixteen zirconium cylinders 99.5% pure nominally 11.1 cm long were saw cut from a 3.3 cm diameter solid round bar 3.0 meter long. The average weight of each cylinder was 0.63 kg. The chemical composition of the zirconium cylinders has been presented previously in Table 2.1.4.

The induction coil used to heat the stainless steel slug and sustain the reaction is the same as described in Section 2.1.2. The coil was placed around the interaction crucible and centered vertically with respect to the stainless steel slug.

The same galvanized pipe used to deliver the zirconium metal to the melt pool in test QT-D was used for this test.

2.2.3 Instrumentation

A total of 67 data channels were used in the QT-E test. Twenty-four of these were thermocouples used to measure axial concrete erosion. An additional 35 thermocouples were used to record the radial/sidewall concrete erosion. Two K-type thermocouples were placed in the stainless steel slug to monitor the initial heatup and melt. One K-type thermocouple was used to measure the gas effluent temperature. The induction power applied to the coil was recorded on two channels and the final three channels were used to measure the CO/CO_2 content of the gas effluent.

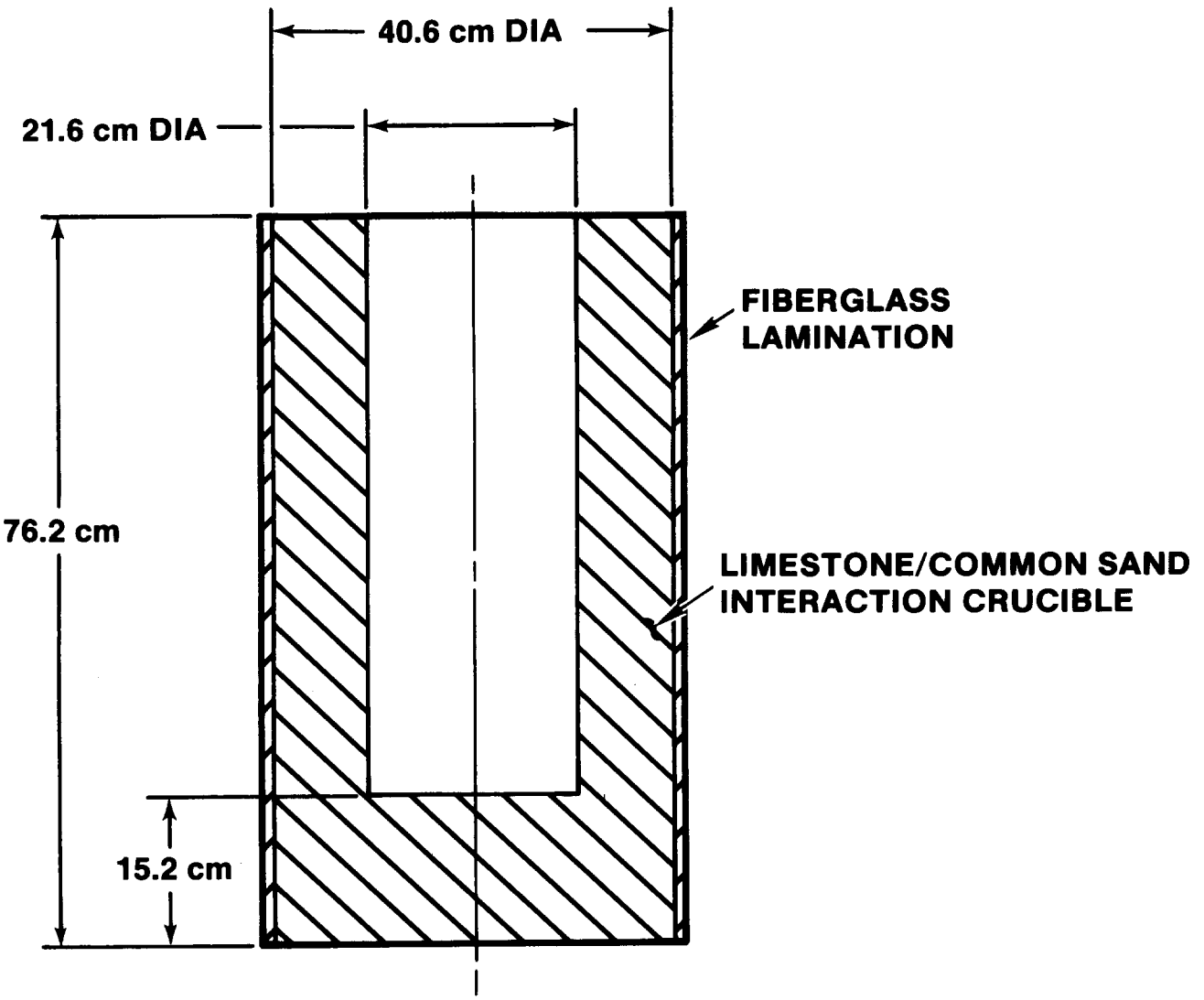

Figure 2.2.2 - QT-E Geometry

Thermocouple Instrumentation

A total of 59 thermocouples were cast into the sidewall and base of the crucible. The relative location of the thermocouples are shown in Figure 2.2.3. Figure 2.1.3 shown previously, defines the nomenclature describing the thermocouple locations using cylindrical coordinates. Table 2.2.1 lists the specific locations of the thermocouples cast into the concrete base and sidewall. Two arrays of 12 thermocouples each are cast into the base. The spacing of the thermocouples in these arrays is 1.0 cm between 0.0 and 7.0 cm. The spacing increases to 1.5 cm between 7.0 and 13.0 cm. One array is located on the axial centerline of the crucible. The other array is located adjacent to the axial array at a radial distance of 5.3 cm. The sheath of each thermocouple was bent at an angle of 90 degrees at a minimum of 10 sheath diameters from the tip (see Figure 2.1.4). The bent tip of the thermocouple was located in a plane parallel to the concrete surface and thus parallel to the propagating isotherm. This was done to minimize the errors caused by heat conduction down the metal sheaths.

A total of five arrays with seven thermocouples in each array were cast into the concrete sidewall at distances of 25.4, 10.16, 0, -5.08 and -10.16 cm with reference to the top surface of the concrete cavity. The spacing of the thermocouples in these arrays was 1.0 cm between 0.0 and 3.0 cm. Then the spacing increased to 1.5 cm between 3.0 and 7.5 cm. These thermocouples were installed to monitor the radial ablation of the concrete.

A calibration test to verify thermocouple locations and thermal properties of the concrete was performed using boiling water. The test was conducted by placing the 304 stainless steel cylinder on 0.64 diameter alumina tubes placed on the surface of the concrete cavity. Water was then added until it filled the crucible. An induction coil was placed around the crucible and vertically centered with respect to the stainless steel slug. A cover was placed over the crucible to help minimize water loss due to vaporization. The induction power supply was set to apply just enough power to the stainless steel slug to maintain a boiling state within the cavity. The temperature of the water at steady state boiling was 369 K. The thermocouple responses as a function of time for all the crucible thermocouples are shown in Appendix C.

Gas Sampling Instrumentation

The gas sampling instrumentation was the same as described in the QT-D test (see Figure 2.1.5), with one exception. The Infrared CO/CO_2 monitor samples were drawn from two, 304 stainless steel tubes, cast into the side of the interaction crucible instead of one tube located above the crucible cover. The sample gas was drawn past a K type thermocouple located a few centimeters down stream from the sample point to measure gas temperature.

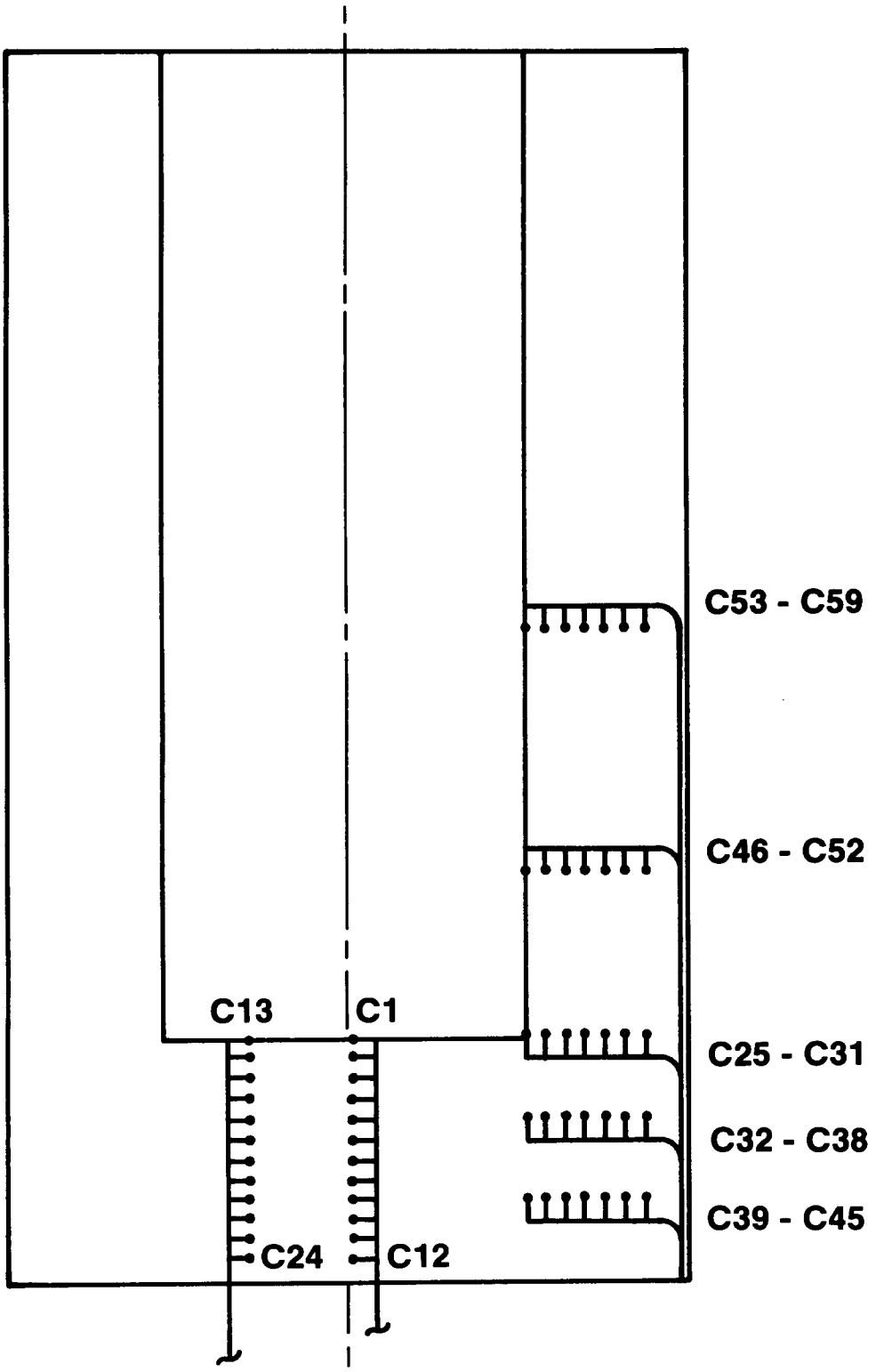

Figure 2.2.3 - Relative Thermocouple Locations - QT-E

TABLE 2.2.1

Thermocouple Locations, Test QT-E

Thermocouple Identification (#)	TC Type (C,K,S)	r (cm)	t (cm)	θ (deg)	Z (cm)
C1	K	0		0	0.0
C2	K	0		0	- 1.0
C3	K	0		0	- 2.0
C4	K	0		0	- 3.0
C5	K	0		0	- 4.0
C6	K	0		0	- 5.0
C7	K	0		0	- 6.0
C8	K	0		0	- 7.0
C9	K	0		0	- 8.5
C10	K	0		0	-10.0
C11	K	0		0	-11.5
C12	K	0		0	-13.0
C13	K	5.33		270	- 0.0
C14	K	5.33		270	- 1.0
C15	K	5.33		270	- 2.0
C16	K	5.33		270	- 3.0
C17	K	5.33		270	- 4.0
C18	K	5.33		270	- 5.0
C19	K	5.33		270	- 6.0
C20	K	5.33		270	- 7.0
C21	K	5.33		270	- 8.5
C22	K	5.33		270	-10.0
C23	K	5.33		270	-11.5
C24	K	5.33		270	-13.0

TABLE 2.2.1 (continued)

Thermocouple Locations, Test QT-E

Thermocouple Identification (#)	TC Type (C,K,S)	r (cm)	t (cm)	θ (deg)	Z (cm)
C25	K		0.0	0	- 0.0
C26	K		1.0	0	- 0.0
C27	K		2.0	0	- 0.0
C28	K		3.0	0	- 0.0
C29	K		4.5	0	- 0.0
C30	K		6.0	0	- 0.0
C31	K		7.5	0	- 0.0
C32	K		0.0	-15	- 5.08
C33	K		1.0	-15	- 5.08
C34	K		2.0	-15	- 5.08
C35	K		3.0	-15	- 5.08
C36	K		4.5	-15	- 5.08
C37	K		6.0	-15	- 5.08
C38	K		7.5	-15	- 5.08
C39	K		0.0	-30	-10.16
C40	K		1.0	-30	-10.16
C41	K		2.0	-30	-10.16
C42	K		3.0	-30	-10.16
C43	K		4.5	-30	-10.16
C44	K		6.0	-30	-10.16
C45	K		7.5	-30	-10.16
C46	K		0.0	+15	10.16
C47	K		1.0	+15	10.16
C48	K		2.0	+15	10.16
C49	K		3.0	+15	10.16
C50	K		4.5	+15	10.16
C51	K		6.0	+15	10.16
C52	K		7.5	+15	10.16

TABLE 2.2.1 (continued)

Thermocouple Locations, Test QT-E

Thermocouple Identification (#)	TC Type (C,K,S)	r (cm)	t (cm)	θ (deg)	Z (cm)
C53	K		0.0	+30	25.40
C54	K		1.0	+30	25.40
C55	K		2.0	+30	25.40
C56	K		3.0	+30	25.40
C57	K		4.5	+30	25.40
C58	K		6.0	+30	25.40
C59	K		7.5	+30	25.40

The induction power instrumentation and calorimetric calibration was also the same as described in the QT-D experiment. All 67 data channels were recorded every 10 seconds during the test using an HP 1000 data acquisition system. In addition, a remote video camera was used to visually record the experiment. These systems are described in Section 2.1.3.

2.2.4 Procedure

After initial calibration runs and pretest checks were performed, power was applied to the coil (Figure 2.2.4) at a rate of 100 kW. Thermocouples located in the stainless steel slug (Figure 2.2.5) were monitored to confirm that 50% ± 4% of the power was being transmitted to the metallic charge. After twenty minutes (t=20) erosion began in the radial direction, and the power level was dropped to 40 kW. At time t=32, erosion began in the axial direction and the power was boosted to 50 kW. The Zr metal was dropped into the crucible at time=46-47 minutes by removing the MgO coverplate and sliding 18 Zr cylinders sequentially into the open crucible via a 5 cm diameter steel pipe canted 45° to the top of the test article. Visual observations showed that most, if not all, of the cylinders failed to penetrate into the melt pool. The coverplate was replaced and the power was boosted to 75 kW in order to mix the Zr metal into the stainless steel. At time t=60 a violent Zr-steel-concrete reaction began. This reaction levitated the MgO coverplate and allowed most of the gas and aerosol effluents to bypass the outlet port. Thermocouple response showed a rapid increase in both the axial and radial erosion rates. Power was dropped to 45 kW in an attempt to slow this erosion at time t=65. Rapid erosion continued, nonetheless, and the outside crucible was breached at time, t=70. This breach allowed the molten metal mixture to contact the induction coil, resulting in immediate shutdown and termination of the test.

2.2.5 Data Presentation and Results

Twenty K-type thermocouples were used to monitor the axial concrete erosion in QT-E. These were grouped in two arrays with a spacing of 1 cm between each thermocouple. Typical data traces from five of the axial erosion thermocouples is shown in Figure 2.2.6. This figure plots temperature as a function of time for the centerline group of axial thermocouples located at the 1, 2, 3, 4, and 5 cm depths in the limestone-common sand concrete. These thermocouples failed (exceeded 1600 K) at times t=38, t=59, t=64, t=66, and t=68.5 minutes. A plot of the failure times for both axial thermocouple groups is shown in Figure 2.2.7. A total of twelve thermocouples failed in the axial direction, 6 from the centerline group and six from the mid-radius group. The initial erosion rate for both groups averages 7 cm/hr during the first twenty minutes of erosion. At time t=47, the Zr metal was added to the crucible and the erosion slowed to 5 cm/hr for approximately 10 minutes. At time t=60, the Zr reaction began,

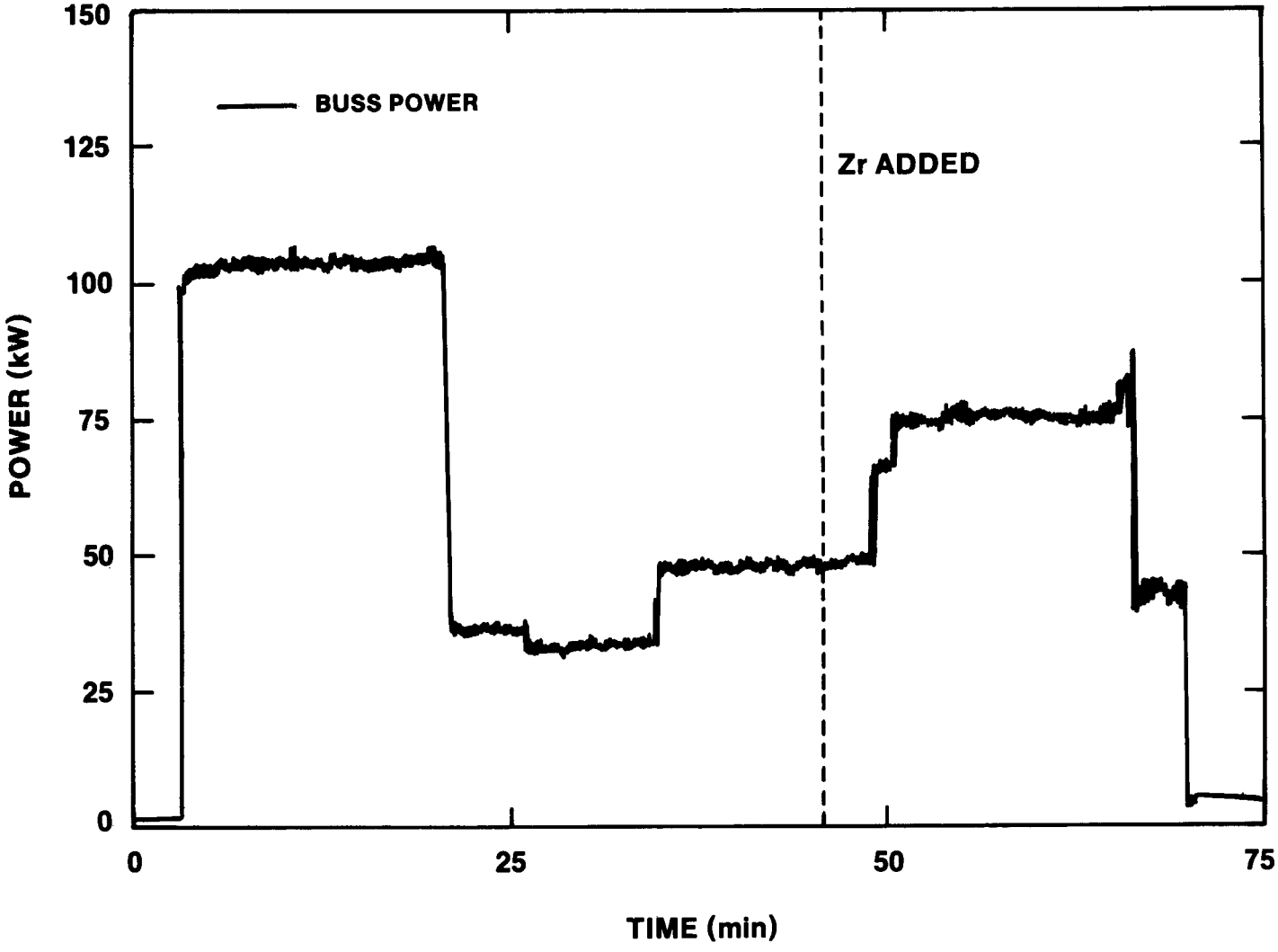

Figure 2.2.4 - QT-E Coil Input Power

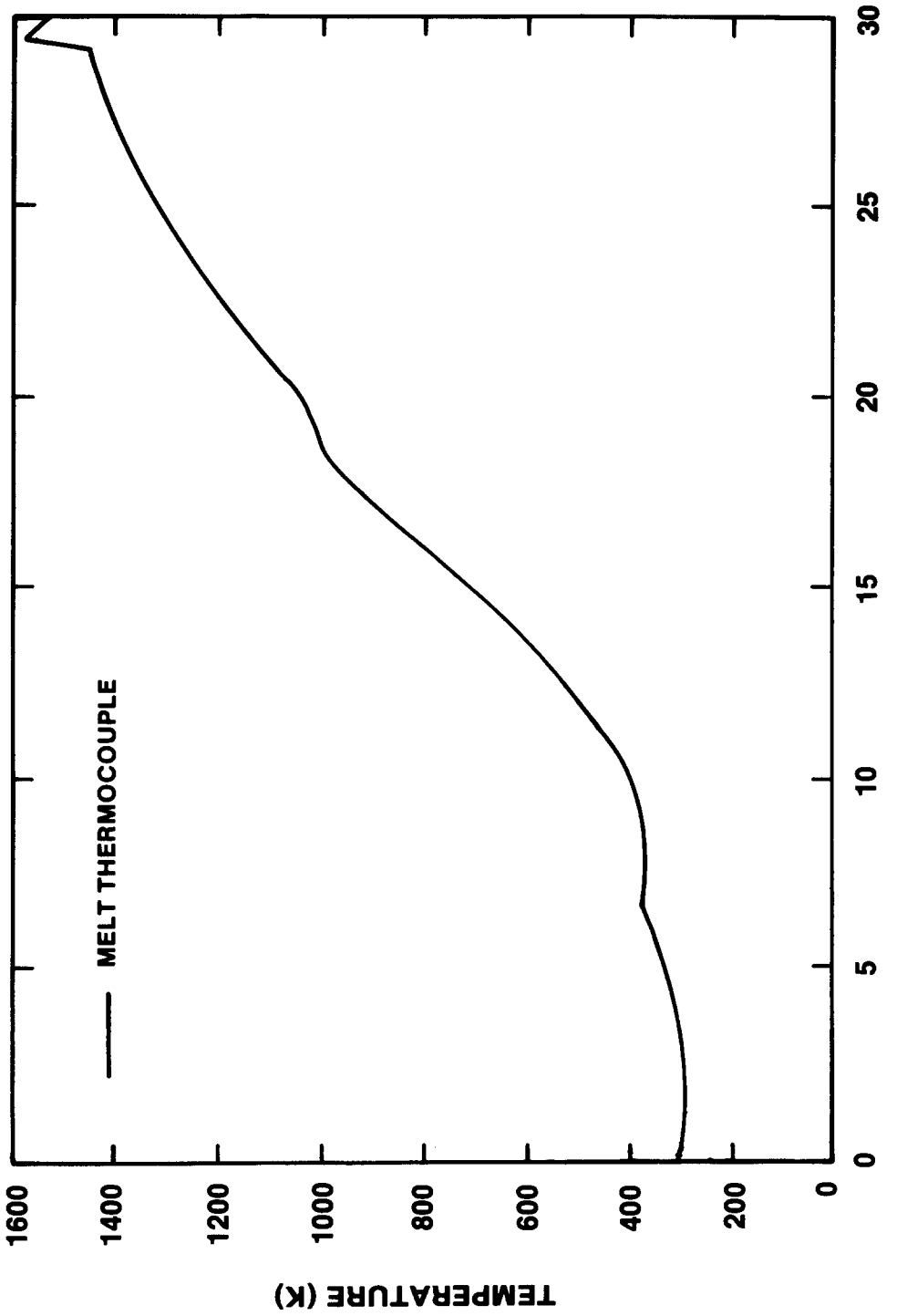

Figure 2.2.5 - Initial Steel Temperature vs. Time

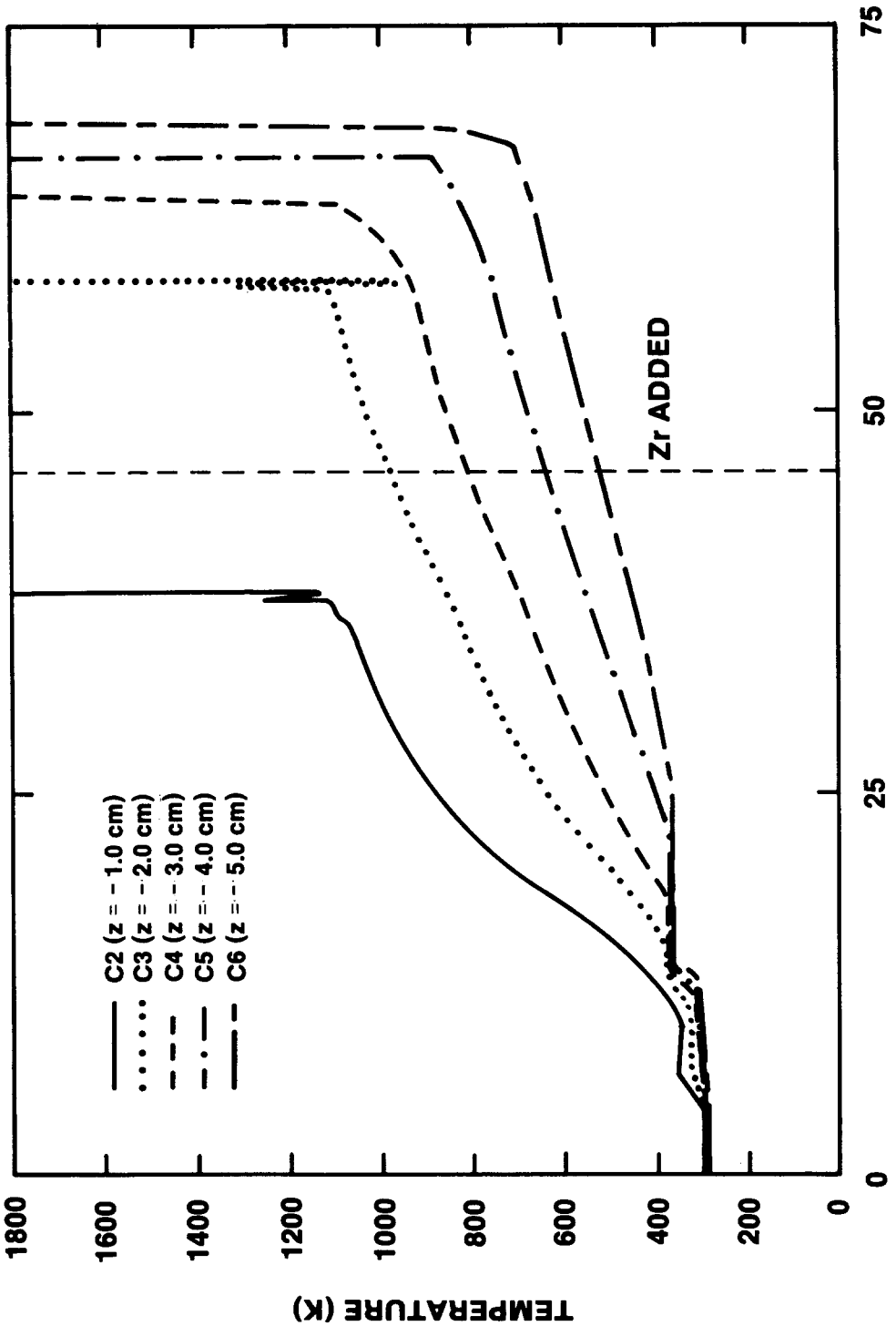

Figure 2.2.6 - Typical Axial Thermocouple Response in QT-E

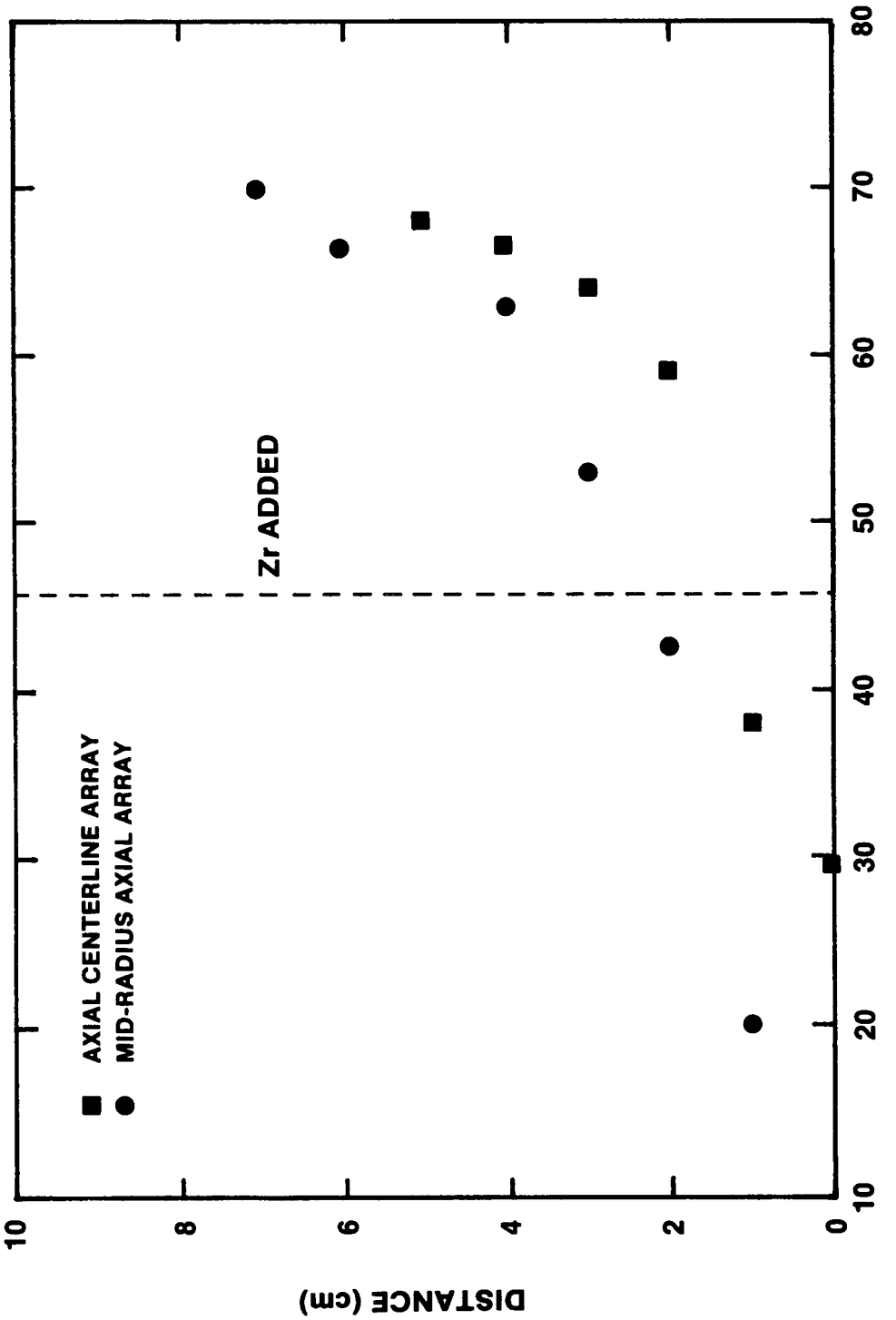

Figure 2.2.7 - Axial Erosion vs. Time for QT-E

followed by a marked increase in the axial erosion rate from ~.7 cm/hr to 23 cm/hr. This rapid ablation continued for 8-10 minutes until time t=70 when the sidewall of the crucible was penetrated.

Thirty-five thermocouples were used to monitor the radial concrete erosion in QT-E. These were grouped in five arrays as described in the Instrumentation section. Typical data traces from five of the radial erosion thermocouples is shown in Figure 2.2.8. This figure plots the temperature vs. time response for the group of radial thermocouples which was located at the initial steel/concrete interface. Failure times for the five thermocouples were at t=25.5, t=44, t=54, t=64.5, and t=66 minutes, respectively. A plot displaying the failure times for four of the five radial thermocouple groups is shown in Figure 2.2.9. This figure indicates that the average erosion rate for two of the groups in the radial direction was ~ 8 cm/hr prior to time t=60 minutes. After t=60, the ablation rate increases to 36 cm/hr as a result of the vigorous Zr-concrete reaction. All four radial groups record this increased ablation rate. The fifth radial erosion thermocouple group was located 10 cm below the initial concrete interface and did not record temperatures in excess of 700 K. At time t=70 minutes, the 10.2 cm thick sidewalls of the crucible were eroded completely at a position adjacent to the original concrete/steel interface as shown by the Z=0. sidewall array in Figure 2.2.6.

The data from the infrared CO/CO_2 detector are shown in Figure 2.2.10. Soon after initial heating (less than five minutes), the CO content exceeded 2000 ppm and the CO_2 content exceeded 20%. At time t=25, the CO reached a maximum concentration of 50%. After the power was lowered at t=20, the CO level dropped to 25% and after the power was increased at time t=35, the CO level increased to 40%. At time t=46, the MgO crucible lid was removed to drop the Zr metal into the melt and then subsequently was replaced. This was marked by a drop in both CO and CO_2 concentrations to near zero for a few minutes followed by an increase to levels in excess of 50% CO and 20% CO_2. At t=60 the CO_2 level begins to drop off until time t=66 when the violent Zr reaction caused melt debris to erupt from the crucible, thus blocking the gas sample ports. Both gas concentrations dropped to zero following the breach of the crucible walls at t=70 minutes. Except for the brief time that the crucible lid was open for the Zr addition, the gas exit port provided the only outlet for gaseous effluents and it is assumed that less than 10% air was pulled into the sampling lines.

2.2.6 Posttest Observations and Conclusions

The QT-E crucible was x-rayed after the test. Figure 2.2.12 shows the result. A total of 8 cm of concrete was eroded in the axial direction during the experiment. In addition, the concrete sidewalls were heavily eroded over a 35 - 40 cm region, which

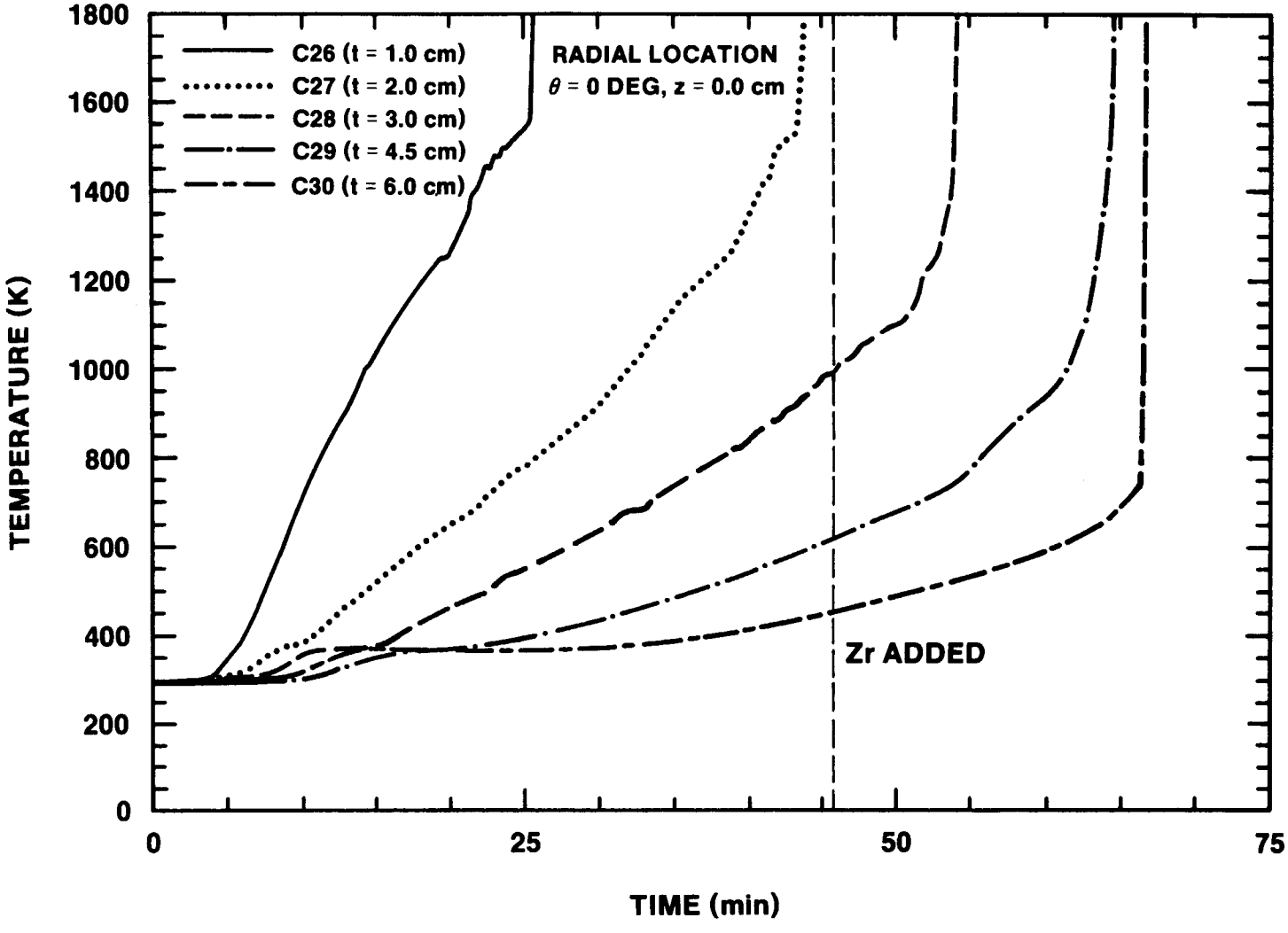

Figure 2.2.8 - Typical Radial Thermocouple Response in QT-E

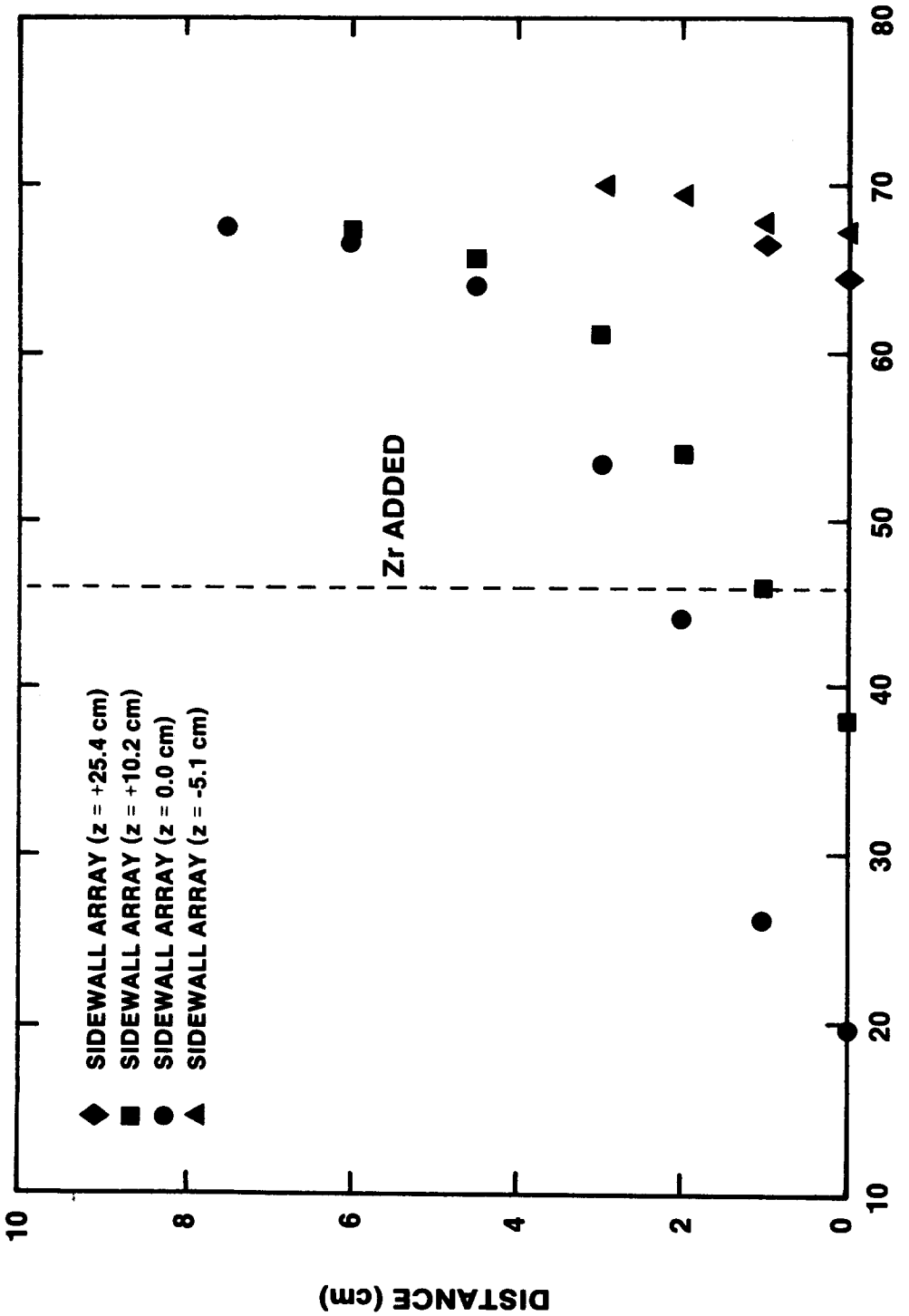

Figure 2.2.9 - Radial Erosion vs. Time for QT-E

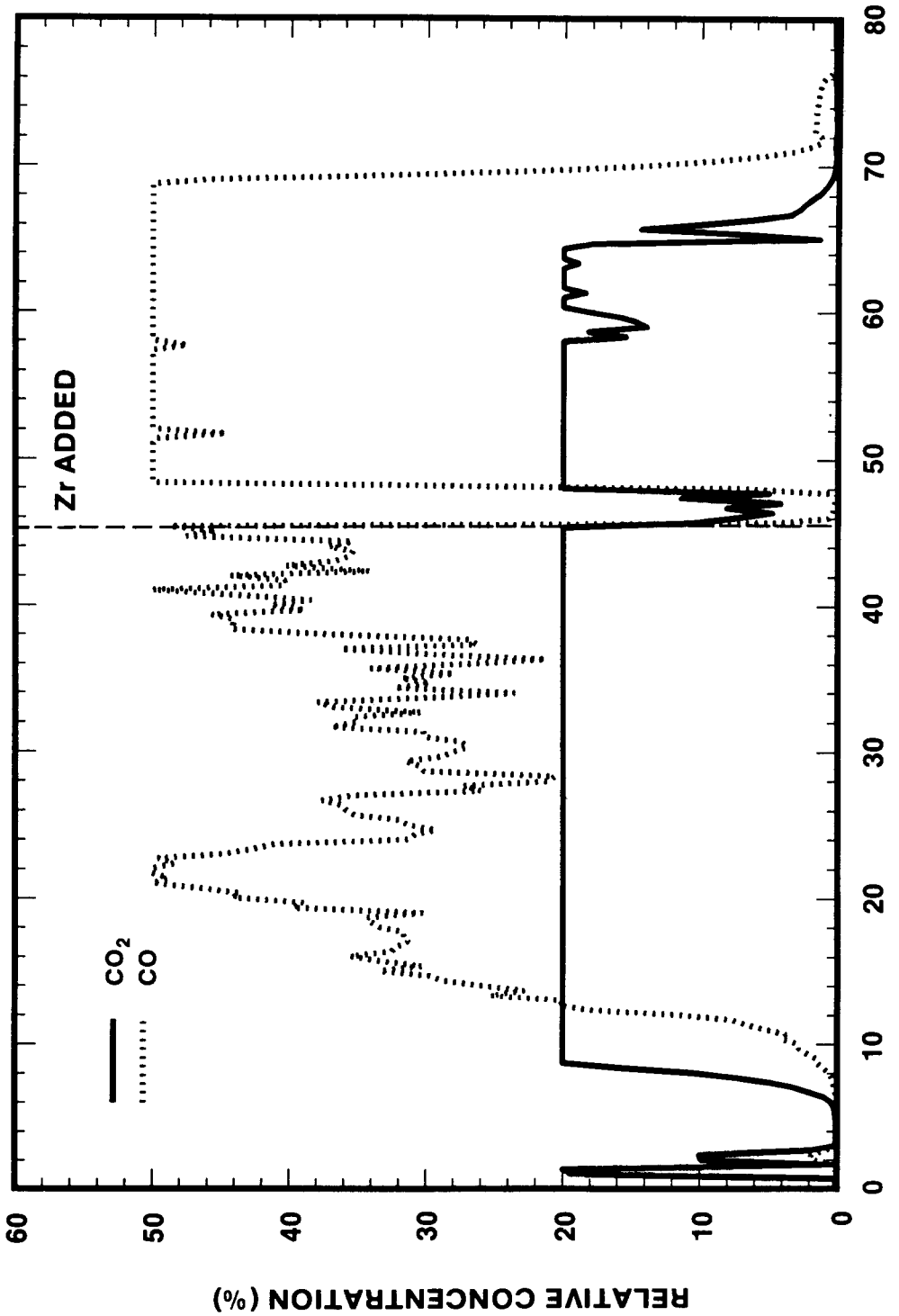

Figure 2.2.10 - CO/CO_2 Gas Effluent Measurement in QT-E

extended from 5 - 8 cm below the original concrete interface to 25 - 30 cm above the interface. The sidewall erosion appeared to be symmetrical in the azimuthal coordinate leaving an average wall thickness of 1 cm at the thinnest point which was located roughly .5 cm above the original steel/concrete interface. The erosion cavity was bulged or swollen in the axial direction such that the central cavity diameter was larger than either the upper or lower cavity. The upper cavity diameter was 30 cm at a position 26 cm above the original concrete interface and the lower cavity diameter was 28 cm at a position 5 cm below the interface as compared to the original cavity diameter of 20.4 cm. There was no steel or Zr remaining in the crucible. Posttest inspection confirmed that all of the melt had flowed from the crucible and that it had flowed between and had bonded to the water-cooled induction coil. Disassembly of the test article resulted in the destruction of both of these items.

The QT-E experiment provided the qualitative and quantitative data necessary to complete the design of the SURC-3 experiment matrix and to complete the instrumentation strategy for those experiments. It also provided important information regarding the two dimensional nature of steel-Zr-concrete interactions.

The thermocouple data showed that the axial and radial erosion rates both increased significantly when the Zr reaction was in progress. The axial rate was seen to increase from 7 cm/hr. to 23 cm/hr. and the radial rate increased from 8 cm/hr. to 36 cm/hr. Significant amounts of gas and aerosol were released during the Zr/concrete reaction which lasted 9 - 10 minutes from onset until the crucible walls failed. The gas effluent was composed of > 50% CO with < 20% CO_2 before the Zr reaction and > 50% CO with < 20% CO_2 just at the onset of the reaction before the gas sampling ports plugged. Here plugging occurred despite the fact that the sample lines were located well (20 cm) above the surface of the melt pool.

Results from the QT tests (QT-D and QT-E) both suggest that a lower amount of Zr metal should be added to the melt in SURC-3 and subsequent tests. The SURC test procedure was amended to allow for 5 kg of Zr metal to be added to a 50 kg steel melt pool rather than 10 kg as was done in QT-E. In addition, the SURC-3A test was constructed entirely with limestone concrete similar to the QT-E test but with significantly thicker (15 cm vs 10 cm) sidewalls. Gas composition and flow sampling ports in the SURC tests included a larger stand-off distance as well as an aerosol filter.

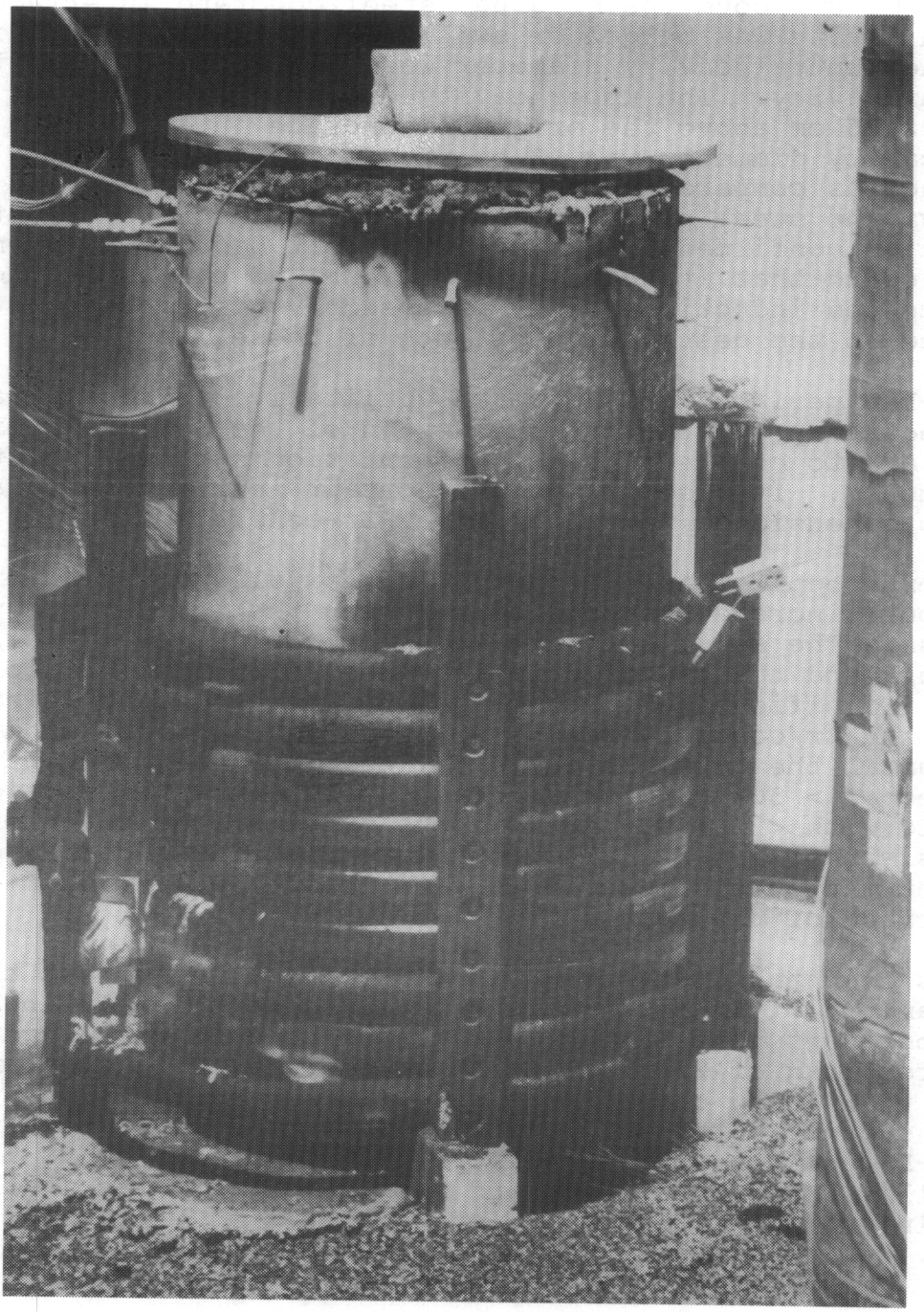

Figure 2.2.11 - QT-E with Zr Reaction in Progress

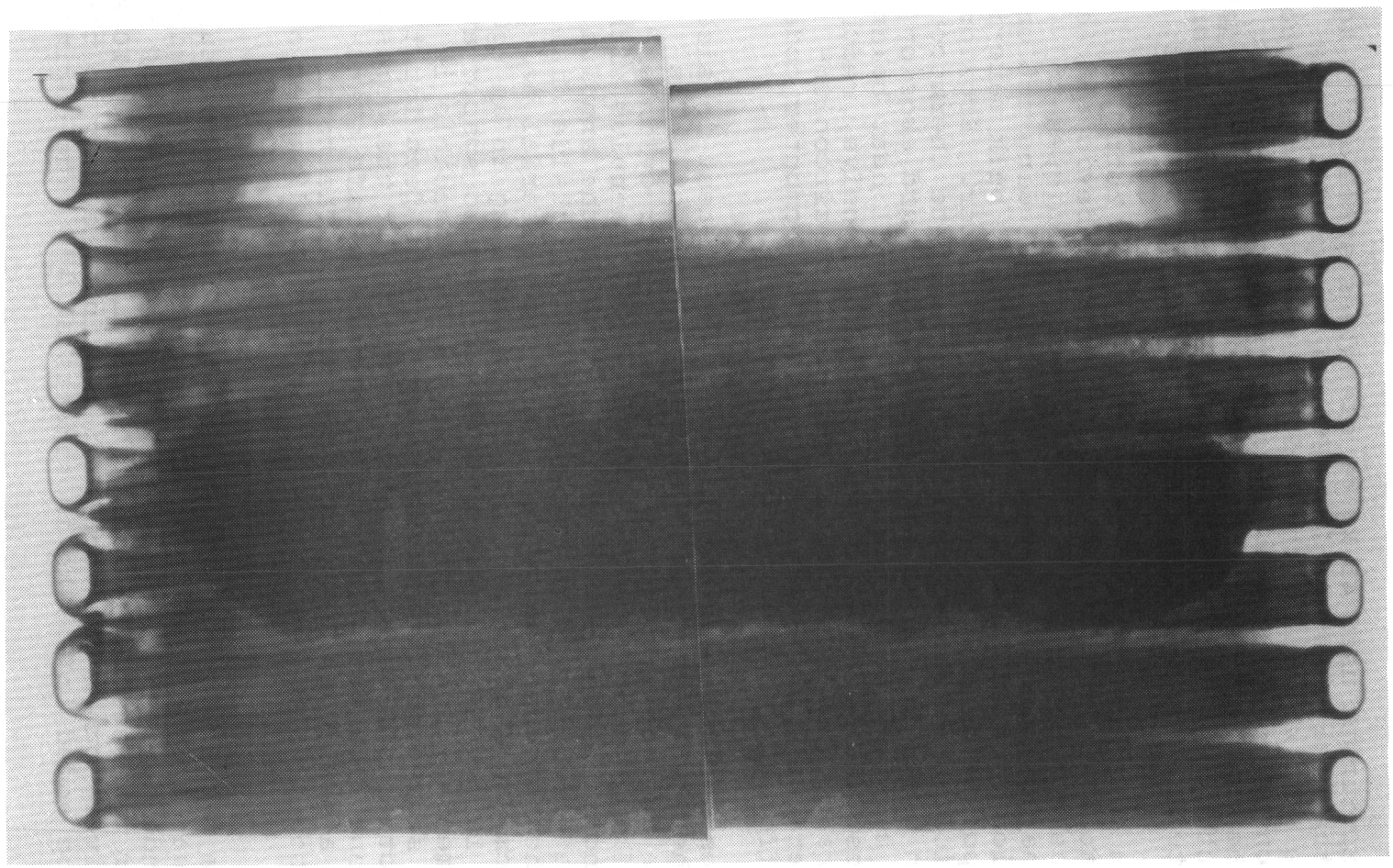

Figure 2.2.12 - Posttest X-ray of QT-E Crucible

2.3 SURC-3 Experiment

2.3.1 General

The SURC-3 experiment used 45 kg of stainless steel and 5 kg of Zr metal as the charge materials. It was designed to be a comprehensive test examining the additional effects of zirconium metal addition to molten steel interacting with limestone concrete. The goals of the experiment were to measure in detail the gas evolution, aerosol generation, and erosion characteristics associated with steel-zirconium-concrete interactions.

Gas evolution was measured in order to determine both gas composition and flow rate using three different devices. Aerosol generation was measured with five different techniques to completely characterize the aerosol source, including not only mass generation rate but also size distribution, bulk material density, composition, and the dynamic shape factor. Erosion characteristics were measured using three separate thermocouple techniques in order to define not just the downward erosion rate but also the meltpool temperature and the overall heat balance. The SURC-3 test was designed to provide comprehensive, redundant, and well-characterized information on the steel-zirconium-concrete interaction which would be suited for computer code validation efforts.

The SURC-3 test article was similar to the QT-E test in size and similar to the QT-D test in materials configuration. The crucible (see Section 2.3.2) was a right circular cylinder consisting of an MgO (K/R cast-98 MgO castible) annulus with a limestone concrete slug poured into the base of the annulus. The height of the crucible was 76 cm and it had an outside diameter of 40 cm. The internal cavity for the charge material had a depth of 60 cm and a diameter of 20.3 cm resulting in an MgO wall thickness of 10 cm. An additional 1 meter ceramic spacer and 2 meter instrumentation tower were bolted to the crucible in order to provide a sealed expansion volume of 10 cubic feet for the concrete reaction effluents, to provide space for the aerosol and gas measurement flow channels, and to provide a safe stand-off distance for a sealed Zr delivery tube system. The total apparatus stood 3.75 meters high with an outside diameter of 40 cm.

The zirconium metal was added to the meltpool via a four-tube remotely actuated sealed delivery system. Each tube contained nine Zr cylinders with diameters of 3.3 cm and a length of 5 cm. Each cylinder weighed 268 g and the total charge weighed 10 kg. The four delivery tubes are each actuated individually so that Zr metal could be added in 2.5 kg increments at any time during the test.

The SURC-3 crucible was positioned in a 13 turn copper induction coil with an inside diameter of 43 cm and a height of 45 cm. The

coil was powered using a 280 kW motor generator set operating at a frequency of 1000 Hz in order to melt and sustain the steel-Zr-concrete interaction. The apparatus was sealed and purged with argon gas in order to direct the majority of the reaction gas and aerosol effluents through a 5 cm diameter flow pipe. The SURC-3 test was run at atmospheric pressure and at an ambient temperature of 18°C.

2.3.2 Geometry and Materials

2.3.2.1 Geometry

The experimental apparatus for SURC-3 is shown in Figure 2.3.1. A similar apparatus was used in the SWISS experiments [Blose et al., 1987]. The apparatus was instrumented to provide measurements of the temperature, pressure, gas evolution and flow rates, aerosol generation, concrete erosion and inductive power during the experiment. The major components shown in Figure 2.3.1 are the "1-D" interaction crucible, zirconium delivery section, expansion chamber and induction coil. These components will be discussed in this section.

Interaction Crucible

The interaction crucible used in this experiment is typical of the cylindrical, "1-D" design used in the previously conducted SWISS experiments. The purpose of the "1-D" design was to limit concrete erosion to the downward or axial direction. The materials used in the construction of the interaction crucible have been discussed in detail in the previous section. The crucible, shown schematically in Figure 2.3.1, consists of an instrumented limestone concrete cylinder 21.6 cm in diameter and 40.0 cm high cast at the base of a MgO annulus, 40.6 cm O.D. and 91.4 cm high. A detailed description of the crucible fabrication is presented in Appendix E. The crucible was cast with an annular recess in the top. This recess matched an annular step cast into the base of the zirconium delivery section which was mounted to the top of the crucible.

The outside of the crucible was laminated with two layers of 207 MN/m^2 tensile strength fiberglass cloth for strength. The glass cloth was 7500 Hexcell with a F16 finish manufactured by Hexcell Corporation, Dublin, California. The cloth was laid up on the crucible using 12 parts TETA curing agent to 100 parts 828 resin. The curing agent is manufactured by Pacific Anchor and the resin by Shell Corporation, Houston, Texas. The total thickness of the fiber glass lamination was 1.5 to 2.0 mm.

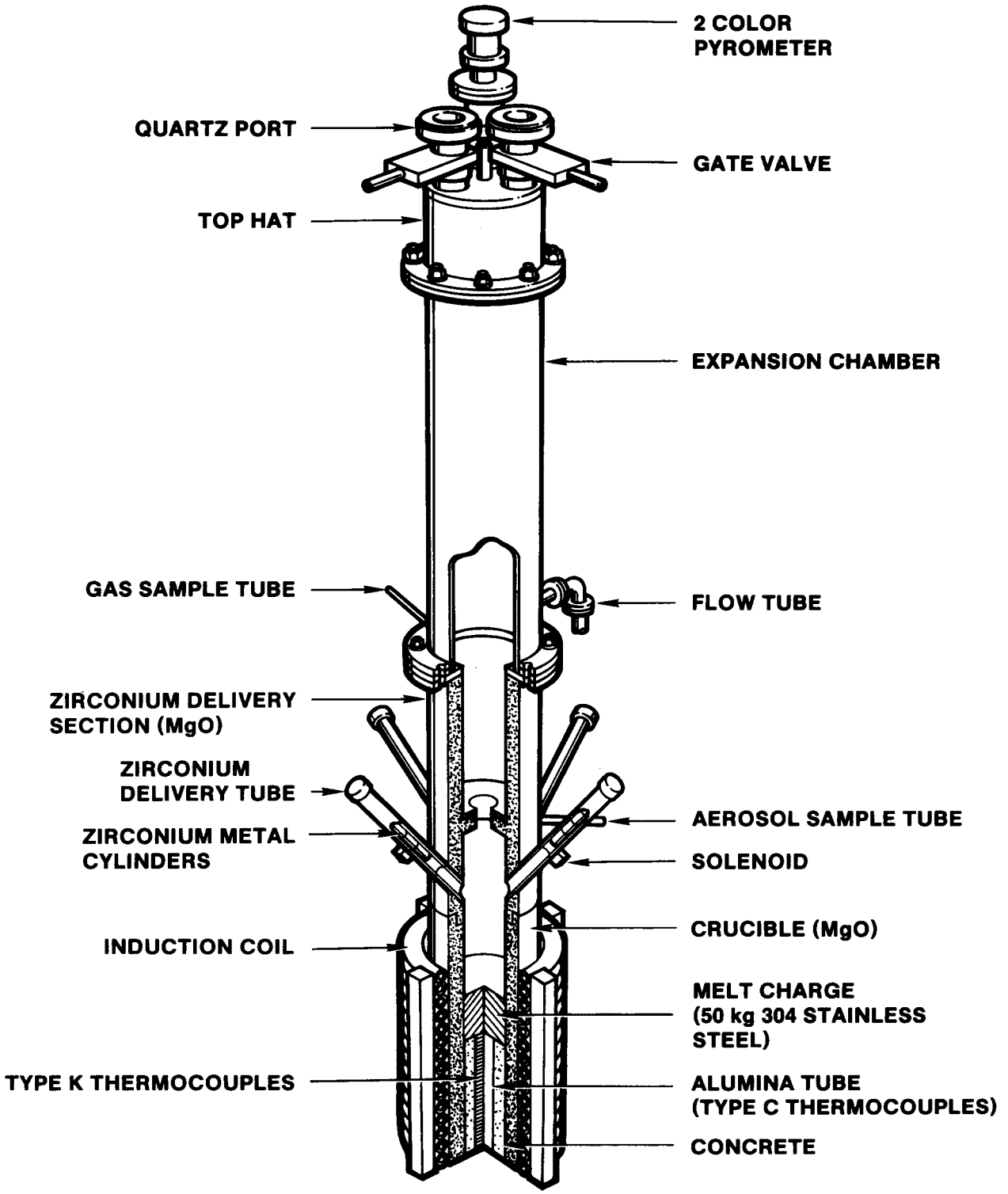

Figure 2.3.1 - Test Apparatus, SURC-3 Experiment

The MgO annulus and concrete cylinder were instrumented with a total of 89 type K (chromel-alumel) thermocouples having an ungrounded, 1.6 mm, 304 stainless steel sheath. These thermocouples were cast into the crucible in 13 arrays to measure thermal response. Figure 2.3.2 shows the relative thermocouple locations and the various arrays cast into the crucible. This figure also shows the nomenclature used to describe the locations of the thermocouples in cylindrical coordinates, specifically r, θ, z and t. Additionally, six type C (tungsten-5% rhenium vs. tungsten-26% rhenium) and six type S (platinum-10% rhodium vs. platinum) thermocouples were installed into three alumina tubes (4/tube) cast into the limestone concrete cylinder to measure melt temperature. These thermocouples had ungrounded, 1.6 mm, tantalum sheaths.

A total of 40 type K thermocouples were cast into the concrete in two arrays. Table 2.3.1 lists the locations and designations of these thermocouples. The array containing thermocouples designated C1 through C20 was located on the axial centerline at odd (0, 1, 3, 5, etc.) centimeter depths. The array containing thermocouples designated C21 through C40 were located on a line parallel to the center axis at a radial distance of 5.4 cm (mid-radius) at even (0, 2, 4, 6 etc.) centimeter depths. The sheath of each thermocouple was bent at an angle of 90 degrees, ten sheath diameters from the tip. This was done to minimize the errors caused by heat conduction down the metal sheath by placing the tip in a plane perpendicular to the anticipated direction of the thermal front propagating into the concrete.

Three, four-hole alumina tubes designated A1, A2, and A3, were cast into the concrete cylinder parallel to the axial centerline, 120 degrees apart at a radial distance of 5.4 cm. Installed in each tube were two type C and two type S thermocouples located at various depths within the concrete cylinder. These thermocouples were used to measure melt temperature and their locations are tabulated in Table 2.3.2. Figure 2.3.3 shows an installation of the two concrete thermocouple arrays and one of three alumina tubes installed with the type C and S thermocouples. Figure 2.3.4 shows a top view of the crucible showing the array orientation of the axial arrays and alumina tubes.

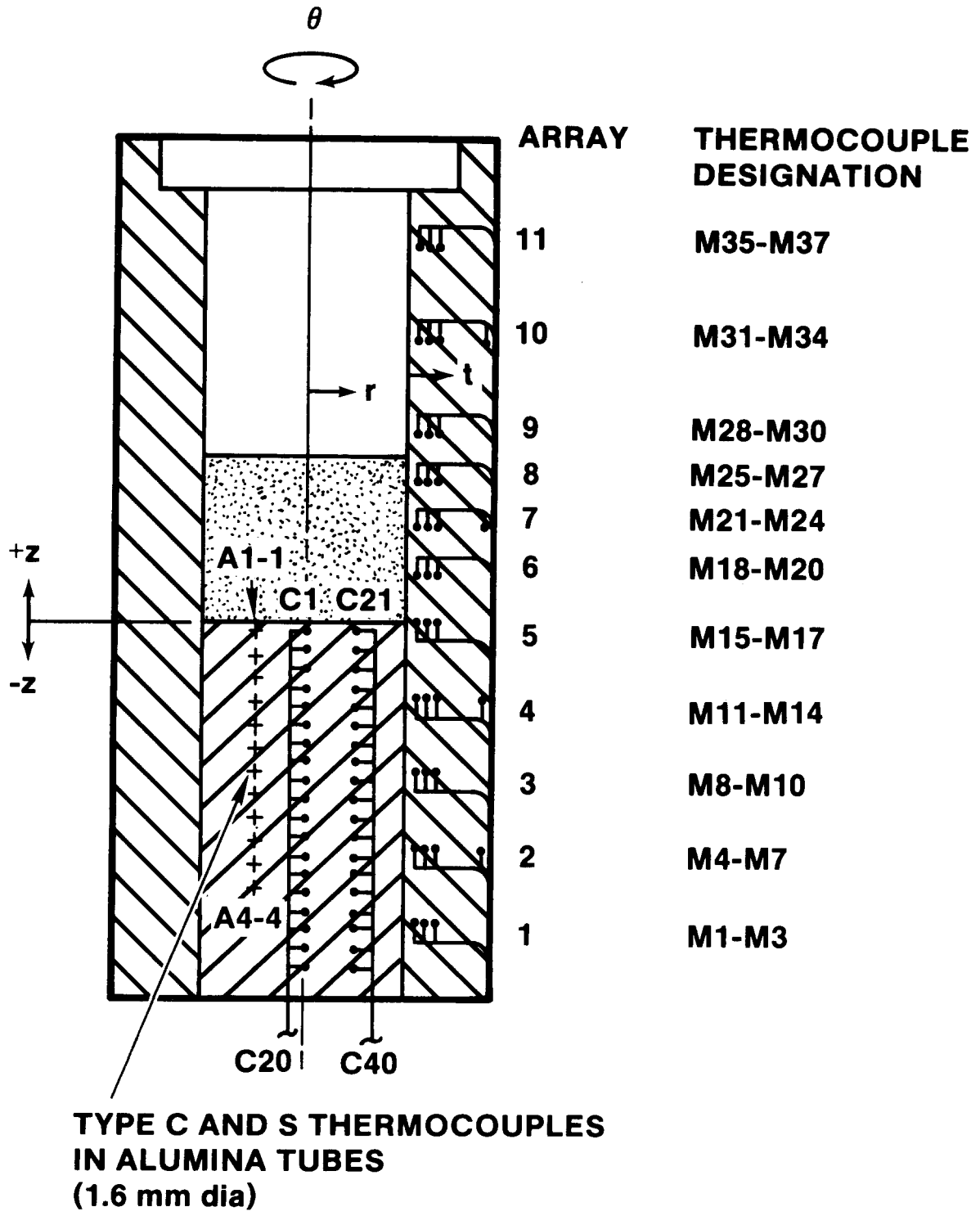

Figure 2.3.2 - Relative Thermocouple Locations, SURC-3 Crucible

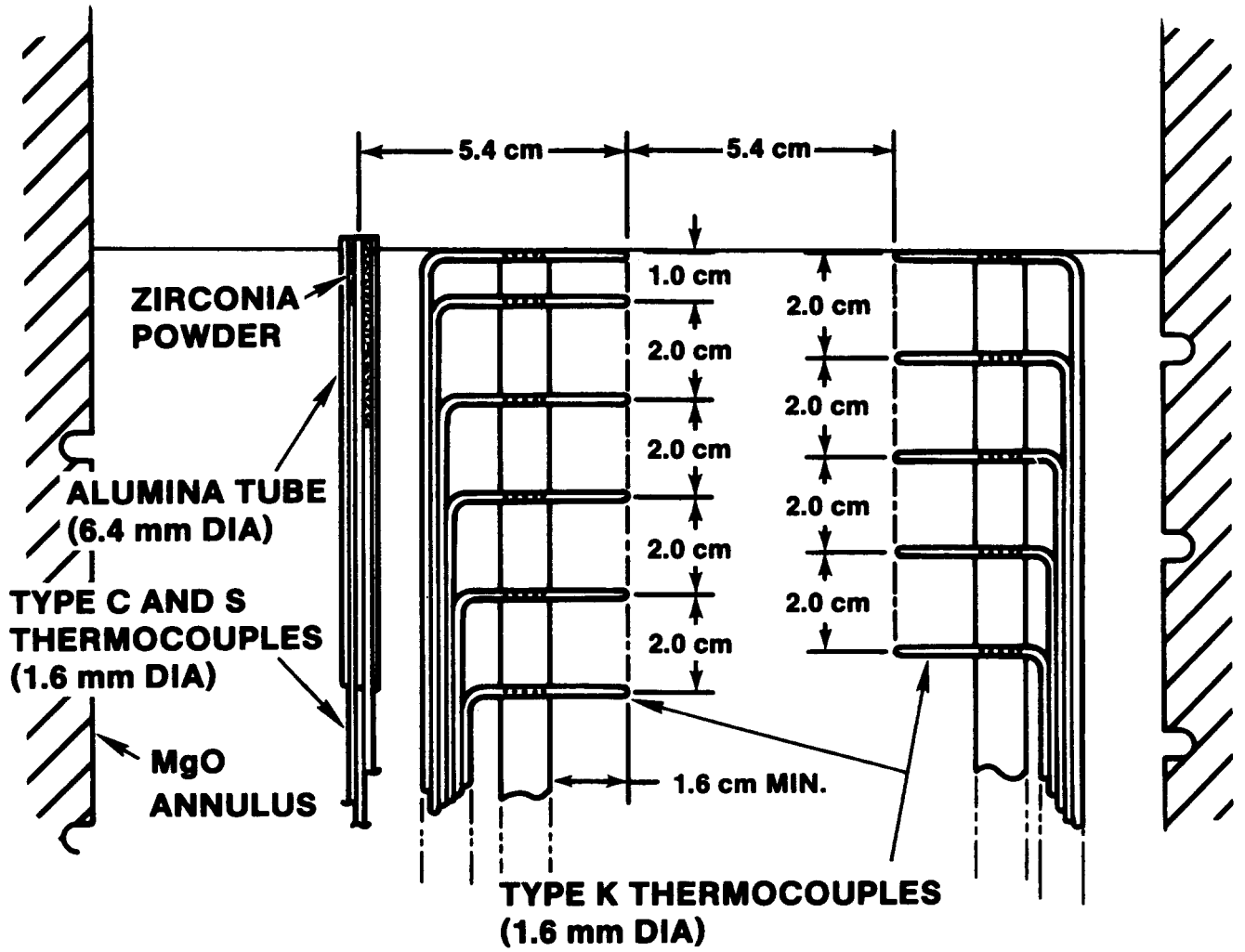

Figure 2.3.3 - Concrete Thermocouple Array, SURC-3

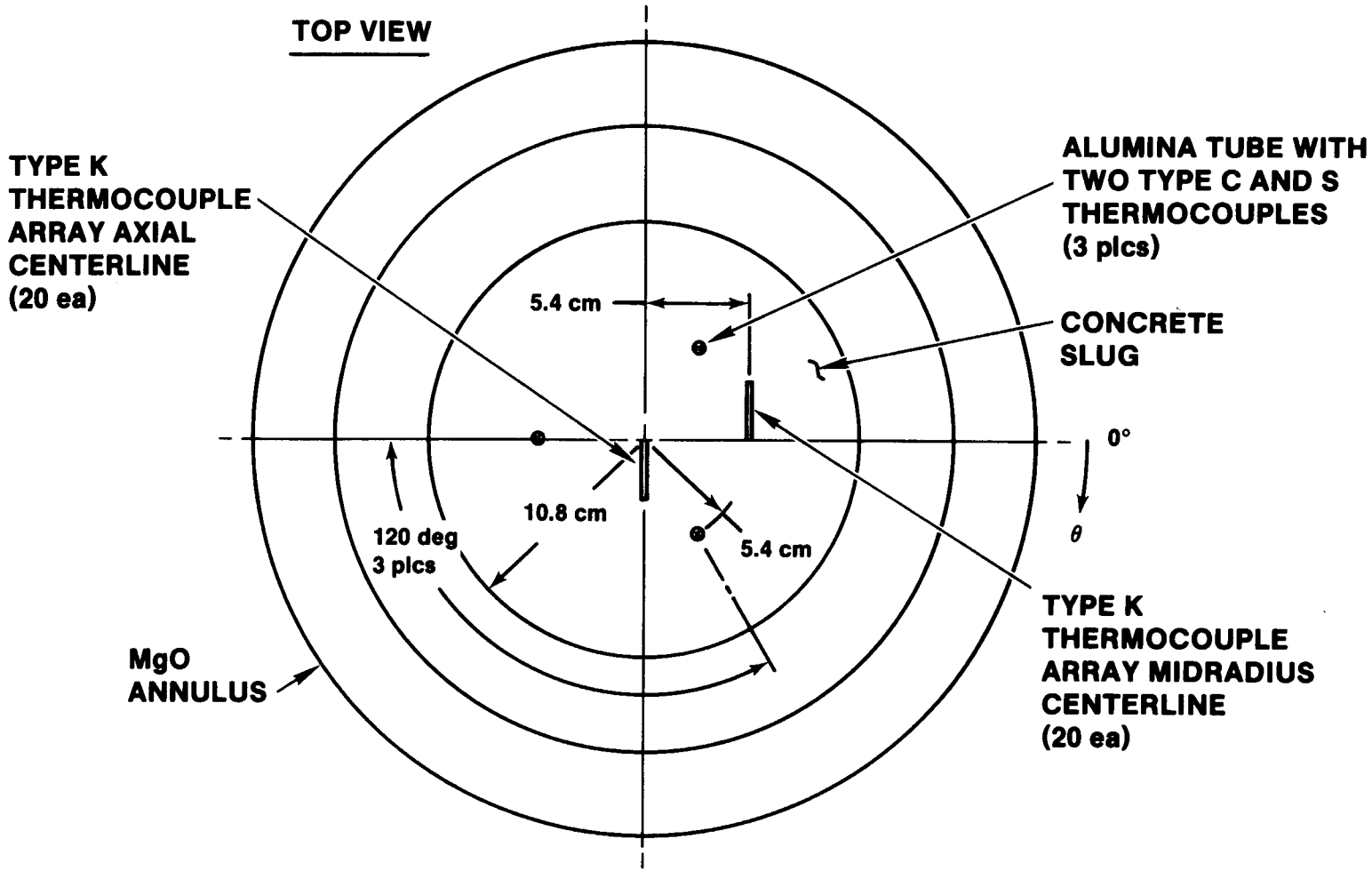

Figure 2.3.4 - Thermocouple Orientation, Concrete Slug, SURC-3

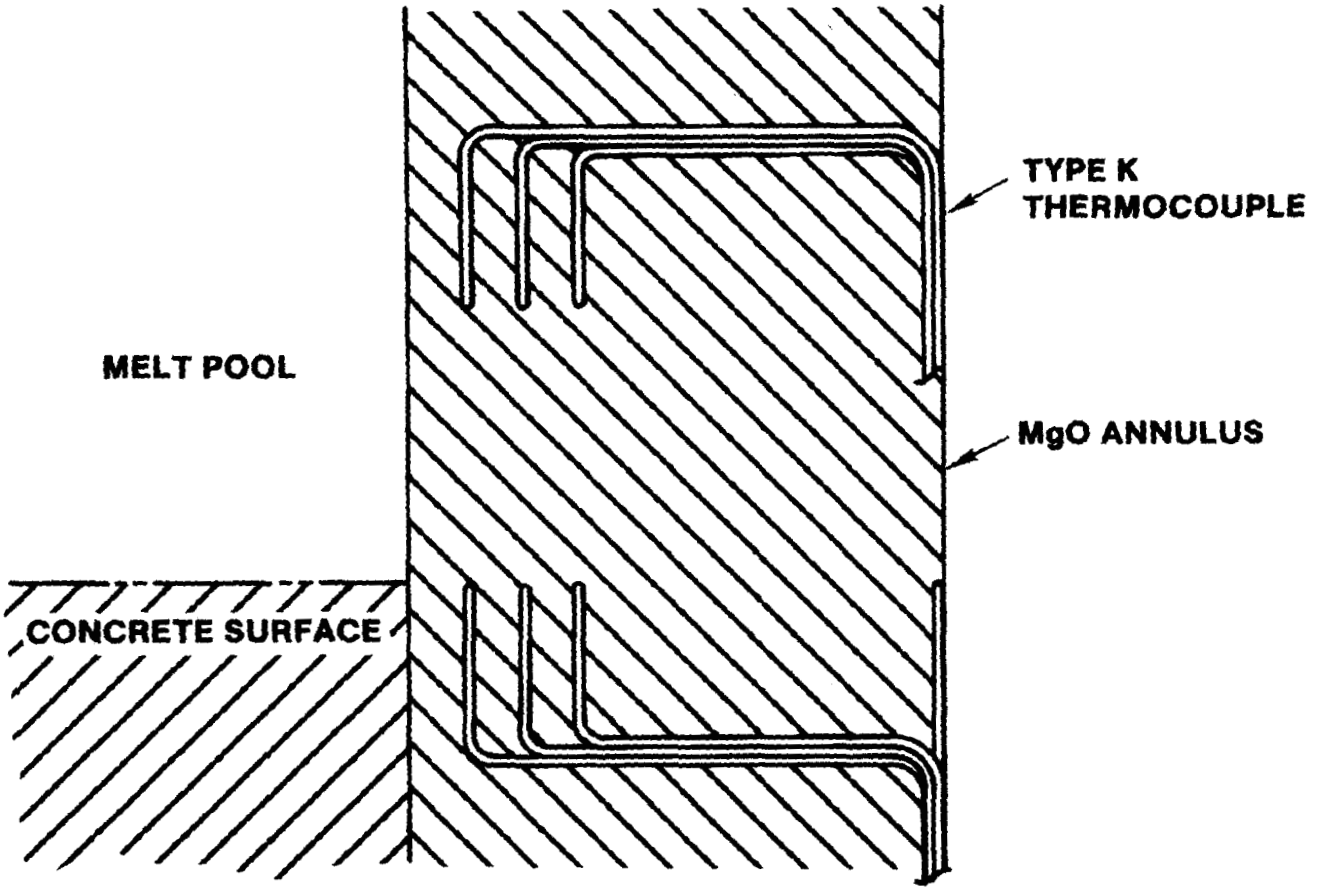

Figure 2.3.5 - Typical Sidewall Thermocouple Array, SURC-3

TABLE 2.3.1

Location of Thermocouples Cast Within the Concrete Slug, SURC-3

(See Figure 2.3.2)

Thermocouple No.	r (cm)	θ (degree)	z (cm)
C1	0	0	-0.2
C2	0	0	-1.2
C3	0	0	-3.3
C4	0	0	-5.2
C5	0	0	-7.2
C6	0	0	-9.2
C7	0	0	-11.2
C8	0	0	-13.2
C9	0	0	-15.2
C10	0	0	-17.2
C11	0	0	-19.2
C12	0	0	-21.2
C13	0	0	-23.2
C14	0	0	-25.2
C15	0	0	-27.2
C16	0	0	-29.3
C17	0	0	-31.3
C18	0	0	-33.2
C19	0	0	-35.2
C20	0	0	-37.3
C21	5.4	0	-0.2
C22	5.4	0	-2.3
C23	5.4	0	-4.2
C24	5.4	0	-6.0
C25	5.4	0	-8.2
C26	5.4	0	-10.1

TABLE 2.3.1 (continued)
Location of Thermocouples Cast Within the
Concrete Slug, SURC-3
(See Figure 2.3.2)

Thermocouple No.	r (cm)	θ (degree)	z (cm)
C27	5.4	0	-12.2
C28	5.4	0	-14.2
C29	5.4	0	-16.2
C30	5.4	0	-18.2
C31	5.4	0	-20.2
C32	5.4	0	-22.2
C33	5.4	0	-24.3
C34	5.4	0	-26.3
C35	5.4	0	-28.3
C36	5.4	0	-30.3
C37	5.4	0	-32.3
C38	5.4	0	-34.3
C39	5.4	0	-36.4
C40	5.4	0	-38.4

TABLE 2.3.2

Location of Thermocouples Installed in the Alumina Tubes Cast Into the Concrete Slug, SURC-3

(See Figure 2.3.2)

Tube No.	Thermocouple No.	Thermocouple Type (C or S)	r	θ	z
A1	1	C	5.4	60	- 1.0
	2	C	5.4	60	- 7.0
	3	S	5.4	60	-15.0
	4	S	5.4	60	-24.0
A2	1	C	5.4	180	- 3.0
	2	C	5.4	180	- 9.0
	3	S	5.4	180	-18.0
	4	S	5.4	180	-27.0
A3	1	C	5.4	300	- 5.0
	2	C	5.4	300	-12.0
	3	S	5.4	300	-21.0
	4	S	5.4	300	-30.0

TABLE 2.3.3

Location of Thermocouples Cast Within

The MgO Sidewall, SURC-3

(See Figure 2.3.2)

Array No.	Thermocouple No.	r (cm)	θ (degree)	z (cm)
1	M1	1.1	0	-32.0
	M2	2.1	0	-32.0
	M3	3.1	0	-32.0
2	M4	1.1	0	-24.1
	M5	2.2	0	-24.1
	M6	3.1	0	-24.1
	M7	9.0	0	-24.0
3	M8	1.2	0	-16.0
	M9	2.2	0	-16.0
	M10	3.1	0	-16.1
4	M11	1.1	270	- 7.9
	M12	2.1	270	- 8.0
	M13	3.3	270	- 8.0
	M14	8.9	270	- 8.4
5	M15	1.3	270	0.1
	M16	2.2	270	0.1
	M17	3.1	270	0.1
6	M18	0.9	270	5.2
	M19	2.0	270	5.4
	M20	3.1	270	5.5
7	M21	1.0	180	10.0
	M22	2.2	180	10.1
	M23	3.0	180	10.6
	M24	9.6	180	11.1
8	M25	1.2	180	14.7

TABLE 2.3.3 (continued)
Location of Thermocouples Cast Within
The MgO Sidewall, SURC-3
(See Figure 2.3.2)

Array No.	Thermocouple No.	r (cm)	θ (degree)	z (cm)
8	M26	2.3	180	15.0
	M27	3.4	180	14.9
9	M28	1.1	180	20.2
	M29	2.3	180	20.2
	M30	3.2	180	20.3
10	M31	0.88	90	30.1
	M32	2.3	90	30.1
	M33	3.2	90	30.3
	M34	8.2	90	31.3
11	M35	1.2	90	40.3
	M36	2.5	90	40.4
	M37	3.7	90	41.3

A total of 37 type K thermocouples configured in 11 arrays were cast into the MgO annulus of the crucible at various elevations to monitor the thermal response of the sidewall. Each array contained either 3 or 4 thermocouples positioned at depths within the annulus nominally 1, 2, 3, and 9 cm measured from the inside surface of the annulus. These thermocouples were bent at 90 degrees, ten sheath diameters from the tip, like those cast into the concrete cylinder. The tips were oriented in a plane perpendicular to the direction of the propagating thermal front. The specific locations of the sidewall thermocouples are tabulated in Table 2.3.3.

Zirconium Delivery Section

The zirconium delivery section was designed to mount on top of the interaction crucible and configured to initially house and later deliver the zirconium metal cylinders to the molten debris at the designated time. The zirconium delivery section was cast entirely of MgO castible and is shown in Appendix E, Figure E-1. It, like the crucible, was also laminated on the outside with the high strength fiberglass. Four brass mounting anchors were cast into the melt generator at the top, 90 degrees apart on a 33.0 cm diameter bolt circle. These anchors were used to securely mount a 2.5 cm thick aluminum transition plate used to connect the expansion chamber with the zirconium delivery section and crucible. Another four anchors were cast into the perimeter 90 degrees apart at a height of 15.2 cm from the base for the purpose of securing the zirconium delivery section to the interaction crucible. This was accomplished by connecting turn buckles between eye bolts screwed into the brass mounting anchors cast into the crucible and zirconium delivery section. The crucible and zirconium delivery section was sealed using a porcelain like cement called Sauereisen No. 31. This is a two component, powder filler and liquid binder cement used for sealing and assembly of high temperature ceramic components. This material has a maximum service temperature of 1366 K.

Four 2-inch black pipe sections were cast into the annulus of this section 90 degrees apart at an angle of 45 degrees with the horizon. The zirconium delivery system consists of an extension tube made of 2-inch black pipe, an inner sleeve of thin walled seamless stainless steel, a small pneumatic cylinder and the zirconium cylinders. The extension tube is connected to the end of the black pipe cast into the side of the melt generator with a union fitting. The thin walled stainless sleeve is inserted into the full length of the black pipe to serve as the slide for the zirconium cylinders. A small 1.1 cm diameter bore pneumatic cylinder mounted to a boss, welded to the extension tube having a 1.3 cm stroke was used to hold the zirconium cylinders in place. Delivery of the cylinders was initiated by activating a solenoid valve causing the pneumatic cylinder to pressurize and withdraw the piston rod holding the cylinders. The zirconium delivery section was installed with four delivery tubes each capable of delivering 2.5 kg of zirconium metal.

A 304 stainless steel aerosol dilution tube 25.4 cm long with a 5.1 cm O.D. was cast into the side of the zirconium delivery section 21 cm above the base. The dilution tube was used to sample aerosols produced during the experiment.

Expansion Chamber

The mild steel expansion chamber was sealed and bolted to the top of the aluminum transition plate mounted to the top of the zirconium delivery section. Three 4.7 mm thick asbestos gaskets and several layers of graphfoil sheet were used to seal the expansion chamber to the zirconium delivery section. The expansion chamber is connected to two vertically mounted pneumatic cylinders (not shown in Figure 2.3.1) having a stroke of about 2 meters. Activating these cylinders lifts the entire expansion chamber allowing access to the zirconium delivery section. The 1.9 cm thick lower flange of the expansion chamber was drilled and tapped for instrumentation feedthroughs, gas sampling, and gas purging. A 2-inch pipe port located 15 cm above the lower flange was used to connect the expansion chamber with the aerosol and gas flow measuring instrumentation. The free volume within the apparatus including the crucible, zirconium delivery section and expansion chamber is estimated to be 0.26 m^3.

Induction Coil

The interaction crucible used in the SURC-3 experiment was installed inside an induction coil fabricated by Inductotherm Corporation, Rancocas, New Jersey. The 12 turn copper coil had a pitch of 5 cm and was centered vertically with the stainless charge. The 53.3 cm I.D., 50.8 cm high coil was supported by six hard rock maple supports equally spaced around the perimeter. The coil was connected to the induction power supply using two, 4.6 meter long, #32 high current, water-cooled, flexible leads. The coil was cooled by a 39/61 mixture of ethylene glycol and water.

2.3.2.2 Materials

The interaction crucible used in this experiment is typical of the cylindrical, "1-D" design used in the SWISS [Blose et al., 1987] experiments. The crucible shown schematically in Figure 2.3.6 consists of an instrumented limestone concrete cylinder 21.6 cm in diameter and 40.0 cm high cast at the base of a MgO annulus 40.6 cm O.D. and 91.4 cm high. A detailed description of the interaction crucible will be discussed later in Section 2.3.3. The MgO castible material (K/R Cast-98) was briefly described earlier in Section 2.1.1 where the basic chemical composition was presented in Table 2.1.1. This material will be further described here with respect to mixing and curing requirements, in addition to the thermal and mechanical properties. The concrete, charge material and fission product simulants will also be discussed in this section.

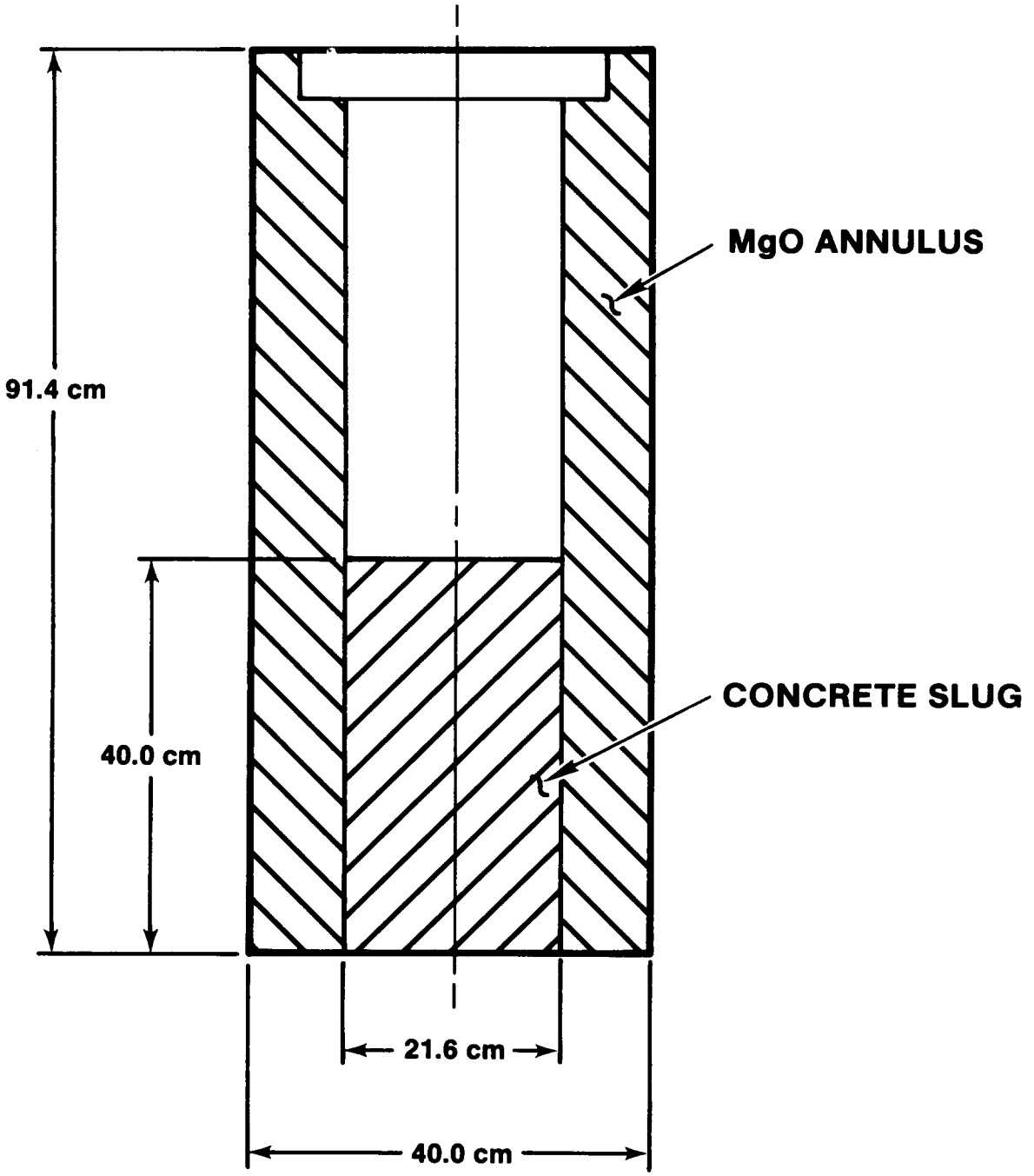

Figure 2.3.6 - "1-D" Interaction Crucible, SURC-3

Magnesium Oxide (MgO) Castible

K/R Cast-98 is a superior MgO castible produced from critically sized 98+% MgO periclase and bonded with a special chromate composition. This material resists melt penetration and provides outstanding resistance to acid slags typically produced from steel melts. K/R Cast-98 has excellent volume stability and is commonly used for crucibles in the steel industry.

The MgO castible was mixed by placing a known mass of dry material into a clean paddle-type mixer. Clean drinking water was then added 5% to 6% by weight to the castible material and mixed for at least two minutes. Once a homogeneous mixture was achieved, the mix was carefully placed into the casting forms with small scoops and shovels. A mechanical vibrator called a "stinger" operating at 10,000 to 12,000 vibrations per minute was inserted into the mix to densify it and to remove entrained air. Three 10.2 cm diameter, 20.3 cm high test cylinders were cast with the annulus to measure the compressive strength of the castible after being cured. The cylinders were tested on the day of the experiment. This was done as a quality assurance procedure to reveal any gross anomalies that may have occurred during the casting process. The compressive strength of the three test cylinders were measured to be 18.2, 18.7 and 18.9 MN/m^2. These strengths are within acceptable limits for the castible material.

After casting, the annulus and compressive cylinders were cured at ambient temperature (20 to 30°C) for 24 hours. Then the forms were placed into an oven and heated to 470 K. The casting was held at temperature for 12 hours. The total curing cycle took 24 hours. During the baking period, two type K thermocouples were connected to a strip chart recorder to monitor the curing temperature. One thermocouple measured the ambient oven temperature, the other was cast into the annulus an measured the actual temperature of the castible material.

The thermal behavior of the K/R Cast-98 was characterized by thermal gravimetric analysis (TGA) and is shown in Figure 2.3.11. This analysis was performed with a Dupont 790 thermal analysis apparatus with a 1870 K DTA cell and Model 950 TGA attachment. The TGA was performed in dry air with a flow rate of 50 cc/min. The heating rate was 10°C/min from room temperature to 1000°C. A 22.11 mg sample of the material was obtained from one of the three tested compressive cylinders cast and cured with the annulus. Weight loss indicated in the thermogram shown in Figure 2.3.7a is attributed to release of free water and $Mg(OH)_2$. This sample shows a 2.0 weight-percent loss due to the release of free water between ambient temperature and 305°C. Figure 2.3.7b shows an expansion of the thermogram between 360 and 475°C. Between 415 and 440°C, an additional 2.0 weight-percent loss was observed, which is probably due to the loss of brucite $Mg(OH)_2$.

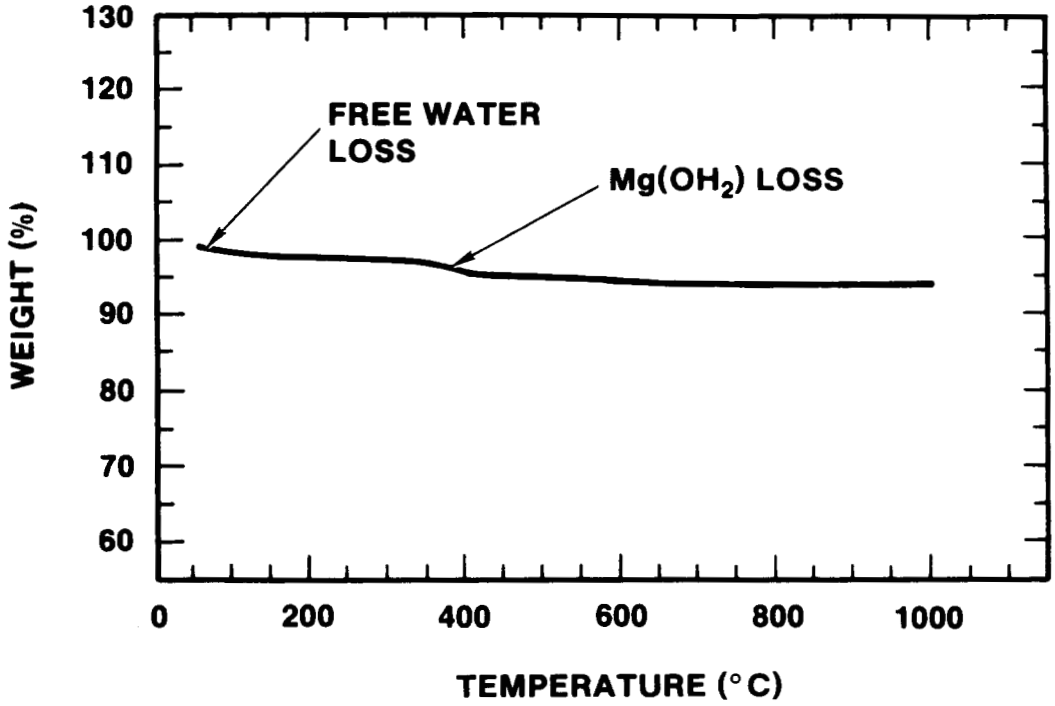

Figure 2.3.7a - Thermogram (TGA) of K/R Cast-98: Air Cured 24 hrs and Baked at 240°C for 12 hours.

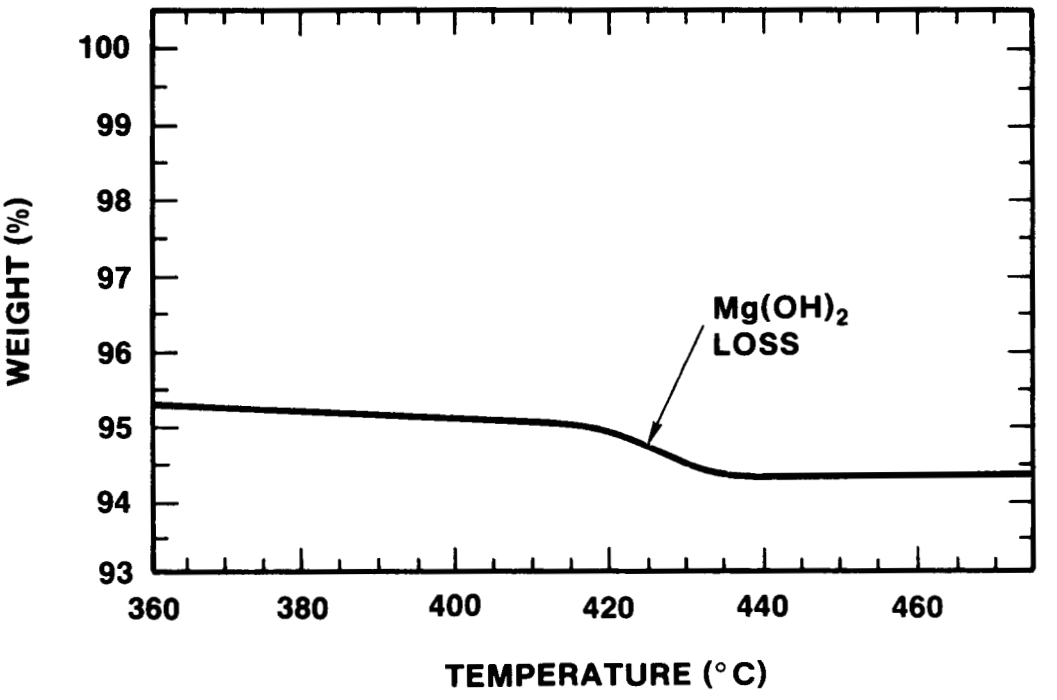

Figure 2.3.7b - Expansion of Thermogram (TGA) of K/R Cast-98 between 360 and 475°C.

The thermal properties of the castible K/R Cast-98 have been extensively investigated. In addition to industry data, experiments were conducted at Sandia to study the thermal response of the MgO to intense heating conditions similar to those expected during an experiment. These experiments were carried out at the Sandia Solar Power Tower where a MgO specimen was subjected to incident solar fluxes in the range of 6.5×10^5 W/m^2 to 1.4×10^6 W/m^2. The test specimen was 45 cm x 45 cm x 8 cm and was cast of the K/R Cast-98 material according to specifications. The test specimen was well instrumented with 17, 1.5 mm diameter type K thermocouples, located from 0.3 cm to 6.3 cm below the exposed surface. The test specimen was mounted in a frame compatible with the Solar Tower assemblies. The incident flux was monitored by heat flux gauges deployed along the top side of the test specimen. The back of the test specimen was well insulated in order to approximate an adiabatic boundary condition.

The data were analyzed by the "PROPTY" code developed by J.V. Beck [Beck, 1985]. The code determines the thermal conductivity of a material that fits a set of temperature response curves for specific interval and boundary conditions.

A typical thermal history of the specimen is shown in Figure 2.3.8. As one can see, the temperature rise is interrupted at 100°C. This is due to the release of free water in the castible material. The material continued to be heated until approximately 1400°C, then the solar heat flux was removed and the test specimen was allowed to cool.

The PROPTY prediction of the thermal conductivity of the MgO is shown in Figure 2.3.9. The presence of the free water within the castible material causes minor problems in the analysis of the experimental data. As shown in Figure 2.3.9, the predicted thermal conductivity is slightly higher for "wet" or uncured material than it is for the "dry" material of fully dehydrated MgO castible. A check of the relative accuracy of the values of the conductivity is demonstrated by comparing the predicted thermal response with the actual experimental data. As shown in Figure 2.3.10, excellent agreement is achieved. The absolute values of thermal conductivity (k) are dependent on the initial value set in the PROPTY code. This value is fixed, and the value of k at other temperatures are allowed to vary in order to determine the best value of k. Thermal conductivity data for 98% dense magnesium oxide are also shown in Figure 2.3.9. It is readily apparent that the thermal conductivity of the K/R Cast-98 is much less than the highly densified MgO. The conductivity of the castible material is quite dependent on density and method preparation. Another determination of the thermophysical properties of K/R Cast-98 was performed by Purdue University and these data are presented in Appendix D.

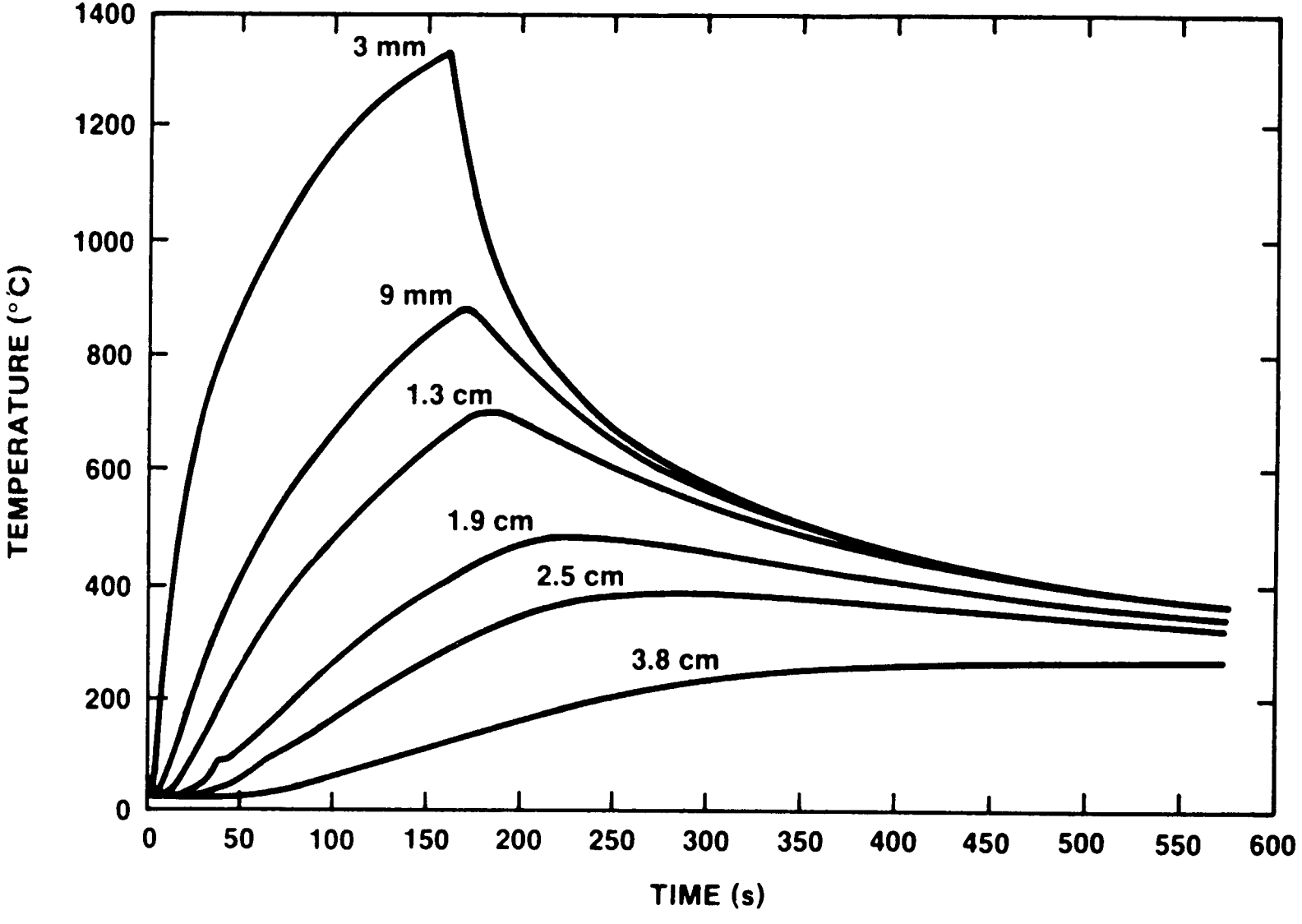

Figure 2.3.8 - Representative Temperature History of an MgO Sample Exposed to Solar Heat Flux 1.4 x 10^6 W/m^2.

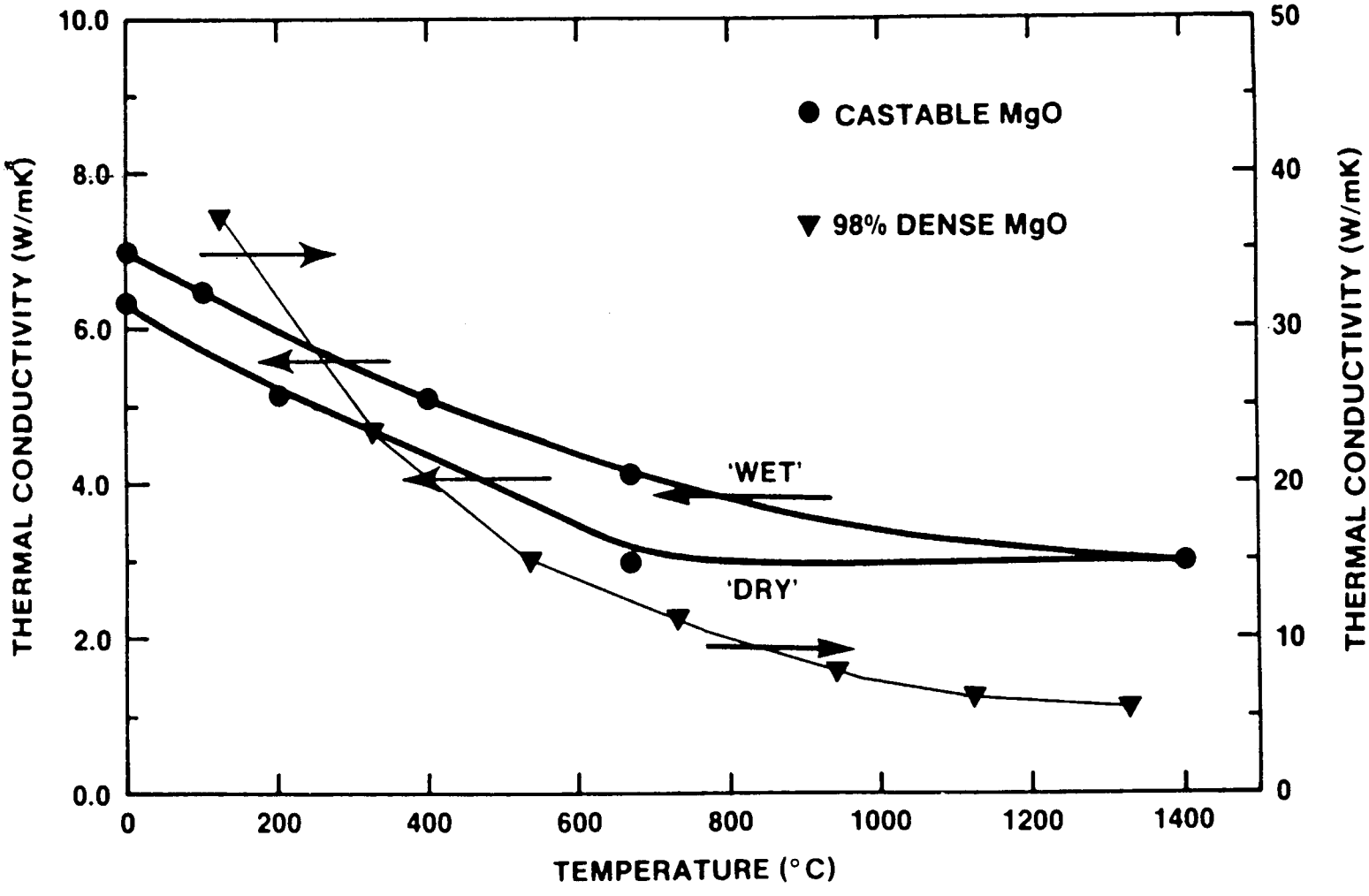

Figure 2.3.9 - "PROPTY" Thermal Conductivity Prediction for Castible MgO Material. Also shown are data for 98% dense material. Note the significantly different scale used for the thermal conductivity of the highly dense material.

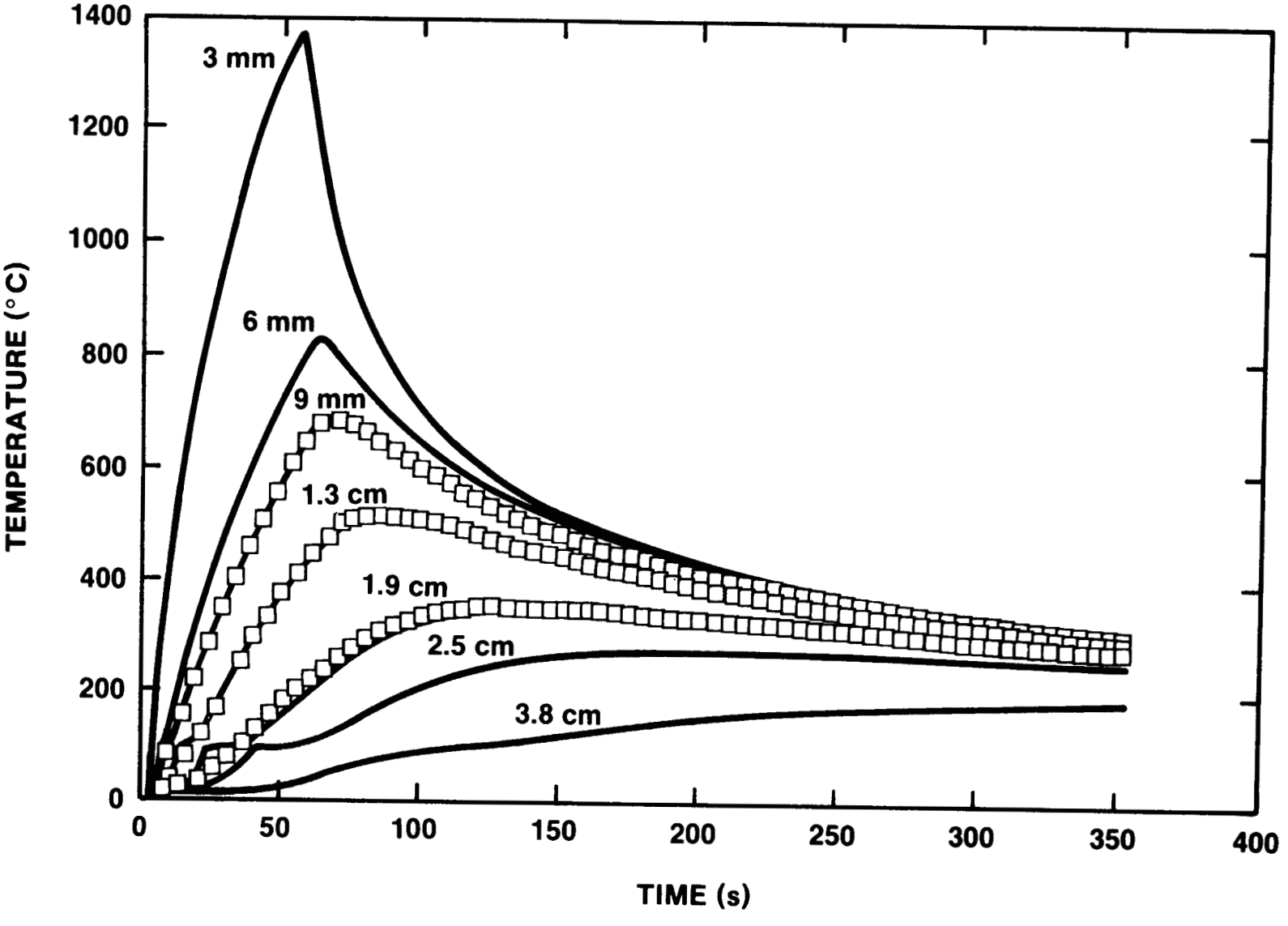

Figure 2.3.10 - Comparison of Experiment Thermal History and Predictions of the "PROPTY" Code. Curves are labelled according to the depth below the surface exposed to the incident heat flux. Data obtained in the experiment are shown as open squares. Results calculated with PROPTY code are shown as solid lines.

The density of the K/R Cast-98 material was also investigated. The bulk density of the material used in SURC-3 was found to be 2680 kg/m^3 as compared to the theoretical density of 3590 kg/m^3.

Concrete Material

The base of the interaction crucible was constructed of limestone concrete. This concrete is used because it is typical of those used in the construction of nuclear power plants. Materials making up this type of calcareous concrete are found throughout the United States. This concrete melts over a range of 1653 to 1873 K and typically liberates 30-35 weight-percent CO_2 gas and 4-5 weight-percent H_2O vapor when heated to melting.

Specifications for the concrete are listed in Table 2.3.4. Tables 2.3.5 and 2.3.6 summarize the engineering and chemical composition of the limestone concrete, respectively. Table 2.3.7 shows comparisons of the size specifications and the distribution of sizes for the coarse and fine aggregate actually used for the concrete mix.

Four 10.2 cm diameter, 20.3 cm high test cylinders were cast with the concrete slug to measure the compressive strength at 7, 14, 28 and 82 days (day of the experiment). The concrete slug was cured at ambient temperature conditions nominally 20 ± 5°C. The compressive strengths measured at the end of each cure period were 22.1, 23.6, 29.4 and 28.7 MN/m^2, respectively. These strengths are within the acceptable limits for this concrete.

The thermal behavior of the concrete can be characterized by thermal gravimetric analysis (TGA). Figure 2.3.11 shows the thermogram produced by TGA for the SURC-3 limestone concrete. Between ambient temperature and 100°C there is a 2.5 weight-percent loss due to the release of free water. There is a 0.7 weight-percent loss between 415 and 440°C. This is attributed to the release of $Ca(OH)_2$. A significant weight loss (29 weight-percent) is observed between 575 and 825°C. This is due to the release of CO_2.

Charge Material

The melt charge used in this experiment was a solid cylinder of 304 stainless steel having a mass of 50 kg. The cylinder had a 21.6 cm diameter and was 17.3 cm high. The standard composition of the 304 stainless steel was presented earlier in Table 2.1.3.

Five kg of zirconium metal was added to the melt concrete interaction after steady-state concrete erosion was observed based on thermocouple data. The zirconium was in the form of solid cylinders having nominal dimensions of 3.3 cm diameter and length of 5 cm. The mass of each cylinder was approximately 278 g. The elemental analysis of the zirconium metal was presented earlier in Table 2.1.4.

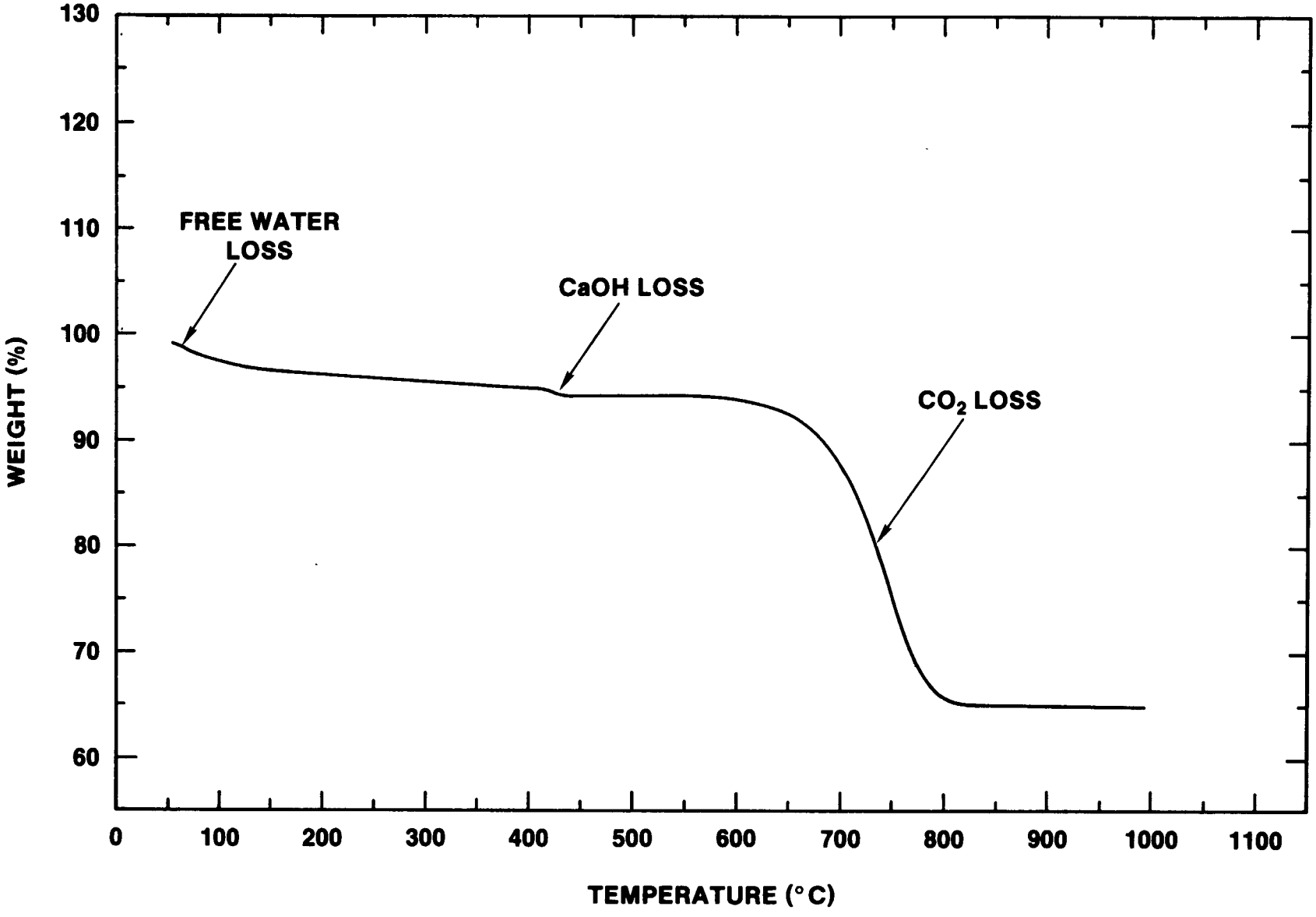

Figure 2.3.11 - Thermogram (TGA) of Limestone Concrete

TABLE 2.3.4

Concrete Specifications

1)	Compressive strength after 90 day cure = 27.5 MPa minimum
2)	Slump = 5 cm
3)	Cement = American Type II Portland Cement
4)	Air Content = 3 to 5% by volume
5)	Air entraining agent per reference (a) below
6)	Composition per reference (b) below
7)	Aggregate size and size distribution per reference (c) below
8)	Water reducing agent per reference (a) below
9)	Mixing, forming, and placing per references (b,c,d,e) below

(a) ASTM C-494-71, Standard Specification for Chemical Admixtures for Concrete, American Society for Testing and Materials, Philadelphia, PA.

(b) ACTI 211. 1-74, Recommended Practices for Normal and Heavy Concrete, American Concrete Institute, Detroit, MI.

(c) ASTM 33-74, Standard Specifications for Concrete Aggregates, American Society for Testing and Materials, Philadelphia, PA.

(d) ACI 347-68, Recommended Practice for Working Concrete, American Concrete Institute, Detroit, MI.

(e) ACI 315-74, Detailing Manual, American Concrete Institute, Detroit, MI.

TABLE 2.3.5

Mix Specification for Limestone Concrete

Concrete Type	Cement (kg)	Water (kg)	Sand (kg)	Coarse Aggregate	Fine Aggregate	Fly Ash	AEA* (ml)	WRA+ (ml)
Limestone	42.6	24.0	0	165.2	118.0	7.3	82.9	83.5

* Air entraining agent

\+ Water reducing agent

TABLE 2.3.6

Chemical Composition of Limestone Concrete and Concrete Constituents

Oxide	Type I & II Cement*	Limestone Aggregate*	Fly Ash*	Limestone Concrete*	Expected Error*
Fe_2O_3	4.11	0.38	11.7	1.2	0.3
Cr_2O_3	0.011	0.012	0.022	0.004	0.01
MnO	0.08	0.04	0.02	0.01	0.02
TiO_2	0.2	0.04	2.24	0.12	0.04
K_2O	0.54	0.36	3.5	0.68	0.4
Na_2O	0.27	0.16	0.34	0.08	0.2
CaO	63.5	47.2	1.3	45.4	1.0
MgO	1.53	0.6	1.14	5.67	0.5
SiO_2	20.1	8.0	51.2	3.6	1.5
Al_2O_3	4.2	1.2	24.5	1.6	0.2
CO_2	ND	38	ND	35.7	1.0
H_2O	ND	ND	0.3	4.1	0.5
SO_2	1.0	ND	ND	< 0.02	0.2

* - All components reported as weight percent

ND = Not Determined

TABLE 2.3.7

Comparison of Specified and Actual Size Distributions for the Fine and Coarse Limestone Aggregate

Screen Opening (cm)	Specified Weight % Passing Through the Screen	Observed Weight % Passing Through the Screen Opening: As Received Limestone
A) COARSE AGGREGATE		
2.5	95-100	100
1.9	90-100	97.29
1.3	25-60	51.83
0.95	20-55	
0.48	0-10	
0.23	0-5	
B) FINE AGGREGATE		
1.3	100	100
0.95	85-100	100
0.48	10-30	20.1
0.23	0-10	0.2
0.12	0-5	0

Fission Product Simulants

In order to evaluate the transport of fission products during the melt concrete interaction, various chemical species, listed in Table 2.3.8, were added to the melt prior to heating. The simulants, composed of both metals and metal oxides, were added to the charge as a homogeneous powdered mixture prior to heating.

TABLE 2.3.8
Fission Product Simulants Used
in the SURC-3 Experiment

FISSION PRODUCT	MASS
Tellurium (Te)	500 g
Molybdenum (Mo)	500 g
Barium Oxide (BaO)	500 g
Zirconium Oxide (ZrO_2)	500 g
Cerium Oxide (CeO_2)	500 g
Lanthunum Oxide (La_2O_3)	500 g
Niobium Oxide (Nb_2O_5)	500 g

2.3.3 Instrumentation

A total of 142 data channels were used to record the results of the SURC-3 test. Of these, 105 were thermocouple channels. Forty thermocouple channels were used to monitor axial erosion in the concrete. An additional 37 thermocouple channels were used to estimate the sidewall heat losses through the MgO annulus. Five thermocouple channels were located in the flow system to measure the effluent gas temperature. Eleven more thermocouple channels were used to monitor the temperature within the aerosol collection system, and the last twelve thermocouple channels were used to record the meltpool temperature. Thirty seven data channels were voltage channels. Nine of these were used to

monitor pressure and flow through the system. One was used to record the melt surface temperature. Six more were used to measure the induction coil power and coolant flow levels. Three were used to monitor the composition of the effluent gas and the last 14 were used to record aerosol data. All of these instrument channels were recorded every 10 seconds during the test using an HP 1000 data acquisition system. In addition to the HP 1000 data system, data was sampled and stored with the SEDS aerosol system (14 channels), the gas grab sample system (32 channels), the Inficon Mass Spectrometer (10 channels), and a video camera/recorder system.

2.3.4 Procedure

Initial calibration runs using a 16-inch diameter-45 kg stainless steel slug were performed in order to determine the coupling efficiency and overall losses for the SURC-3 coil geometry. Power to the coil was set at 150 kW. Thermocouples placed in the slug indicated a temperature rise of 375°C in ten minutes followed by losses of 200°C in ten minutes after power shutdown. These results indicated a net efficiency of 18.7 percent (28 kW total to the steel slug) with overall losses of 10 kW. Following these power calibration tests, the SURC-3 apparatus was assembled and leak tested. Results of the leak tests using argon gas as the flow medium indicated a cold leak rate of .3 cfm at an inlet flow rate of 6.0 cfm (5% losses) and an overpressure of 2 psi in the SURC-3 expansion crucible.

After the final calibration and pretest checkouts were performed, power was applied to the coil (Figure 2.3.12) at the maximum allowable rate of 168 kW. This constituted the start of SURC-3 at time = 26 minutes. The temperature adjacent to the steel charge was monitored (Figure 2.3.13) at the concrete interface to confirm that approximately 20% of the power was being transmitted to the metallic slug. After twenty-five minutes of constant heating at time = 50, the power supply was shut down to inspect the SURC-3 apparatus and cool the zirconium delivery tubes which had heated to 300°C due to incidental coupling with the induction field. Full power was resumed at time = 55 and continued at a steady 168 kW until time = 90. At that time, the power supply was shut down to conduct field repairs on the aerosol sampling system. The remote actuation system for the aerosol apparatus had malfunctioned and was replaced with a manual system. The manual aerosol sampling setup required that the power supply be shut down for 1-2 minutes each time filter samples were taken. Subsequent shutdowns for aerosol sampling occurred at times = 105, 127, 176, 204, and 224. Erosion of the concrete in SURC-3 began around time = 90 as indicated by thermocouple failures in the concrete. After 6 to 8 cm of erosion, the power supply was shutdown at time = 133 to add the zirconium metal to the melt. Two of the four zirconium delivery tubes were actuated, adding 5 kg of Zr metal to the steel-concrete interaction. Full power to

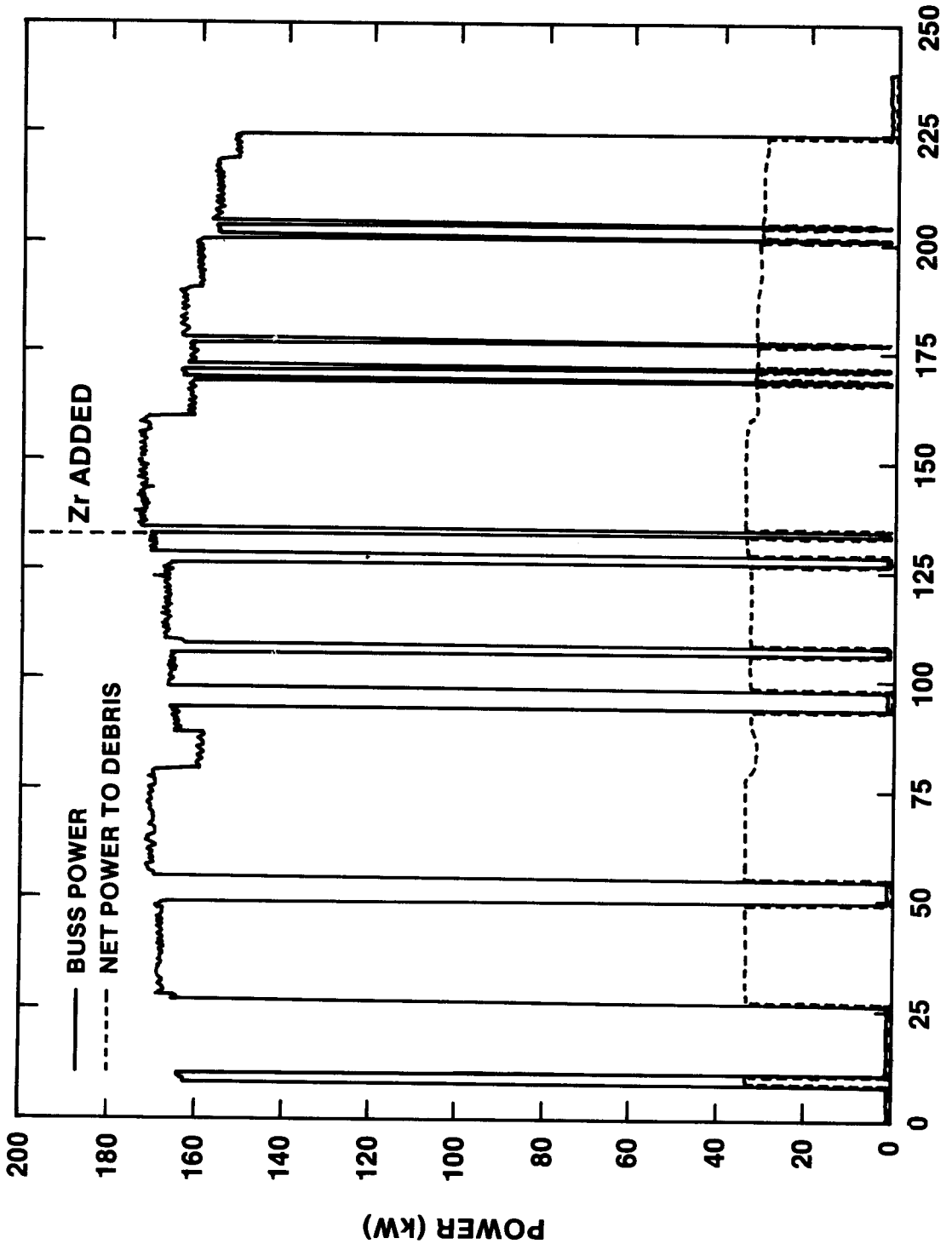

Figure 2.3.12 - Coil Power - SURC-3

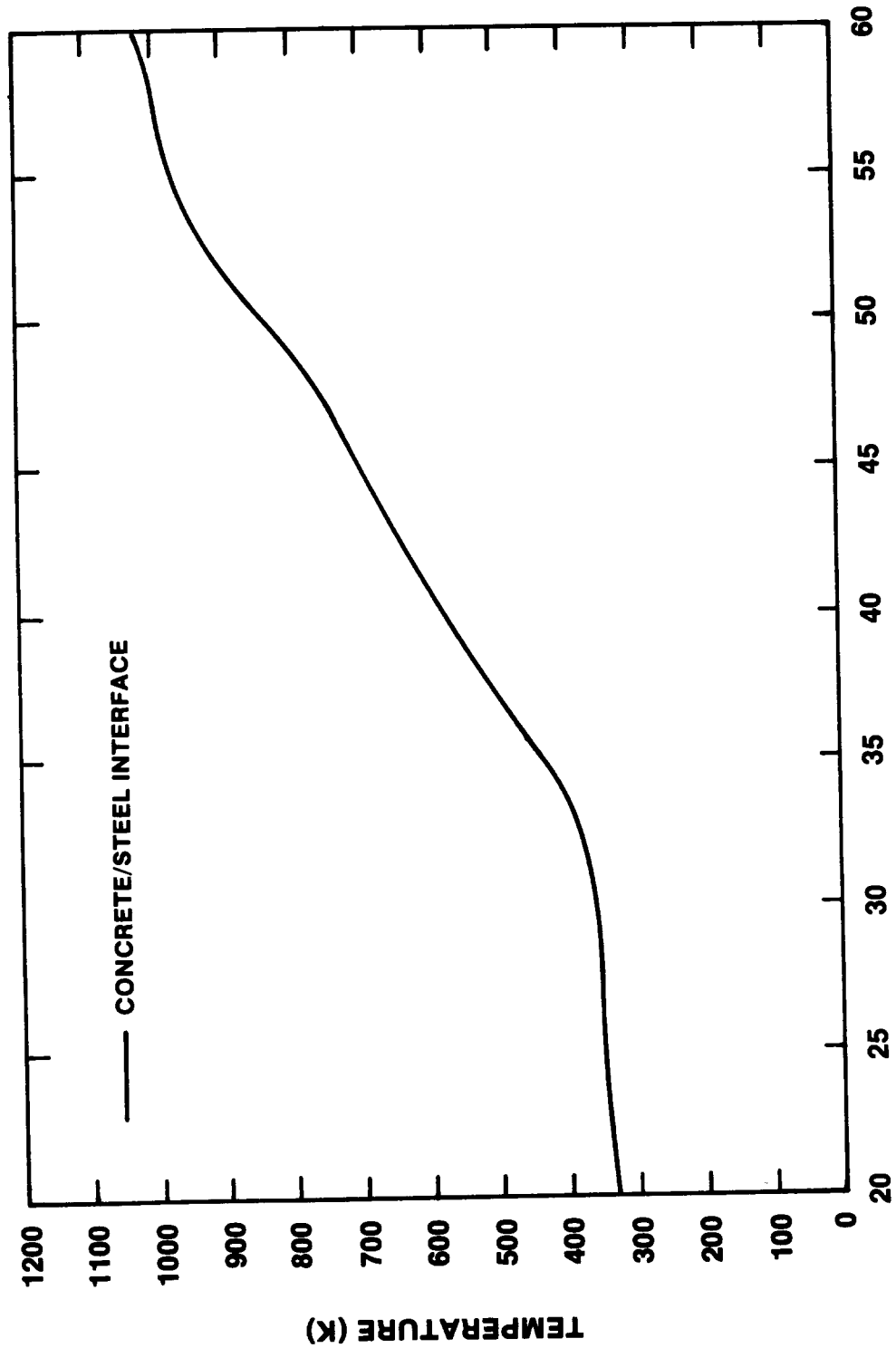

Figure 2.3.13 - Initial Steel Temperature - SURC-3

the coil was then resumed. A significant Zr-steel-concrete interaction ensued which lasted for about 15 minutes. After the Zr reaction was complete, twenty minutes of steel-concrete erosion was recorded before a second addition of Zr metal was attempted at time = 177. Thermocouple failures indicated 23-25 cm of erosion to that point. The power supply was again shut down and the remaining two Zr delivery tubes were actuated. This also added 5 kg of Zr metal to the steel-concrete interaction. Full power was again resumed at time = 178. No significant changes in erosion, aerosol production, flow rate, or gas composition occurred following the second Zr drop. The steel-concrete interaction was allowed to continue for forty minutes to ensure that there were no latent effects of the second Zr addition. A total erosion depth of 34 cm was indicated at time = 220. At time = 225, the power was shut down and the SURC-3 experiment was concluded. During the 200-minute test, a total of 10 power interruptions occurred to allow for inspections and aerosol sampling. These interruptions accounted for a total of twenty minutes of down time, thus, reducing the average power to the melt by 10 percent.

2.3.5 Posttest Observations

Posttest x-rays (radiographs) were taken of the SURC-3 crucible as seen in Figure 2.3.14. These x-rays indicated several layers of overlying crust above the solidified metallic charge. The uppermost crust was 21 cm above the original steel concrete interface and 1 cm above the original meltpool height. This top crust was 15 cm thick, relatively dense, and appeared to have as many as 16 Zr cylinders embedded in it. Below this uppermost crust was a 15-20 cm bell-shaped void, then a second crust. This middle crust was also relatively dense, 2-6 cm thick, and appeared to be composed entirely from molten oxide material. The bottom surface of this crust was nearly horizontal and located 4.5-5 cm below the original steel/concrete interface. A second cylindrical-shaped void extended 7-8 cm below the middle crust to the top of the final meltpool surface. The top of the final meltpool was a third oxide crust, somewhat less dense and roughly 7.5 cm thick. The upper surface of the final meltpool crust was 12 cm below the original melt/concrete interface. The solidified metal pool lay just below the third oxide crust. This pool was 20 cm in diameter and 14-15 cm deep. The bottom of the solidified melt was 33.5 cm below the original melt/concrete interface and roughly bowl shaped with one side 2-3 cm higher than the other. The MgO sidewalls of the SURC-3 crucible remained nearly vertical and the diameter of the cavity varied less than 1 cm (21.5-22.5) over its entire height, thus indicating a minimum of sidewall erosion. The SURC-3 crucible was sectioned vertically after the posttest x-rays were examined. Figure 2.3.15 shows the crucible after a 120° section has been removed to examine the interior. The upper crust of the SURC-3 cavity was covered with Zr cylinders which were slightly oxidized but otherwise intact. Nine cylinders (2.5 kg) were

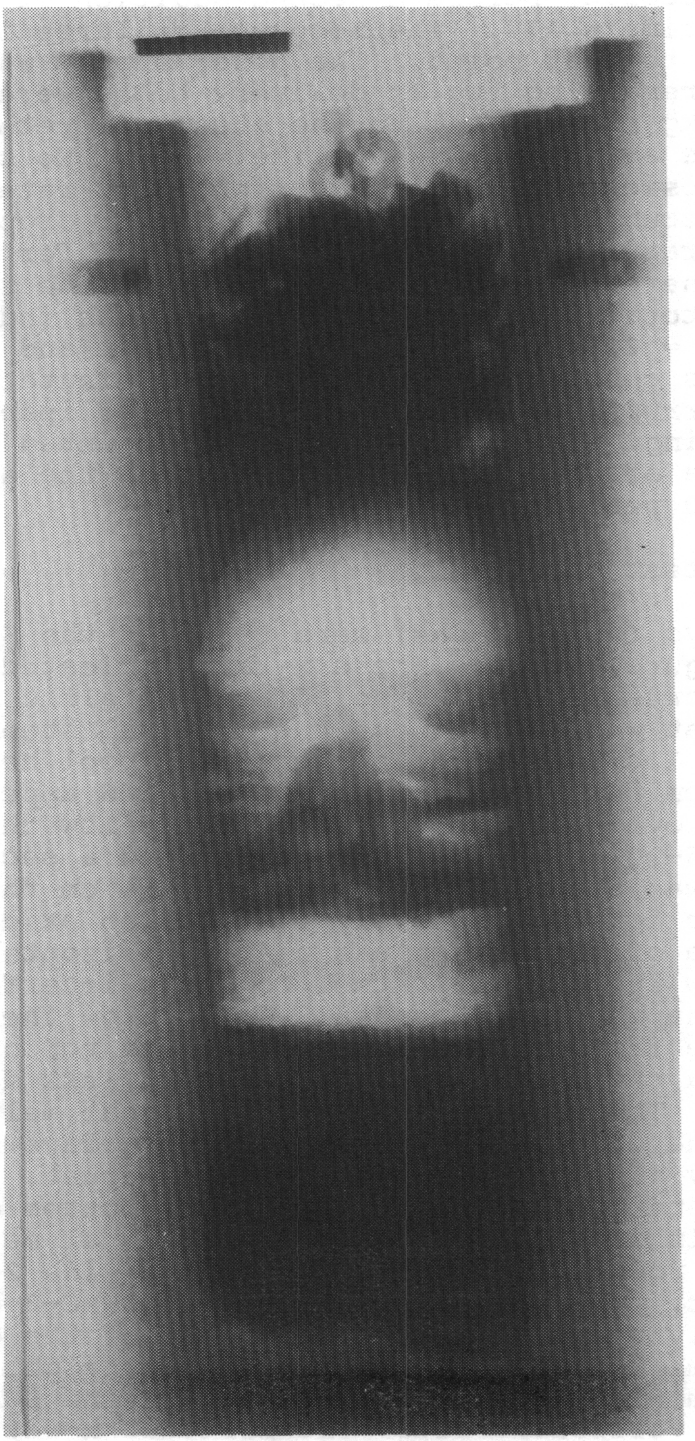

Figure 2.3.14 - SURC-3 Posttest X-ray

Figure 2.3.15 - SURC-3 Posttest Crucible Section

loosely piled on top of a slag mixture which contained an additional 5 cylinders (1.4 kg). This indicated that only four cylinders (1.1 kg) from the first Zr drop entered the steel meltpool at time 133 and that none of the Zr cylinders from the second drop at time 177 had a chance to interact with the melt. Examination of the open crucible also showed that the upper two crusts in the cavity were dense oxide melt debris while the third crust was a somewhat more porous oxide layer at the bottom of the cavity. The MgO sidewalls were slightly discolored and showed hairline cracks in several locations but were otherwise intact and showed no signs of interaction with the meltpool. The concrete in the bottom of the cavity was porous and discolored immediately next to the frozen melt to a depth of 1 cm. Four or five centimeters of concrete remained unaffected in the bottom of the cavity for a total erosion depth of 35 - 36 cm during the test.

2.3.6 Temperature Data Presentation

The 50 kg, 304 stainless steel charge, doped with fission product simulants was inductively heated for approximately 90 minutes prior to the onset of melting and concrete erosion. At t = 133 min, after eroding approximately 7 cm of concrete, and establishing a steady-state ablation rate, 5 kg of zirconium metal was released to the meltpool. At t = 177 min, after ablating approximately 23 cm of concrete, another 5 kg of zirconium was released to the meltpool. The test was terminated at t = 224 min after ablating 34 cm of concrete. The thermal response of the interaction crucible before, during and after the zirconium additions will be discussed in this section.

Three important regions of the melt/concrete interaction in SURC-3 are shown in Figure 2.3.16. The pool region is the high temperature melt that attacks the concrete. The pool consists primarily of stainless steel, but it also contains zirconium metal and condensed products of concrete decomposition and fission product compounds which may be molten. The "dry" region consists of the concrete that is dehydrated, decomposing to yield CO_2, and beginning to melt. The "wet" region is the concrete that still contains water in the concrete pores. The boundary between the "wet" and the "dry" region is taken here to be the point at which pore water undergoes the phase change to vapor.

Surrounding the three important regions of the melt/concrete interaction in the SURC-3 test, is the magnesium/oxide annulus. In an ideal circumstance, the confining annulus of the test would be totally inert. That is, it would neither conduct heat, off-gas, nor mechanically interact. Clearly, no such totally inert material exists and it is necessary to consider how the magnesia annulus affects the melt/concrete interaction.

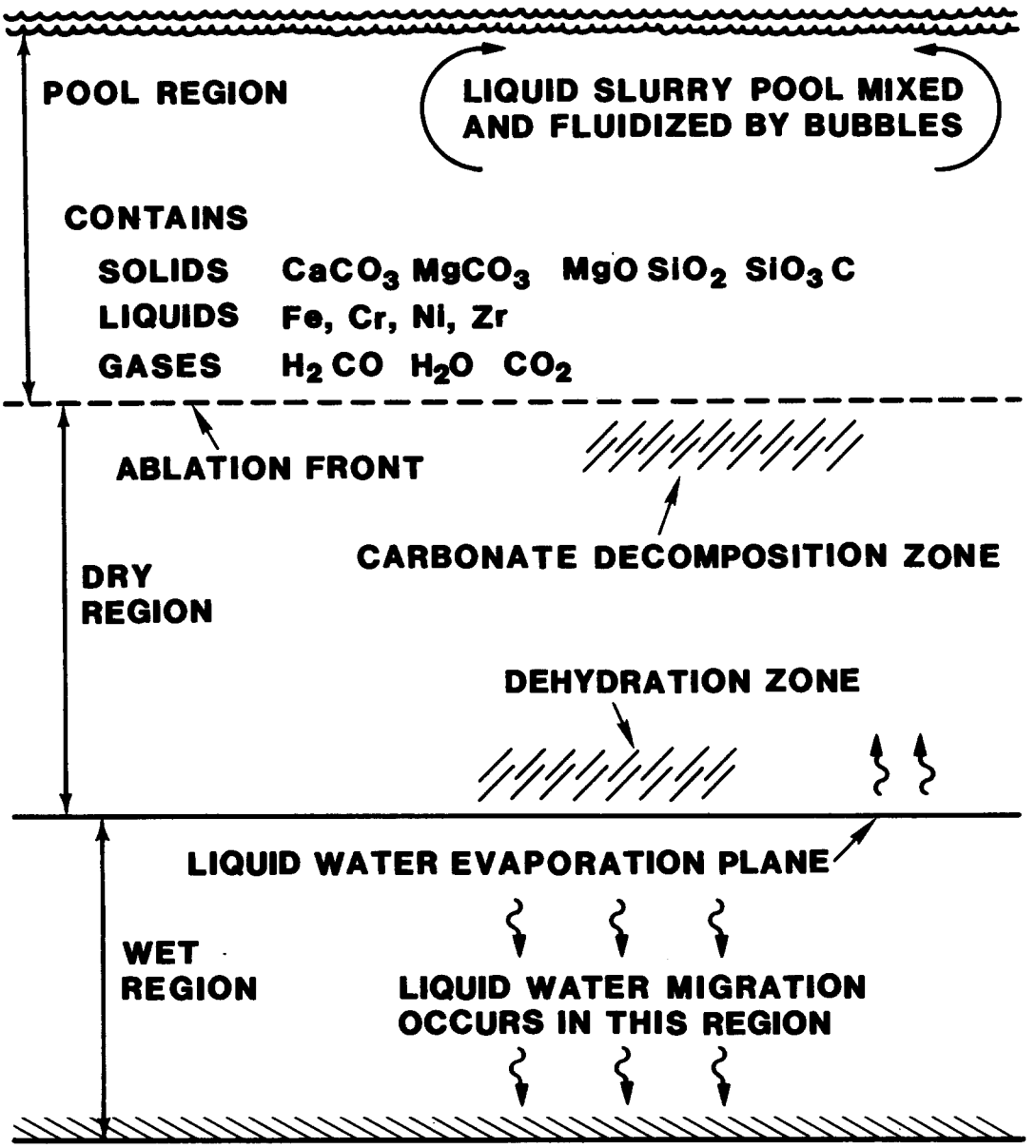

Figure 2.3.16 - Three Regions of Melt-concrete Interaction

In this section, the temperature data obtained in the SURC-3 experiment will be used to describe the three important regions of melt/concrete interactions and the magnesium oxide annulus.

The Concrete Slug

Some typical temperatures plotted as a function of time, indicated by thermocouples embedded in the concrete slug and during a period of steady-state ablation, are shown in Figure 2.3.17. Temperatures rise slowly to between 400 and 600 K followed by a rapid increase to failure caused by contact with the meltpool. The failure temperature for type K thermocouples is approximately 1645 K.

The propagation of the interface between the "wet" and the "dry" zones may be characterized in the SURC-3 test by the motion of the 400 K isotherm. The location of this isotherm is shown plotted as a function of time in Figure 2.3.18. The isotherm moves rapidly into the concrete between t = 34 and t = 45 min. Motion of the interface assumes a steady-state rate between t = 45 and t = 140 min. Approximately 7 min after the first zirconium addition, at t = 140, the motion of the isotherm increases significantly and remains constant for the next 30 minutes of the test. After t = 170, the interface velocity slows to a lower steady rate. The second addition of 5 kg of zirconium, delivered at t = 177 min, did not sffect the motion of the interface between the "wet" and "dry" zones and the motion of the interface continued at a reduced rate for the duration of the test. During the time period between t = 45 min to the end of the test the power supply was turned off numerous times from 1 to 5 minutes. None of these power excursions appeared to have an effect on the motion of this interface.

Linear regression of the interface position data indicates that the velocity of the interface prior to the first addition of zirconium and before it had time to react with the stainless and concrete is 8.2 ± 0.6 cm/hr. The time period considered for this calculation is between t = 45 and t = 140 min. The increased velocity of this interface after the initial zirconium addition observed between t = 140 and t = 170 min was calculated to be almost three times the initial rate or 24 ± 1.5 cm/hr. After t = 170, interface velocity drops to 12 ± 1 cm/hr.

The limestone concrete used in the SURC-3 experiment melts over the temperature range of 1653 to 1873 K. The temperature at which physical ablation of the melting concrete occurs is not precisely known. Here it is assumed ablation occurs at 1600 K for the purpose of measuring the propagation of the erosion front. This was done as a matter of convention and could have been any value between 1000 K and 1800 K since the delay time from 1000 K to failure for any thermocouple was less than 30 seconds as seen in Figure 2.3.17. The position of the 1600 K isotherm as a function of time is shown in Figure 2.3.19. Ablation began at approximately t = 82 min and arrested at t = 92

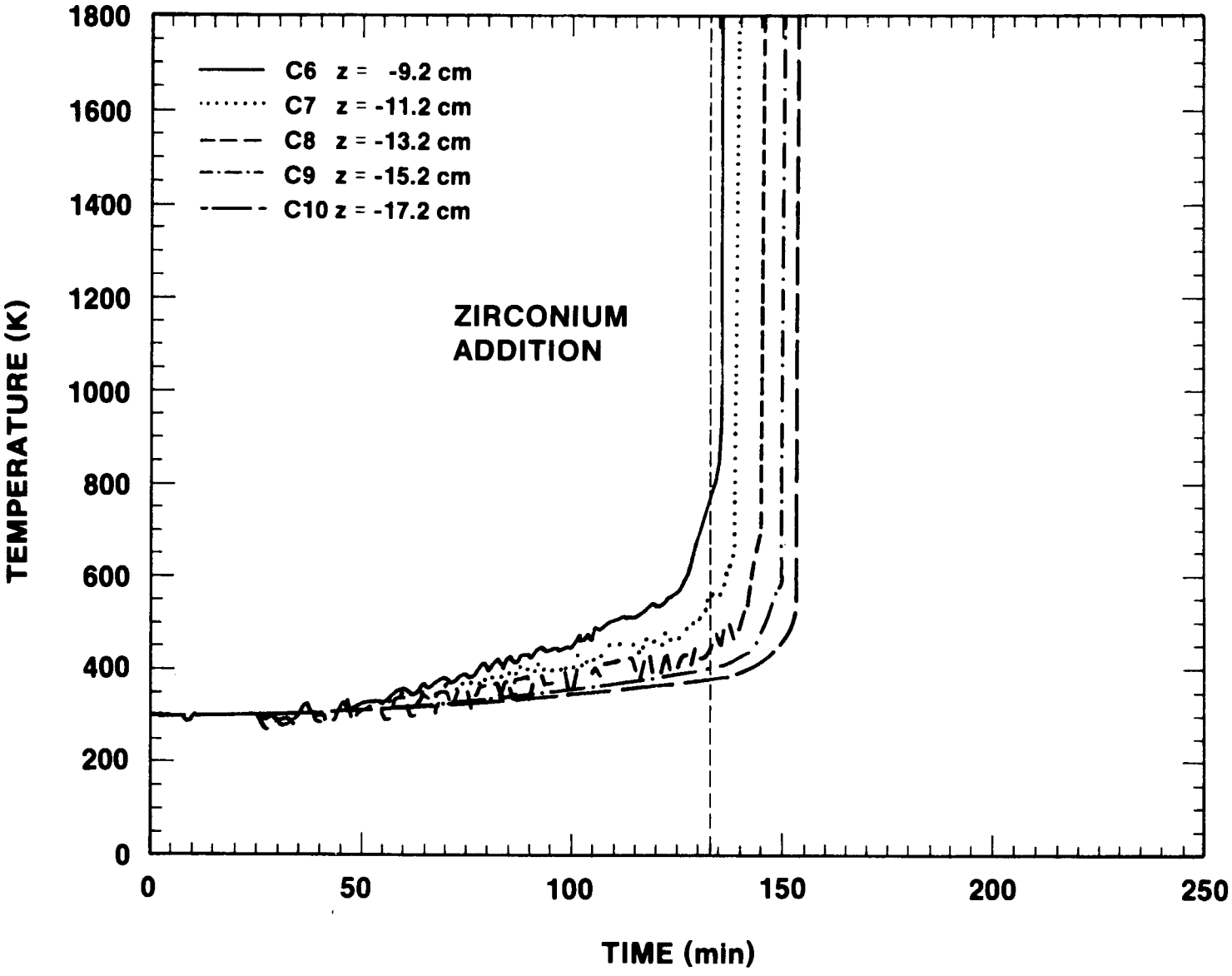

Figure 2.3.17 - Typical Temperatures Indicated by Thermocouples Embedded in the Concrete Slab

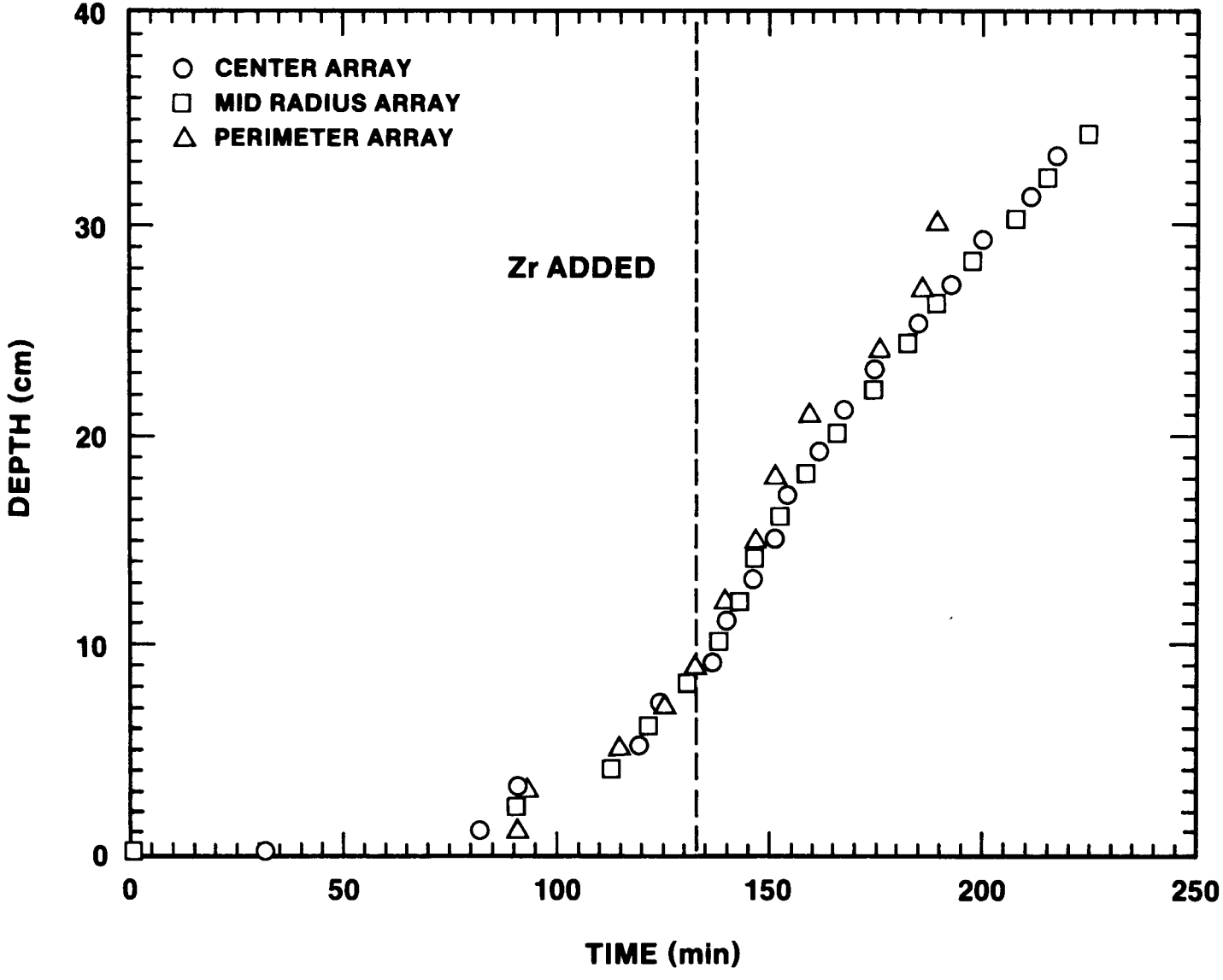

Figure 2.3.18 - SURC-3 Dehydration Front. This is a plot of the 400 K isotherm location in the concrete.

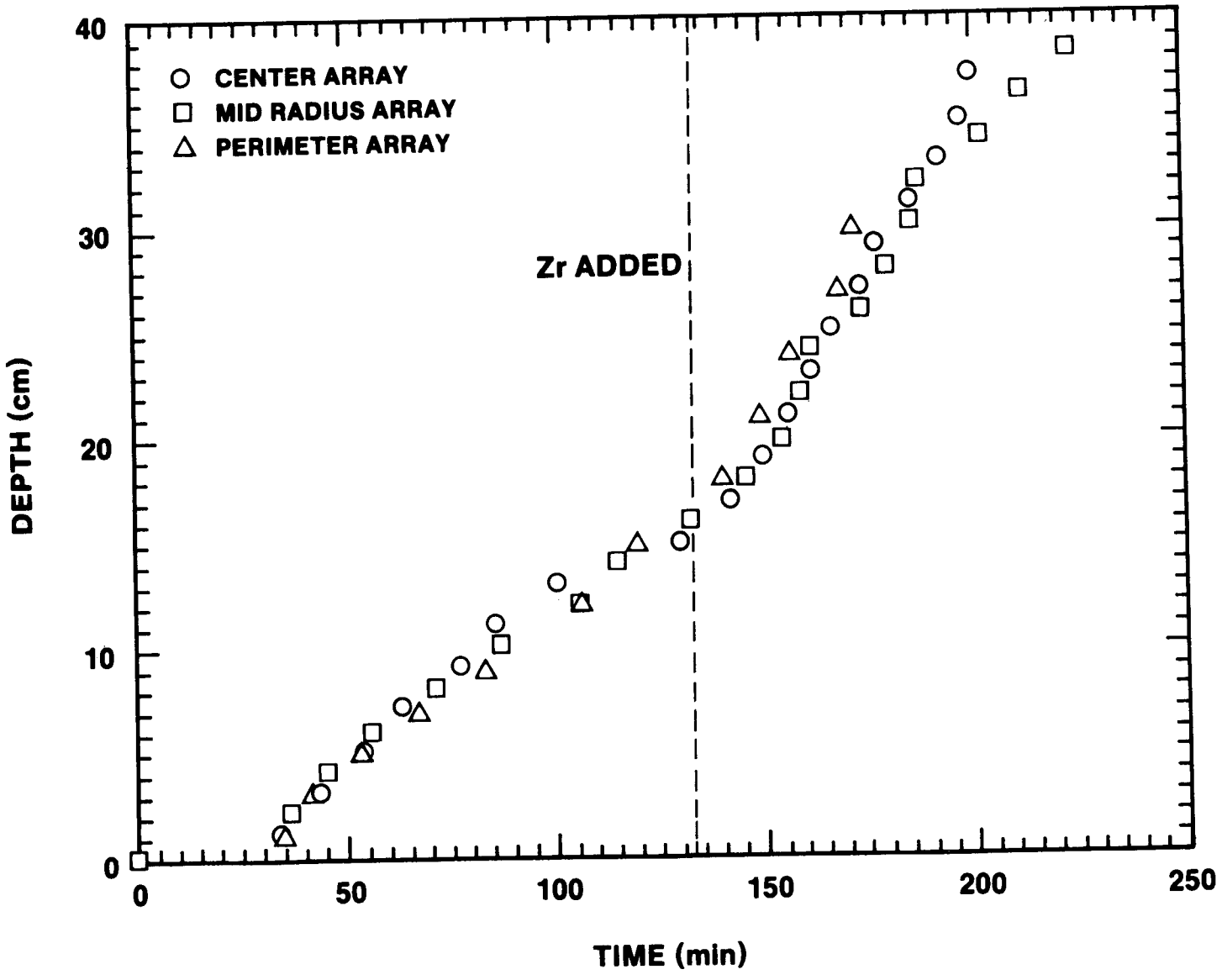

Figure 2.3.19 - Ablation Event History for the SURC-3 Experiment. This is a plot of the 1600 K isotherm location in the concrete.

min. After a 21 minute pause, the ablation front began advancing again moving at nearly a constant rate between t = 113 and t = 135 min. The inductive power supply was turned off twice during the arrest period between t = 92 and 113 min. The power supply was turned off the first time at t=93 min for approximately 4.4 minutes and was turned off the second time for a period of 1.7 minutes at t = 106 min. During the 21 minute arrest period, the power supply was off a total of 6.1 minutes. After a successful zirconium addition at t = 133 min the motion of the ablation front noticeably increases between t = 135 and t = 155 min. After t = 155 min the motion of the ablation front again decreases to what appears to be the initial rate prior to the zirconium addition. The second attempt to add zirconium was unsuccessful and no effect on the motion of the ablation front was observed.

Applying a linear regression analysis to the data for the three distinct ablation periods observed in Figure 2.3.16 yields the ablation velocities. During the initial period prior to zirconium addition between t = 113 and t = 133 min the velocity of the ablation front was calculated to be 13.9 ± 0.3 cm/hr. The propagation rate after the zirconium addition between t = 133 and t = 159 was calculated to be 26.7 ± 0.8 cm/hr. This is slightly less than double the initial rate. The velocity of the ablation front during the latter period of the test between t = 159 and t = 224 min was nearly the same as the initial rate. The velocity of the ablation front during this period was calculated to be 14.1 ± 1.0 cm/hr.

The depth to which the concrete was dehydrated can be determined by comparing the the position of the 400 K (wet/dry interface) and 1600 K (ablation front) isotherm at a specific time. Figure 2.3.20 shows a plot comparing data representing the 400 and 1600 K isotherms. The depth of the dehydrated concrete is initially 8 cm at t = 90 min. The 1600 K isotherm converges to within 3 to 4 cm of the 400 K isotherm near t = 155 min. After this time the 400 K isotherm precedes the ablation front by 5 cm on the average for the remainder of the test.

The Steel/Zr Meltpool

Melt temperatures were also measured during the experiment with six type C and S thermocouples installed in alumina tubes and cast at various depths within the concrete slug. A typical temperature response of these thermocouples plotted against time is shown in Figure 2.3.21. Other individual plots of melt temperature can be found in Appendix H. The figure shows that the temperature increases slowly between 300 and 600 K. The temperature then rises rapidly upon contact with the advancing melt front arresting at a peak usually lasting several minutes. These plateaus closely match the failure times of the type K thermocouples from the center array. Figure 2.3.22 shows a plot of the peak-meltpool temperatures prior to failures during the test. The meltpool temperature ranged between 1950 and 2050 K.

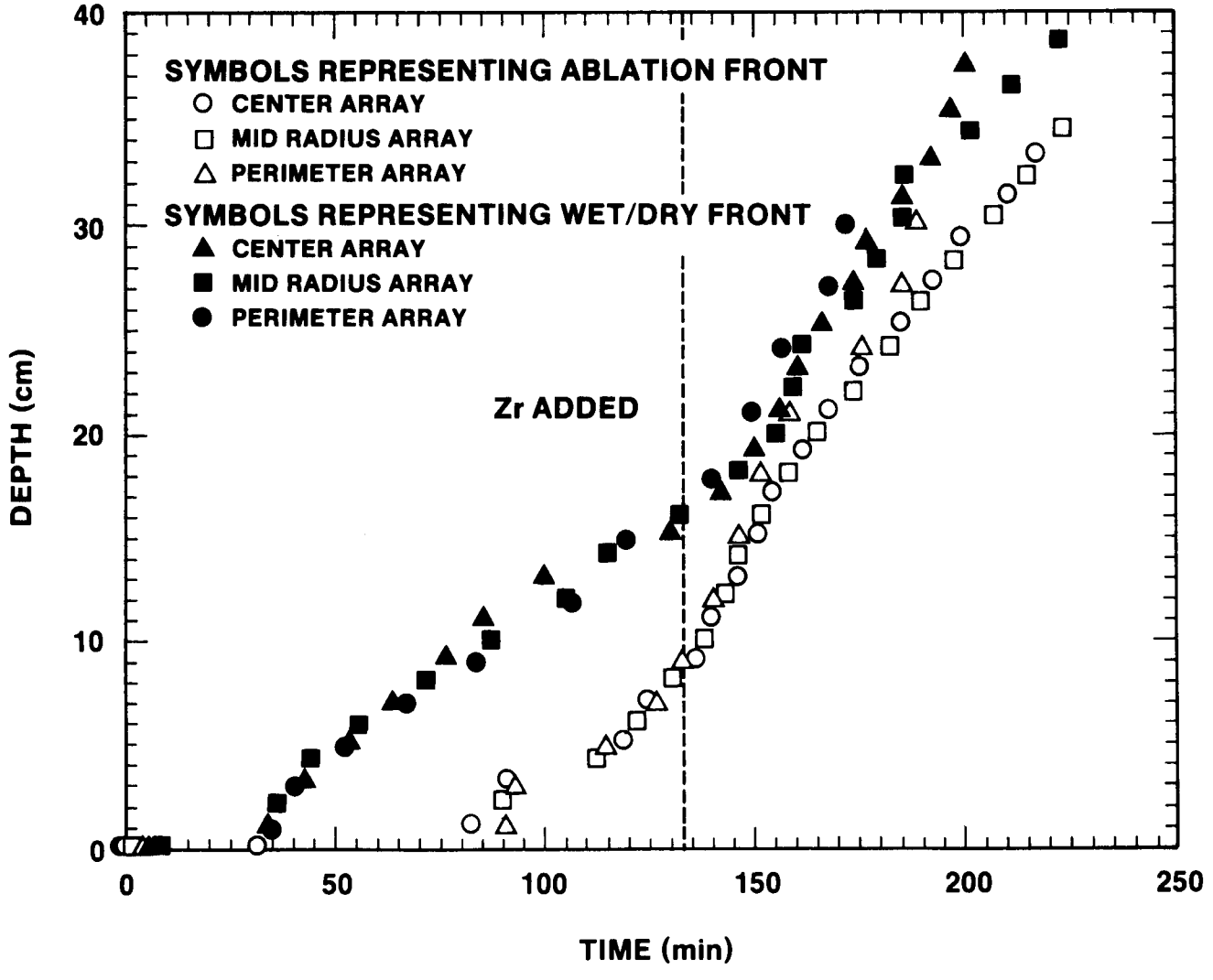

Figure 2.3.20 - Comparison of the location of the 400 K and 1600 K Isotherms.

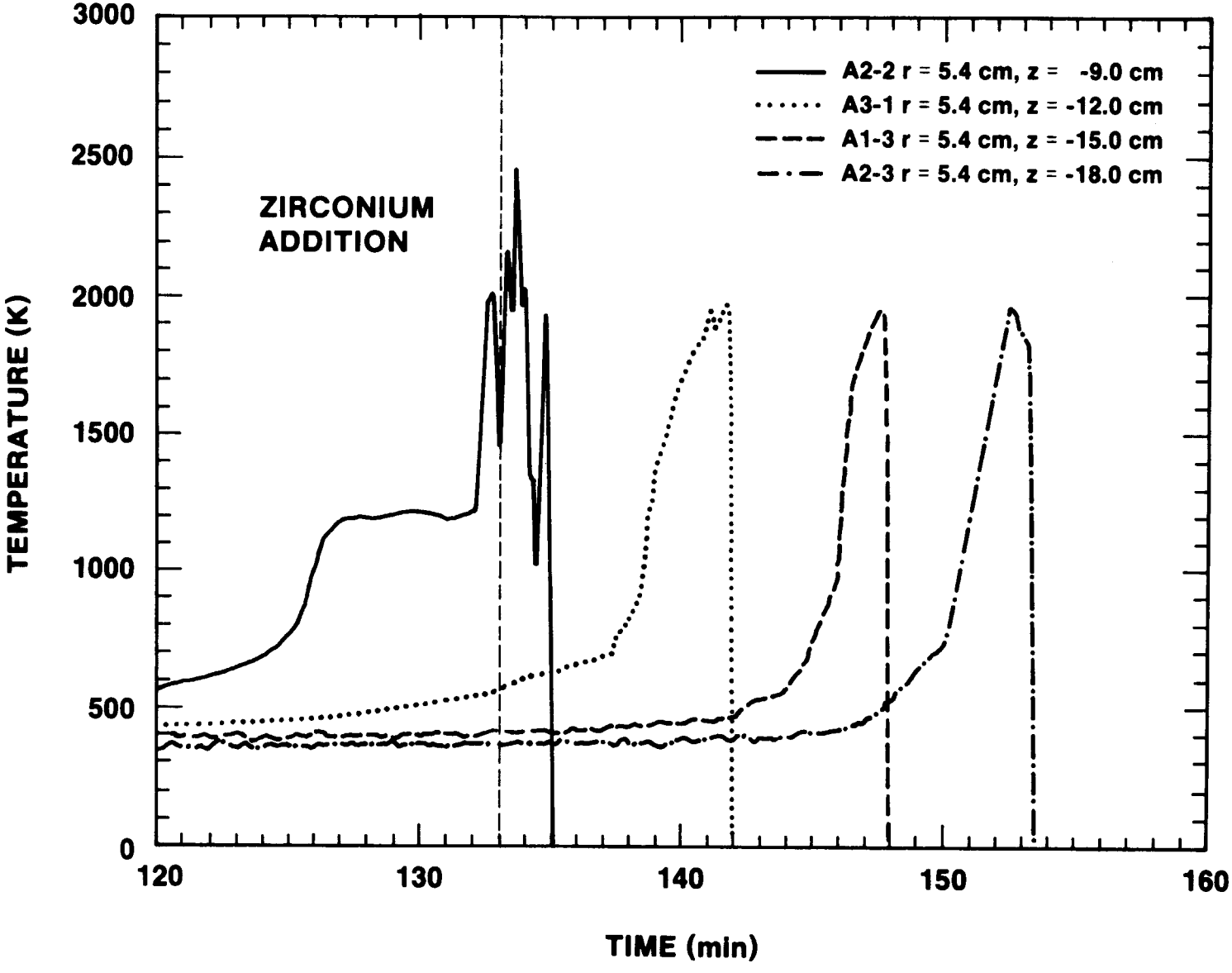

Figure 2.3.21 - Typical Temperatures Indicated by Type C and S Thermocouples Installed into Alumina Tubes, Embedded in the Concrete Slug.

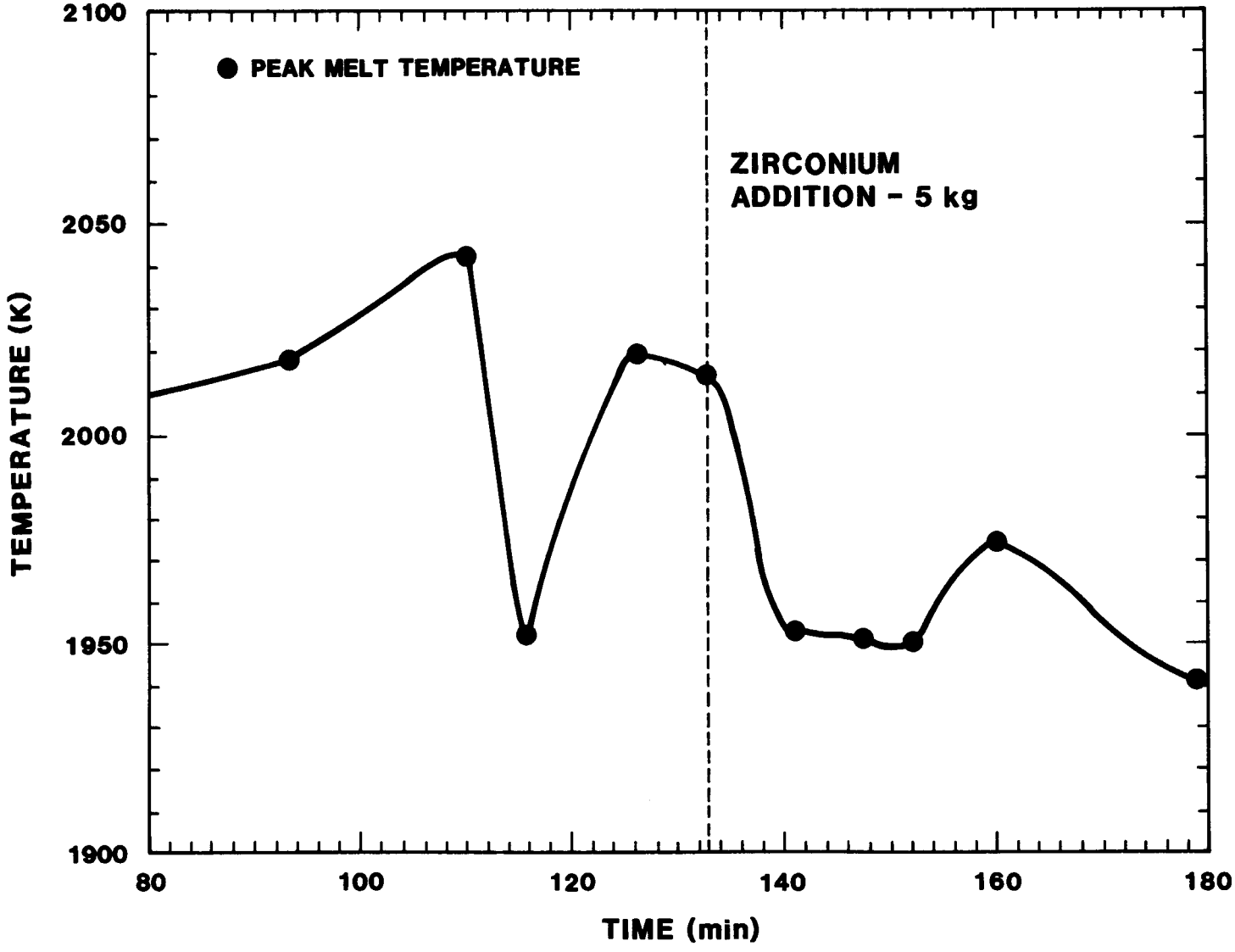

Figure 2.3.22 - Peak Melt Temperatures Indicated by Type C and S Thermocouples Installed in Alumina Tubes and Embedded into the Concrete Slug.

This amounted to a superheat in the steel of between 250 and 350 K. The results show that the 304 stainless steel reached its melt point of 1700 K at 80 minutes into the test. After 90 minutes, concrete erosion began along with a meltpool temperature increase from 1700 to 1950 K, indicating a superheat of 250 degrees. These temperatures were maintained for 40 minutes during which 8 to 10 cm of concrete were eroded. Zirconium was then added to the melt at time 133. Melt temperatures after 130 minutes rose briefly to 2020 K then decreased to 1950 K for the remainder of the test. There was no observed effect on the meltpool temperature after the second attempt to add zirconium at t = 177 minutes.

MgO Sidewalls

The heat transfer into the MgO sidewalls during the interaction has a global effect on the energy balance and therefore, the heat transfer to the concrete. As discussed in Section 2.3.2 thermocouple arrays were installed at various locations within the MgO annulus to determine the thermal response of the sidewalls to the heat flux imparted by the meltpool. A typical temperature versus time history for the sidewall array located adjacent to the melt at an elevation of z = 10 cm is shown in Figure 2.3.23. Thermocouple M21 located at a depth of 1.0 cm rises rapidly and fails at approximately t = 92 min. Thermocouples M22 and M23 located at depths of 2.2 and 3.0 cm respectively, peaked at a temperature of 1450 K and declined to a value of 1200 K at t = 250 min. The thermocouple located at a depth of 9 cm near the perimeter of the annulus rises gradually and peaks at a temperature of 1150 K at t = 220 min. The temperature versus time histories measured by thermocouples in other arrays, cast into the MgO sidewall, are presented in Appendix H.

The calculation of heat of heat flux to the MgO walls is a classic example of an "inverse" heat conduction problem (IHCP) [Beck, 1985] where the boundary condition (e.g., heat flux) is determined from known interior temperatures. Of the available methods for solving the IHCP, the one that appears to be most successful for the widest variety of applications is the non-linear estimation technique proposed by Beck [1985]. In this method, the value of the calculated heat flux minimizes the square of the difference between the calculated and the experimental temperatures. A computer code, IHCP, has been written by Bradley [1986] based on Beck's methods. The code was tested using a variety of exact solution problems and was found to perform excellently. The accuracy of this method is strongly dependent upon the thermocouple data and the material property data. In general, it was found that the greater the number of thermocouples utilized in the analysis, the greater the accuracy of the solution. However, Bradley found beyond three thermocouples, the improvement in accuracy was not sufficient to justify additional thermocouples. The

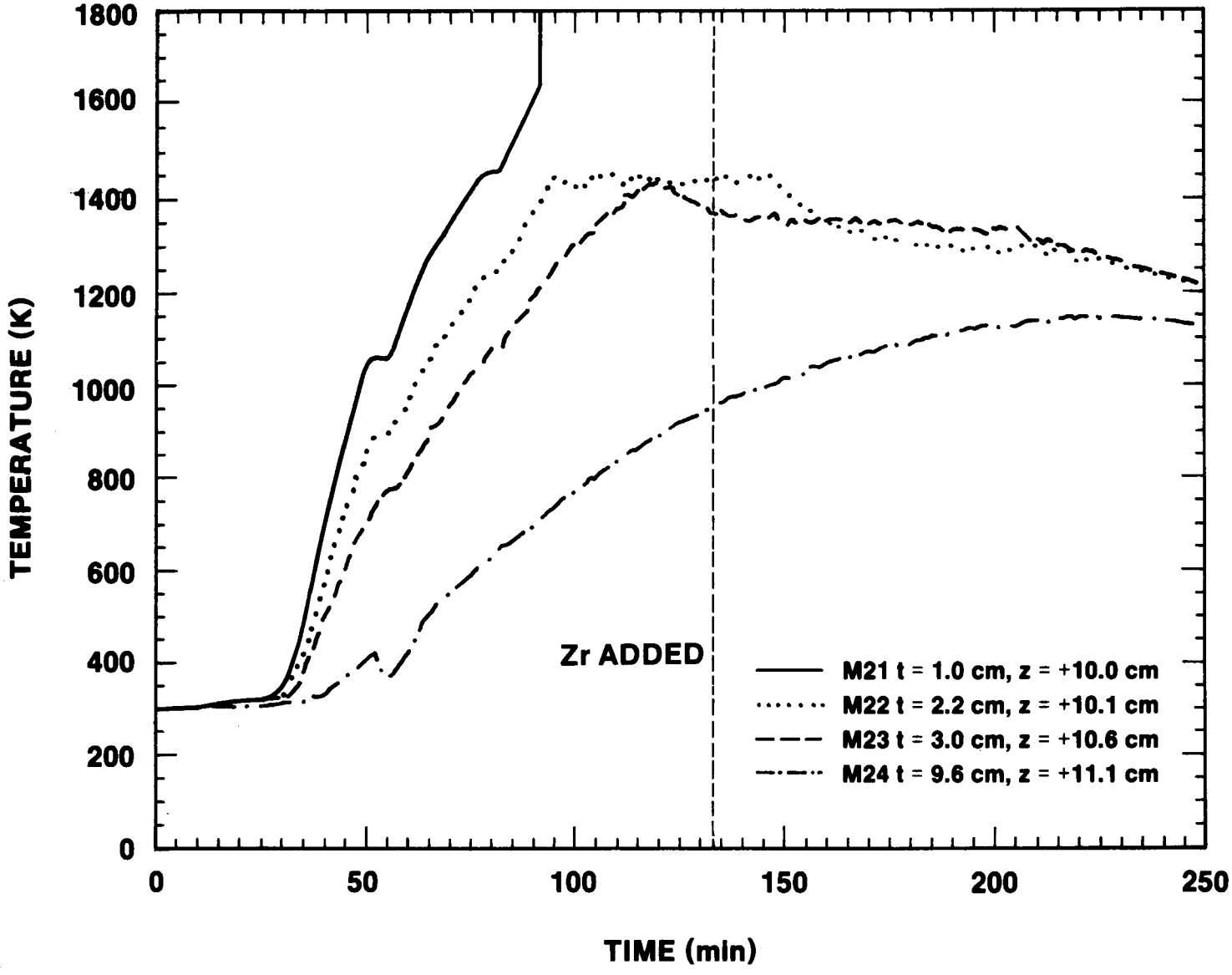

Figure 2.3.23 - Typical Thermocouple Data Measured by the Sidewall Array located at Z = 10.0 cm.

experimental data recorded, and utilized in the IHCP, consisted of at least three thermocouples at depths from the surface of 1, 2 and to 3 cm into the MgO sidewall and an occasional one at 9 cm. The IHCP solution was calculated for each array of the thermocouples that was imbedded in the MgO sidewall at various locations above and below 0 cm, the original location of the concrete surface.

The thermal properties for the MgO used to calculate the sidewall heat fluxes are listed below:

Density (kg/m^3)	2640
Specific Heat (J/kg K)	1250
Thermal Conductivity (W/m K)	$k = aT + b$

Where: $a = -5.0 \times 10^{-3}$
$b = 8.193$
T = temperature in K

Minimal Thermal Conductivity (W/m K) = 1.955

Shown in Figure 2.3.24, 2.3.25 and 2.3.26 are the heat flux histories for the sidewall arrays initially below the melt, adjacent to the melt and above the melt, respectively. Heat flux histories for other sidewall arrays are shown in Appendix H. Figure 2.3.24 shows the heat flux at z = -24.1 cm. The heat flux slowly increases to a value 2×10^4 W/m^2 at t = 160 min and sharply increases peaking at a value of 2.5×10^5 W/m^2 at t = 185 min. This peak corresponds with the position of the ablation front. The heat flux then gradually decreases to 1×10^5 W/m^2 at t = 245 min. as the MgO wall is heated.

The thermocouples in the array located at z = 10.0 cm (Figure 2.3.25) were directly adjacent to the melt during the heating, melting and the early period of erosion. The heat flux history at this elevation is sensitive to fluctuations in the power delivered to heat and sustain the melt. The power supply is initially turned on at t = 7.9 min at a power setting of 165 kW for 2.6 minutes and turned off. As can be seen in Figure 2.3.25 the heat flux increases from 3.5×10^2 W/m^2 to 5.5×10^3 W/m^2. During the period between t = 10.5 and t = 26.6 min the power supply is off and the heat flux decreases during this period to 4×10^3 W/m^2. The power supply is turned on again at t = 26.3 min and the heat flux increases rapidly to a value of 1.05×10^5 W/m^2 at t = 42 min. The heat flux calculated for this location remains in a range between 1.07×10^5 and 4.9×10^5 W/m^2 for the duration of the test. Small decreases in the heat flux history appearing as shallow valleys in the data are caused by the power supply being turned off for short durations (1 to 5 minutes). There appears to be no significant effect on the heat flux from adding the zirconium at time 133.

Thermocouples in the sidewall array at z = 30.1 cm (Figure 2.3.26) were always above the melt during the experiment. The

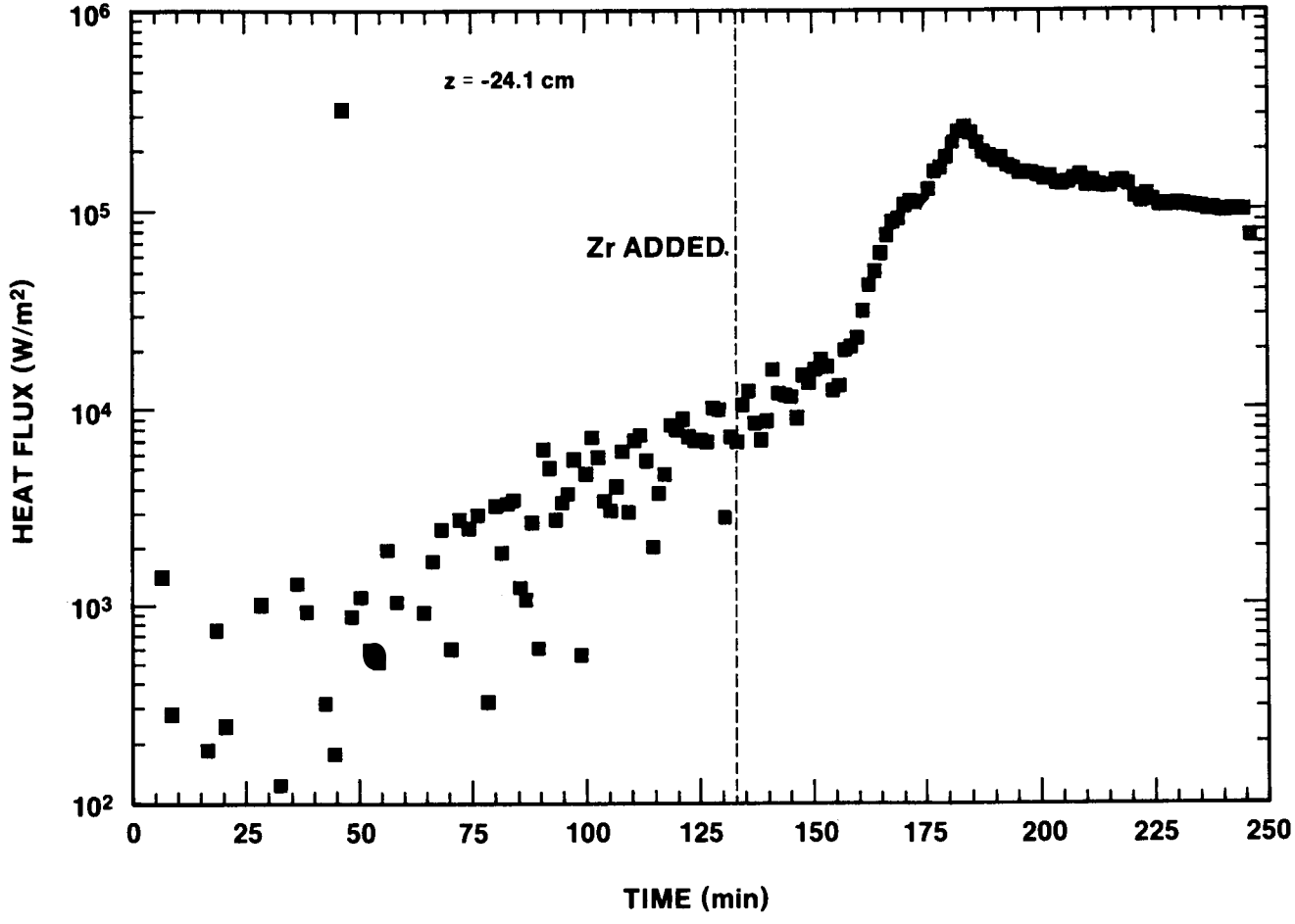

Figure 2.3.24 - MgO Sidewall Heat Flux History for z = -24.1 cm, Test SURC-3.

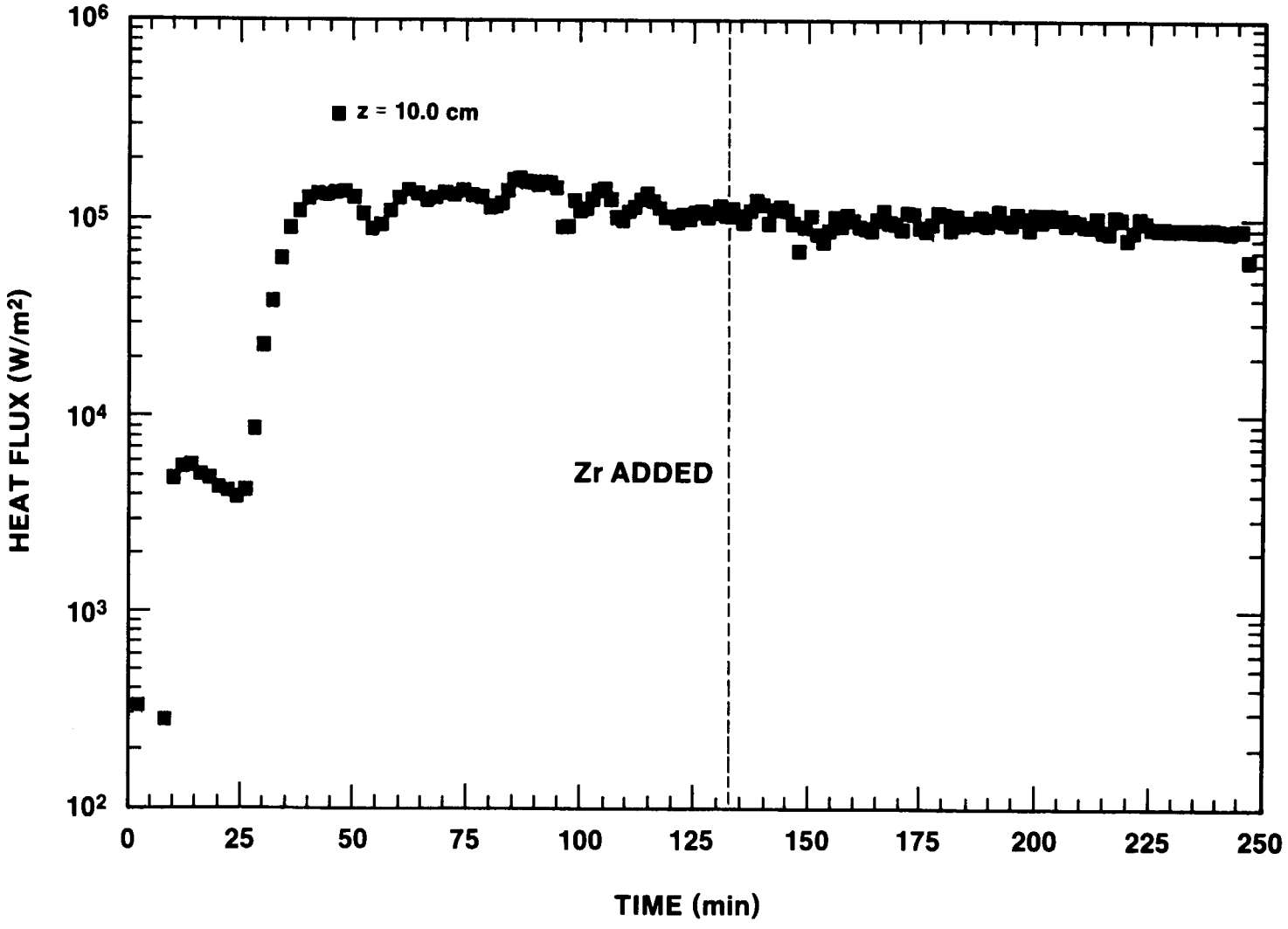

Figure 2.3.25 - MgO Sidewall Heat Flux History for z = 10.0 cm, Test SURC-3.

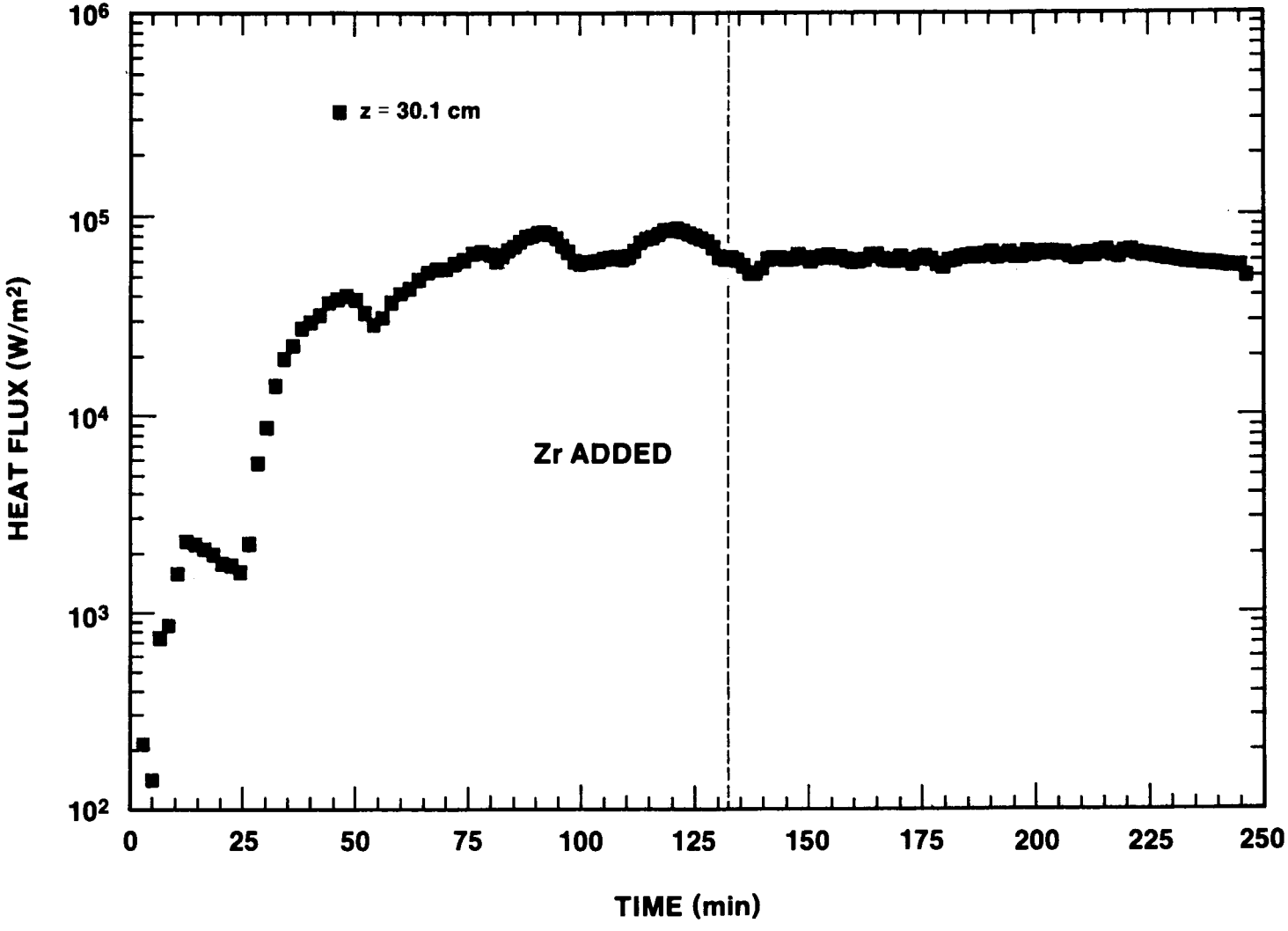

Figure 2.3.26 - MgO Sidewall Heat Flux History for z = 30.1 cm, Test SURC-3.

heat flux history at this elevation is also sensitive to the power delivered to the melt. This can be observed by the peaks and dips observed between t = 0 and t = 140 min. which correspond to the power supply fluctuations recorded in Figure 2.3.12. The value of heat flux calculated at this elevation peaks at 8 x 10^4 W/m^2 at t = 90 and again at t = 120 min. The heat flux decreases gradually to a value of 6 x 10^4 W/m^2 and remains constant for the remainder of the test.

In summary, the heat flux when the melt was directly adjacent to the MgO sidewall arrays was calculated to be between 4.9 x 10^4 and 1.05 x 10^5 W/m^2. The array located above the melt inferred heat fluxes in the range of 5.5 x 10^4 and 8.0 x 10^4 W/m^2. Heat fluxes indicated by the array embedded in the sidewalls below the concrete surface, increased to a value near 2.0 x 10^5 W/m^2 when the melt was directly adjacent to the array. This value decreased to a value between 7.5 x 10^4 and 1.0 x 10^5 W/m^2 as the melt continued to penetrate the concrete and pass the array.

2.3.7 Flow Data Presentation

Five different devices were used to measure the reaction gas flow rate in SURC-3: A 1.02 cm orifice plate, a laminar flow element, a turbine meter, a Rockwell 450 gas clock, and a Rockwell 750 gas clock. Figure 2.3.27 shows a flow train schematic of the hardware for SURC-3.

The orifice plate flowmeter is probably the most widely used flowmeter in service today. It is found mostly in field use and is simple, rugged, reliable, accurate, and inexpensive. The principles of operation and pertinent equations for orifice plate flowmeters are well established [Baker, 1983]. Orifice plates used for gas measurement are considered to be accurate to 1-2% based on physical dimensions and published correction factors alone. It should be noted, however, that uncertainties in differential pressure (the measured parameter), temperature, line pressure, and gas density can easily overwhelm the laboratory calibration. One disadvantage of the orifice plate is that a 10:1 change in differential pressure results from only a 3:1 change in flow due to the square root relationship between differential pressure and flow. Thence, 50% of expected full flow is measured in 20% of expected differential pressure. This makes low flow rates difficult to measure accurately.

The orifice flowmeter used in the SURC-3 experiment had an opening of 1.02 cm and was mounted between flanges in a 5 cm i.d. pipe. This pipe was mounted to the SURC-3 expansion chamber so that 80 cm of straight pipe preceded the flow device and at least 50 cm of straight pipe followed the device. Three Validyne pressure transducers were used in conjunction with the orifice plate. Two of these were used to record the differential pressure across the plate and had operational ranges of either 0-2 psia or 0-10 psia. The third pressure transducer was used to measure the system pressure and had a range of 0-10 psig. All of

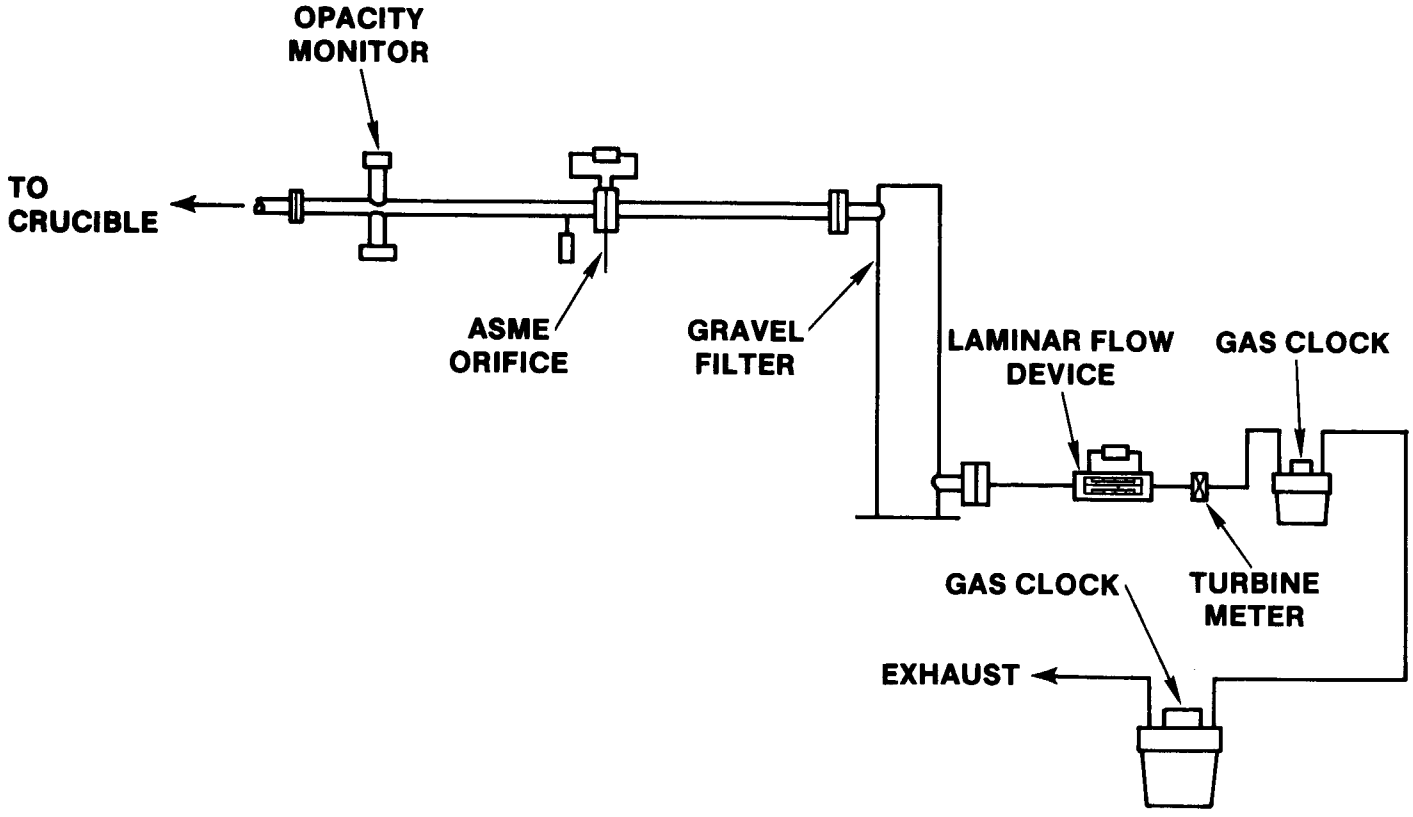

Figure 2.3.27 - Flow Instrumentation Schematic

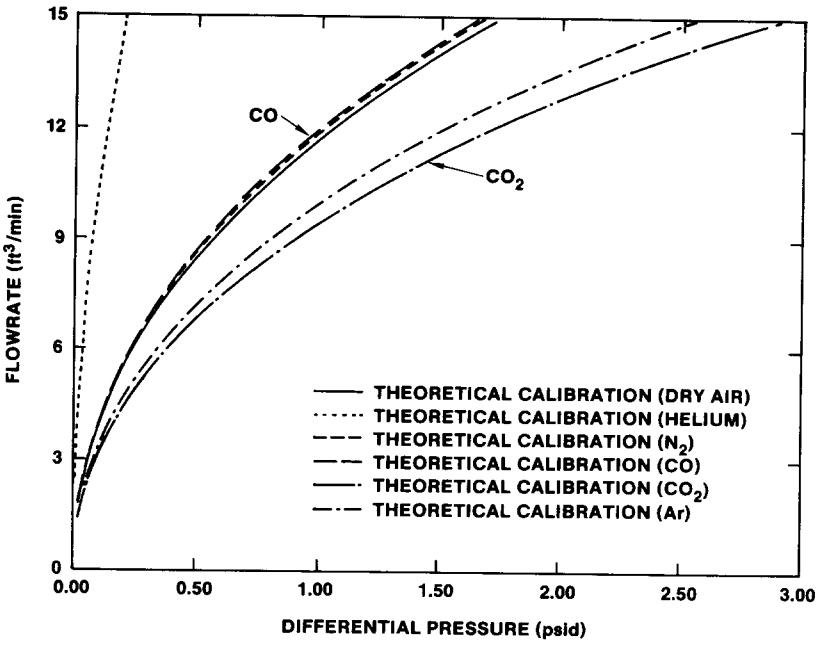

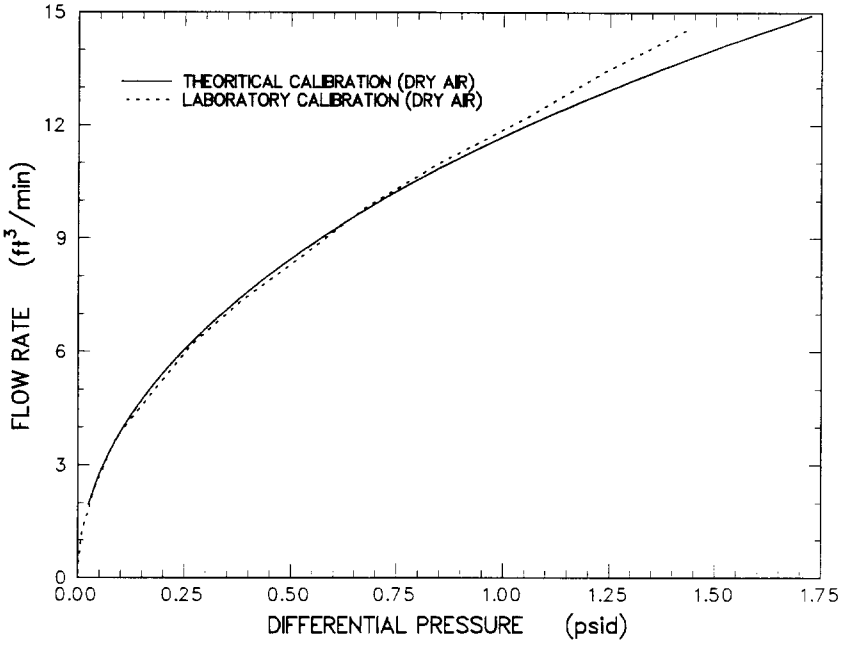

Figure 2.3.28 - Laboratory Calibration of the ASME Orifice Plate

these devices were calibrated as a set--both in the laboratory and at the test site--using several different gases and a range of flow rates. Results of the laboratory calibration are shown graphically in Figure 2.3.28.

The laminar flow element (LFE) is a group of capillary tubes bundled together to form a matrix such that the flow through each passage is laminar, even though the total flow upstream of the device may be turbulent. The LFE is not as sensitive to piping configuration as an orifice plate so that one or two pipe diameters (instead of 5 or 10) is usually sufficient to provide a well-characterized flow pattern. The equations governing the operation of LFE devices are described by Baker [Baker, 1983]. One advantage of an LFE is that the relationship between differential pressure (the measured parameter) and flow is linear for the range of flows for which it is designated. Calibration of the device should be done against a primary standard and is a function of gas viscosity which is itself a function of gas composition. A potential disadvantage is that the small passages in the flow matrix are susceptible to plugging when the gas contains aerosols or water vapor, although they are easy to clean.

The LFE used in the SURC-3 experiment was designed and built by Calibrating and Measuring Equipment (CME) and has a nameplate flow range of 0-300 slpm for air at standard conditions. The LFE is contained in a 50 cm pipe with an i.d. of 3.6 cm. Differential pressure is measured using a Validyne differential transducer with a range of 0-2 psia. The device was calibrated both in the laboratory and at the test site. Laboratory calibration (Figure 2.3.29) was done using a variety of gases with NBS-traceable critical orifices as the primary standard.

The turbine flow meter [Baker, 1983] consists of a freely rotating blade or propeller mounted concentrically in a pipe. The force of the gas striking the blades causes them to rotate at an angular velocity proportional to the gas velocity so that the volumetric gas flow is directly proportional to the rotational speed of the propeller. A magnetic pickup in the rotor causes a voltage to be generated in an external electrical coil. The magnitude of the voltage is then directly proportional to the volumetric flow rate for the designated flow range of the device. The output of the device is in actual liters per minute (ALPM) and must be corrected to STP. Turbine flow meters must be calibrated to determine the coefficient of discharge but once this is done are considered to be accurate to about 1%. Some advantages of the turbine floweter are that it is insensitive to gas composition and it produces a linear response over its design flow range. Some disadvantages are that it is susceptible to drag if the gas contains aerosols or water and that the magnetic pickup can be affected by an induction or electrical field.

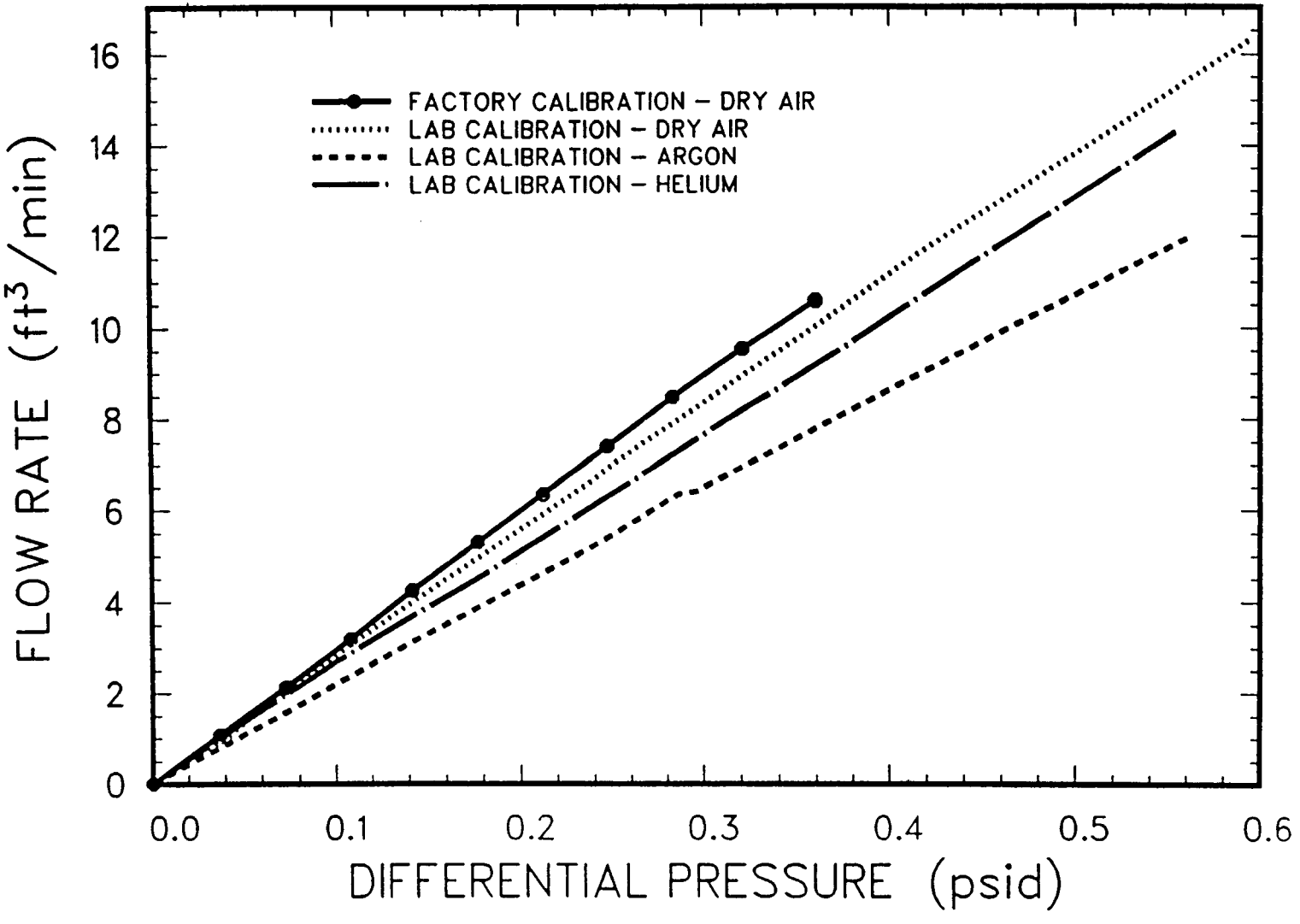

Figure 2.3.29 - Laboratory Calibration of the LFE

The turbine meter used in SURC-3 was made by Flow Technology, Inc., and is contained in a 50 cm long pipe with an i.d. of 2 cm. The operating range of the device is 0-280 slpm as indicated by a voltage output of 0-10 volts d.c. The turbine meter was calibrated in the laboratory and at the test site using Ar, He, air, and CO_2. Results of the laboratory calibration are shown in Figure 2.3.30.

The Rockwell gas clocks used in SURC-3 are dry gas meters. These devices have four bellows-type chambers that alternately fill and empty known volumes of gas. The slide valves that control the cycle are attached to mechanical counters that totalize the volume of gas that passes through the meter. These devices are very rugged and bulky [Baker, 1983] and register the total volume in ALPM. They are impervious to the aerosol or water content in the gas and measure total volume independently without corrections for density or viscosity. Once the volume of the bellows is known, their accuracy is within 1%. The major disadvantages of the dry gas meter are its size and lack of sensitivity to transient flow perturbations.

The Rockwell 415 was manufactured by Rockwell and has a stated operational range of 0-200 lpm at STP. The device has a sensitivity of 28.3 liters per bellows cycle. The Rockwell 750 was also manufactured by Rockwell and has an operational range of 0-350 lpm at STP. The Rockwell 750 gas clock has a sensitivity of 283 liters per bellows cycle. Both devices were calibrated in the laboratory and at the test site with different gases and a range of flow rates. The laboratory calibration is shown in Figure 2.3.31.

After the experimental setup was completed for the SURC-3 test, an insitu calibration was performed using N_2, Ar, and CO_2. This was done to insure that the laboratory calibrations were still valid, to evaluate the entire flow system, and to determine the system pressure as a function of flow rate. Results of the in-situ calibration for the orifice flowmeter, LFE, turbine meter, and system pressure are given in Table 2.3.9. In addition, a systems leak test was performed by valving off the flow train and pressurizing the crucible and expansion chamber. A pressure decay chart for this procedure is given in Table 2.3.10. Based on the insitu checks, the initial leak rate from the crucible was calculated to be 10 slpm at a system pressure of 2.0 psig or 6% of the 165 lpm flow rate.

Results

Five time periods are of interest for the SURC-3 flow data. These are the onset of gas release from concrete from time 50-80, the gas release associated with the start of concrete ablation between time 80-95, the steady-state erosion gas release from time 105-125, the increased reaction rate due to Zr interactions between time 135-150, and the return to steady-state erosion at

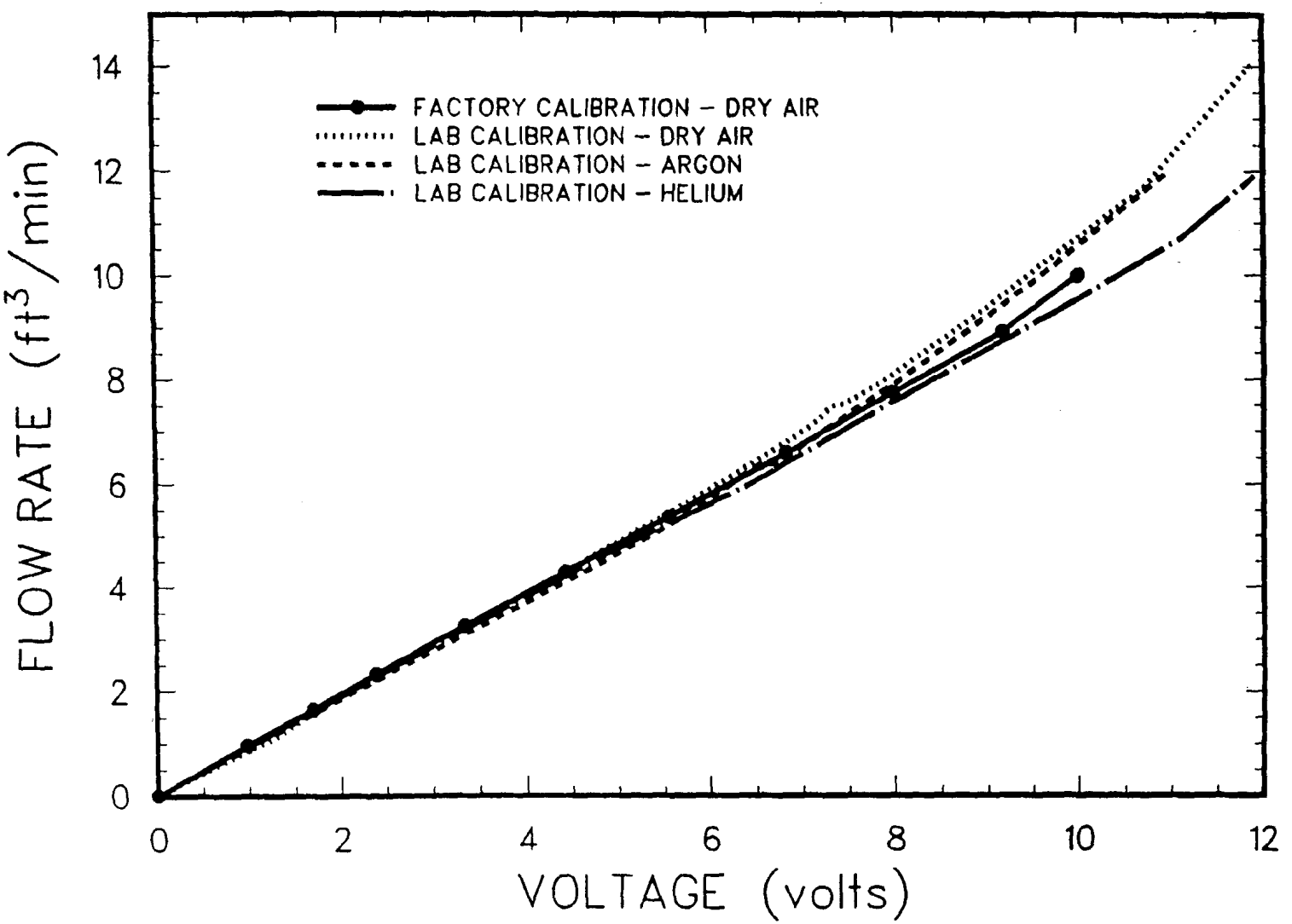

Figure 2.3.30 - Laboratory Calibration of the Turbine Meter

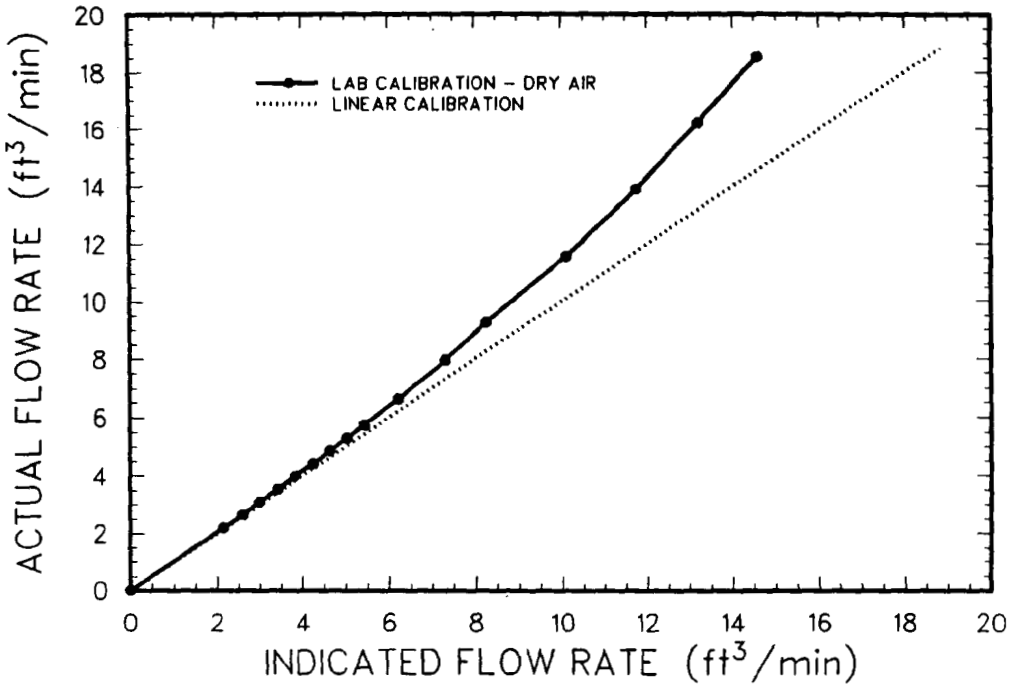

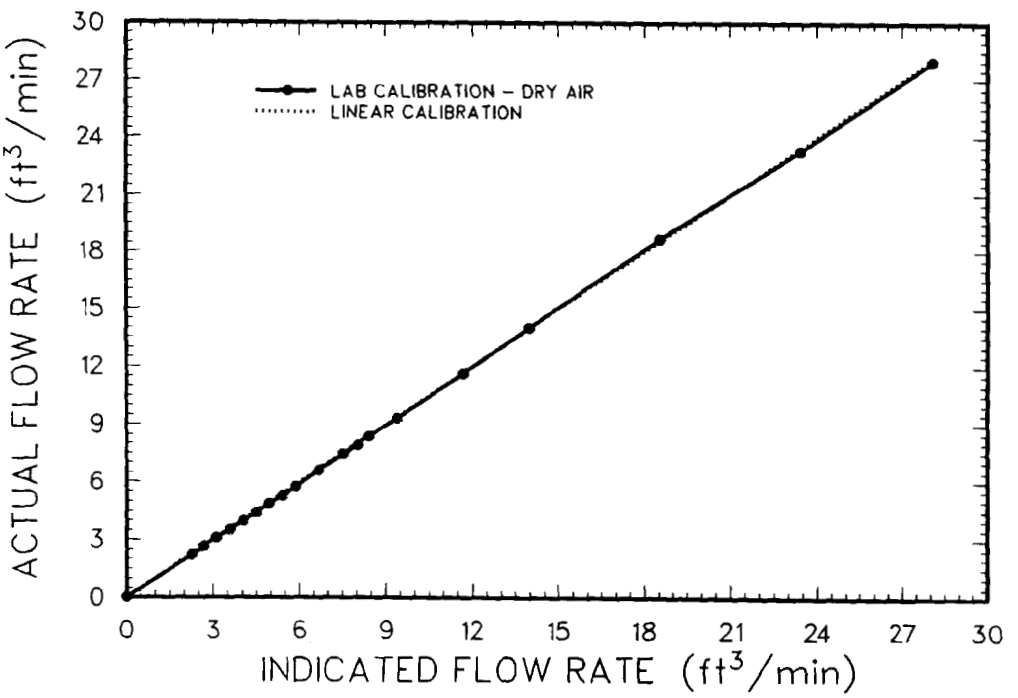

Figure 2.3.31 - Laboratory Calibration of the Rockwell Gas Clocks

TABLE 2.3.9

Insitu Calibration* for SURC-3 Flow Devices

Inlet Flow SLPM	System Pressure PSIG	ASME Orifice SLPM	LFE SLPM	Outlet Turbine SLPM
175	2.0	167	164	161
121	1.1	115	118	110
61	.3	56	60	58

* Calibration done with argon gas.

TABLE 2.3.10

Pressure Decay and Leakrate for SURC-3
Crucible, Expansion Chamber and Flow Train*

Time (min)	Pressure (PSIG)
0.0	5.0
1.0	4.1
2.0	3.45
3.0	2.86
5.0	2.0
6.0	1.65
8.0	1.08
10.0	.68

* Calibration done with argon gas.

times after 155. Events during the SURC-3 test that caused fluctuations in the data include power excursions, argon back-flushing, the addition of Zr metal, and an increasing leakage rate due to cracking and thermal decomposition of the refractory crucible.

The power excursions create a temporary decrease in the concrete ablation rate which results in a flow decrease. These occurred at times 50, 95, 105, 127-133, 165-177, and 203-207 in order to conduct field repairs and take aerosol samples. Argon backflushing results in a sharp flow increase and was done at times 120, 147, 160, 173, 185, and 210 to clear the gas composition sampling lines. Zr metal was added at times 133 and 177. The leakage rate increased continuously during the SURC-3 test resulting in a gradual loss of flow.

The gas temperature was monitored in four locations. These were at the argon carrier gas inlet, in the SURC expansion chamber, in the flow train near the orifice plate, and at the exit port. Of these, the gas temperature in the expansion chamber was the only one which varied significantly during the test. The gas temperature inside the expansion chamber started out at 35°C then climbed to a maximum value of 80°C at a run time of 140 minutes followed by a return to 48°C at time 160 and throughout the remainder of the test. The argon inlet temperature at the orifice plate varied between 40-50°C throughout the test as did the temperature at the outlet port. Data plots for these temperatures are shown in Appendix H.

The argon carrier gas inlet flow was monitored using a Kulite pressure transducer in conjunction with a 20 slpm calibrated critical orifice. The pressure behind the orifice registered a pressure of 30-31 psi throughout the test yielding a constant argon input flow rate of 33 ± 2 slpm.

An approximation of the increasing crucible leak rate during the test can be derived by comparing the concrete erosion data (Section 2.3.2) and the raw data from either the 415 or 750 (Figure 2.3.32) gas clock. Thermogravametric analysis of the SURC-3 concrete indicates that 37.8 l of H_2/H_2O and 127.5 l of CO/CO_2 will be liberated for each centimeter of concrete heated to 850°C. In a leak-free system, the gas clocks would record the volume of gas released from the concrete plus the 33 slpm argon carrier gas volume less 5 slpm removed from the system for gas analysis. At time 60, 2011 standard liters of gas should have been collected by the 450 gas clock whereas, 1840 were actually measured, thus indicating a leakrate of 8% during that period. This compares to a cold leakrate of 6% as determined during pretest calibrations. Similar computations yield a leakrate of 7.5% during the 60-114 minute period, a leakrate of 26% during the 114-148 minute period, 43% leakage during the 148-207 time period, and 40% leakage during the 207-242 minute time frame. During the entire test, the 750 gas clock sampled 9585 standard

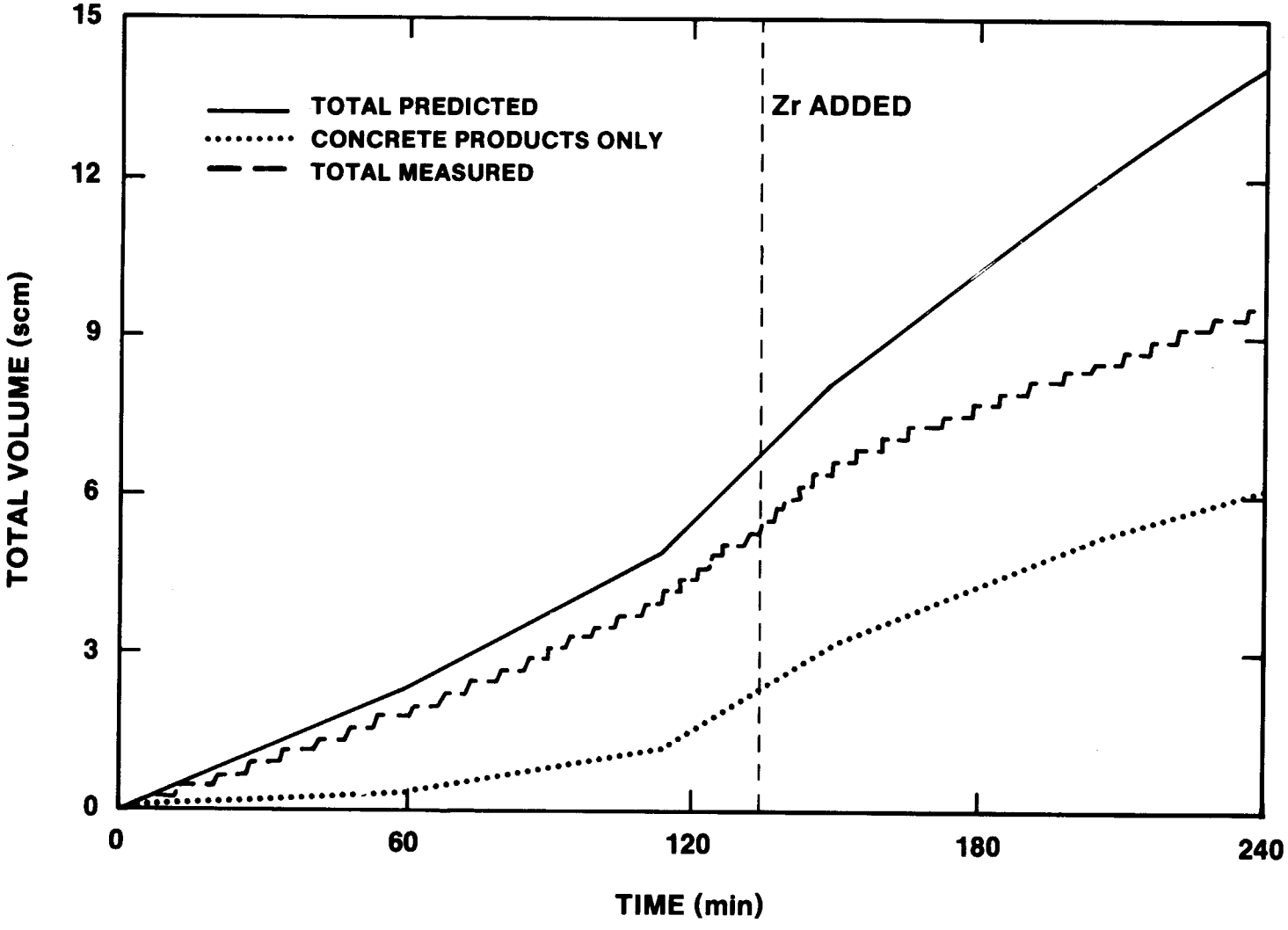

Figure 2.3.32 - 750 Gas Clock Data - SURC-3

liters of gas as compared to a projected total of 13,894 std l for an overall efficiency of 69%. The 450 gas clock sampled a total of 9414 standard liters.

The raw data for the turbine meter are shown in Figure 2.3.33. The raw data indicate an initial argon flow of 38 alpm. Degassing of the concrete is seen to start about time = 50 minutes and is marked by an increase in total measured flow to 40-48 alpm. Between 80 to 90 minutes, the total flow increases from 40 to 70 alpm in conjunction with the onset of concrete ablation. The flow then fluctuates between 80 to 110 alpm during the steady-state ablation period prior to Zr addition at time = 133 minutes. After time 133, the flow increases sharply to 160 alpm then coasts down to 45 alpm at time 150. After time 150, the total flow holds steady at 40 to 45 alpm until the test was concluded at time 247. When corrections for leakage, standard temperature, and standard pressure are made and the argon carrier gas is subtracted from the total flow, a plot of the gas release due to steel/concrete interactions both with and without Zr added results. The reduced data for the turbine meter are shown in Figure 2.3.34. The corrected turbine meter results indicate the onset of concrete interaction at time = 45 minutes when the flow rate increases to roughly 10 slpm. This is followed by an increase to 25 slpm at the onset of concrete ablation at time = 90 minutes. The flow then fluctuates between 45 to 75 slpm during the steady ablation period prior to Zr addition at time = 133 minutes. After Zr is added, the interaction flow rate increases dramatically to a peak value of 195 slpm. After 10 to -15 minutes of markedly increased flow between 90 to 120 slpm, the flow rate drops back to a steady-state value of roughly 25 slpm for the remainder of the test. A total of 5416 standard liters of gas can be accounted for using the integrated results of the corrected turbine meter data as compared to a total predicted value of 5775 standard liters of gas.

Similar results are shown in Figures 2.3.35 and 2.3.36 for the orifice flow device and for the laminar flow element. Both of these devices are sensitive to gas composition, hence, a range of output is shown using either argon or nitrogen as the basis for data reduction. As with the turbine meter, these results have been corrected for leakage, temperature, pressure, and the carrier gas flow. The critical orifice (Figure 2.3.35 indicates the onset of gas evolution at time = 40 minutes with a flow rate of 15 slpm followed by an increase to 30 slpm when ablation started at time = 90 minutes. The steady-state ablation period from time 105 to 125 is marked by 40 to 75 slpm flow rates before Zr addition at time 133. After Zr addition, the orifice plate indicates a flow increase to 165 to 195 slpm followed by a coastdown to 25 to 30 slpm for the remainder of the test. The laminar flow device (Figure 2.3.36 indicates the onset of gas evolution at time = 45 minutes with a flow rate of 7 slpm followed by an increase to 32 slpm when ablation started at time = 90 minutes. The steady-state erosion period prior to Zr

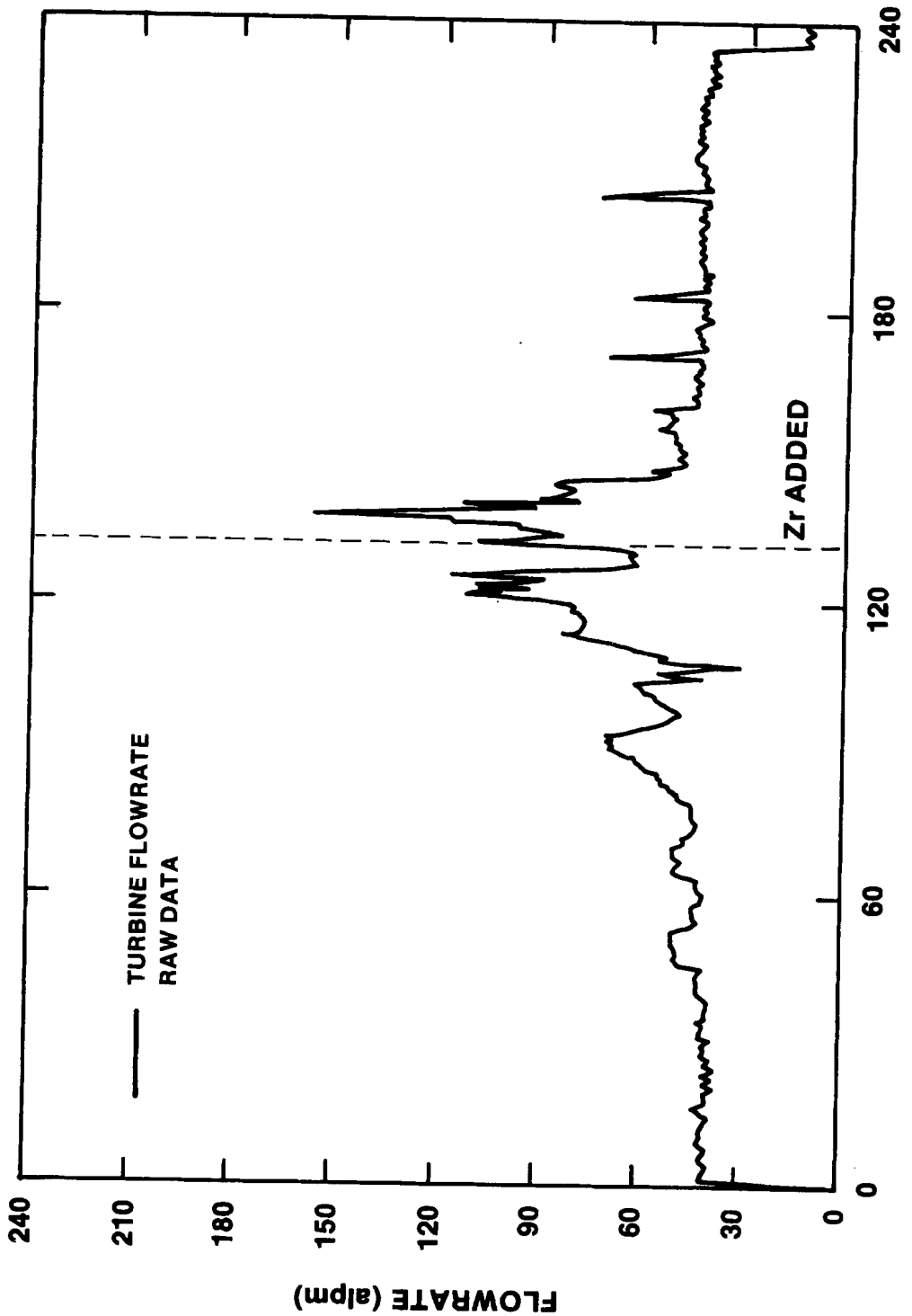

Figure 2.3.33 - Turbine Data (Raw) for SURC-3

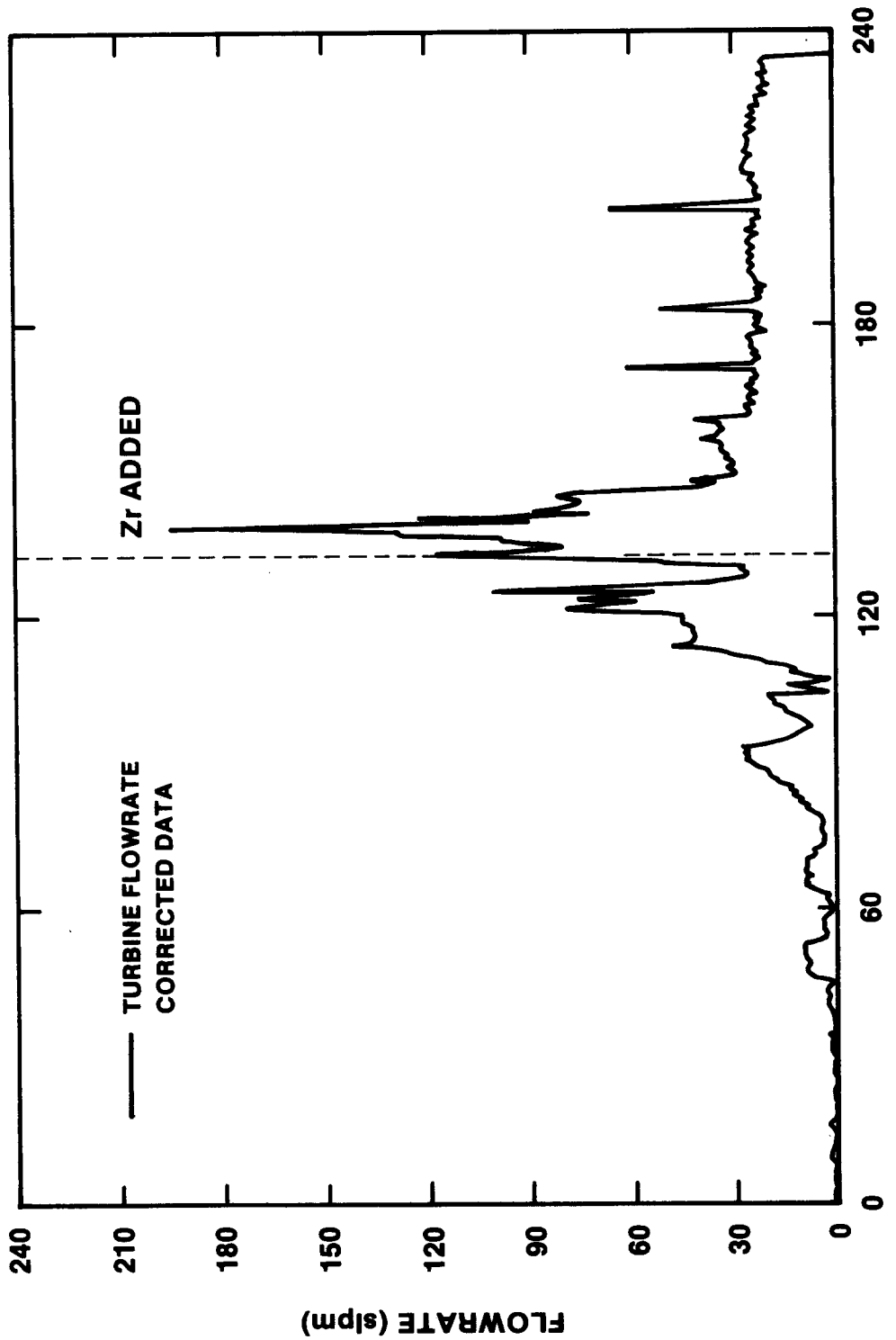

Figure 2.3.34 - Turbine Data (Corrected) for SURC-3

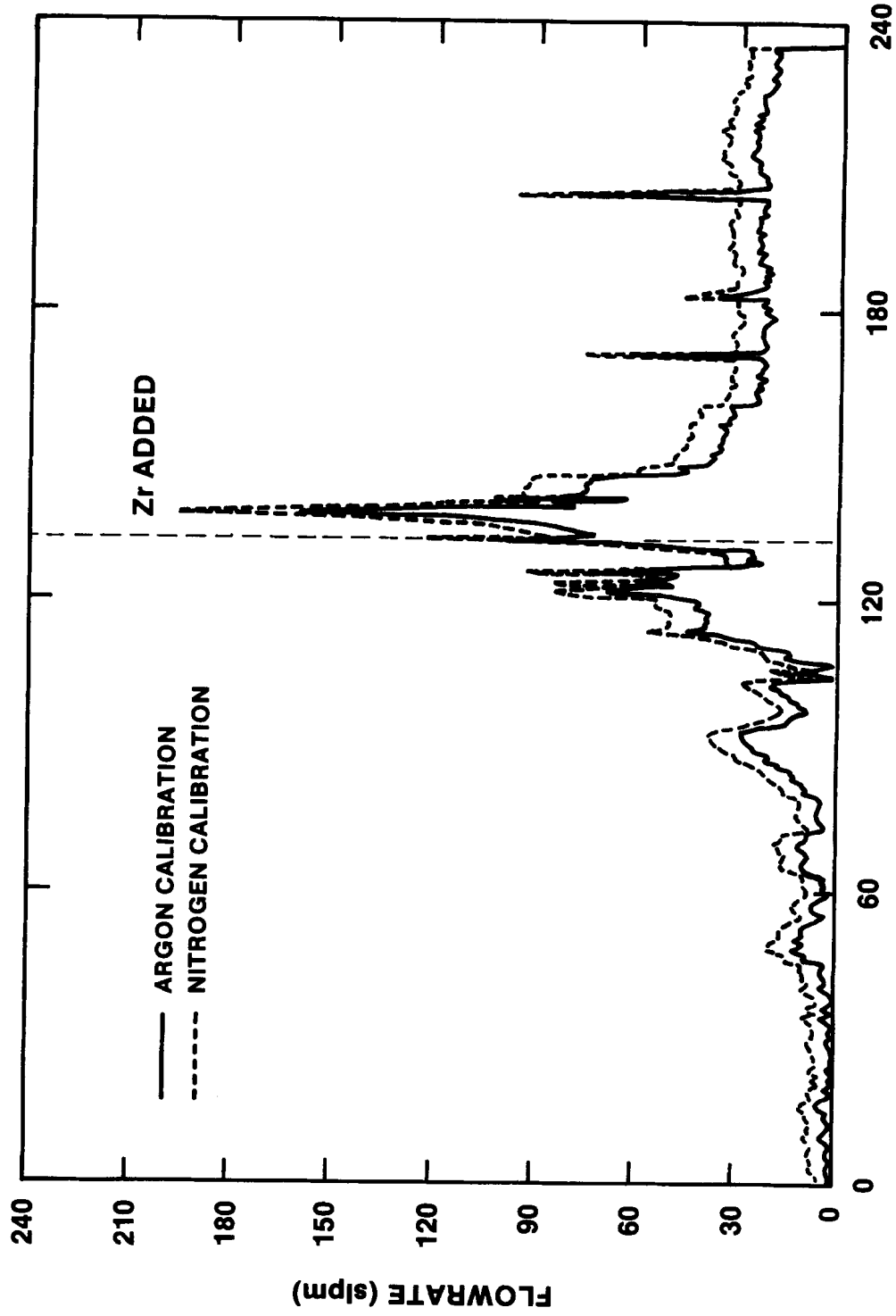

Figure 2.3.35 - Orifice Plate Data for SURC-3

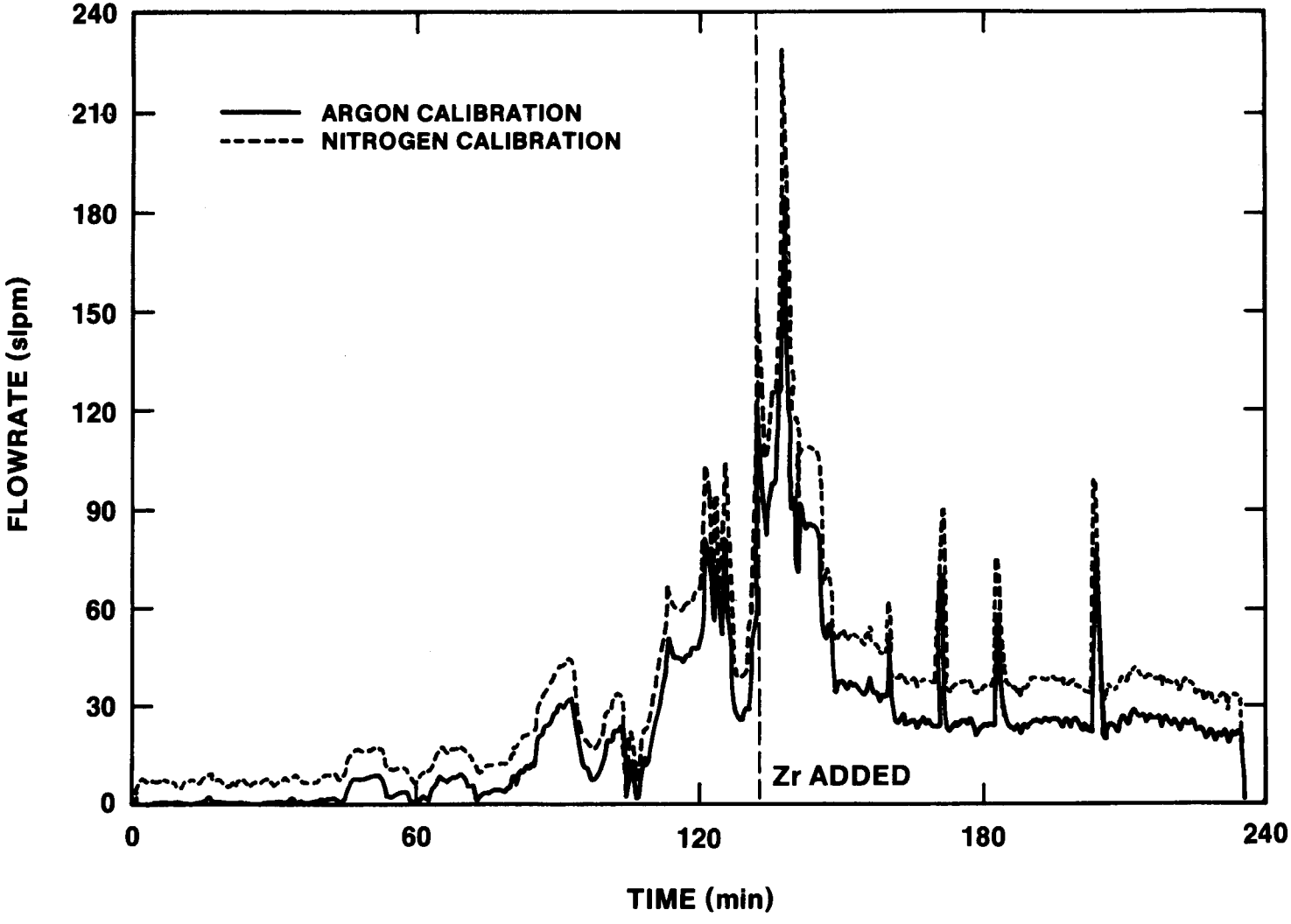

Figure 2.3.36 - LFE Data for SURC-3

addition at time 133 is marked by 45 to 80 slpm flow rates. After Zr addition, the laminar flow element indicated a flow increase to 180 to 225 slpm followed by a coastdown to 25 to 30 slpm for the final steady-state period. A total of 5300 standard liters of gas can be accounted for by integrating the argon calibration results for the orifice plate flowmeter as compared to 5500 standard liters of gas for the laminar flow element.

2.3.8 Aerosol Data Presentation

The objectives of aerosol measurement in the SURC test series are to measure and characterize the melt/concrete aerosol source term in the test, to provide a data base for model validation, and to provide additional details of the source term such as aerosol shape factors and size dependent composition [Powers, 1986].

The elements of the aerosol source term are (1) the aerosol mass generation rate, (2) the aerosol size distribution, (3) the aerosol bulk material density, (4) the aerosol dynamic shape factor, and (5) the aerosol composition. These elements are time dependent quantities and must be corrected to melt composition and temperature and to gas evolution rate. Elements (3), (4), and (5) may be size dependent quantities as well [Brockmann, 1987].

Aerosol Instrumentation

The aerosol instrumentation placed on the SURC-3 test is described below. It has been designed to provide data which will allow calculation of the aerosol source term. Figure 2.3.37 is a schematic diagram of the SURC-3 test article showing the sample points and location of aerosol instrumentation.

Figure 2.3.38 is a schematic diagram of the aerosol instrumentation fielded for the SURC-3 test. This assembly of samplers and diluters comprises the sample extraction dilution system (SEDS) designed to sample the high temperature and high concentration aerosols produced in the SURC-3 test.

An aerosol sample is drawn from the crucible volume through the crucible wall into the sample extraction dilution system (SEDS). Figure 2.3.39 is a schematic diagram of the crucible sample point. An important feature is the diluter integrated into the crucible wall. This diluter delivers dilution gas to the drawn sample, cooling it and reducing the aerosol concentration as it first enters the SEDS. This integral diluter corresponds to diluter D0 in Figure 2.3.38.

Dilution of the sample by the diluters D0, D1, D2, D3, and D4 serves three purposes. The first is to reduce the high aerosol concentration to a level that is within the instrument range. The second is to cool the flow by the addition of the cooler dilution gas. The third is to reduce the variation in gas

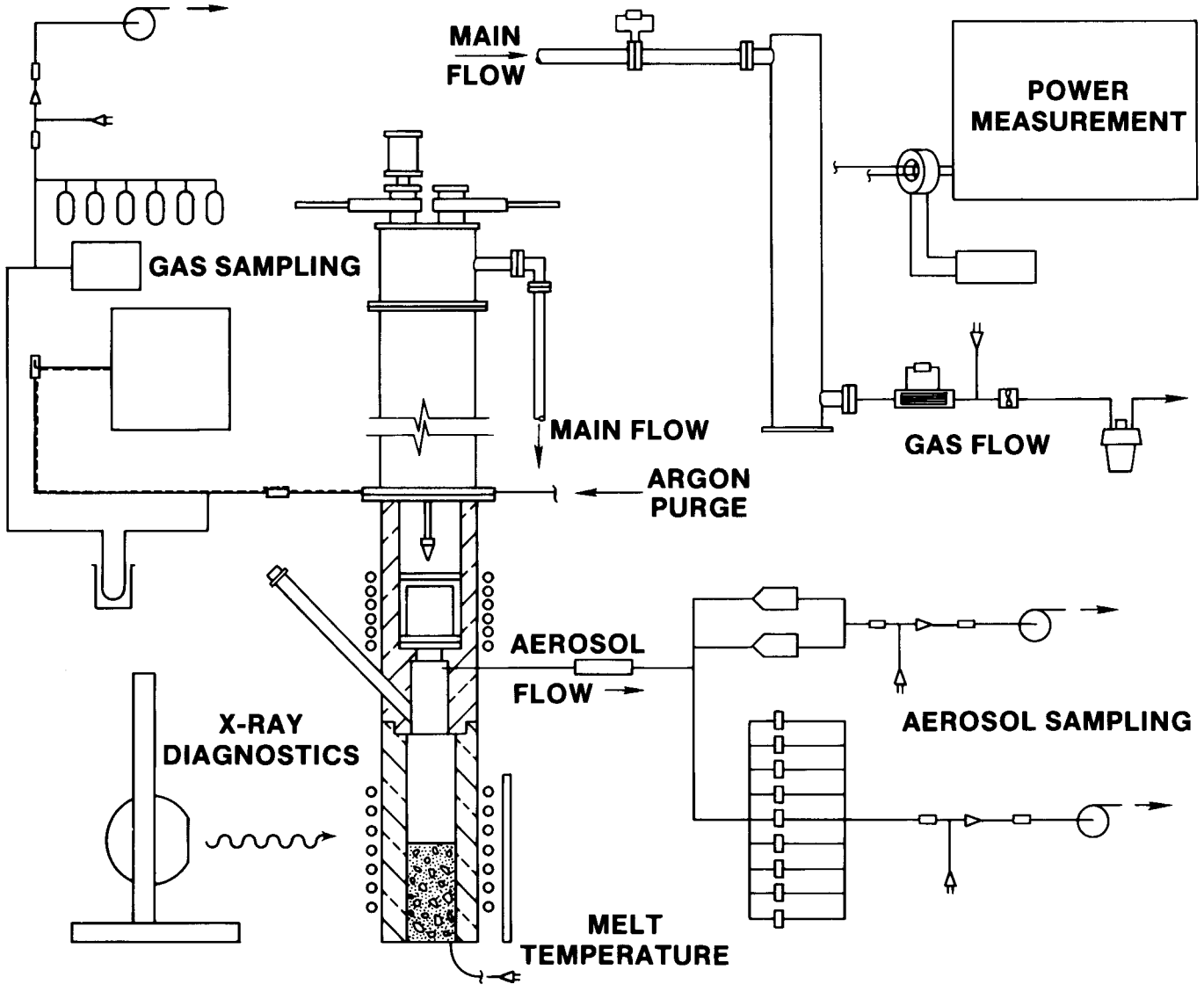

Figure 2.3.37 - SURC-3 Test Article Schematic

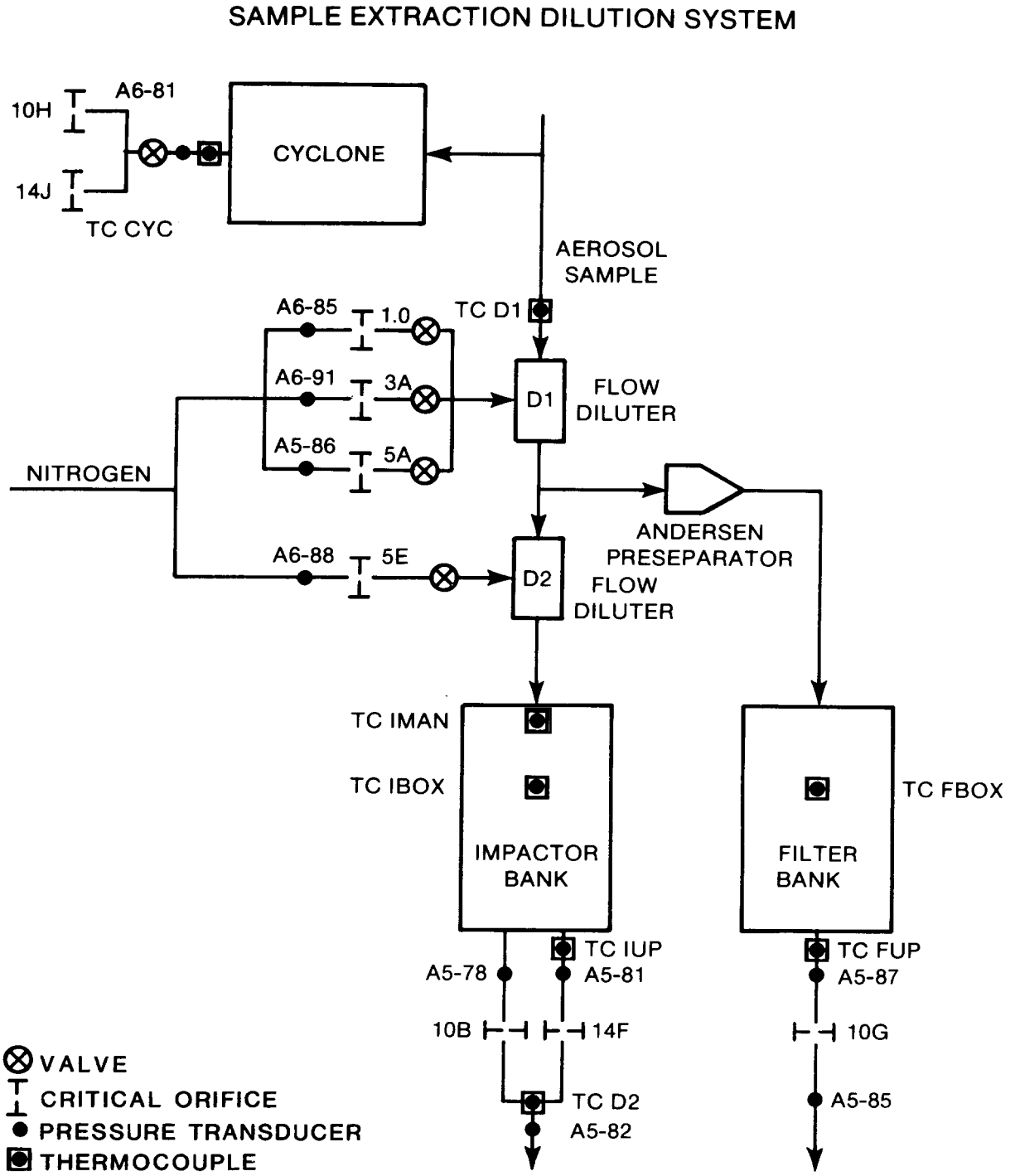

Figure 2.3.38 - SEDS Schematic

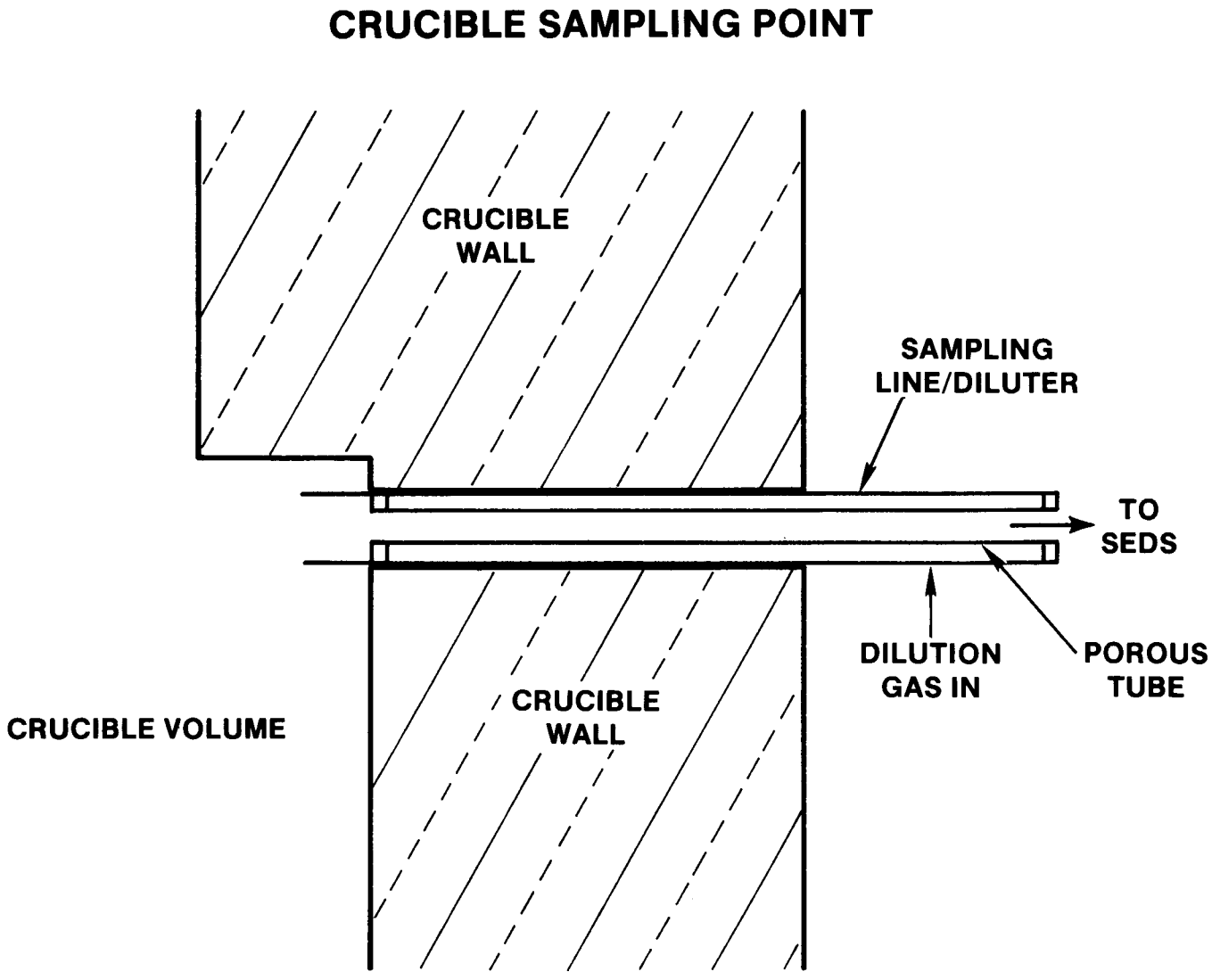

Figure 2.3.39 - Crucible Sample Point

Figure 2.3.40 is a schematic diagram of the flow diluter designed for this test series. The diluter consists of an aluminum outer tube 6.35 cm in diameter and 15 cm long and a 1.9 cm diameter sinterred stainless steel inner tube. End caps hold the tubes in place. Dry dilution gas is passed through a 1/4" swagelok fitting in the outer tube to the annular plenum region between the two tubes. Gas passes through the porous walls of the inner tube diluting the aerosol sample flowing through it.

The total flow out of the diluter, Q_T, is measured and the dilution flow into the diluter, Q_D, is measured. The dilution ratio DR, is then defined as Q_T divided by the difference between Q_T and Q_D.

A practical upper limit of DR is about 5. The dilution ratio is calculated using the difference between two numbers and when those numbers are of similar magnitude, the error in the difference can become large.

The dilution flow is controlled by a critical orifice manufactured by Millipore and calibrated at Sandia's Primary Standards Lab.

The cascade cyclone, manufactured by Sierra, inertially classifies aerosol particles and yields a mass distribution with respect to aerodynamic equivalent particle diameter. A cyclone is capable of collecting much more material than an impactor and can be used to collect size classified material for bulk analysis. The Sierra cascade cyclone is a series of six cyclones (of increasing capability to collect smaller particles) followed by a glass fiber backup filter. The aerosol sample is brushed out of the collection cup of each cyclone for weighing. The cascade cyclone is of stainless steel construction and when assembled is 12.7 cm in diameter at the widest point and about 60 cm in length. The calibration provided by the manufacturer is used.

Figure 2.3.41 is a schematic diagram of how the cascade cyclone is plumbed into the SEDS (Figure 2.3.39). Sample flow is controlled by two Millipore critical orifices in parallel to give a nominal sample flow of 24 liters per minute. Their calibrated flow is given in Table 2.3.11. A remotely actuated valve manufactured by ASCO is used to take the sample.

Figure 2.3.42 is a schematic diagram of the filter box on the SEDS. This box contains 12 Gelman in-line stainless steel filter holders. This stainless steel 5.9 cm diameter 5.7 cm long filter holder (Gelman catalog number 2220) is designed for pressure applications of up to 200 psig. It uses 47 mm diameter Durapore Membrane filtration media from Millipore (catalog designation HVLP 047). The effective filtration area is 9.67 cm^2.

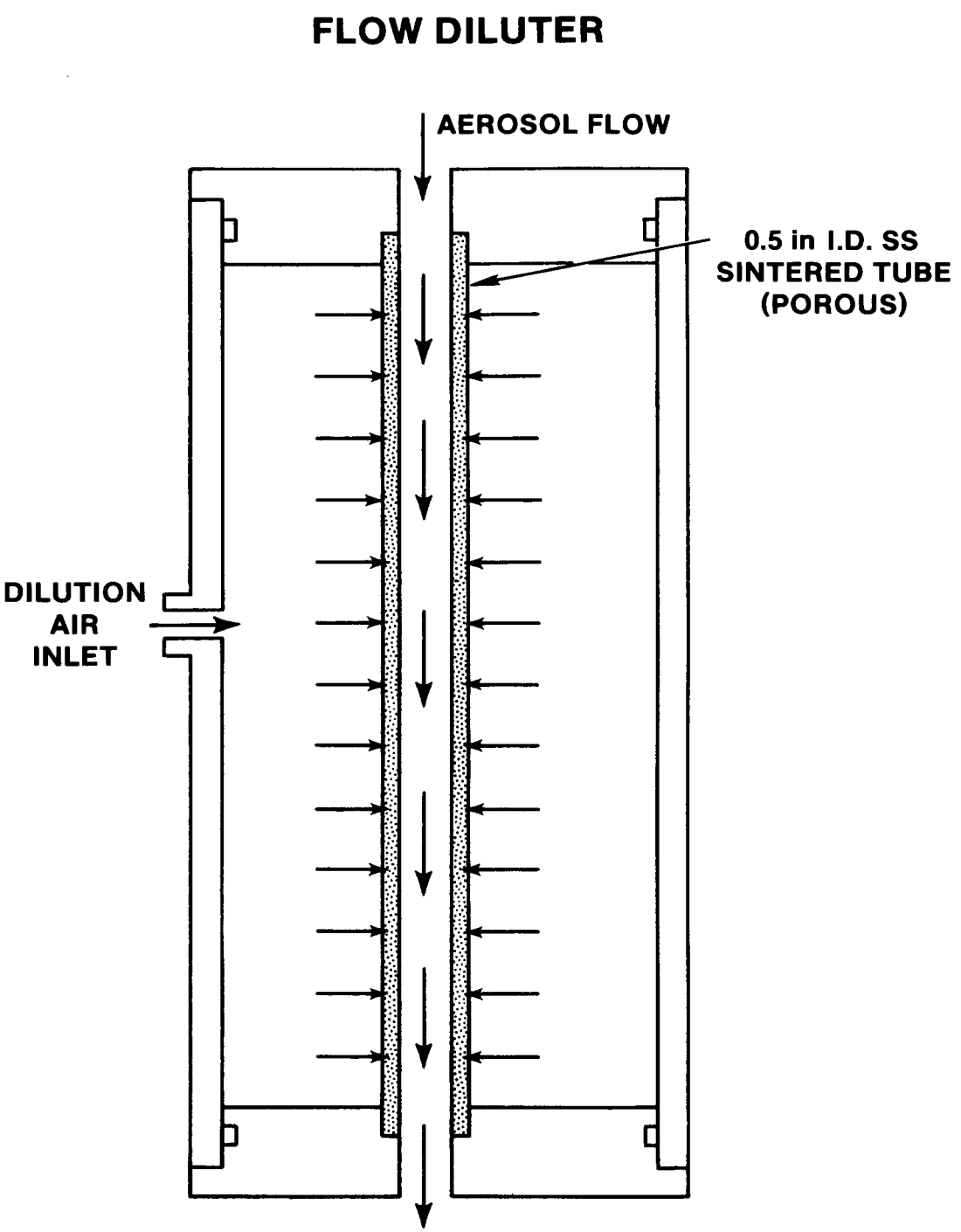

Figure 2.3.40 - Flow Diluter Schematic

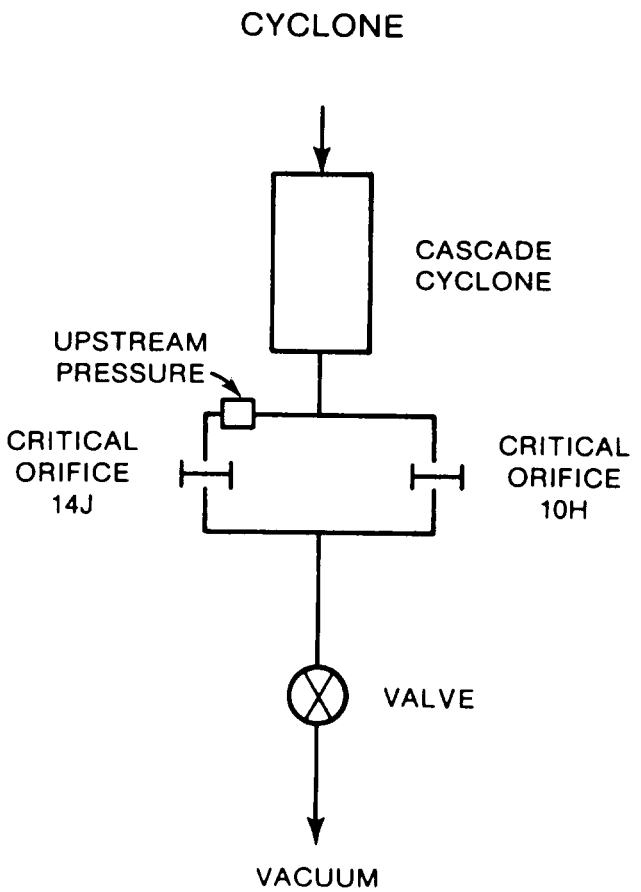

Figure 2.3.41 - Cascade Cyclone Schematic

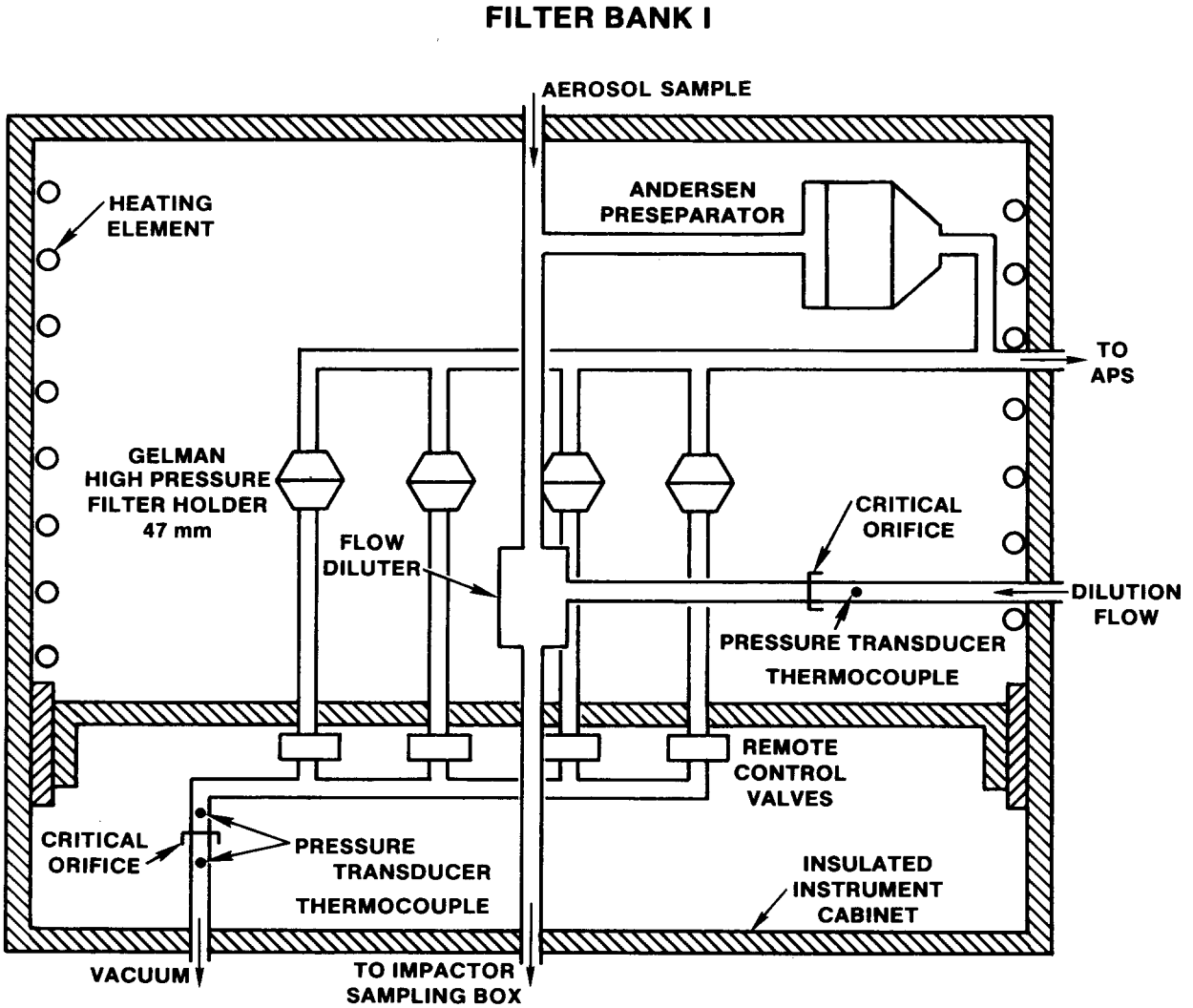

Figure 2.3.42 - Filter Sample Box Schematic

TABLE 2.3.11

SEDS Hardware Calibration

Instrument	Orifice Designation	Critical Calibration Flow (cc/sec) Q_{CO}
Filter	10 G	170.8
Impactor	10 B	174.8
Impactor	14 F	241.5
Cyclone	14 J	423.5
	10 H	
Diluter 0	5 D	72.5
Diluter 1*	1-1	19.05
Diluter 2	3 A	46.0
Diluter 3*	1-3	14.58
Diluter 4	5 C	72.2

*Calibration by flowmeter in lab

The inlet of this filter sample section is connected to a preseparator which removes particles larger than 10 to 15 micrometers aerodynamic equivalent diameter. This preseparator is manufactured by Anderson and is of stainless steel construction, 8.2 cm in diameter and 12.8 cm long. The preseparator collects course material in an impaction cup, and passes the finer aerosol to the filter sample section.

The filter sample provides a collected mass of aerosol with aerodynamic equivalent particle diameter less than 10 to 15 micrometers. This sample allows calculation of the aerosol mass concentration of these smaller particles. The collected material can also be chemically analyzed. The filter sample is the principal measurement in determining aerosol mass source rate and elemental composition. The filter to be used to take a sample is selected by opening and closing a remotely actuated valve (ASCO). Flow is controlled by a Millipore critical orifice common to all the filters. The orifice calibrated flow is given in Table 2.3.11.

The filter sample section is mounted in an insulated box and electrically heated to avoid water condensation. The heaters are controlled by an Omega Model 920 temperature controller with a type K thermocouple.

Figure 2.3.43 is a schematic of the impactor sample section. Anderson MkIII cascade impactors are used. An Anderson MkIII cascade impactor inertially classifies aerosol particles into nine size bins. It consists of eight stages and an after filter and employs glass fiber collection substrates. It yields a mass distribution of aerosol with respect to aerodynamic equivalent particle diameter. The Anderson MkIII cascade impactor is 8.2 cm in diameter and 18 cm long and is constructed of stainless steel.

A preseparator which removes particles nominally larger than 15 micrometers aerodynamic diameter was used to avoid overloading (more than 15 to 30 mg of material on any one stage) of the impactor with large particles. It effectively collects material which would otherwise be collected on the first two stages of the impactor. The preseparator collects material in an impaction cup, which is brushed out to retrieve the collected sample. The preseparator is of stainless steel construction, 8.2 cm in diameter and 12.8 cm long. It threads into the front of the impactor. The assembled preseparator-impactor is 8.2 cm in diameter and 29.8 cm long.

Two impactors are ganged together and run simultaneously in parallel at different flow rates. The two flow rates are nominally 15 liters per minute and 10 liters per minute. Flow is controlled by two Millipore critical orifices and sample selection is accomplished with ASCO remotely actuated valves. The orifice calibrated flow and location are given in Table 2.3.11 for each instrument.

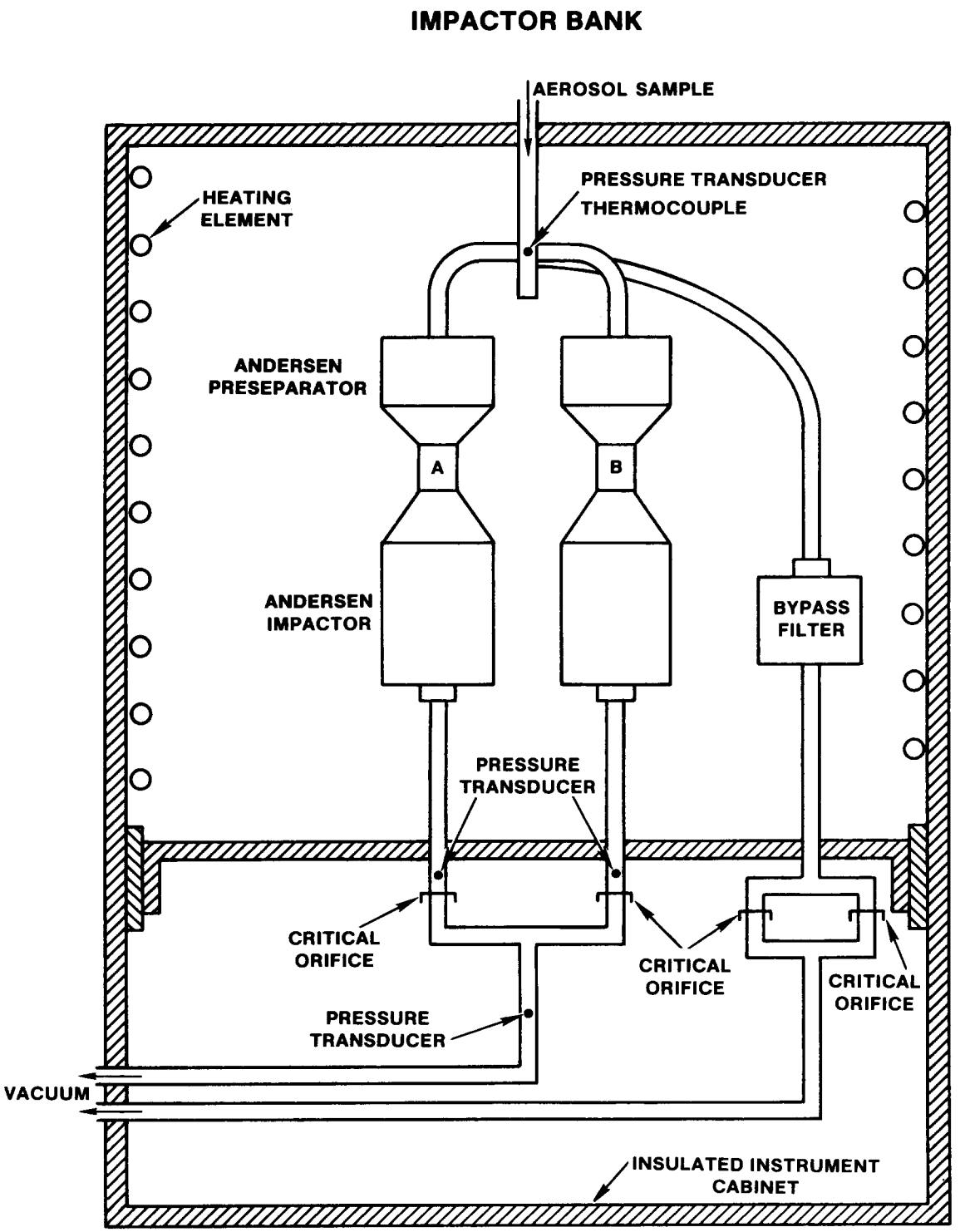

Figure 2.3.43 - Impactor Sample Box Schematic

The impactor assemblies are mounted in an insulated box similar to the one used for the filter sample section. This box is also electrically heated to avoid water condensation and is controlled using type K thermocouples and Omega controlled devices.

The aerodynamic particle sizer (APS) is manufactured by TSI, Inc. It yields a real time measurement of the aerosol number distribution with respect to particle aerodynamic diameter. Flow through this instrument is controlled by a pump whose speed is regulated by a feedback system that keeps the pressure drop across the instrument constant.

The APS requires further dilution of the aerosol sample. This is accomplished through the use of pinhole diluters. Figure 2.3.44 is a schematic diagram of a pinhole diluter. A pinhole diluter is made by drilling a small hole through the capped end of a Gelman cartridge filter from the upstream side to the downstream side. This allows a small portion of unfiltered gas to pass through the filter and mix with the filtered gas. Dilution rates are determined by calibration.

Figure 2.3.45 is a schematic diagram of the Dynatron Model 301 opacity meter placed in the exhaust line of the test article before the gravel filter and flow measurement devices. This device measures the attenuation of a light beam as it travels through an aerosol. Light attenuation correlates with mass loading. Correlation of the opacity meter output with the mass measured by the filter samples provides a continuous record of mass concentration in the 3-inch pipe exhausting gas and aerosol from the interaction crucible in the SURC test. The windows allowing light transmission are kept clean and free of aerosol deposition by a purge gas flow.

The remotely actuated valves are operated by a Modicon Micro 80 programmable controller manufactured by Gould.

Pressure Transducer Calibration

Kulite 0 to 100 psia pressure transducers were used to monitor the pressure of the gas upstream of the orifices in the diluters and the pressures in the sample extraction-dilution system. The transducers were calibrated insitu by pressurizing the upstream side of the diluters to known pressures. This was performed on twice before the test and rechecked the day of the test. The pressure transducers on one of the five original diluters did not repeat the original calibration and was not included in the test.

The calibration data are given in Figures 2.3.46 and 2.3.47 along with the response functions also found in Table 2.3.12. The response functions developed for the diluter pressure transducers are based on the best fit of the calibration data at the pressure at which the dilution gas was supplied.

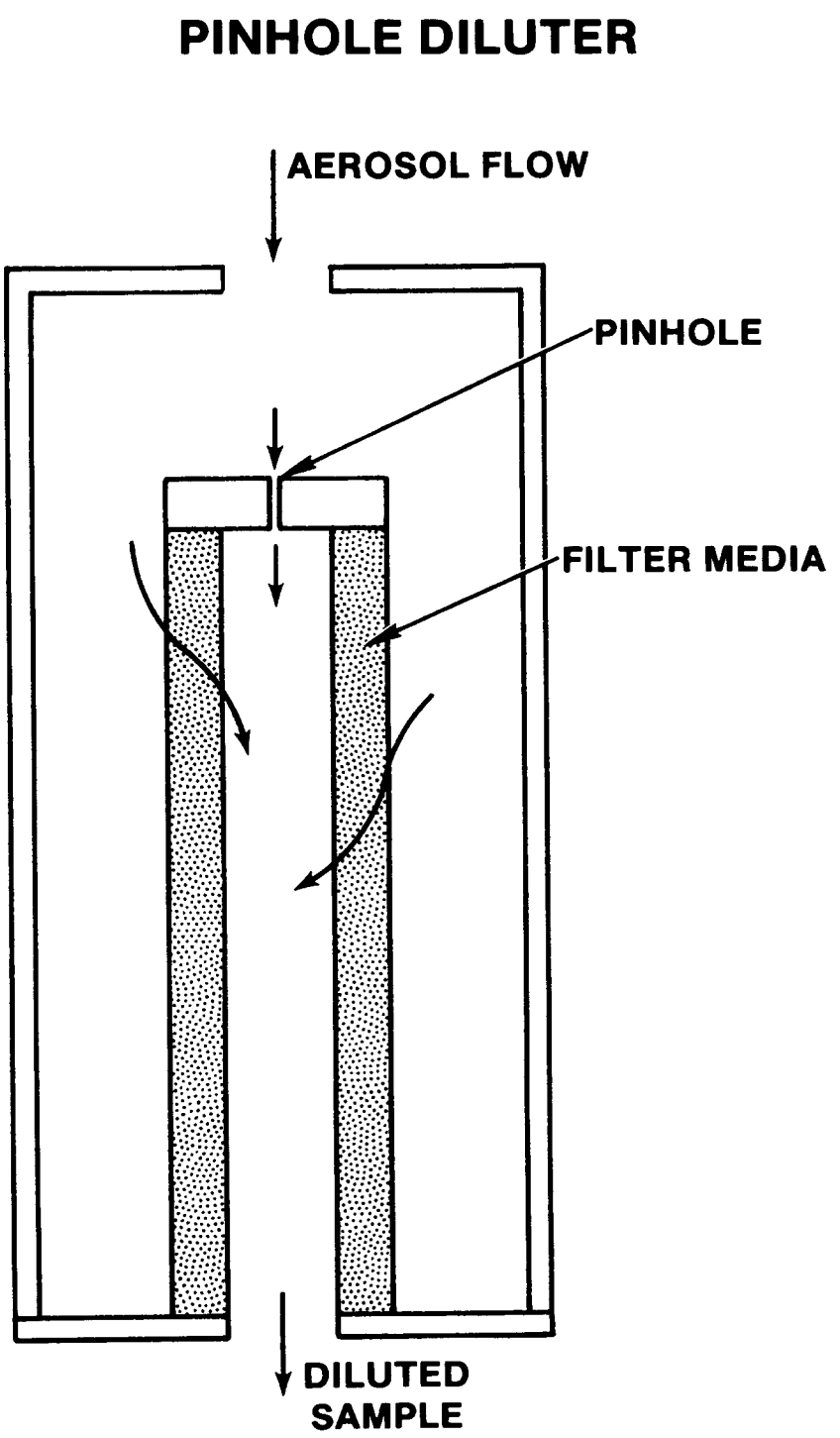

Figure 2.3.44 - Pinhole Diluter Schematic

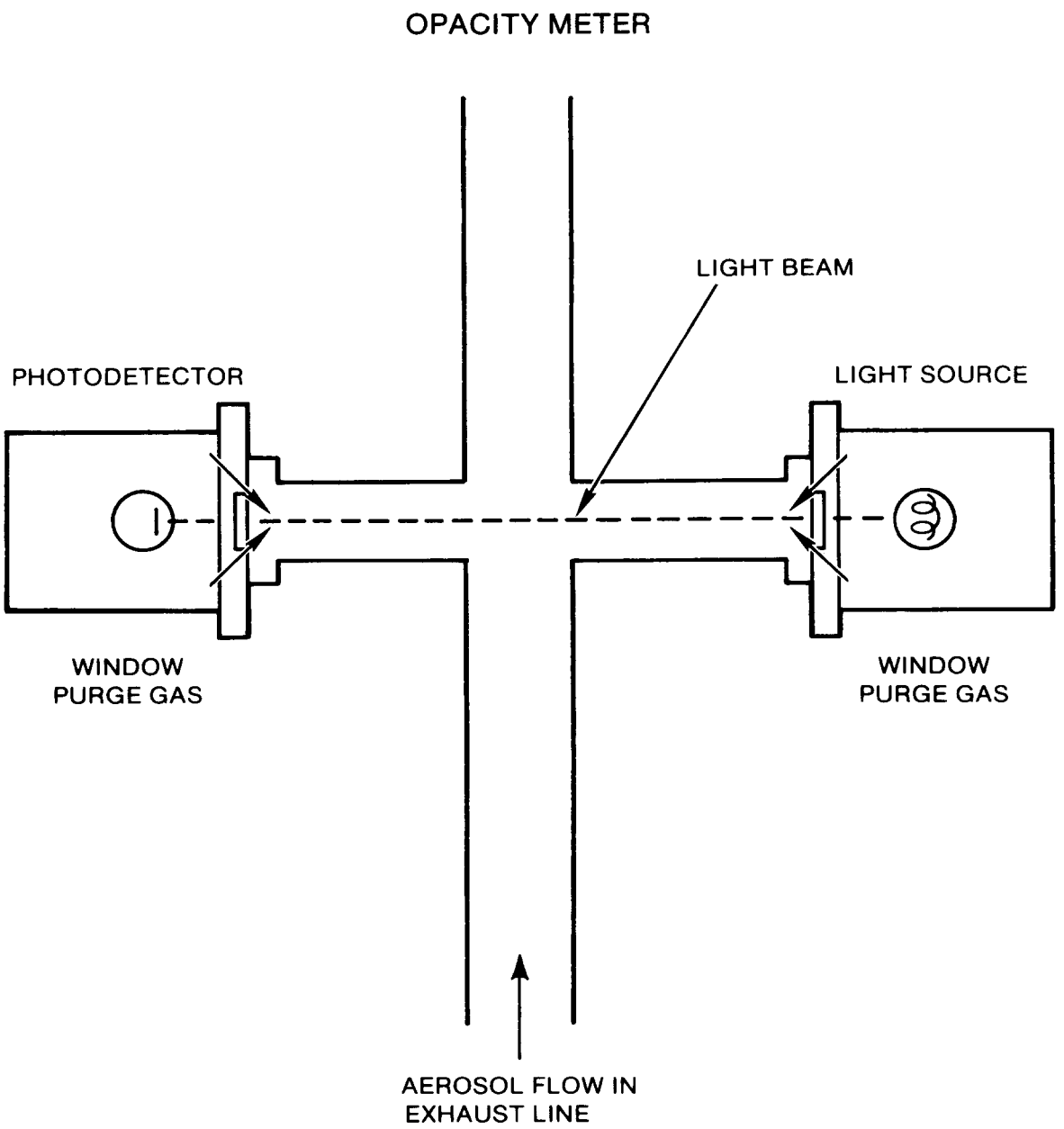

Figure 2.3.45 - Opacity Meter Schematic

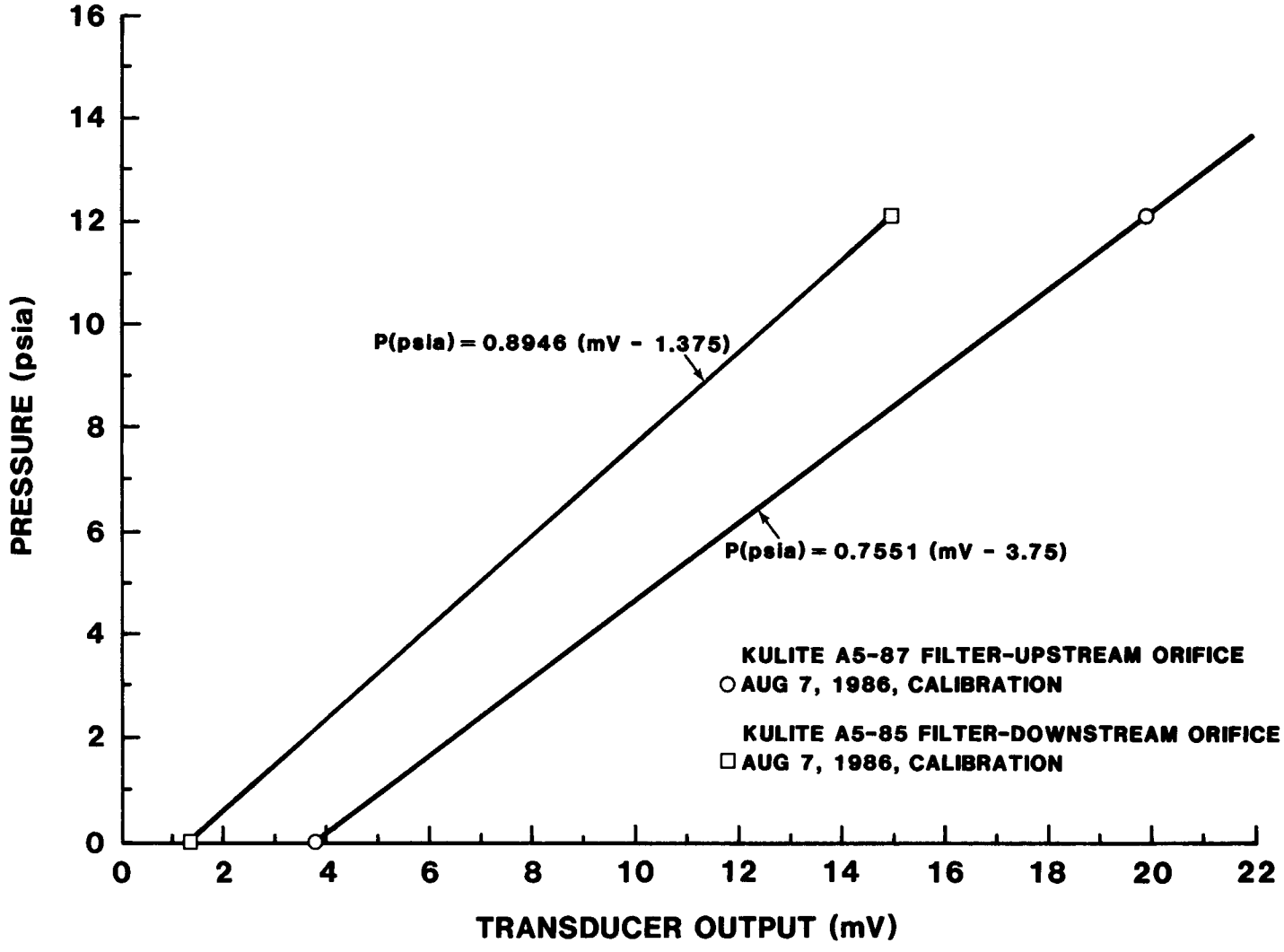

Figure 2.3.46 - Aerosol Pressure Transducer Calibration

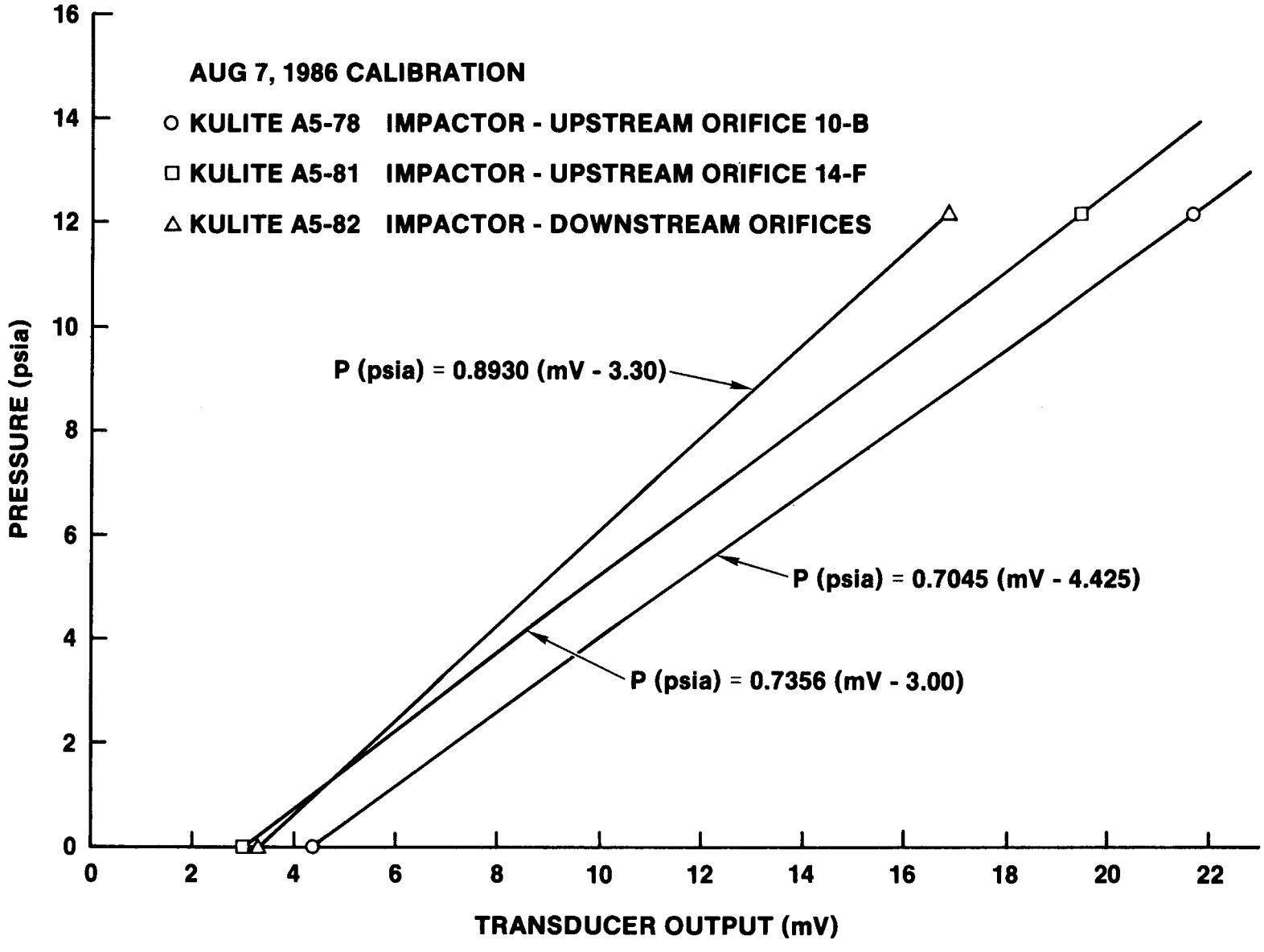

Figure 2.3.47 - Aerosol Pressure Transducer Calibration

TABLE 2.3.12

SEDS Pressure Transducer Hardware

Pressure Transducer Location	Pressure Transducer Designation	a (mV)	S (psi/mV)	Calibration
Filter-Upstream Orifice	A5-87	3.75	0.7551	At Site
Downstream 10-B orifice	A5-85	1.375	0.8946	At Site
Impactor-Upstream 10-B orifice	A5-78	4.425	0.7045	At Site
Upstream 14 F orifice	A5-81	3.0	0.7356	At Site
Downstream Orifices	A5-82	3.3	0.8930	At Site
Cyclone-Upstream Orifices	A6-91	-1.886	1.24	
Diluter 0-Upstream Orifice	A4-3	-0.970	1.429	At Site
Diluter 1-Upstream Orifice				
Diluter 2-Upstream Orifice	A6-38	0.4093	0.9926	At Site
Diluter 4-Upstream Orifice	A4-5	1.828	1.619	At Site
System-SEDS manifold	A4-6	-1.67	1.13	

NOTE: Response of pressure transducers is defined as P(psia) = S (output-a) where S and a are constants from the above table.

The pressure transducers located upstream and downstream of the flow controlling orifices in the aerosol samplers were calibrated insitu by a simple two point method. Readings were taken with the values closed and while pulling a vacuum to give a zero pressure reading. Readings taken with the values opened and no flow (i.e., no vacuum) gave the values for ambient Albuquerque pressure of 12.2 psia. These two points gave the calibration for these transducers as indicated in Figures 2.3.46 and 2.3.47 and Table 2.3.12.

From the insitu calibration of the pressure transducers located upstream and downstream of the flow controlling orifices, the pressure drop across the filter and impactors was determined as was the downstream operating pressure for critical flow determination.

The impactor operating with orifice 10 B had a pressure drop of 0.46 psi and the one operating with orifice 14 F had a pressure drop of 0.55 psi. The downstream pressure of these orifices was 2.8 psia which assured critical flow operation of the orifices.

The filter operating with orifice 10 G had a pressure drop of 0.59 psi. The downstream pressure at this orifice was 2.4 psia assuring critical flow operation.

An insitu calibration of the pressure transducer located upstream of the flow controlling orifices of the cascade cyclone could not be performed. Instead, the calibration supplied with the Kulite pressure transducer was used to give a pressure drop measurement across the cyclone of 1.61 psi.

The pressure drops across each of the sampling instruments are listed in Table 2.3.13.

TABLE 2.3.13

Aerosol Sampler Pressure Drops

Cyclone Pressure Drop	= 1.61 psi
Filter Pressure Drop	= 0.59 psi
10 lpm Impactor Pressure Drop	= 0.46 psi
15 lpm Impactor Pressure Drop	= 0.55 psi

Impactor Calibration

The Andersen Mark III cascade impactor has been calibrated by Cushing et al., 1976. We have employed this experimentally-determined calibration in the reduction of data taken with the Andersen Mark III impactors.

Each impactor stage is assumed to collect all particles larger than some characteristic size and pass along all particles smaller than that size. This characteristic size is called the cut point. Thus, in a cascade impactor (an impactor composed of a series of stages with successive smaller cut points) each stage collects particles of a size between the cut point of that stage and that of the previous stage. The impactor yields a distribution of aerosol mass as mass between successive cut points.

The cut point of an impactor can be expressed as a Stokes number:

$$Stk = \frac{\rho_o D_{ae}^2 U}{18 L \mu}$$

where ρo is the density of 1 g/cm^3, D_{ae} is the aerodynamic equivalent diameter, U is the velocity through the orifice, μ is the absolute viscosity of the gas, and L is the diameter of the orifice. Impactor theory holds that for a given stage, the characteristic Stokes number is constant [Marple and Willeke, 1979]. Thus, changing the flow (or U) through the impactor changes the cut point for that stage. The aerodynamic equivalent diameter corresponding to the cut point for each stage for impactors operating at 10 and 15 liters per minute are given below:

Aerosol Transport Calibration

Aerosol transport through the sample extraction and dilution system (SEDS) is not universally efficient. It is dependent upon particle size and flow conditions. A transport model of the SEDS has been compiled and transport data for the system have been taken to test it. The aerosol mass source rates are calculated by multiplying the measured aerosol concentration by the exhaust gas flow rates. Delay times for the aerosol to flow from the crucible volume to the sampling point are taken into account by calculating the time to flow through the intervening volume [Gronger, 1986; Davies, 1982; Jayasekera, 1980].

Experimental measurements of penetration through a series of 90° bends and through the SEDS plumbing from inlet to filter sample point and to impactor sample point have been made. The calibration aerosol was monodisperse oleic acid particles generated with the vibrating orifice generator manufactured by TSI, Inc. [Berglund and Liu, 1973]. Measurements of total counts made by a

TSI aerodynamic particle counter (APS-33) both upstream and downstream of the penetration section were made to obtain the penetration efficiency. Table 2.3.14 gives the results for the 90° bend and Figure 2.3.48 shows these results plotted as efficiency vs Stokes number along with the theoretical curve. For these high levels of penetration, the theory and data match well, however, for larger particles or higher flows resulting in lower penetration, theory may be in error.

Figure 2.3.49 is the room temperature penetration of a 4.56 micrometer diameter particle through the SEDS plumbing to the filter sample point. The curve is the theoretical penetration calculated by the model discussed above. Figure 2.3.49 also holds for the impactor sample point.

TABLE 2.3.14

Particle Penetration Through a 90° Bend

D_p (μm)	Q (cc/sec)	l (cm)	Stk (-)	P_{exp} (--)	P_{model} (--)
4.56	136	1.092	$8.3 \cdot 10^{-3}$	.978-.987	.987
4.56	208	1.092	$1.26 \cdot 10^{-2}$	.961-.972	.980
4.56	136	1.727	$2.1 \cdot 10^{-3}$	.972-1.00	.997
4.56	208	1.727	$3.2 \cdot 10^{-3}$	.981-1.00	.995
7.24	136	1.727	$5.2 \cdot 10^{-3}$	.945-.985	.992
9.12	136	1.727	$8.3 \cdot 10^{-3}$	.942-.967	.987

In both cases, the calibration gave only slightly lower penetration than the model calculated: about 30% low for the filters and 15% low for the impactors. This indicated that particles between 01 and 10 microns would be sampled efficiently during the SURC-3 test [Brockmann, 1987].

Procedures

Twelve filter holders were loaded with 12 preweighed filters and installed into the SEDS filter sampler box. Eight impactors were loaded with preweighed collection substrates and installed into the SEDS impactor sampler box.

The Dynatron opacity meter was adjusted and the zero set according to the manufacturers specifications.

The samplers and SEDS were set up and the site calibration performed on the pressure transducers. The transducer on diluter 3 did not repeat earlier calibrations and diluter 3 was shut down and not used.

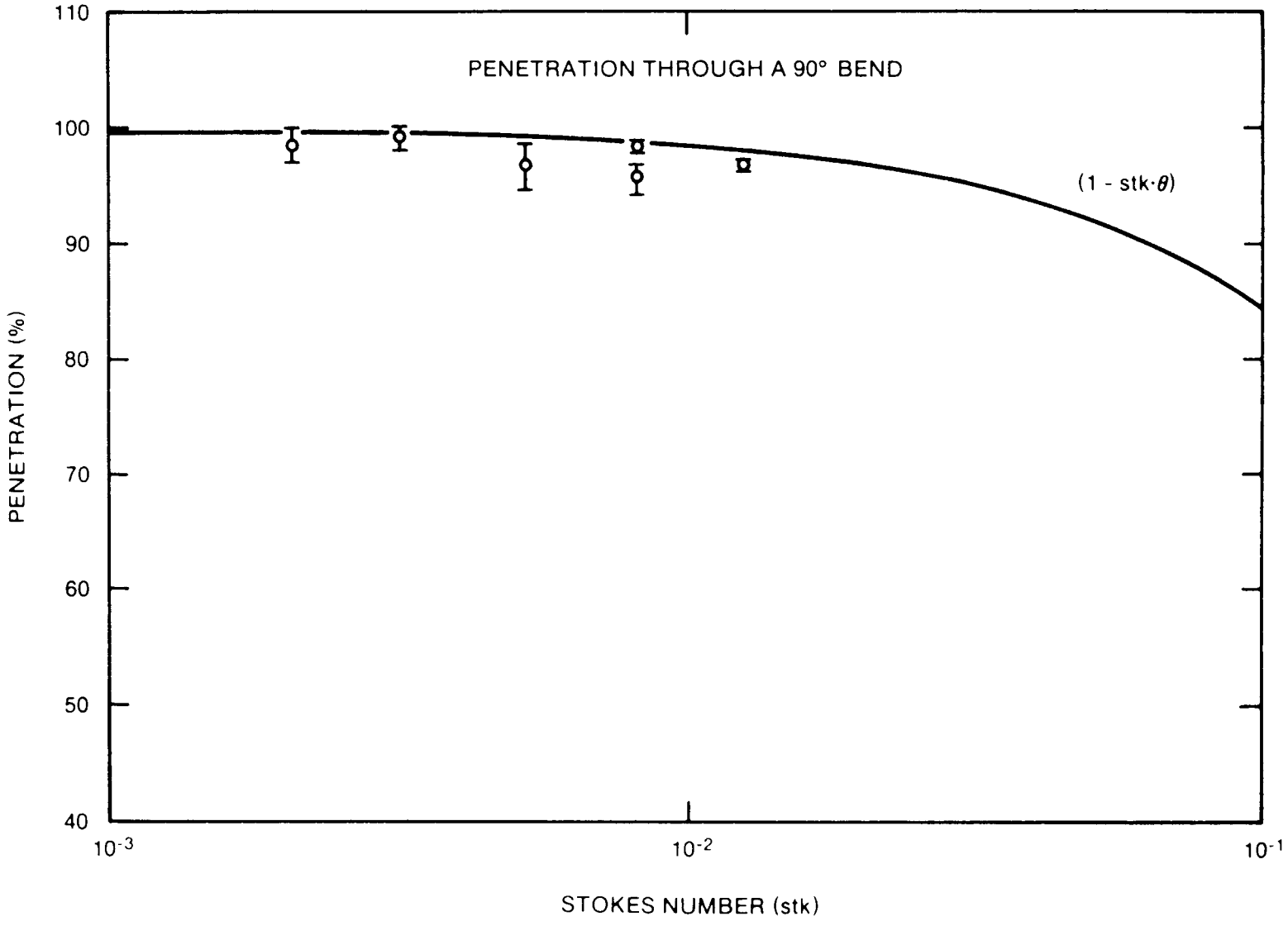

Figure 2.3.48 - Aerosol Penetration Through a 90° Bend

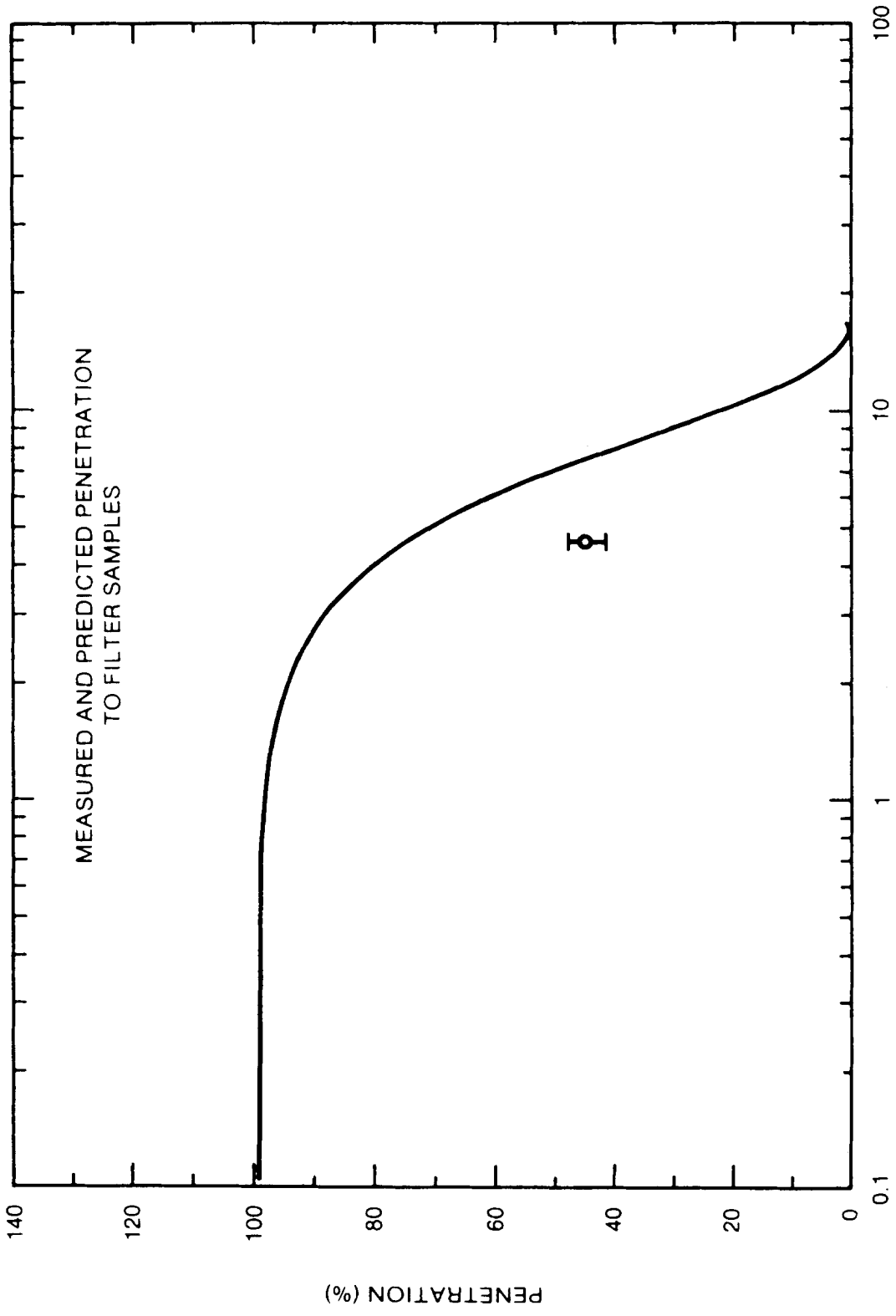

Figure 2.3.49 - Measured and Predicted Aerosol Penetration

The pressures determined for the desired dilution ratios were set by adjusting metering valves upstream of the diluter orifices. The remote valves opening and closing flow to the diluters were cycled to check that the pressures returned to their set values. During this time, the readings from the transducer on diluter 1 failed to come back to the original setting. The signal from that transducer was considered to be unreliable and diluter 1 was shut down and not used.

The Modicon 80 programmer was programmed to take 12 samples; each at the determination of the operator. The samples were of two types. Four were of the first type which utilized a gang of two impactors, a filter, the cyclone, and diluters for 30 seconds and then shut them off. Eight of the second type which utilized the impactor by-pass, a filter, the cyclone, and diluters for 30 seconds and then shut them off.

Diluter 2 (D2) was manually operated. Its use was determined by the system pressure; a system over pressure in excess of 1.6 psi would require diluter D2 to be switched on.

Table 2.3.11 identifies the orifice and its calibrated flow associated with each sampler and diluter.

At the time the test was run, melt was achieved and aerosol flowed through the SEDS to the APS plugging the pinhole diluter. The plugging of the diluter prevented any APS data from being obtained but protected the instrument from damage by overloading. This initial aerosol was detected on the photometer analog readout, but was not recognized as being as intense a source as it was. This unexpected level of aerosol generation, coupled with the lack of two diluters in the SEDS led to the plugging of the APS pinhole diluter and the elimination of APS data.

For an undetermined reason, the Modicon 80 failed to trigger the samples and some of them had to be manually triggered. Table 2.3.15 gives the sampling schedule which resulted. It indicates which samplers and diluters were switched on and whether or not the cyclone was operating. Only the last four samples were successfully taken by a normal remote execution of the Modicon 80.

During normal test operations the pressure and thermocouple readings were swamped with noise from the induction furnace. At some of the sample times, however, the power supply was shut down so that noise-free measurements could be recorded.

TABLE 2.3.15

SURC-3 - Sampling Schedule

Sample Time (min)	Sample Duration (sec)	Filter	Impactors	Cyclone	Diluters
105.12	60	F1(A)	I2(A) & I2(B)	None	None
106.12	60	F12(L)	None	None	None
126.12	60	F2(B)	I3(C) & I4(D)	None	D2
128.12	30	F3(C)	I5(E) & I6(F)	None	D2
139.12	30	F4(D)	I7(G) & I8(H)	Yes	D0, D2, D4
141.12	35	F7(G)	None	Yes	D0, D2, D4
151.12	30	F5(E)	None	Yes	D0, D4
156.12	30	F8(H)	None	Yes	D0, D4
176.12	30	F9(I)	None	Yes	D0, D4
204.12	30	F(10)J	None	Yes	D0, D4
224.12	30	F11(K)	None	Yes	D0, D4

Data and Analysis

The procedure for data reduction and analysis is diagrammatically shown in Figure 2.3.50. The instruments used and the quantities measured which are used to give the various elements of the source term are shown. We have mass concentration data from the filter and impactor samples which combined with the exhaust gas flow measurements give the aerosol mass source term. Even though the impactors were, for the most part, overloaded, they do give a good idea of the aerosol mass distribution. The filter sample data along with the aerosol mass source term was analyzed to give an elemental aerosol mass source term for some of the elements.

The photometer provided continuous qualitative aerosol concentration data. The APS was plugged before data could be obtained and the cyclone operated for too little time to collect enough material for analysis. This lack of data prevent us from determining the dynamic shape factor, the aerosol material density and the elemental mass distribution of the aerosol [Brockmann et al., 1987].

The three most important elements of the source term, mass source term, elemental mass source term, and mass distribution can be determined from the filter and impactor data which have successfully been taken.

SURC-3 AEROSOL INSTRUMENTATION/
AEROSOL SOURCE TERM FLOW CHART

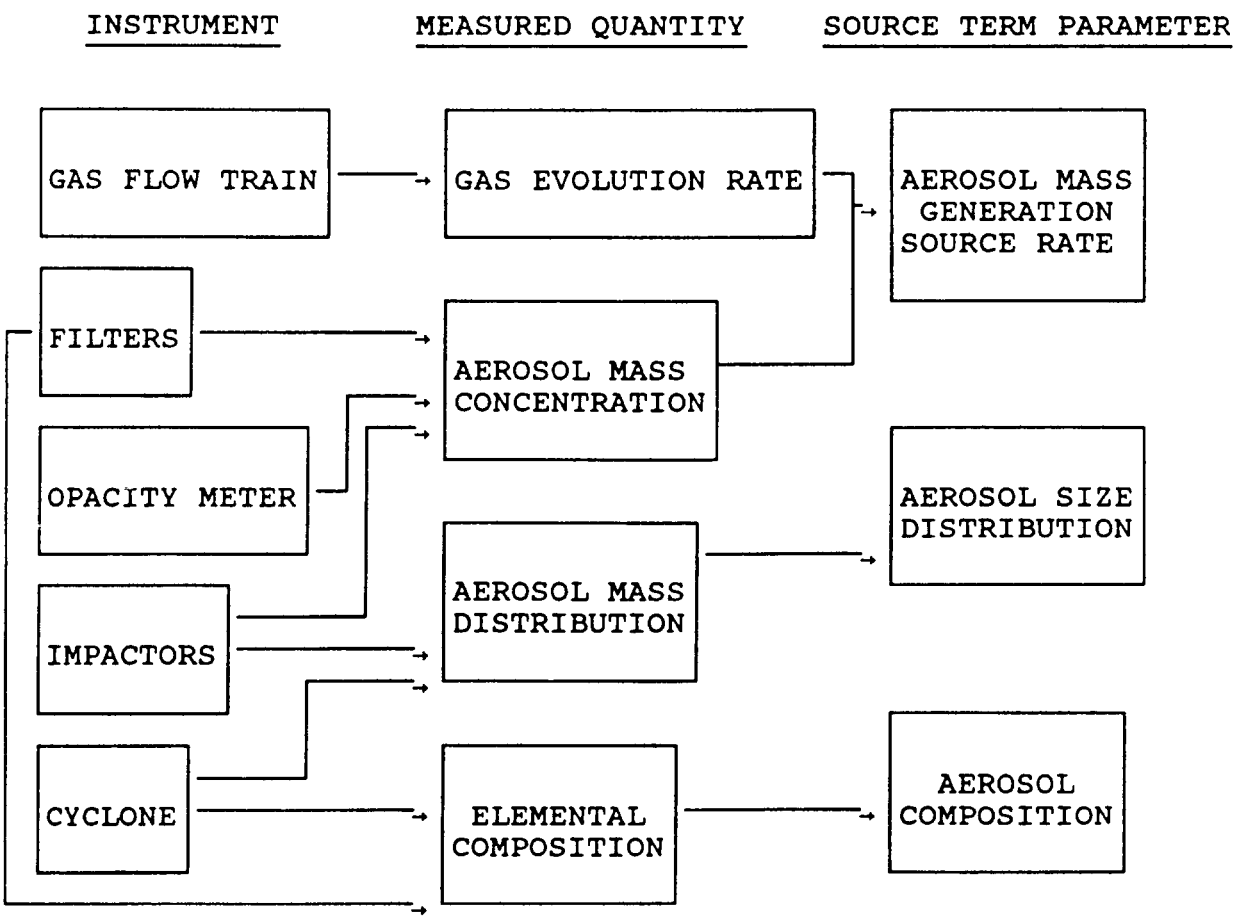

Figure 2.3.50 - Aerosol Data Analysis Technique

The mass concentration is determined from the aerosol mass collected in the filter or impactor sample and the volume of gas which was sampled. This result is corrected for dilution and transport efficiency using the following equation:

$$M = \frac{\Delta m \; DR}{Q_s \; \Delta t} \cdot \frac{1}{\eta}$$

where M = aerosol mass concentration,
Δm = aerosol mass collected,
DR = dilution rate,
Q_s = sample flow rate,
Δt = sample time, and
η = integral transport efficiency.

The filters and impactors have critical orifices which control the flow. Volumetric flow through a critical orifice is calculated from:

$$Q = Q_c \left[\frac{T}{T_c} \cdot \frac{MW_c}{MW} \right]^{1/2}$$

where Q = volumetric flow upstream of the orifice,
Q_c = volumetric flow upstream at calibration condition,
MW = molecular weight of gas,
T = upstream gas temperature, and
c = subscript denotes calibration conditions.

This equation also applies to the dilution gas delivered through critical orifices [Holman, 1966].

The molar flow is calculated from this Q using the perfect gas law.

$$\dot{n} = PQ/RT$$

where $\dot{n}$ = molar flow rate,
Q = volumetric flow rate,
R = universal gas constant,
T = gas temperature, and
All quantities evaluated upstream of the orifice.

In the case of the impactors and filters. The pressure (P) used is the system pressure, P_s, minus the pressure drop across the sampler, ΔP.

Dilution is calculated based on the molar flows in the SEDS from the following equation:

$$DR_i = \frac{\dot{n}_{oi}}{\dot{n}_{oi} - \dot{n}_{Di}} = \frac{\dot{n}_{si} + \dot{n}_{Di}}{\dot{n}_{si}}$$

where DR_i = the dilution rate of the i^{th} diluter,

$\dot{n}_{oi}$ = the total molar flow out of the diluter,

$\dot{n}_{si}$ = the molar flow of sample gas into the diluter, and

$\dot{n}_{Di}$ = the molar flow of dilution gas into the diluter.

All flows in the SEDS are known and the resulting dilution rates are calculated. The APS flow is not controlled by a critical orifice but is internally controlled to maintain a constant pressure drop across an orifice. This will cause the molar flow through the APS to vary inversely with system pressure. We have assumed a constant molar flow of $3.3 \cdot 10^{-3}$ moles/second which is the ambient setting. The pressure increase should, all else being constant, cause the molar flow to decrease [Brockmann, 1984]. However, the output from the APS mass flow meter indicates mass flows varying higher and lower than the initial setting. The increasing pressure in the system could have forced more gas through the APS than the pump and pressure feedback system could handle. In future tests, the APS will not be used on a pressurized sample port. This flow through the APS introduces additional uncertainty into the dilution rates calculated. The values used to calculate the molar flows and dilution rates are given in Tables 2.3.16 and 2.3.17.

After the test, the samples were taken to the laboratory where the filters and impaction substrates were removed and weighed. The weights of aerosol collected on the filters are given in Table 2.3.18 and the aerosol mass collected in the impactor preseparators and each stage and backup filter are given in Table 2.3.19. The total moles of gas sampled through each sampler and the total dilution rate for each sampler are also given in these tables.

The cyclone was opened but had not collected enough material for analysis. This was because it had only been operated for a few relatively short times at the end of the test.

The opacity meter (photometer) output shown in Figure 2.3.51 indicates high aerosol concentrations in the exhaust line at six distinct times (indicated by the six peaks). Aerosol sampling came from the crucible volume above the melt crust while the

opacity meter data came from the exhaust line farther down the flow path. No correlation other than timing between aerosol samples and opacity meter data was possible.

Table 2.3.20 gives the aerosol mass concentrations and the aerosol mass source term as determined by the filter samples in SURC-3. Figure 2.3.52 is a graphic representation of these data.

The aerosol mass concentration as determined from the impactor samples are given in Table 2.3.21 along with the concentrations determined from the concurrent filter samples. Figures 2.3.53 through 2.3.56 are the aerosol mass distributions determined by the impactors samples. Impactors A and B show a bimodal distribution with the mass roughly divided equally between the two modes. The smaller mode is centered at about 1.5μm aerodynamic diameter and the larger mode lies beyond 10μm aerodynamic diameter.

TABLE 2.3.16

Orifice Temperatures During SURC-3

Cyclone Orifice Temperature	= 300 K
Filter Orifice Temperature	= 340 K
10 1pm Orifice Temperature	= 318 K
15 1pm Orifice Temperature	= 318 K
DO Orifice Temperature	= 308 K
D2 Orifice Temperature	= 300 K
D4 Orifice Temperature	= 341 K

TABLE 2.3.17

System and Diluter Pressures

Sample Time (min)	System Pressure (psia)	Upstream For DO (psia)	Orifice Diluters D2 (psia)	Pressure D4 (psia)
105.12	12.6	off	off	off
106.12	12.6	off	off	off
126.12	13.2	off	40.2	off
128.12	13.2	off	40.2	off
137.12	14.1	87.9	40.2	29.0
141.12	13.3	87.9	40.2	29.4
151.12	12.7	87.9	off	29.0
156.12	12.7	87.9	off	29.0
176.12	12.6	87.9	off	29.5
204.12	12.6	87.9	off	29.1
224.12	12.6	87.9	off	28.6

TABLE 2.3.18

Aerosol Filter Data - SURC-3

Gas Sampled, Dilution Rate and Mass Collected in Filters (mg)

Filter	Mass (mg)	Sampled Gas Rate (moles)	Dilution
A	125.97	0.323	1
B	214.74	0.337	1.29
C	80.93	0.169	1.29
D	4.03	0.211	3.34
E	19.19	0.162	2.32
F	15.56	--	--
G	11.41	0.169	3.99
H	658.07	0.162	2.32
I	14.02	0.161	2.36
J	5.39	0.161	2.35
K	2.38	0.161	2.34
L	458.90	0.323	1

TABLE 2.3.19

Aerosol Impactor Data - SURC-3

Gas Sampled, Dilution Rate, and Mass Collected in Impactors (mg)

	A	B	C	D	E	F	G	H
Pre-Separator	91.49	87.82	168.19	22.42	14.53	22.76	12.96	21.60
Stage 1	30.75	33.33	45.93	2.38	1.72	2.70	1.63	3.46
Stage 2	10.29	9.18	33.85	1.67	1.04	1.64	0.52	2.35
Stage 3	11.78	10.77	50.50	3.24	1.66	2.70	0.69	2.25
Stage 4	7.26	15.23	70.00	7.10	1.99	3.77	1.03	2.67
Stage 5	23.66	33.87	263.99	93.22	4.05	7.01	1.13	2.89
Stage 6	46.20	98.66	100.91	85.80	8.13	17.64	0.97	2.60
Stage 7	32.70	39.50	36.94	30.68	11.51	22.92	0.83	3.35
Stage 8	17.30	19.25	13.11	6.98	12.03	18.39	0.85	2.46
Filter	30.98	34.48	37.05	6.64	23.82	31.86	0.95	18.10
Total	304.41	382.09	820.47	260.13	80.48	131.39	21.56	61.73
Sampled Gas (moles)	0.343	0.473	0.358	0.494	0.179	0.247	0.225	0.310
Dilution Rate	1	1	1.29	1.29	1.29	1.29	4.88	4.88

TABLE 2.3.20

Aerosol Filter Concentrations and Mass Source Term

Sample Time (min)	Filter Sample	Aerosol Concentration (mg/std liter)	Exhaust Gas (std liter/min)	Mass Source Rate (mg/sec)
105	F1	16.1	43	11.5
106	F12	59	43	42.3
126	F2	34	78	44.2
128	F3	26	78	33.8
139	F4	2.6	185	8.0
141	F7	11.1	185	34.2
151	F5	11.4	68	12.9
176	F9	8.5	60	8.5
204	F10	3.3	60	3.3
244	F11	1.43	60	1.43

TABLE 2.3.21

Aerosol Data - SURC-3 Impactors

Concentration mg/std liter

Time	Impactor	Pre-Separator	Stages	Total
105	A	11.0	25.7	36.7
105	B	7.7	25.7	33.3
126	C	25.1	97.4	122.5
126	D	2.42	25.7	28.2
128	E	4.3	19.7	24.0
128	F	4.9	23.5	28.3
139	G	11.6	7.7	19.3
139	H	14.0	26.1	40.1

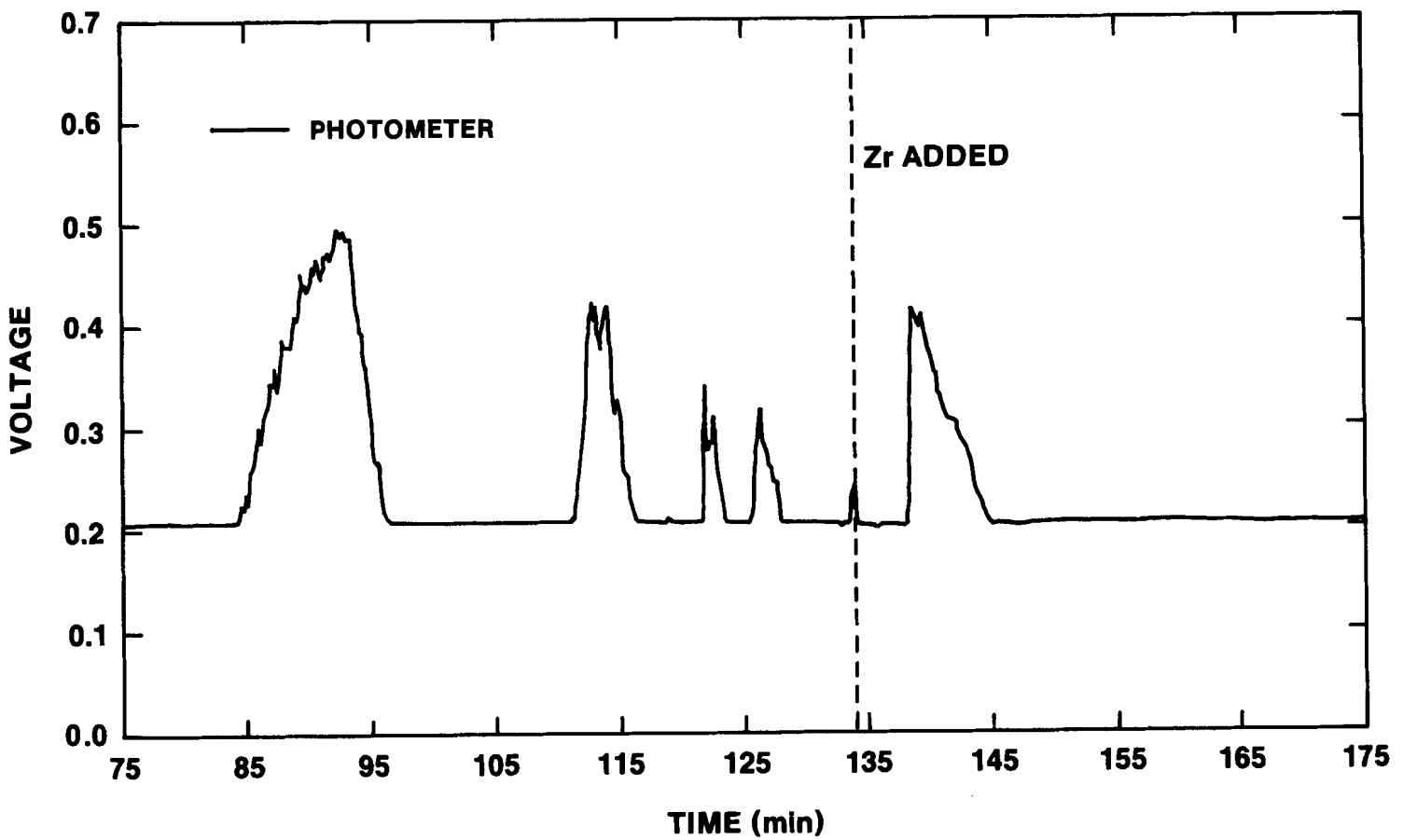

Figure 2.3.51 - SURC-3 Opacity Meter

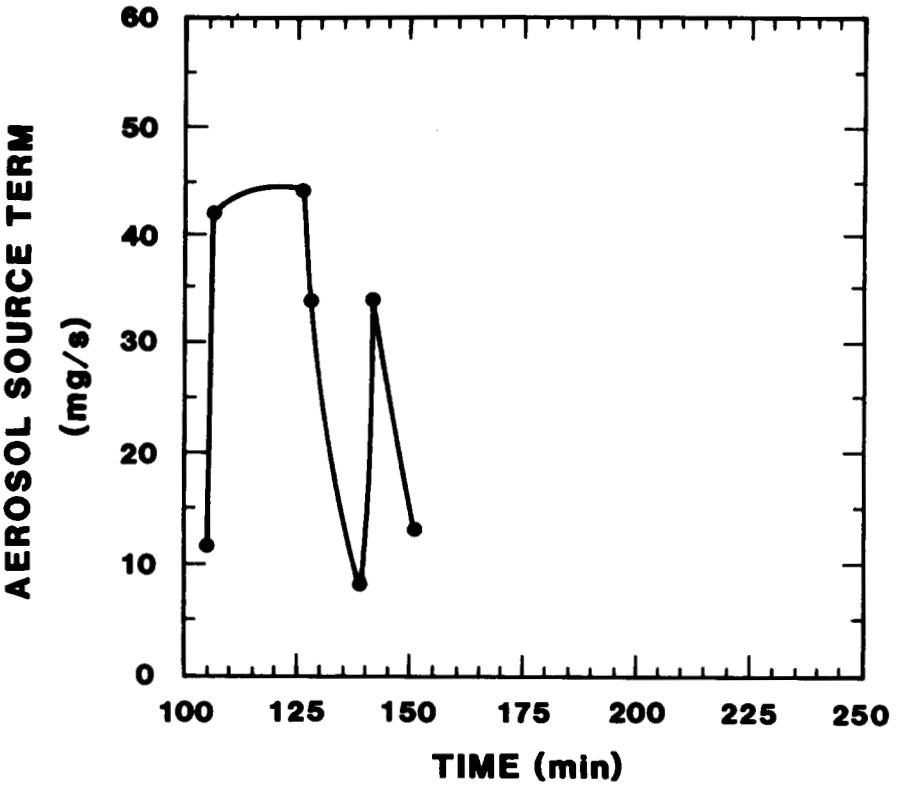

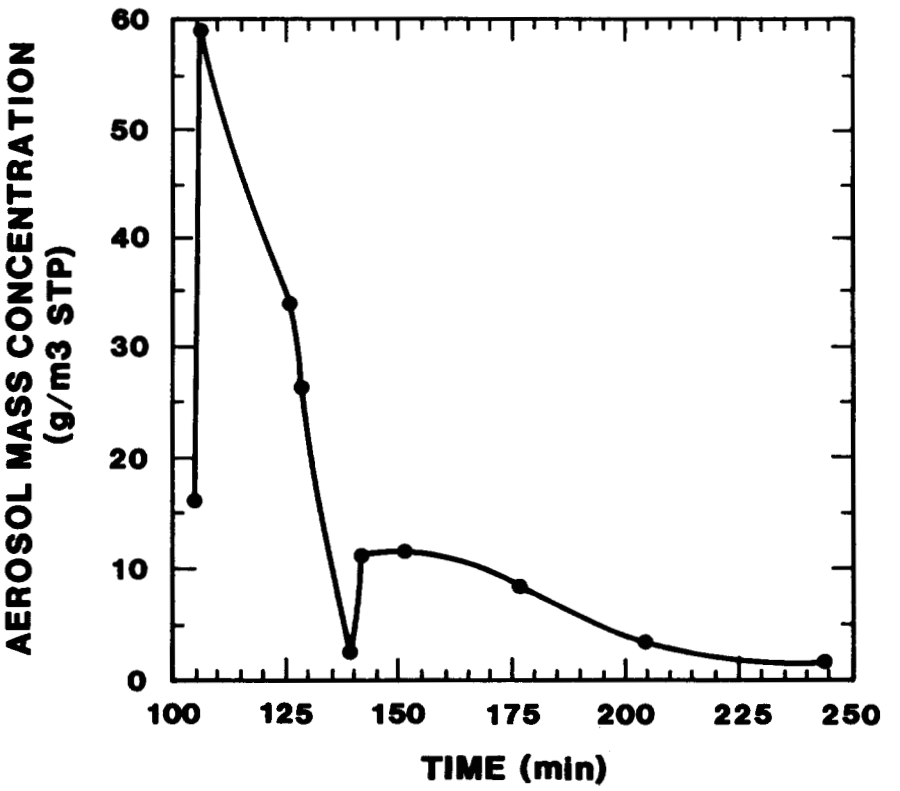

Figure 2.3.52 - SURC-3 Aerosol Mass Source Term

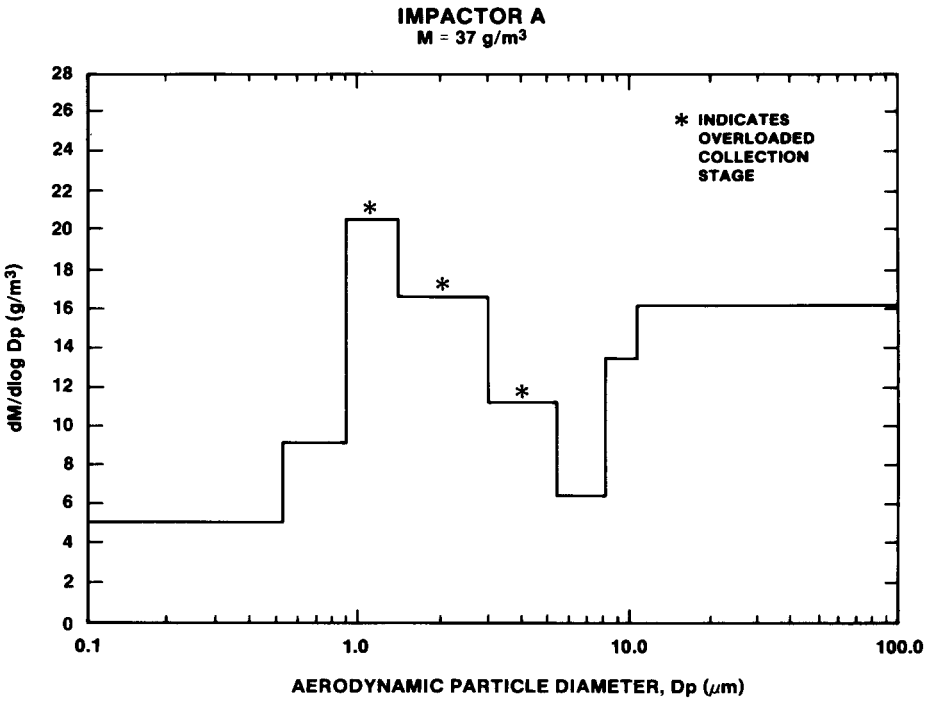

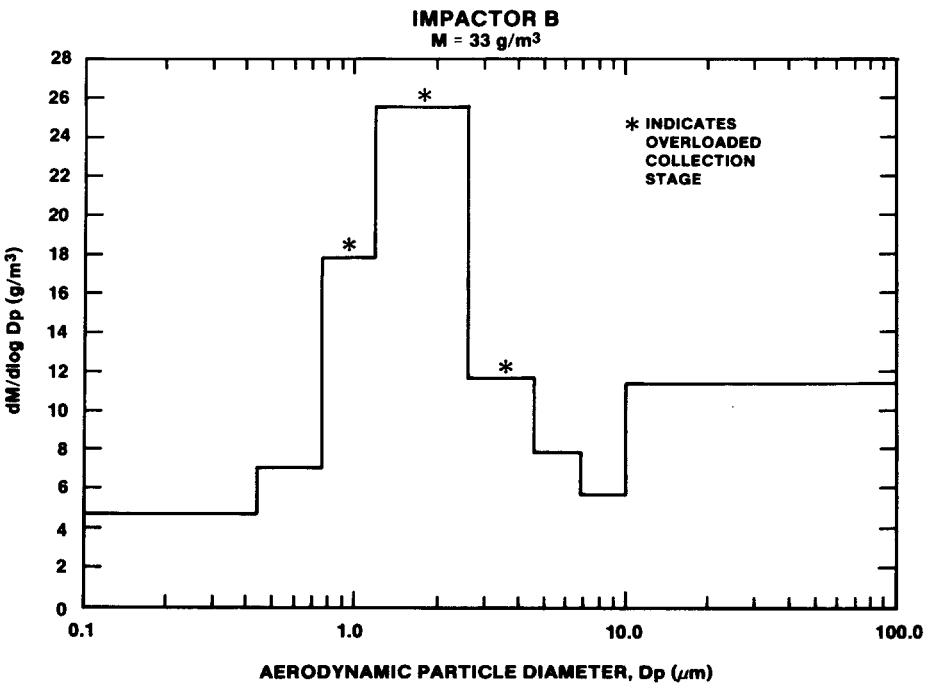

Figure 2.3.53 - Aerosol Size Distribution - Impactor A & B

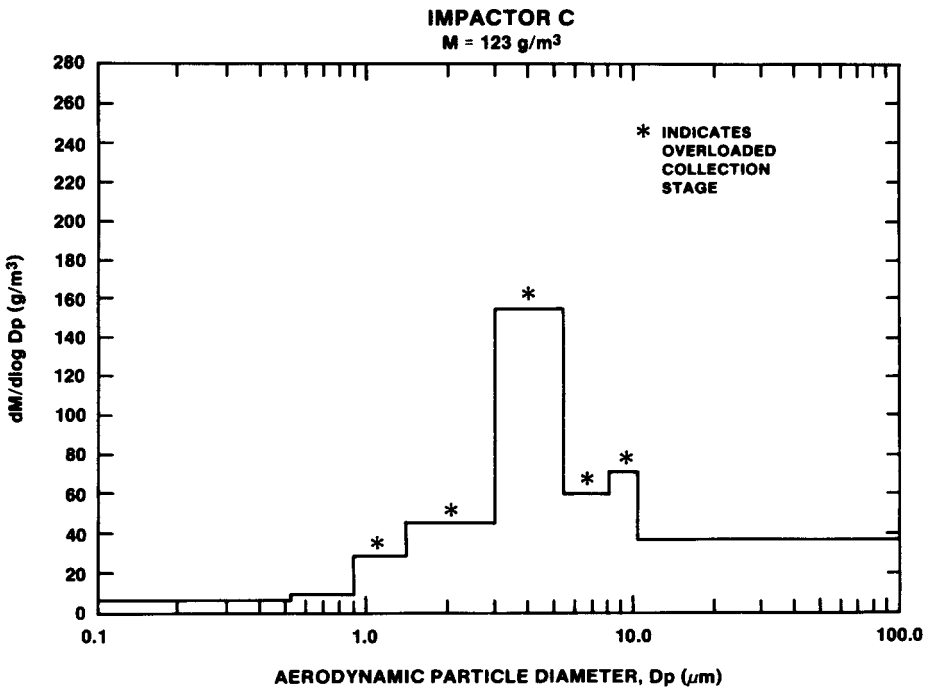

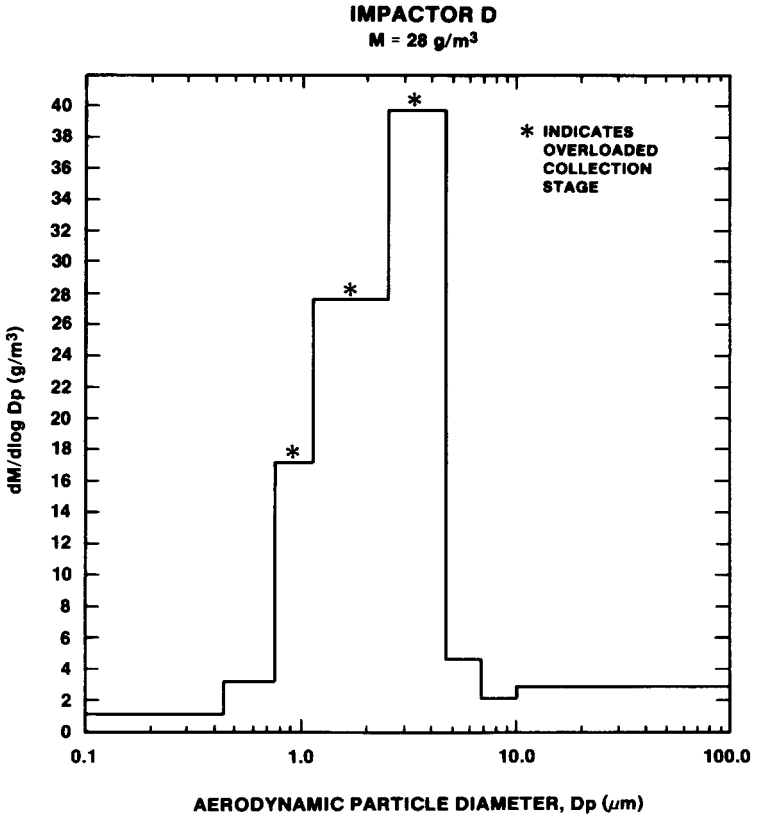

Figure 2.3.54 - Aerosol Size Distribution - Impactor C & D

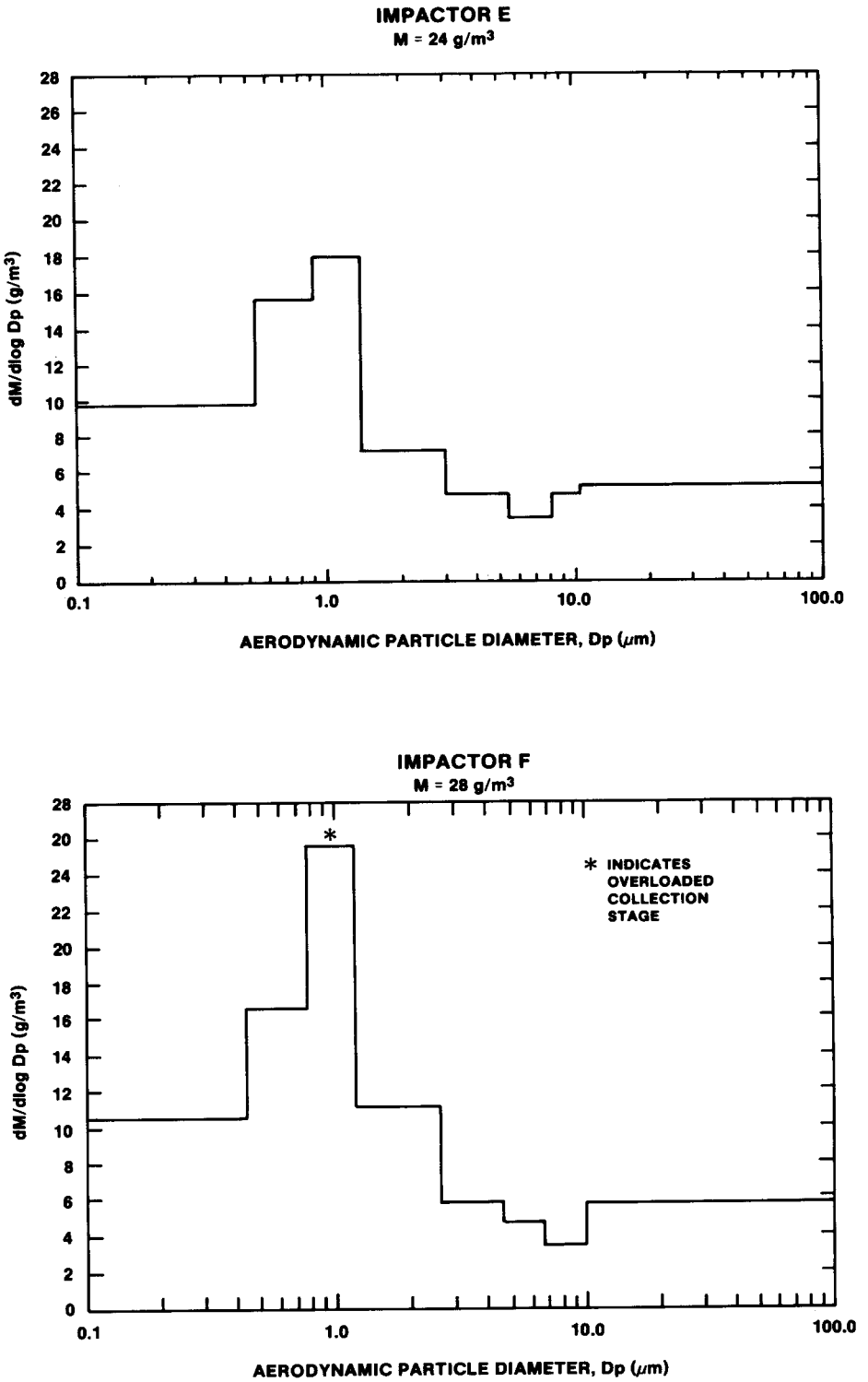

Figure 2.3.55 - Aerosol Size Distribution - Impactor E & F

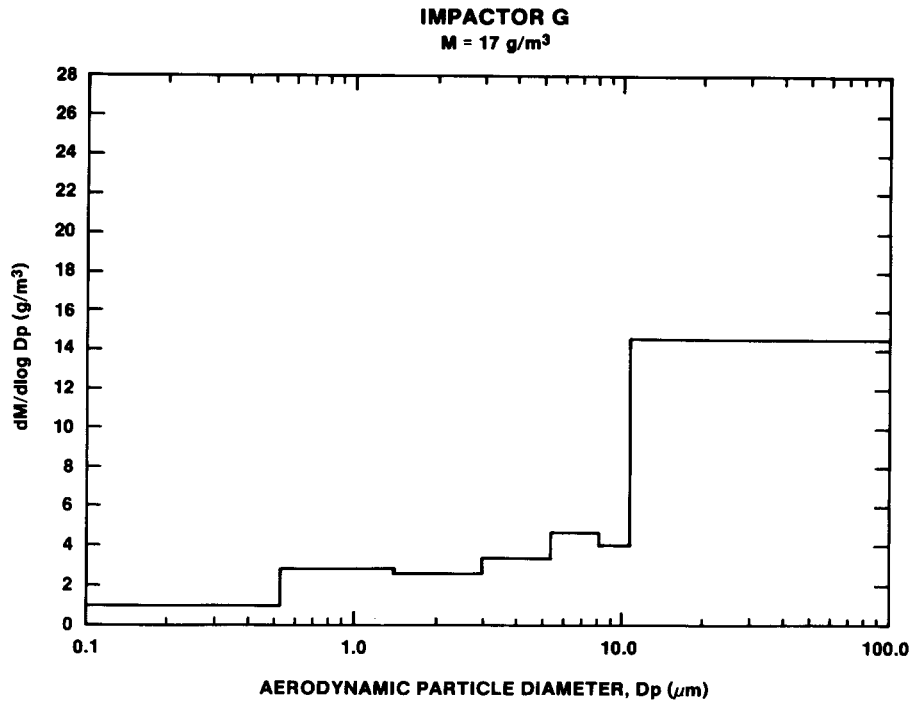

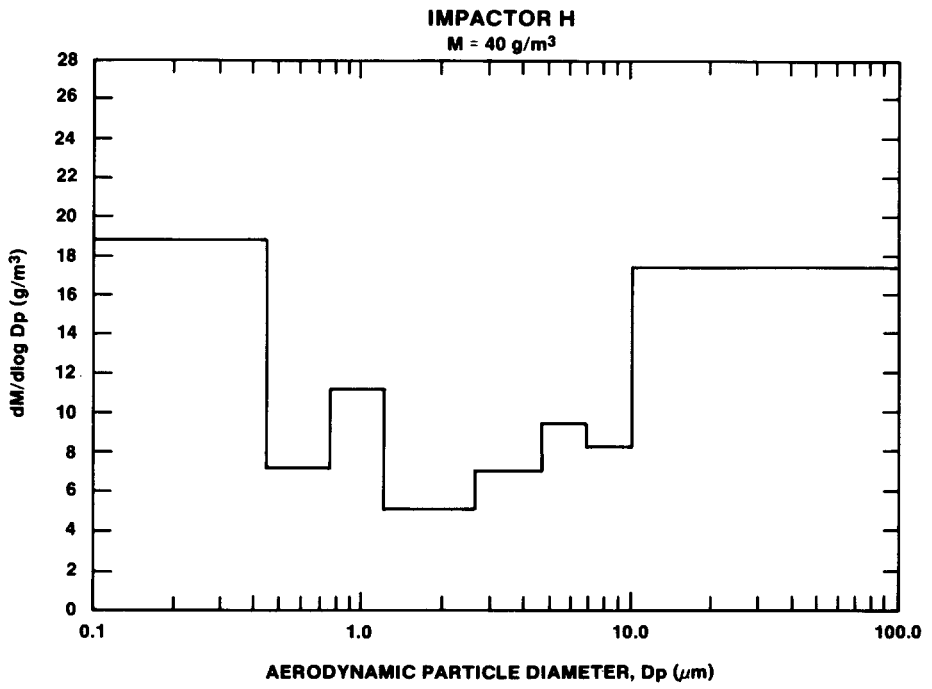

Figure 2.3.56 - Aerosol Size Distribution - Impactor G & H

Impactors C and D show a more unimodal distribution centered at about 4μm. The inordinately high concentration indicated by impactor C is noted. No explanation beyond the possibility of a leak in C has been discovered.

Impactors E and F show distributions similar to those of A and B. The smaller mode is closer to 1μm and contains more mass than the larger mode at about 10μm.

Impactors G and H do not give very well resolved distributions. They indicate a broad size distribution with a substantial mass concentration above 10μm. These samples were taken at late times and may include material re-entrained from the exhaust line.

Inductively coupled plasma (ICP) emission spectrocopy elemental analysis was conducted on selected filter samples. The laboratory first did a hydrofluoric acid digestion on some of these samples. Virtually no tellurium was found in these samples. It was later determined that the tellurium may have been lost as a volatile fluoride during the digestion. Other samples were analyzed without performing a digestion and showed tellurium to be a major constituent of the aerosol (from 27.5 w/o to 86.8 w/o).

Table 2.3.22 gives the elemental analysis for the filter samples F1-A, F12-L, F2-B, F-3C, F-4D, F7-C, F8-H, F9-I, F10-J and F11-K. The sample marked with an asterisk indicate samples analyzed by ICP at Sandia which have valid data for tellurium. These are F12-4, F2-B, F7-G, and F8-H. Potassium and sodium are also present at weight percent levels. Entries preceded by a "<" character are the lower detectability limit and indicate that the element was not detected. Entries of "NA" indicate that the element was not analyzed in that particular sample.

TABLE 2.3.22 Elemental Analysis of SURC-3 Aerosol
(Weight Percent of Element in Sample)

Element	F1-A	F12-4	F12-4*	F2-B*	F3-C	F4-D	F7-G*	F8-H*	F9-I	F10-J	F11-K
Fe	0.34	1.06	1.06	2.72	1.36	1.54	1.58	1.48	0.66	0.89	0.42
Ni	0.007	0.049	0.81	0.14	0.043	0.050	0.14	0.11	0.050	0.056	0.042
Cr	0.79	1.29	1.18	2.86	1.11	1.86	3.48	3.93	2.9	3.3	3.3
Mn	1.03	2.83	2.87	6.78	4.7	3.0	2.97	3.23	1.14	1.71	2.1
Mg	0.119	0.283	0.302	1.86	0.72	1.14	0.59	1.05	0.36	0.56	0.71
Ba	0.007	0.024	0.022	<0.02	0.007	<0.025	<0.02	<0.02	<0.007	0.037	<0.04
Na	0.95	2.10	1.72	2.4	1.48	4.5	2.59	2.04	1.28	1.39	2.8
K	5.1	7.77	5.49	NA	16.2	21.0	NA	NA	6.1	9.1	18.5
Si	0.22	0.25	0.191	0.23	0.26	0.60	0.31	0.10	0.128	0.30	1.05
Ca	0.007	0.024	0.022	0.10	0.044	0.149	0.37	0.08	<0.04	0.148	<0.2
Te	0.008	0.115	86.8	27.5	0.173	1.27	73.0	45.1	0.070	1.26	1.68
La	<0.004	<0.009	<0.015	<0.02	<0.006	<0.125	<0.02	<0.02	<0.04	<0.09	<0.2
Mo	0.002	0.0016	<0.015	<0.02	0.001	<0.02	<0.02	<0.02	<0.00	<0.02	<0.04
Ce	0.002	0.003	<0.015	<0.02	0.007	0.025	<0.02	<0.02	0.014	0.019	0.042
Nb	<0.002	<0.005	<0.015	<0.02	<0.004	<0.07	<.02	<0.02	<0.02	<0.056	<0.126
Zr	0.005	0.0016	<0.015	<0.02	0.002	0.025	<0.02	<0.02	0.007	0.019	0.042

* Valid data for tellurium.

2.3.9 Gas Composition Data Presentation

Gas sampling for the SURC-3 test was done using three techniques: An Infocon Model IQ200 mass spectrometer, an Infrared Industries Model 700 CO/CO_2 detector, and integral grab samples. The first two techniques yield real-time data which is viewed on-line and stored on computer disks. The grab samples are stored and analyzed posttest using both gas chromatography and mass spectrometry. A schematic layout of the SURC-3 gas composition sampling apparatus is shown in Figure 2.3.57.

All sample lines for gas collection were 6.4 mm (.250 in) O.D. stainless steel with Swagelok stainless steel fittings and Nupro plug valves. The sample system manifold consisted of a normal and backup line and also a 40 psi argon source for backflushing filters. There were two types of inline filters used for SURC-3, 15 micron stainless Nupro filters and .3 micron Gelman HEPA filters with an element of acrylic copolymer.

K type thermocouples were used to monitor sample gas temperatures in two different locations. A stainless steel cold trap with a volume of 75cc and cooled with liquid nitrogen was used to condense excess water vapor and prevent it from fouling the analysis equipment (Figure 2.3.58). One Gast diaphragm type air pump was used to support the main gas flow while another supplied the CO/CO_2 monitor. Flow indication for the system was measured by self-indicating rotameters. The CO/CO_2 supply was monitored with a Dwyer 0-10 scfh air rotameter and the main gas flow with a Gilmont 0-13 lpm rotameter.

Samples from the grab sample system were analyzed by gas chromatography/mass spectrometry using a Tracor MT-150g gas chromatograph and a Finnigan Mat 271/45 mass spectrometer. The samples were contained in 75cc stainless steel bottles with Nupro JB series regulating valves for closures. A Validyne absolute pressure transducer with a range of 1-1000 torr and a 0-10 volt output was used to keep track of sampling events by monitoring manifold pressure. Vacuum in the bottles was maintained prior to sampling by a Welch two-stage belt drive vacuum pump with 175 lpm free air capacity. A remote control panel housed valve position indicator lights and four-position switches for controlling the multi-port valves used in acquiring grab samples (Figure 2.3.59).

The CO/CO_2 analyzer operates on an infrared absorption technique using Infrared Industries Models 702 and 703 detectors (Figure 2.3.60). The carbon monoxide is monitored on a range of 0-50% and the carbon dioxide is monitored on a range of 0-20%. Response time is 5 seconds for 90% of the reading with a sensitivity of $\pm$ 2%. Output for the detectors to the data acquisition system is 0-5 volts.

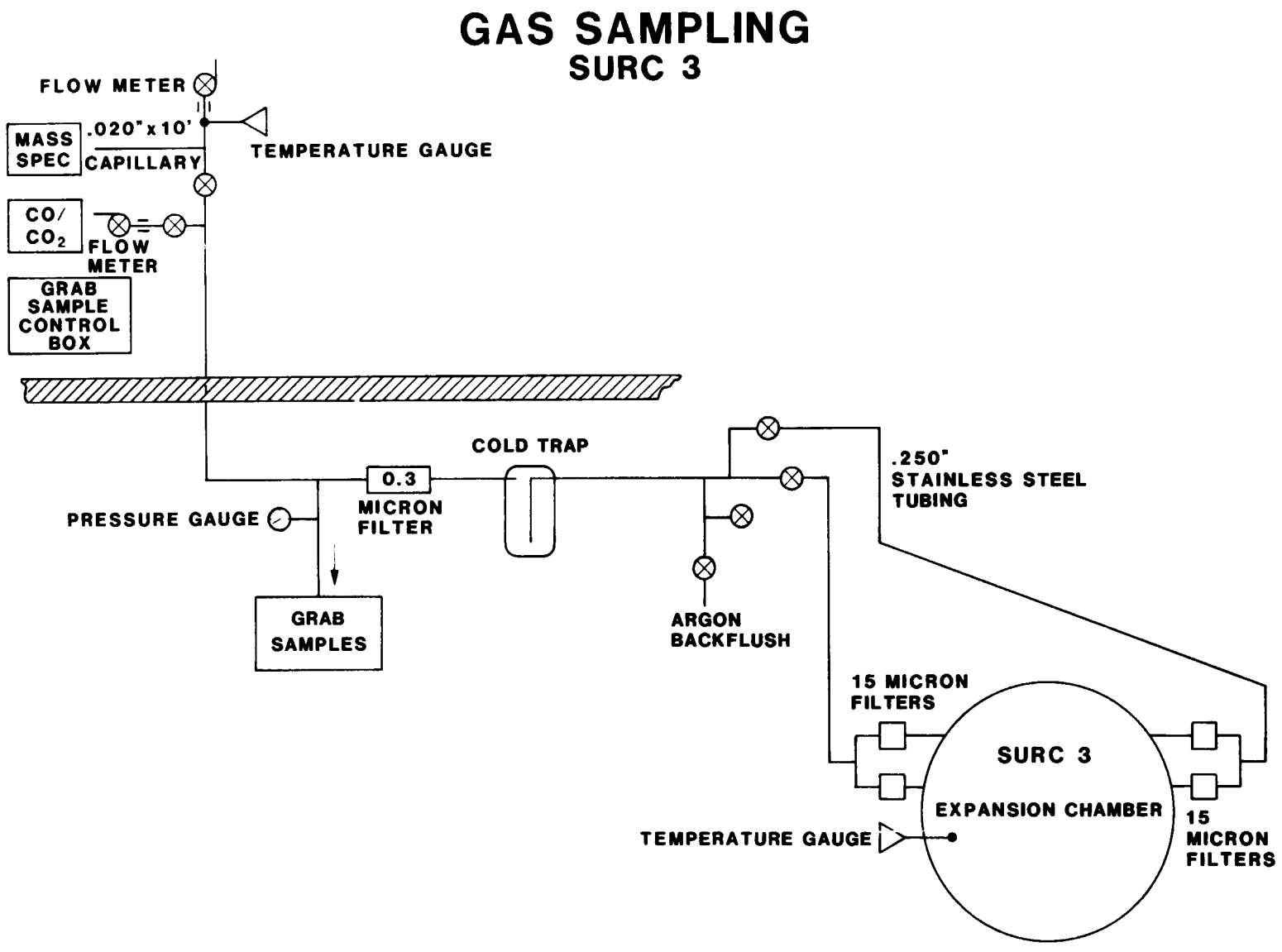

Figure 2.3.57 - Gas Sampling - SURC-3 Schematic

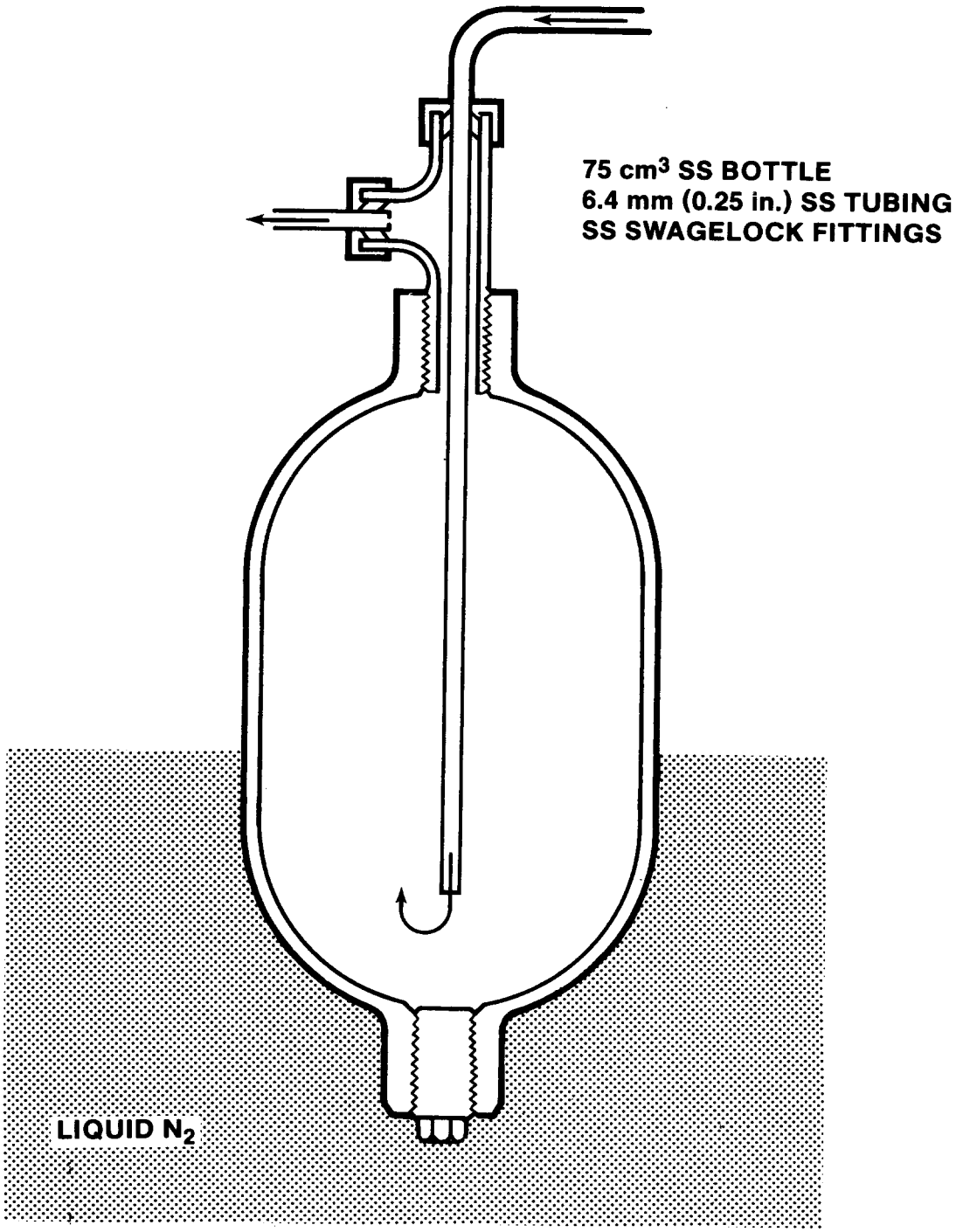

Figure 2.3.58 - Gas Sampling Nitrogen Cold Trap

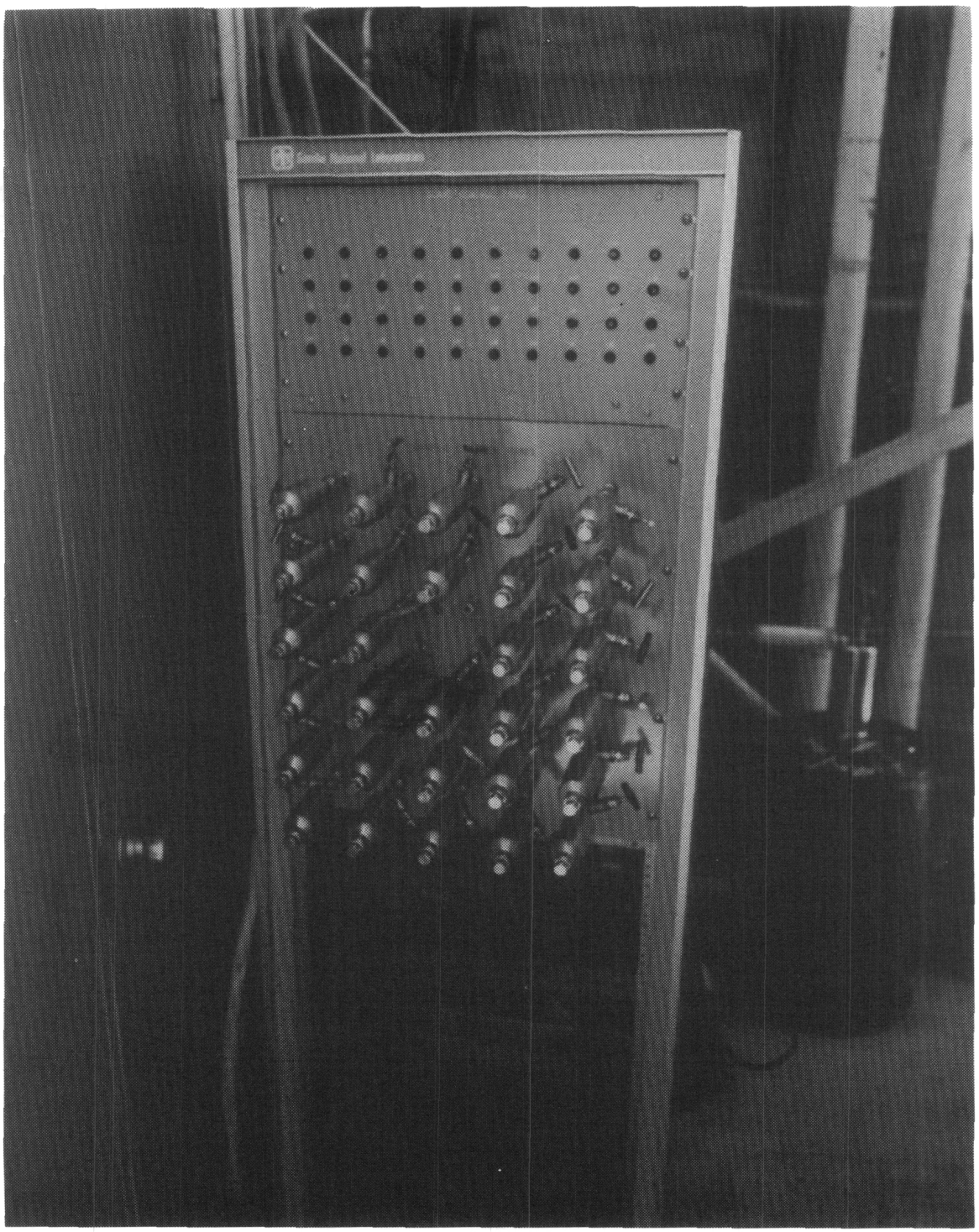

Figure 2.3.59 - Grab Sampling Apparatus

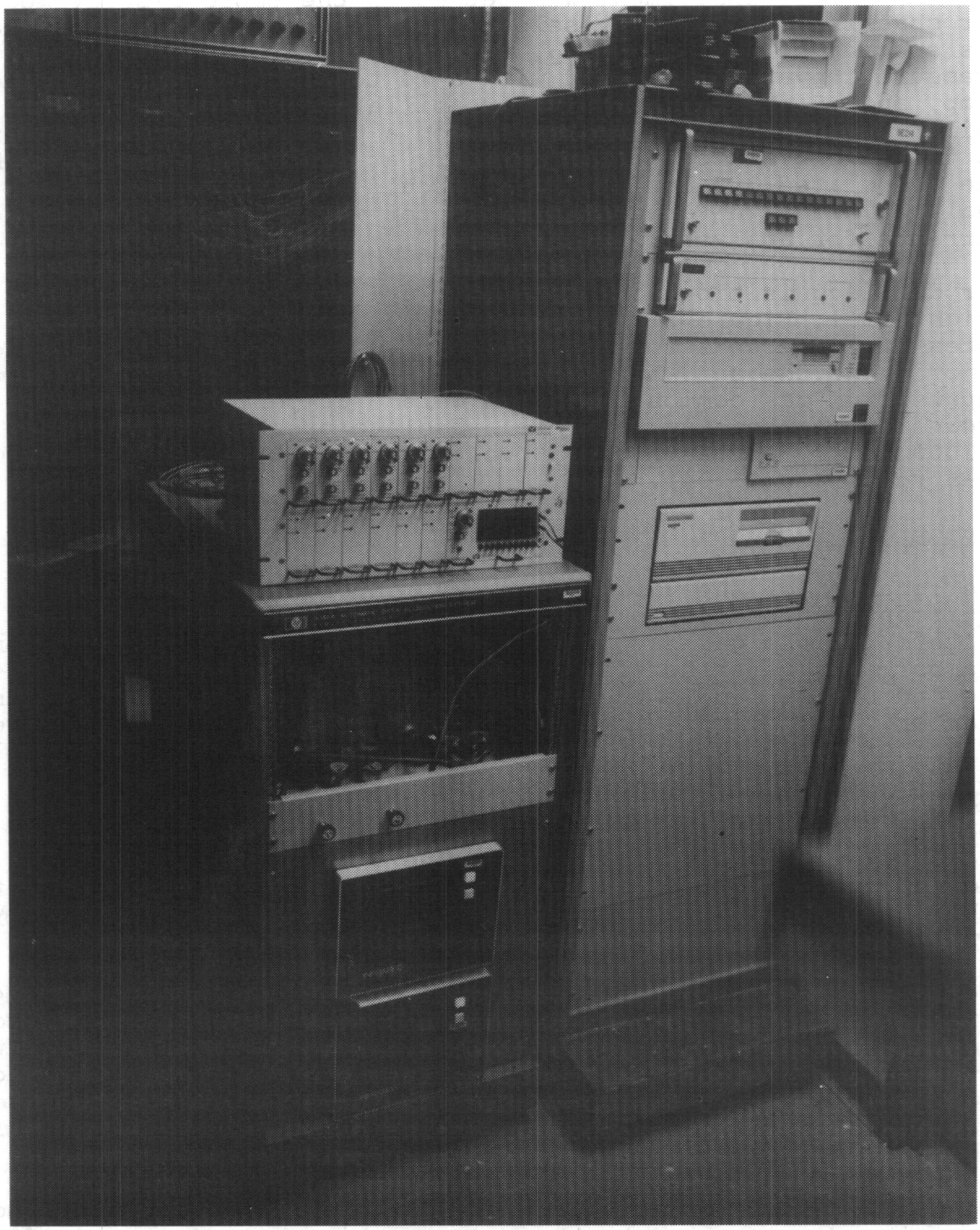

Figure 2.3.60 - CO/CO_2 Analyzer and Data Acquisition System

Another diagnostic tool for gas data used for the SURC-3 test was a quadruple residual gas analyzer, Inficon model IQ200 (Figure 2.3.61). This instrument was set up in the table display mode for scanning specifically selected masses corresponding to the gas species of interest: H_2, H_2O, CO, O_2, Ar, and CO_2. A pressure converter manifold with a 10 torr orifice, 27 lpm vacuum pump, and .5 mm (.020 in.) I.D. capillary tube provided the ability for continuous sampling from a pressure of 2 atmospheres at the sample source down to 10 torr at the analyzer supply where the associated 150 lps turbo pump could maintain 10^{-6} torr at the analyzer head. A Faraday cup detector was used to produce the currents for analysis.

For data acquisition, a Hewlett Packard 1000 series computer (right side, Figure 2.3.60) system was used with acquisition rates of 10 seconds for the test warm-up and 3 seconds for the majority of the run where test events necessitated a faster rate. Inputs from gas composition data were: temperature from the expansion chamber thermocouple, absolute pressure (0-10 volts for 0-1000 torr), percent CO (0-5 volts per 0-50%), and percent CO_2 (0-5 volts per 0-20%).

Layout and Location

The location of the various support components and analysis equipment can be seen on Figure 2.3.57. The stainless steel filters for the gas sample lines were mounted on the expansion chamber/melt generator flange approximately 15 cm downstream from the end of the sample tube which was located inside the expansion chamber. Temperature inside the expansion chamber was measured by one of the K type thermocouples while the other thermocouple measured the gas temperature at the mass analyzer sample tee. The HEPA filter, cold trap, and argon backflush manifold were located just upstream of the grab sample line approximately 7.5 m (24.5 ft) from the test article. One diaphragm air pump and flowmeter were located at the CO/CO_2 monitor supply line and the other air pump and flowmeter were downstream of the mass analyzer sample tee.

The grab sample system tied into the main gas line using a 6.4 mm (.250 in) O.D. stainless steel tube with a dead volume of 50cc. The grab sample equipment rack housed the sample bottles, multi-port valves, and pressure transducer and was located outside on the test pad approximately 7.6m (25 ft.) from the SURC-3 vessel. The control panel was located in the shielded computer room along with other instrumentation.

The CO/CO_2 instrument was located in the shielded computer room where it was connected to the main gas line by a 6.4 mm (.250 in) O.D. stainless steel tube. A diaphragm pump and flowmeter supplied the sample gas from the main gas stream for the infrared detectors. The distance upstream to the SURC-3 test article was 9.5 m (31 ft).

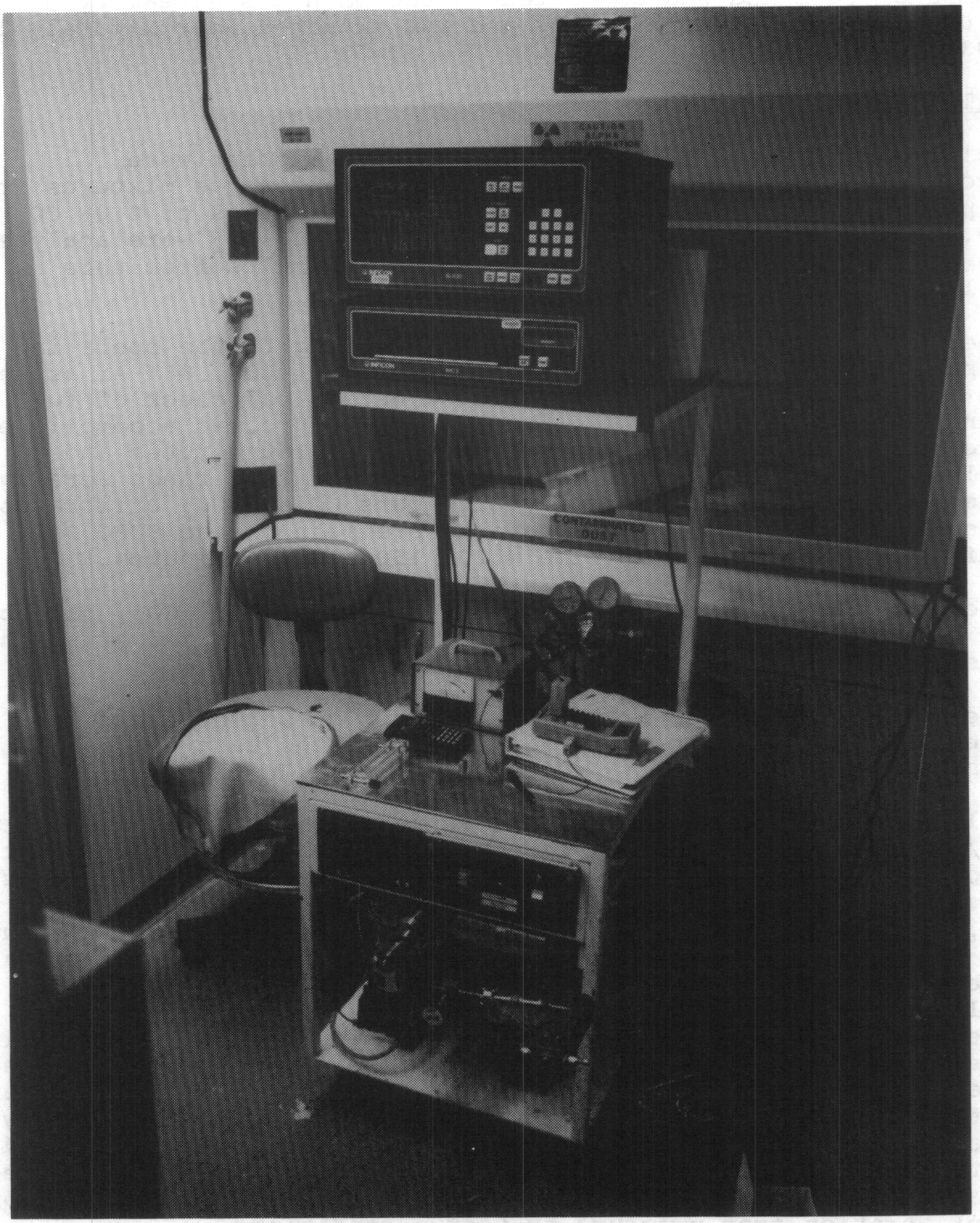

Figure 2.3.61 - Infocon Mass Spectrometer

The Inficon mass spectrometer was also located in the shielded computer room and was connected to the main gas stream by a .5 mm (.020 in) I.D. capillary tube and was situated approximately 10 m (33 ft) from the test vessel.

Calibrations

Calibrations for the different sampling equipment were accomplished with primary standard calibration gas mixtures from Alphagaz. For the grab sample analysis, mixtures of 2.0% CO, 10.0% CO_2, 88% Ar and 45.0% CO, 15.0% CO_2, 40% N_2 were analyzed in addition to the SURC-3 test samples. Results from this calibration are listed on Table 2.3.23.

The CO/CO_2 analyzer was calibrated according to the operating manual using a gas mixture of 2.0% CO, 10.0% CO_2, 88% Ar as well as pure nitrogen as a zero gas and a mechanical check of full range indications. This calibration procedure was accomplished pretest. During the test at a run time of 150 minutes and following the test completion, the zero and full range were again checked for significant drift using pure CO and CO_2 calibration gas. Results of these calibrations are seen on the SURC-3 infrared CO/CO_2 plots at time = 20, 150 and 240 minutes.

The same calibration gas mixture of 2.0% CO, 10.0% CO_2, balance Ar was used for the mass spectrometer both before and after the test. No anomalies were noted in either case.

Operational checks of all of the support components were done in the laboratory, insitu following setup of the test apparatus, and posttest.

Following the operational checks performed in the laboratory, the CO/CO_2 monitor and mass spectrometer were placed in their test locations in the sample system. Primary standard gas mixtures of 45.0% CO, 15.0% CO_2, balance N_2 and 2,0% CO, 10.0% CO_2, balance Ar, as well as a welding mixture of 25% CO_2 in Ar were introduced at different times into the expansion chamber as an operational check on these two instruments. After the SURC-3 test, the calibration procedure for the CO/CO_2 monitor and the mass spectrometer was completed again and showed no significant drift. Operational checks of the support components included response of the thermocouples from below ambient to above ambient as compared with other K type thermocouples in the same environment. Flow measurement through the self-indicating rotameters was matched with several other similar flowmeters. Output of the pressure transducer was monitored while changing the grab sample manifold configuration from pressure to vacuum conditions.

TABLE 2.3.23

Results of GS/MS Analysis
on Calibrated Gas

SAMPLE DATE	SAMPLE #	CO	CO_2	N_2	Ar
21AUG86	10A	2.03	9.85	N.D.*	87.90
21AUG86	45N	44.52	15.58	39.84	

* Not detected.

Procedures

Operational procedures for support components and analysis equipment were accomplished in the following manner. The output from the K type thermocouple installed in the expansion chamber was continuously monitored and recorded by the data acquisition system while the output from the other thermocouple mounted in the sample stream was monitored about every 5 minutes with a portable temperature meter.

Gas flow through the sample line was established several minutes before the start of the test by energizing both diaphragm pumps. The flow was manually regulated to provide 6 scfh to the CO/CO_2 monitor and 3 lpm for the main gas flow line. Monitoring of sample line flow was done every 2-5 minutes and when a substantial decrease in flow was indicated, argon was introduced into the sample line to backflush the stainless steel filters.

The grab sample bottles were evacuated before the test and then individually subjected to vacuum just prior to sample collection. Samples were taken manually and recorded on computer disk as indicated by pressure spikes. Because of the dead volume in the grab sample line leading to the main gas stream, two grab samples were taken per sampling event. After the test, two additional sample bottles were filled with calibration gas.

The CO/CO_2 monitor was warmed up for at least 30 minutes before the pretest calibrations. The data acquisition system recorded the output signals and the visible readout was monitored locally at the instrument and remotely in the control room. Following the test, another calibration check was performed on the instrument.

The mass spectrometer system was in operation under a low vacuum of 100m torr for one week prior to establishing a vacuum of 10^{-6} torr for three days before the test date. The analyzer display was continuously monitored locally. On-line data was recorded every few minutes during periods of low activity and almost every minute during more critical events.

Results

Four periods of time are of interest for the SURC-3 gas composition data: the onset of concrete ablation between 85 and 95 minutes, steady-state erosion between 105 and 125 minutes, the Zr addition and ensuing reaction between 133 and 145 minutes, and the return to steady-state erosion from 150 to 175 minutes. Notable events during the test which affected the gas composition data were: power excursions at times 90, 105, 127, and 133; temporary blockage of the gas flow lines at times 120 and 147; addition of Zr metal at times 133 and 177; and argon purge/backflush at times 122, 150, 160, and 172.

A total of 3.2 ml of water was recovered from the gas line cold trap. This would have added 4.8 l of H_2O vapor to the 170 l of collected CO, CO_2, and H_2 yielding an average water content of 2-3% in addition to the reported gas compositions for CO, CO_2, and H_2.

Gas temperature was measured at the mass spectrometer sample tee. This temperature remained fairly constant at 29-31°C throughout the test. The gas temperature was also measured inside the expansion chamber. This temperature stayed at 35°C until the first Zr drop at time=133 minutes. At time 140, this temperature reached a maximum value of 80°C, then returned to 48°C for the remainder of the test.

The 15 micron stainless steel filters interrupted gas flow to the CO/CO_2 monitor and mass spectrometer when they became clogged with aerosol particulate at run times of 120 and 147 minutes. In each instance, the filters were backflushed with argon and flow was reestablished in about 5 minutes. Backflushing was only partially successful when the lines became clogged at later times and almost no gas flow other than Argon could be detected after time 180.

The results from the CO/CO_2 monitor are shown in Figure 2.3.62. The raw data, shown here as percent CO and percent CO_2 in the sampling flowline, indicate the onset of ablation at time=83 minutes. A steady-state erosion is indicated from 100-130 minutes followed by a large increase in CO production at 135-145 minutes due to the Zr reaction. After time 145, a second steady-state condition is observed between time 150 and 175. Normalized data for these time periods are shown in Table 2.3.24. The data was normalized to eliminate the effects of the argon carrier gas and to include the effect of H_2 so that the CO/CO_2 monitor results can be compared to grab sample and mass spectrometer data. The normalized data for the CO/CO_2 monitor indicates a CO concentration of 79-80% and a CO_2 concentration of 15-16% during the onset of ablation at times 87-95. During the ensuing steady-state erosion (time 110-120) the gas composition averages 84% CO and 11% CO_2. After Zr addition at time 133, the CO concentration

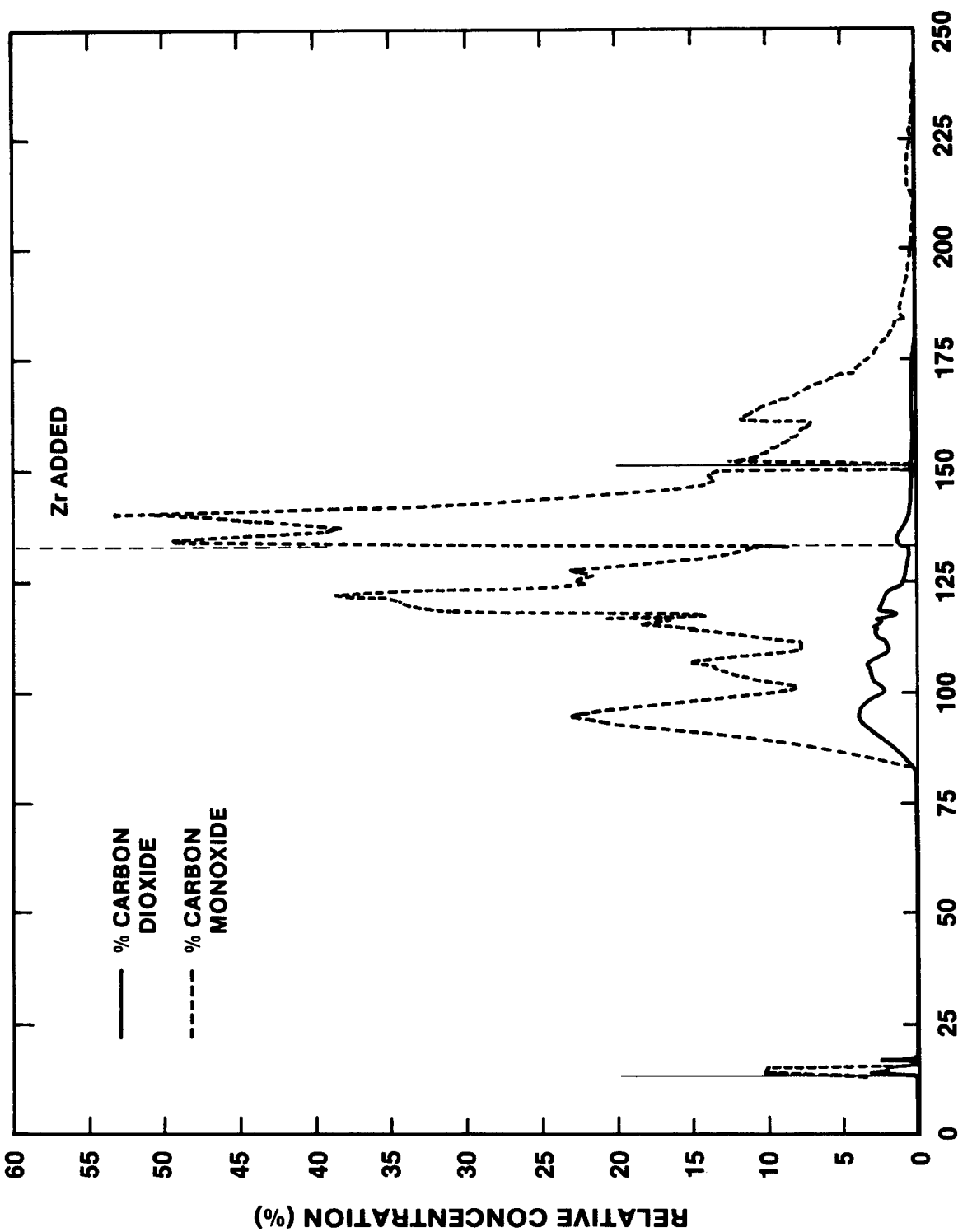

Figure 2.3.62 - CO/CO_2 Data for Test SURC-3

TABLE 2.3.24

Normalized Data - CO/CO_2 Monitor

Time	CO	CO_2	H_2 (Assumed)
87	78.8	16.2	(5.0)
89	79.0	16.0	(5.0)
91	79.7	15.3	(5.0)
93	80.8	14.2	(5.0)
95	80.2	14.8	(5.0)
110	81.6	13.4	(5.0)
112	76.9	18.1	(5.0)
114	81.3	13.7	(5.0)
116	85.8	9.2	(5.0)
118	88.0	7.0	(5.0)
120	88.6	6.4	(5.0)
135	92.6	2.4	(5.0)
137	93.0	2.0	(5.0)
139	94.0	2.0	(5.0)
141	94.3	.7	(5.0)
143	94.1	.9	(5.0)
145	93.9	1.1	(5.0)
165	92.5	2.5	(5.0)
167	92.8	2.8	(5.0)
169	92.0	3.0	(5.0)
171	91.8	3.2	(5.0)

increases to 94% and CO_2 drops to 1%. The final steady-state plateau at time 165-171 has a composition of 92% CO - 3% CO_2. After time 175, the CO/CO_2 monitor showed a carrier gas concentration in excess of 97%, probably due to gas line clogging.

Raw data from the mass spectrometer are shown in Table 2.3.25. These data indicate the onset of ablation at 89 minutes, a steady-state condition from 105-120 minutes, the Zr reaction period from 134-152 minutes, and a return to steady-state erosion at 162-176 minutes. Normalized data for these time periods are also shown in Table 2.3.25. The mass spectrometer indicates an initial concentration of 6% H_2 - 79% CO - 15% CO_2 at times 89-96. This changes to 2.5% H_2 - 87% CO - 10% CO_2 during the steady-state erosion times before Zr addition. After Zr addition at time 133, the CO concentration increases with respect to CO_2 resulting in a gas composition of 2% H_2 - 94% CO - 3% CO_2. The CO/CO_2 ratio then decreases yielding a final steady-state composition of 5% H_2 - 84% CO - 11% CO_2 between times 162 - 176. After time 181, the mass spectrometer showed a carrier gas concentration in excess of 95%, again probably due to gas sample line clogging.

The grab sample results for SURC-3 are shown in Table 2.3.26. The carrier gas for these samples includes air as well as argon in total amounts ranging from 55 - 99%. The normalized H_2 concentration during the test ranged from 2.7 - 6.4% with an average value of 4.1%. The normalized CO_2 concentration ranged from 1 to 11% with an average value of 6.6% and the CO concentration ranged from 84 - 96% with an average value of 89.3%. Eleven samples were taken in which no other gases besides H_2, O_2, CO, CO_2, N_2, and Ar were detected.

2.3.10 Data Summary and Conclusions

The SURC-3 experiment used 45 kg of 304 stainless steel and 5 kg of Zr metal as reactor core simulant materials. It was designed to be a comprehensive test examining the additional effects of zirconium metal addition to molten steel interacting with limestone concrete. The goals of the experiment were to measure in detail the gas evaluation, aerosol generation and erosion characteristics associated with steel-zirconium-concrete interactions.

The SURC-3 experiment was conducted in a 40 cm diameter interaction crucible constructed with a 20 cm diameter limestone concrete cylinder in the base of a magnesium oxide (MgO) annulus. An additional 1 meter ceramic spacer and 2 meter instrumentation tower were bolted to the top of the interaction crucible in order to provide a sealed expansion volume of 10 cubic feet for reaction effluents. A 280 kW induction power supply and coil were used to heat and melt the 45 kg stainless steel charge within the test article and to sustain the interaction for the duration of the experiment. Additionally, 5 kg of fission

TABLE 2.3.25

Gas Chromatography Analysis of SURC-3 Grab Samples

RAW DATA - VOLUME PERCENT

SAMPLE DATE (MIN.)	SAMPLE #	H_2	O_2	CO	CO_2	N_2	Ar
84	10-4	0.80	13.61	10.51	1.21	47.85	26.02
114	10-1	1.20	3.16	42.52	0.38	23.52	29.22
115	9-2	1.07	8.16	17.91	2.17	29.41	41.28
138	9-3	1.03	9.29	28.02	0.30	40.98	20.38
139	9-4	0.92	1.25	3.61	0.84	6.38	87.0
187	8-2	0.03	10.17	0.79	0.06	35.12	53.83
188	8-3	0.04	0.76	0.97	0.07	3.21	94.95
198	8-4	0.02	1.22	0.42	0.02	4.24	94.08
199	7-2	0.02	0.58	0.38	0.05	1.84	97.13
224	7-3	0.02	0.99	0.37	0.03	3.42	95.17
225	7-4	0.01	0.46	0.33	0.03	1.56	97.61

NORMALIZED DATA - VOLUME PERCENT

TIME (MIN.)	H_2O	CO	CO_2
84	6.4	83.9	9.7
114	2.7	96.4	.9
115	5.0	84.6	10.3
138	3.5	95.4	1.0
139	17	67.2	15.6
187	3.4	89.8	6.8
188	3.7	89.8	6.5
178	4.3	91.0	4.3
199	4.4	84.4	11.1
224	4.8	88	7.1
225	2.7	89.2	8.1

TABLE 2.3.26

Mass Spectrometer Data for SURC-3 Test

RAW DATA - VOLUME PERCENT

RUN TIME (min)	H_2	H_2O	CO	Ar	CO_2	NOTES
31	0.4		2.6	96.7	0.3	
40		1.7	4.2	94.1		
46	0.3	1.6	4.1	94.0		
50		1.7	6.4	91.9		
66	0.3	1.7	4.2	93.8		
69	0.3	1.7	4.3	93.6		
72	0.4		4.4	95.3		
75	0.3		4.3	95.4		
80	0.3		4.3	95.4		
82	0.3		4.3	95.4		
84	0.7		6.6	92.7		
89	1.1		12.0	84.2	2.8	
92	1.3		16.5	79.1	3.2	
96	1.6		21.0	73.3	4.1	
101	1.1		17.4	81.6		
105	1.3		25.7	73.0		
109	0.6		20.8	75.9	2.6	
114	1.1		41.7	53.8	3.5	
118	0.9		34.6	60.2	4.3	
120	0.8	4.1	36.7	55.0	3.4	Flow Blocked
125			76.7	17.7	5.6	Filter Backflushing
134	1.4		36.5	60.1	1.9	Zr Drop
138	1.2		55.3	41.5	2.0	
141	1.2		67.5	29.4	1.9	
145	2.0		79.3	15.3	3.3	
147			64.5	32.3	3.2	Flow Blocked
152			60.0	38.7	1.8	

TABLE 2.3.26 (continued)

RUN TIME	H_2	H_2O	CO	Ar	CO_2	NOTES
162	0.4		13.6	85.0	1.0	Backflush
166	0.4		10.8	88.1	0.7	
168	0.4		7.7	90.5	1.3	
173	0.4		6.8	92.0	0.9	
176	0.4		6.8	92.0	0.9	Zr Drop
181			4.6	94.5	0.9	
184	0.3		2.0	97.1	0.5	
191	0.3		1.7	97.4	0.6	
198	0.3		1.7	97.6	0.4	
201	0.3			99.3	0.5	
206	0.3			99.0	0.7	
209	0.3			99.3	0.5	
214	0.3			99.0	0.5	
216			0.9	98.4	0.7	
222	0.3		1.1	98.0	0.7	
224	0.3		1.1	98.2	0.5	
236			2.6	96.9	0.5	

NORMALIZED DATA - VOLUME PERCENT

89	7.0	75.9	17.7
92	6.2	78.9	15.3
96	6.0	78.7	15.3
109	2.5	86.3	10.8
114	2.4	90.2	7.6
118	2.3	86.9	10.8
134	3.5	91.5	4.8
138	2.1	94.5	3.4
141	1.7	95.6	2.7
145	2.4	93.6	3.9
166	3.4	90.7	5.9
168	4.2	81.1	13.7
173	4.9	84.0	11.0
176	4.9	84.0	11.0

product simulants were added to the melt to study fission product release. Flow rates of generated gases were measured using a sharp edge concentric orifice, a laminar flow device, a turbine meter and two dry gas clocks. Gaseous effluents produced during the experiment were monitored and sampled using an infrared gas analyzer, mass spectrometer, and by an integral grab sample technique. Aerosols were captured on filters, cascade impactors, and a cascade cyclone. Erosion characteristics were measured using type K, S and C thermocouples in order to define the meltpool temperature and overall heat balance as well as the axial erosion rate. The SURC-3 apparatus was sealed and purged with argon gas in order to direct the majority of the reaction gas and aerosol effluents through a 5 cm diameter flow pipe. The test was run at atmospheric pressure (.83 atm) and at an ambient temperature of 18°C.

The SURC-3 test ran for a total of 200 minutes. During this time an average power of 28±3 kW was applied to the 45 kg slug. After the slug became molten and 6-8 cm of concrete had been eroded, 1.1 kg of zirconium metal was added to the melt followed by the erosion of an additional 25 cm of limestone concrete in the final 80 minutes of the test.

Four time periods during the test are of particular interest. These are the onset of gas release from the concrete between 50 and 90 minutes, steady concrete erosion due to molten metal attack between 90 and 130 minutes, the increased attack due to Zr addition to the melt during the 135-150 minute time frame and a return to steady concrete erosion for the remainder of the test.

During the initial heatup period between 50 and 90 minutes, the temperature of the steel charge increased from 800 K to 1700 K and became molten. The concrete basemat started to dehydrate during this time at an average rate of 8 cm/hr producing a reaction gas flow rate of 10 slpm. The composition of this initial effluent gas was 6% H_2 - 79% CO - 15% CO_2. No aerosol samples were taken during this period and the opacity meter did not register an aerosol density greater than 10 g/m^3.

Concrete erosion began after 90 minutes. This was accompanied by an increase in average meltpool temperature from 1700 K to 1950 K. Aerosol release was indicated by the photometer immediately after the onset of ablation at an average density of 25 g/m^3. Molten steel-concrete attack proceeded at an average rate of 14 cm/hr until the Zr metal was added at 133 minutes. The gas release rate during this period ranged from 25 to 75 slpm and had a typical composition of 2.5% H_2 - 87% CO - 10% CO_2.

At time = 133 minutes, the Zr metal was added to the meltpool. A total of 1.1 kg of Zr became mixed with the 45 kg of 304 stainless steel resulting in a mixture of 98 w/o steel - 2 w/o zirconium. A vigorous oxidation reaction consumed the zirconium metal during the next 10-15 minutes. This reaction was marked by

an increase in ablation, flow rate and carbon monoxide production. The ablation rate increased from 14 cm/hr to 27 cm/hr during the zirconium oxidation phase and the effluent gas flow rate increased from 50 slpm to 100 slpm. The effluent was rich in carbon monoxide throughout the oxidation phase and had a typical composition of 2% H_2 - 94% CO - 3% CO_2. The meltpool temperature was 1950 K prior to the Zr addition increased to 2020 K during the oxidation period and was 1950 K at the end of the oxidation phase. Aerosols produced during this time period had an average density of 12 g/m^3.

At times after 150 minutes the melt-concrete reaction rates returned to values comparable to those seen prior to the zirconium oxidation phase. The meltpool temperatures remained near 1950 K for times between 150 minutes and 200 minutes. The effluent flow rate averaged 25 slpm and had a typical composition of 5% H_2 - 84% CO - 11% CO_2. Ablation of the concrete proceeded at 14 cm/hr during this timeframe and the aerosol source term was measured at 10 g/m^3.

Two important conclusions can be drawn from the SURC-3 data with regards to the effects of zirconium metal reactions during severe reactor accidents. First and most obvious is the fact that significant increases in gas production, aerosol generation and concrete ablation do occur even at relatively low (2%) percentages of zirconium metal content. Second, that these reactions cannot be described correctly using the "coking" gas phase reaction model by itself since a complete reduction of CO_2 does not necessarily occur. The SURC-3 data is also well suited for code validation efforts in the areas of core-concrete heat transfer, aerosol production and flammable gas concentration due to the consistency and redundancy of the measurements.

2.4 SURC-3A Experiment

2.4.1 General

The SURC-3A experiment also used 50 kg of stainless steel and 5 kg of Zr metal as the charge materials. In addition, the interaction crucible for SURC-3A was constructed entirely with limestone concrete. This test was designed to examine not only the additional effects of zirconium metal inclusion to molten steel interacting with limestone concrete, but also the relative rates of radial as well as the axial erosion when Zr metal is a melt-pool component. The primary goals for SURC-3A were to measure the gas evolution, aerosol generation, and erosion characteristics associated with two dimensional steel-zirconium-concrete interactions in order to provide validation data for chemistry models in CORCON, particularly with regard to the severity and duration of any coking effects, which are predicted to produce extraordinary amounts of CO immediately after the Zr oxidation phases are complete. [Bradley, 1986; Powers, 1986; Gronager, 1986].

SURC-3A was instrumented to provide comprehensive, redundant, and well-characterized information on the steel-zirconium-concrete interaction. Gas evolution was measured in order to determine both gas composition and effluent flow rate using four flow rate devices and three independent gas analysis techniques. Aerosol generation was measured with four different techniques to completely characterize the aerosol source including not only mass generation rate, but also size distribution, bulk material density, and elemental composition. Erosion characteristics were measured using three separate thermocouple techniques in order to define the meltpool temperature and overall heat balance as well as the axial and radial erosion rates.

The SURC-3A test article was similar to the SURC-3 test in design and dimensions and similar to the QT-E test in materials configuration. The crucible (see Section 2.4.2) was made entirely from limestone concrete and was 40 cm in diameter and 90 cm high. The meltpool cavity was 20 cm in diameter and 50 cm high, leaving 10-cm thick sidewalls and a basemat 40 cm thick. An additional one meter refractory spacer was bolted to the interaction crucible in series with a 2 meter instrumentation tower. This provided a sealed expansion volume of approximately 10 cubic feet for the concrete reaction effluents, additional space for the aerosol and gas measurement apparatus, and a safe standoff distance for the sealed Zr delivery system. The total apparatus stood 3.75 meters high and had an outside diameter of 40 cm.

The zirconium metal was added to the meltpool via a two-tube remotely actuated delivery system attached directly to the expansion top hat. Each tube contained nine Zr cylinders. each cylinder had a diameter of 3.3 cm and a length of 5 cm. Each cylinder weighed 268 g and the total charge weighed 5 kg. The two tubes are each actuated individually so that Zr metal could

be added in 2.5 kg increments at any time during the test. In addition to the Zr metal, fission product simulants were added to the metallic change in order to determine their potential to become aerosolized during the melt-concrete interaction. These simulants were added to the charge in powder form during the assembly stage of the experiment and were thus heated and incorporated into the initial melt along with the stainless steel. Equal amounts of Te, NG_2O_5, Mo, ZrO_2, La_2O_3, BaO, and CeO_2 totalling 3.5 kg made up these fission product mocks.

The SURC-3A crucible was positioned in a 13 turn copper induction coil with an inside diameter of 43 cm and a height of 45 cm. The coil was powered using a 280 kW motor generator set at a frequency of 1000 Hz in order to melt and sustain the steel-Zr-concrete interaction. The apparatus was sealed and purged with both argon and helium gas in order to provide background flow for the reaction gas and aerosol effluents. The total flow containing both carrier gas and the reaction effluents was directed through a 5 cm instrumented flow pipe which was routed through a gravel filter bed then exhausted to atmosphere. The SURC-3A test was run at local atmospheric pressure (.83 atm) and at an ambient temperature of 20°C.

2.4.2 Geometry and Materials

2.4.2.1 Geometry

The experimental apparatus used in the SURC-3A experiment was the same as that used in the SURC-3, except that the crucible was cast entirely of limestone concrete. The major components of the experimental apparatus have been previously discussed in detail in Section 2.3.3 and are shown in Figure 2.3.1. The crucible geometry and thermocouple locations will be described in this section.

Interaction Crucible

The interaction crucible used in the SURC-3A experiment was constructed in a cylindrical geometry typical of that used in the SURC-3 test and is shown in Figure 2.4.1. The cavity dimensions were the same as that of the SURC-3 crucible having an ID of 21.6 cm and a depth of 51.4 cm. In anticipation of significant sidewall erosion, the crucible was cast having a 14.6 cm thick annulus, 50.8 cm OD and 91.4 cm height. The crucible was cast with an annular recess in the top to facilitate mounting the zirconium delivery section. The outside of the crucible was laminated with two layers of fiber glass cloth for strength as described earlier.

The concrete annulus and slug were instrumented with the same number and type of thermocouples installed in relatively the same location as the SURC-3 crucible. A total of 40 type K

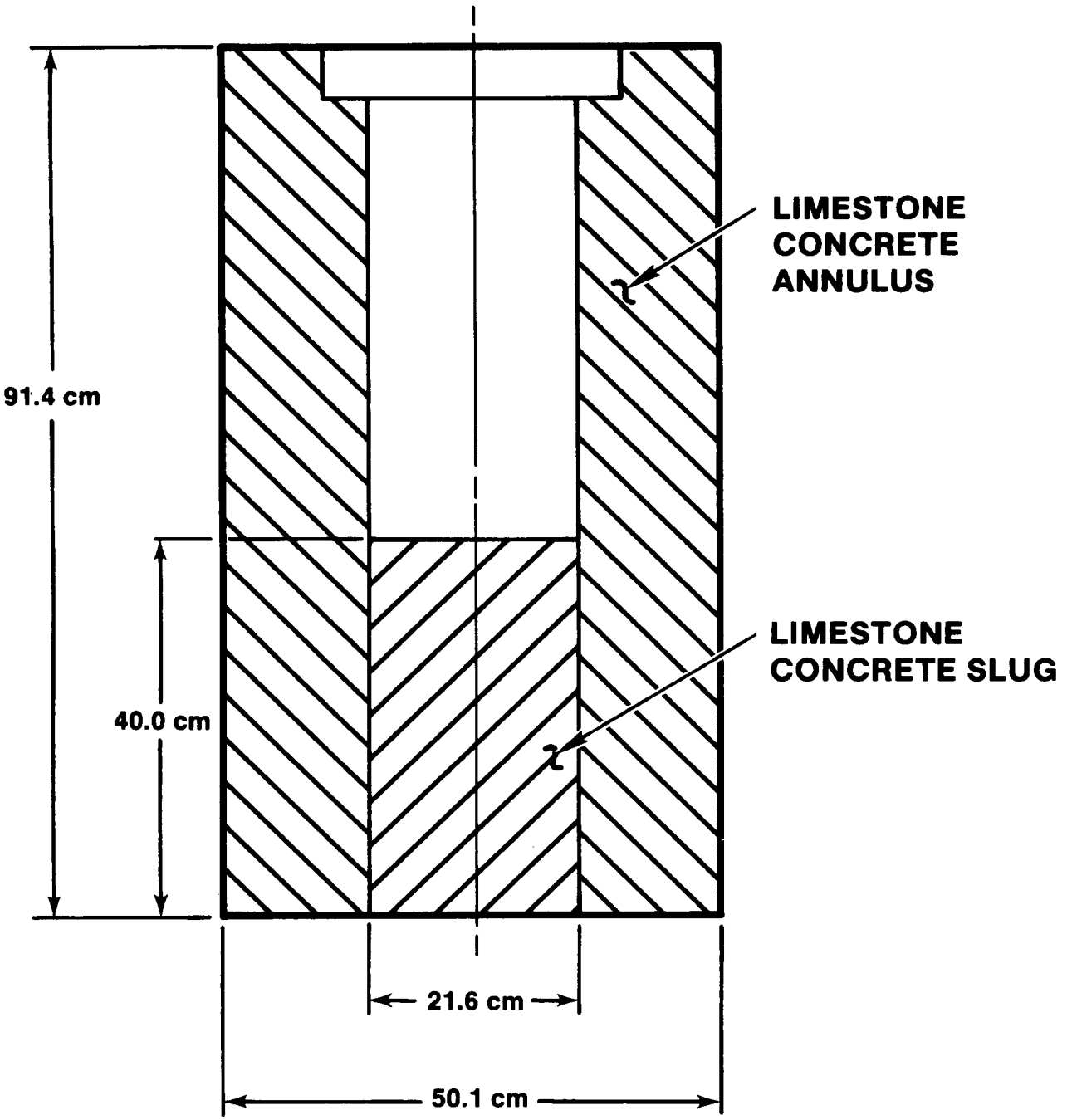

Figure 2.4.1. Interaction Crucible, SURC-3A

thermocouples were cast into the concrete slug in two arrays to measure the thermal response and monitor concrete erosion. An additional six type S and six type C thermocouples were installed into alumina tubes and cast into the concrete slug to measure melt temperature. The locations of the type K thermocouples cast into the concrete slug are tabulated in Table 2.4.1. The location of the type S and C thermocouples installed in the alumina tubes and embedded in the concrete slug are listed in Table 2.4.2.

A total of 37 type K thermocouples, installed in 11 arrays were cast into the concrete annulus of the crucible at various elevations to monitor the thermal response and erosion of the sidewall and erosion. These thermocouples were installed in relatively the same location as in the SURC-3 crucible. The specific locations of the sidewall thermocouples are tabulated in Table 2.4.3.

2.4.2.2 Materials

The materials used in the SURC-3A experiment were the same as those used in SURC-3, except the interaction was cast entirely (annulus and base) with limestone concrete. The zirconium delivery section was cast using K/R Cast-98, MgO castible. Both of these materials have been described in detail with regard to mixing specifications, chemical composition and thermal properties in Section 2.3.2.

Concrete Material

In order to verify the concrete curing strength, four 10.3 cm diameter, 20.3 cm high compressive test cylinders were cast with both the annulus and base of the interaction crucible. The crucible was cured at ambient temperature conditions (nominally 20 ± 5°C). A cylinder cast with concrete typical of the annulus and base was tested at 7, 14, 28 and 107 (day of the experiment) days. The compressive strengths measured at the end of each cure period are tabulated in Table 2.4.4. The two samples tested at 28 days representing the concrete cast into the annulus and base of the crucible had a compressive strength of 26.3 and 28.9 MN/m^2, respectively. These strengths exceed the minimum 28 day specification of 17.2 MN/m^2. The other specification was that the concrete achieve a minimum compressive strength of 27.5 MN/m^2 after 90 days. No test cylinders were tested at the end of 90 days, however, a cylinder sample taken from the annulus and the base were tested at 107 days, the day of the experiment. The cylinder tested from the base concrete yielded a strength of 30.4 MN/m^2. This is well above the specification requirement of 27.5 MN/m^2. The strength of the test cylinder cast with the concrete forming the annulus measured 26.1 MN/m^2. This is slightly under the suggested specification, but is acceptable.

TABLE 2.4.1

Location of Thermocouples Cast Within the Concrete Slug, SURC-3A

(See Figure 2.3.4)

Thermocouple No.	r (cm)	θ (degree)	z (cm)
C1	0	0	-0.0
C2	0	0	-1.0
C3	0	0	-2.9
C4	0	0	-4.9
C5	0	0	-6.9
C6	0	0	-8.9
C7	0	0	-10.9
C8	0	0	-12.9
C9	0	0	-15.0
C10	0	0	-17.0
C11	0	0	-19.0
C12	0	0	-21.0
C13	0	0	-23.0
C14	0	0	-25.1
C15	0	0	-27.1
C16	0	0	-29.0
C17	0	0	-31.0
C18	0	0	-33.0
C19	0	0	-35.1
C20	0	0	-37.1
C21	5.4	0	-0.2
C22	5.4	0	-2.0
C23	5.4	0	-4.0
C24	5.4	0	-6.0
C25	5.4	0	-8.0
C26	5.4	0	-10.0

TABLE 2.4.1 (continued)
Location of Thermocouples Cast Within the
Concrete Slug, SURC-3A
(See Figure 2.3.4)

Thermocouple No.	r (cm)	θ (degree)	z (cm)
C27	5.4	0	-12.0
C28	5.4	0	-14.0
C29	5.4	0	-16.0
C30	5.4	0	-18.0
C31	5.4	0	-20.0
C32	5.4	0	-22.0
C33	5.4	0	-24.0
C34	5.4	0	-26.0
C35	5.4	0	-28.0
C36	5.4	0	-30.0
C37	5.4	0	-32.0
C38	5.4	0	-34.0
C39	5.4	0	-36.1
C40	5.4	0	-38.1

TABLE 2.4.2

Location of Thermocouples Installed in the Alumina Tubes Cast Into the Concrete Slug, SURC-3A

(See Figure 2.3.4)

Tube No. (#)	Thermocouple No. (#)	Thermocouple Type (C or S)	r	θ	z
A1	1	C	5.46	0	- 1.0
	2	C	5.4	60	- 7.0
	3	S	5.4	60	-15.0
	4	S	5.4	60	-24.0
A2	1	C	5.4	180	- 3.0
	2	C	5.4	180	- 9.0
	3	S	5.4	180	-18.0
	4	S	5.4	180	-27.0
A3	1	C	5.4	300	- 5.0
	2	C	5.4	300	-12.0
	3	S	5.4	300	-21.0
	4	S	5.4	300	-30.0

TABLE 2.4.3
Location of Thermocouple Cast Within
The Sidewall, SURC-3A
(See Figure 2.3.4)

Array No.	Thermocouple No.	t (cm)	θ (degree)	z (cm)
1	M1	1.2	0	-32.1
	M2	2.3	0	-32.1
	M3	3.3	0	-32.1
2	M4	0.9	0	-24.2
	M5	2.1	0	-24.2
	M6	3.2	0	-24.2
	M7	9.9	0	-24.2
3	M8	1.2	0	-16.1
	M9	2.1	0	-16.1
	M10	3.3	0	-16.1
4	M11	1.1	270	- 8.5
	M12	2.0	270	- 8.5
	M13	3.1	270	- 8.5
	M14	8.9	270	- 8.5
5	M15	1.1	270	0.5
	M16	1.9	270	0.5
	M17	3.1	270	0.5
6	M18	1.0	270	4.5
	M19	2.0	270	4.5
	M20	3.0	270	4.5
7	M21	1.1	180	9.8
	M22	2.2	180	9.8
	M23	3.2	180	9.8
	M24	9.3	180	9.8
8	M25	1.0	180	14.9

TABLE 2.4.3 (continued)
Location of Thermocouple Cast Within
The Sidewall, SURC-3A
(See Figure 2.3.4)

Array No.	Thermocouple No.	t (cm)	θ (degree)	z (cm)
8	M26	1.9	180	14.9
	M27	2.8	180	14.9
9	M28	1.0	180	20.0
	M29	2.0	180	20.0
	M30	3.0	180	20.0
10	M31	0.8	90	30.3
	M32	1.9	90	30.3
	M33	3.0	90	30.3
	M34	9.6	90	30.3
11	M35	0.5	90	39.9
	M36	1.9	90	39.9
	M37	2.7	90	39.9

TABLE 2.4.4

Limestone Concrete Compressive Strengths,

Test SURC-3A

Crucible Section	Cure Days (No.)	Failure Stress (MN/m^2)
Annulus	7	23.3
	14	22.5
	28	26.3
	107	26.1
Base	7	21.1
	14	22.1
	28	28.9
	107	30.4

The thermal behavior of the concrete was characterized by thermal gravimetric analysis. A representative sample was tested using concrete cast in the annulus and the base. The thermograms for the annulus and base material are presented in Figures 2.4.2 and 2.4.3, respectively. The procedure for testing these samples was the same as described in Section 2.3.2. A 22.39 mg sample of the annulus materials and a 21.29 mg sample of the slug material was tested. Both thermograms show a 1.9% weight loss between ambient temperature and 100°C. This is due to the release of free water in the concrete. Figures 2.4.2a and 2.4.2b show a 34% and 36% weight loss, respectively, between 565 and 817°C. This is representative of the loss of CO_2 from the limestone concrete. Figures 2.4.3a and 2.4.3b are expansions of the thermograms between 360 and 475°C. These two figures reveal a 0.3 and 0.4% weight loss for both samples between 405 and 435°C caused by the decomposition of $Ca(OH)_2$. The thermograms presented are representative of limestone concrete.

Charge Material and Fission Product Simulants

The charge material, zirconium metal and fission product simulants are the same in mass, geometry and chemistry as those used in the SURC-3 experiment and are described in Section 2.3.2. In order to evaluate the transport of fission products during the melt concrete interaction, various chemical species, listed in Table 2.4.5, were added to the melt. These fission product simulants were added to the interaction crucible as a homogeneous powdered mixture prior to heating the stainless steel. Half of the simulant mass (1.75 kg) was placed directly on top of the concrete surface to help serve as an insulator during the initial heating of the steel to minimize concrete dehydration. The other half of the mass was placed on top of the stainless steel cylinder.

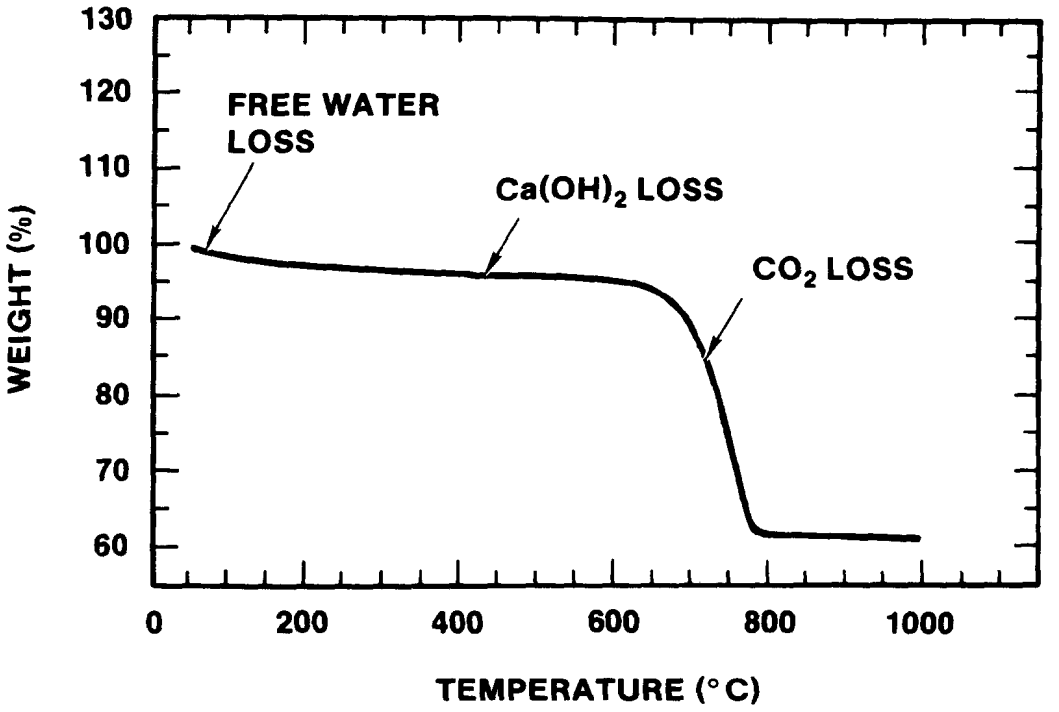

Figure 2.4.2a. Thermogram (TGA) of the Limestone Concrete used in the Annulus of the Crucible, SURC-3A.

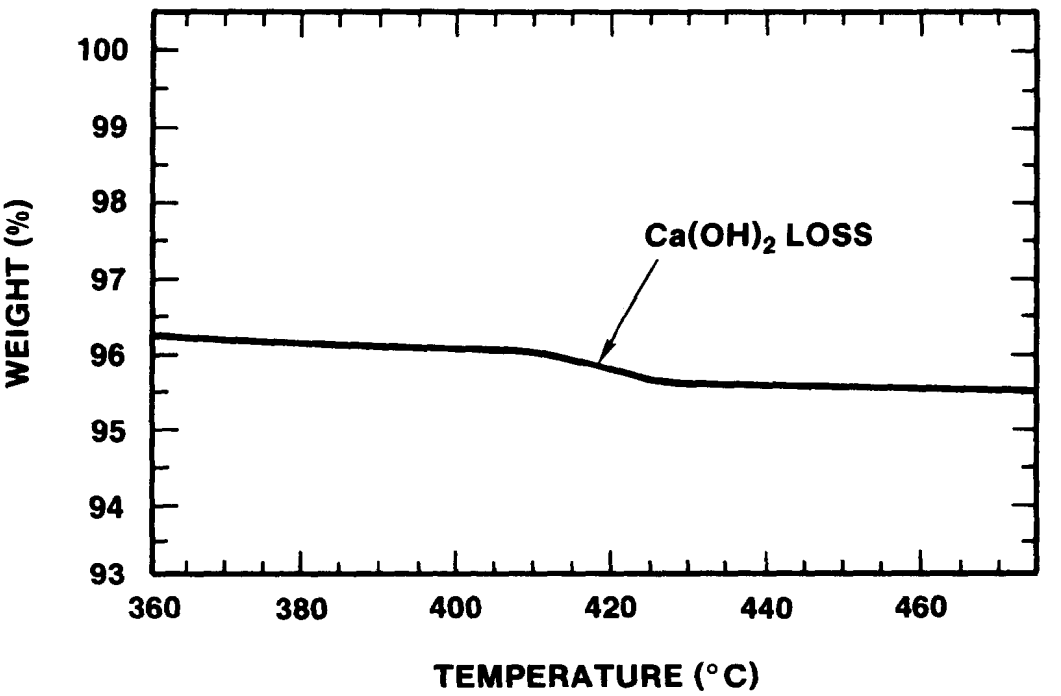

Figure 2.4.2b. Expansion of Thermogram (TGA) of the Limestone Concrete used in the Annulus of the Crucible, SURC-3A.

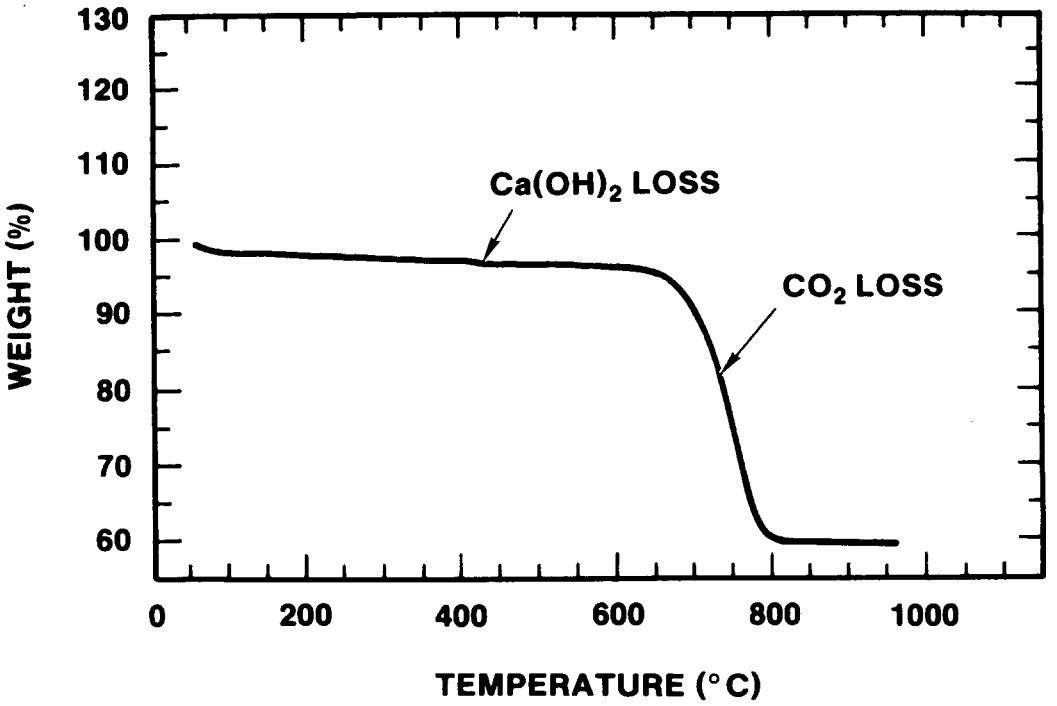

Figure 2.4.3a. Thermogram (TGA) of the Limestone Concrete used in the Base of the Crucible, SURC-3A.

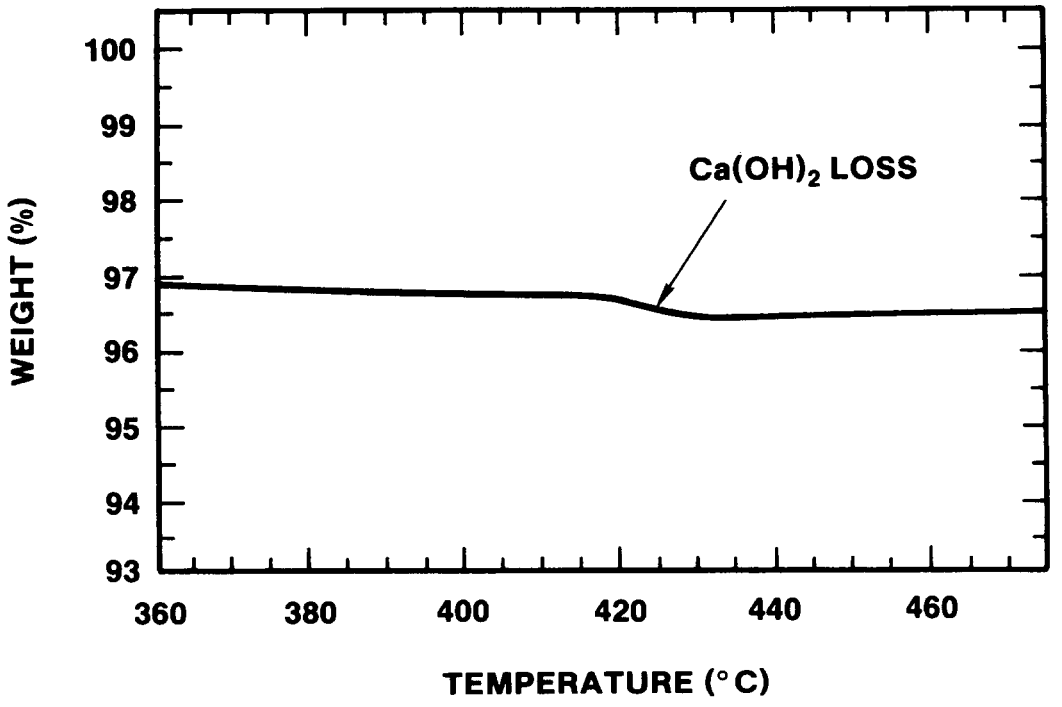

Figure 2.4.3b. Expansion of Thermogram (TGA) of the Limestone Concrete used in the Base of the Crucible, SURC-3A.

TABLE 2.4.5
Fission Product Simulants Used
in the SURC-3A Experiment

Fission Product	Mass
Tellurium (Te)	500 g
Molybdenum (Mo)	500 g
Barium Oxide (BaO)	500 g
Zirconium Oxide (ZrO_2)	500 g
Cerium Oxide (CeO_2)	500 g
Lanthunum Oxide (La_2O_3)	500 g
Niobium Oxide (Nb_2O_5)	500 g

2.4.3 Instrumentation

A total of 138 data channels were used to record the results of the SURC-3A test. Of these, 92 were thermocouple channels. Two arrays of twenty K-type thermocouples were used to monitor axial erosion in the concrete. An additional 37 K-type thermocouples were used to record the sidewall heat losses and radial erosion. These radial thermocouples were arranged in groups of 3 or 4 at eleven different heights along the crucible sidewall. Seven thermocouple channels were located in the expansion chamber and along the flow stream to measure the effluent gas temperature. Five more thermocouple channels were used to monitor the temperatures within the aerosol collection system. The last twelve thermocouple channels were used to record the meltpool temperature. Six of these were C-type thermocouples and six were S-type thermocouples.

Thirty-four data channels were voltage channels. Twelve of these were used to monitor pressure and flow through the system. One was used in conjunction with a two-color pyrometer to record the melt surface temperature. Five more were used to measure the induction coil power and coolant flow levels. Three were used to monitor the CO/CO_2 composition of the effluent gas and the last 13 were used to record data for the aerosol collection system. One of the aerosol channels recorded the output of the optical photometer used to qualitatively measure the aerosol density while the other 12 recorded flow and pressure information for the quantitative aerosol analysis. All of these instrument channels, voltage and thermocouple, were recorded every 10 seconds during

the early phase of the test using the HP 1000 data acquisition system. This sample rate was increased to once every three seconds after concrete erosion began. In addition to the HP 1000 data system, data was sampled and stored with the SEDS aerosol system (14 channels), the gas grab sample system (32 channels), the Infocon mass spectrometer (10 channels), and a video camera/recorder system.

2.4.4 Procedure

Initial calibration runs for the SURC-3A metallic charge using the 280 kW power supply indicated an initial maximum power level of 165 kW. This was nearly identical to the initial maximum power level of 168 kW achieved in SURC-3. These results indicated a net efficiency of 18.5 percent for power delivered to the 50 kg charge. Following these power calibration tests, the SURC-3A apparatus was leak tested. Results of the leak tests using argon gas as the flow medium indicated a cold leak rate of 11 alpm at a system pressure of 1.4 psi or 8% of the indicated flow rate of 138 alpm.

After the final calibration and pretest checkouts were performed, power was applied to the coil (Figure 2.4.4) at a rate of 158 kWw. This constituted the start of SURC-3A at time = 6 minutes. The temperature in the steel charge was monitored (Figure 2.4.2) to confirm that 18.5% of the power was being transmitted to the slug. These thermocouples indicated a temperature rise of 775°C in twenty minutes as compared to a 375°C rise over a ten minute period during the SURC calibration run reported in Section 2.3.4. Those results indicated a net efficiency of 18.7% with overall losses of 10 kW. Assuming similar losses for SURC-3A results in a net efficiency of 19 ± 1%.

After 35 minutes of constant heating at a power supply setting of 158 kW, the steel charge became molten and concrete ablation started at time = 40 minutes. Power was subsequently increased to the maximum achievable level of 168 kW in order to duplicate the SURC-3 power history as closely as possible. At time = 66 minutes, the laminar flow element and turbine flow meter became plugged with aerosol. Flow through the system rapidly decreased with a corresponding increase in system pressure. A bypass valve was activated in order to lower the system pressure and restore flow at time = 70 minutes. This bypass effectively removed the laminar flow element, turbine meter, and gas clocks from the instrumented flow stream, leaving the aerosol collection system and the orifice plate flow device intact. Steady-state erosion of the two-dimensional limestone crucible continued and at time = 75 minutes, approximately 4 cm of axial and 2 cm of radial erosion were indicated. The Zr metal was added to the meltpool at time = 75 minutes. Both insertion tubes were actuated so that the total Zr addition was 5 kg. Power to the induction coil was subsequently boosted to 172 kW to reflect the maximum achievable value after Zr addition and to compensate somewhat for the increase in meltpool mass. A substantial increase in flow and

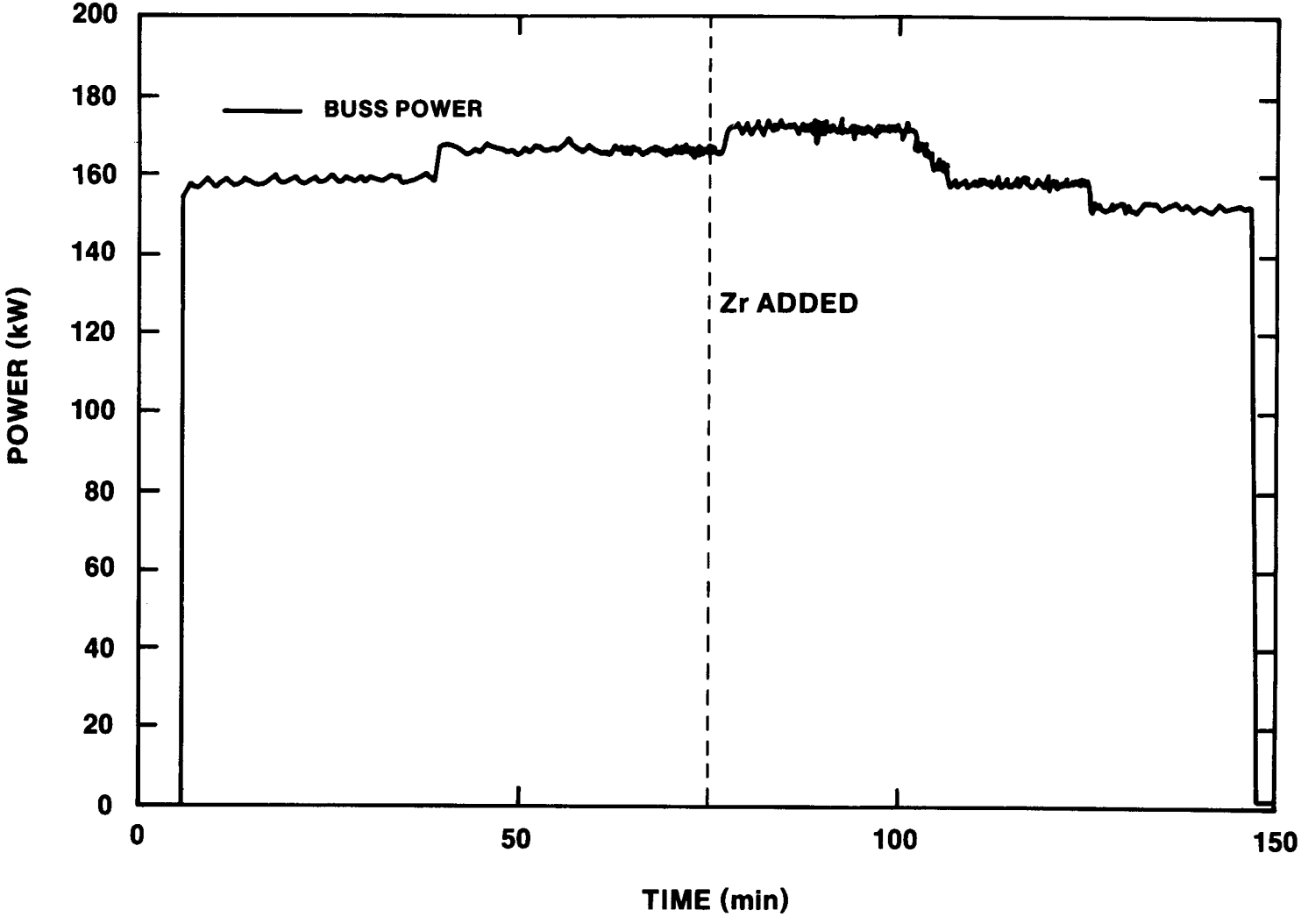

Figure 2.4.4 SURC-3A Power History

aerosol production closely followed the Zr addition at time = 75 minutes. At time = 90 minutes, pressure in the expansion chamber again began to rise with a corresponding drop in measured flow. At time = 100 minutes, the bypass valve became fully plugged with aerosol debris. This forced a second bypass of the flow train such that all of the flow was routed through the aerosol collection system thus eliminating the orifice plate flow device and the plugged bypass valve. Power was reduced at time = 105 minutes to 160 kW while field repairs were made to restore flow through the orifice plate section of the flow train. At time = 120 minutes, flow through the measurement system was restored. After time = 125 minutes, the axial erosion rate appeared to slow down with a corresponding increase in radial erosion. Total axial erosion at time = 125 minutes was 22 cm with radial erosion greater than 3 cm in two locations. Three additional locations in the crucible indicated radial erosion greater than 3 cm during the period from time 130-145 minutes. Although the measured flow rate in the system appeared to hold steady, the maximum achievable power to the coil decreased from 160 kW to 153 kW during this period. Since crucible sidewall failure appeared imminent and all of the established goals for SURC-3A had been met, the test was terminated at time = 148 minutes. A total of 5 power fluctuations occurred during the SURC-3A test. The range of total power to the coil was from 153 to 172 kW with a mean value of 163 kW. In all, the SURC-3A experiment eroded 25 cm of concrete in the axial direction and 3-5 cm of concrete in the radial direction during 100 minutes of interaction and was successful in observing and recording the effects of Zr addition to steel-concrete attack.

2.4.5 Posttest Observations

Posttest x-rays of the SURC-3A crucible were taken and are shown in Figure 2.4.5. These x-rays indicated a thick upper layer of dense crust material, a large, irregular central voided area, a distended lower interaction region filled with medium density oxide material, and an off-center bottom region which contained the remainder of the metallic charge. The upper layer of dense crust material was 4-8 cm thick and appeared to contain part of the original stainless steel slug. This material was located 29 cm above the original meltpool height and 49 cm above the original steel-concrete interface. Half of this upper crust was composed of dense material resembling the top 3 cm of the original steel slug with the remainder composed of less dense slag material. Below this upper crust was a large, irregular voided area which was 38-42 cm in height and 13-27 cm in diameter. The top of the voided area was located roughly 20 cm above the original meltpool height with the bottom being roughly 5 cm below the original steel-concrete interface. A relatively dense slag material 2 to 6 cm thick lined the cavity wall and formed the boundaries of this central void. The limestone concrete walls of the interaction crucible adjacent to the voided region were correspondingly enlarged to a diameter of 23-32 cm vs. an original diameter of 21 cm. Below the central voided area was a distended lower interaction region. This region was filled

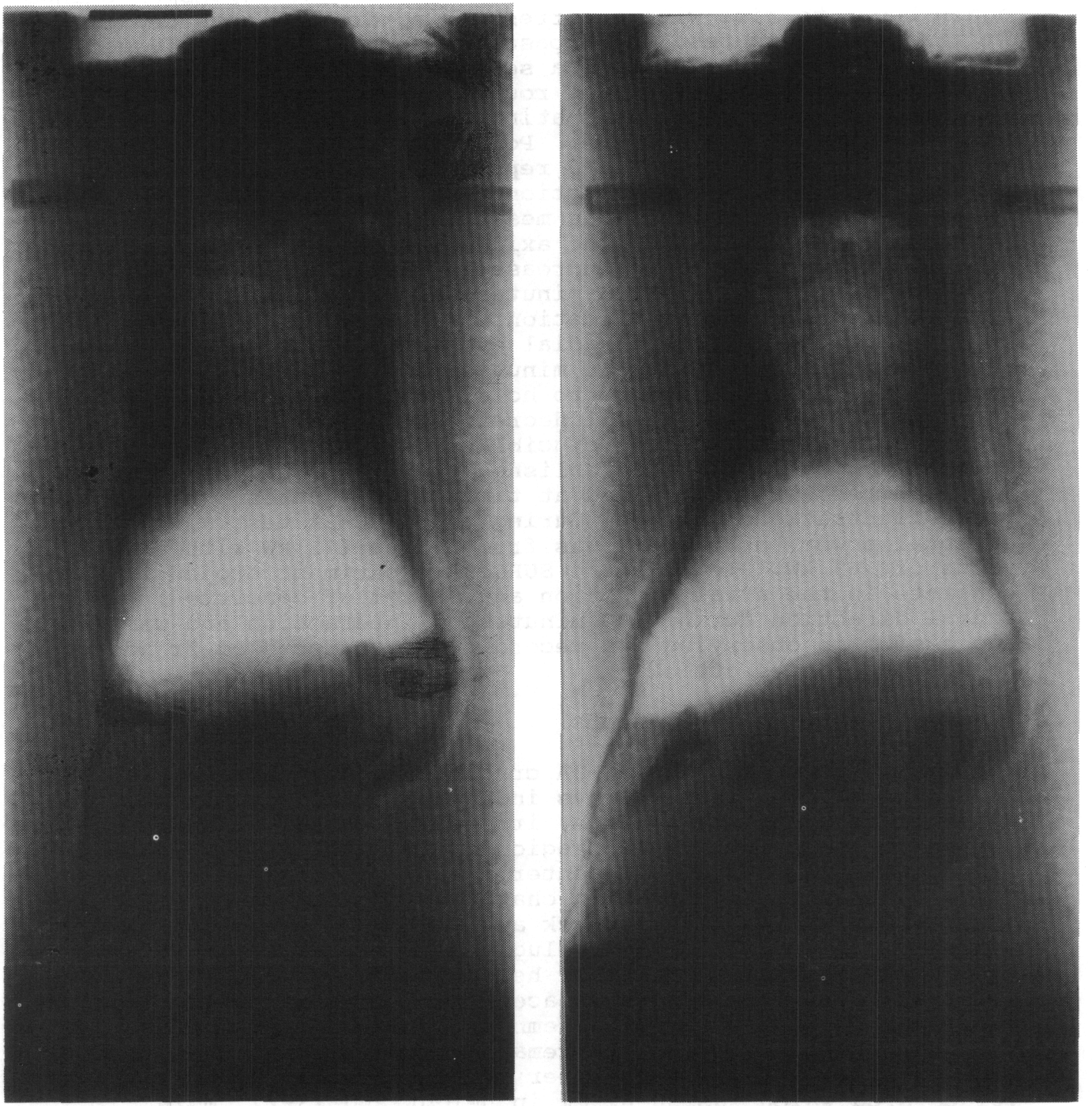

0° 90°

Figure 2.4.5 SURC-3A Posttest X-ray

with medium density material and measured 20-25 cm in depth and 20-31 cm in diameter. The bottom of this region lay 25 cm below the original steel-concrete interface. The remainder of the limestone crucible which surrounded this interaction region was highly asymmetric and skewed with one sidewall being 5-25 cm thick and its opposite being 1-5 cm thick, indicating that the steel-concrete interaction was proceeding considerably off-center after 20 cm of erosion had occurred. The bottom region of the cavity contained the bulk of the solidified metallic charge for SURC-3A. This region was 20-27 cm in diameter and 6.5-7 cm thick. The centroid of the solidified pool lay 10-11 cm to one side of the concrete cavity centerline. The bottom and sides of this region marked the greatest extent of axial and radial penetration and were located 30-31 cm below the original steel-concrete interface and nearly 20 cm to one side of the cavity centerline.

The SURC-3A crucible was sectioned vertically after the posttest x-rays were examined. Figure 2.4.6 shows the crucible after a 180° section was removed to examine the interior. The Zr delivery system was found to be partially blocked due to the expansion of the upper crust in the cavity section of the crucible and 7 of the 18 Zr cylinders were removed intact from the Zr delivery system. An additional 4 cylinders were found embedded in the upper debris, leaving 8 cylinders (2.2 kg) to enter the meltpool and interact with the steel-concrete mixture. In addition to the Zr cylinders, the top of the original steel slug was found in the upper crust debris. It had a diameter of 20 cm and varied from 3-5 cm in thickness with an estimated weight of 7-10 kg. There was a substantial hole in the slug (Figure 2.4.5) which was slightly off-center, measured 13 cm x 6.5 cm, and covered 25% of the available surface area. The remainder of the upper crust was below the steel slug, 4-5 cm thick, and oxidic in nature. The central cavity of the sectioned crucible was filled with a dark grey powder. A total of 22 kg of this material was removed in order to expose the metallic charge and the slag covered walls. This oxidic power had an approximate density of 2.0 g/cc and is believed to be a mixture of trapped aerosol material consisting of iron oxide and concrete by-products. The sidewalls of the SURC-3A cavity were covered with a denser slag material which had a thickness of 1-3 cm and appeared to have been molten at one time. The bulk (26-30 kg) of the solidified steel charge was located off-center in the bottom of the interaction cavity; however, several additional kilograms of metallic material were uncovered at higher locations. This material was 5-15 cm above the bottom pool and appeared to be splashed or precipitated material which became trapped against the sidewalls when the pool cooled.

The concrete on the sidewalls of the SURC-3A limestone crucible was discolored and porous. In particular, the limestone aggregate in the exposed sidewall concrete had changed from grey to white indicating at least partial thermal decomposition. A total of 15-18 cm of concrete were unaffected in the plane of the

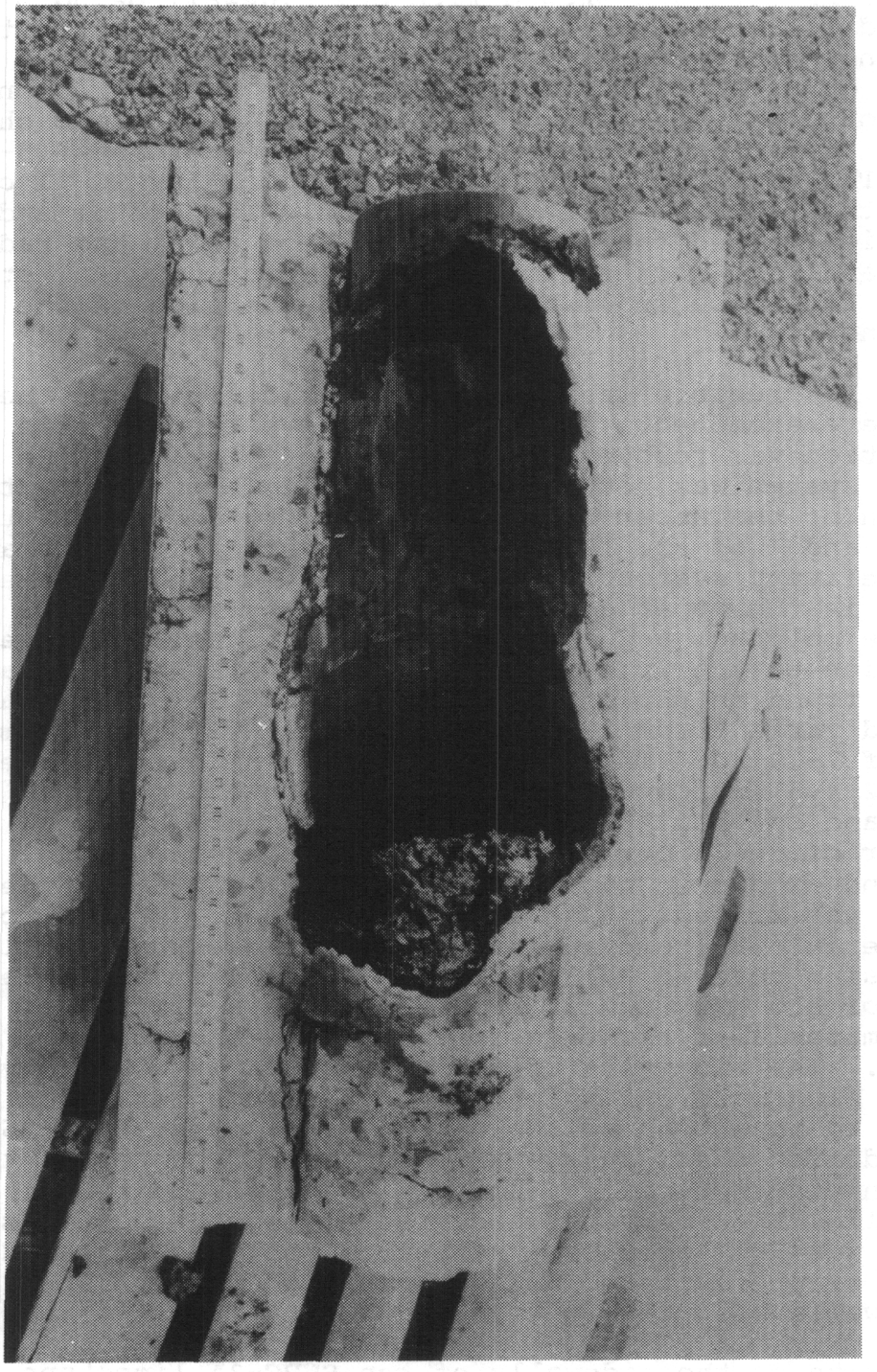

Figure 2.4.6 SURC-3A Crucible Section

sectioned crucible which corresponds to the 90° x-ray view shown in Figure 2.4.5. Since the erosion pattern was severely skewed, the maximum radial and axial erosion values were not exposed in this view.

2.4.6 Temperature Data Presentation

The 50 kg, 304 stainless steel charge, doped with fission product simulants, was inductively heated for approximately 55 minutes prior to the onset of melting and concrete erosion. Four type K thermocouples were installed in the steel charge to measure the heating profile. Two of the four thermocouples functioned during the heating period. These thermocouples were located 7.6 cm below the top surface of the cylinder one at a radius of 5.1 cm and the other at 9.4 cm from the axis of the cylinder. The temperature response of these thermocouples is shown in Figure 2.4.7. The data shows a steady temperature increase of approximately 36 K/min beginning at t = 5 minutes, until failure occurs near the operational limits of this thermocouple at 1645 K. At t = 75 minutes, after eroding approximately 6 cm of concrete, and after establishing a steady-state ablation rate, 5 kg of zirconium metal was released to the meltpool. The test was terminated at t = 147.5 minutes after eroding 27 cm of concrete. The thermal response of the interaction crucible before, during and after the zirconium addition will be discussed in this section.

The Concrete Slug

Typical temperatures indicated by the thermocouples embedded in the concrete slug are shown in Figure 2.4.8. The temperature versus time histories measured by the rest of the thermocouples embedded in the concrete slug are presented in Appendix I. Temperatures rise slowly to between 400 and 500 K followed by a rapid increase to failure caused by contact with the meltpool.

The propagation of the interface between the "wet" and the "dry" zones may be characterized in the SURC-3A test by the motion of the 400 K isotherm. The location of this isotherm plotted is shown plotted as a function of time in Figure 2.4.9.

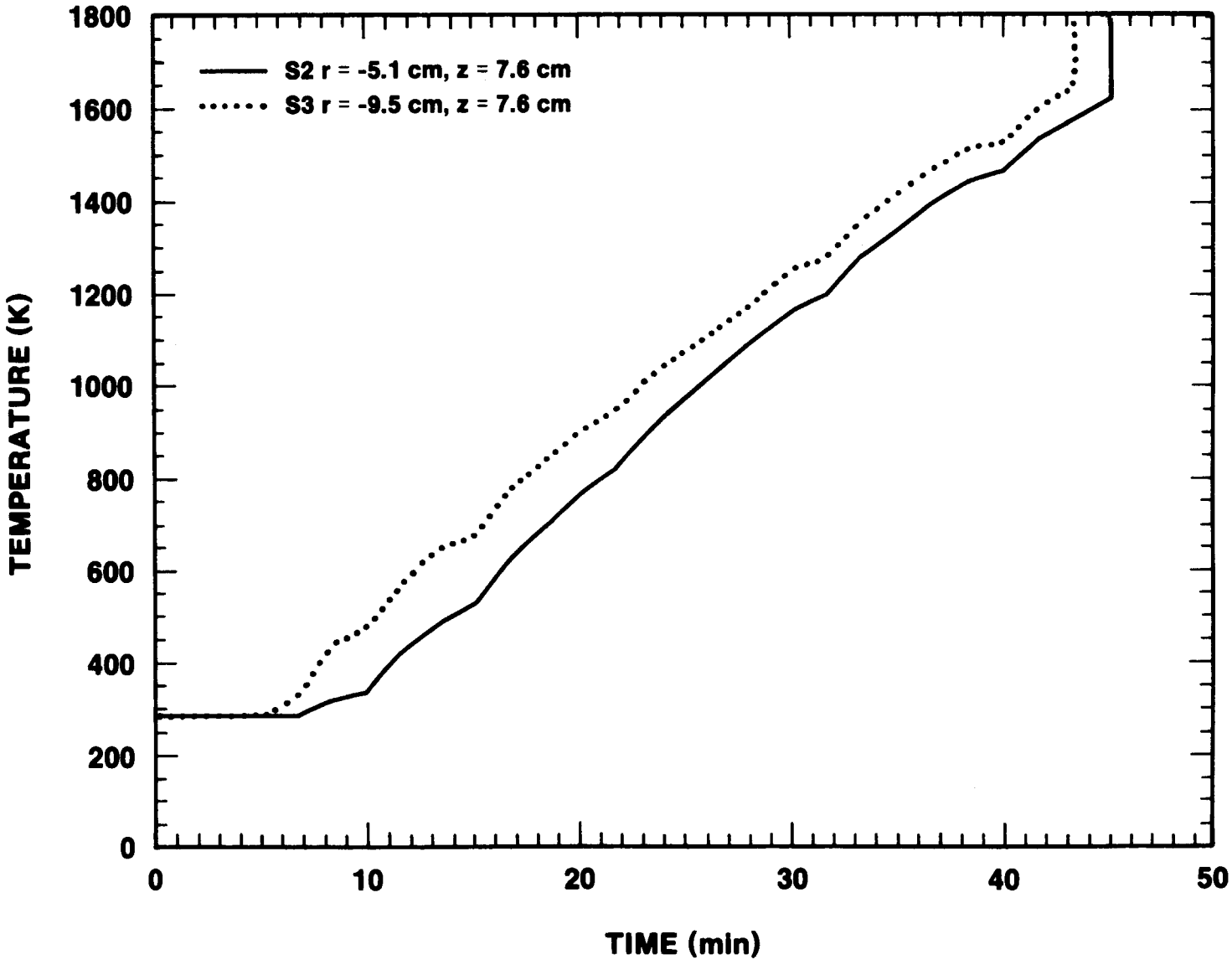

Figure 2.4.7 Initial Steel Temperature in SURC-3A

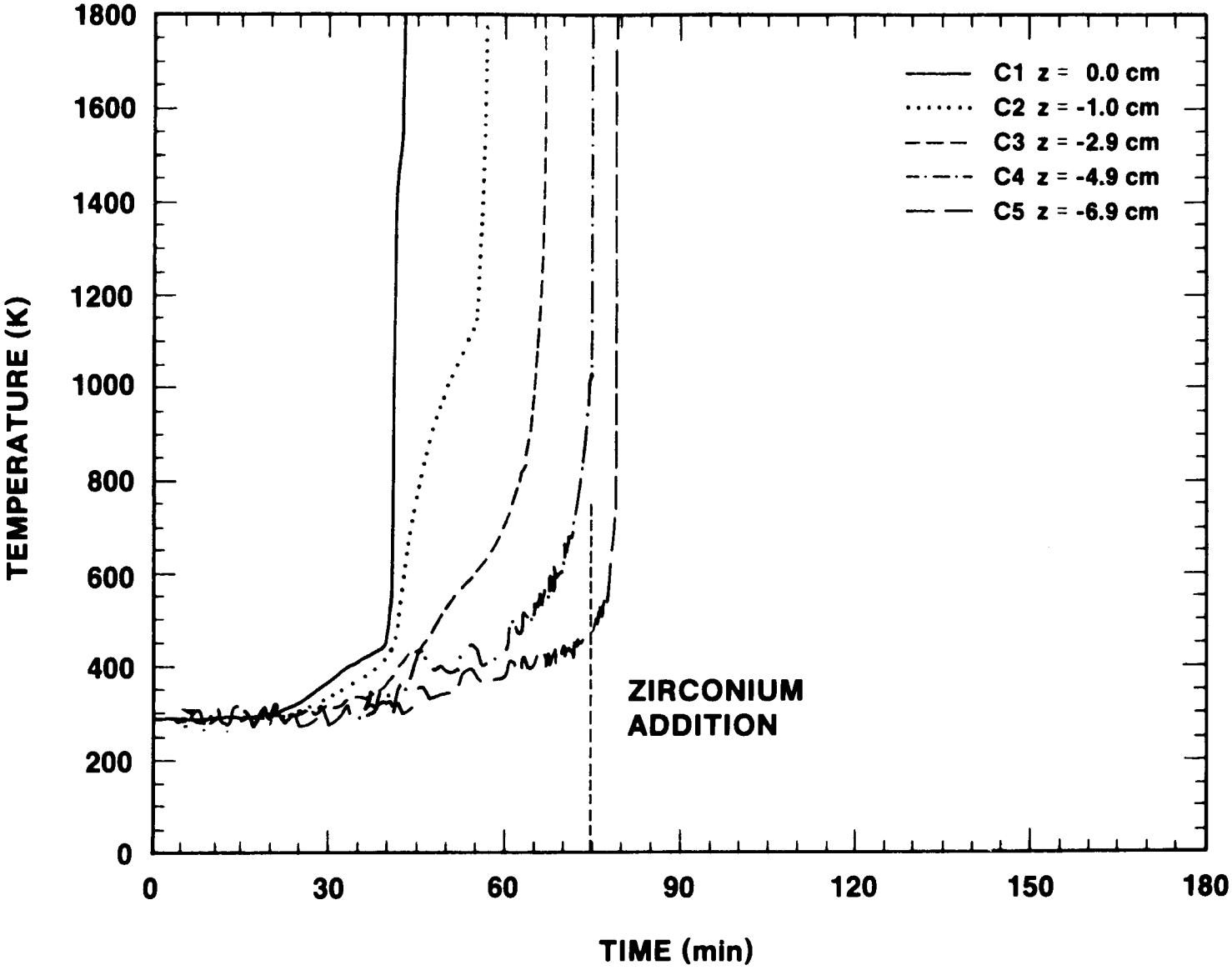

Figure 2.4.8 Typical Axial Thermocouple Response - SURC-3A

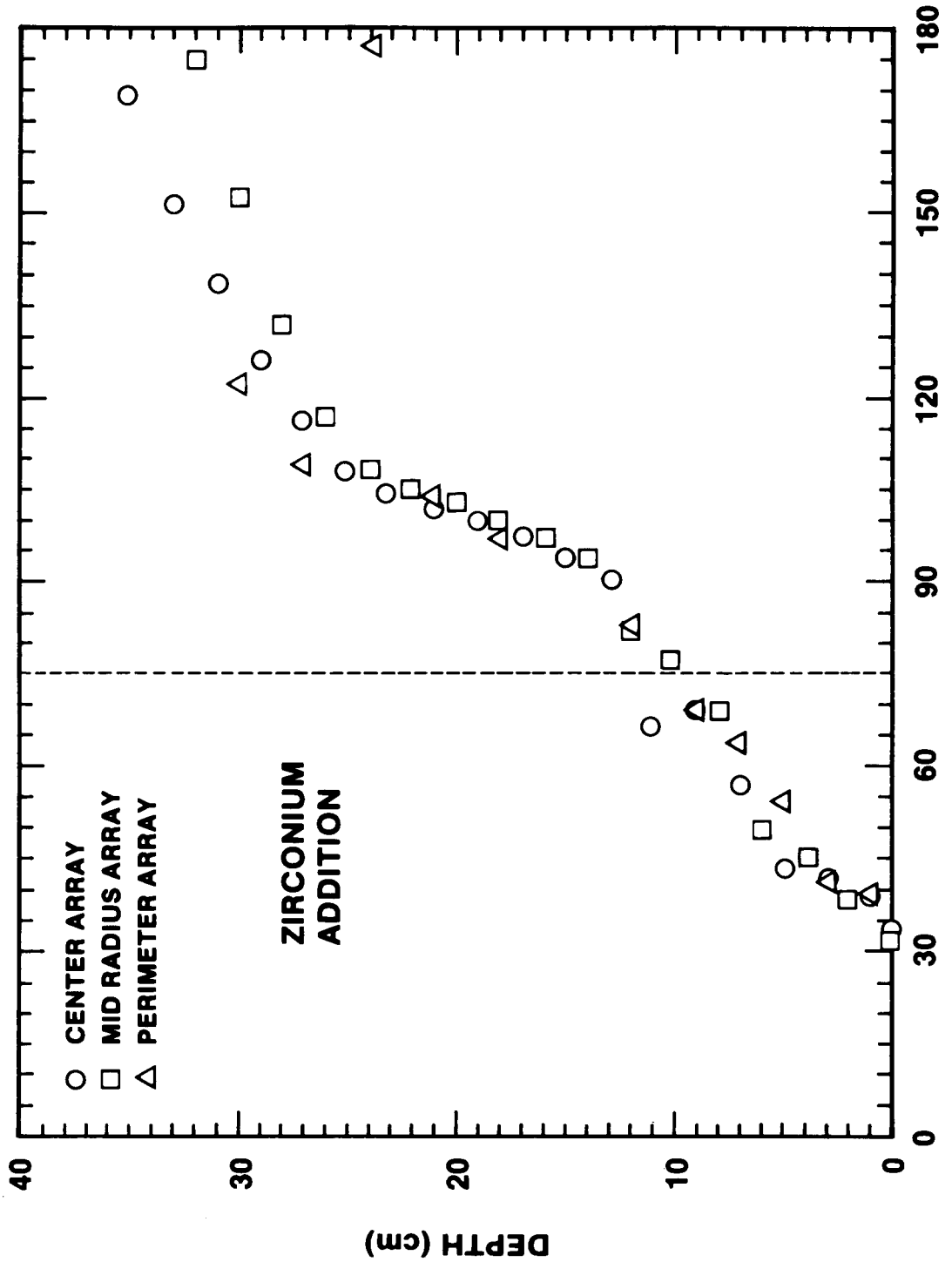

Figure 2.4.9 400 K Isotherm - SURC-3A

This isotherm begins to move into the concrete at t = 32 minutes. In order to determine the velocity of this isotherm at various stages selected data was linearly fit by a least squares routine. Between t = 40 and 95 minutes, the velocity is nearly constant moving at 11.8 ± 0.7 cm/hr. Approximately 15 minutes after the zirconium was added, the motion of the isotherm increases significantly to 42.7 ± 0.8 cm/hr and remains constant between t = 90 and 110 minutes. The velocity of this isotherm then decreases to a rate of 7.0 ± 1.5 cm/hr for the duration of the test.

The position of the erosion front can be approximated by the 1600 K isotherm moving through the concrete. Figure 2.4.10 shows the position of the 1600 K isotherm plotted as a function of time. Ablation begins between t = 43 and 48 minutes when the two surface thermocouples indicate 1600 K. The ablation front propagates at almost a constant rate of 20.0 ± 0.4 cm/hr between t = 65 and 95 minutes. Approximately 20 minutes after the zirconium addition the velocity of the ablation front increased to 50.0 ± 1.1 cm/hr between t = 95 and 105 minutes. The rate of propagation then decreases to 14.7 ± 0.9 cm/hr between t = 105 and 130 minutes.

The depth to which the concrete was dehydrated can be determined by comparing the position of the 400 K (wet/dry interface) and 1600 K (ablation front) isotherm at a specific time. Figure 2.4.11 shows a plot comparing data representing the 400 and 1600 K isotherms. The depth of the dehydrated concrete at the onset of ablation was approximately 4 to 5 cm between t = 43 and 48 minutes. Beyond this time the two fronts converge and appear to maintain a 2 to 4 cm separation.

Melt Temperatures

Melt temperatures were measured during the experiment with six type C and six type S thermocouples installed in alumina tubes and cast at various depths within the concrete slug. A typical temperature response of these thermocouples plotted against time is shown in Figure 2.4.12. Other plots of melt temperature can be found in Appendix I. The figure shows a peak usually lasting from a few seconds to several minutes. The thermocouple later becomes unstable due to eventual junction oxidation caused by the melt. Figure 2.4.13 shows a plot of the peak melt temperatures measured by these thermocouples during the test. These peaks closely match the failure times of the type K thermocouples from the center array. The meltpool temperature ranged between 1950 and 2100 K. This amounted to a superheat in the steel of between 250 and 350 K. The results show that the 304 stainless steel reached its melt point of 1700 K at 40 minutes into the test. At time = 45 minutes, concrete erosion began alon with a meltpool temperature increase from 1700 to 1950 K indicating a super heat of 250 degrees. These temperatures increased to 2000 K as 4-6 cm of concrete were

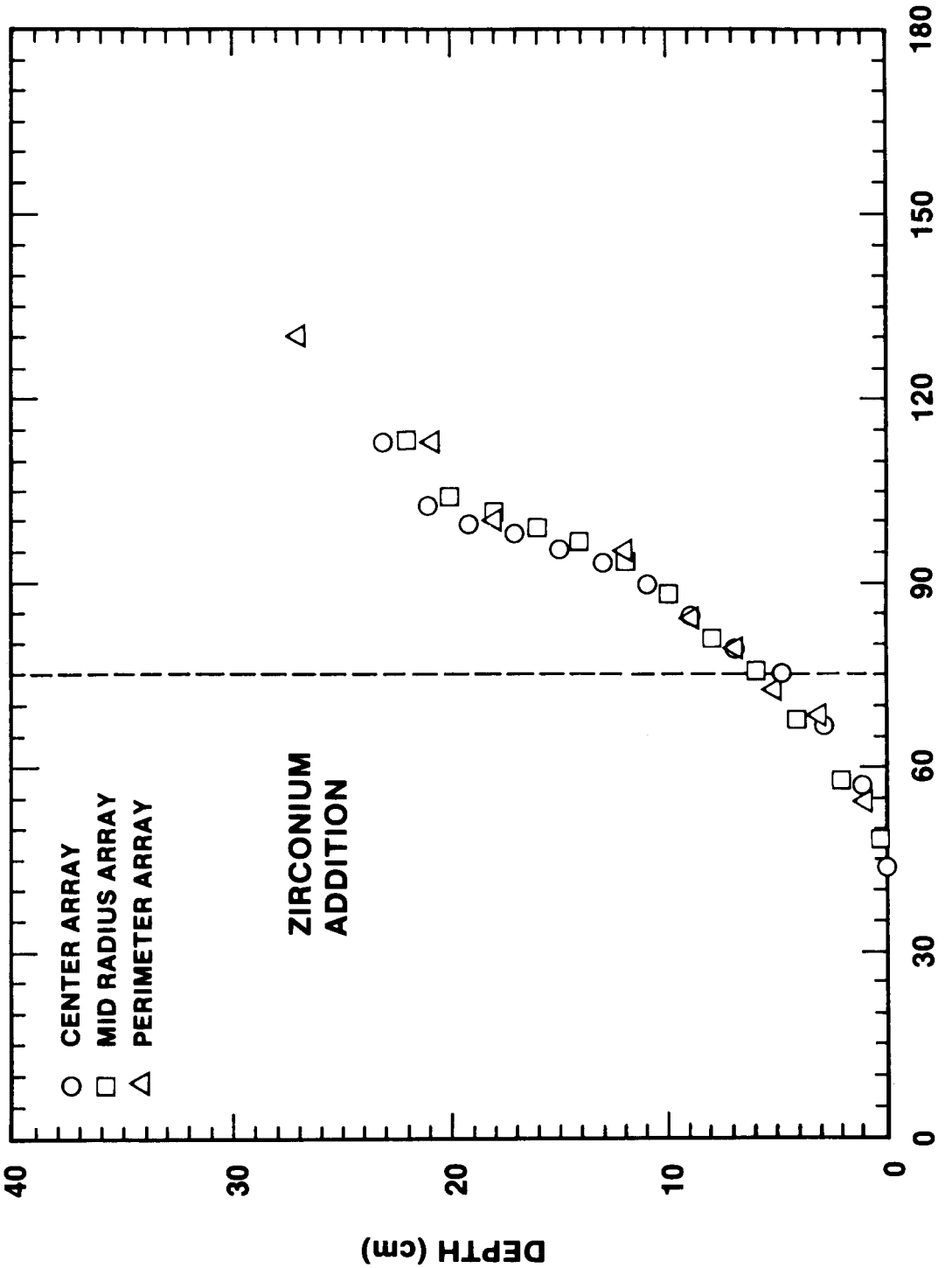

Figure 2.4.10 1600 K Isotherm in SURC-3A

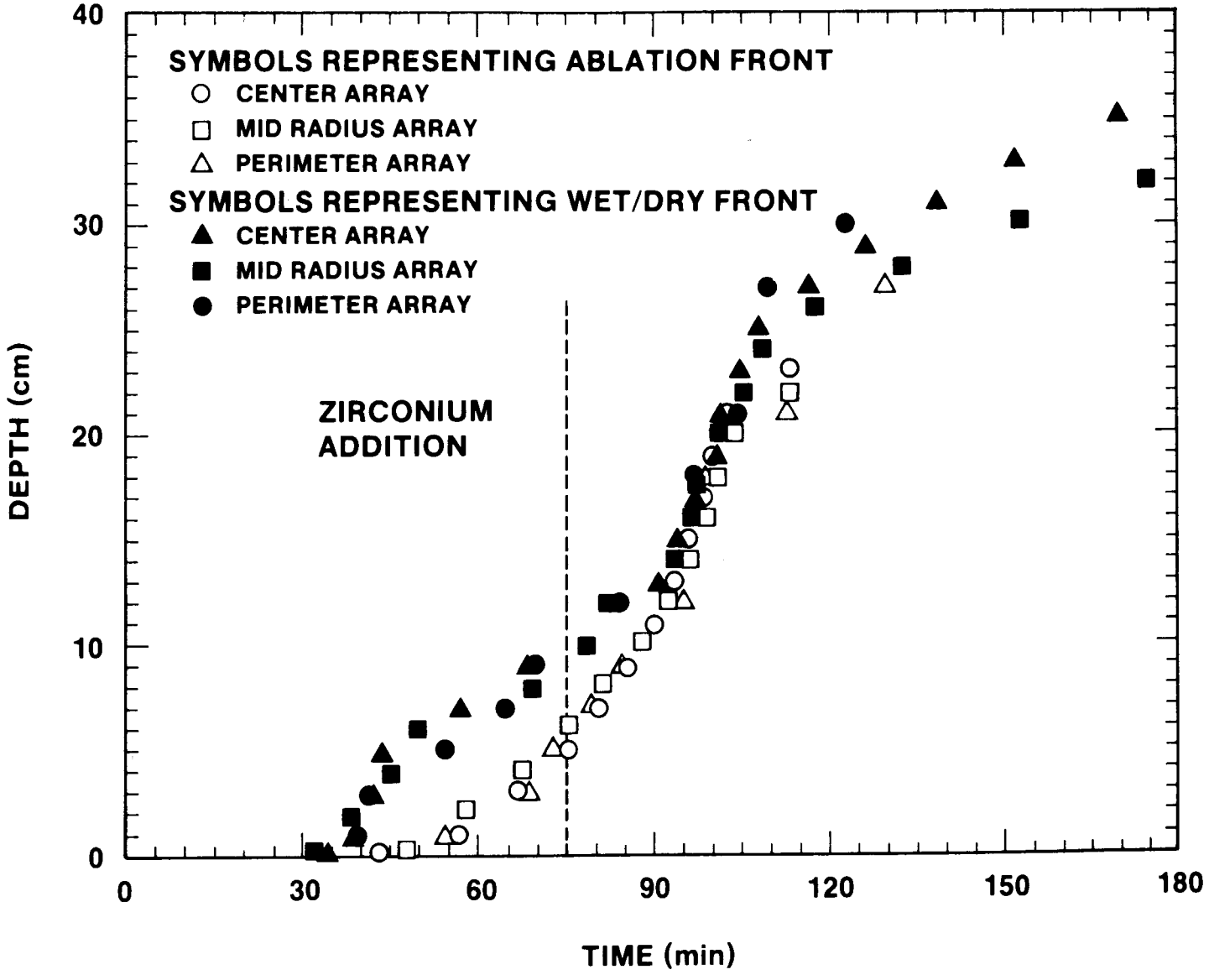

Figure 2.4.11 Comparison of the Location of the 400 K and 1600 K Isotherms

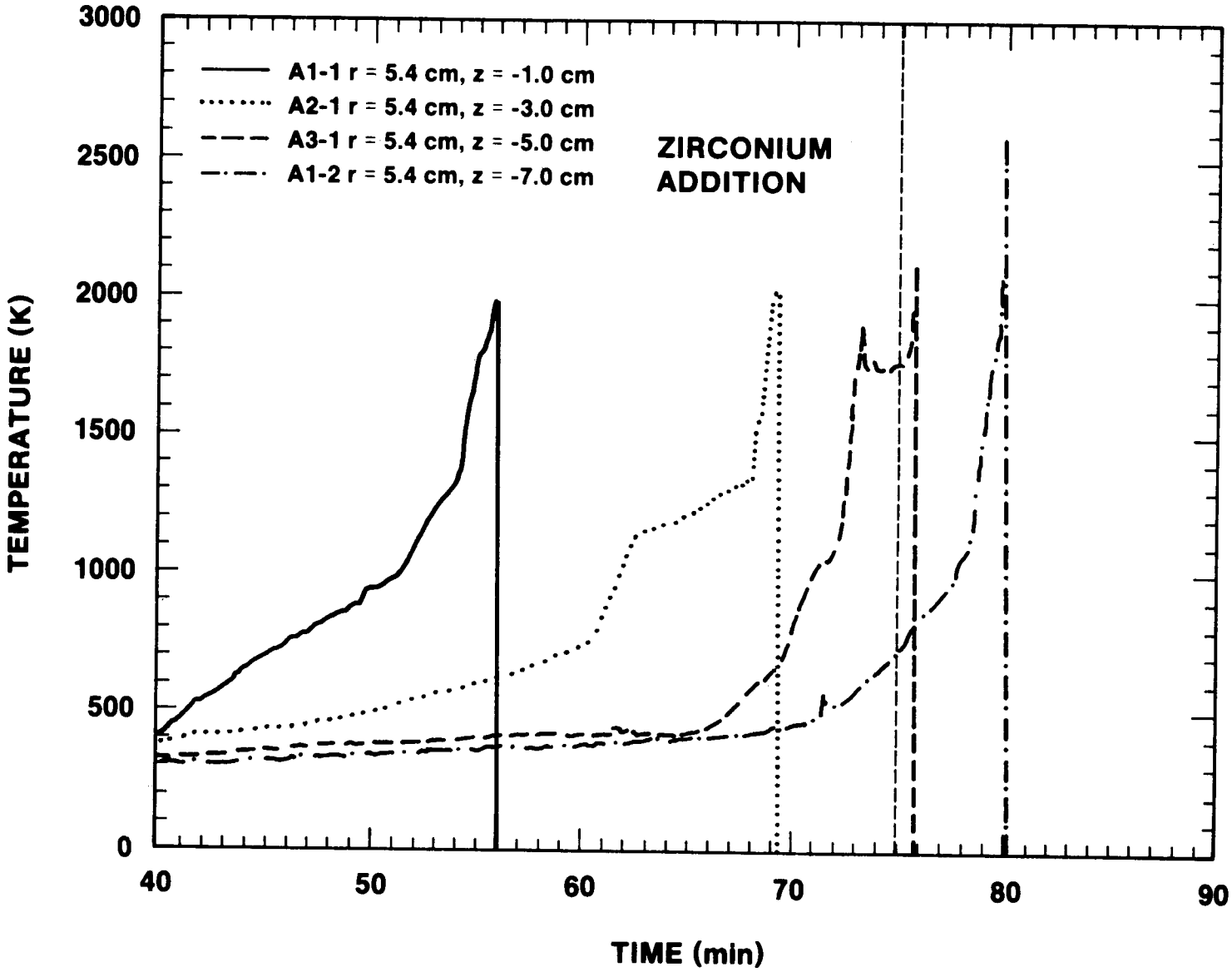

Figure 2.4.12 Typical Meltpool Thermocouple Response in SURC-3A

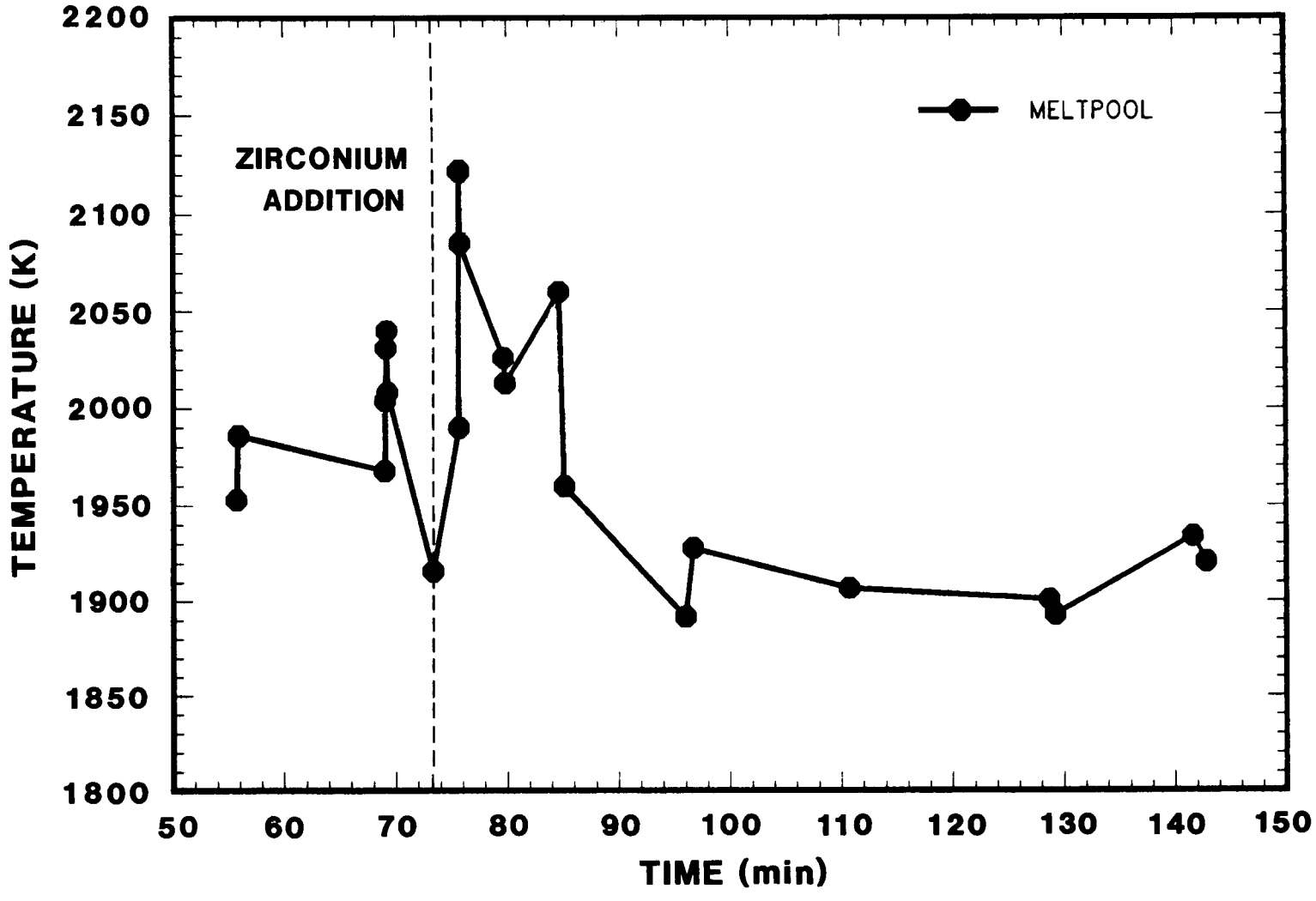

Figure 2.4.13 Melt Temperature in SURC-3A

eroded axially between time = 45 minutes and time = 75 minutes. Zirconium was then added to the melt at time = 75 minutes. Melt temperatures after 75 minutes rose briefly to 2100 K then gradually decreased to 2000 K between 80 - 85 minutes. After time = 85 minutes, meltpool temperatures eroded an additional 15 - 20 cm of limestone concrete in the axial direction.

Concrete Sidewalls

The thermal response of the concrete annulus was measured by type K thermocouples configured in 11 arrays of 3 to 4 each located at various elevations. Three typical sidewall thermocouple array responses initially located below (z = -24.2 cm), adjacent (z = 4.5 cm), and well above the melt (z = 30.3 cm) are shown in Figures 2.4.14, 2.4.15 and 2.4.16, respectively. The temperature histories measured by thermocouples cast into the concrete sidewall are presented in Appendix I. The temperatures indicated by the four thermocouples located in the array at z = -24.2 cm (Figure 2.4.14) begin to increase from a baseline of 290 K at t = 100 minutes, but never rise above 500 K prior to the termination of the test. The three thermocouples located adjacent to the melt at z = 4.5 cm (Figure 2.4.15) indicate a rapid temperature rise beginning at t = 8 minutes. The first two thermocouples located at a depth of 1.0 ad 2.0 cm failed at t = 52 and 64 minutes, respectively. The thermocouple located at a depth of 3.0 cm did not fail, but peaked at a temperature of 1610 K at t = 85 minutes. The data from the array of four thermocouples located at z = 30.3 cm approximately 13 cm above the melt surface are shown in Figure 2.4.16. These thermocouples measured temperatures through the test without failure. The temperatures begin to rise significantly at t = 48 minutes. The temperature indicated by the thermocouple located at a depth of 1.0 cm peaks at 1350 K at t = 77 minutes. The thermocouple embedded in the concrete at a depth of 9.6 cm indicated a maximum temperature of 500 K prior to test termination.

The sidewall erosion profile is shown in Figure 2.4.17 and the angular location of each thermocouple set is listed in Table 2.4.3. These data are based on the failures of thermocouples embedded in the annulus and provide an indication of the azimuth and depths where significant sidewall erosion occurred during the experiment.

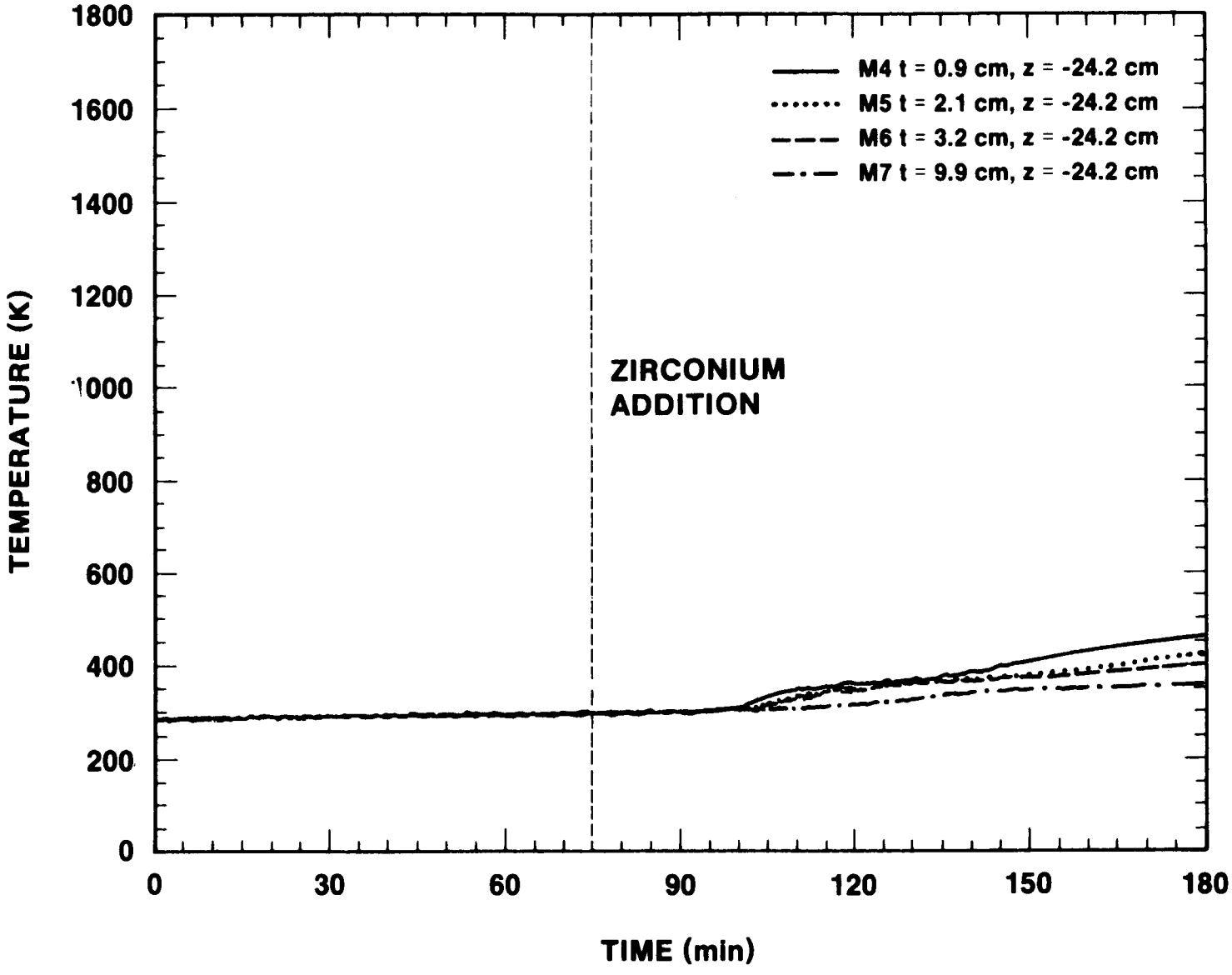

Figure 2.4.14 Typical Sidewall Thermocouple Response Below the Melt

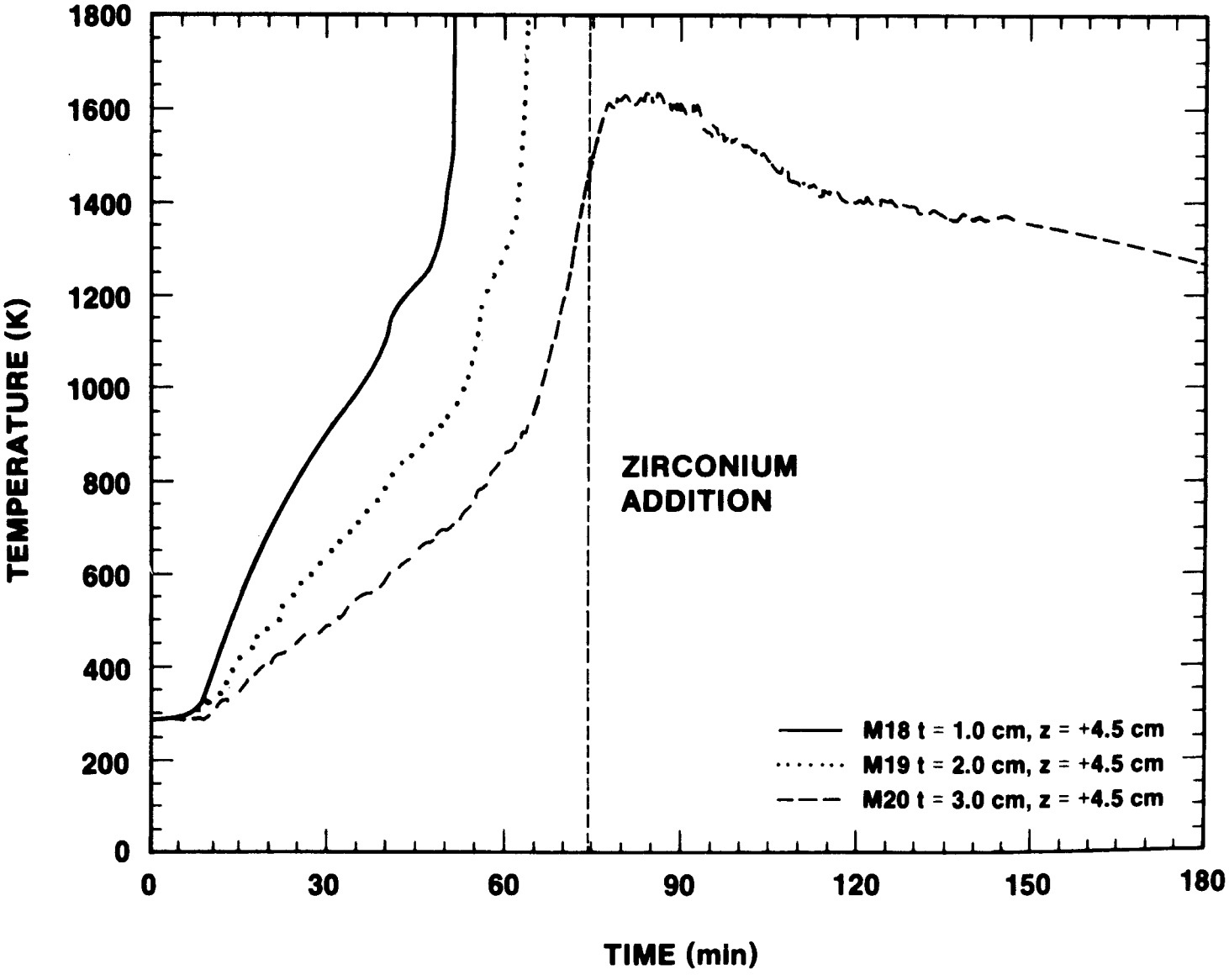

Figure 2.4.15 Typical Sidewall Thermocouple Response Adjacent to the Melt

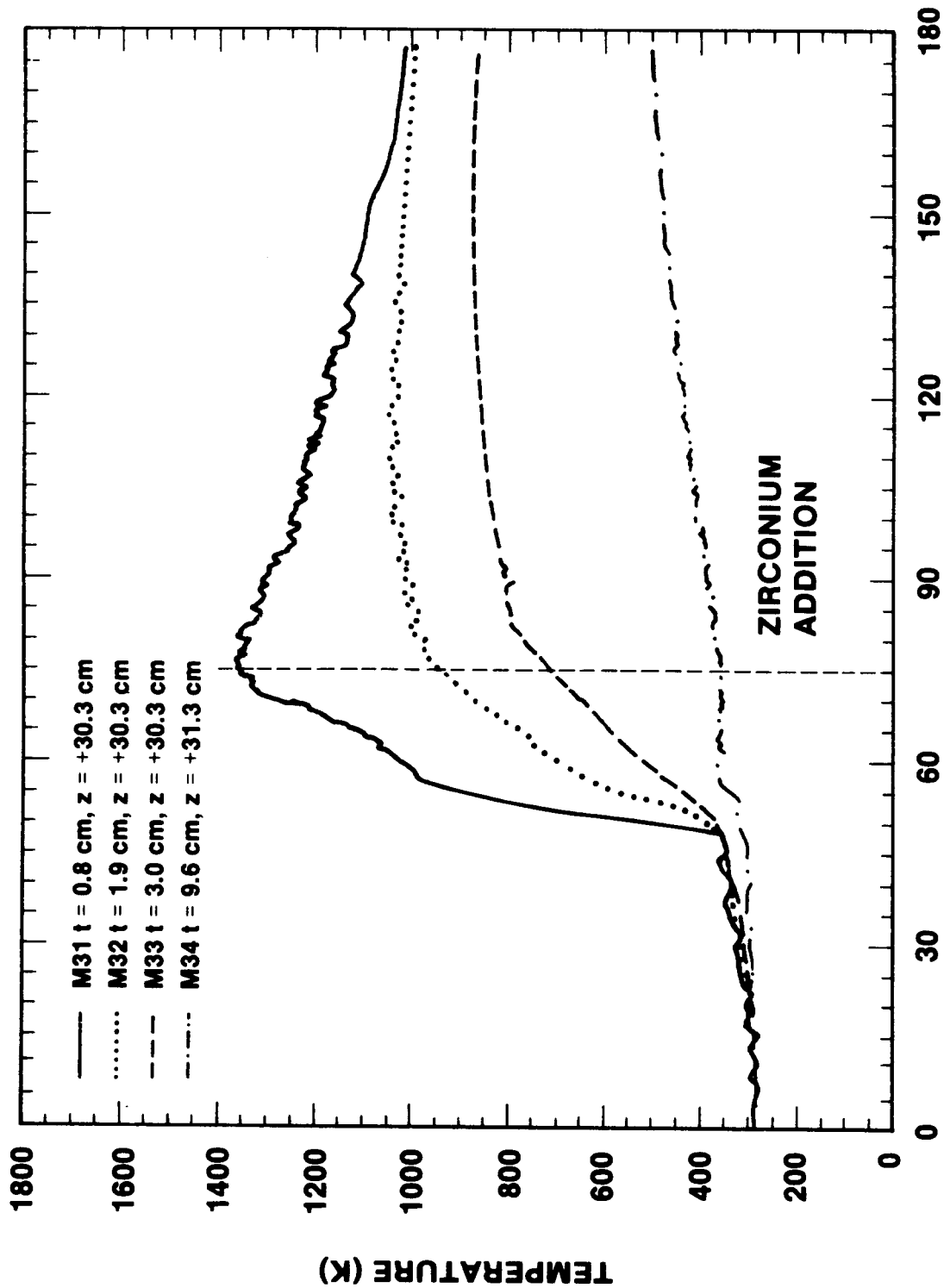

Figure 2.4.16 Typical Sidewall Thermocouple Response Above the Melt

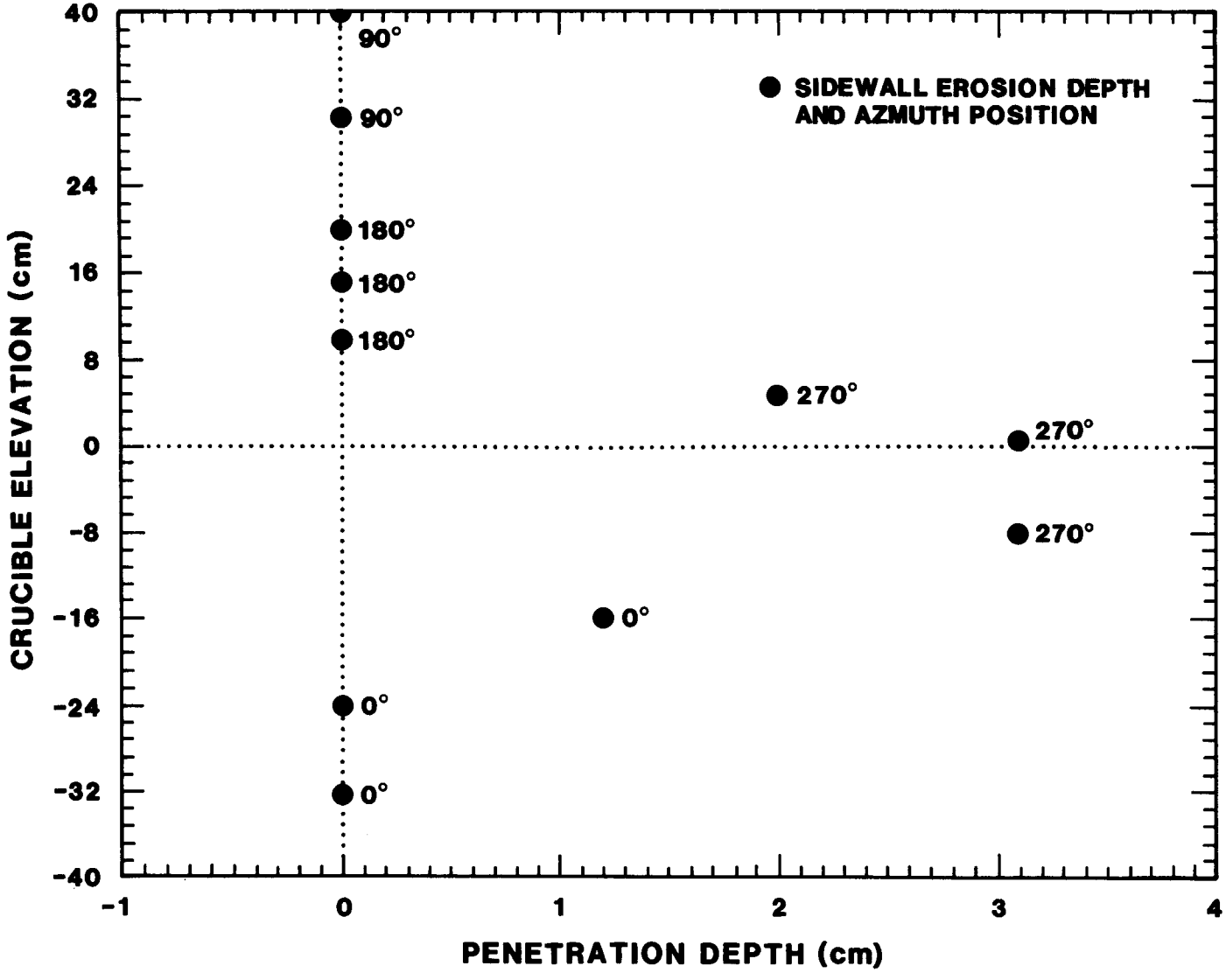

Figure 2.4.17 SURC-3A Sidewall Erosion Profile

2.4.7 Flow Data Presentation

Five different flow devices were used to measure the gas flow rate in SURC-3A: a 1.02 cm orifice plate, a laminar flow element, a turbine meter, and two gas clocks. This is the same instrumentation as was used in the SURC-3 test. A schematic of the instrumentation flow train is shown in Figure 2.3.27 and the hardware descriptions including calibration data for the SURC-3A flow devices is covered in Section 2.3.7.

As with the SURC-3 test, an insitu calibration was performed prior to SURC-3A using argon as the flow medium. This was done to insure that the laboratory calibrations were still valid, to evaluate the SURC-3A flow system, to determine the system pressure as a function of flow rate, and to compare the pretest status of SURC-3A with that of SURC-3. Results of the insitu calibration for the orifice flow meter, LFE, turbine meter, and system pressure for SURC-3A are given in Table 2.4.6. These results also include a downstream gage pressure at a location beyond the turbine meter and before the gas clocks. This pressure was monitored in order to better locate the sources of system pressure drop so that more accurate posttest corrections to STP values could be made. Following the insitu test, a systems leak check was performed by valving off the flow train and pressurizing the crucible and expansion chamber. A pressure decay chart for this procedure is given in Table 2.4.7. Based on the insitu checks, the SURC-3A initial leakrate from the crucible was calculated to be 9.2 slpm at a system pressure of 1.4 psig or 8% of the 113 slpm flow rate.

TABLE 2.4.6

Pressure Decay and Leakrate for SURC-3A
Crucible/Expansion Chamber

Time (min)	Pressure (psig)	Leakrate (SLPM)
0.	7.53	
.5	5.92	44.6
1.0	5.25	35.8
2.0	3.75	28.9
3.0	2.66	21.1
4.0	1.88	15.0
6.0	.93	9.2
7.0	.65	5.4
8.0	.46	3.8

TABLE 2.4.7

SURC-3A InSitu Flow Calibration

Inlet Flow (ALPM)	System Pressure (PSIG)	Orifice Plate ΔP (PSIA)	LFD ΔP (PSIA)	Turbine (ALPM)	Exit Pressure (PSIG)
278	7.4	.94	.437	284	3.8
230	4.3	.57	.359	228	2.0
170	2.1	.275	.26	166	.8
117	1.0	.12	.18	110	.3
58	.3	.027	.084	53	.07

The gas temperature in SURC-3A was monitored in five locations. These were at the argon gas inlet, at the helium gas inlet, in the SURC-3A expansion chamber, in the flow train near the orifice plate, and at the exit port from the gas clocks. Of these, the temperature in the expansion diameter was the only one which varied significantly during the test. The expansion chamber temperature started at 30°C and rose gradually to 42°C at time = 45 minutes. Steel melt and concrete ablation occurred after time = 45 minutes and the expansion chamber temperature rose to a temperature of 145°C at time = 65 minutes. After time 65, the expansion chamber temperature first dropped to 65°C just after Zr addition at time 75, then rose dramatically to a peak of 350°C at time = 100 minutes and coasted down to a final value of 100°C at time 150. Despite these temperatures within the expansion chamber, the bulk temperature in the gas at the flow measurement devices remained steady at 30-35°C throughout the test. The inlet temperatures also were fairly constant at 30°C for the duration of the experiment.

The carrier gas for SURC-3A was comprised of both argon and helium. Argon was input below the flow outlet pipe in the expansion chamber and just beyond the critical orifice plate at the aerosol photometer. Two 14 slpm NBS traceable critical orifices (calibrated for dry air) were backpressured at 24.5 ± 1 psia yielding an argon input flow rate of 38 ± 2 slpm. Helium was input above the flow outlet pipe at the top of the expansion chamber in order to maintain two unobscured viewing ports over the SURC-3A crucible. One 10 slpm critical orifice (again calibrated for dry air) was backpressured at 21.5 ± 1 psia yielding a helium input flow rate of 38 ± 2 slpm. Total input flow rate for the SURC-3A experiment was the combination of the two or 76 ± 3 slpm.

Results

Three time periods are of interest for the SURC-3A flow data. These are the onset of concrete ablation from time 45 to 75, the additional effects of Zr addition from time 75-100, and the return to steady-state ablation at times after 120. Several events during the execution of SURC-3A caused fluctuations in the data. The most notable of these were aerosol plugging of the laminar flow device at time = 65 minutes, the addition of Zr metal at time 75, at the aerosol plugging of the relief flow valve at time = 120 minutes. In addition, there was an increasing leakage rate from the crucible throughout the test due to cracking and thermal decomposition.

The plugging of the laminar flow device at time 65 caused a brief cessation in measured flow until time = 70 minutes. A bypass valve which circumvented the laminar flow device, turbine meter, and the two gas clocks was employed to restore the flow through the orifice plate flow meter. Consequently, the orifice plate is the only device used to measure flow rate after time = 70 minutes. At time = 75 minutes the Zr metal was added to the melt pool resulting in significant increases in both flow and system pressure. Later in the experiment, the flow bypass valve became clogged with aerosol debris at time = 100 minutes, resulting in a 20 minute data gap. Field repairs restored flow through the orifice plate at time 120. The leakage rate from the crucible results in decreased flow. This leakage was originally 6-8% based on insitu calibrations and comparison of inlet flow (76 ± 3 slpm) to measured turbine outlet flow (72 ± 2 slpm). A comparison of inlet flow to outlet flow was conducted after the test was concluded and the debris/crucible configuration had cooled. This test indicated only 30% of the inlet flow was being measured posttest at a system pressure of .5 psig and an input flow rate of 150 slpm resulting in a 70% leakrate. The time dependent nature of the leakrate during SURC-3A is difficult if not impossible to determine precisely due to the loss of the volumetric flow gas clocks at time 65 and due to the irregular radial erosion patterns during the test. A gross estimate of the leakrate based on a comparison of the orifice plate data and the erosion rates from Section 2.4.3 is 8% leakage from time 0-50, 25% leakage from time 50-100, and 50% leakage from time 100-150. The difficulty in estimating the leakrate for SURC-3A is compounded by partial plugging of the orifice plate by aerosols produced during the test. Posttest examination and calibration checks show that the orifice plate measured a flow rate of 106 alpm with a differential pressure of 1.22 psi as compared to .13 psi in pretest calibrations. This means that the indicated flow rate on the orifice plate was as much as a factor of three higher than the actual flow rate, especially at times after 120 minutes. The increasing leak rate during the test is thus offset by a corresponding increase in indicated flow. The net result is that the total flow due to concrete ablation as measured by the orifice plate is within 5% of the predicted total volume of 13,000 standard liters of gas based on final erosion patterns.

No corrections for either leakage or aerosol plugging were applied to any of the flow data after time 60. The reported results for the orifice plate after that time should not be considered to be as quantitatively accurate as they are qualitatively correct.

Results for the turbine meter are shown in Figure 2.4.18. Here total flow (raw data) includes the argon-helium carrier gas and concrete products flow does not. The raw data indicates an initial flow rate of 72 slpm. Degassing of the concrete is seen to start around time = 25 minutes and is marked by an increase in total measured flow to 110 slpm at time = 45 minutes. Between times 45-75, the total flow increases to an average value of 200 slpm in conjunction with steady-state concrete ablation. Aerosol plugging then caused the turbine meter to be bypassed at time 60 and no further data were recorded. The corrected data for flow rate due to steel-concrete interactions alone indicate flow starting at time 25-30 and rising to 40-50 slpm before concrete ablation begins. Onset of concrete ablation is marked by an increase in flow to a peak of 165 slpm at time 55 followed by a coast-down to 100-110 slpm at time 60 when the turbine meter was bypassed.

The laminar flow device shows similar results as seen in Figure 2.4.19. Two calibration gases, nitrogen and argon, were used to reduce the data. The flow rate for steel-concrete interactions above is seen to start at time = 40 minutes and rise to peak values of 135-165 slpm at time 55 before aerosol plugging of the device necessitated flow bypass at time 60. The gas clock results are shown in Figure 2.4.20. Before time 66, the 450 gas clock collected a total of 7446 standard liters of gas as compared to 7286 standard liters of gas collected by the 750 gas clock. Approximately 2750 standard liters of the gas was concrete reaction products with the remainder being argon and helium. This compares to a total of 2666 standard liters of steel-concrete reaction gases measured by the turbine meter and 2200-2500 standard liters of gas collected by the laminar flow device. Erosion at time 66 was approximately 5 cm downward and 2 cm in the radial direction yielding a projected total of 2723 standart liters of gas, 70% of which is due to radial concrete decomposition. Heating of the concrete sidewalls above the melt-pool would account for additional amounts of gas, especially CO_2 and H_2O, which did not react with the meltpool.

The orifice plate flow meter was the only device which recorded data for the entire duration of SURC-3A. As previously noted, these measurements were obscured after time = 66 minutes by leakage from the crucible and aerosol plugging. Figure 2.4.21 shows the details of the orifice plate flow measurements for the three periods of interest. Flow begins at time = 27-30 minutes and rises to a value of 45-55 slpm before concrete erosion begins at time = 45 minutes. Flow rate then increases to a peak of 150-170 slpm at time 55 and coasts down to a value of 75 slpm

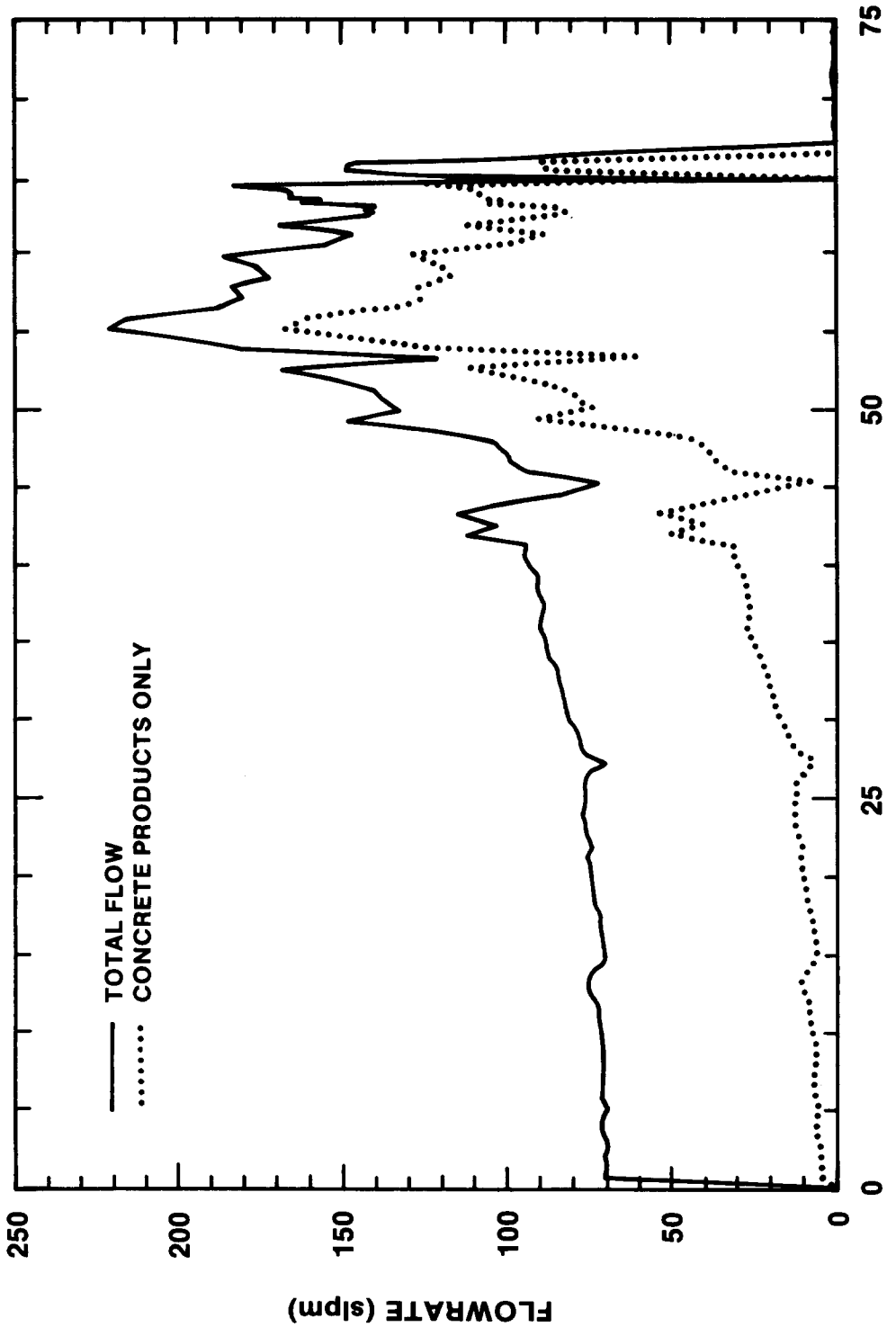

Figure 2.4.18 SURC-3A Flow Rate - Turbine

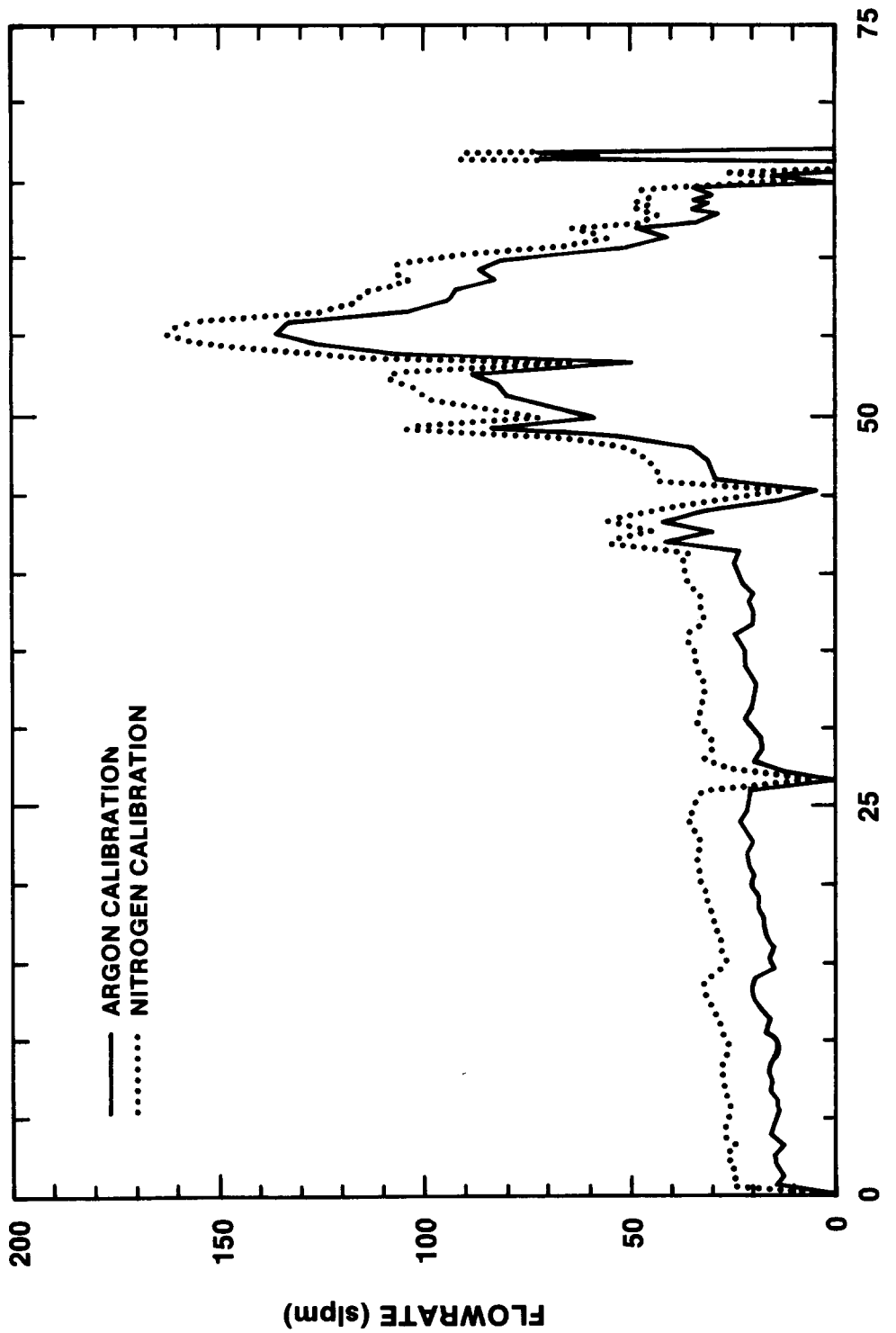

Figure 2.4.19 SURC-3A Flow Rate - LFD

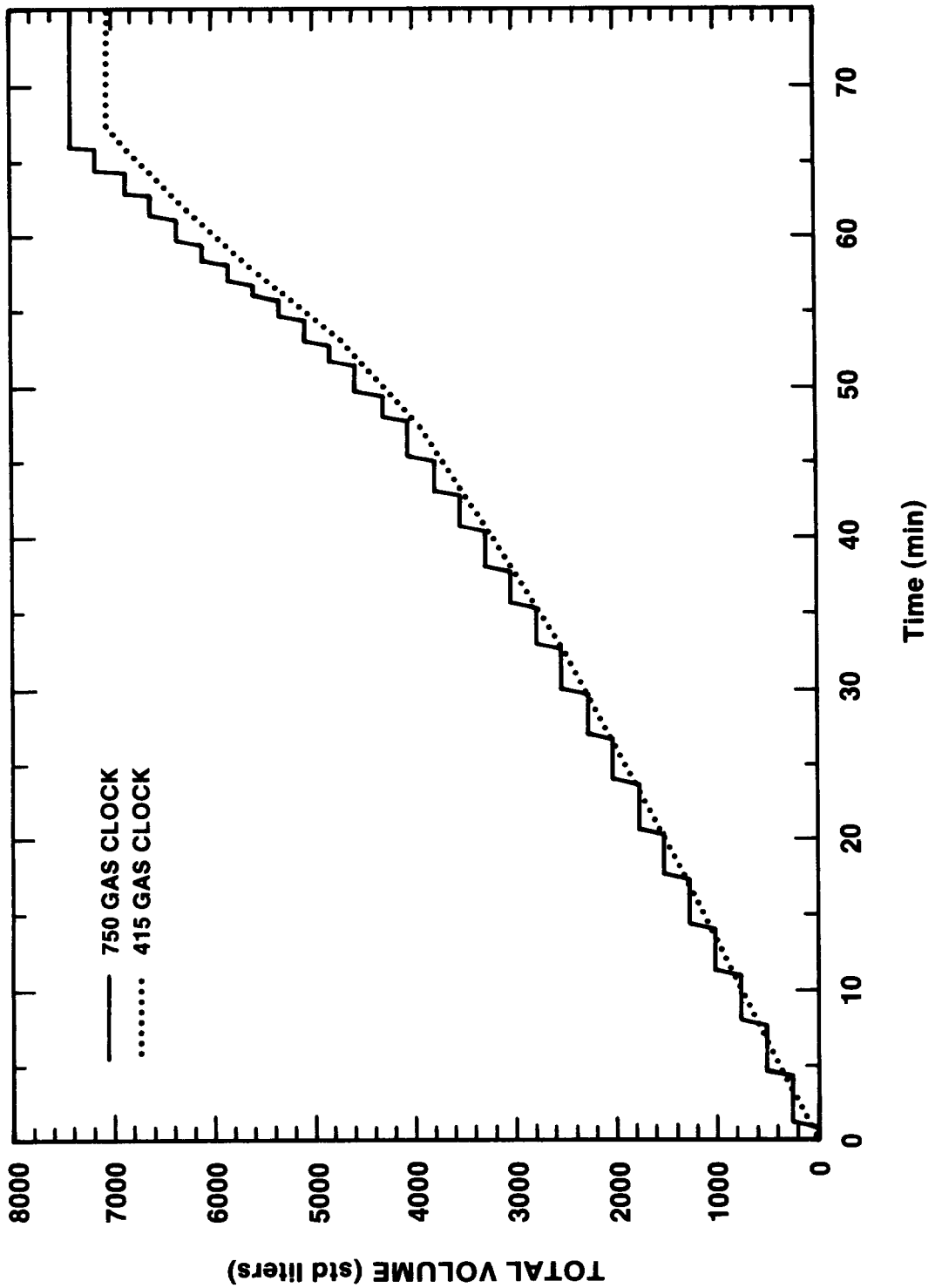

Figure 2.4.20 SURC-3A Total Flow - 750 Gas Clock

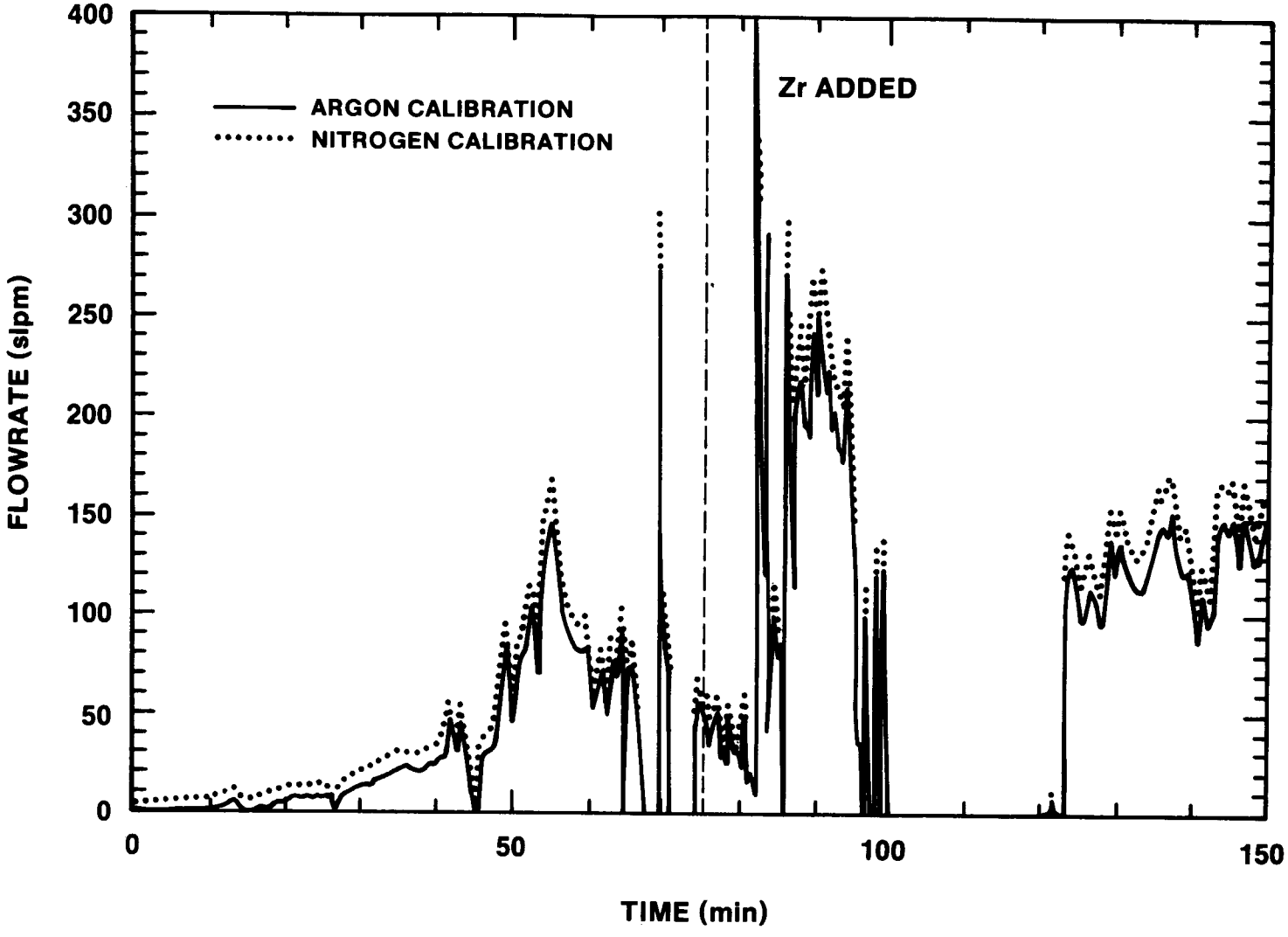

Figure 2.4.21 SURC-3A Flow Rate - Orifice Plate

during the steady-state concrete erosion phase from time = 45-75 minutes. After the Zr metal is added at time 75, the flow rate first drops to 30 slpm at time = 82 minutes, then rises dramatically to 200-250 slpm for an extended period of time. The orifice plate data was lost during time 100-120 due to flow bypass. After time 120 flow was restored and flow rates of 110-160 slpm were recorded for the remainder of the SURC-3A test.

2.4.8 Aerosol Data Presentation

The aerosol data taken in the SURC-3A test is similar to that taken in the SURC-3 test, though not as extensive. Section 2.3.8 describes the instrumentation, calibration, sampling and data reduction techniques common to both tests.

Aerosol Instrumentation

The aerosol instrumentation placed on the SURC-3A test is described below. (The reader is referred to Section 2.3.8 for more detail). It is designed to provide data which will allow calculation of the aerosol source term. Figure 2.4.22 is a schematic diagram of the SURC-3A test article showing the sample points and location of the aerosol instrumentation.

An aerosol sample was drawn from the crucible volume through the crucible wall into a Sierra Cascade Cyclone. No dilution on this sample was performed. The automatic value control system was set up to take a cyclone sample each time a filter sample was being drawn. Thus, the cyclone sample may be viewed as the average aerosol sample of all the filter samples.

The filter bank described in Section 2.3.8 was used with a single diluter running at a constant 86.8 standard liters per minute. The heating system described in 2.3.8 was used to heat the filters to about 70°C.

An impactor bank was not included in the SURC-3A test. Instead, three impactors (Andersen, Mk IV) were used to sample from a box into which a small quantity of exhaust gas was directed. The function of this box was to provide dilution and a means of sampling the aerosol with the APS (see Section 2.3.8) without pressure fluctuations. The impactors sample simultaneously from this roughly 1 m^3 box.

The opacity meter was also connected in the exhaust line as described in Section 2.3.8.

The pressure transducers and critical orifices used in SURC-3 and described in Section 2.3.8 were also used in SURC-3A. The filter bank operated with orifice 10G. The impactors A, B and C operated with orifices 14B, 14C and 14E, respectively. Table 2.4.8 lists the flow controlling orifices, their calibrated flow values, and the pressure transducers used.

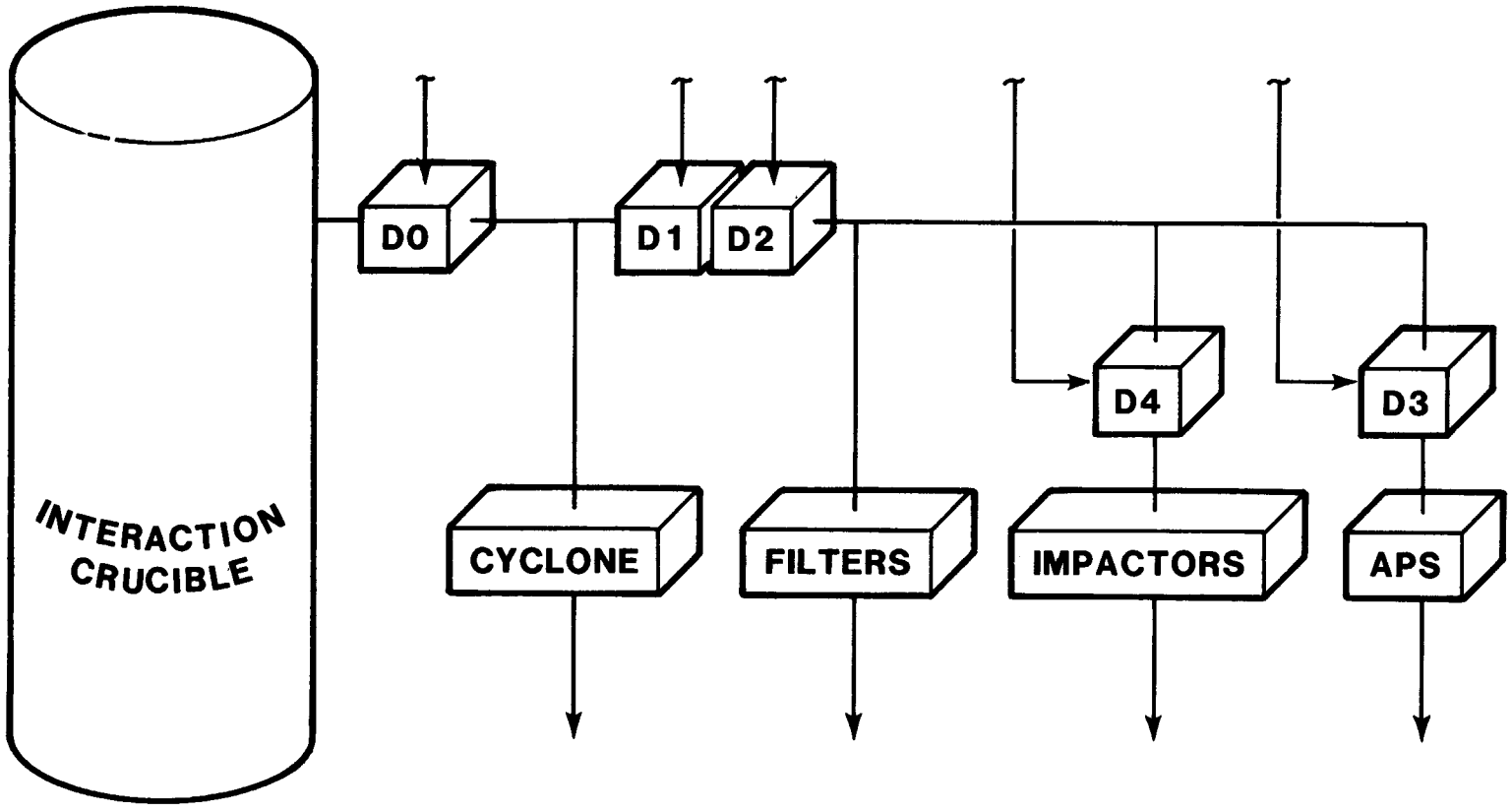

Figure 2.4.22 SURC-3A Aerosol Instrumentation Schematic

TABLE 2.4.8

Flow Controlling Devices Used in SURC-3A Aeosol Collection

Impactor A	Orifice 14B (237 cm^3/s)
Upstream pressure:	LV-47
Downstream pressure:	A6-38
Impactor B	Orifice 14C (255 cm^3/s)
Upstream pressure:	LV-33
Downstream pressure:	A6-38
Impactor C	Orifice 14E (247 cm^3/s)
Upstream pressure:	A4-3
Downstream pressure:	A6-38
Filter Bank	Orifice 10G (170.8 cm^3/s)
Upstream pressure:	A5-87
Downstream pressure:	A5-85
Cascade Cyclone	Orifice 10H and 14J(423.5 cm^3/s)
Upstream pressure:	A6-95
Diluter	Orifice 3A (46 cm^3/s)
Upstream pressure:	A6-91

The calibrations described in Section 2.3.8 are also applicable for test SURC-3A.

Procedures

Twelve filter holders were loaded with 12 pre-weighed filters and installed into the SEDS filter sampler box. The Dynatron opacity meter was adjusted and the zero set according to the manufacturer's specifications.

The pressure determined for the desired dilution ratio was set on the diluter to the filter bank by adjusting the metering valve upstream of the diluter flow controlling orifice. The remote valve opening and closing flow to the diluter was cycled to check that the pressure returned to the set value of 28.3 psia.

The Modicon 80 programmer was programmed to take 12 filter samples, each at the determination of the operator. The cyclone was programmed to sample during each of the filter samples. For three of the filter samples, a simultaneous impactor sample was taken from the aerosol box. The filter and impactor samples were of 60 seconds in duration (except filter 9I which sampled for 79 seconds). Table 2.4.9 gives the sampling schedule for the SURC-3A test.

The impactors and the APS sampled from the aerosol box. The box tapped into the exhaust line. A remotely actuated valve allowed a short time duration flow of aerosol laden exhaust gas into the box. The amount of aerosol flowing into the box was small compared to the volume of the box resulting in high effective dilution. Simultaneous sampling with the APS and impactors was to provide data for dynamic shape factor assessment; however, the valve cycling time was too long and the aerosol concentration in the box rapidly overloaded the APS, causing the small inlet nozzle to become partially blocked. The impactor data from the box is of good quality and compares well to the size distribution data from the cyclone.

Valve cycling was performed for aerosol impactor samples A and B. At about 100 min. it became necessary to vent the exhaust gas through the aerosol box. Impactor sample C was taken at this time. It yields distribution data and mass concentration data in good agreement with filter sample 3C.

The diluter to the filter bank operated continuously during the test. The dead volume in the sample line from the sampling point to the diluter is about 130 cm^3 and in the filter bank is about 500 cm^3. The time to clear the entire dead volume in the filter sampling system is about 6% of the total sampling time. The contribution of sampling line dead volume to sample uncertainty is also about 6%.

TABLE 2.4.9

SURC-3A Sampling Schedule

Sample Time (min)	Sample Duration (sec)	Filter	Impactor	Cyclone
44.18	60	4D	-	on
49.13	60	5E	-	on
60.01	60	6F	-	on
61.85	60	7G	-	on
63.15	60	8H	-	on
70.6	60	1A	A	on
77.3	79	9I	-	on
88.3	60	2B	B	on
102.5	60	3C	C	on
108.3	60	10J	-	on
130.45	60	11K	-	on
142.0	60	12L	-	on

During the test, interference from the induction power supply produced severe noise in a number of the pressure transducer and thermocouple signals. For the most part, the signals relating to the aerosol measurements were not useful. Notable exceptions were the pressure records of the upstream filter control orifice and the upstream impactor control orifices. These records gave verification of sample times and duration for the impactors and filters. The upstream temperature of the filter sample control orifice could be determined to within 5°C over the test period, while the temperature inside the filter box was known accurately only at the beginning and end of the test. This was also the case for the diluter orifice upstream pressure.

Data and Analysis

Data and sample retrieval and the analysis methods for the SURC-3A test were the same as for the SURC-3 test.

Aerosol transport efficiency to the filters, impactors, and cyclone is assumed to be better than 95% for the size distributions measured based on the transport data illustrated in Figures 2.3.48 and 2.3.49.

The filter sample data for SURC-3A is given in Table 2.4.10. This lists the filter sample, sample time, sample duration, aerosol mass concentration and calculated mass source rate along with other quantities used to calculate the concentration and source rate. The aerosol concentration fluctuates between 2 to 20 mg/standard liter. The mass source varies between 5 and 90 mg/s. The uncertainty in mass source is ±30% arising from the uncertainty in gas flow due to leakage. Figure 2.4.23 is a graph of the aerosol concentration and mass source term in SURC-3A based on the filter data.

Figure 2.4.24 is a graph of the aerosol filter concentrations shown with the opacity meter signal. The signal may be degraded by noise from the power supply; however, the trends in the filter concentration fluctuations match the fluctuations in the opacity signal.

The aerosol impactor samples taken from the aerosol box give an indication that the aerosol is unimodal, narrowly distributed about 1μm aerodynamic equivalent diameter. The impactor data are given in Table 2.4.11.

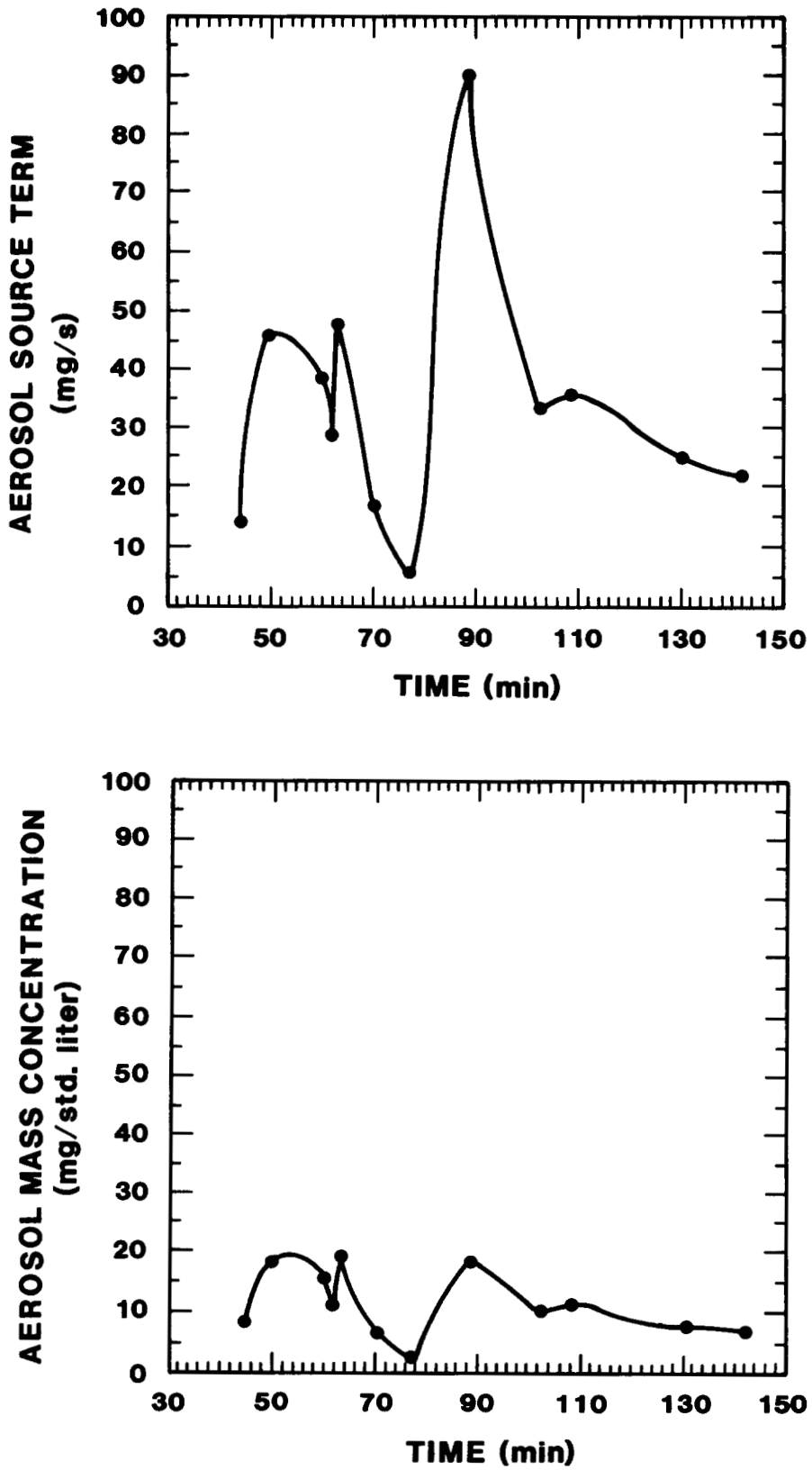

Figure 2.4.23 SURC-3A Aerosol Concentration - Filter Data

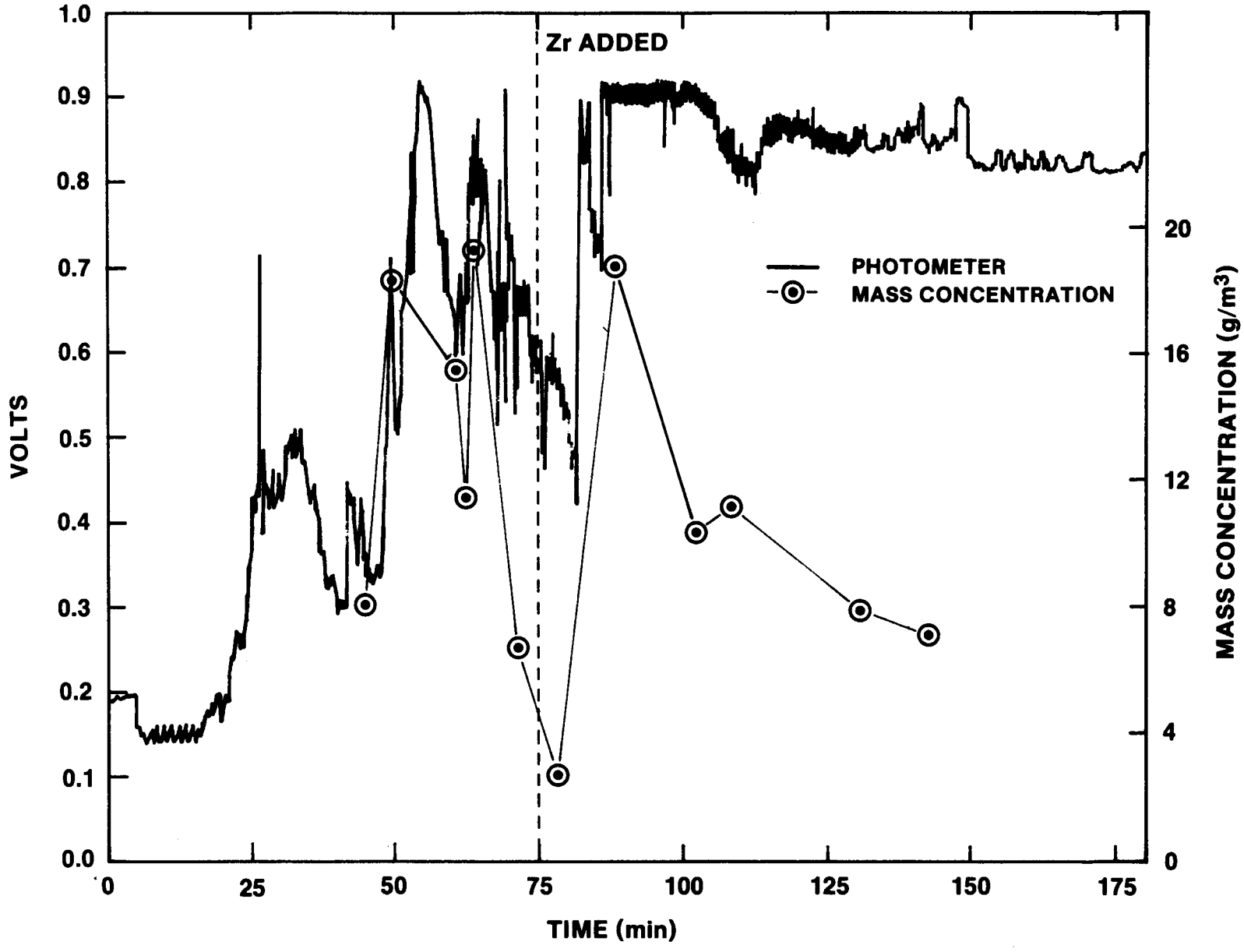

Figure 2.4.24 SURC-3A Aerosol Concentration - Opacity Meter

TABLE 2.4.10

SURC-3A Filter Sample Data

Filter Sample Source	Sample Time (min)	Collected Mass (mg)	System Pressure (psia)	Filter Orifice Temp (K)	Gas Sampled (std. liters)	Dilution Ratio	Total Exhaust Gas Flow (std. liters/ min.)	Mass Concentration (mg/std liter)	Mass Source (mg/s)
4D	44.18	25.35	12.7	305	8.17	2.66	100	8.25	13.8
5E	49.13	65.58	13.5	306	8.68	2.42	150	18.28	45.7
6F	60.01	62.50	14.2	307	9.12	2.27	150	15.56	38.9
7G	61.85	46.13	14.2	307	9.12	2.27	150	11.48	28.7
8H	63.15	77.14	14.2	307	9.12	2.27	150	19.20	48.0
1A	70.6	19.33	12.6	309	7.99	2.76	150	6.68	16.7
9I	77.3	10.13	12.3	310	10.23	2.84	120	2.81	5.6
2B	88.3	62.43	13.3	310	8.43	2.53	290	18.74	90.6
3C	102.5	27.76	12.3	310	7.77	2.91	190	10.40	32.9
10J	108.3	30.11	12.3	310	7.77	2.91	190	11.28	35.7
11K	130.45	20.94	12.4	313	7.76	2.92	190	7.88	25.0
12L	142	19.31	12.4	313	7.76	2.92	180	7.27	21.8

Filter sample drawn through orifice 10G at 171 actual cm^3/s.

Dilution gas flow constant at 86.8 standard cm^3/s.

TABLE 2.4.11

Aerosol Impactor Data - SURC-3A

Impactor	A	B	C
	Collected Mass (mg)		
Pre-Separator	0.10	0	0.12
Stage 1			
Stage 2			
Stage 3	0.12	0.01	0.15
Stage 4	0.12	0.18	0.42
Stage 5	0.62	0.34	1.20
Stage 6	3.84	2.13	19.41
Stage 7	4.30	4.58	59.03
Stage 8	3.38	2.85	24.96
Filter	.92	1.2	5.04
TOTAL (mg)	13.4	11.3	110.3
Gas Sampled (std. liters)	11.7	12.6	12.2
Concentration (mg/std. liter)	1.15	0.90	9.0

Figures 2.4.25, 2.4.26, and 2.4.27 show the impactor size distributions plotted as the fraction of total collected mass per logarithmic size interval versus the aerodynamic equivalent particle diameter. The data reduction was performed using the calibration data of Cushing, et al (1976). The size distributions agree well with one another, even though the concentrations collected on impactor C are an order of magnitude higher than on A or B. The sample impactor C was taken during the venting of exhaust gas through the filter box. This concentration measured by impactor C, 9 mg/standard liter is in good agreement with the filter sample 3C taken at the same time, 10.4 mg/standard liter.

The size distributions given by the impactor are in good agreement with the size distribution measured by the cyclone. Table 2.4.12 gives the cyclone data and Figure 2.4.28 is a plot of the size distribution measured by the cyclone. The size distribution is presented in the same way as the impactor size distributions.

The cyclone sampled from a volume in the crucible just above the melt while the impactors sampled from a box which drew the aerosol from an exhaust line after the aerosol had been transported through the crucible and exhaust plumbing. The impactor and cyclone size distributions show remarkable agreement. Differences may be explained by uncertainties in parameters such as gas sampling rate and gas properties, or in the instrument calibration used.

Elemental analysis using inductively coupled plasma (ICP) emission spectroscopy was performed on some of the filter samples and the cyclone samples. Dissolution of the samples was in hydrofluoric acid, as with the SURC-3 samples, and it is highly likely that the tellurium was lost before analysis as a volatile fluoridate. Our assumption that tellurium is a major component in the SURC-3A aerosol does not have the support of analysis (as is the case in the SURC-3 analysis), but similarity of the SURC-3 and 3A tests along with the lack of any other highly dominant constituent in the SURC-3A samples would suggest it.

Table 2.4.13 gives the elemental analysis of filter samples 2B, 3C, 5E,6F, 8H, 10J and 12L for a number of elements. When a value is preceded by a "<" character, the element was not detected and the number given is the detectability limit. Sodium and potassium are present at several weight percent.

Table 2.4.14 gives the elemental analysis for the samples collected in the cyclone by stage.

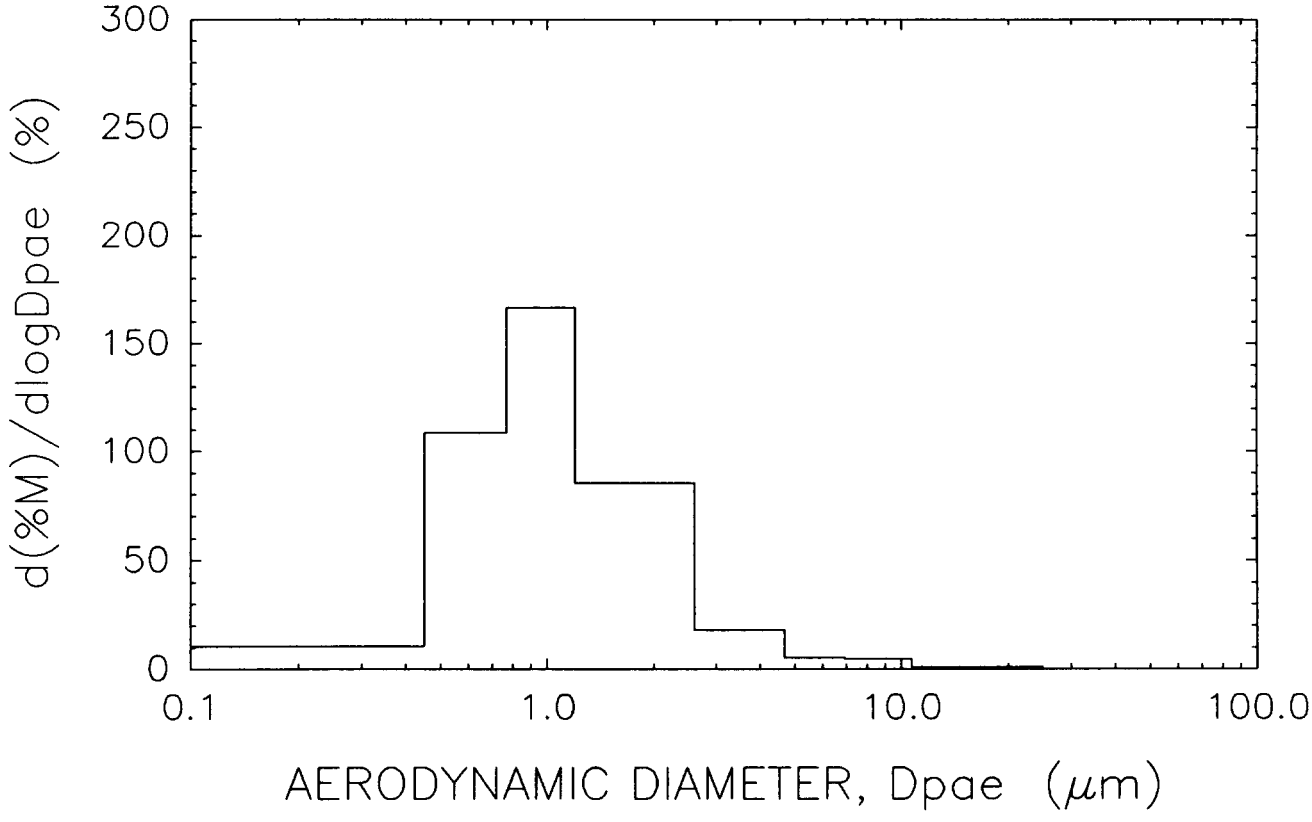

Figure 2.4.25 Aerosol Size Distribution - Impactor A

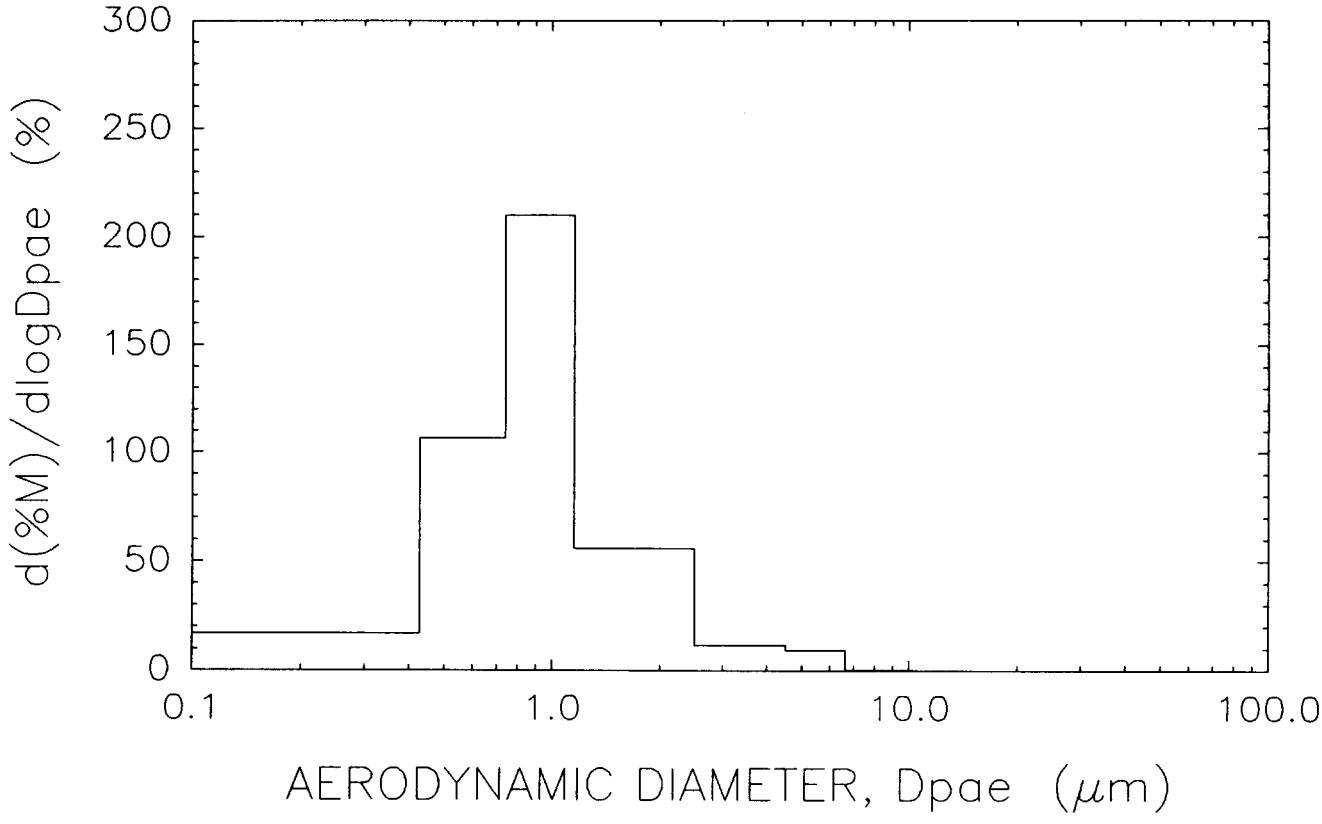

Figure 2.4.26 Aerosol Size Distribution - Impactor B

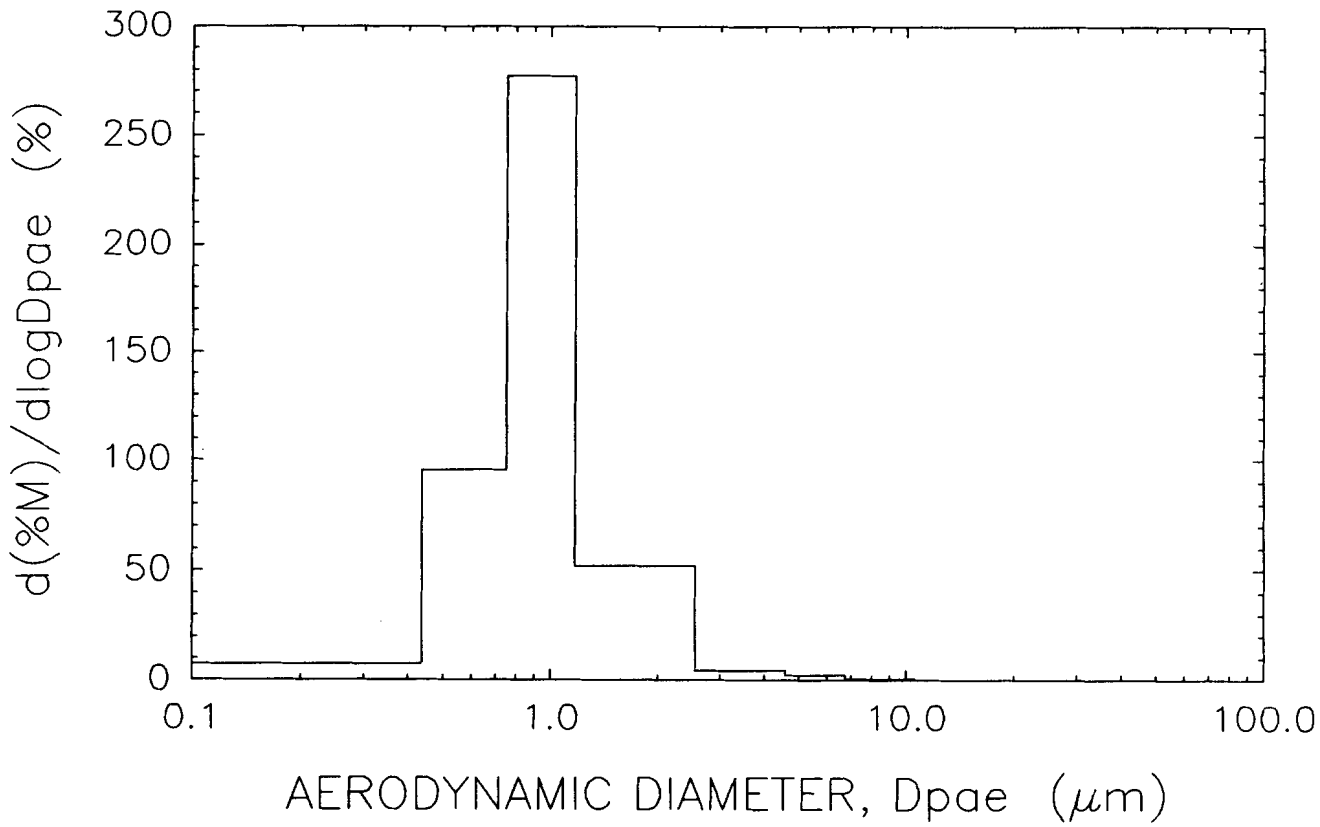

Figure 2.4.27 Aerosol Size Distribution - Impactor C

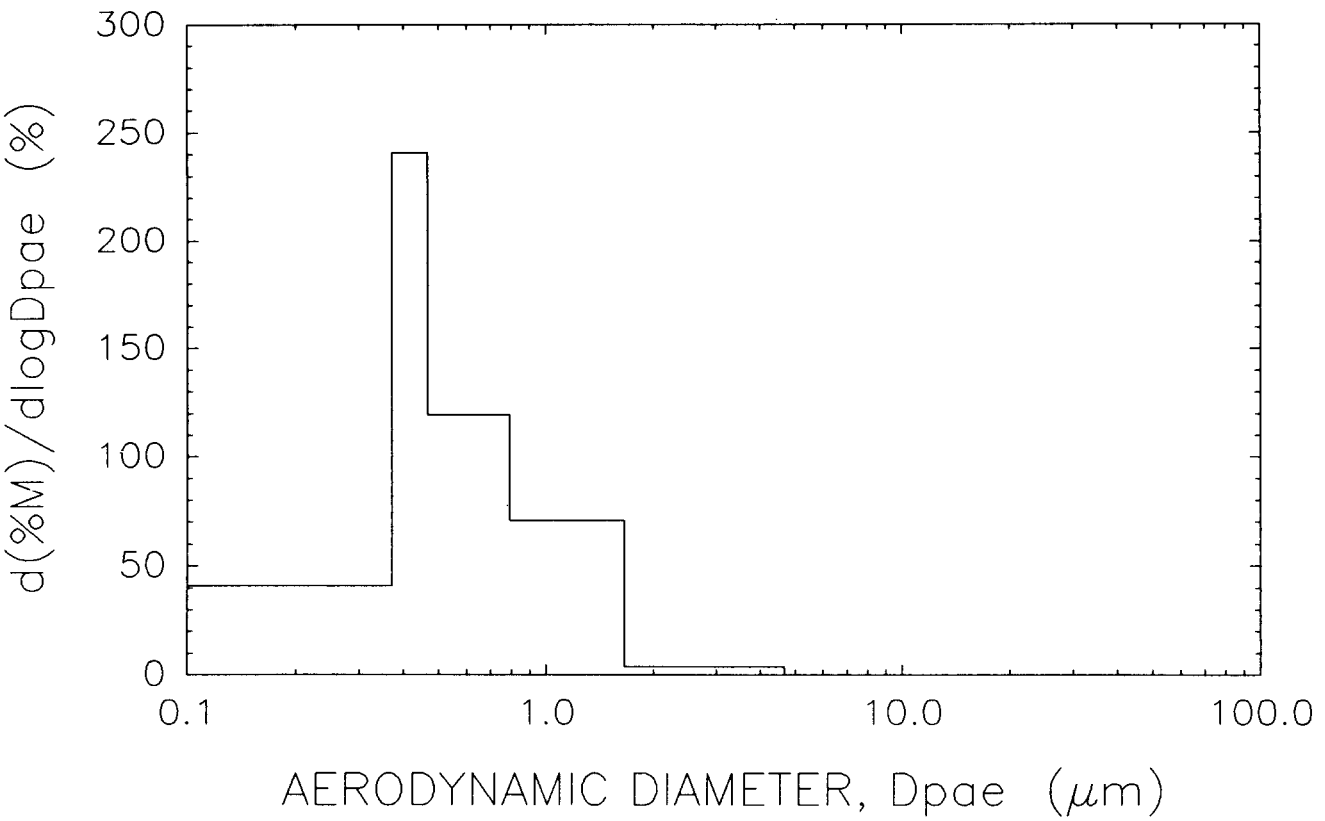

Figure 2.4.28 Aerosol Size Distribution-Cyclone

TABLE 2.4.12

Cyclone Data - SURC-3A

Cyclone Stage	Mass Collected (mg)	Size Range* (μm)
1	0	>4.7
2	0	
3	33.2	1.69 to 4.7
4	441.65	0.79 to 1.69
5	518.13	0.47 to 0.79
6	466.73	0.37 to 0.47
F	444.46	<0.37
TOTAL	1904	

*Aerodynamic equivalent diameter based on manufacturer's calibration.

TABLE 2.4.13

Elemental Analysis of SURC-3A Filter Data
Weight Percent of Element in Sample

Element	F2-B	F3-C	F5-E	FG-F	F8-H	F10-J	F12-L
Fe	0.099	0.108	0.69	0.99	0.112	0.183	0.115
Ne	0.006	0.007	0.011	0.006	<0.001	0.020	<0.005
Cr	0.040	0.007	0.113	0.96	0.006	0.103	<0.005
Mn	0.27	0.054	0.120	0.04	0.025	0.106	0.005
Mg	0.022	0.0108	0.143	0.24	0.008	0.007	<0.031
Ba	<0.002	<0.004	0.006	0.005	0.013	0.003	<0.005
Na	4.0	2.56	0.85	1.28	1.56	4.65	1.81
K	18.3	22.4	7.47	12.0	15.7	30.2	28.5
Si	0.040	0.40	0.168	0.147	0.025	0.040	0.021
Ca	0.019	<0.022	0.52	0.59	0.181	<0.020	0.062
La	<0.008	<0.018	<0.008	<0.008	<0.006	<0.017	0.145
Mo	0.003	0.69	0.035	0.050	0.064	0.030	1.04
Ce	<0.002	<0.004	<0.008	0.005	<0.005	<0.007	<0.005
Nb	0.005	<0.011	<0.005	0.005	<0.004	<0.010	<0.016
Zr	0.082	0.025	0.87	0.62	0.98	1.16	0.021

TABLE 2.4.14

Elemental Analysis of SURC-3A Cyclone Data
Weight Percent of Element in Sample

Element	#3	#4	#5	#6	Filter
Fe	1.14	0.046	0.044	0.39	0.146
Ni	0.093	0.003	0.001	<0.001	0.005
Cr	0.244	0.024	0.017	0.013	0.011
Mn	0.051	0.038	0.036	0.089	0.072
Mg	0.60	0.008	0.006	0.008	0.83
Ba	0.42	<0.001	<0.001	<0.001	0.025
Na	3.6	1.2	2.4	1.8	2.5
K	6.6	8.7	13.6	9.2	15.7
Si	8.1	0.004	0.015	0.012	6.3
Ca	1.14	<0.001	0.010	<0.005	5.7
La	<0.015	<0.001	<0.001	<0.001	<0.001
Mo	0.087	0.036	0.026	0.062	0.160
Ce	0.039	0.005	0.001	<0.001	0.0016
Nb	0.009	0.001	0.001	<0.001	<0.0002
Zr	4.2	0.55	0.061	0.007	0.010

2.4.9 Gas Composition Data Presentation

Gas sampling for the SURC-3A test was done using three techniques: the Inficon Model IQ 200 mass spectrometer, the Infrared Industries Model 700 CO/CO_2 monitor, and integral grab samples. These were the same instruments as were used in the SURC-3 experiment. The first two techniques provide real-time data which can be viewed on-line and is stored on computer disks. The grab samples are stored and analyzed posttest using both gas chromatography and mass spectrometry. A schematic layout of the SURC-3A gas composition sampling apparatus is shown in Figure 2.4.29.

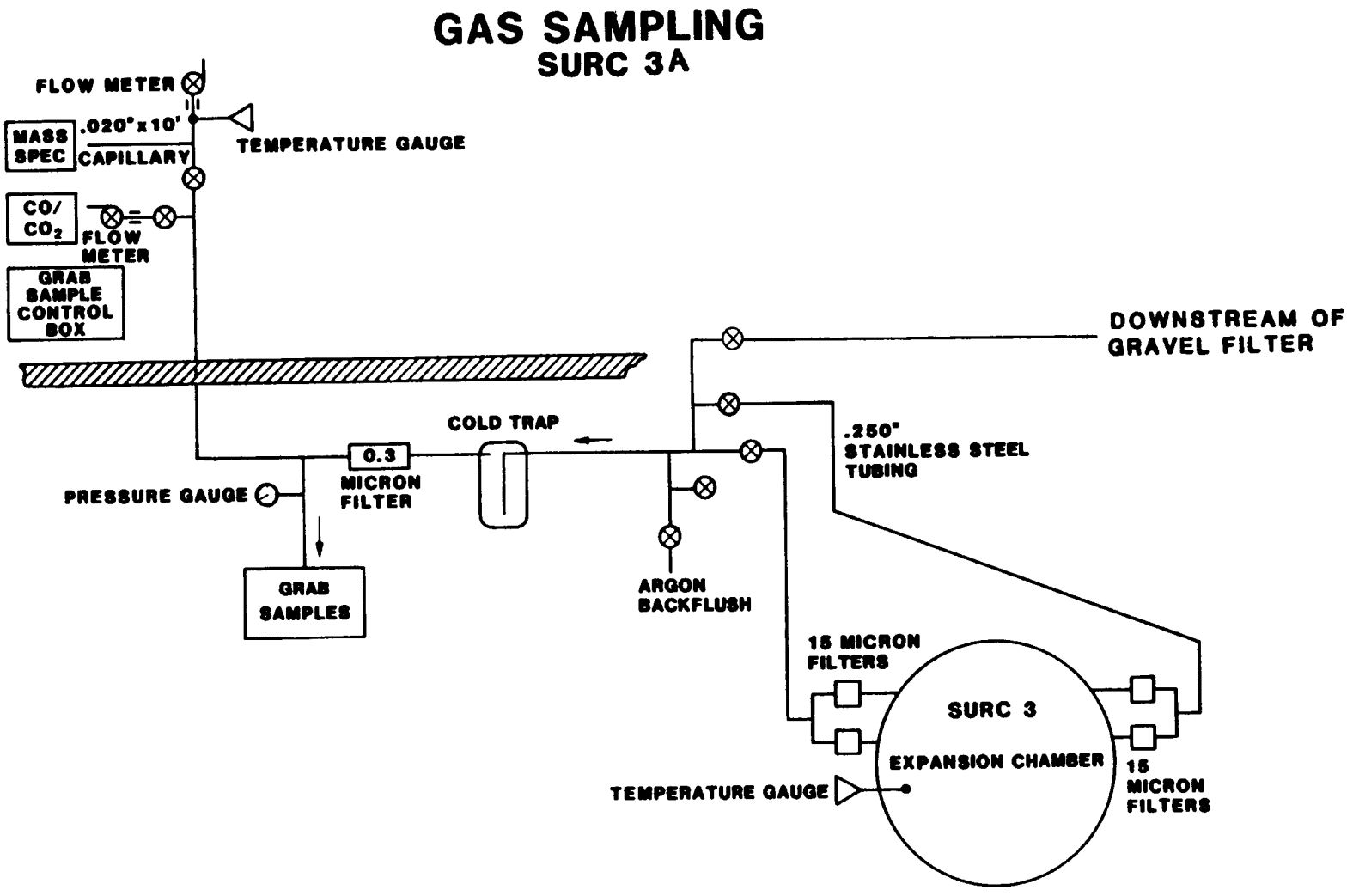

Figure 2.4.29 SURC-3A Gas Composition Instrumentation Schematic

Hardware

Support equipment for SURC-3A is described in this section. All sample lines for gas collection were 6.4 mm (.250 in.) O.D. stainless steel tubes with Swagelok stainless steel fittings and Nupro plug valves. There was a normal and standby line from the expansion chamber and a third line connected downstream of the gravel filter. Two 15 micron stainless steel filters in parallel were attached to both of the expansion chamber sample lines while only one was used on the gravel filter line. Forty psi argon was available for backflushing the stainless steel filters and a .3 micron Gelman HEPA filter was in-line with a stainless steel cold trap to prevent water vapor from getting to the analysis equipment (Figure 2.3.58).

K type thermocouples were used to monitor sample gas temperature in two different locations. One Gast oilless diaphragm air pump was used to support the main gas flow while another supplied the CO/CO_2 monitor. Flow indication for the system was measured by self-indicating rotameters. The CO/CO_2 supply had a Dwyer 0-10 scfh air rotameter and the main gas flow used a Gilmont 0-13 lpm air rotameter.

A small helium flow was directed on the quartz windows inside the expansion chamber at the top to allow for clear photography and argon was used as the purge gas throughout the test.

The grab sample system was designed to take gas samples for post-test analysis by using 75 cc stainless steel bottles with Nupro JB series closures. A Validyne absolute pressure transducer with a range of 0-1000 torr was used to monitor manifold pressure. All this equipment plus a Welch 2-stage belt drive vacuum pump with 175 lpm free air capacity was installed in a standard test rack (Figure 2.3.59). The control box contained the valve position lights and four-way switches to control the multiposition sample valves. The grab samples were analyzed posttest by Gas Chromatography/mass spectrometry using a Tracor MT-150g Gas Chromatograph and a Finnigan Mat 271/45 mass spectrometer.

The CO/CO_2 analyzers are the primary means for collecting CO/CO_2 data furnished as real time information. They operate on an infrared absorption technique using Infrared Industries detector models 702 and 703 (Figure 2.3.60). The carbon monoxide is monitored on a range of 0-50% and the carbon dioxide on a range of 0-20%. Response time is 5 seconds for 90% of the reading. Both detectors have a 0-5 volt output with an overrange capability of 2 volts.

The mass spectrometer was an Inficon IQ200 Quadrupole Residual Gas Analyzer set up to display real time data by continuously scanning specifically selected masses of H_2, H_2O, CO/N_2, O_2, Ar, and CO_2.

A pressure converter manifold provided the ability for continuous sampling from a pressure of 2 atmospheres at the sample source down to 10 torr at the analyzer where the associated 150 lps turbo pump could maintain $1x10^{-6}$ torr at the sensor. A Faraday cup sensor was used to provide the currents for analysis (Figure 2.3.61).

For data acquisition, the Hewlett Packard 1000 series computer was used at acquisition rates of 10 seconds for test warm up and 3 seconds for the majority of the run where test events necessitated a faster rate (Figure 2.3.60). Inputs to the data acquisition system for gas composition were: temperature from the expansion chamber, grab sample manifold pressure 0-10 volts per 0-1000 torr, percent CO 0-5 volts per 0-50%, and percent CO_2 0-5 volts per 0-20%.

Layout and Location

Figure 2.4.29 shows the general location for the support equipment and major gas sampling components. Stainless steel filters for the gas sample lines were mounted on the expansion chamber/melt generator flange ~15 cm from the end of the sample tube located inside the expansion chamber and also on the line downstream of the gravel filter.

One K type thermocouple was located inside the expansion chamber ~1 meter from the melt charge and another in the main sample line at the mass spectrometer sample tee. The HEPA filter, cold trap, and argon backflush manifold were located just upstream of the grab sample line approximately 7.5 m (24.5 ft) from the test article. One diaphragm air pump and rotameter were used at the CO/CO_2 supply line while the other pump and rotameter were downstream of the sampling tees drawing the main gas flow.

The grab sample system tied into the main gas line using a 6.4 mm (.250 in) O.D. stainless steel tube with a dead volume of 50 cc. The equipment rack was located outside on the test pad 7.6 m (25 ft) down the line from the crucible. The control box was operated from the computer room.

The CO/CO_2 analyzers were located in the computer room where they were connected to the main gas line with a 6.4 mm (.250in) O.D. stainless steel tube and a diaphragm pump supplying the sample gas through a Dwyer rotameter. The distance from the CO/CO_2 monitor to the test crucible was 9.5 m (31 ft).

The Inficon mass spectrometer was also located in the computer room and was connected to the main gas line by a .5 mm (.020 in) I.D. x 10 ft capillary tube. The sample tee was situated 10 m (33 ft) from the SURC-3A crucible.

Calibrations and System Checks

Calibrations for the different sampling equipment were accomplished with primary standard gas mixtures from Alphagaz. The CO/CO_2 analyzers were calibrated using a gas mixture of 2.0% CO_2, 200 ppm CO, 98% argon. In addition, the instrument zero was checked with a zero gas of nitrogen and the full range checks were done by mechanical means. This calibration was accomplished pretest as well as posttest to check for significant drift.

This same primary standard gas mixture was introduced into the mass spectrometer system prior to the test and monitored. This mixture as well as another was used for the calibration check on the mass spectrometer system after the test.

As an operational check on the whole system, a calibration gas was introduced into the expansion chamber and the results monitored by the mass spectrometer and CO/CO_2 systems. Pressure was monitored from the grab sample manifold while switching from constant gas flow to grab sampling events. All three sample locations were checked in this way.

Other operational checks included comparing the thermocouples used in the test with others known to be operationally acceptable. The flow meters were also matched with other calibrated rotameters in use.

Procedures

For SURC-3A, support equipment was operated in the following manner: The output from the thermocouple installed in the expansion chamber was monitored continuously by the data acquisition system while the thermocouple at the mass spectrometer sample tee was read every 5 minutes with a portable meter.

Gas flow through the sample lines was established several minutes before the start of the test by energizing both diaphragm pumps. The flow was manually regulated to provide 6 scfh to the CO/CO_2 monitor and 3 lpm for the main gas flow line. Monitoring of sample line flow was done every 2-5 minutes and when a substantial decrease in flow was indicated, argon was introduced into the sample line to backflush the stainless steel filters.

The grab sample bottles were evacuated before the test and maintained under vacuum until the multi-port valves were positioned to evacuate a sample of gas from the main gas stream. Samples were taken manually and recorded on computer disk as indicated by pressure spikes from the manifold transducer.

The CO/CO_2 monitors were warmed up at least 20 minutes before use. During the test, the 0-5 volt signal was continuously monitored by the data acquisition system while percent displays were monitored locally at the instrument and remotely in the control room.

The mass spectrometer was under a vacuum of 100 torr for at least one week before establishing a vacuum of 10-6 torr for two days prior to testing. The analyzer display was continuously monitored at the instrument. On-line data was recorded every 5 minutes during periods of low activity and every minute during more critical events.

Results

Four periods of time are of interest for the SURC-3A gas composition data: the onset of concrete ablation between 25-55 minutes, steady-state erosion between 55-75 minutes, the Zr addition and ensuing reaction between 75-100 minutes, and the return to steady-state erosion from 100-150 minutes. Notable events during SURC-3A which affected the gas composition results were: a temporary filter blockage of the gas analysis flow line at time 39-44, delivery of the Zr metal at time 75, and a permanent blockage of the gas analysis flow line at time 91 which necessitated a change in gas sampling location from the expansion chamber to the gravel filter chamber.

A total of 3.3 ml of water was recovered from the gas analysis line cold trap. This would have added 5.0 l of H_2O vapor to the 370 liters of collected concrete reaction gas yielding an average water vapor content of 1-2% in addition to the reported gas compositions for H_2O, H_2, CO, and CO_2.

Gas temperature of the sample line was measured at the mass spectrometer sampling tee. This temperature remained fairly constant through the test at a value of 30-31°C. The gas temperature was also monitored inside the expansion chamber. At that location, the gas temperature ranged from 42°C at time = 45 minutes to a peak value of 350°C at time = 100. Gas temperatures in the flow stream are discussed further in Section 2.4.6.

The 15 micron stainless steel filters interrupted the normal sample line gas flow at a run time of 39 minutes due to aerosol blockage. These filters were backflushed with argon at time = 40 minutes and flow was re-established at time = 44 minutes. At time 99, the filters for both the normal sample line and the secondary sample line from the expansion chamber became clogged and backflushing did not prove to be effective. The sample location was then switched to the gravel filter volume at the end of the main exhaust line for the remainder of the test. Two checks of the normal and secondary sampling lines at times 112 and 120 verified that those lines were permanently plugged.

The results from the CO/CO_2 monitor are shown in Figure 2.4.30. The raw data, shown here as percent CO and CO_2 in the sampling flow line indicates the onset of concrete decomposition at time = 20 minutes. Between time =20 and the onset of concrete erosion at time 45, the CO_2 concentration in the gas was higher than the CO concentration. After time 45, the CO concentration rose and CO_2 concentration fell so that the CO concentration was much higher than the CO_2 concentration. A further increase in CO production was noted after time 80 when the Zr reaction began. This increase continued until time 125 when the Zr reaction was complete and steady-state values were re-established. Normalized data from the CO/CO_2 monitor is shown in Table 2.4.15. The data was normalized by subtracting the amounts of argon-helium carrier

TABLE 2.4.15

Normalized Gas Composition Data for SURC-3A -- CO/CO_2 Monitor

Time	% CO	% CO_2	% H_2/H_2O (Assumed)
20	14.0	78.0	(8.0)
25	16.7	75.3	(8.0)
30	14.3	77.7	(8.0)
35	16.5	75.5	(8.0)
40	25.5	66.5	(8.0)
45	34.3	57.7	(8.0)
50	56.6	35.4	(8.0)
55	73.3	18.7	(8.0)
60	77.0	15.0	(8.0)
65	82.0	10.0	(8.0)
70	82.5	9.5	(8.0)
75	83.5	8.5	(8.0)
80	85.9	6.1	(8.0)
85	89.4	2.6	(8.0)
90	90.9	1.1	(8.0)
95	89.1	2.9	(8.0)
100	84.3	7.7	(8.0)
105	86.6	5.6	(8.0)
110	89.0	3.0	(8.0)
115	84.9	7.1	(8.0)
120	77.5	14.5	(8.0)
125	78.6	13.4	(8.0)
130	82.8	9.2	(8.0)
135	81.1	10.9	(8.0)
140	79.4	12.6	(8.0)
145	78.4	13.6	(8.0)
150	78.0	14.0	(8.0)

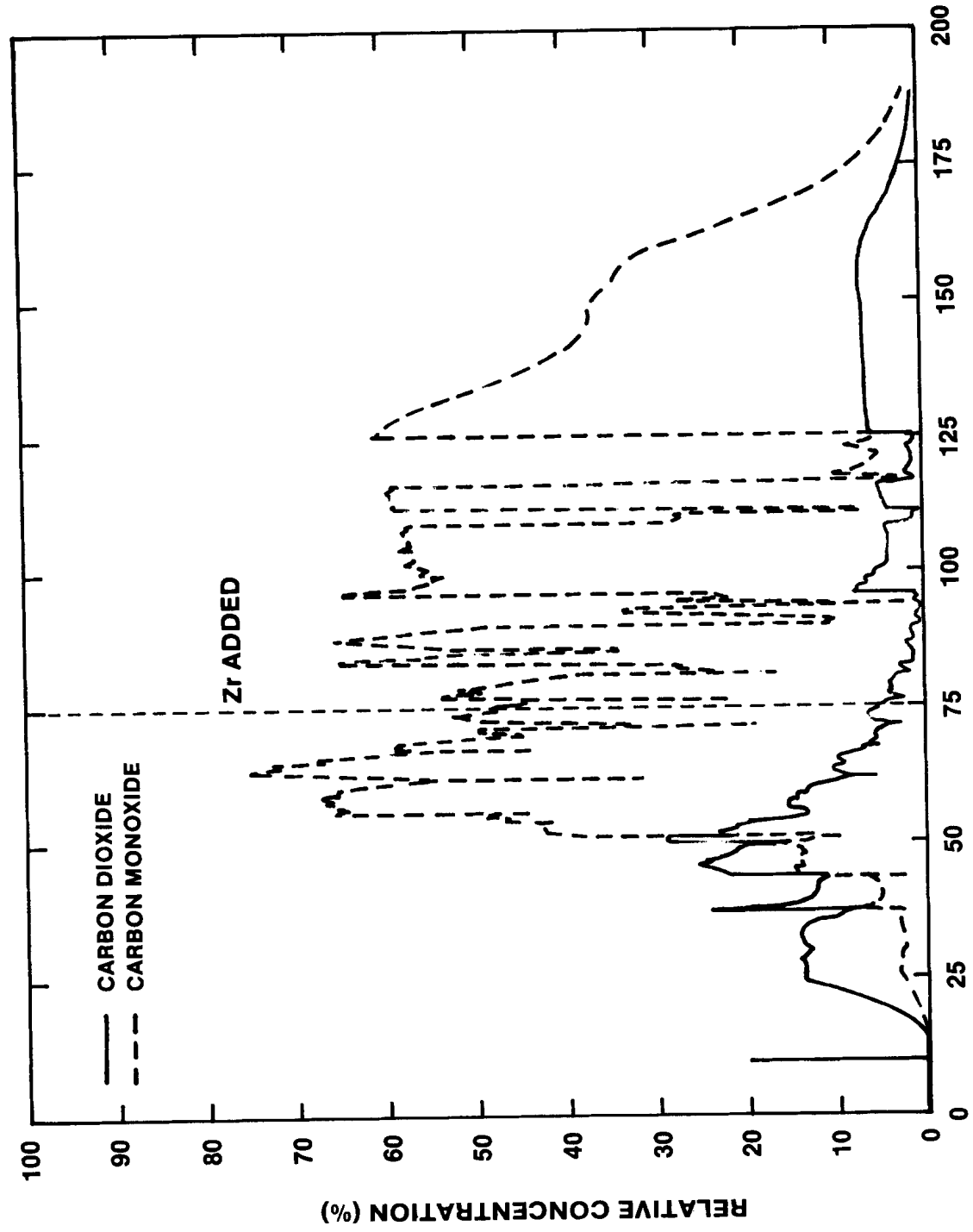

Figure 2.4.30 SURC-3A Gas Composition - CO/CO_2 Monitor

gas while including amounts for the H_2 and H_2O so that the CO/CO_2 monitor results can be compared to grab sample and mass spectrometer data.

The normalized data for the CO/CO_2 monitor indicates a CO concentration of 14-25% and a CO_2 concentration of 60-75% while the limestone concrete in SURC-3 is thermally decomposing prior to time 50. After time = 50 minutes, concrete attack begins and the CO concentration arises to 75 to 80% with a corresponding drop in CO_2 concentration to 10-20%. After the Zr metal is added to the pool at time 75, there is a slight rise in CO concentration from 85 to 90 percent and a decrease in CO_2 concentration from 8 percent to 1 percent. Steady-state values are reestablished after time 100 when the CO concentration goes back to 80-85 percent and the CO_2 concentration rises to 7-10 percent.

Raw data from the mass spectrometer are shown in Table 2.4.16. These data indicate the onset of concrete ablation between 22-45 minutes, steady-state erosion between 47-75 minutes, the additional effects of Zr addition to the meltpool between 81-111 minutes, and the return to steady-state erosion after time 126. Normalized data from the mass spectrometer for these time periods are shown in Table 2.4.17.

The data from the mass spectrometer indicate an initial concentration of 2 to 3% H_2 - 6% H_2O - 30 to 45% CO - 50 to 70% CO_2 at times 25-45 minutes. This changes to: 2 to 3% H_2 - 3 to 9% H_2O - 60 to 80% CO - 10 to 30% CO_2 during the steady-state erosion times before Zr addition. After Zr addition at time = 75 minutes, the CO and H_2 concentrations increased slightly with respect to H_2O and CO_2 resulting in a gas composition of 4% H_2 - 3 to 7% H_2O - 83% CO - 5 to 10% CO_2. The H_2/H_2O and CO/CO_2 ratios then go to a final steady-state concentration of 5 to 7% H_2 - 4 to 7% H_2O - 70 to 80% CO - 9 to 17% CO_2.

The grab sample results for SURC-3A are shown in Table 2.4.18. The background has for six of the seven samples included air as well as argon and helium in total amounts ranging from 50 - 90%. The normalized H_2 concentration (which also includes H_2 from H_2O vapor) during the test ranged from 2-20 percent with an average value of 11.7%. The normalized CO_2 concentration ranged from 4 to 12% after ablation began with an average value of 8.5% and the CO concentration ranged from 72-86% with an average value of 79.8%. Seven samples were taken in which no other gases besides H_2, O_2, CO, CO_2, N_2, Ar, and He were detected.

TABLE 2.4.16

SURC-3A Gas Composition [Mass Spectrometer - Raw Data]

VOLUME PERCENT

TIME (min)	H_2	He	H_2O	CO	Ar	CO_2	REMARKS
22	.3			3.8	87.0	8.9	
25	.3			4.8	83.0	11.9	
30				11.2	76.4	12.4	~900 slug
39				36.5	52.2	11.3	filters plugged
42			16.5	45.0	24.8	13.6	backflushing
45	1.1		2.8	19.0	55.8	21.4	grab #1 6-4
47	1.4	1.8	7.2	31.9	36.2	21.4	
52	1.4	2.2	3.5	37.8	34.7	20.5	grab #2 6-3
57	1.0	4.2	2.6	54.5	21.7	16.0	
63	1.3	5.6	1.5	50.6	30.9	10.1	grab #3 5-4
64	1.3	4.3	2.1	57.9	25.0	9.5	
67	1.6	4.1	8.2	63.3	12.2	10.6	
72	1.2	7.4	3.0	45.9	34.8	7.8	time 75:Zr drop
78	1.6		4.1	47.2	41.0	6.1	grab #4 5-3
81	1.1	10.1	2.7	24.1	59.0	3.1	
85	2.4	5.0	4.0	46.0	40.0	2.6	
88	2.0		10.2	66.0	15.2	6.6	
91*			15.8	79.1		5.1	filters plugged
94*			26.1	65.4		8.5	~0 gas flow
97	1.9	6.1	1.4	45.2	38.9	6.5	gravel samples
100	3.1	6.5	1.2	46.7	37.5	5.0	
103	3.9	3.4	2.7	53.1	32.0	4.9	grab #5 5-2
111	5.1	3.9	3.1	55.6	26.3	6.1	grab #6 4-4 from normal line
126	5.3	4.0	3.2	58.2	21.8	7.4	
130	5.2	3.9	3.1	52.7	26.8	8.3	
134	4.3	3.7	3.0	46.4	35.2	7.4	
139	3.2	3.9	3.1	40.5	42.1	7.2	
142	3.2	3.9	3.1	40.1	41.7	8.1	grab #7 4-3
146	3.1	7.5	3.0	38.9	40.3	7.4	
147	2.6	7.8	3.1	35.8	42.0	8.7	power off
150	2.7	8.2	3.3	33.6	44.2	8.1	
162	2.0	8.5	3.4	26.4	51.9	7.8	
183	.8	10.2	4.1	41.7	40.7	2.6	
193		10.1	4.0	36.4	47.5	1.9	* data not used

TABLE 2.4.17

SURC-3A Gas Composition
Normalized Mass Spectrometer Data

Time (min)	% H_2	% H_2O	% CO	% CO_2
25	2.3	---	29.2	68.5
30	---	---	47.5	52.5
45	2.5	6.3	43.0	48.2
52	2.2	5.5	59.9	32.5
63	2.0	2.3	79.7	15.9
72	2.1	5.2	79.4	13.5
81	3.6	8.7	78.0	10.0
85	4.4	7.3	83.6	4.7
97	3.5	2.5	82.2	11.8
111	7.3	4.4	79.6	8.7
126	7.1	4.3	78.4	10.0
139	5.9	5.7	75.0	13.3
150	5.7	6.9	70.6	17.0

TABLE 2.4.18

SURC-3A Gas Composition
Grab Samples

Volume Percent - Raw Data

TIME	#	H2	He	N2	O2	Ar	CO	CO2	CO/CO2
45	6-4	4.02	4.76	37.03	10.14	25.47	7.87	10.71	.73
52	6-3	4.72	10.45	0.76	0.33	18.06	58.81	6.87	8.56
63	5-4	3.36	8.68	15.37	3.72	26.52	37.55	4.80	7.82
78	5-3	5.22	7.91	29.69	7.78	17.32	30.15	1.93	15.62
103	5-2	7.84	7.94	35.73	8.98	10.80	27.22	1.49	18.27
111	4-4	2.80	3.97	44.81	12.14	24.03	10.84	1.36	7.97
142	4-3	.15	.40	69.52	18.98	4.51	5.64	.80	7.05

Volume Percent - Normalized

TIME	H_2	CO	CO_2
45	17.8	34.8	47.4
52	6.7	83.5	9.8
63	7.4	82.1	10.5
78	14.	80.8	5.2
103	21.5	74.5	4.1
111	12.	72.0	9.0
142	2.3	85.8	12.2

A total of 750 standard liters of gas were collected by the gas analysis system. An average of 50% or 370 standard liters of the total gas collected was either H_2, CO, H_2O, or CO_2. It should be noted that a significant fraction of the concrete reaction gas collected (up to 10%) was undoubtedly a result of thermal decomposition of limestone concrete above the meltpool. As indicated by early time test results, this tends to enrich the effluent gas in CO_2 and H_2O thus decreasing the CO/CO_2 and H_2/H_2O ratios to values lower than would be measured if the total gas collected were from steel-Zr-concrete interactions alone.

2.4.10 Data Summary and Conclusions

The SURC-3A experiment used 50 kg of stainless steel and 5 kg of Zr metal as the charge materials. This test was designed to examine not only the additional effects of zirconium metal inclusion to molten steel interacting with limestone concrete, but also the relative rates of radial as well as axial erosion when Zr is a meltpool constituent. The primary goals for SURC-3A were to measure the gas evolution, aerosol generation and erosion characteristics associated with two-dimensional steel-zirconium-concrete interactions in order to provide validation data for chemistry models in the CORCON core-concrete interaction code.

The SURC-3A test article was similar to the SURC-3 test in design and dimensions and similar to the QT-E test in mateials configuration. The crucible was made entirely from limestone concrete and was 40 cm in diameter and 90 cm high. The meltpool cavity was 20 cm in diameter and 50 cm high, leaving 10 cm thick sidewalls and a basemat of 40 cm. An additional one meter refractory spacer was bolted to the interaction crucible in series with a 2 meter instrumentation tower. This provided a sealed expansion volume of 10 cubic feet for reaction effluents. A 280 kW induction power supply and coil were used to heat and melt the 50 kg stainless steel charge within the test article and to sustain the interaction for the duration of the experiment. Additionally, 5 kg of fission product simulants were added to the melt to study fission product release. Flow rates of generated gases were measured using a sharp edge concentric orifice, a laminar flow device, a turbine meter and two dry gas clocks. Gaseous effluents produced during SURC-3A were monitored and sampled using an infrared CO/CO_2 gas analyzer, a mass spectrometer and an integral grab sampling technique. Aerosols were captured on filters, cascade impactors and a cascade cyclone. Erosion characteristics and meltpool temperatures were recorded using type K, S and C thermocouples in over twenty separate arrays. The SURC-3A apparatus was sealed and purged with helium and argon gases in order to direct the majority of reaction gas and aerosol effluents through a 5 cm diameter flow pipe. The test was run at local atmospheric pressure (.83 atm) and at an ambient temperature of 20°C.

The SURC-3A test ran for a total of 148 minutes. During the molten interaction phase of the experiment, a net power of 32±3 kW was applied to the 50 kg slug. After 40 kg of slug material became molten and approximately 4 cm of axial and 2 cm of radial erosion were indicated, 2.2 kg of Zr metal was added to the meltpool. This was followed by additional erosion of 25 cm in the axial direction and 9 cm in the radial direction during the final 75 minutes of the test.

Four time periods were of particular interest during the test. These are the onset of concrete ablation between 25-45 minutes, steady-state erosion between 45-75 minutes, the Zr metal addition and ensuing reaction between 75-100 minutes and the return to steady-state erosion from 100-150 minutes.

During the initial heatup period between 25 and 45 minutes, the temperature of the stainless steel charge increased from 950 K to 1700 K and became molten. The concrete basemat began to dehydrate during this time producing a reaction gas flow rate ranging from 0-50 slpm. The composition of this initial effluent gas was 2 to 3% H_2 - 1 to 6% H_2O - 30 to 45% CO - 50 to 70% CO_2. Two aerosol samples were taken at the end of this period. These samples indicated an aerosol concentration ranging from 8-18 g/m^3.

After 45 minutes, concrete ablation began. This was followed by an increase in meltpool temperature from 1700 K to 1950 K and an increase in gas flow rate from 50 to 100 slpm. A total of 4 cm of limestone concrete was eroded in the axial direction as well as 2 cm in the radial direction during the ensuing 45-75 minute time period. Aerosol release was recorded throughout the steady erosion at levels of 6-19 g/m^3 and the flow rate ranged from 75 to 160 slpm. Meltpool temperatures increased from an initial value of 1950 K to a peak of 2030 K at 69 minutes, then dropped to near 1900 K at 75 minutes just prior to the time of Zr addition. The typical composition of gas during this time frame was 2 to 3% H_2 - 3 to 9% H_2O - 60 to 80% CO - 10 to 30% CO_2.

At time = 75 minutes the Zr metal was added to the meltpool. A total of 2.2 kg of Zr became mixed with 40 kg of stainless steel resulting in a mixture of 95 w/o steel - 5 w/o zirconium. A vigorous oxidation reaction consumed the zirconium metal during the next 20-30 minutes. This reaction was marked by an increase in temperature, flow rate and carbon monoxide production. The meltpool temperature increased from 1900 K to a peak value of 2120 K shortly after the Zr metal addition, then decreased to values ranging from 1950 K to 2000 K. Flow rate increased dramatically to 200-250 slpm and the carbon monoxide content of the effluent rose slightly resulting in a gas composition which was 4% H_2 - 3 to 7% H_2O - 83% CO - 5 to 10% CO_2. The aerosol concentration was measured at 10-18 g/m^3 during this time frame which, when coupled to the flow rate, resulted in mass production rates two to three times greater than those measured earlier in the test.

At times after 100 minutes the melt-concrete reaction rates returned to values comparable to those seen prior to the zirconium oxidation phase. The meltpool temperatures remained near 1900 K for times between 100 and 150 minutes. The effluent flow rate ranged from 110 to 160 slpm and had a typical composition of 5 to 7% H_2 - 4 to 7% H_2O - 70 to 80% CO - 9 to 17% CO_2. The aerosol source term was measured twice during the final 50 minutes of the test and was found to have an average density of 7-8 g/m^3.

A total of 25 to 30 cm of limestone concrete were ablated in the axial direction and 2-9 cm in the radial direction during the test. The major observations gleaned from this information and from the rest of the SURC-3A data are that both axial and radial erosion increase during the zirconium interaction phase and that carbon monoxide was produced continuously throughout the test. These results are conclusive proof that significant increases in gas production, aerosol generation and concrete ablation do occur when zirconium metal is present in the melt. The SURC-3A test was also marked by high gas generation rates, prolific aerosol mass source terms and a highly assymmetric erosion profile. All of these features can generally be attributed to the inclusion of radial concrete decomposition with axial decomposition to yield total ablation. In addition to these observations, the SURC-3A data can be used for supplemental code validation efforts in the areas of heat transfer, aerosol production and gas chemistry.

3. COMPARISON AND SUMMARY OF RESULTS

The SURC-3 test series used 10-50 kg of 304 stainless steel combined with up to 20 w/o Zr metal as reactor core simulant materials. They were designed to be both qualitative and quantitative tests for the specific purpose of examining the comprehensive effects of zirconium metal addition to molten steel interacting with highly calcareous concrete. The goals of the experiments were to measure in detail the gas evolution, aerosol generation and erosion characteristics associated with steel-zirconium-concrete interactions.

Four tests were included in the SURC-3 series. The first two, QT-D and QT-E, were partially instrumented tests performed in open crucibles using limestone-common sand concrete as the basemat material. The final two experiments, SURC-3 and SURC-3A, were fully instrumented tests performed in closed crucibles using limestone concrete as the basemat. Together, QT-D, QT-E,1 SURC-3 and SURC-3A provide comprehensive, redundant and well-characterized information which is well suited for code validation efforts.

3.1 QT-D

The QT-D experiment ablated 12-15 cm of concrete axially during 50 minutes of interaction on limestone-common sand concrete using a 10 kg charge of 304 stainless steel to which 2kg of zirconium metal was added subsequent to the onset of erosion.

This test was the first of its kind ever attempted. Up until the execution of QT-D, no data existed pertaining strictly to Zr-core debris-concrete interactions and there was some doubt as to whether or not an effect would be seen. The primary purpose for QT-D was first to determine if a significant difference between steel-concrete interactions and steel-Zr-concrete interactions existed, and to determine if the difference lasted long enough to allow gas, aerosol and temperature measurements to be taken.

Two secondary goals were also set for QT-D. One of these was to test a new measurement technique for obtaining meltpool temperatures. This technique utilizes multiple C-type or S-type thermocouples set in an alumina sheath and cast into the concrete substrate. The stainless steel melt is expected to erode the concrete substrate but not the alumina sheathed thermocouples, thus allowing them to penetrate into the meltpool from below. By using S-type thermocouples, continuous pool temperature measurements could be taken up to 1760°C and C-type thermocouples could potentially measure pool temperatures as high as 2200°C. Another secondary goal of the QT-D tet was to measure the composition of effluents coming from Zr-concrete interactions. Large amounts of CO and CO_2 were expected to be produced.

The QT-D test article (Figure 2.1.1) was a right circular cylinder consisting of an MgO (K/R cast-98 MgO castible) annulus with a limestone common-sand concrete slug poured into the base of the annulus. The overall height of the test article was 40 cm. The MgO walls were 5 cm thick, leaving an inside cavity diameter of 20 cm. The limestone-common sand concrete plug filled the bottom 30 cm of the annulus. The stainless steel meltpool material was a solid cylinder of 304 stainless 10 cm in diameter and 15 cm in thickness. Zirconium metal was added to the meltpool in the form of right circular cylinders. Six cylinders, each with a diamter of 3.3 cm and a length of 6 cm were used. The total weight of Zr metal was 2.0 kg.

Based on the thermocouple data, on visual observations and on the posttest observations, the addition of Zr metal to molten steel interacting with concrete definitely results in a significant reaction. The measured ablation rate in QT-D increased from 12 cm/hr to 100 cm/hr after Zr metal was added and large amounts of flammable gas with entrained aerosols were observed. This reaction was contained by the MgO crucible and lasted at least ten minutes, indicating that comprehensive gas, aerosol and temperature measurements would be feasible in future tests. The meltpool temperature measurement technique was successful in obtaining consistent values ranging from 1993 K to 2124 K over a period of twelve minutes with each of the four C-type thermocouples registering the maximum pool temperature value for at least 20 seconds. Finally, attempts to measure gas composition in QT-D were successful. Carbon monoxide was measured at 43% during the period that molten steel was eroding the limestone common sand concrete basemat. At the time of Zr addition, the subsequent reaction caused oxidic crusts to quickly rise and block or plug the gas sampling tube. Subsequent attempts to measure the gas effluent would include a protected gas sampling port and an inert gas purge.

3.2 QT-E

The QT-E experiment was also designed as a scoping test to prepare for the SURC-3 experiments. It was executed for two reasons: (1) to obtain information on a larger scale than the QT-E experiment and (2) to determine the extent and nature of the steel-zirconium-concrete reaction when the crucible was cast entirely with concrete. The execution of QT-E resulted in the ablation of 10 cm of limestone-common sand concrete axially and 10 cm radially during 35 minutes of sustained interaction using 50 kg of stainless steel and 10 kg of zirconium as the melted constituents.

The QT-E test used a 50 kg slug of steel and 10 kg of Zr metal as the charge material. This represented a factor of five increase in melt mass over the QT-D experiment, which utilized 10 kg of steel and 2 kg of Zr metal. The geometry in QT-E was meant to be as nearly identical to the SURC-3 geometry as was practicable so

as to obtain enough information to finalize the instrumentation strategies for the SURC-3 test and subsequent experiments. In addition, the QT-E experiment was performed in a crucible cast entirely from limestone-common sand concrete instead of the concrete-filled MgO annulus used in QT-D. This would allow us to discern whether or not MgO was a major contributor to the vigorous reaction observed in QT-D and also to measure two-dimensional erosion patterns which result from the steel-zirconium-concrete interaction.

Posttest analysis of the QT-E crucible indicated that there was a considerable amount of radial erosion during the experiment which ultimately resulted in the failure of the crucible sidewalls. A substantial amount of axial erosion was also indicated. The thermocouple data showed that the axial and radial erosion rates both increased significantly when the Zr reaction was in progress. The axial rate was seen to increase from 6 cm/hr to 24 cm/hr and the radial rate increased from 9 cm/hr to 36 cm/hr. Significant amounts of gas and aerosol were released during the Zr/concrete reaction which lasted 9 - 10 minutes from onset until the crucible walls failed. The gas effluent was composed of > 50% CO with < 20% CO_2 before the Zr reaction and just at the onset of the reaction before the gas sampling ports plugged. Here plugging occurred despite the fact that the sample lines were located well above (20 cm) the surface of the meltpool.

Results from the QT tests (QT-D and QT-E) both suggest that a lower amount of Zr metal should be added to the melt in SURC-3 and SURC-3A tests. The SURC test procedure was amended to allow for 5 kg of Zr metal to be added to a 50 kg steel meltpool rather than 10 kg as was done in QT-E. In addition, the SURC-3A test was constructed entirely with limestone concrete similar to the QT-E test but with significantly thicker (15 cm vs 10 cm) sidewalls. Gas composition and flow sampling ports in the SURC tests included a larger standoff distance as well as an aerosol filter.

3.3 SURC-3

The SURC-3 experiment used 45 kg of 304 stainless steel and 5 kg of Zr metal as reactor core simulant materials. It was designed to be a comprehensive test examining the additional effects of zirconium metal addition to molten steel interacting with limestone concrete. The goals of the experiment were to measure in detail the gas evaluation, aerosol generation and erosion characteristics associated with steel-zirconium-concrete interactions.

The SURC-3 experiment was conducted in a 40 cm diameter interaction crucible constructed with a 20 cm diameter limestone concrete cylinder in the base of a magnesium oxide (MgO) annulus. An additional 1 meter ceramic spacer and 2 meter instrumentation tower were bolted to the top of the interaction crucible in order

to provide a sealed expansion volume of 10 cubic feet for reaction effluents. A 280 kW induction power supply and coil were used to heat and melt the 45 kg stainless steel charge within the test article and to sustain the interaction for the duration of the experiment. Additionally, 5 kg of fission product simulants were added to the melt to study fission product release. Flow rates of generated gases were measured using a sharp edge concentric orifice, a laminar flow device, a turbine meter and two dry gas clocks. Gaseous effluents produced during the experiment were monitored and sampled using an infrared gas analyzer, mass spectrometer and by an integral grab sample technique, aerosols were captured on filters, cascade impactors, and a cascade cyclone. Erosion characteristics were measured using type K, S and C thermocouples in order to define the meltpool temperature and overall heat balance as well as the axial erosion rate. The SURC-3 apparatus was sealed and purged with argon gas in order to direct the majority of the reaction gas and aerosol effluents through a 5 cm diameter flow pipe. The test was run at atmospheric pressure (.83 atm) and at an ambient temperature of 18°C.

The SURC-3 test ran for a total of 200 minutes. During this time an average power of 28±3 kW was applied to the 45 kg slug. After the slug became molten and 6-8 cm of concrete had been eroded, 1.1 kg of zirconium metal was added to the melt followed by the erosion of an additional 25 cm of limestone concrete in the final 80 minutes of the test.

Four time periods during the test are of particular interest. These are the onset of gas release from the concrete between 50 and 90 minutes, steady concrete erosion due to molten concrete attack between 90 and 130 minutes, the increased attack due to Zr addition to the melt during the 135-150 minute timeframe and a return to steady concrete erosion for the remainder of the test.

During the initial heatup period between 50 and 90 minutes, the temperature of the steel charge increased from 800 K to 1700 K and became molten. The concrete basemat started to dehydrate during this time at an average rate of 8 cm/hr producing a reaction gas flow rate of 10 slpm. The composition of this initial effluent gas was 6% H_2 - 79% CO - 15% CO_2. No aerosol samples were taken during this period and the opacity meter did not register an aerosol concentration greater than 10 g/m^3.

Concrete erosion began after 90 minutes. This was accompanied by an increase in average meltpool temperature from 1700 K to 1950 K. Aerosol release was indicated by the photometer immediately after the onset of ablation at an average density of 25 g/m^3. Molten steel-concrete attack proceeded at an average rate of 14 cm/hr until the Zr metal was added at 133 minutes. The gas release rate during this period ranged from 25 to 75 slpm and had a typical composition of 2.5% H_2 - 87% CO - 10% CO_2.

At time = 133 minutes, the Zr metal was added to the meltpool. A total of 1.1 kg of Zr became mixed with the 45 kg of 304 stainless steel resulting in a mixture of 98 w/o steel - 2 w/o zirconium. A vigorous oxidation reaction consumed the zirconium metal during the next 10-15 minutes. This reaction was marked by an increase in ablation, flow rate and carbon monoxide production. The ablation rate increased from 14 cm/hr to 27 cm/hr during the zirconium oxidation phase and the effluent gas flow rate increased from 50 slpm to 100 slpm. The effluent was rich in carbon monoxide throughout the oxidation phase and had a typical composition of 2% H_2 - 94% CO - 3% CO_2. The meltpool temperature was 1900 K just prior to the Zr addition, increased to 2020 K during the interaction period and was 1950 K at the end of the oxidation phase. Aerosols produced during this time period had an average concentrastion of 12 g/m^3.

At times after 150 minutes the melt-concrete reaction rates returned to values comparable to those seen prior to the zirconium oxidation phase. The meltpool temperatures remained near 1950 K for times between 150 minutes and 200 minutes. The effluent flow rate averaged 25 slpm and had a typical composition of 5% H_2 - 84% CO - 11% CO_2. Ablation of the concrete proceeded at 14 cm/hr during this timeframe and the aerosol source term was measured at 10 g/m^3.

Two important conclusions can be drawn from the SURC-3 data with regards to the effects of zirconium metal reactions during severe reactor accidents. First and most obvious is the fact that significant increases in gas production, aerosol generation and concrete ablation do occur even at relatively low (2%) percentages of zirconium metal content. Second, that these reactions cannot be described correctly using the "coking" gas phase reaction model since a complete reduction of CO_2 does not occur. In addition to these observations, the SURC-3 data is well suited for code validation effort in the areas of core-concrete heat transfer, aerosol production and flammable gas concentration.

3.4 SURC-3A

The SURC-3A experiment used 50 kg of stainless steel and 5 kg of Zr metal as the charge materials. This test was designed to examine not only the additional effects of zirconium metal inclusion to molten steel interacting with limestone concrete, but also the radial erosion effects as well as the axial erosion rate when Zr is a meltpool constituent. The primary goals for SURC-3A were to measure the gas evolution, aerosol generation and erosion characteristics associated with two-dimensional steel-zirconium-concrete interactions in order to provide validation data for chemistry models in the CORCON core-concrete interaction code.

The SURC-3A test article was similar to the SURC-3 test in design and dimensions and similar to the QT-E test in materials configuration. The crucible was made entirely from limestone concrete and was 40 cm in diameter and 90 cm high. The meltpool cavity was 20 cm in diameter and 50 cm high, leaving 10 cm thick sidewalls and a basemat of 40 cm. An additional one meter refractory spacer was bolted to the interaction crucible in series with a 2 meter instrumentation tower. This provided a sealed expansion volume of 10 cubic feet for reaction effluents. A 280 kW induction power supply and coil were used to heat and melt the 50 kg stainless steel charge within the test article and to sustain the interaction for the duration of the experiment. Additionally, 5 kg of fission product simulants were added to the melt to study fission product release. Flow rates of generated gases were measured using a sharp edge concentric orifice, a laminar flow device, a turbine meter and two dry gas clocks. Gaseous effluents produced during SURC-3A were monitored and sampled using an infrared CO/CO_2 gas analyzer, a mass spectrometer and an integral grab sampling technique. Aerosols were captured on filters, cascade impactors and a cascade cyclone. Erosion characteristics and meltpool temperatures were recorded using type K, S and C thermocouples in over twenty separate arrays. The SURC-3A apparatus was sealed and purged with helium and argon gases in order to direct the majority of reaction gas and aerosol effluents through a 5 cm diameter flow pipe. The test was run at local atmospheric pressure (.83 atm) and at an ambient temperature of 20°C.

The SURC-3A test ran for a total of 148 minutes. During the molten interaction phase of the experiment, a net power of 32±3 kW was applied to the 50 kg slug. After 40 kg of slug material became molten and approximately 4 cm of axial and 2 cm of radial erosion were indicated, 2.2 kg of Zr metal was added to the meltpool. This was followed by additional erosion of 25 cm in the axial direction and 9 cm in the radial direction during the final 75 minutes of the test.

Four time periods were of particular interest during the test. These are the onset of concrete ablation between 25-45 minutes, steady-state erosion between 45-75 minutes, the Zr metal addition and ensuing reaction between 75-100 minutes and the return to steady-state erosion from 100-150 minutes.

During the initial heatup period between 25 and 45 minutes, the temperature of the stainless steel charge increased from 950 K to 1700 K and became molten. The concrete basemat began to dehydrate during this time producing a reaction gas flow rate ranging from 0-50 slpm. The composition of this initial effluent gas was 2 to 3% H_2 - 1 to 6% H_2O - 30 to 45% CO - 50 to 70% CO_2. Two aerosol samples were taken at the end of this period. These samples indicated an aerosol concentration ranging from 8-18 g/m^3.

After 45 minutes, concrete ablation began. This was marked by an increase in meltpool temperature from 1700 K to 1950 K and an increase in gas flow rate from 50 to 100 slpm. A total of 4 cm of limestone concrete was eroded in the axial direction as well as 2 cm in the radial direction during the ensuing 45-75 minute time period. Aerosol release was recorded throughout the steady erosion at levels of 6-19 g/m^3 and the flow rate ranged from 75 to 160 slpm. Meltpool temperatures increased from an initial value of 1950 K to a peak of 2030 K at 69 minutes, then dropped to near 1900 K at 75 minutes just prior to the time of Zr addition. The typical composition of gas during this time frame was 2 to 3% H_2 - 3 to 9% H_2O - 60 to 80% CO - 10 to 30% CO_2.

At time = 75 minutes the Zr metal was added to the meltpool. A total of 2.2 kg of Zr became mixed with 40 kg of stainless steel resulting in a mixture of 95 w/o steel - 5 w/o zirconium. A vigorous oxidation reaction consumed the zirconium metal during the next 20-30 minutes. This reaction was marked by an increase in temperature, flow rate and carbon monoxide production. The meltpool temperature increased from 1900 K to a peak value of 2120 K shortly after the Zr metal addition, then decreased to values ranging from 1950 K to 2000 K. Flow rate increased dramatically to 200-250 slpm and the carbon monoxide content of the effluent rose slightly resulting in a gas composition which was 4% H_2 - 3 to 7% H_2O - 83% CO - 5 to 10% CO_2. The aerosol concentration was measured at 10-18 g/m^3 during this time frame which, when coupled to the flow rate, resulted in mass production rates two to three times greater than those measured earlier in the test.

At times after 100 minutes the melt-concrete reaction rates returned to values comparable to those seen prior to the zirconium oxidation phase. The meltpool temperatures remained near 1900 K for times between 100 and 150 minutes. The effluent flow rate ranged from 110 to 160 slpm and had a typical composition of 5 to 7% H_2 - 4 to 7% H_2O - 70 to 80% CO - 9 to 17% CO_2. The aerosol source term was measured twice during the final 50 minutes of the test and was found to have an average density of 7-8 g/m^3.

A total of 25 to 30 cm of limestone concrete were ablated in the axial direction and 2-9 cm in the radial direction during the test. The major observations gleaned from this information and from the rest of the SURC-3A data are that both axial and radial erosion increase during the zirconium interaction phase and that carbon monoxide was produced continuously throughout the test. These results are conclusive proof that significant increases in gas production, aerosol generation and concrete ablation do occur when zirconium metal is present in the melt. The SURC-3A test was also marked by high gas generation rates, prolific aerosol mass source terms and a highly asymmetric erosion profile. All of these features can be attributed to the inclusion of radial concrete decomposition with axial decomposition to yield total

ablation. In addition to these observations, the SURC-3A data can be used for supplemental code validation efforts in the areas of heat transfer, aerosol production and gas chemistry.

3.5 Summary

Together, the results of QT-D, QT-E, SURC-3 and SURC-3A paint a consistent and clear picture describing the phenomena associated with Zr laden meltpools interacting with limestone-based concretes. A table summarizing these phenomena is shown in Table 3.1.

In all four tests the meltpool temperature, ablation rate and gas release rate increased when Zr metal was added to the core-concrete interaction. This is a strong indicator of the exothermic oxidation reactions taking place. In addition, the gas reaction products of these exothermic reactions contained increased amounts of carbon monoxide gas and decreased amounts of carbon dioxide. This is a strong indicator that at least part of the reaction is occurring between Zr metal and CO_2. Finally, there is a strong indication that a complete coking reaction between Zr and CO_2 does not occur since carbon monoxide is continuously produced in large quantities. In addition to these conclusions the data from the four tests are well suited for additional modeling and validation efforts in the areas of core concrete heat transfer, aerosol production and flammable gas production.

TABLE 3.1

Summarized Results from Zr-Steel Reactions with Limestone Concrete

	QT-D	QT-E	SURC-3	SURC-3A
Test Size and and Geometry	20cm dia 1D	40 cm dia 2D	40 cm dia 1D	40 cm dia 2D
Steel Mass	10 kg	50 kg	45 kg	40 kg
Zr Added	2 kg	10 kg	1.1 kg	2.2 kg
Total Erosion	18 cm	10 cm axial 10 cm radial	33 cm	25 cm axial 9 cm radial
Meltpool Temperature Before Zr Addition	2000 K	--	1950 K	1950 K
Meltpool Temperature After Zr Addition	2125 K	--	2020 K	2100 K
Ablation Rate(s) Before Zr Addition	12 cm/hr	6 cm/hr axial 9 cm/hr radial	14 cm/mr 14 cm/mr	8 cm/hr axial 4 cm/hr radial
Ablation Rate(s) After Zr Addition	100 cm/hr	24 cm/hr axial 36 cm/hr radial	27 cm/hr	20 cm/hr axial 6 cm/hr radial
Gas Release Rate Before Zr Addition	--	--	50 slpm	120 slpm
Gas Release Rate After Zr Addition	--	--	100 slpm	220 slpm
Aerosol Release Before Zr Addition	Moderate	Moderate	25 g/m^3 .02 g/sec	6-19 g/m^3 .02 g/sec
Aerosol Release After Zr Addition	Heavy	Heavy	12 g/m^3 .02 g/sec	10-15 g/m^3 .04 g/sec
Gas Composition Before Zr Addition	High CO	High CO Some CO_2	87% CO-10% CO_2 2.5% H_2	70% CO-20% CO_2 3% H_2-7%H_2O
Gas Composition After Zr Addition	--	--	94% CO-3% CO_2 2% H_2	83% CO-7% CO_2 4% H_2-6% H_2O

APPENDIX A

Calorimetric Test Data and Equations, Test SURC-3 and 3A

Experimental Apparatus

Data obtained in the calorimetric test of the induction power supply are shown in this appendix. Calorimetric tests were conducted to verify the calibration of the coil power transducer, on a well characterized stainless steel cylinder. A 50 kg cylinder of 304 stainless steel 20.3 cm in diameter and 19.6 cm high was used as the heat sink for the induction power. The cylinder was instrumented with type K thermocouples installed in the top of the cylinder at radial distances of 0.0, 2.5, 5.1, and 8.9 cm from the axis and approximately 7.6 cm deep. The outputs of the thermocouples were recorded on a data acquisition system. The uninsulated, instrumented cylinder was placed into a crucible cast of MgO having the same radial dimensions as the test article used in the SURC-3 and 3A tests. The induction coil was placed around the MgO crucible and vertically centered with respect to the stainless steel cylinder.

Energy Based on Calorimetry Calculations

Two calibration tests were performed at nominal input powers of 155 and 165 kW, based on power meter readings on the control console of the power supply. The outputs of the power transducer connected to the buss bars and the thermocouple were connected to a Hewlett-Packard HP-1000 data acquisition system for collection and posttest plotting and analysis.

The calorimeter test was initiated by starting the data acquisition system, establishing baseline data for the power supply and recording the initial stainless cylinder temperature. After taking a few seconds of baseline data, the induction power supply was started and a constant input power was applied to the stainless steel cylinder. For the initial test the input power was 155 kW. The power supply was turned off when the thermocouple closest to the perimeter (radius = 8.9 cm) reached 1473 K. The cylinder heating profile for the various thermocouple locations is shown in Figure A-1. The cylinder does not heat uniformly. The perimeter heats more rapidly than the center. The power history transducer heating is shown in Figure A-2.

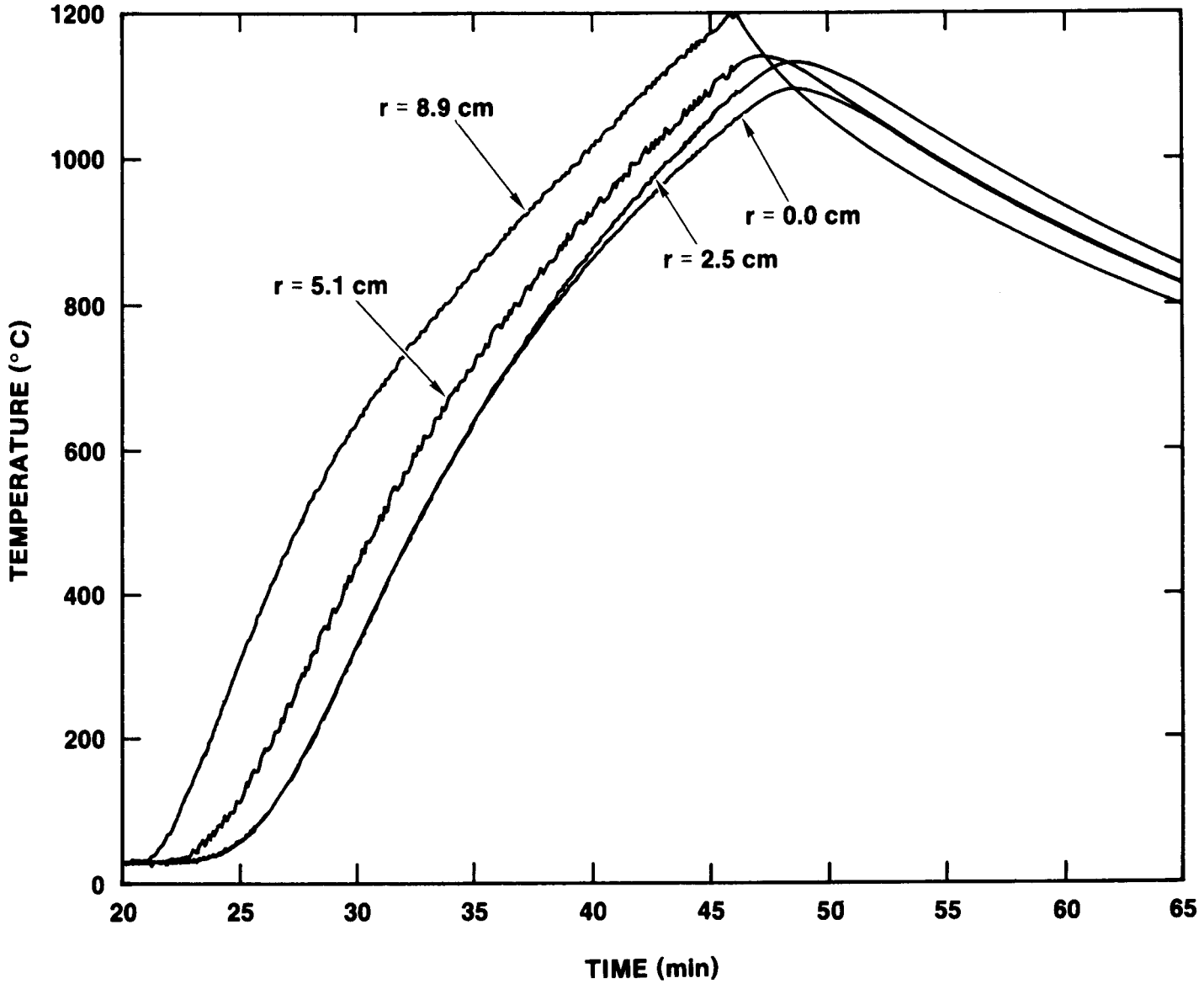

Figure A-1. Thermocouple Response vs. Time, Stainless Steel Cylinder, 155 kW Test

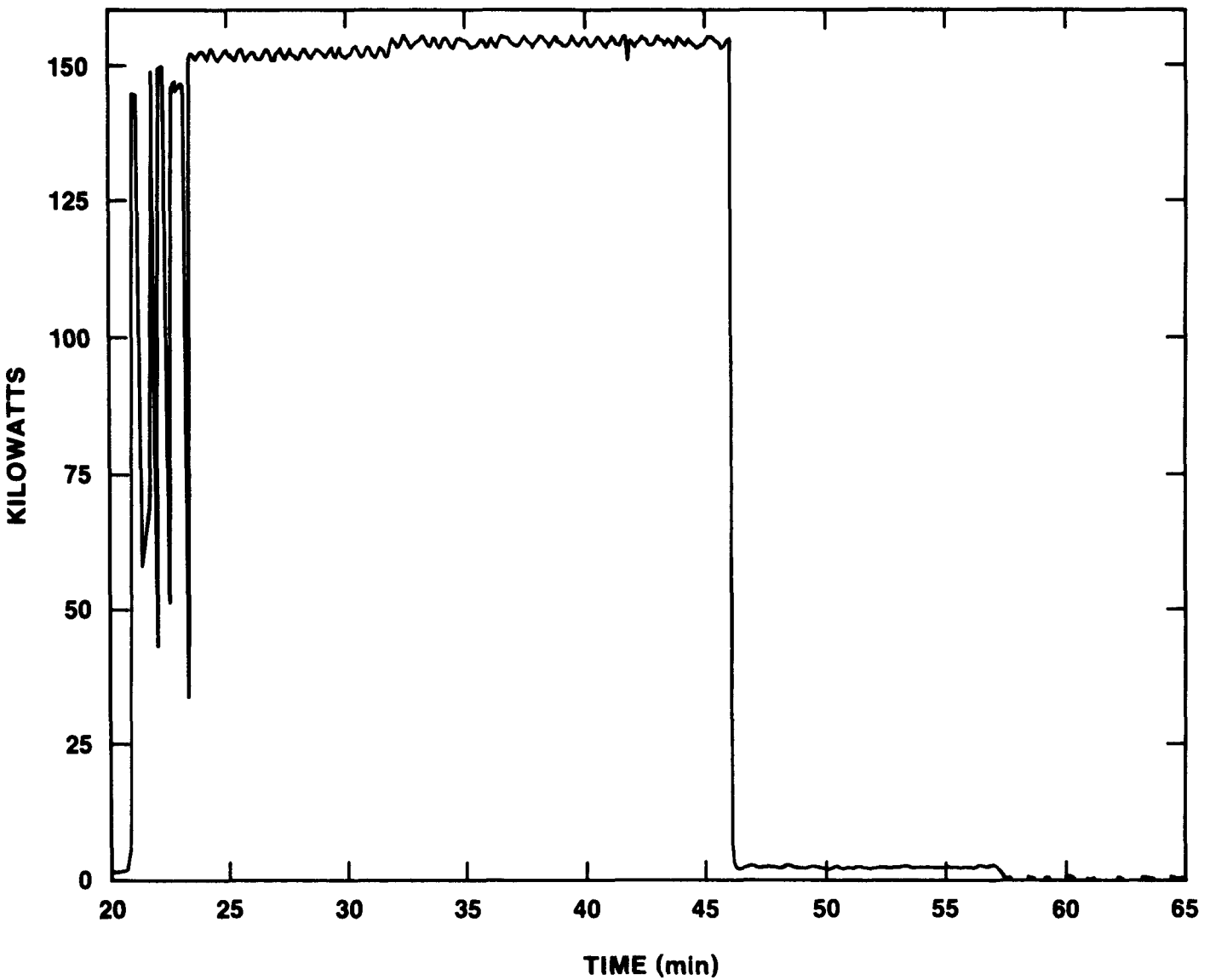

Figure A-2. Power vs. Time, 155 kW Calorimetric Test

The stainless steel slug was allowed to come to thermal equilibrium. This occurred 26.7 minutes after the power supply was started and the equilibrium temperature was measured to be 1409 K. The amount of energy deposited into the stainless steel cylinder for the heating period is given by:

$$E_s = m\ C_p\ (T_{eq} - T_I) \qquad \text{(A-1)}$$

where

E_s = energy deposited (MJ),
m = mass of stainless steel cylinder (kg),
C_p = specific heat Ref stainless (J/kg K),
T_{eq} = equilibrium temperature of cylinder (K), and
T_I = initial temperature of the cylinder (K).

Thermal properties for 304 stainless steel are listed in Table A-1. The value of specific heat was selected using the mean temperature $(T_{eq} - T_I)/2$ of the stainless steel cylinder during heatup phase. The value selected was 585 J/kg K. The initial temperature T_I was measured to be 309 K. Substituting into Equation (A-1) and solving yields a value of 32.2 MJ of energy deposited into the stainless steel.

TABLE A-1

Specific Heat(1) for 304L Stainless Steel

Temperature (K)	Specific Heat (J/kg K)
300	510.0
400	523.4
500	536.8
600	550.2
700	564.0
800	577.4
900	590.8
1000	604.2
1100	617.6
1200	631.4
1300	644.8
1400	658.1
1500	671.5
1600	685.3
1700(s)	698.7
1700(l) to 3000	795.0

(1) Choong S. Kim, Thermophysical Properties of Stainless Steels, Argon National Laboratories, Argon, IL 60439, Report ANL-75-55, September 1975.

For the calorimetric test to be accurate, thermal heat losses, even though small, had to be accounted for since the cylinder was not insulated. Figure F-1 also shows the cooling history of the stainless cylinder. The thermal energy lost during the 26.7 minute period required for the cylinder to reach thermal equilibrium is characterized by the slope of the temperature versus time curve after the point the equilibrium temperature was reached. The energy lost during this period is approximated by:

$$E_t = 1/2[m\ C_p\ (\Delta T/\Delta t)\ t_{eq}] \qquad \text{(A-2)}$$

where

E_t = cylinder thermal losses (J),
ΔT = temperature difference (K),
Δt = time difference (s), and
t_{eq} = time to reach temperature equilibrium (s).

The mass (m) of the stainless cylinder was defined in Equation (A-1) and the specific heat (C_p) here is taken at the equilibrium temperature of 1409 K and is 659 J/kg K. The slope of the cooling profile at the equilibrium temperature was measured to be 21.8 K/min. The time (t_{eq}) for the cylinder to reach an equilibrium temperature from the start of the power supply was measured to be 26.7 minutes. Substituting the appropriate values into equation A-2, and solving results in a total energy loss of 9.6 MJ over the period considered. Based on these calculations, the total energy input to the stainless steel cylinder was equal to the energy deposited E_s = 32.2 MJ (equation A-1) plus the energy lost E_t = 9.6 MJ, Equation (A-2) or 41.8 MJ. The deposited energy calculated from calorimetry will be used as the standard for comparison with the energy measured by the power transducer.

Energy Measured by the Power Transducer

The total energy measured at the buss bars by the power transducer is found by integrating the power curve shown in Figure F-2 and is mathematically represented by the equation shown below:

$$E_b = \int_{t_1}^{t_2} P\ dt \qquad \text{(A-3)}$$

where

E_b = energy measured at the buss bars and

$\int_{t_1}^{t_2} P\ dt$ = Area under the power versus time curve between the limits of t_1 and t_2 (J) (See Figure 2).

The total energy delivered to the coil was calculated to be 221.6 MJ.

The coupling efficiency of the system is defined by

$$\text{Efficiency} = E_s/E_b \times 100 \qquad \text{(A-4)}$$

where

Efficiency = coupling efficiency (%)
E_s = Energy deposited into the stainless cylinder (MJ)
E_b = Energy measured by the power transducer (MJ)

Substituting into Equation (A-4), for the 155 kW test the coupling efficiency is calculated to be 18.9%.

Temperature profiles for the stainless steel cylinder and corresponding input power profiles for the 165 kW calorimetry test are shown in Figures A-3 and A-4, respectively. Based on these results, the coupling efficiency for the 165 kW power level was calculated to be 21.4. The calculated coupling efficiency for the 155 and 165 kW tests are presented in Table A-2. The efficiencies range between 18.9 and 21.4 for input powers between 155 and 165 kW. The net power delivered to the stainless cylinder is taken to be the input power measured at the buss bars times the efficiency derived from the calorimetric tests.

TABLE A-2

System Coupling Efficiency

Method 1

Input Power Console Power Meter	Energy Measured at Buss Bars (MJ)	Energy Deposited in Stainless Cylinder (MJ)	Coupling Efficiency (%)
155	221.6	41.8	18.9
165	174.1	37.2	21.4

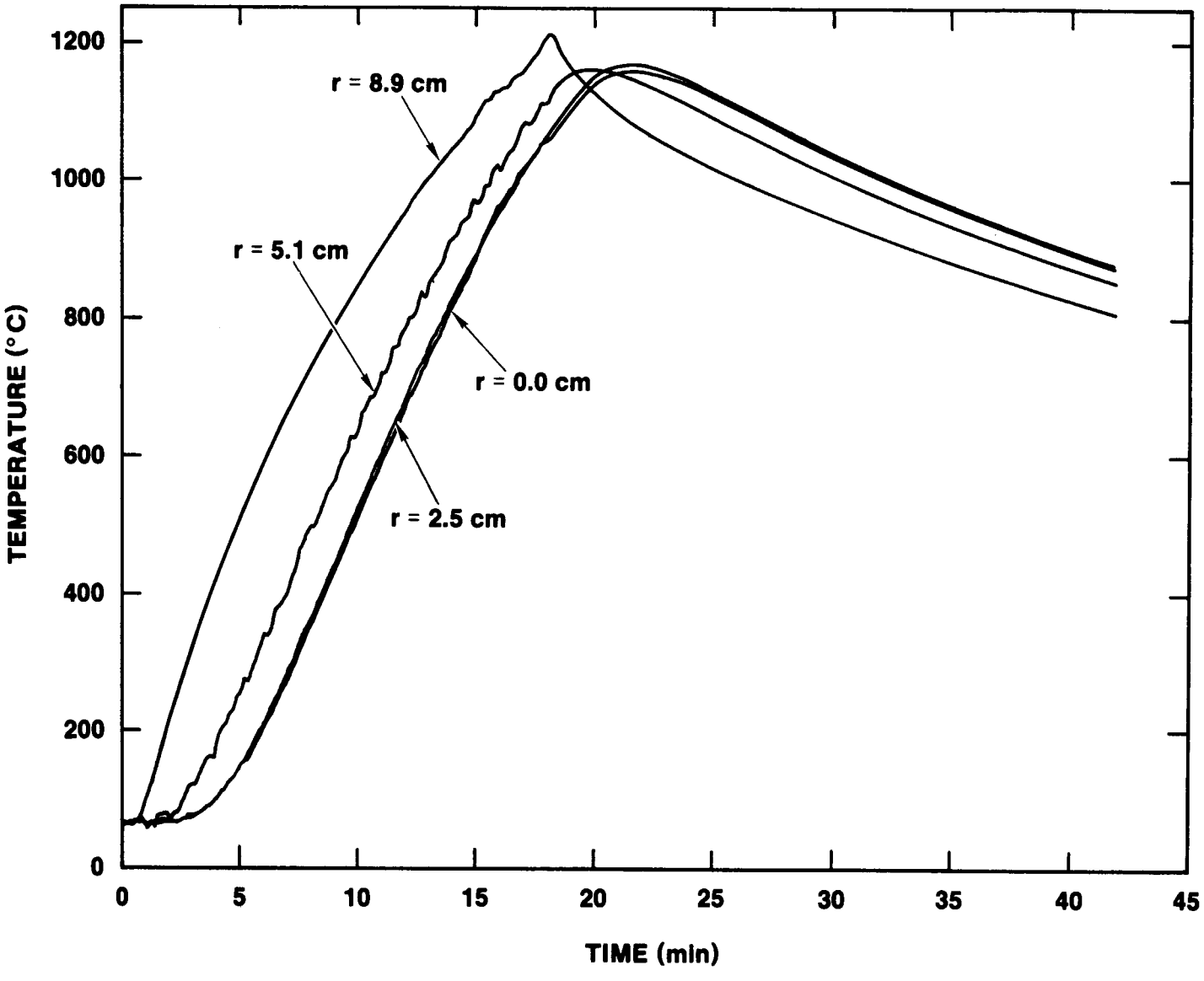

Figure A-3. Thermocouple Response vs. Time, 165 kW Test

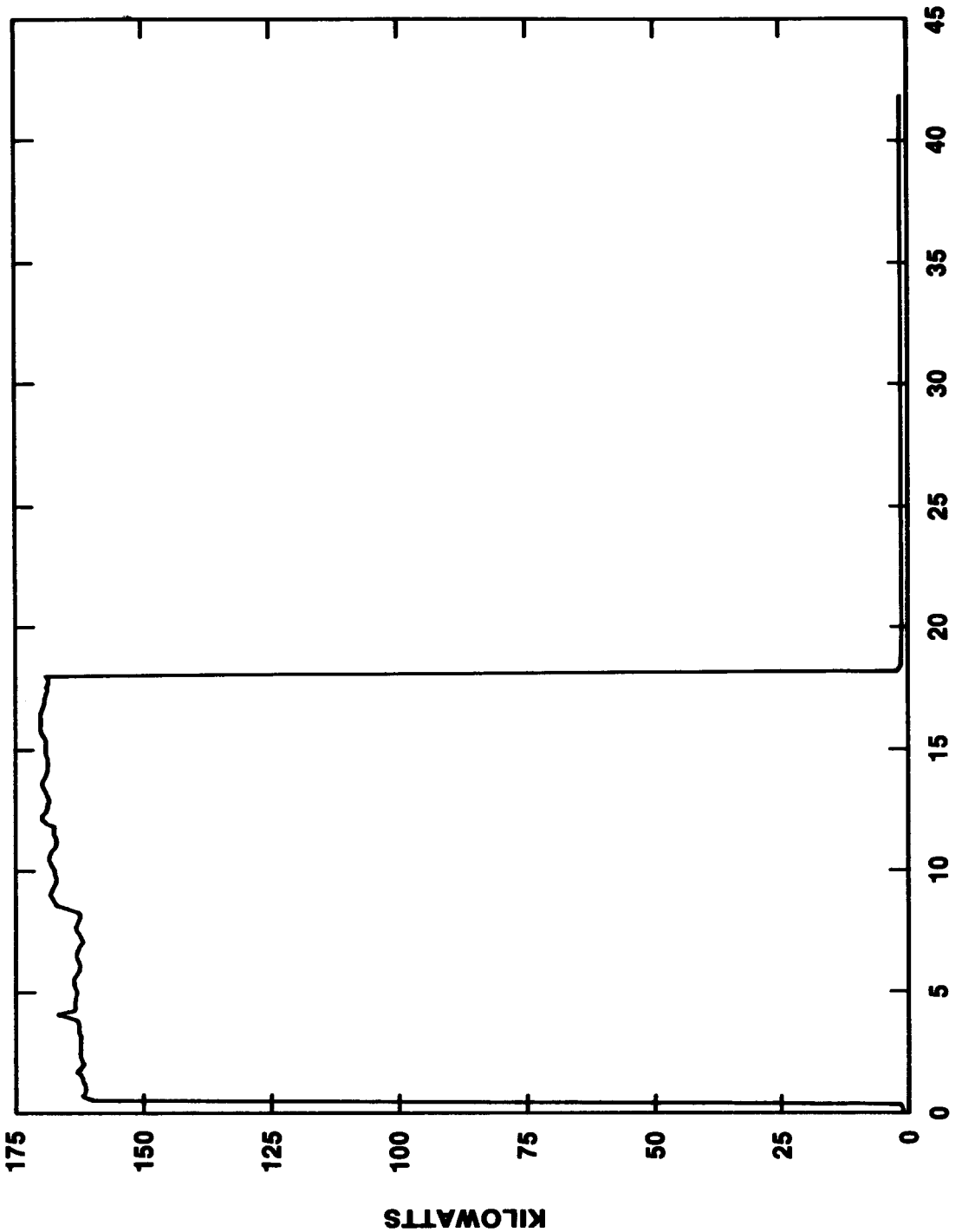

Figure A-4. Power vs. Time, 165 kW Calorimetric Test

Mass Segment Calorimetry Calculations

An alternate approach to the calculation of net power to the slug and coupling efficiency is to consider that the thermal response of the four thermocouples embedded in the slug can be used to characterize the rates of energy addition and loss for four segments of the slug. The center thermocouple is assumed to represent the interior segment from radius r = 0.0 to 1.25 cm; the thermocouple at 2.5 cm is assumed to represent the inner segment from r = 1.25 to 3.8 cm; the thermocouple at 5.1 cm is assumed to represent the outer segment from r = 5.1 to 7.0 cm; and the thermocouple at 8.9 cm is assumed to represent the perimeter segment from r = 7.0 to 10.2 cm. The masses of the four segments of the slug are 0.78, 6.25, 16.60 and 26.37 kg, respectively.

The rate of energy addition to each segment is determined from the slope of the thermocouple plots (see Figures A-1 and A-3) during the last 10 to 15 minutes of the heating period. The energy addition rate is calculated by

$$P_{add} = \sum_{i = 1,3} m_i \, c_{pi} \, (\Delta T/\Delta t)_i \qquad \text{(A-5)}$$

Where m_i is the mass of segment i, c_{pi} is the average specific heat of segment i during the time period, and $(\Delta T/\Delta t)_i$ are the slopes taken from the temperature plots.

Similarly, the rate of energy loss can be calculated from the slopes of the temperature plots during the cool down phase. Once the steel slug has reached thermal equilibrium, each segment of the slug cools at approximately the same rate. It is this rate that is used in the loss calculation. Here,

$$P_{loss} = M \, c_p \, (\Delta T/\Delta t) \qquad \text{(A-6)}$$

where m is the total mass of the slug, c_p is the specific heat evaluated at the equilibrium temperature, and $\Delta T/\Delta t$ is the slope taken from the thermocouple plot.

The total power input to the slug is the sum of P_{add} and P_{loss}. Comparing the total power input calculated in this manner to the power measured at the buss bar gives the efficiency of inductive coupling. The results calculated for the 155 kW and 165 kW power levels are shown in Table A-3.

Summary

Two different methods were used to calculate the coupling efficiency of the system on data produced from calorimetric tests. The energy method of determining the coupling efficiency resulted in a slightly higher value for efficiency

compared to the mass segment method. The average efficiency for the two power runs using the energy method averaged 20.2%. The average coupling efficiency calculated for the mass segment method was 19.2, slightly less than the energy method. Based on these independent calculations the efficiency was determined to be 20% with a calculated uncertainty of ± 2%.

TABLE A-3

System Coupling Efficiency

Method 2

Input Power Console Power Meter	Energy Addition Rate (kW)	Energy Loss Rate (kW)	Coupling Efficiency (%)
155	16.3	11.6	18.0
165	24.2	9.5	20.4

APPENDIX B

Thermistor Bridge Calibration Curve

The calibration of the millivolt signal from the thermistor bridge used to indicate the differential water temperature between inlet and outlet of the coil used in the QT test series is shown in Figure B-1. The calibration procedure for the thermistor bridge is described below.

The differential water temperature measurement was made using two Omega ON-970-44008 thermistor probes configured in a half bridge circuit. The thermistor bridge was calibrated prior to the experiment. For this calibration, the two thermistor probes were placed in separate ambient temperature water baths along with type K thermocouples to measure the bath temperatures. The bridge was excited with 10.0 volts using a regulated DC power supply. The bath temperature of one of the probes was increased using a hot plate. Data were recorded by measuring the temperature of the two baths and the bridge output voltage. The results of the thermistor bridge calibration are shown in Figure B-1.

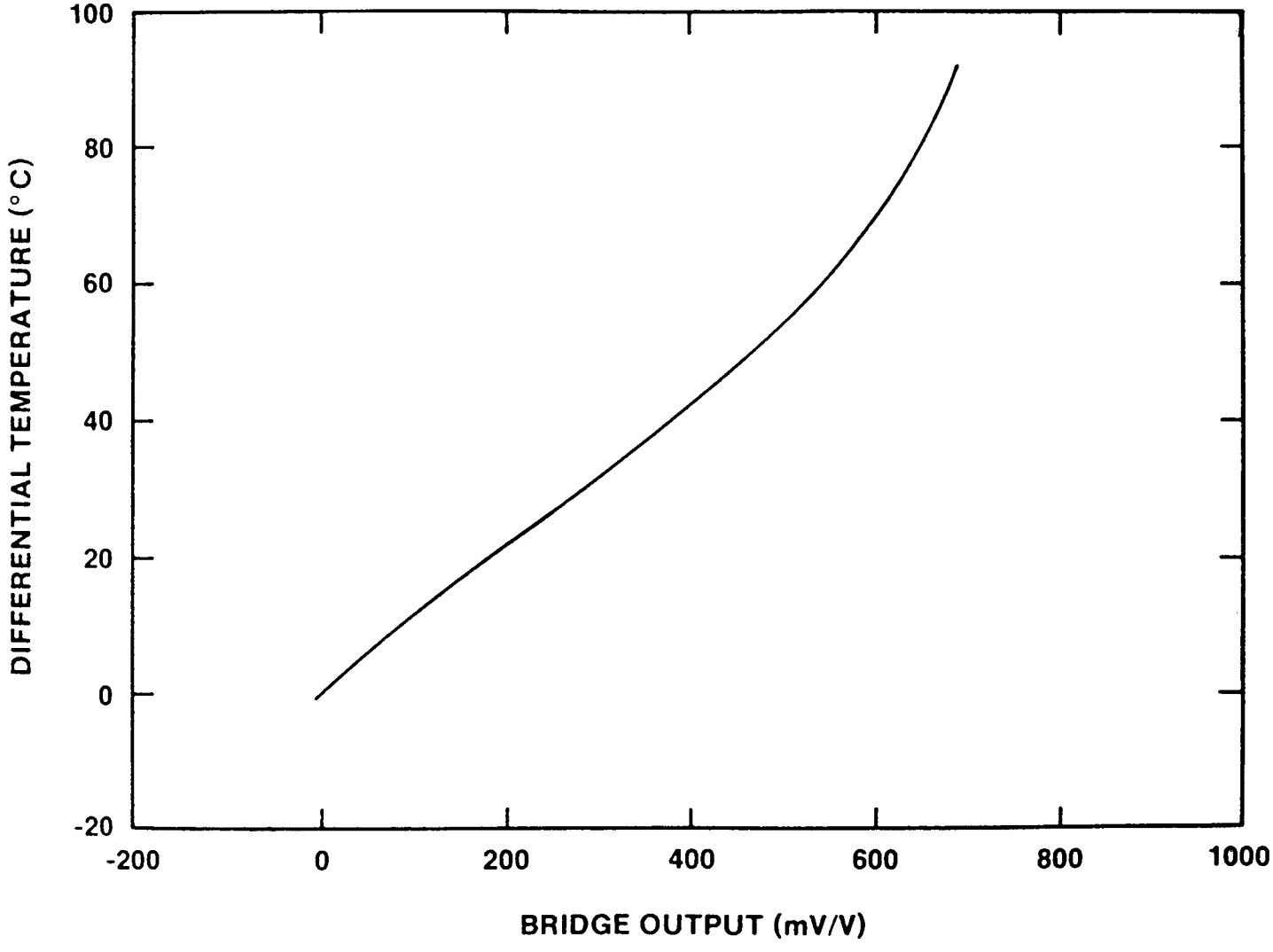

Figure B-1. Thermistor Bridge Calibration Curve to Measure the Differential Water Temperature Across the Crucible Coil.

APPENDIX C

Temperature Data From Boiling Water Calibration, Test QT-E

Temperature data obtained by boiling water inside the cavity of the interaction crucible used in the QT-E experiment are shown in Figures C-1 through C-9. The locations and labels for the thermocouples are described in Table 2.2.1 in the text. Results of this activity were used to verify thermocouple locations and to determine the thermal response of the concrete.

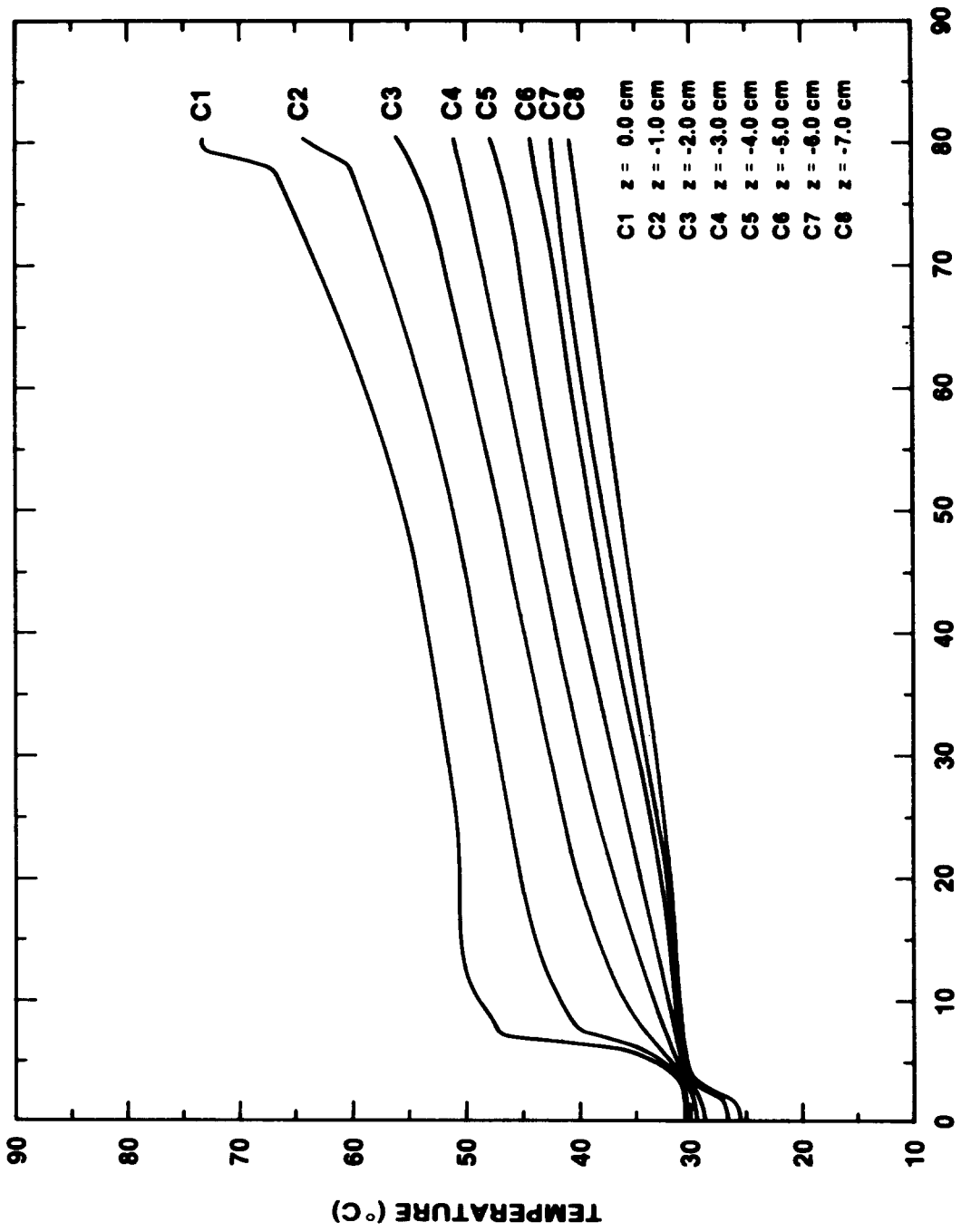

Figure C-1. Center Array Thermocouple Response During Boiling Water Test

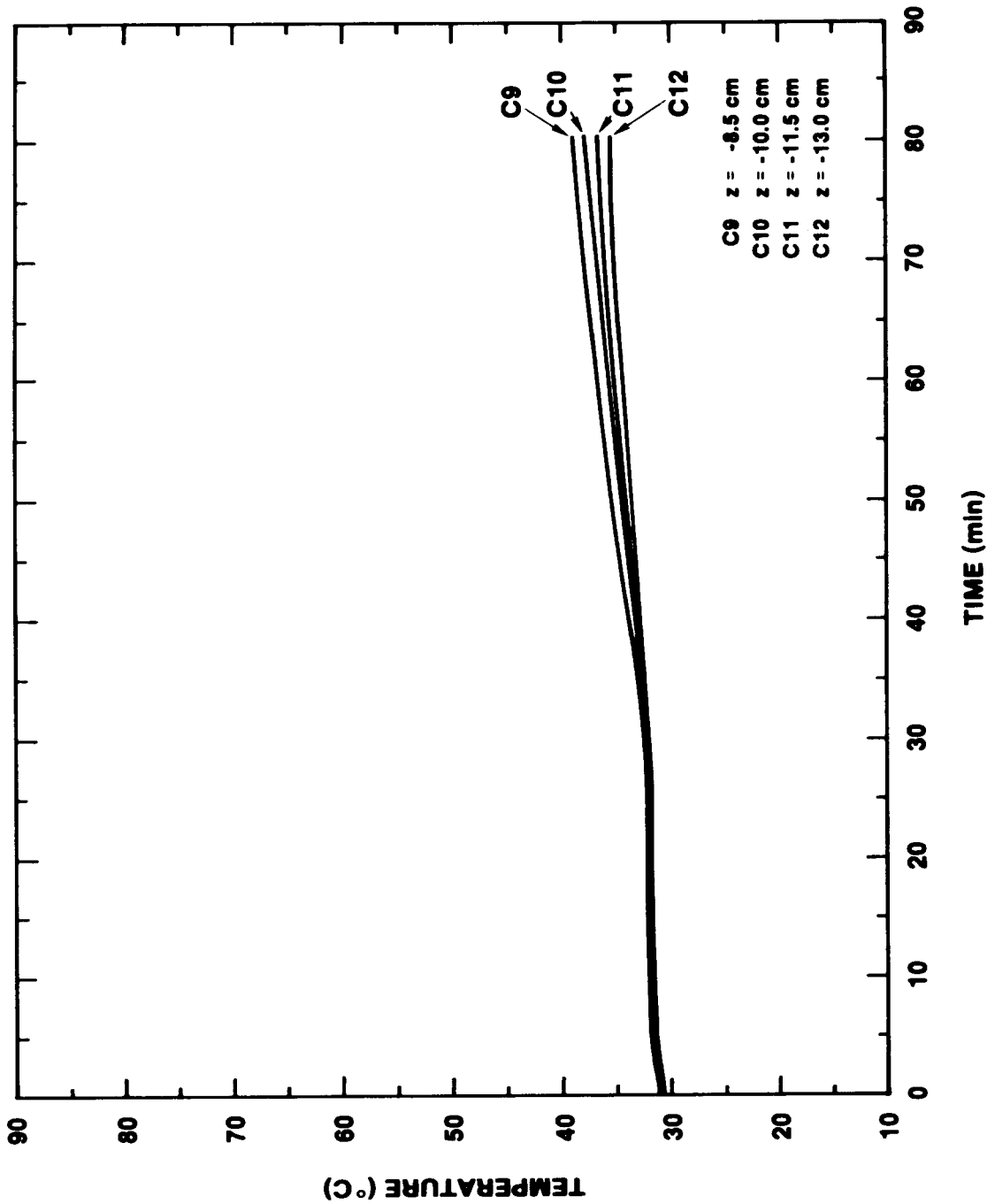

Figure C-2. Center Array Thermocouple Response During Boiling Water Test

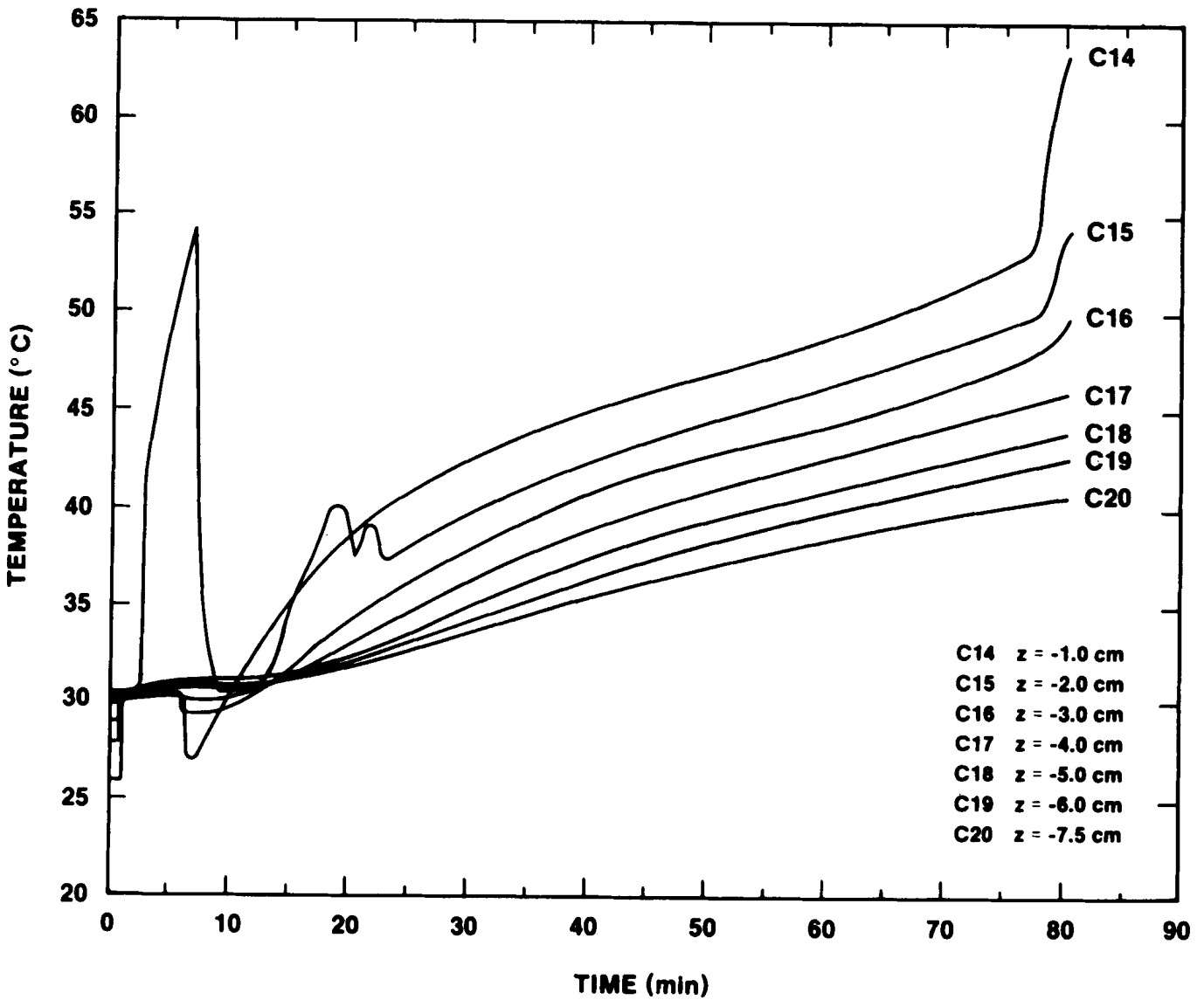

Figure C-3. Mid-Radius Array Thermocouple Response During Boiling Water Test

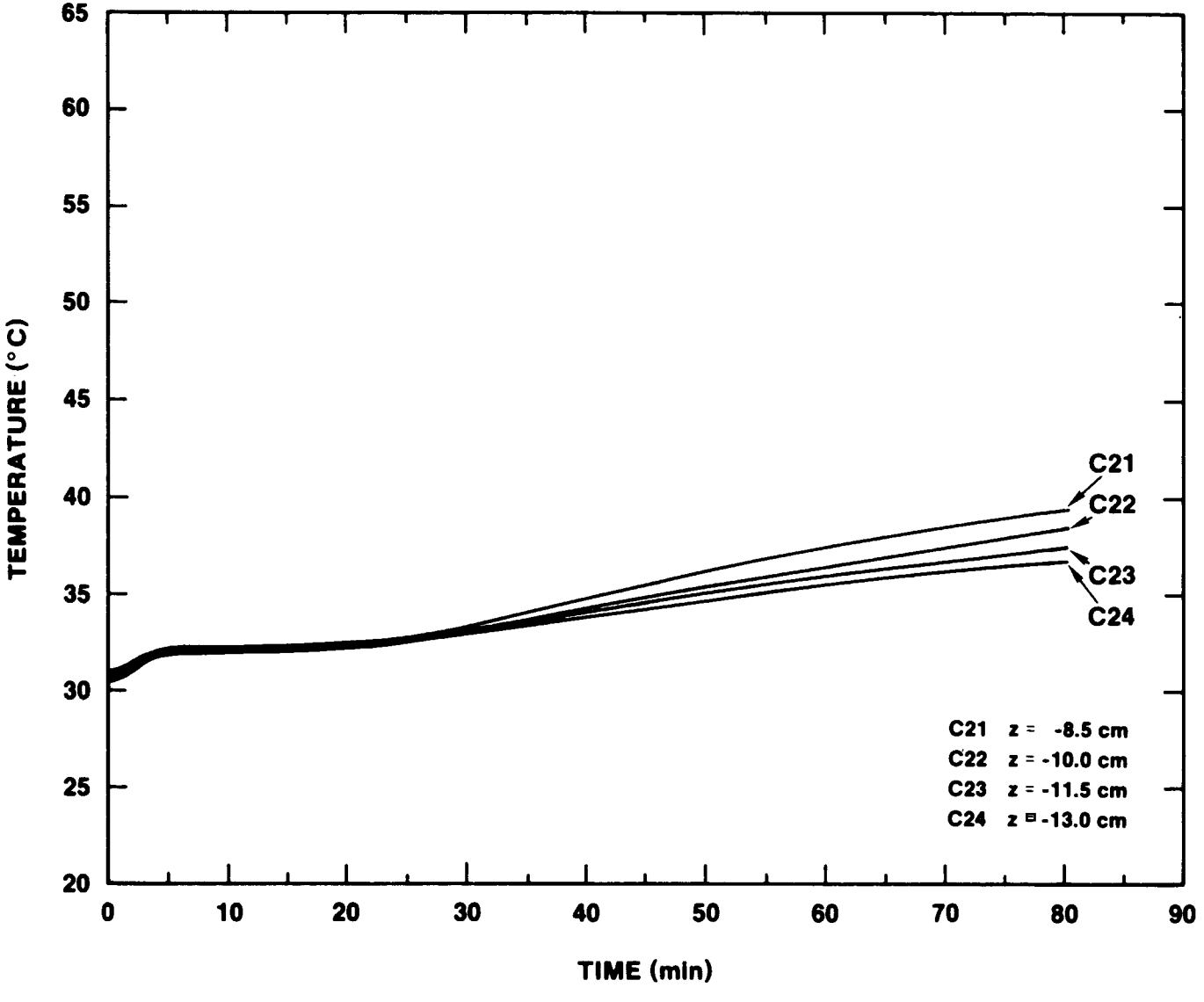

Figure C-4. Mid-Radius Array Thermocouple Response During Boiling Water Test

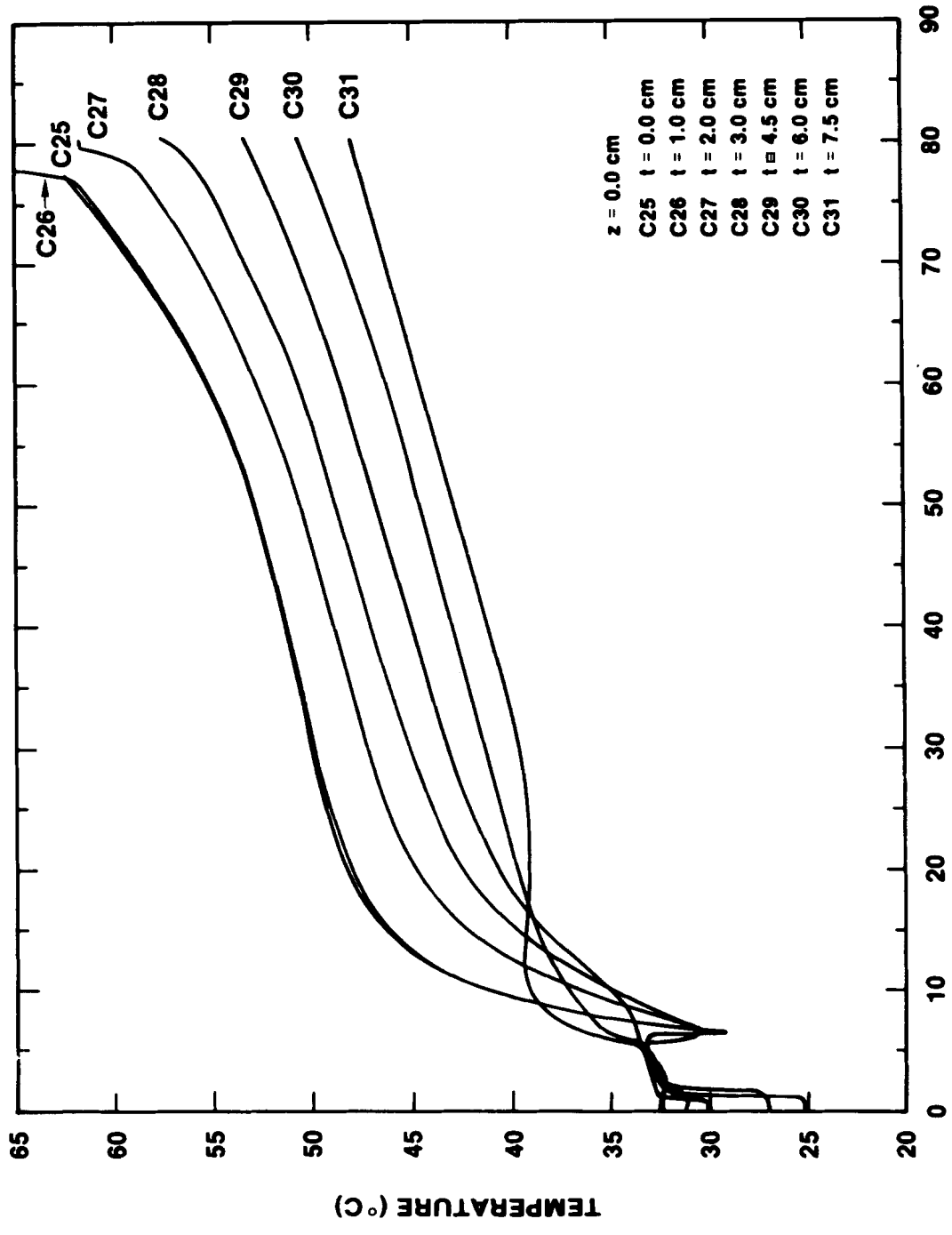

Figure C-5. Interface Wall Array Thermocouple Response During Boiling Water Test

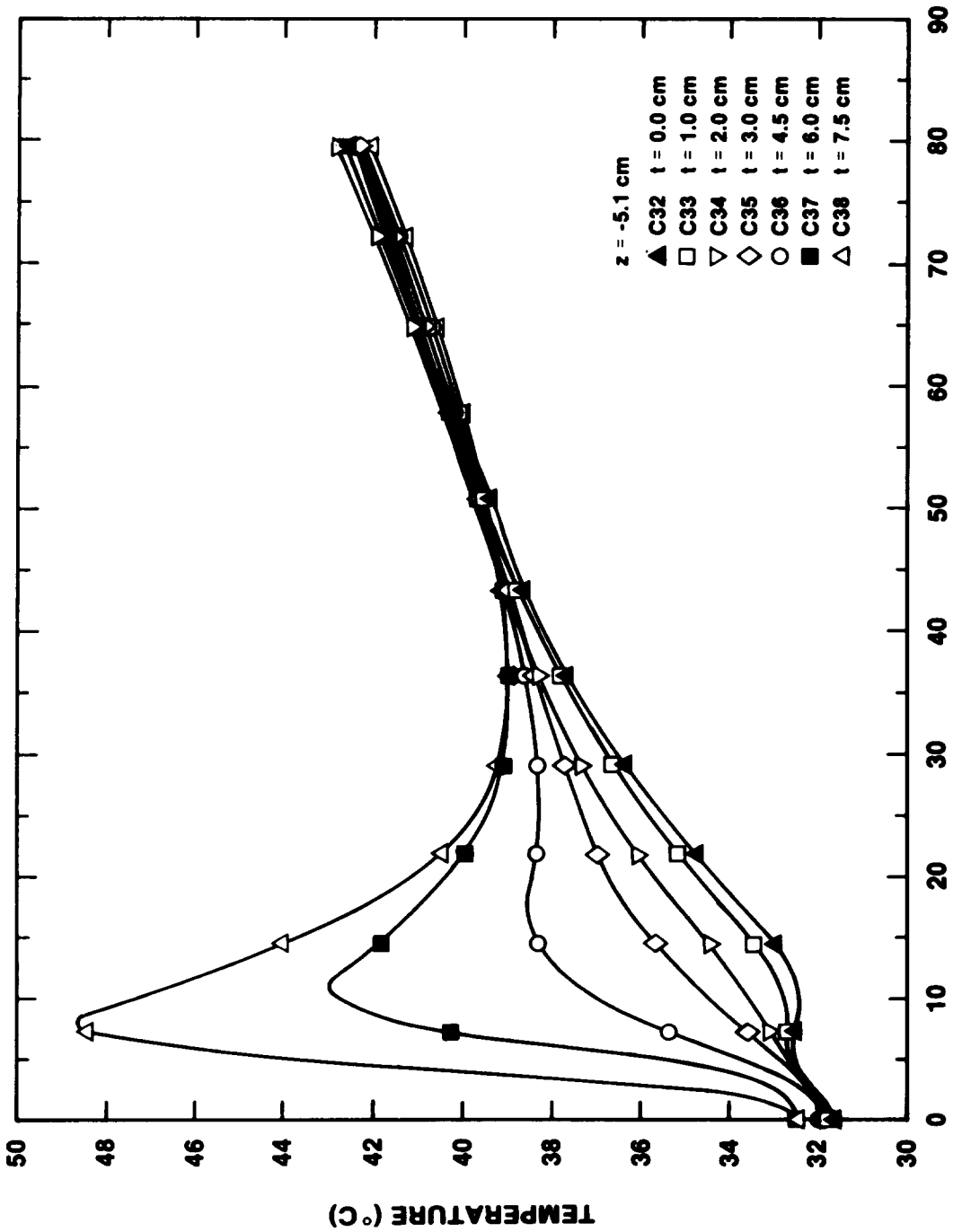

Figure C-6. Wall Array Thermocouple Response for Boiling Water Test at Z = -5.1

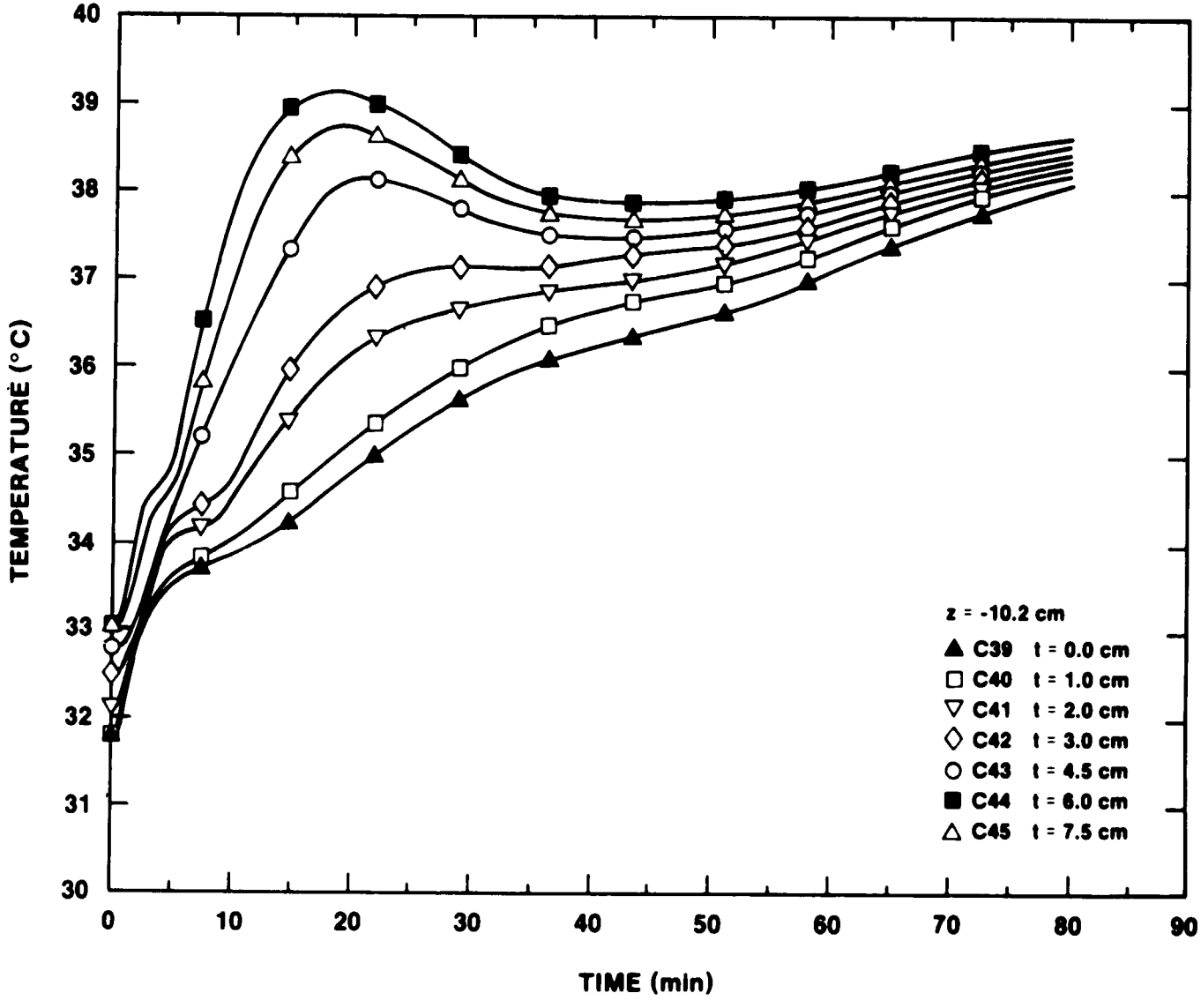

Figure C-7. Wall Array Thermocouple Response for Boiling Water Test at Z = -10.2

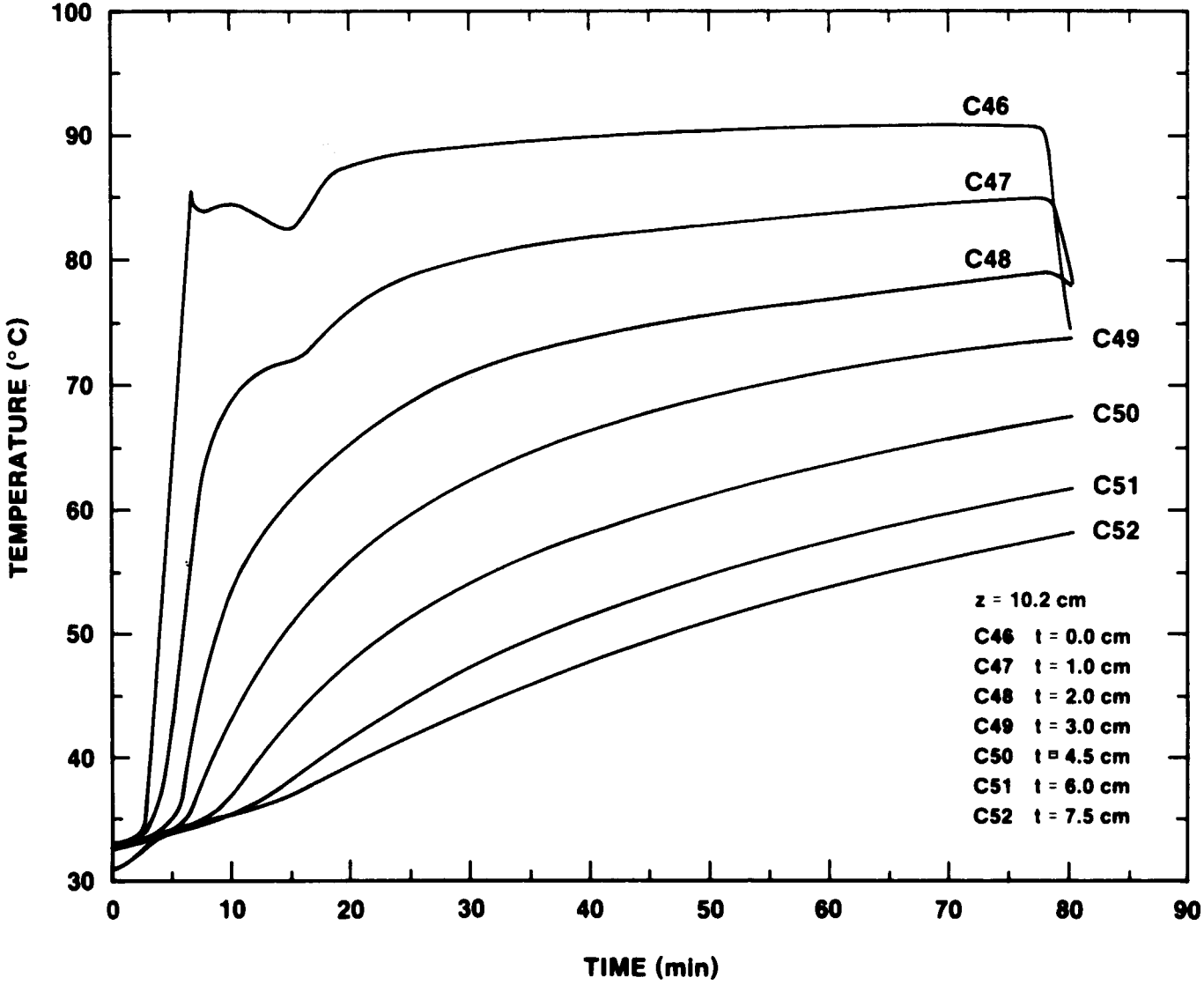

Figure C-8. Wall Array Thermocouple Response for Boiling Water Test at Z = +10.2

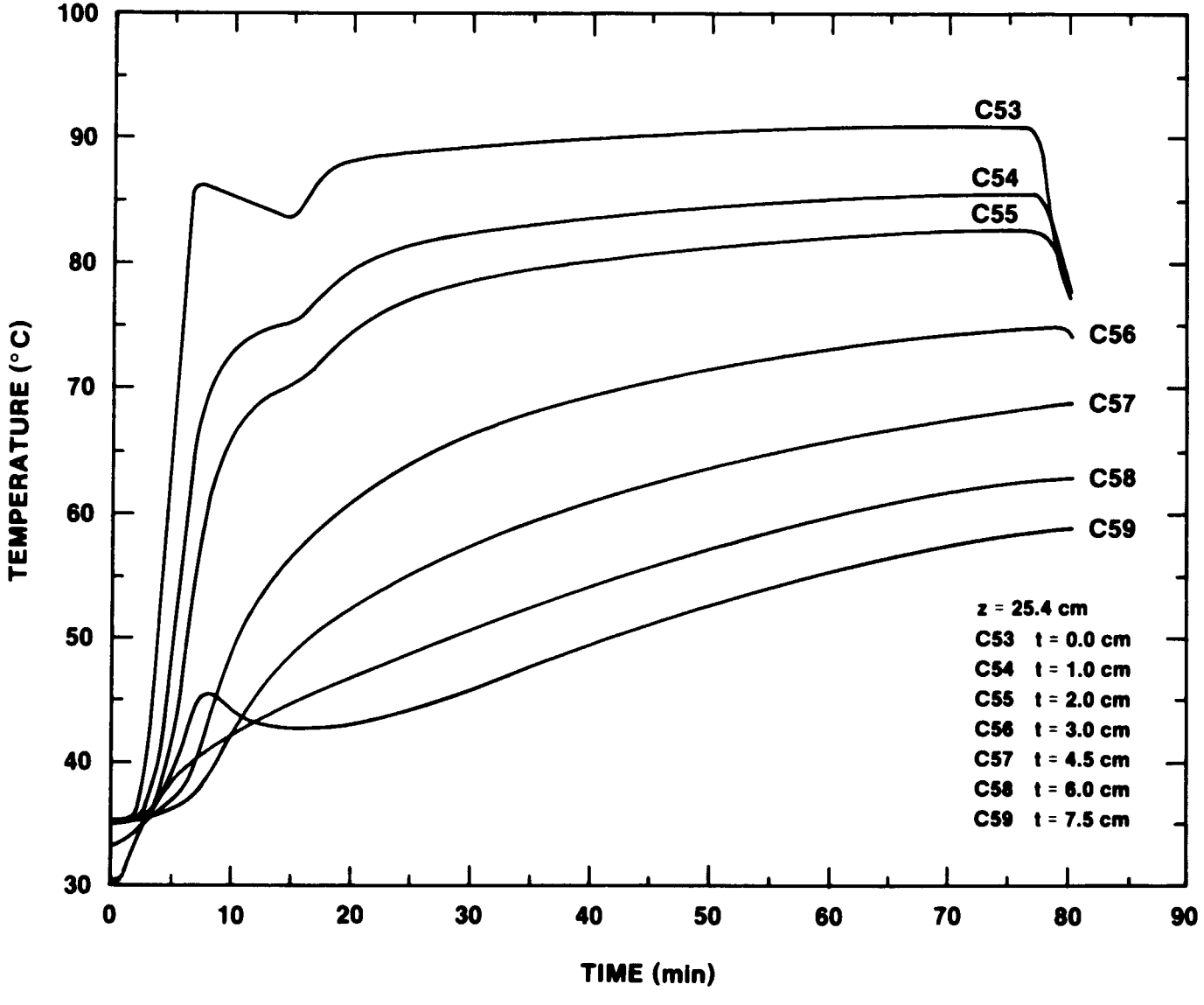

Figure C-9. Wall Array Thermocouple Response for Boiling Water Test at Z = 25.4

APPENDIX D

Thermophysical Properties of Cast MgO, K/R Cast-98

Introduction

Samples of cast MgO were submitted by R. Acton, Sandia National Laboratories (SNLA) for thermophysical property testing at Purdue University. R. E. Taylor and H. Groot of Purdue measured the bulk density (d), thermal diffusivity (α) and specific heat (C_p). The thermal conductivity (λ) is the product of these quantities, i.e. $\lambda = \alpha C_p d$. The results of this study have been summarized in a Purdue University Report, TPRL 447 and issued to SNLA and the data are presented in this appendix.

A Perkin-Elmer Model DSC-II Differential Scanning Calorimeter was used to measure specific heat. A reference and a sample holder in this apparatus are equipped with heaters and temperature sensors. These sensors detect fluctuations of the sample holder temperature. A closed-loop electronic system provides differential electrical power to the heater to compensate for fluctuations. This differential power is read out directly in millicalories per second and is equivalent to the rate of energy absorption or evolution of the sample. By comparing this rate with the rate measured during the heating of a known mass of sapphire, the specific heat could be calculated. The experiments are performed under computer control and the specific heat is automatically calculated at equal temperature intervals.

The flash method, in which the front face of a small disc-shaped sample was subjected to a short laser burst and the resulting rear face temperature rise was recorded, is used in over 80% of the present thermal diffusivity measurements throughout the world. A highly developed apparatus exists at TPRL and Purdue University has been involved in an extensive program to evaluate the technique and broaden its uses. The apparatus consists of a Korad K2 laser, a high vacuum system including a bell jar window for viewing the sample, a tantalum tube heater surrounding a sample holding assembly, a spring-loaded thermocouple or an infrared detector, appropriate biasing circuits, amplifiers, A-D converters, crystal clocks and a minicomputer-based digital data acquisition system capable of accurately taking data in the 40 microsecond and longer time domain. The computer controls the experiment, collects the data, calculates the results and compares the raw data with the theoretical model.

Results and Discussion

Sample dimensions, masses and bulk density values are given in Table D-1. The densities ranged from 2.68 to 2.81 gm cm^3 for the samples used in the diffusivity measurements. Specific heat results are given in Table D-2 and are plotted in Figure D-1. Four runs were made. During Run 1, the specific heat of the as-received materials was measured to 227°C. A peak near 100°C was noted. Run 2 was a duplicate of Run 1 and no peak was observed. Thus, the peak observed in Run 1 was undoubtedly due to the evaporation of moisture. Run 3 covered the range up to 527°C. During this run, a large peak was noted around 430°C. The total weight decrease from the as-received sample of Run 3 to the conclusion of Run 3 was from 0.12990 to 0.11643 gms. No peaks were observed. Thus, the peak observed in Run 3 was probably due to the release of bound water. The results of Run 4 were then extrapolated to 1200°C for purposes of calculating thermal conductivity values.

Previous diffusivity measurements on thinner samples were 0.0316, 0.0244, and 0.0815 cm^2 sec^{-1}. The thin sample with the relatively large diffusibility value was composed mainly of one grain which extended through the entire thickness of the sample. Therefore, thicker samples were obtained. Thermal diffusivity results on the thicker samples are given in Table D-3 and are plotted in Figure D-2. The diffusivity values for the four samples ranged from 0.0279 to 0.0352 cm^2 sec^{-1} at room temperature. Measurements made on Sample 51-6323-1 during cooling agreed with the heating curve to 800°C but were substantially lower at lower temperatures, indicating microcracking. Data were obtained on Sample 51-6323-3 to 600°C and then the sample was cooled to room temperature. The room temperature value was significantly lower than that of the as-received sample. The value at 600°C obtained during reheating was lower by about the same amount. Diffusivity values at higher temperatures approached the values which would be obtained by extrapolating the first run data. This behavior is typical of that observed in heating of microcracked materials.

Thermal conductivity calculations are given in Table D-4. The results are plotted in Figure D-3. Thermal conductivity values for Sample 51-6323-3 are divided into two parts - one obtained during heating to 600°C and the other obtained after cooling to room temperature and reheating to high temperatures. The results for Sample 51-6323-1 and for Sample 51-6323-3 up to 600°C are for as-received samples. Conductivity values decreased during thermal cycling.

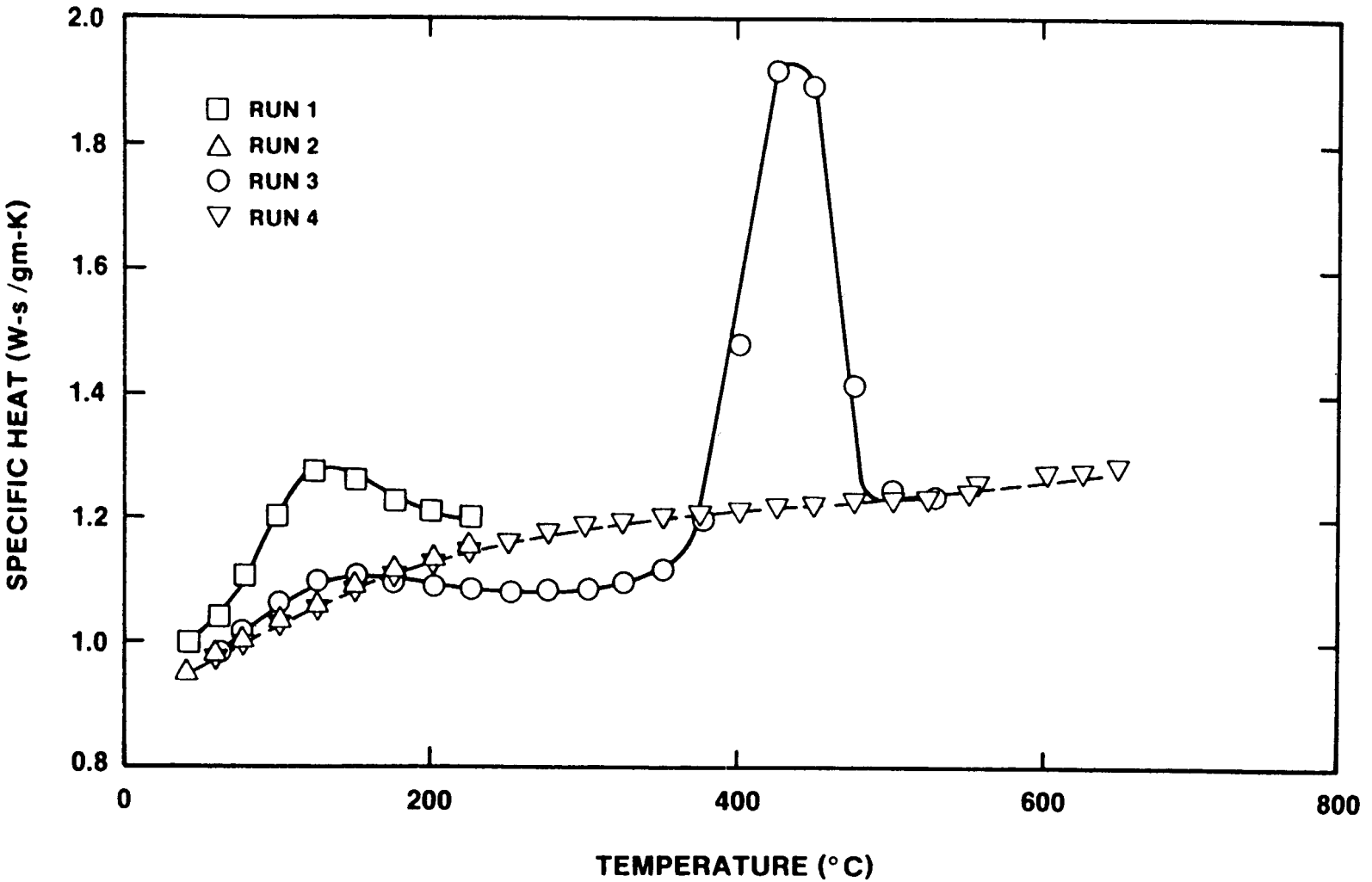

Figure D-1. Specific Heat

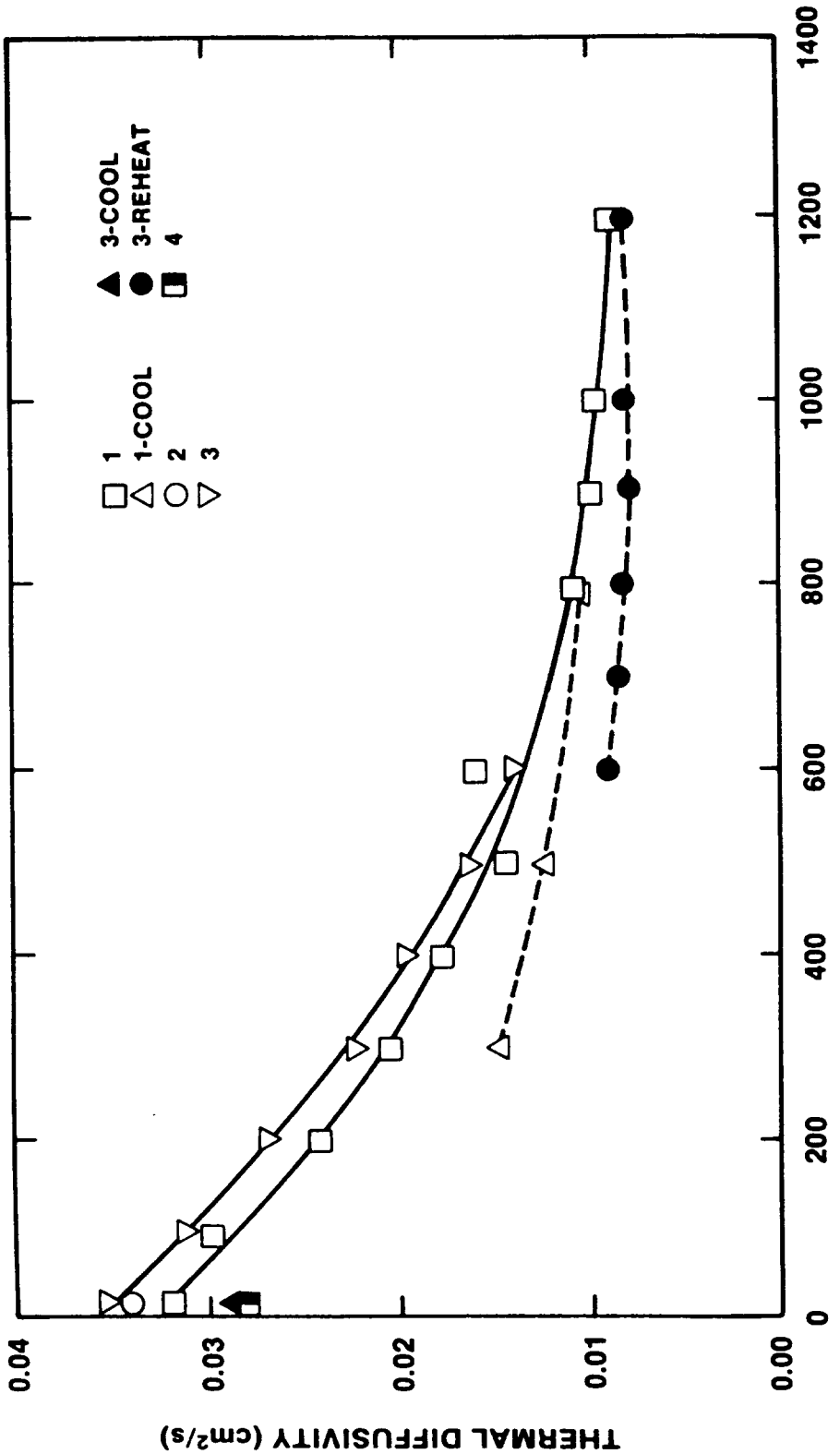

Figure D-2. Thermal Diffusivity

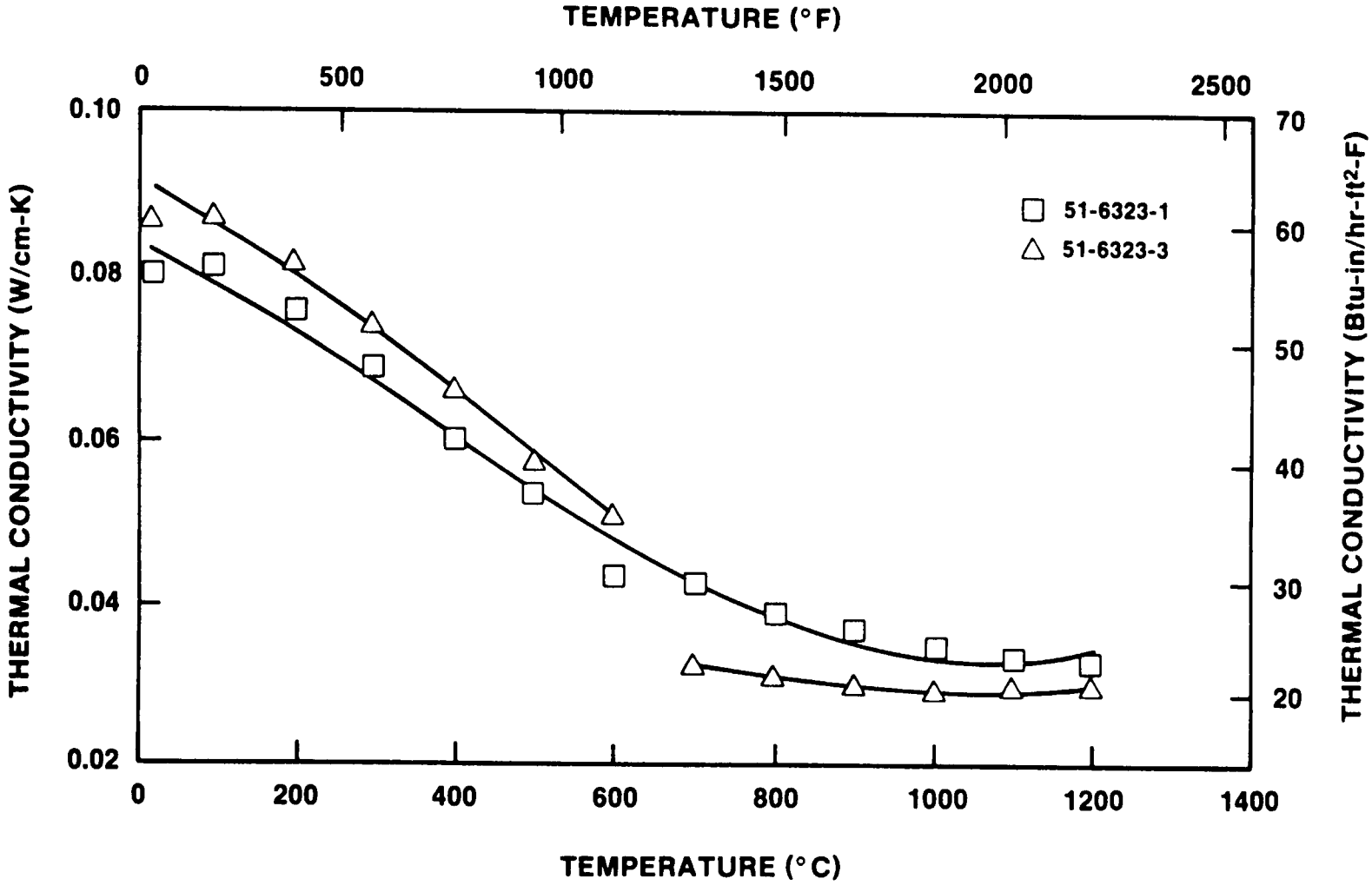

Figure D-3. Thermal Conductivity

TABLE D-1

Sample Dimensions, Masses and Bulk Density Values

Sample Designation	Thick (in.)	Diameter (in.)	Mass (gms)	Density (gm cm^{-3})
51-6323-1	0.2016	0.5005	1.8045	2.776
51-6323-2	0.2015	0.5005	1.8252	2.810
51-6323-3	0.2025	0.5007	1.8234	2.791
51-6323-4	0.1990	0.5007	1.7236	2.684

TABLE D-2

Specific Heat Results*

Temperature (C)	Run 1	Run 2	Run 3	Run 4
42.0	0.9971	0.9504		
62.0	1.0442	0.9783	0.9867	0.9671
77.0	1.0971	0.9970	1.0132	0.9907
102.0	1.2029	1.0269	1.0601	1.0203
127.0	1.2731	1.0552	1.0983	1.0496
152.0	1.2578	1.0815	1.1036	1.0778
177.0	1.2246	1.1069	1.0959	1.1035
202.0	1.2054	1.1322	1.0891	1.1257
227.0	1.2032	1.1579	1.0831	1.1447
252.0			1.0809	1.1605
277.0			1.0841	1.1742
302.0			1.0882	1.1847
327.0			1.0939	1.1924
352.0			1.1169	1.1987
377.0			1.2007	1.2049
402.0			1.4802	1.2112
427.0			1.9173	1.2162
452.0			1.8922	1.2200
477.0			1.4146	1.2251
502.0			1.2454	1.2296
527.0			1.2359	1.2340
552.0				1.2420
557.0				1.2543
602.0				1.2681
627.0				1.2740
652.0				1.2800

* W s $gm^{-1}K^{-1}$

TABLE D-3

Thermal Diffusivity Results

Sample Designation	Temperature (°C)	Diffusivity (cm^2 sec^{-1})	Remarks
51-6323-1	23	0.0318	
	100	0.0298	
	200	0.0241	
	300	0.0202	
	400	0.0176	
	500	0.0143	
	600	0.0158	
	800	0.0105	
	900	0.00988	
	1000	0.00966	
	1200	0.00886	
	800	0.0107	Cooling
	500	0.0124	Cooling
	300	0.0148	Cooling
51-6323-2	23	0.0342	
51-6323-3	23	0.0352	
	100	0.0311	
	200	0.0268	
	300	0.0222	
	400	0.0195	
	500	0.0162	
	600	0.0139	
	23	0.0285	Cooling
	600	0.00910	Reheat
	700	0.00844	Reheat
	800	0.00827	Reheat
	900	0.00766	Reheat
	1000	0.00811	Reheat
	1200	0.00810	Reheat
51-6323-4	23	0.02789	

TABLE D-4

Thermal Conductivity Calculations

Sample (No.)	Temp. (C)	Density (gm cm^{-3})	Specific Heat (W s $gm^{-1}K^{-1}$)	Diffusivity (cm^2sec^{-1})	Conductivity (W $cm^{-1}K^{-1}$)	Conductivity (BTU units*)	Temp. (F)
51-6323-1	22.0	2.776	0.8850	0.03260	0.08009	55.53	71.6
51-6323-1	100.0	2.776	1.0180	0.02860	0.08082	56.04	212.0
51-6323-1	200.0	2.776	1.1230	0.02420	0.07544	52.31	392.0
51-6323-1	300.0	2.776	1.1840	0.02090	0.06869	47.63	572.0
51-6323-1	400.0	2.776	1.2110	0.01790	0.06018	41.72	752.0
51-6323-1	500.0	2.776	1.2420	0.01560	0.05379	37.29	932.0
51-6323-1	600.0	2.776	1.2680	0.01240	0.04365	30.26	1112.0
51-6323-1	700.0	2.776	1.2850	0.01200	0.04281	29.68	1292.0
51-6323-1	800.0	2.776	1.3000	0.01080	0.03898	27.02	1472.0
51-6323-1	900.0	2.776	1.3070	0.01010	0.03665	25.41	1652.0
51-6323-1	100.00	2.776	1.3140	0.00950	0.03465	24.03	1832.0
51-6323-1	1100.0	2.776	1.3250	0.00910	0.03347	23.21	2012.0
51-6323-1	1200.0	2.776	1.3300	0.00880	0.03249	22.53	2192.0
51-6323-3	22.0	2.791	0.8850	0.03510	0.08670	60.11	71.6
51-6323-3	100.0	2.791	1.0180	0.03070	0.08723	60.48	212.0
51-6323-3	200.0	2.791	1.1230	0.02600	0.08149	56.50	392.0
51-6323-3	300.0	2.791	1.1840	0.02240	0.07402	51.32	572.0
51-6323-3	400.0	2.791	1.2110	0.01950	0.06613	45.85	752.0
51-6323-3	500.0	2.791	1.2420	0.01670	0.05789	40.14	932.0
51-6323-3	600.0	2.791	1.2680	0.01440	0.05096	35.33	1112.0
51-6323-3	700.0	2.791	1.2850	0.00910**	0.03264	22.63	1292.0
51-6323-3	800.0	2.791	1.3000	0.00860	0.03120	21.63	1472.0
51-6323-3	900.0	2.791	1.3070	0.00820**	0.02991	20.74	1652.0
51-6323-3	100.00	2.791	1.3140	0.00800**	0.02934	20.34	1832.0
51-6323-3	1100.0	2.791	1.3250	0.00800**	0.02958	20.51	2012.0
51-6323-3	1200.0	2.791	1.3300	0.00810**	0.03007	20.85	2192.0

* (BTU in $hr^{-1}ft^{-2}F^{-1}$)

** After Cooling

APPENDIX E

Zirconium Delivery Section and Crucible Fabrication

In order to conduct these tests two items had to be fabricated for each experiment. The first was a zirconium delivery section used to retain the zirconium metal cylinder prior to delivery to the meltpool. And the second was the test article instrumented for measurement of melt temperature, concrete erosion rates and thermal response of the system. The zirconium delivery section was designed to mount directly above the test article. Hardware such as anchors were cast into both items to facilitate transportation, mounting hardware and securing instrumentation. Stainless tubing and steel pipes were also cast into each item to serve as feed through for instrumentation and other devices necessary to fulfill the experimental and data acquisition requirements.

Zirconium Delivery Section

The zirconium delivery section, shown in Figure E-1 was cast using K/R Cast-98 magnesium oxide castible refractory described in Sections 2.3.2. Prior to casting, the geometry of the zirconium delivery section was configured using SONOTUBE stripable, cardboard, column forms and plywood securely mounted to a mild steel casting base 1.3 cm thick. The zirconium delivery section casting assembly, shown schematically in Figure E-2, consists of three concentric cylindrical cavities of various diameters and lengths, cast within a 40.0 cm diameter, 91.4 cm high right circular cylinder. Four brass mounting anchors were cast into the zirconium delivery section at the top, 90 degrees apart on a 33.0 cm diameter bolt circle. These anchors were used to attach and seal the instrumented expansion chamber to the zirconium delivery section. Another four anchors were cast into the perimeter 90 degrees apart at a height of 15.2 cm from the base for the purpose of securing the zirconium delivery section to the interaction crucible. Four 5.1 cm diameter steel pipes were cast into the zirconium delivery section 90 degrees apart at an angle of 45 degrees with the axis. These pipes were used to house and deliver the zirconium metal to the interaction crucible. The axis of these pipes intersected the outside diameter at a height of 20.0 cm from the base. A 304 stainless steel aerosol dilution tube 25.4 cm long having an OD of 5.1 cm was cast into the zirconium delivery section sidewall at a height of 21 cm from the base. The tube is shown in Figure E-3. This dilution tube was used to sample aerosols and particulate produced during the experiment. This was the only instrumentation cast into the zirconium delivery section.

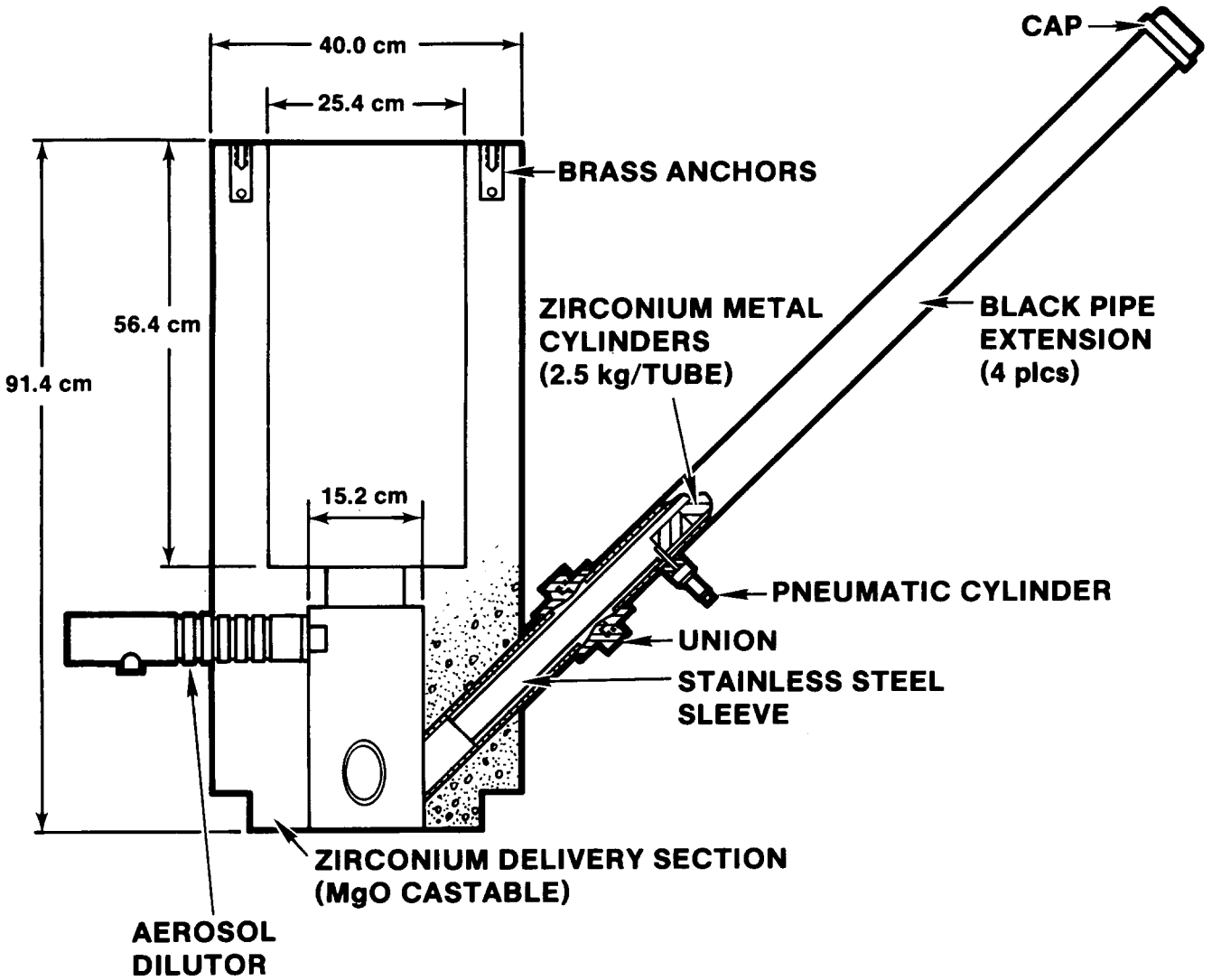

Figure E-1. Zirconium Delivery Section, SURC-3 and 3A

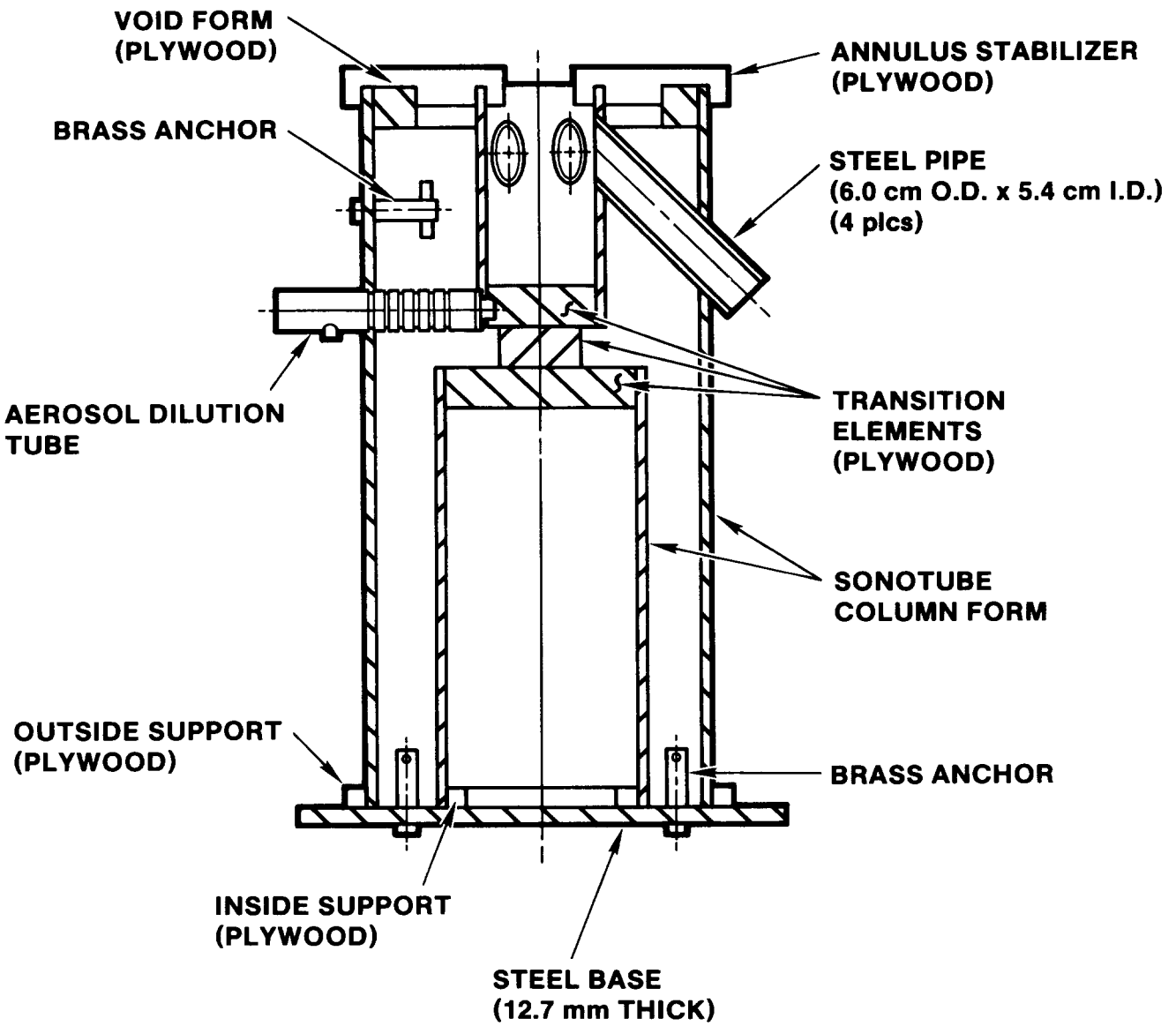

Figure E-2. Casting Assembly, Zirconium Delivery Section, SURC-3 and 3A

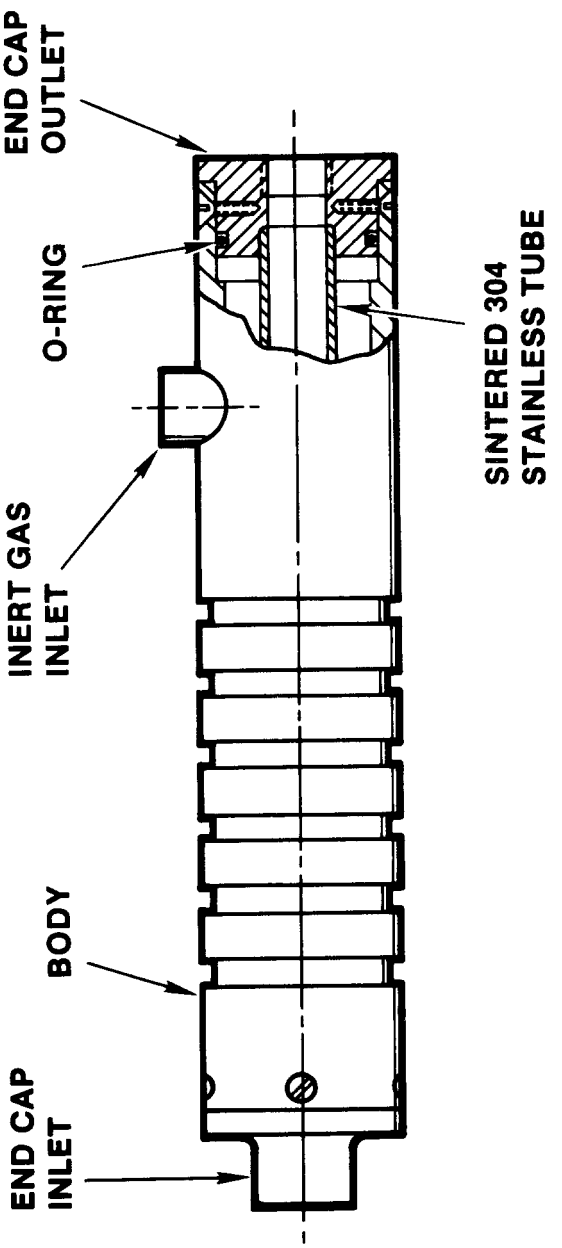

Figure E-3. Aerosol Dilution Tube

The circumferential step shown at the base of the zirconium delivery section was formed out of layers of plywood firmly attached to the inside diameter of the large SONOTUBE. After the forms were secured and all the instrumentation and hardware was installed and the locations documented, the inside of the forms were sprayed with dry film lubricant (teflon), which served as mold release. At various stages of the assembly photographs were taken for the purpose of documentation.

The MgO castible was mixed by placing a known mass of the dry material into a paddle-type mixer. Clean drinking water was then added 5% to 6% by weight to the castible material and mixed for at least two minutes. After the castible had been placed into the crucible forms it was vibrated. A pneumatic concrete vibrator, operating at 10,000 to 12,000 vibrations per minute was used to densify the mix and remove entrained air.

After casting, the mix was cured at ambient temperature (20 to 30°C) for 24 hours. Then it was placed into an oven and heated at a rate of 40°C/hr to 205°C. The casting was held at temperature for 24 hours. During the oven bake, the temperature of the oven was monitored with a type K thermocouple and recorded on a strip chart recorder to document the proper curing.

After the zirconium delivery section had cooled from the elevated temperature cure, the SONOTUBE forms were stripped off and the outside diameter was fiberglass laminated with three (3) 0.03 cm thick layers of 207 MN/m^2 glass fabric for sealing and structural reinforcement. A data sheet was initiated with each zirconium delivery section cast identifying the location of critical instrumentation, mixing ratios, casting dates, curing methods and other important data.

Interaction Crucible

The crucible used in these tests is typical of a design used in the past Sustained Heated Metallic Melt Concrete Interaction with and Overlaying Water Pool (SWISS) experiments. The crucible, shown schematically in Figure E-4, consisted of an instrumented concrete slug 21.6 cm in diameter and 40.0 cm in height, cast at the base of a MgO annulus, 40.6 cm outside diameter and 91.4 cm in height.

Crucibles with a cylindrical geometry have been designed to contain the melt and instrumented to measure the thermal response during the interaction phase in these two experiments [Blose, 1987]. The crucible was fabricated in two major steps: first the construction of the MgO annulus and second the casting of the concrete slug within the base of the annulus.

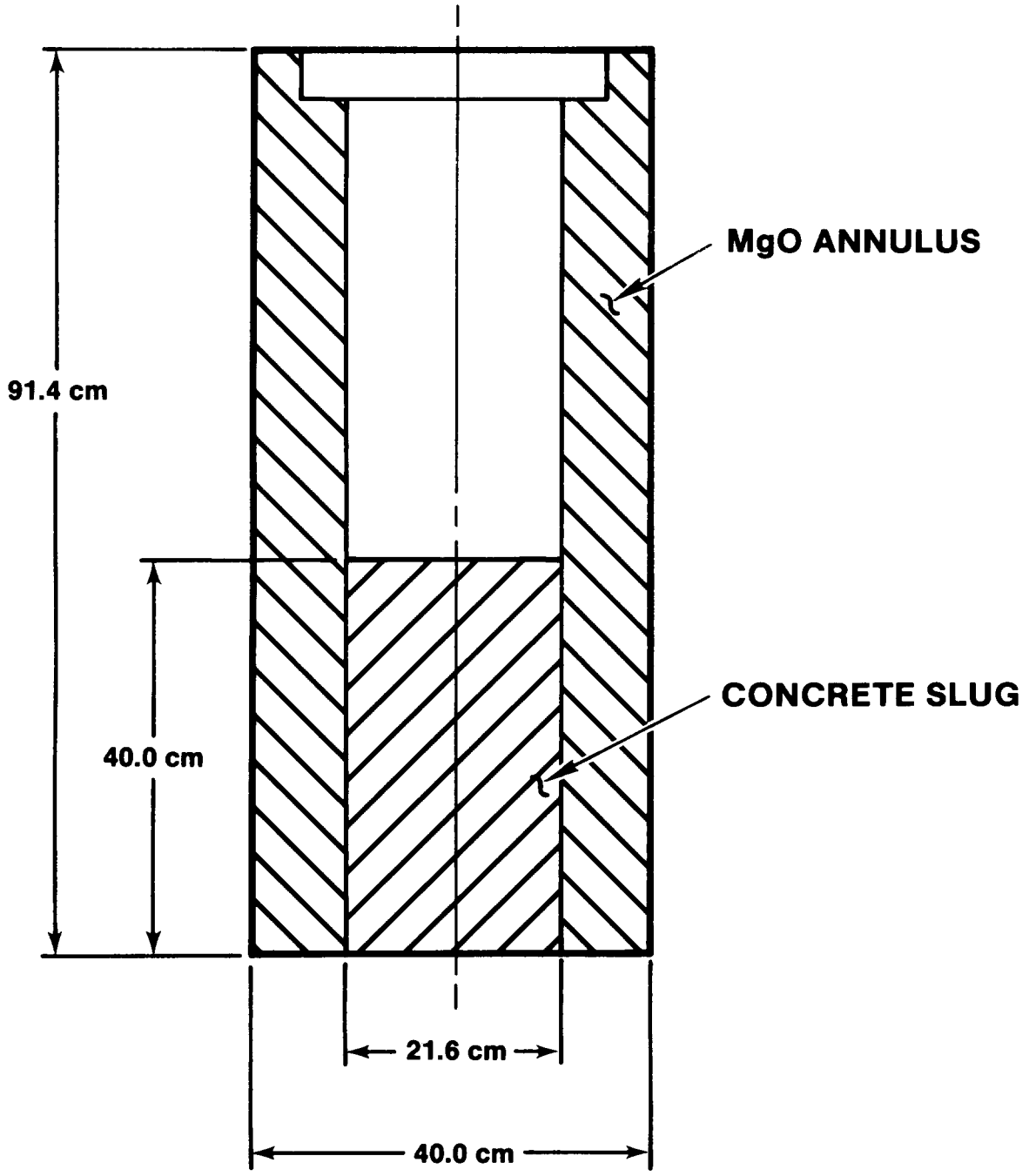

Figure E-4. Interaction Crucible, SURC-3

The crucible casting assembly, shown in Figure E-5 and the photograph in Figure E-6, was constructed like the zirconium delivery section using SONOTUBE strippable column forms. The MgO annulus was fabricated by arranging two SONOTUBE forms concentric with each other mounted to a 1.3 cm thick mild steel plate. The circumferential step shown at the top of the interaction crucible (Figure E-4) was formed out of layers of plywood firmly attached to the perimeter of the SONOTUBE forming the crucible cavity as shown in Figure E-7. This was followed by installation of the sidewall thermocouple arrays and four brass mounting anchors at the perimeter of the large form 15.2 cm from the top. The brass mounting anchors were installed for the purpose of securing the zirconium delivery section to the crucible. The sidewall thermocouple arrays, shown in Figure E-8 and in the photograph in Figure E-9, were placed into a positioning fixture and spot welded to a 0.04 cm thick, 1.0 cm wide, stainless steel ribbon, as shown in Figure E-10. K-type, 0.16 cm diameter, thermocouples having a 304 stainless steel sheath were used. The pre-assembled arrays were installed into the annulus by stretching the stainless ribbon between the inner and outer SONOTUBE forms through slots cut in the wall as shown in Figure E-9. The arrays were secured by spot welding a piece of 0.15 cm, stainless steel, wire to the ends of the stainless ribbon protruding through the SONOTUBE forms. The sheaths of the thermocouples were secured to the wall of the outside SONOTUBE with small diameter wire. All sidewall thermocouple sheaths were routed down the wall of the crucible.

In the region where the concrete slug was cast, a wire wrap 0.6 to 1.0 cm diameter, by 4.0 cm pitch, was installed to improve the bonding between the concrete slug and MgO annulus.

Prior to casting, the location of each thermocouple was independently measured by two individuals and the position documented. The SONOTUBE forms were sprayed with teflon used as a mold release. The annulus was cast and cured using K/R Cast-98 following the procedures described earlier.

Once the annulus had cooled to room temperature, the inner SONOTUBE form and wire wrap were removed, and a plywood platform was installed 40.0 cm from the base of the MgO annulus with a diameter of 21.6 cm (this was the same region where the wire wrap was installed). Thermocouple arrays were prepared using a form as previously described and spot welded to the stainless steel ribbon. Again type K thermocouples were used. The installation of the thermocouple arrays is shown in Figure E-11 and in the photograph in Figure E-12. The two arrays, located on the axial centerline and mid-radius centerline, were installed by stretching the stainless steel ribbon between the plywood platford and a structural support located above the crucible. As before, two independent measurements of the thermocouple locations were made and documented prior to casting.

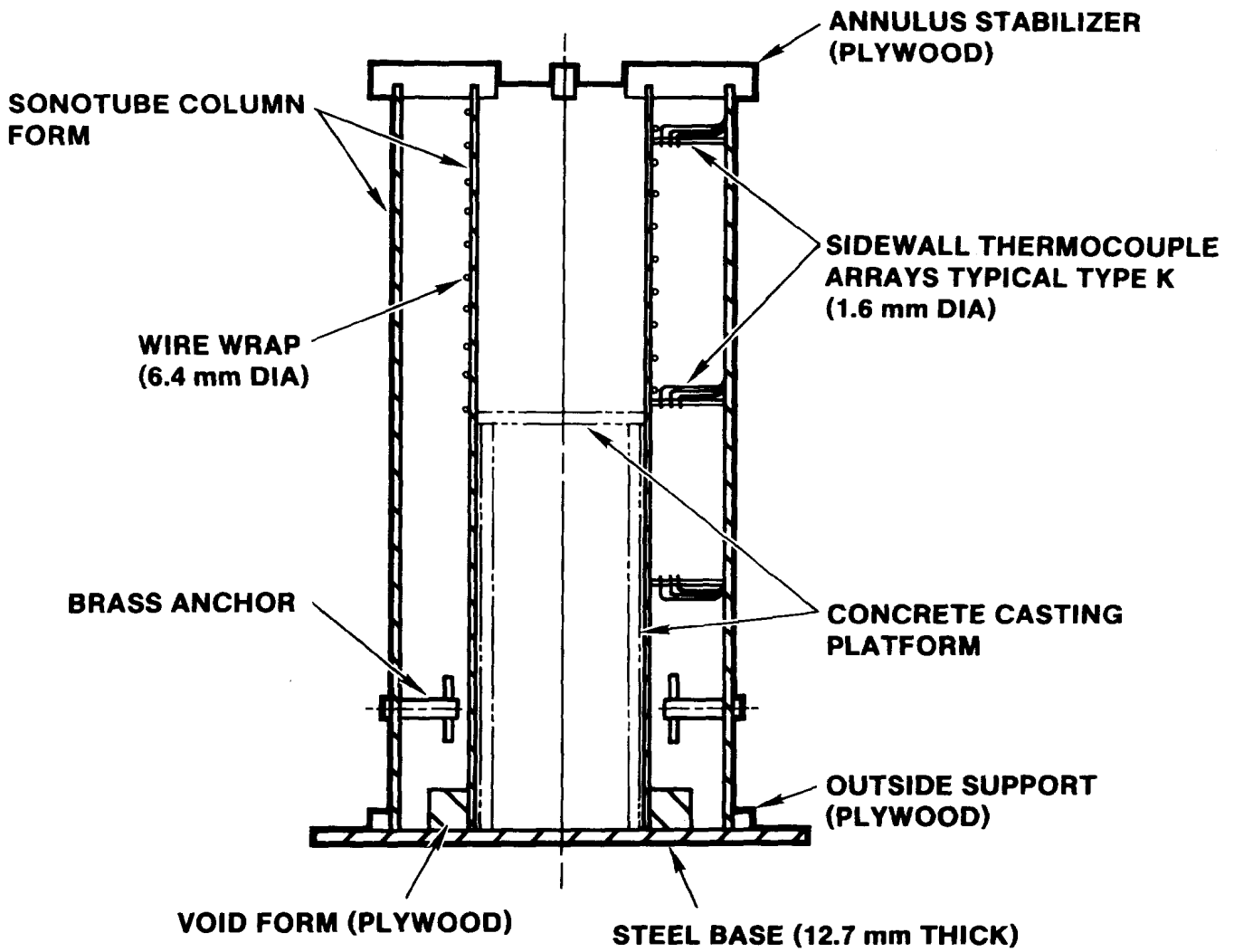

Figure E-5. Casting Assembly, MgO Annulus, Interaction Crucible, SURC Experiments 3 and 4

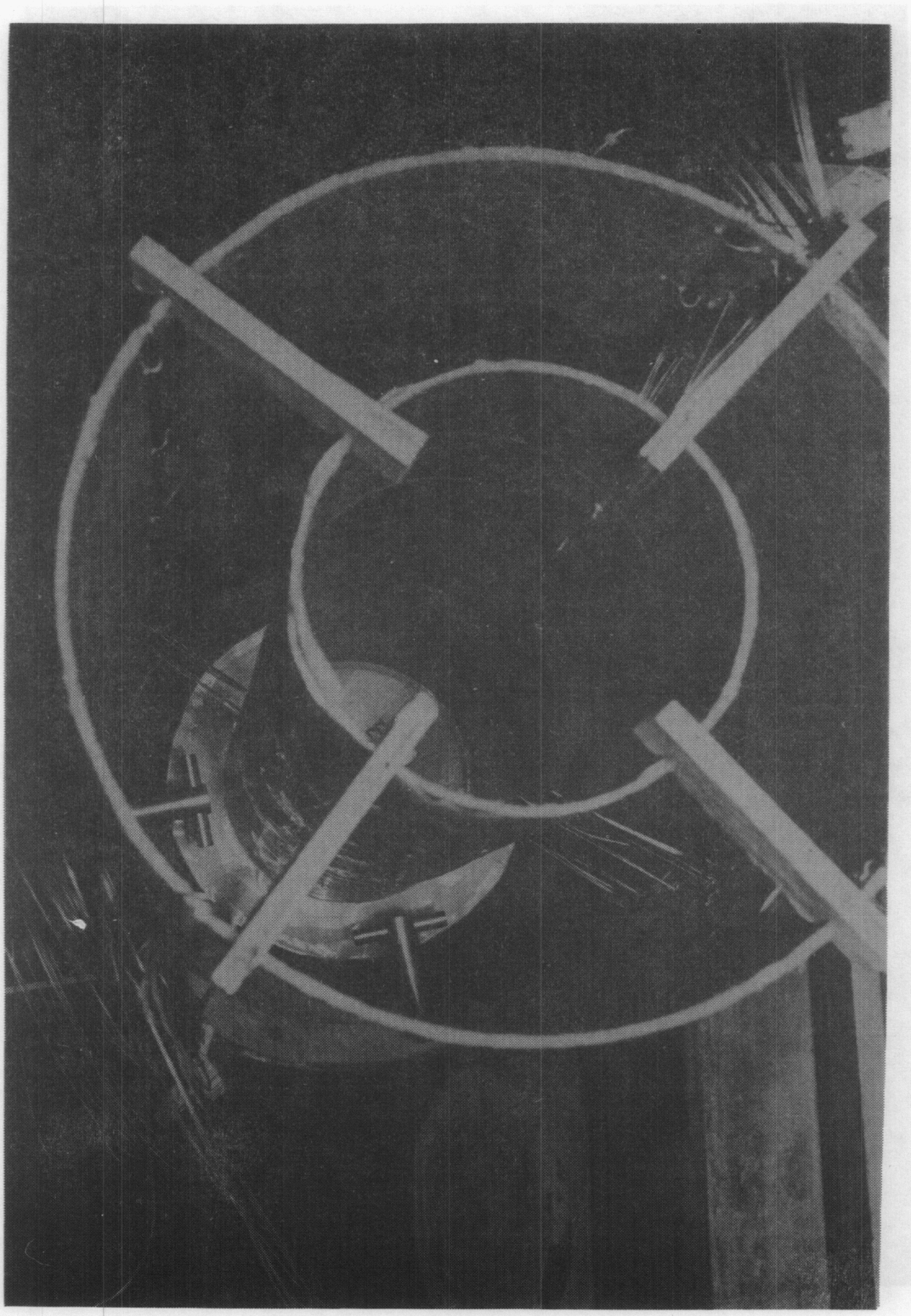

Figure E-6. Casting Assembly, MgO Annulus, Interaction Crucible, SURC Experiments 3 and 4

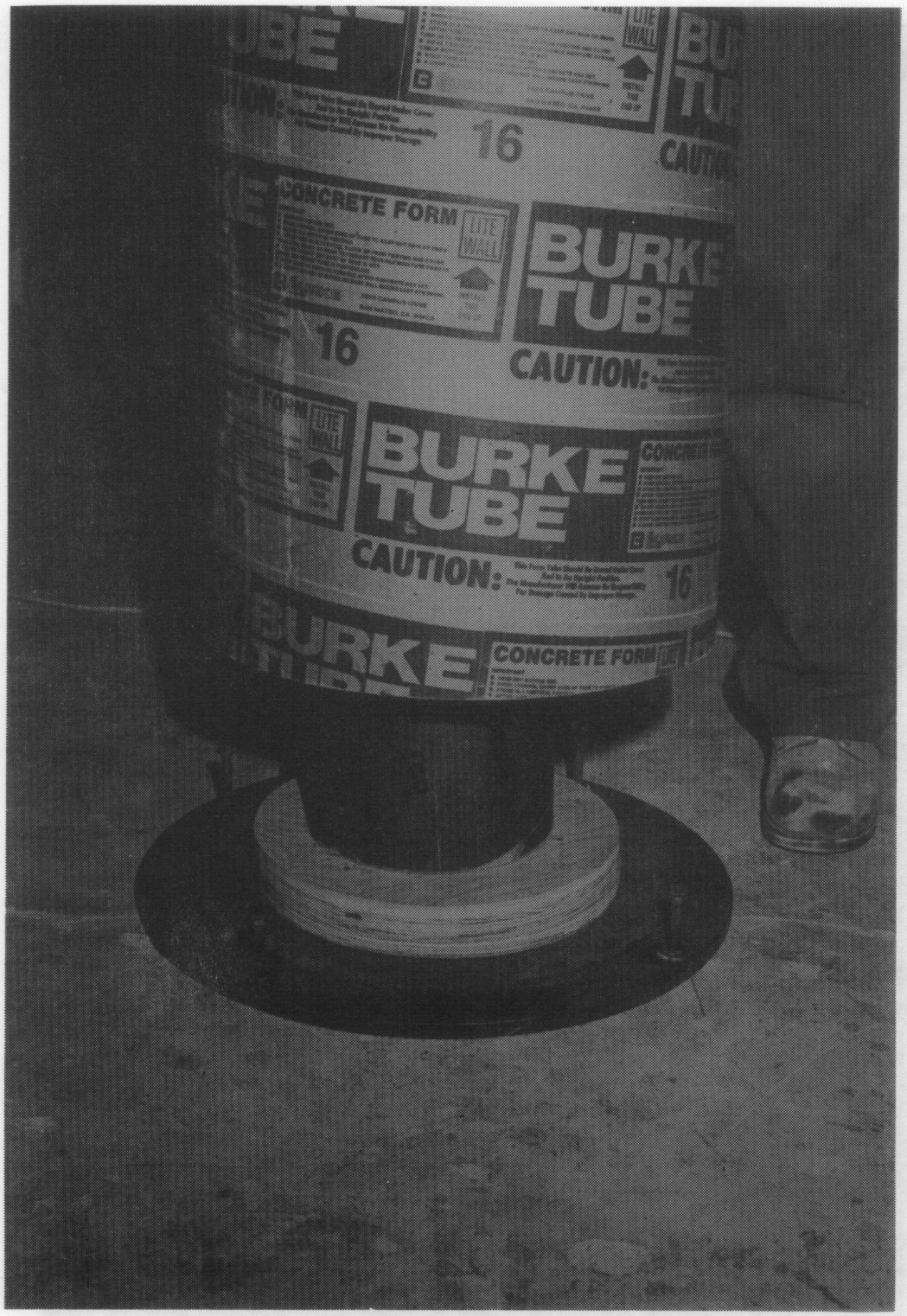

Figure E-7. Method of Forming Circumferential Step at Top of Interaction Crucible

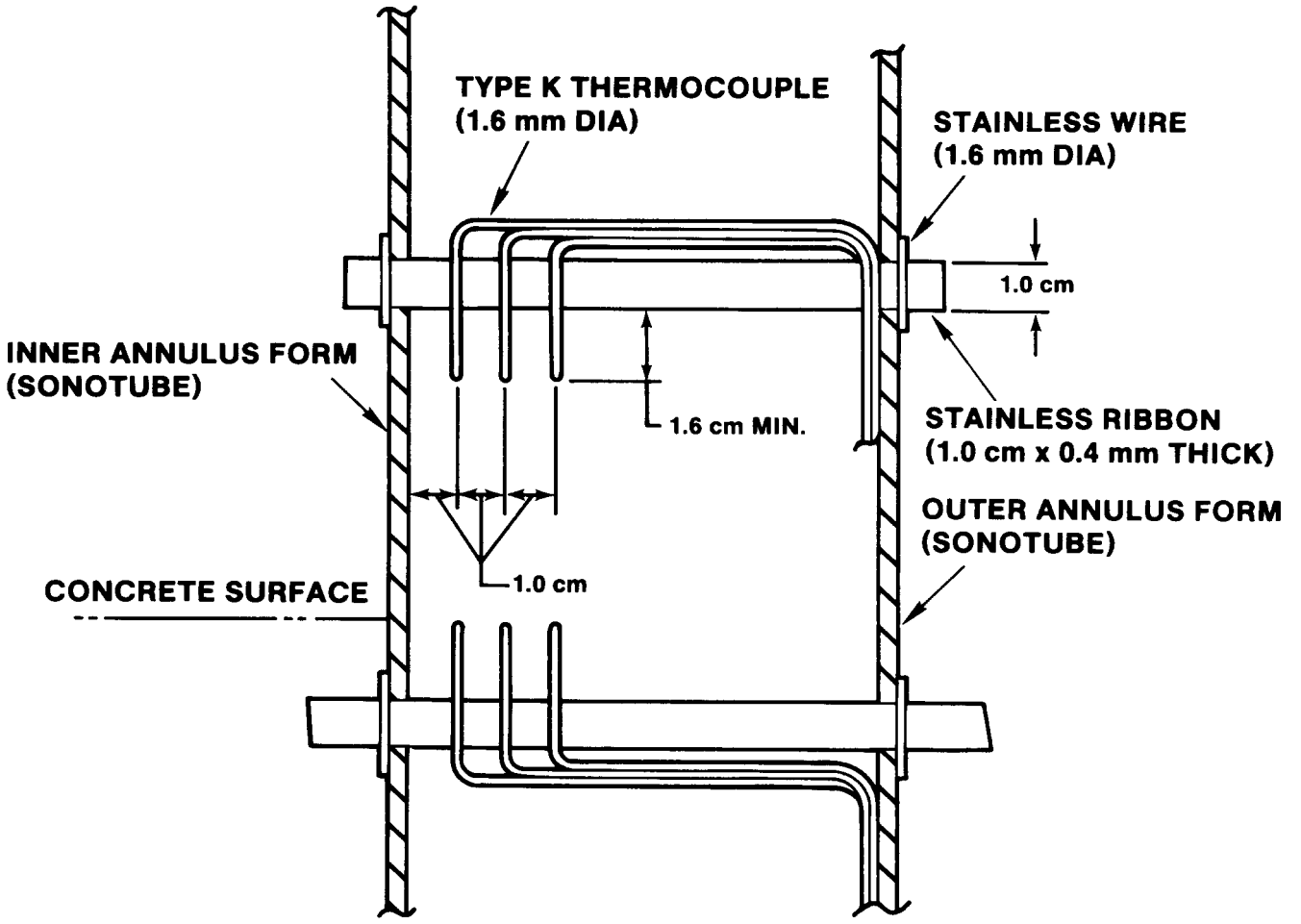

Figure E-8. MgO Annulus Thermocouple Arrays, SURC Experiments 3 and 3A

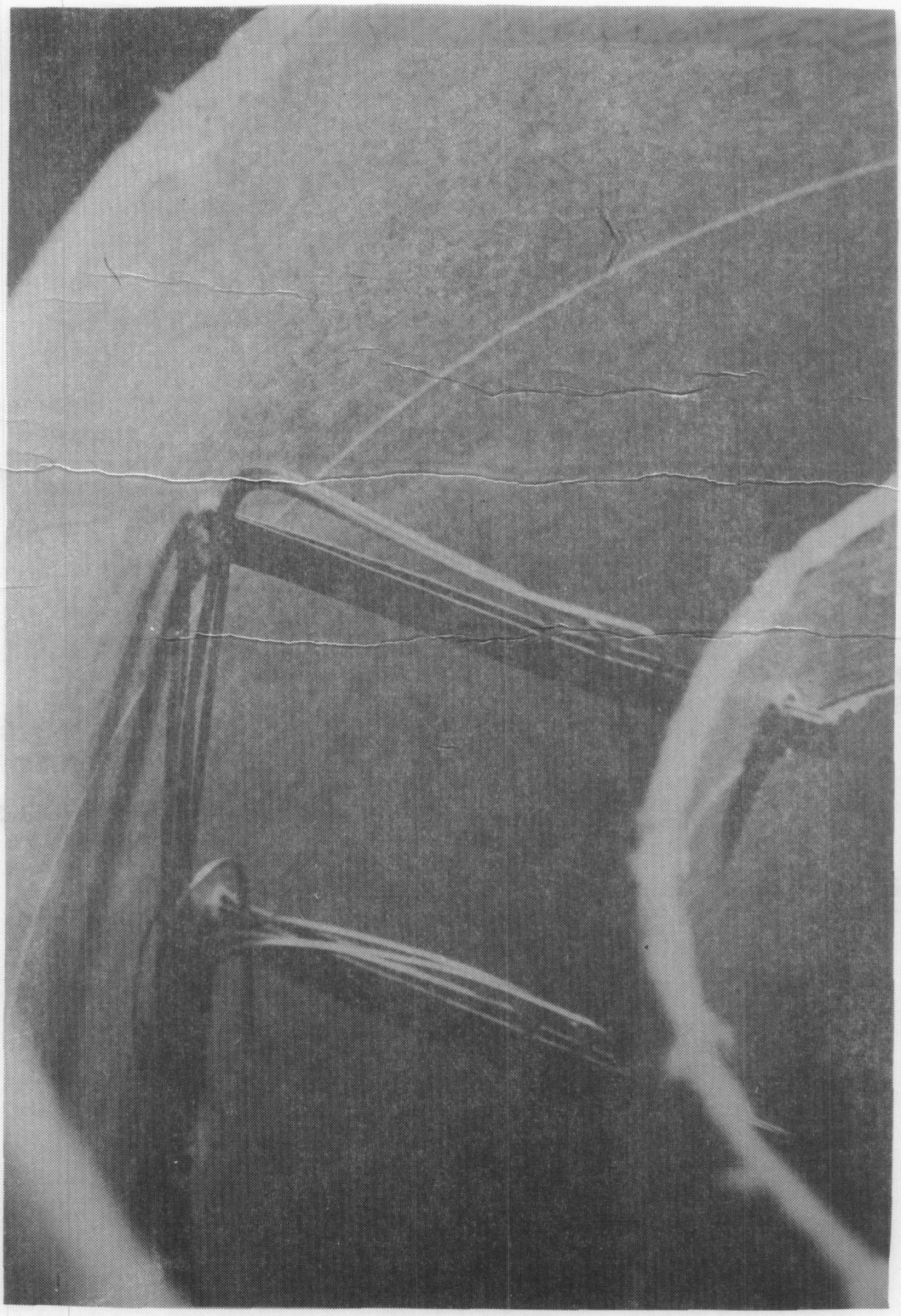

Figure E-9. Typical Installation of Type K Sidewall Thermocouple Arrays

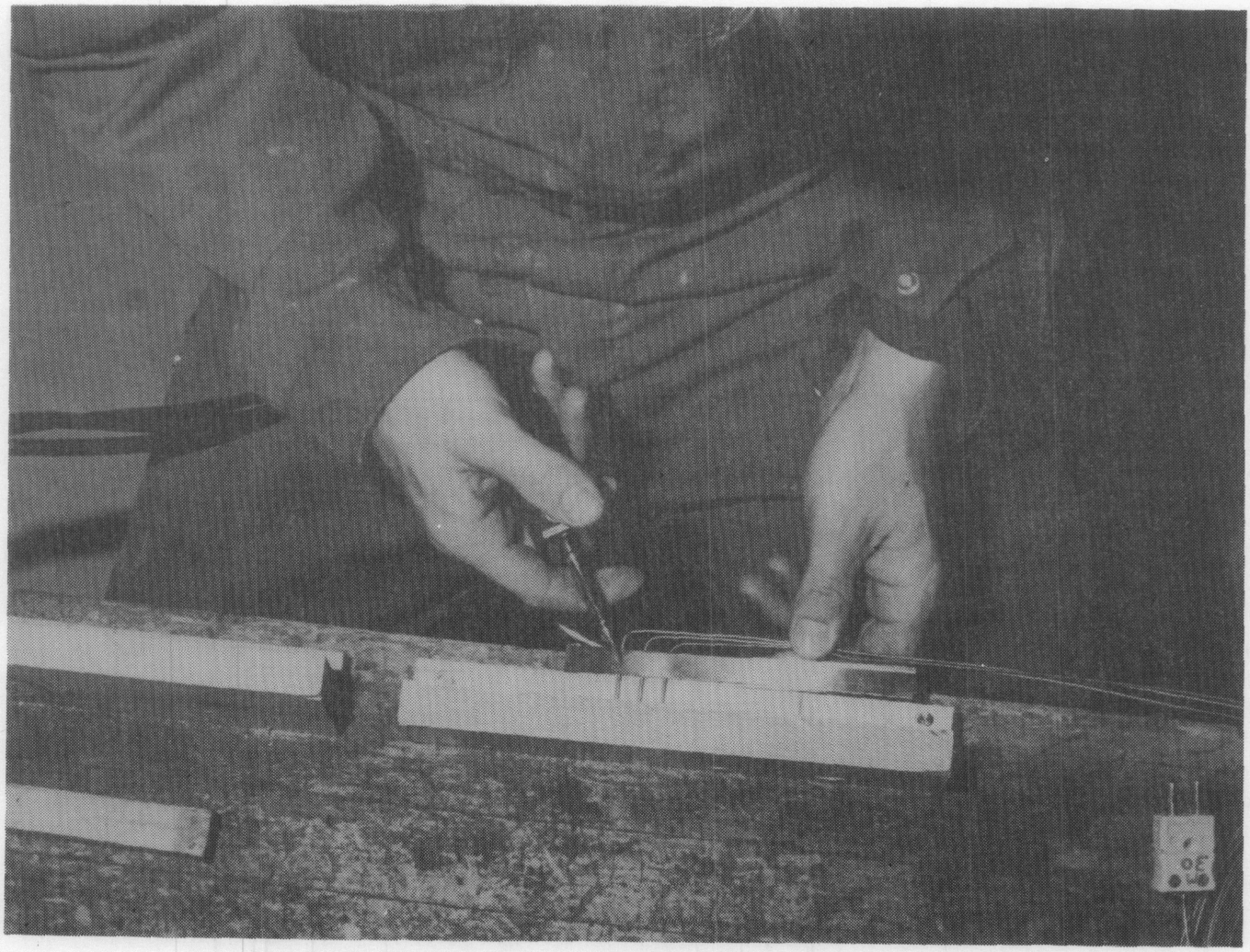

Figure E-10. Spot Welding of Sidewall Thermocouple Arrays to Stainless Steel Ribbon

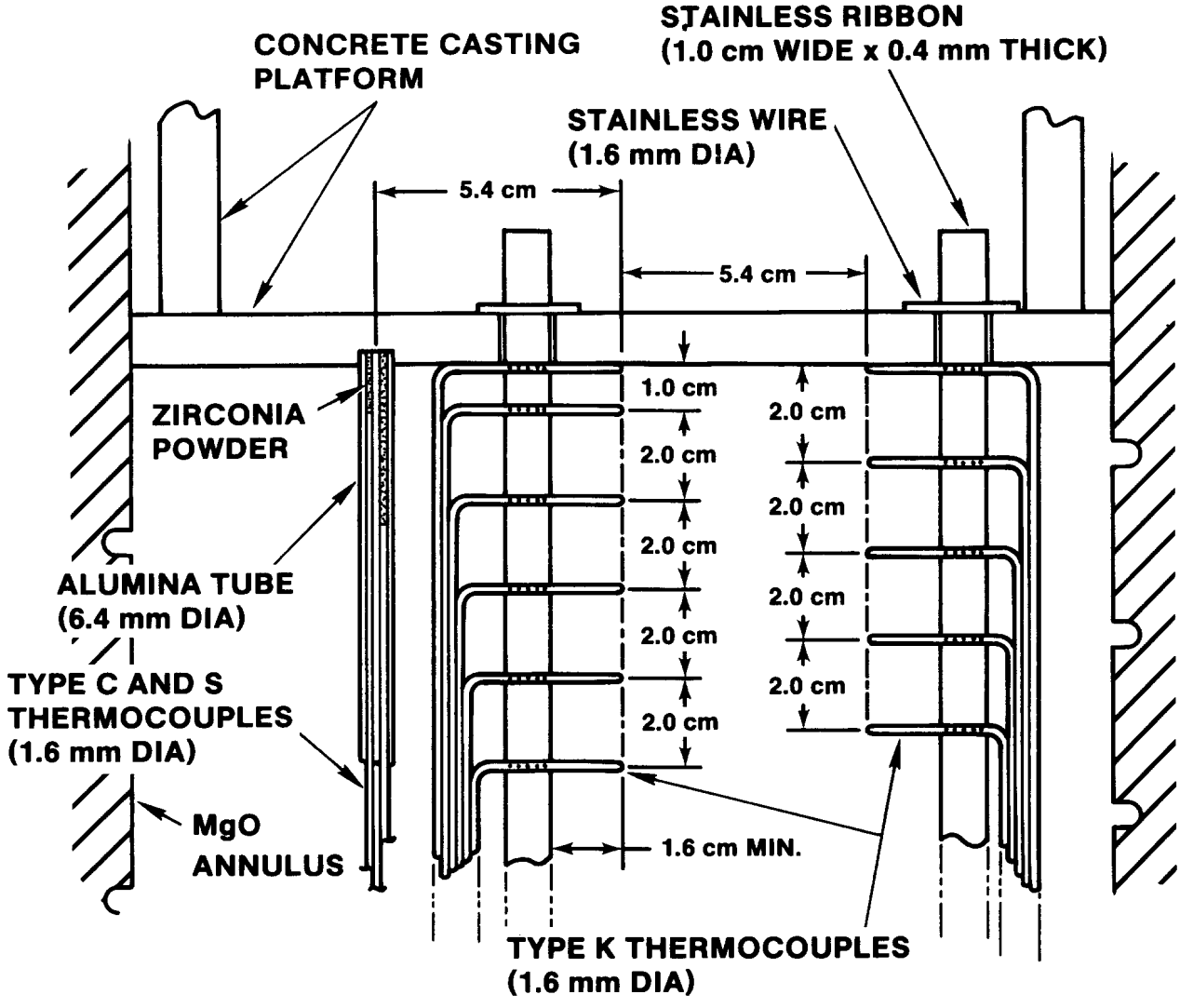

Figure E-11. Concrete Thermocouple Array, SURC-3 and 3A

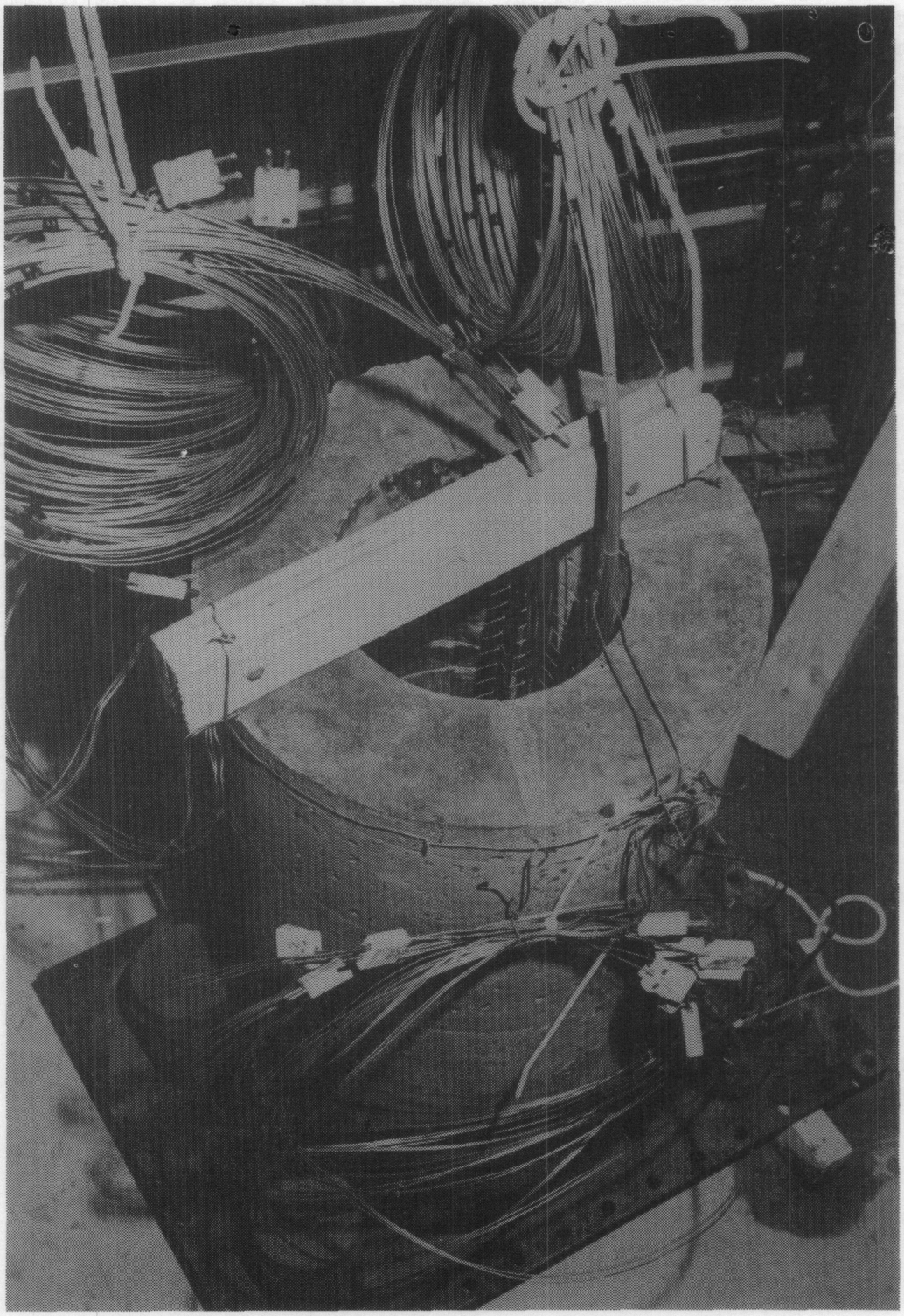

Figure E-12. Installation of Axial Thermocouple Arrays Cast Into the Concrete Slug, SURC-3 and 3A

Three, 0.64 cm diameter alumina tubes, with four 0.2 cm diameter holes, fitted with two type C (Tungsten-5% Rhenium versus Tungsten-26% Rhenium) and two type S (Platinum vs Platinum-10% Rhodium) thermocouples were cast into the concrete slug to measure melt temperature. These thermocouples had a 0.16 cm diameter tantalum sheaths. The configuration and installation of the alumina tubes is shown in Figure E-11. Each tube was installed into a counter-bored hole drilled into the plywood platform. The free end was supported using a fixture attached to the base of the crucible. The tubes were located on the mid-radius circle 10.8 cm in diameter, at 60, 180, and 300° from the type K thermocouple bundle. Figure E-13 shows a top view of the concrete slug and the orientation of thermocouple arrays and alumina tubes. Figure E-14 shows the instrumented crucible just prior to casting the concrete slug.

The casting of the concrete was performed by mixing the concrete constituents in a clean paddle mixer. Once a homogeneous mixture had been achieved, the mix was carefully placed into the casting forms using small scoops and shovels so as not to disturb any of the instrumentation locations. A pneumatic concrete vibrator, operating at 10,000 to 12,000 vibrations was used to densify the mix and remove entrained air.

Approximately 0.09 m^3 of MgO castible and 0.05 m^3 of concrete was required per crucible cast. The estimated total mass of the crucible was:

Annulus - MgO Castible

volume - 0.09 m^3 @ 2950 kg/m^3 = 265.5 kg

Concrete - Limestone

volume - 0.015 m^3 @ 2400 kg/m^3 = 36.0 kg

total mass 301.5 kg

A data sheet was initiated with each interaction crucible fabricated documenting the construction history.

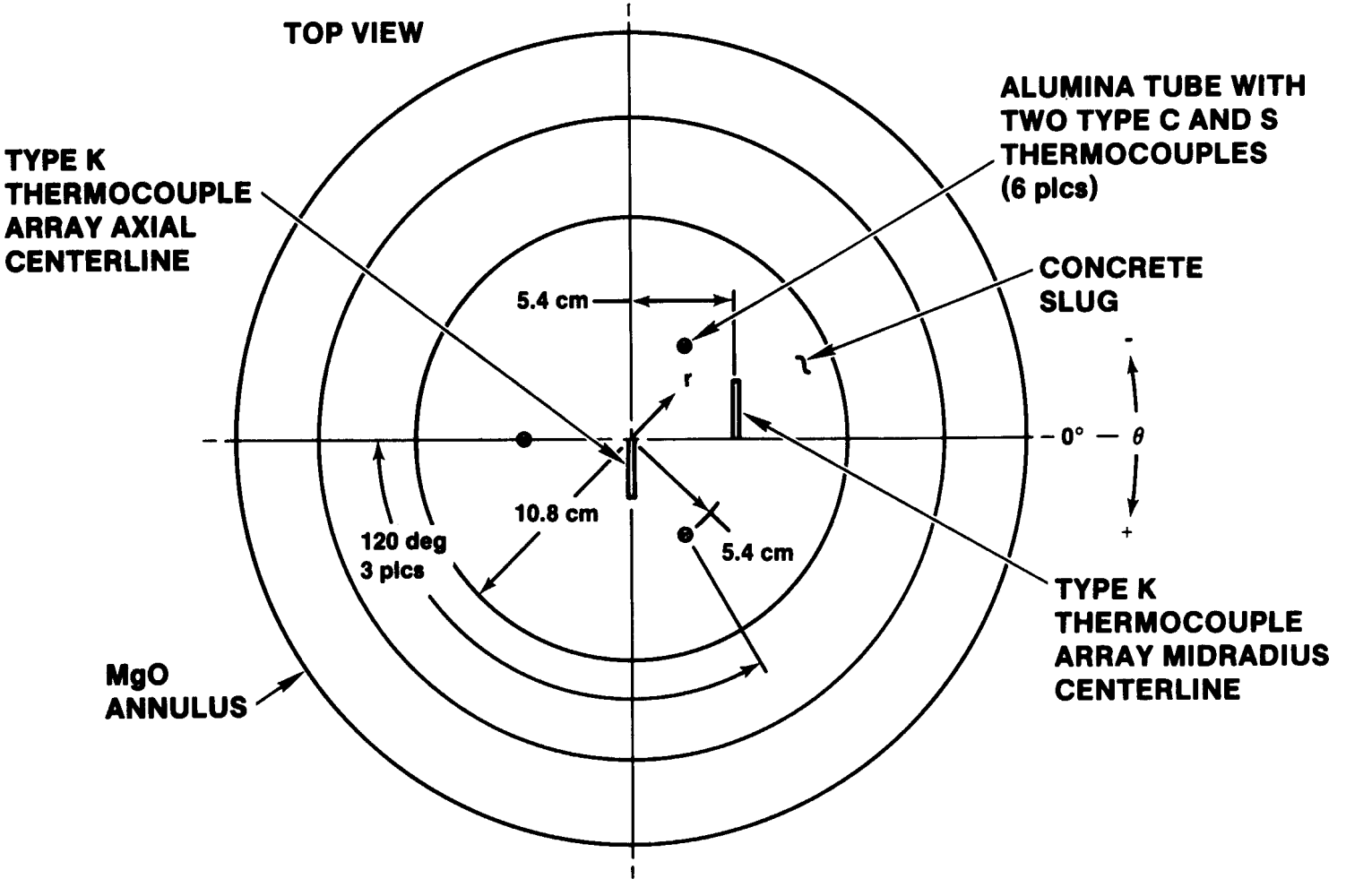

Figure E-13. Thermocouple Orientation, Concrete Slug, SURC-3 and 3A

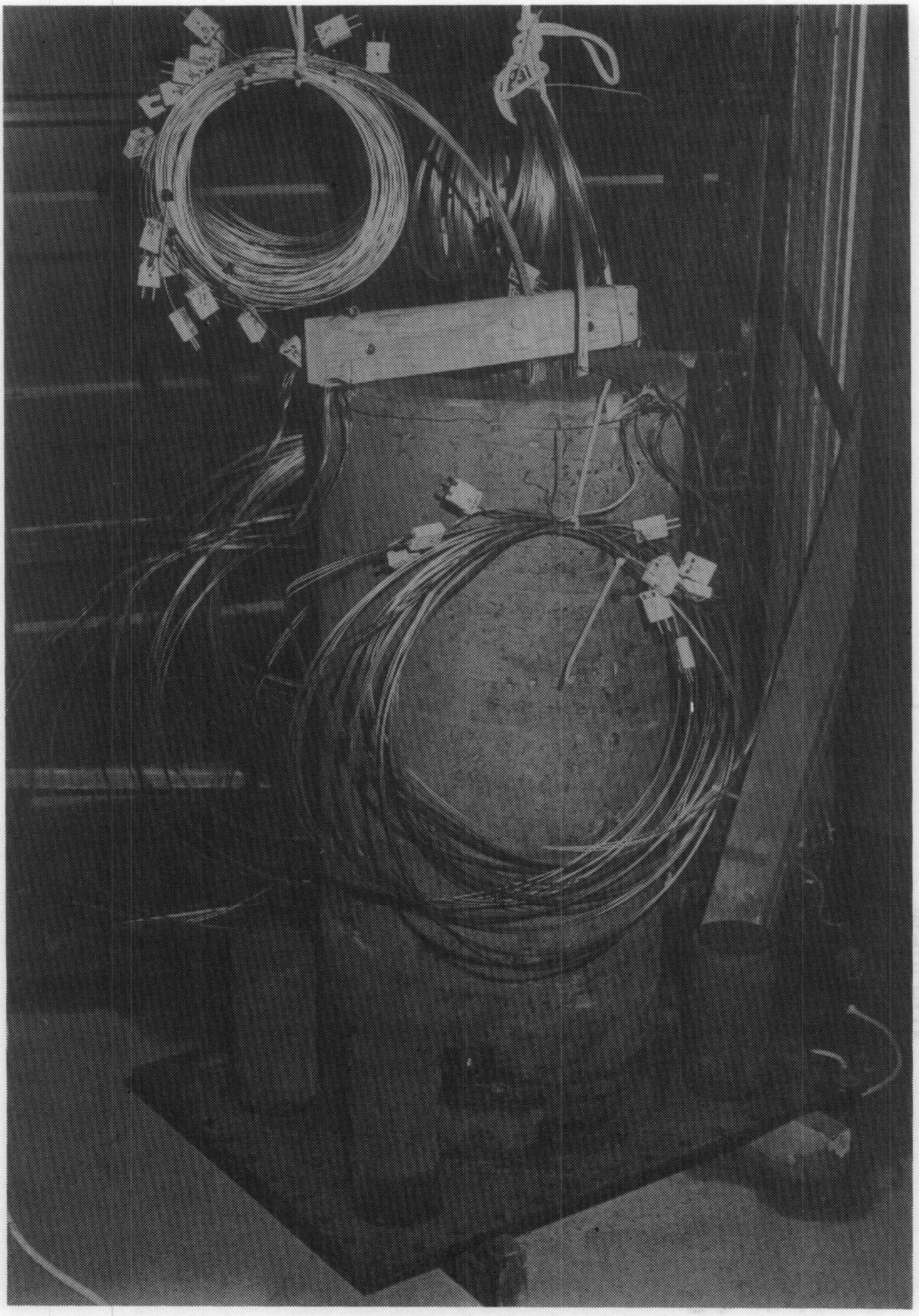

Figure E-14. Instrumented Interaction Crucible Prior to Casting

APPENDIX F

Thermocouple Data From Test QT-D

A total of 23 thermocouples were used in test QT-D to record the meltpool temperature and ablation history. Ten K-type thermocouples (designated C1 through C10) were placed along the axial centerline at intervals of 1 cm. Two additional arrays of four K-type thermocouples (designated A1A-A1D and A3A-A3D) were placed at mid-radius locations with an axial spacing of 2 cm. One set of four C-type thermocouples was positioned at a mid-radius location (designated A2A-A2D) with an axial spacing of 2 cm and there was one K-type thermocouple (Designated M1) attached to the steel slug to record the initial melt temperature. Details of these thermocouples and their placement are given in Section 2.1.3 and Table 2.1.5. Figures F-1 through F-6 show the data recorded from the QT-D thermocouples.

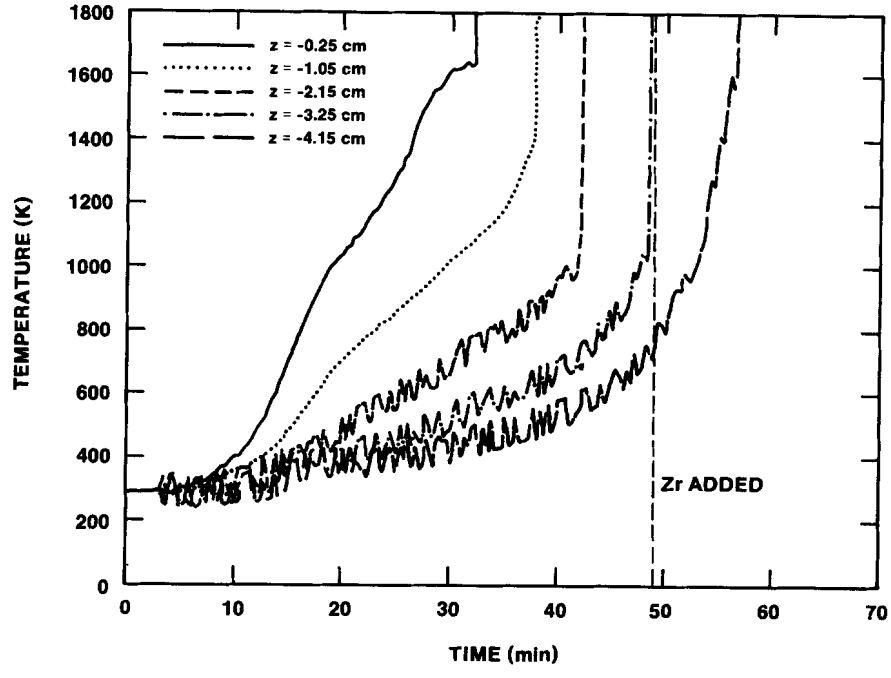

Figure F-1. Axial Thermal Response

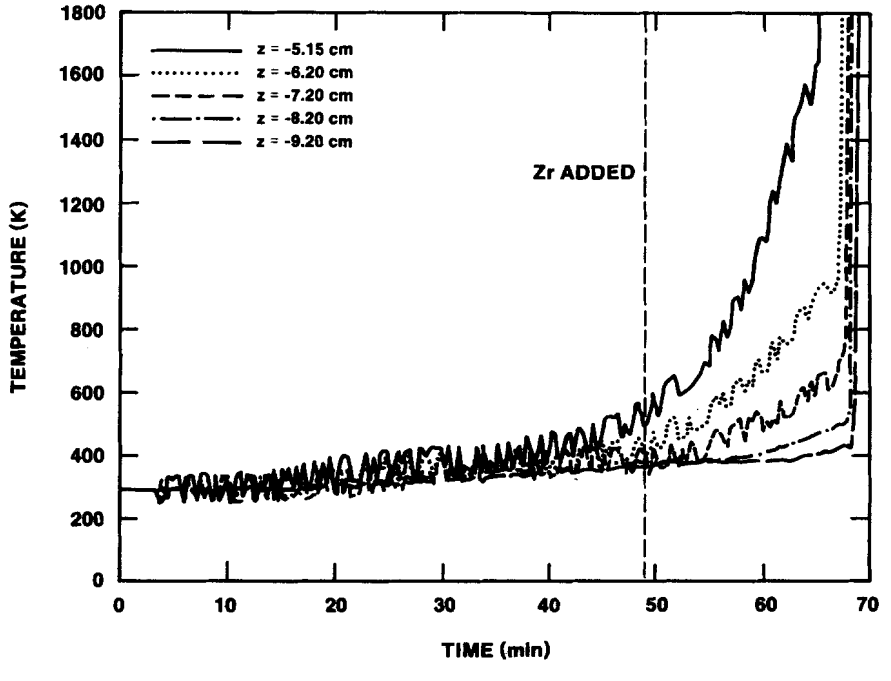

Figure F-2. Axial Thermal Response

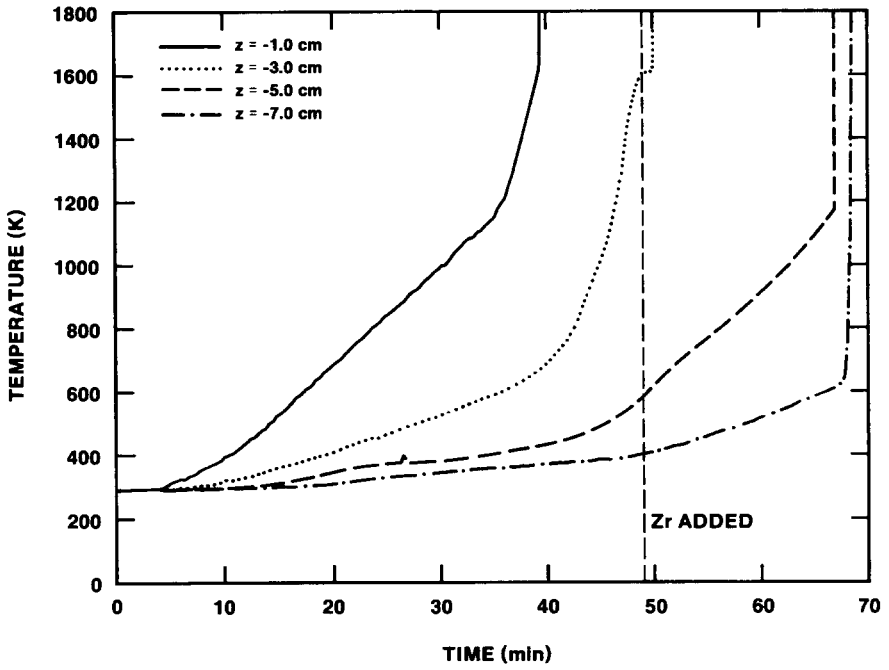

Figure F-3. A-1 Array Thermal Response

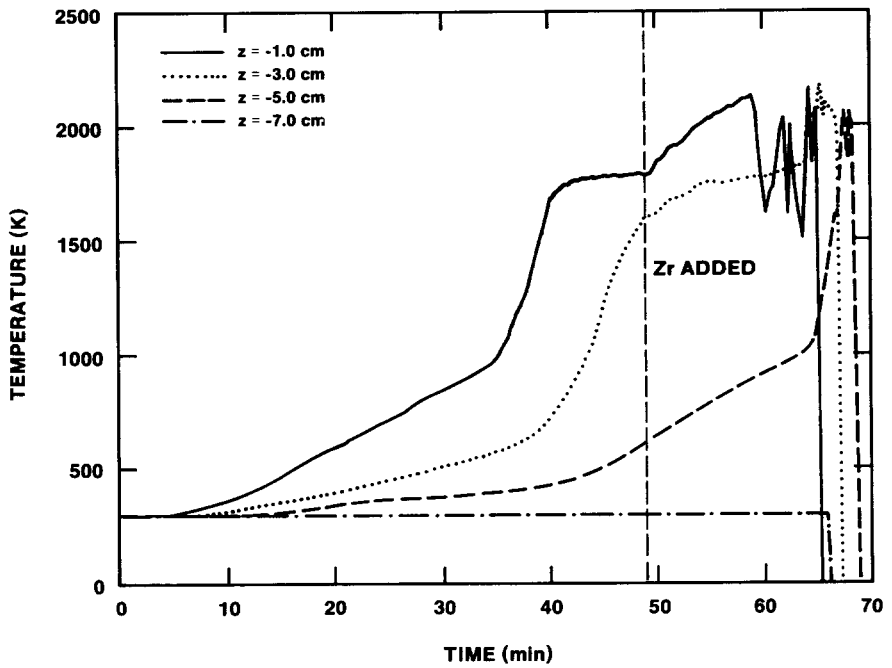

Figure F-4. A-2 Array Thermal Response

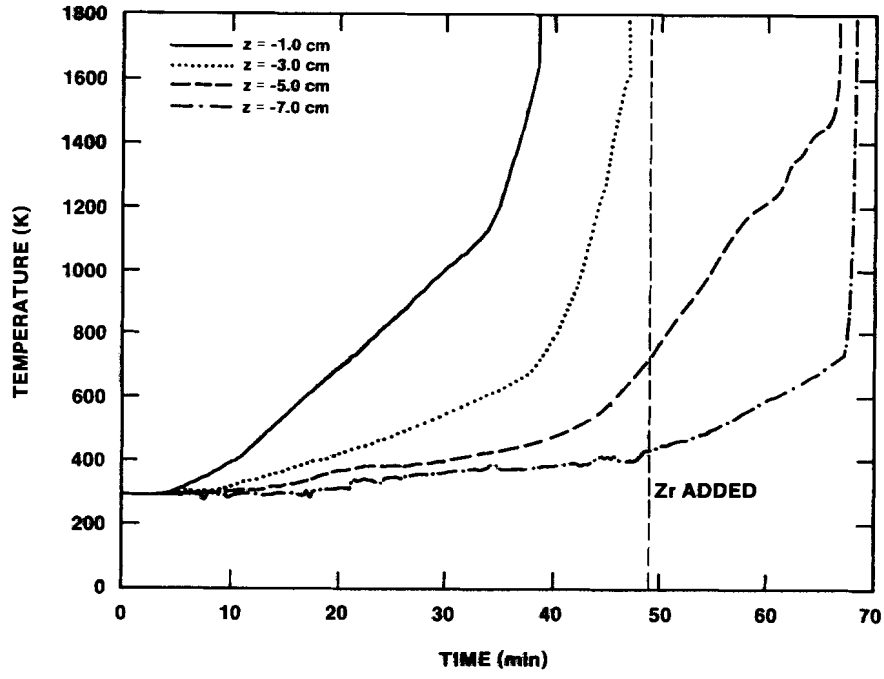

Figure F-5. A-3 Array Thermal Response

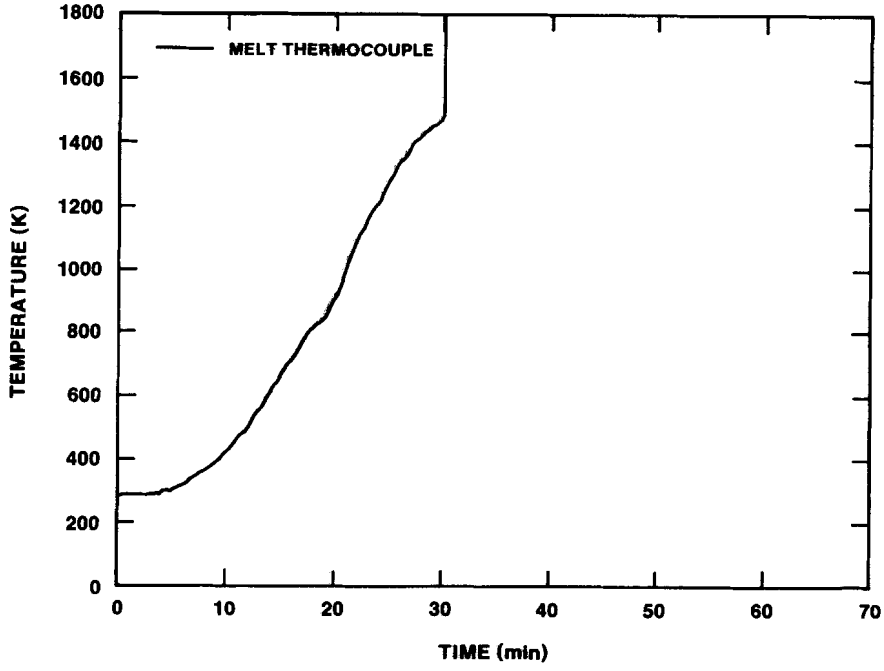

Figure F-6. Initial Melt Temperature

APPENDIX G

Thermocouple Data from Test QT-E

G.1 Temperatures Indicated by Thermocouples Cast Into the Base of the Interactor Crucible, Test QT-E

Temperature data obtained with thermocouples embedded in the base of the interactor crucible used in the QT-E test are shown in Figures G-1 through G-6. The locations and labels for these thermocouples can be found in Table 2.2.1 of the text. Thermocouple C12 became erratic at approximately t = 70 minutes. The thermal response of the other 23 thermocouples cast into the base appeared to be normal.

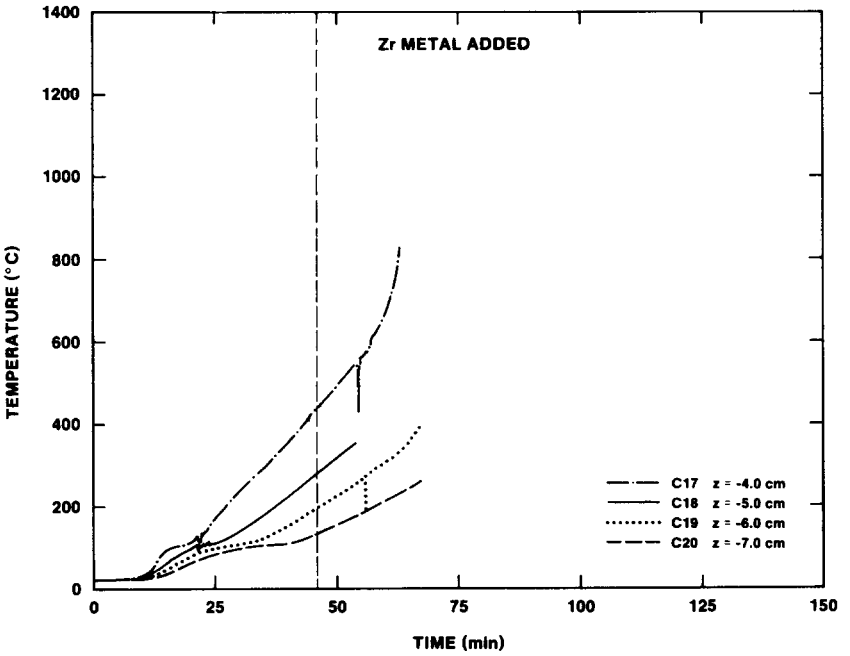

Figure G-5. Concrete Radial Array

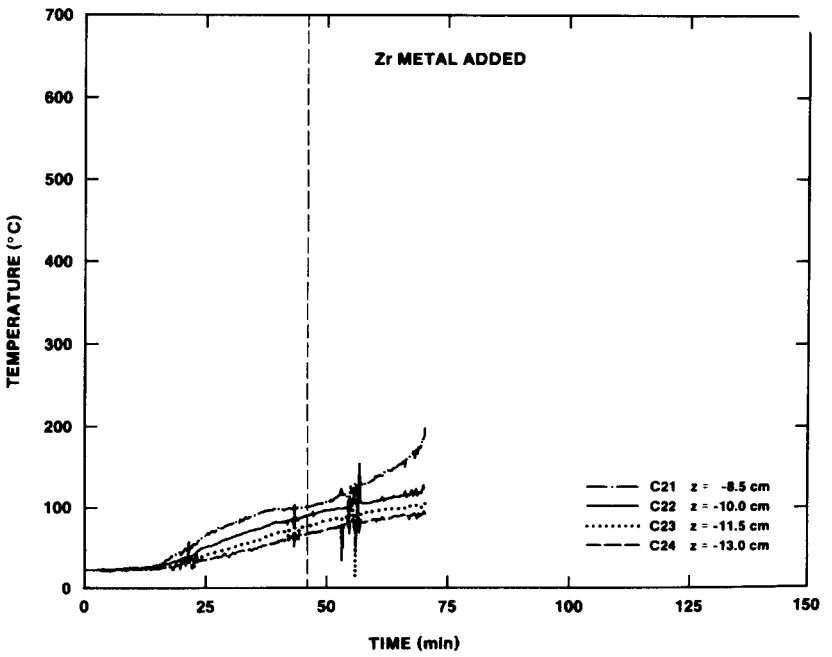

Figure G-6. Concrete Radial Array

G.2 Temperatures Indicated by Thermocouples Cast Into the Concrete Annulus, Test QT-E

Temperature data obtained with thermocouples cast into the concrete sidewalls of the QT-E crucible are shown in Figures G-7 through G-11. The locations and labels for these thermocouples are described in Table 2.2.1 of the text. All 35 thermocouples produced data and appeared to respond normally.

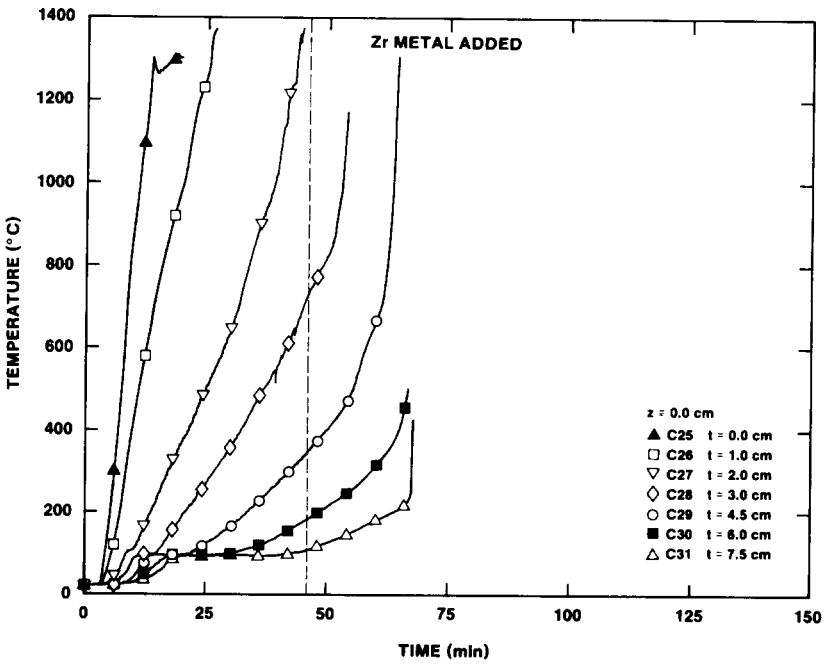

Figure G-7. Z = 0 Array

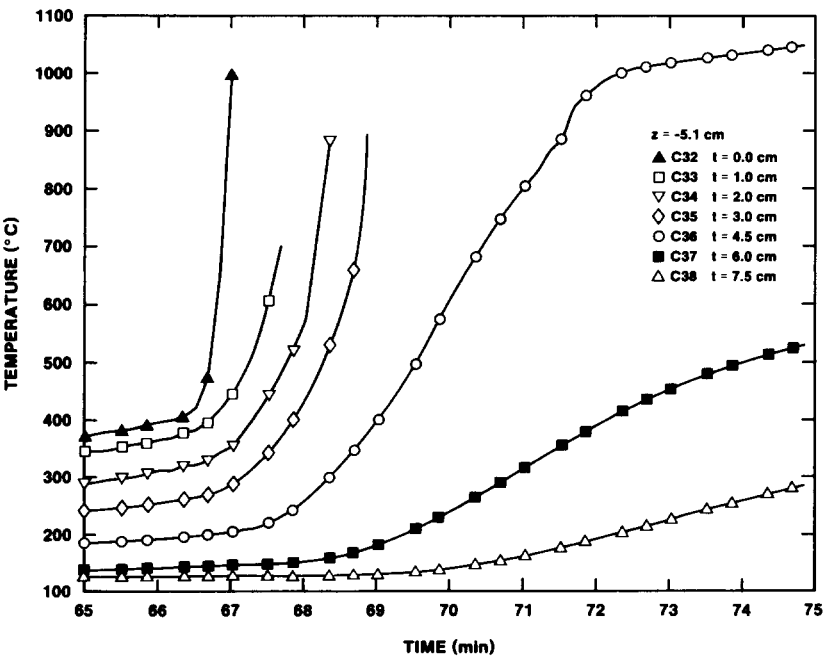

Figure G-8. Z = -5.1 Array

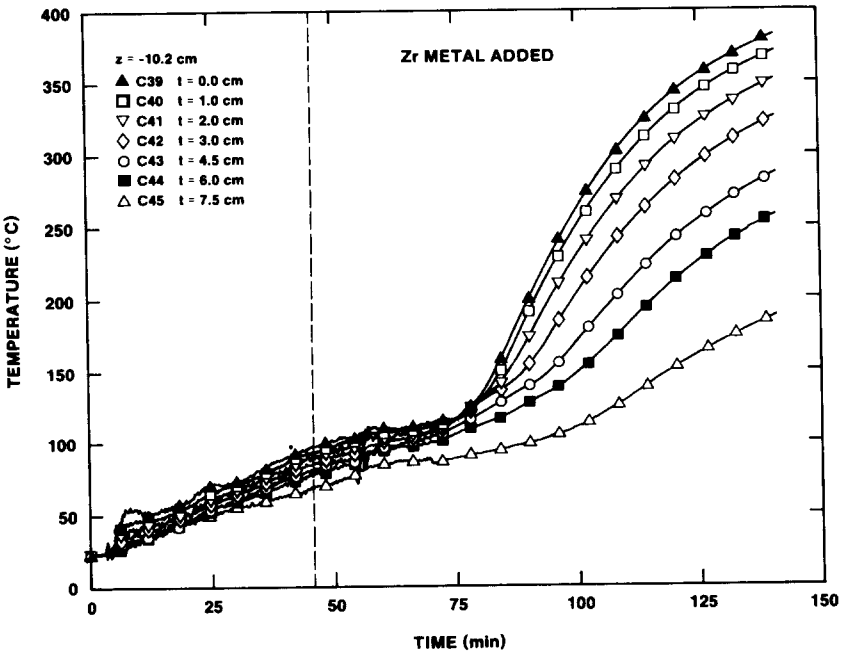

Figure G-9. Z = -10.2 Array

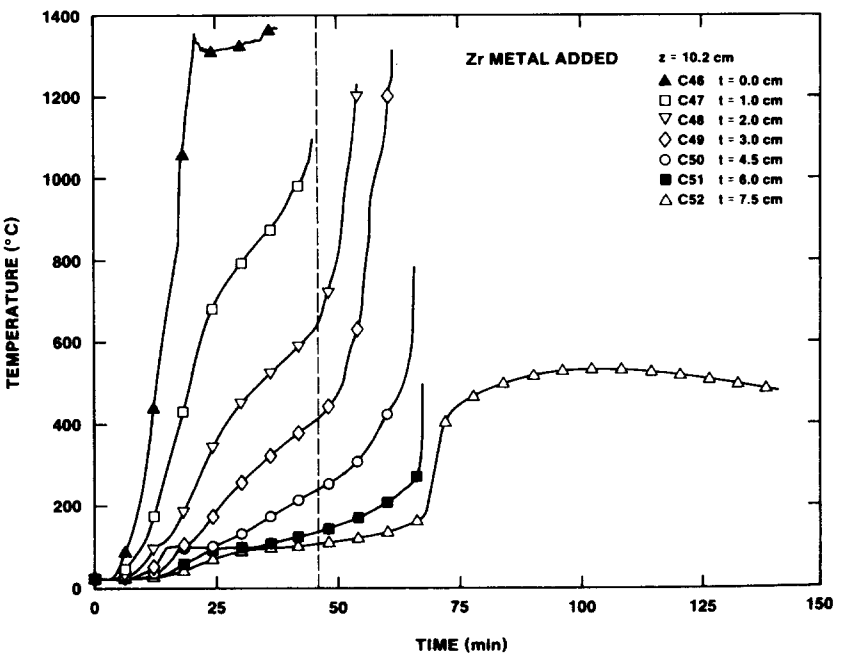

Figure G-10. Z = +10.2 Array

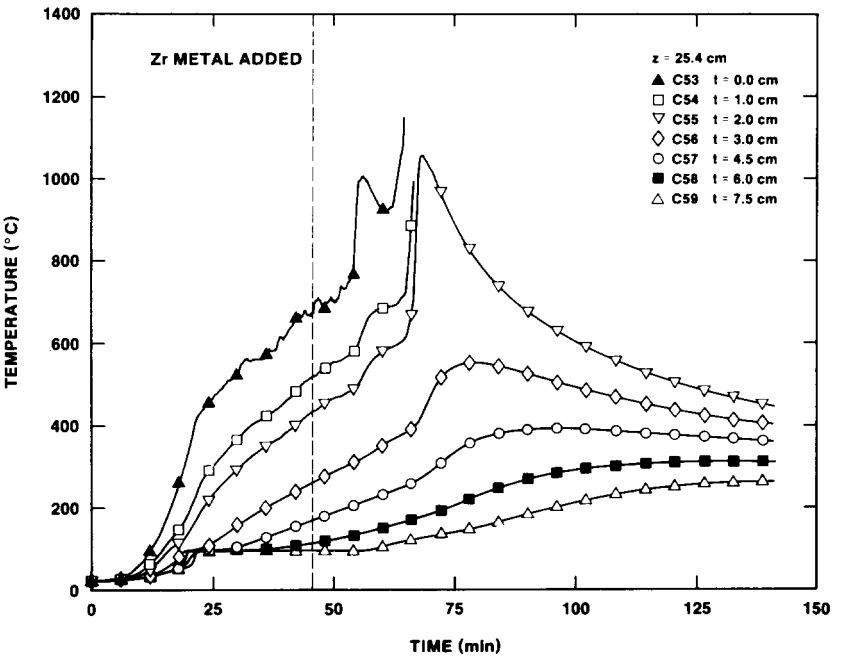

Figure G-11. Z = +25.4 Array

APPENDIX H

Thermocouple and Heat Flux Results From Test SURC-3

H.1 Temperatures Indicated by Thermocouples Cast Into the Concrete Slug, Test SURC-3.

Temperature data obtained with thermocouples embedded in the concrete slug used in the SURC-3 test are shown in Figures H-1 through H-8. The locations and the labels for these thermocouples can be found in Table 2.3.6 of the text. Thermocouples C1 (Figure H-1) and C21 (Figure H-5) failed prior to the start of the test.

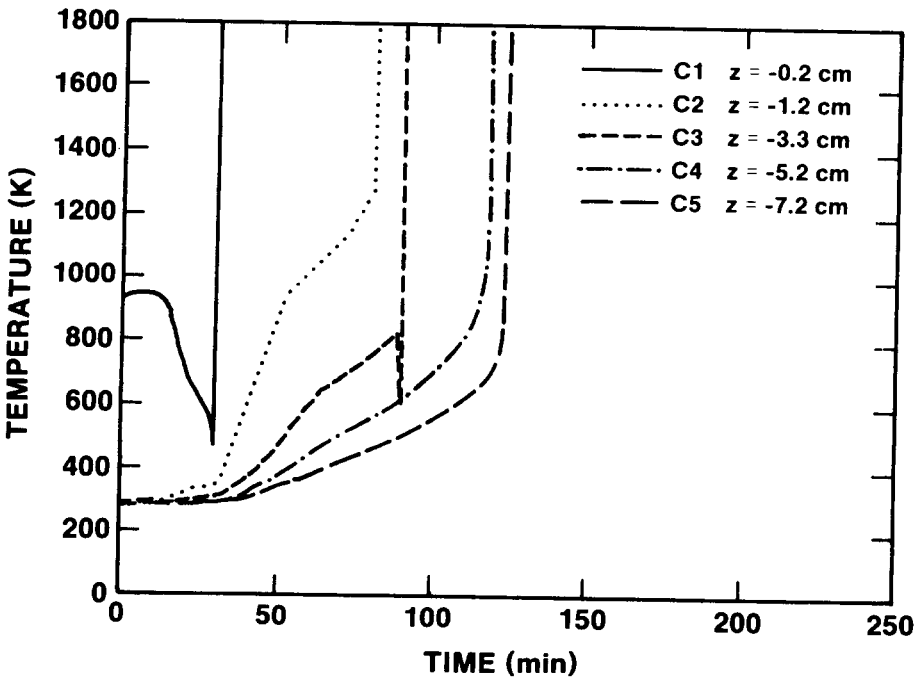

Figure H-1. Concrete Temperature Data Measured by Thermocouples Located on the Axial Centerline at z = -0.2, -1.2, -3.3, -5.2 and -7.2 cm, SURC3

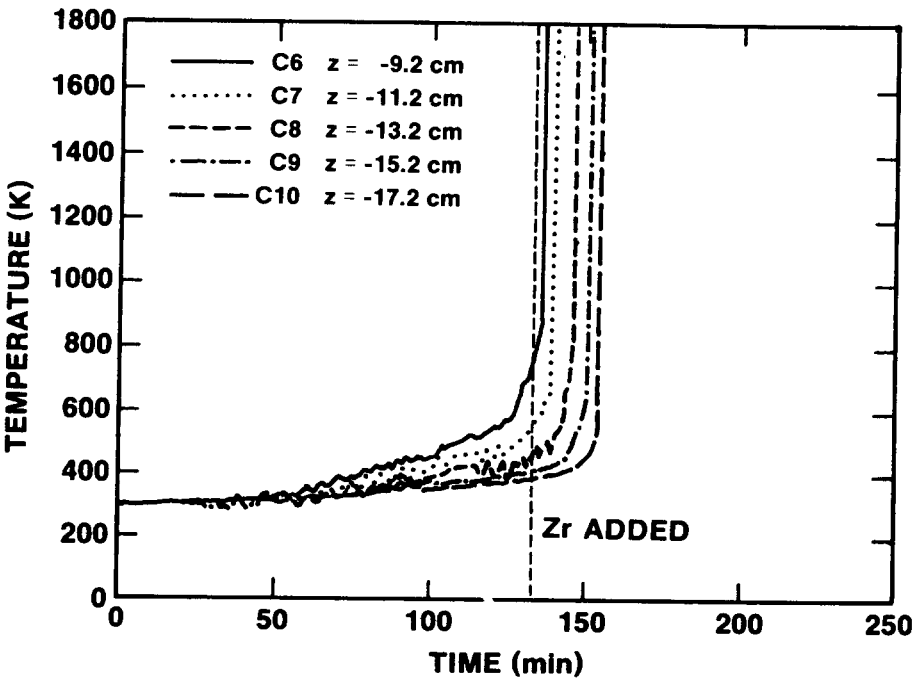

Figure H-2. Concrete Temperature Data Measured by Thermocouples Located on the Axial Centerline at z = -9.2, -11.2, -13.2, -15.2, and -17.2 cm, SURC-3

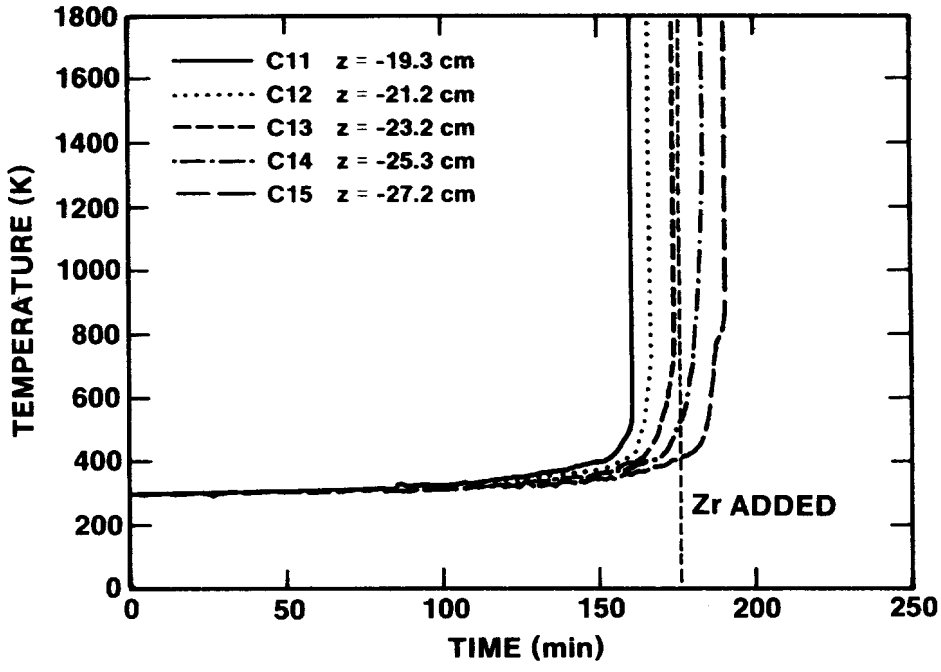

Figure H-3. Concrete Temperature Data Measured by Thermocouples Located on the Axial Centerline at z = -19.3, -21.2, -23.2, -25.3 and -27.2 cm, SURC3

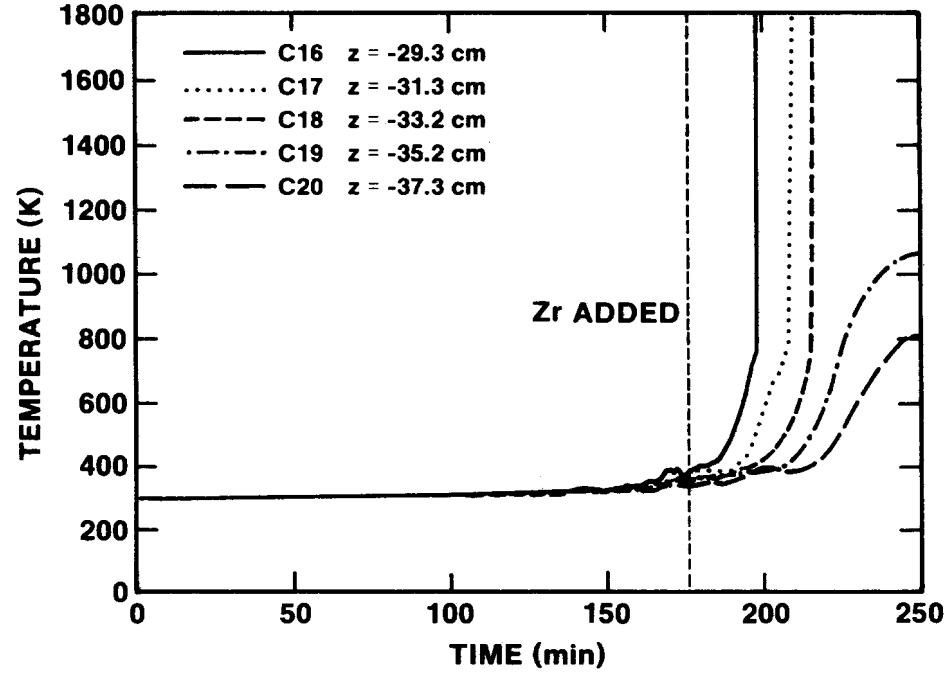

Figure H-4. Concrete Temperature Data Measured by Thermocouples Located on the Axial Centerline at z = -29.3, -31.3, -33.2, -35.2, and -37.3 cm, SURC-3

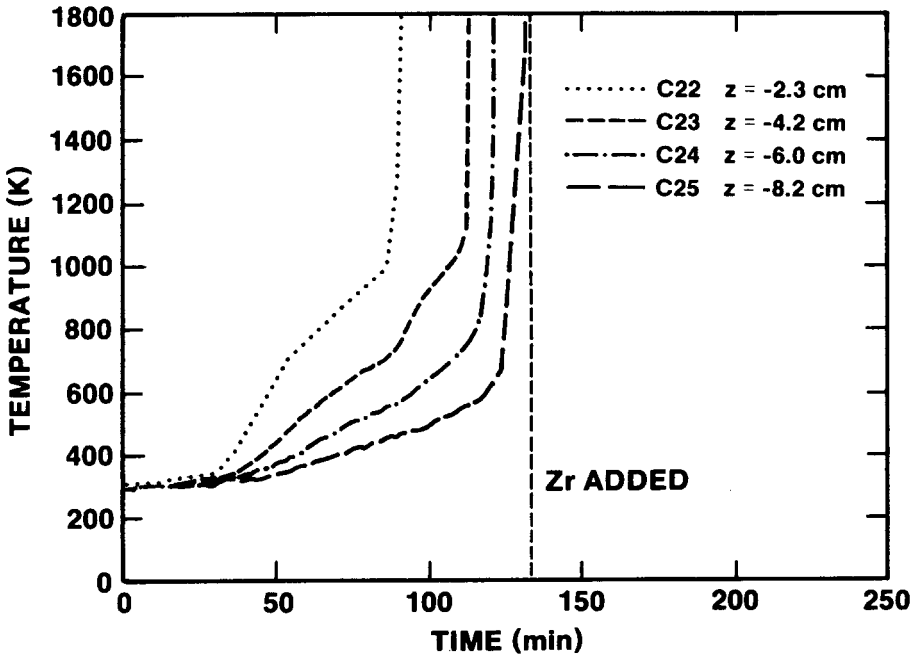

Figure H-5. Concrete Temperature Data Measured by Thermocouples Located on the Axial Centerline at z = -0.2, -2.3, -4.2, -6.0 and -8.2 cm, SURC3

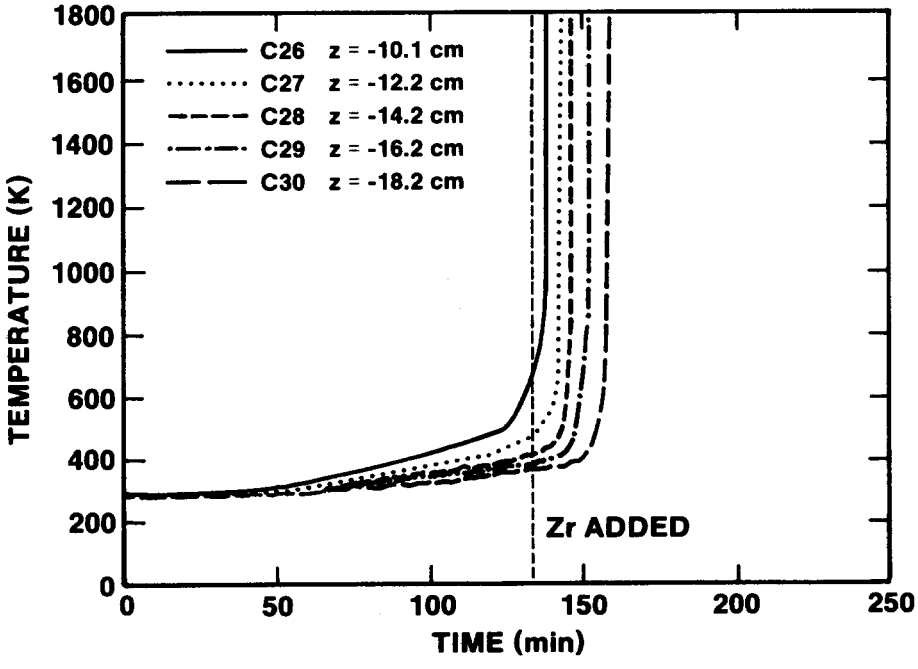

Figure H-6. Concrete Temperature Data Measured by Thermocouples Located on the Axial Centerline at z = -10.1, -12.2, -14.2, -16.2, and -18.2 cm, SURC-3

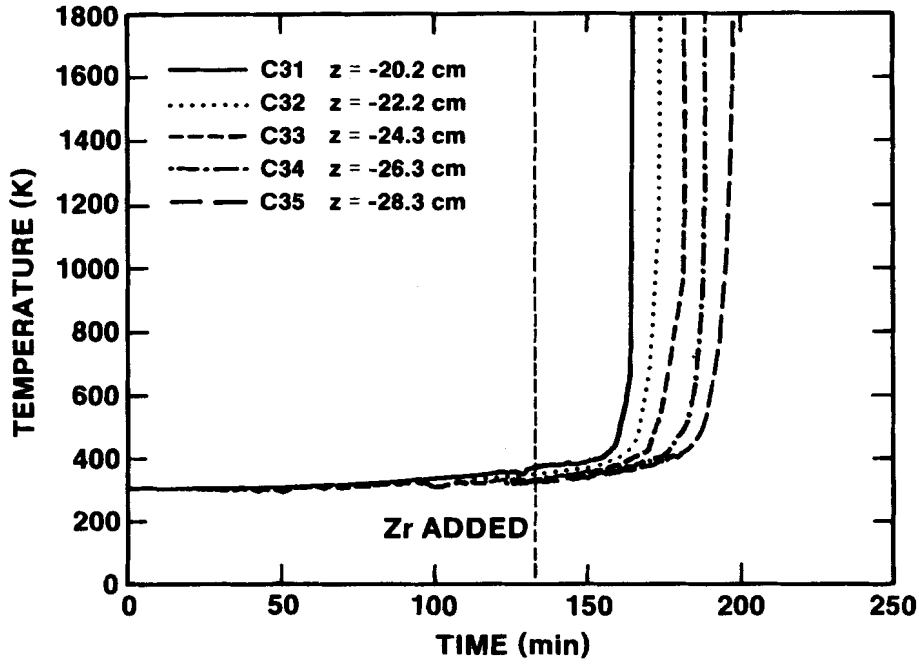

Figure H-7. Concrete Temperature Data Measured by Thermocouples Located on the Axial Centerline at z = -20.2, -22.2, -24.3, -26.3 and -28.3 cm, SURC-3

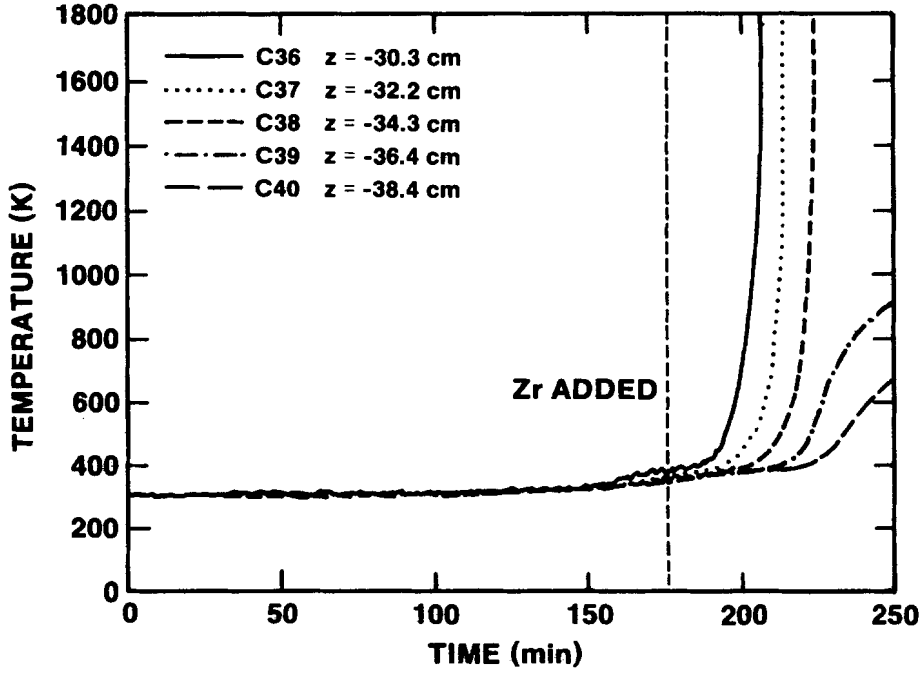

Figure H-8. Concrete Temperature Data Measured by Thermocouples Located on the Axial Centerline at z = -30.3, -32.2, -34.3, -36.4, and -38.4 cm, SURC-3

H.2 Temperatures Indicated by C and S Type Thermocouples Installed in Alumina Tubes and Cast Into the Concrete Slug, Test SURC-3

Several type C and S thermocouples were installed into alumina tubes and cast into the concrete slug to measure melt temperature. Temperatures indicated by these thermocouples are shown as a function of time in Figures H-9 through H-11. The locations and the labels for these thermocouples can be found in Table 2.3.7 of the text. The output of the thermocouple was set to a reading of zero when the operational range was exceeded. All the thermo-couples except A2-4 and A3-4, (Figure H-11) failed due to extended contact with the meltpool. The thermocouples identified above were below the erosion front at test termination.

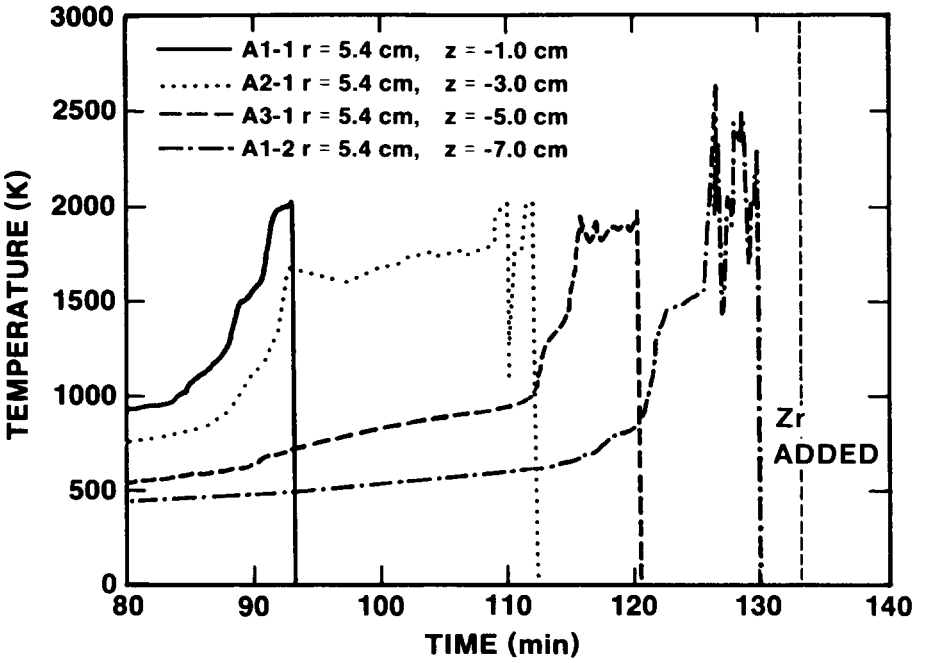

Figure H-9. Melt Temperature Data Measured by Type C and S Thermocouples Cast Into the Concrete Slug at z = -1.0, -3.0, -5.0, and -7.0 cm, SURC-3

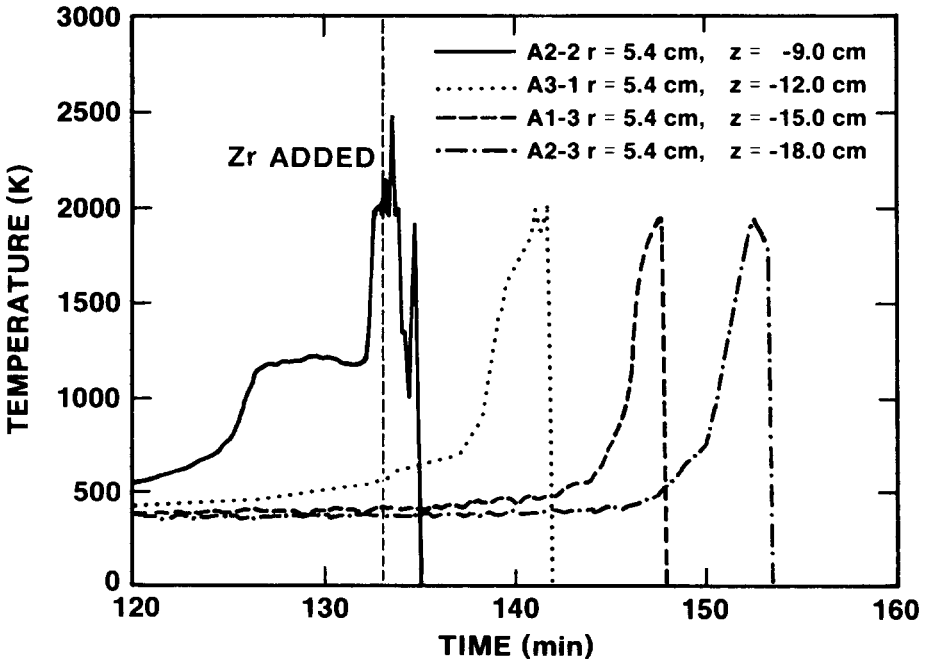

Figure H-10. Melt Temperature Data Measured by Type C and S Thermocouples Cast Into the Concrete Slug at z = -9.0, -12.0, -15.0, and -18.0 cm, SURC-3

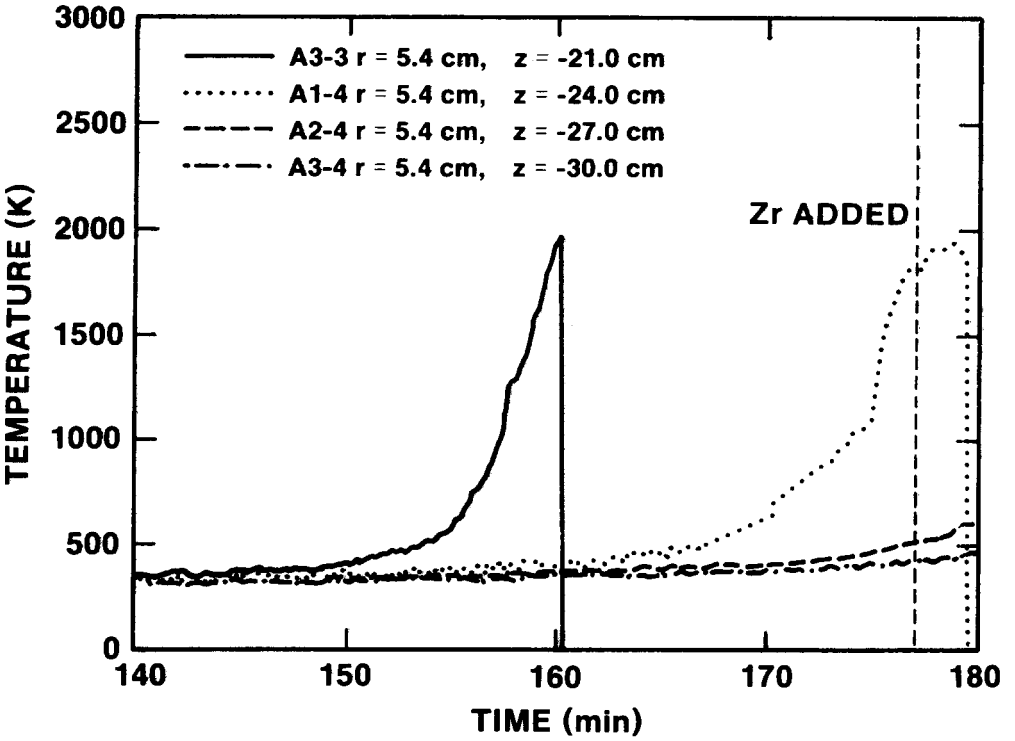

Figure H-11. Melt Temperature Data Measured by Type C and S Thermocouples Cast Into the Concrete Slug at z = -21.0, -24.0, -27.0, and -30.0 cm, SURC-3

H.3 - Temperatures Indicated by Thermocouples Cast Into the MgO Sidewall, Test SURC-3

Temperature data obtained with thermocouples cast into the magnesia walls of the SURC-3 crucible are shown in Figures H-12 through H-22. The locations and labels for the thermocouples are described in Table 2.3.8 of the text. Thermocouple M3 (Figure H-12) fails prematurely at t = 45 minutes into the test. Thermocouples M15 and M16 behave erratically at approximately t = 120. The reason for this is not known. All the other thermocouples cast into the annulus responded as expected.

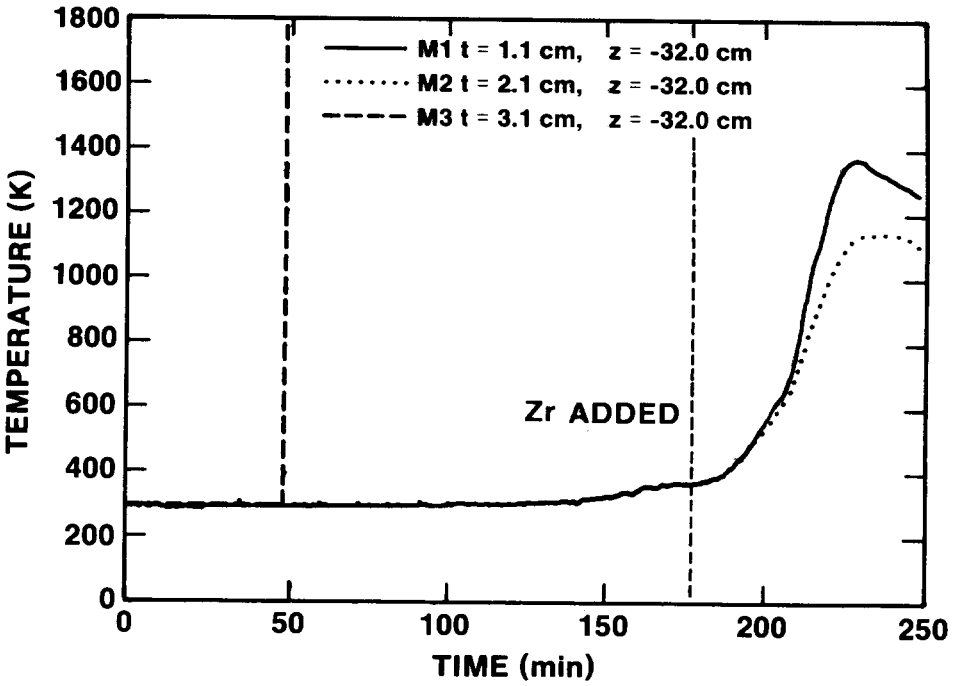

Figure H-12. MgO Sidewall Temperature Data Measured by Thermocouples in the Array Located at z = -32.0 cm, SURC-3

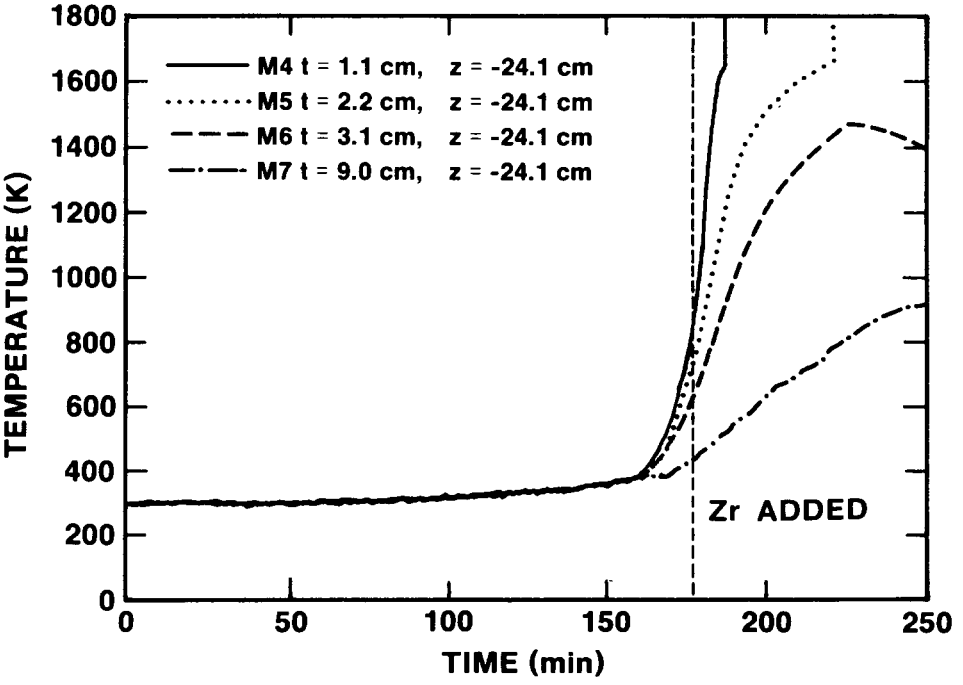

Figure H-13. MgO Sidewall Temperature Data Measured by Thermocouples in the Array Located at z = -24.1 cm, SURC-3

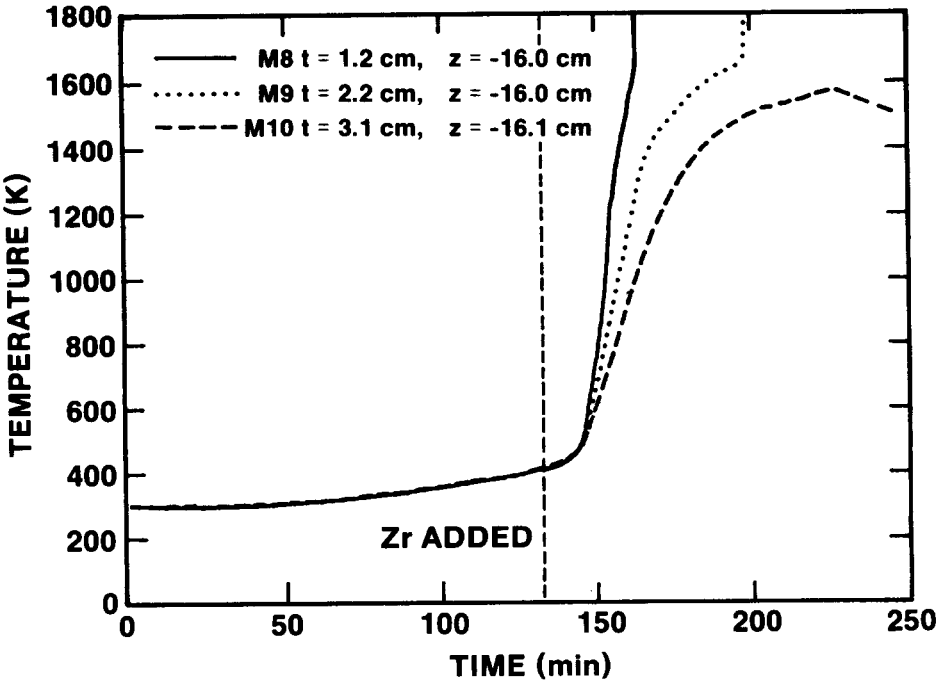

Figure H-14. MgO Sidewall Temperature Data Measured by Thermocouples in the Array Located at z = -16.0 cm, SURC-3

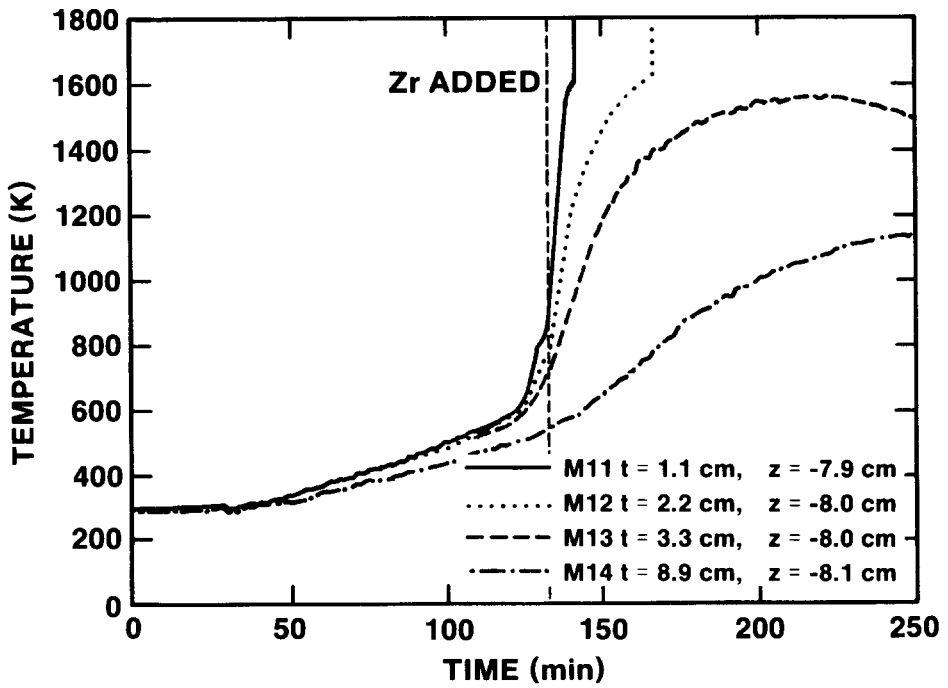

Figure H-15. MgO Sidewall Temperature Data Measured by Thermocouples in the Array Located at z = -8.0 cm, SURC-3

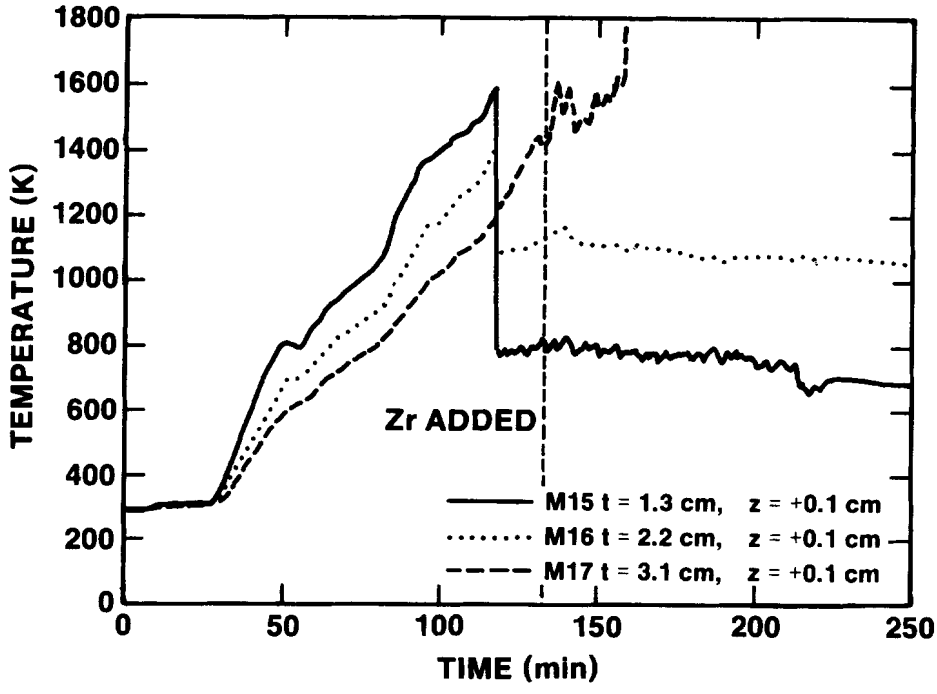

Figure H-16. MgO Sidewall Temperature Data Measured by Thermocouples in the Array Located at z = -0.1 cm, SURC-3

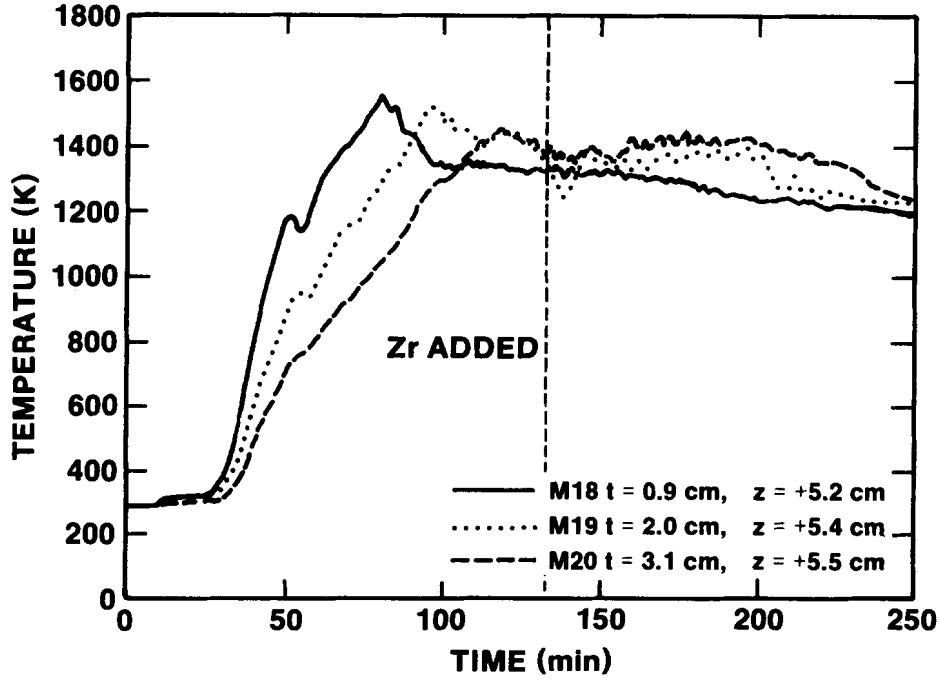

Figure H-17. MgO Sidewall Temperature Data Measured by Thermocouples in the Array Located at z = -5.4 cm, SURC-3

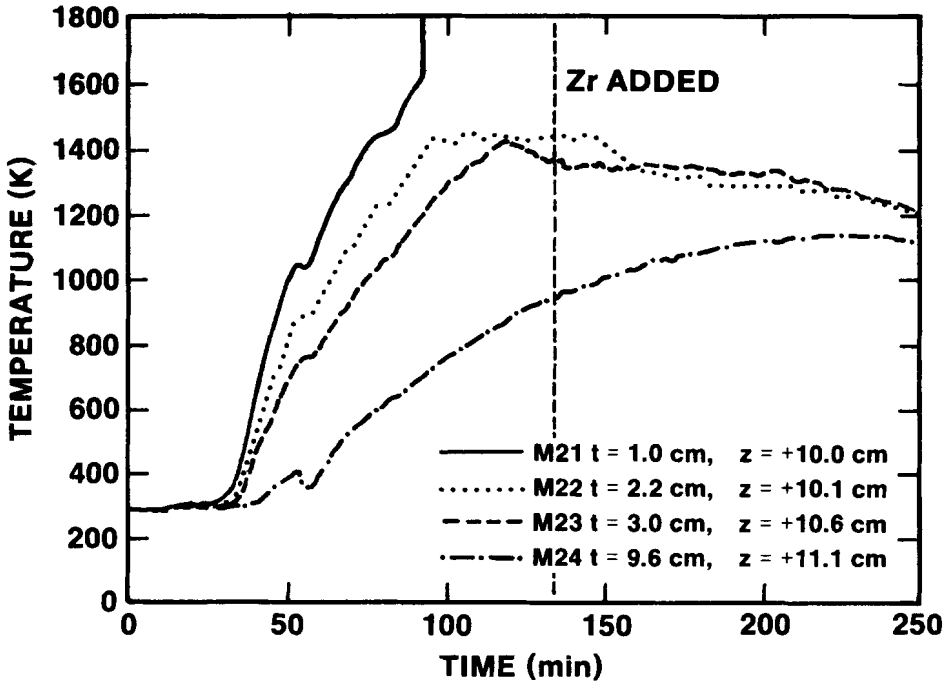

Figure H-18. MgO Sidewall Temperature Data Measured by Thermocouples in the Array Located at z = -10.1 cm, SURC-3

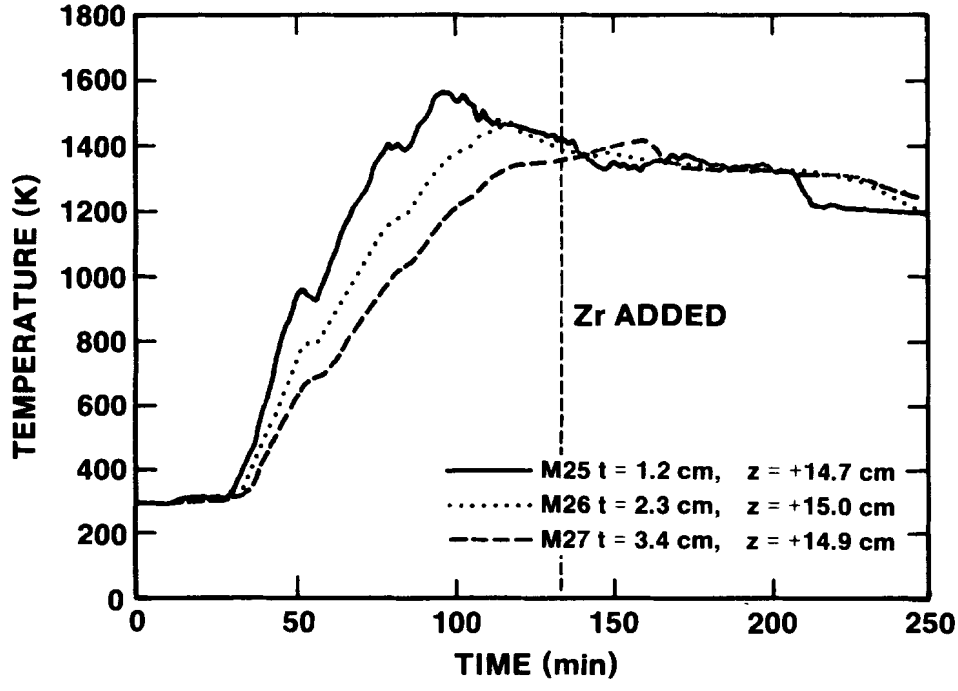

Figure H-19. MgO Sidewall Temperature Data Measured by Thermocouples in the Array Located at z = -14.9 cm, SURC-3

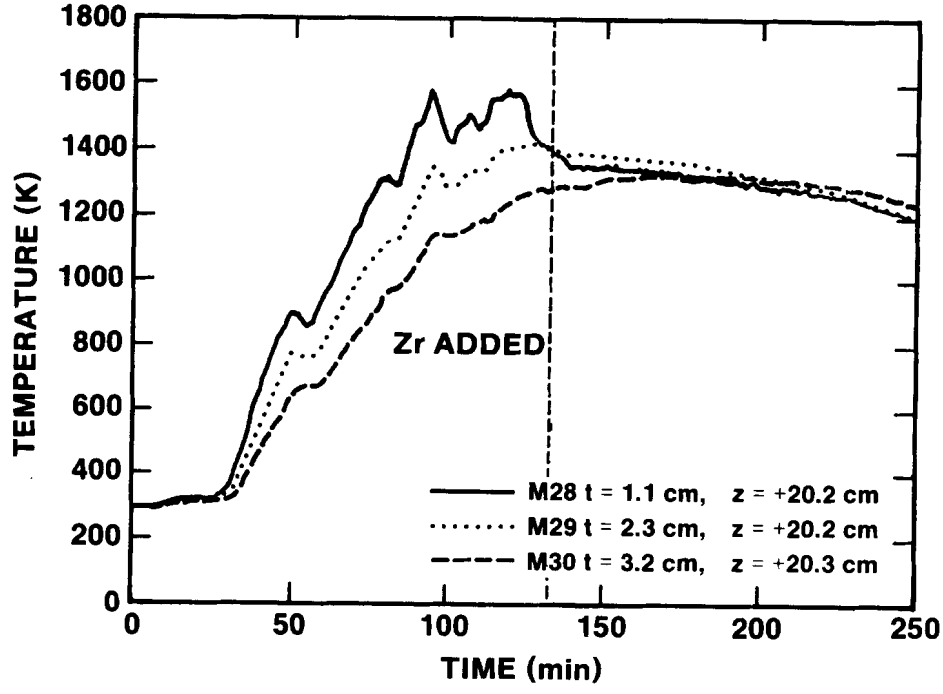

Figure H-20. MgO Sidewall Temperature Data Measured by Thermocouples in the Array Located at z = -20.2 cm, SURC-3

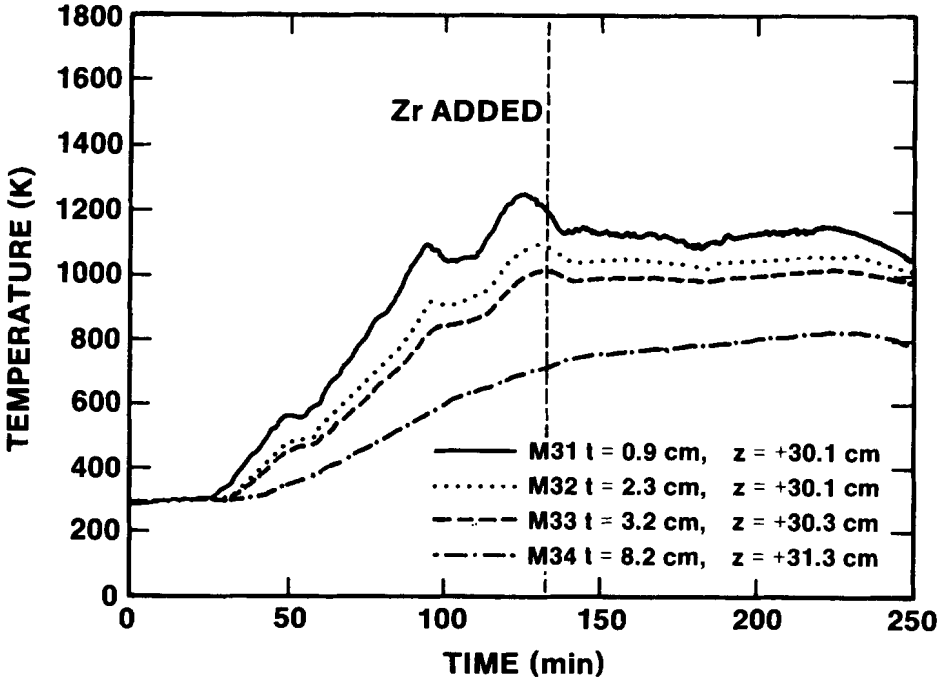

Figure H-21. MgO Sidewall Temperature Data Measured by Thermocouples in the Array Located at z = -30.1 cm, SURC-3

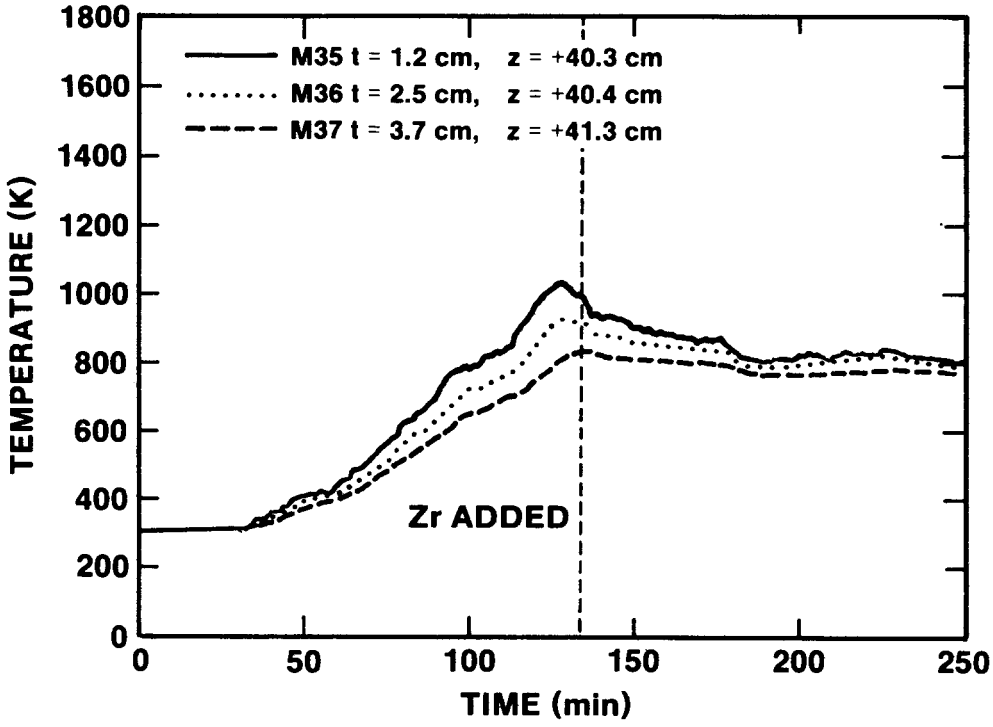

Figure H-22. MgO Sidewall Temperature Data Measured by Thermocouples in the Array Located at z = -40.3 cm, SURC-3

H.4 - Heat Fluxes Derived from Data Produced by Thermocouples Cast Into the MgO Sidewall, Test SURC-3

Heat fluxes derived by the inverse heat flux method from temperature data for the magnesia crucible walls in the SURC-3 test are shown in Figures H-23 through H-33. The locations for these heat flux determinations are described in Table 2.3.8 of the text. Heat flux calculations are terminated early in Figures H-25 through H-28 due to decomposition of the sidewalls in contract with the melt. This affected the material property data and the accuracy of calculations beyond the times shown would be suspect.

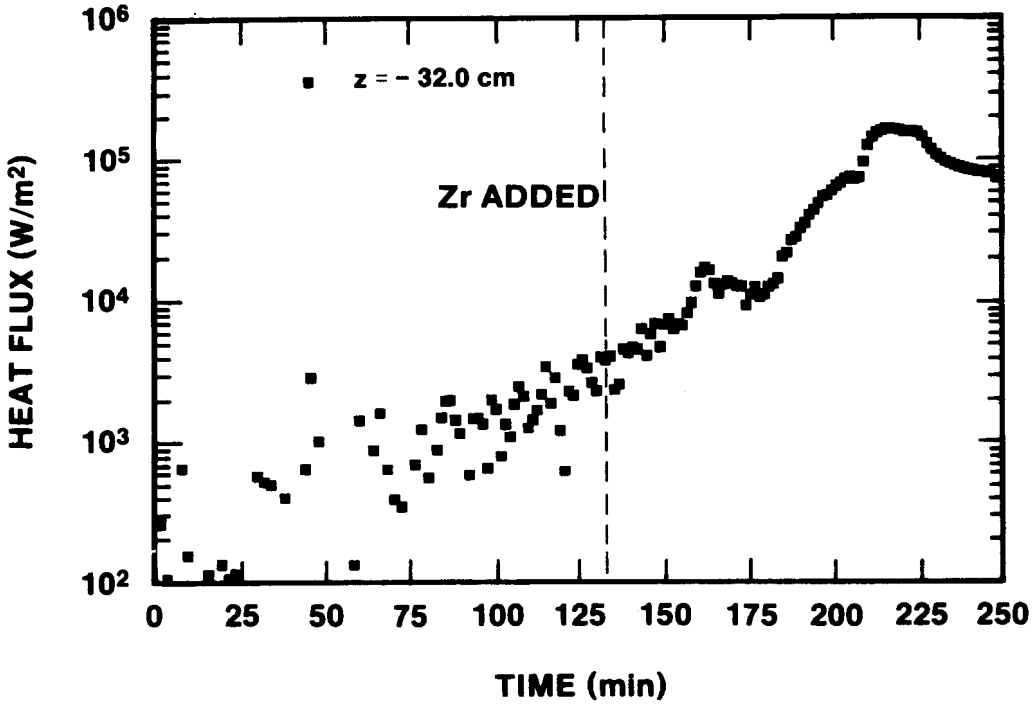

Figure H-23. MgO Sidewall Heat Flux Calculated From Thermocouple Data for the Array Located at z = -32.0 cm, SURC-3

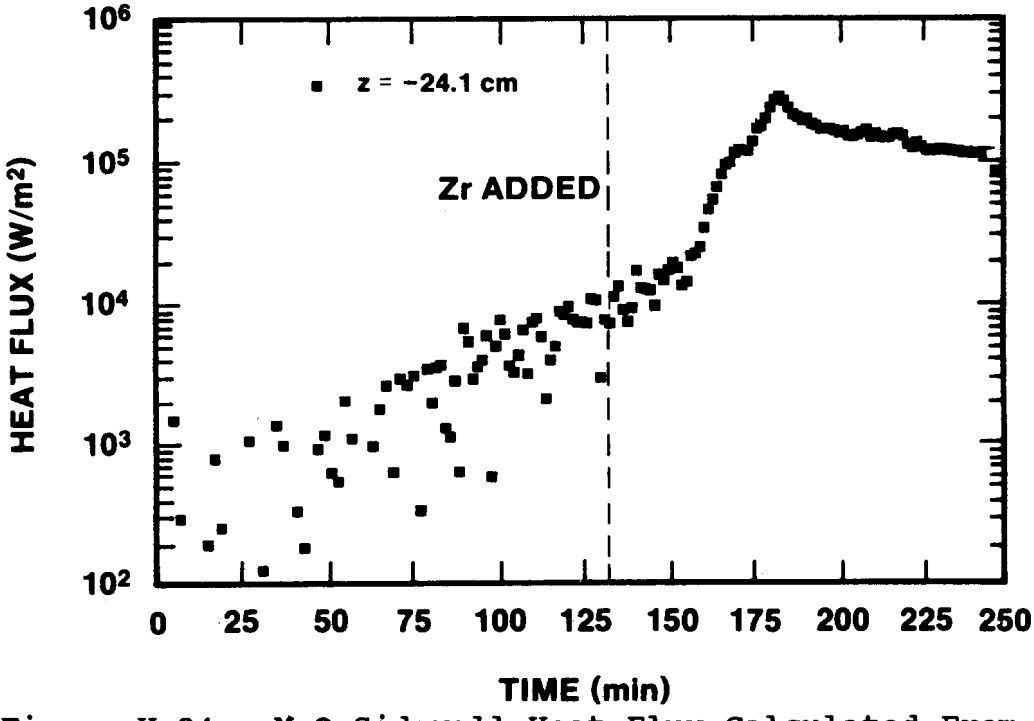

Figure H-24. MgO Sidewall Heat Flux Calculated From Thermocouple Data for the Array Located at z = -24.1 cm, SURC-3

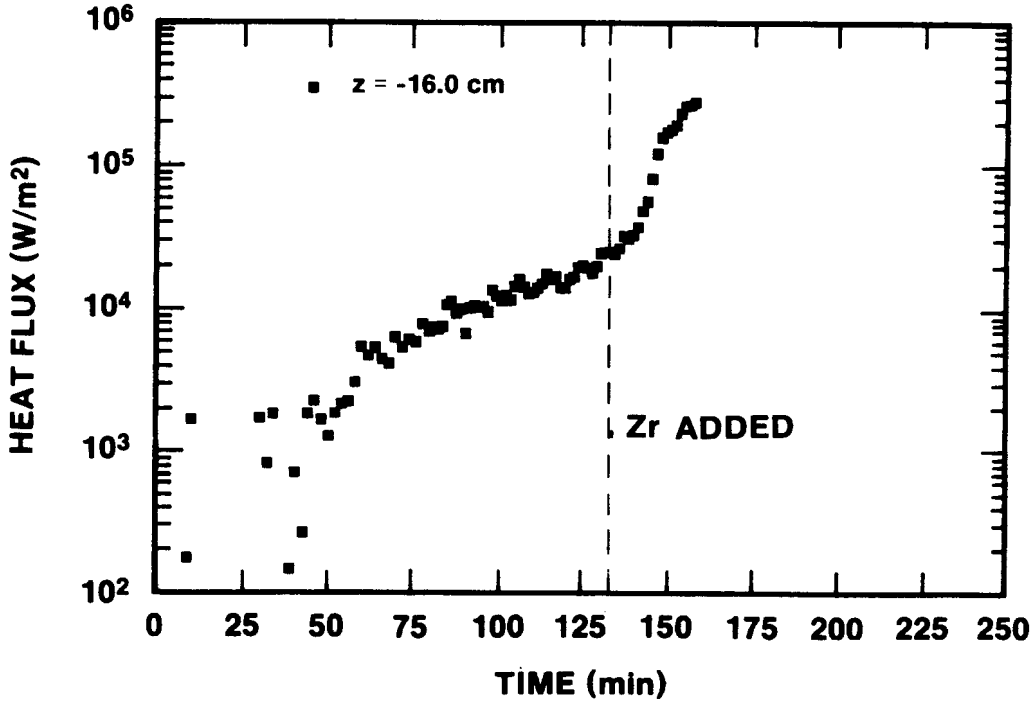

Figure H-25. MgO Sidewall Heat Flux Calculated From Thermocouple Data for the Array Located at z = -16.0 cm, SURC-3

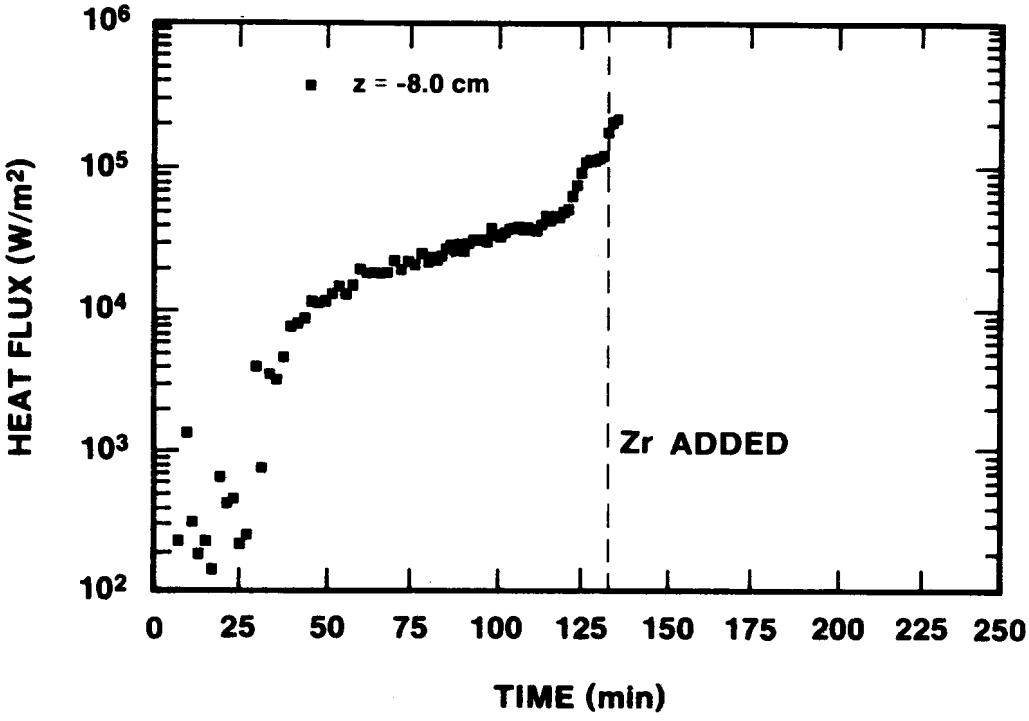

Figure H-26. MgO Sidewall Heat Flux Calculated From Thermocouple Data for the Array Located at z = -8.0 cm, SURC-3

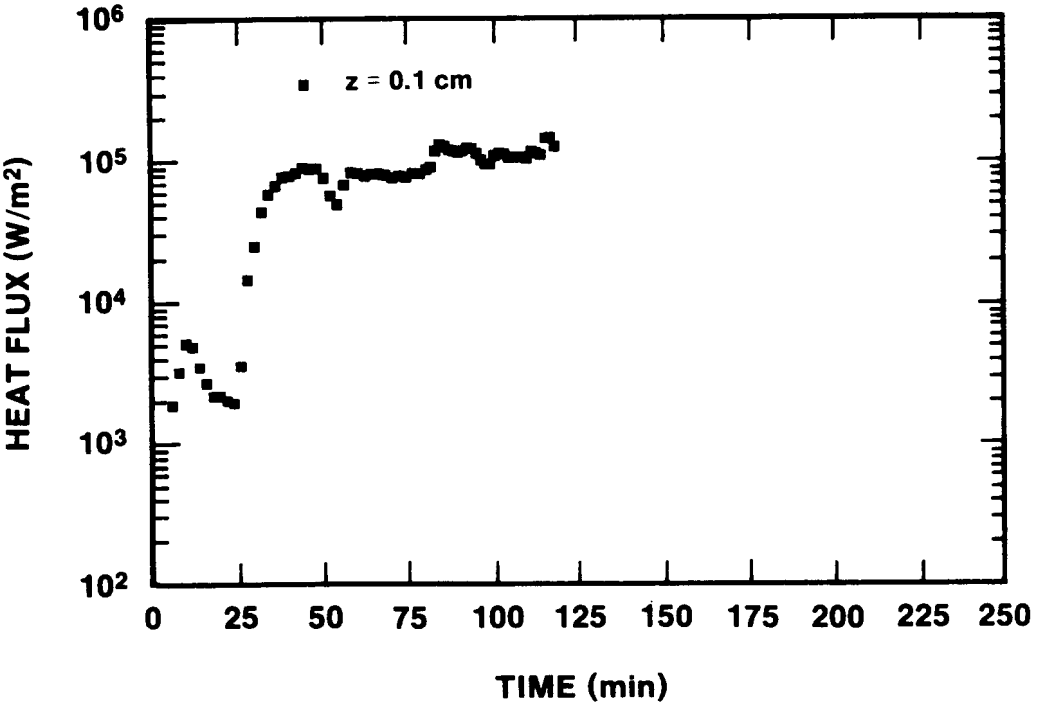

Figure H-27. MgO Sidewall Heat Flux Calculated From Thermocouple Data for the Array Located at z = -0.1 cm, SURC-3

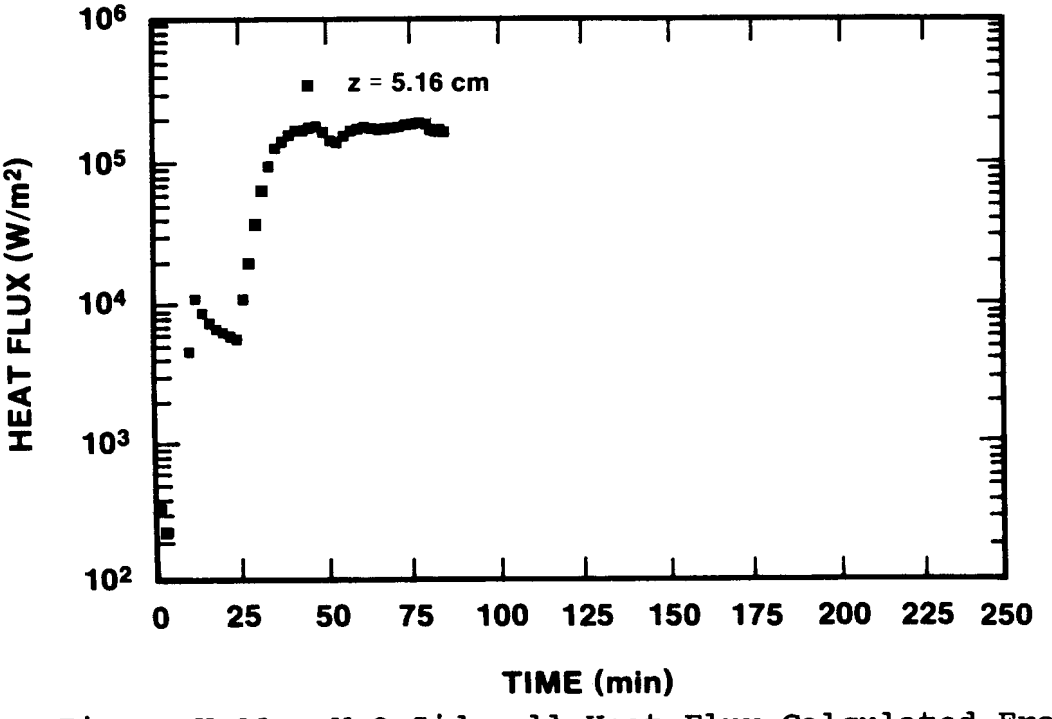

Figure H-28. MgO Sidewall Heat Flux Calculated From Thermocouple Data for the Array Located at z = -5.4 cm, SURC-3

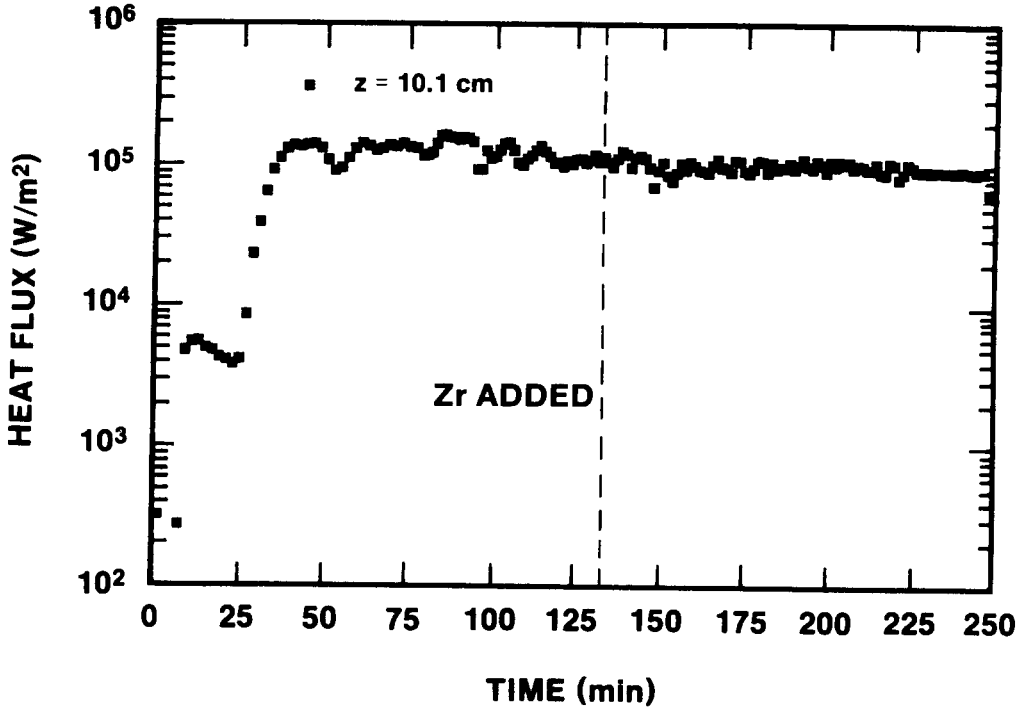

Figure H-29. MgO Sidewall Heat Flux Calculated From Thermocouple Data for the Array Located at z = -10.1 cm, SURC-3

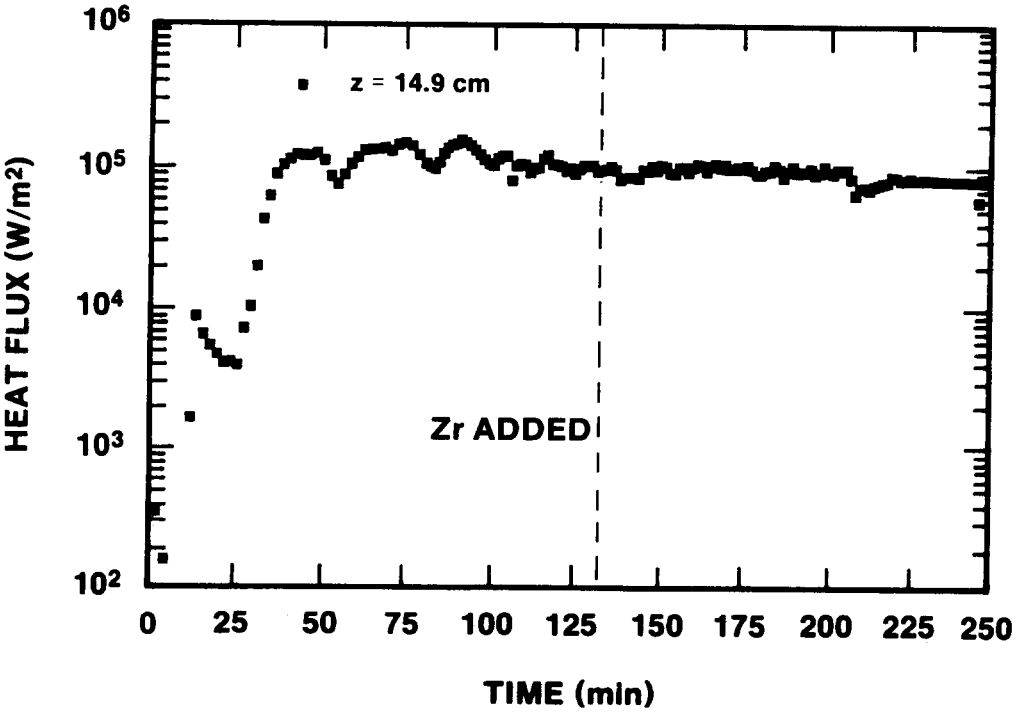

Figure H-30. MgO Sidewall Heat Flux Calculated From Thermocouple Data for the Array Located at z = -14.9 cm, SURC-3

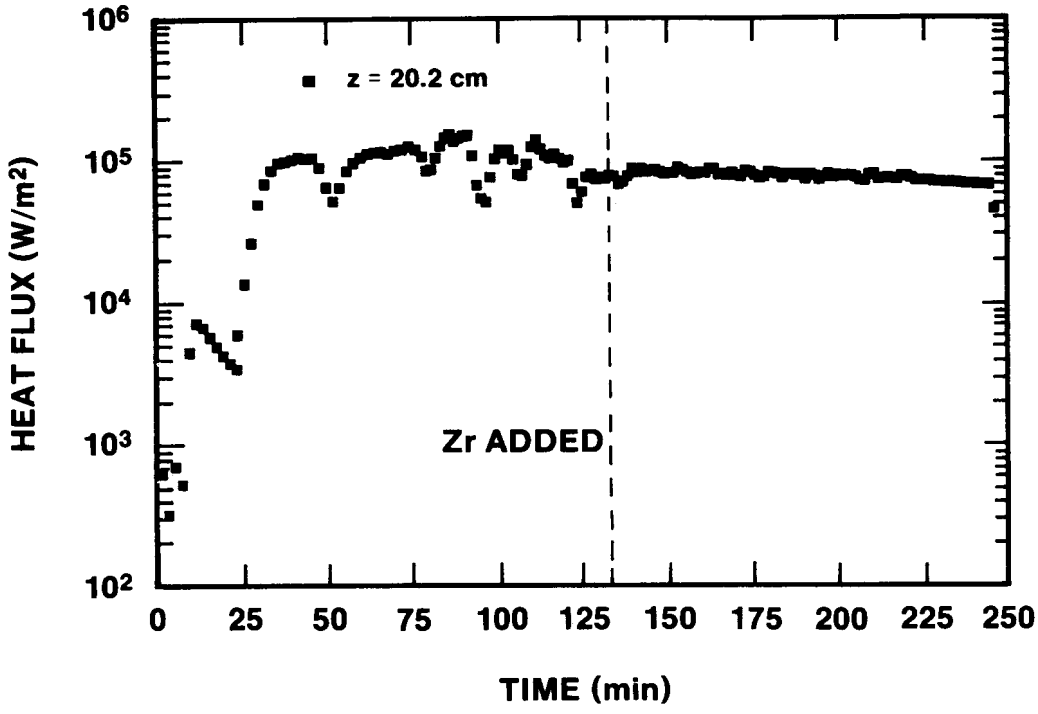

Figure H-31. MgO Sidewall Heat Flux Calculated From Thermocouple Data for the Array Located at z = -20.2 cm, SURC-3

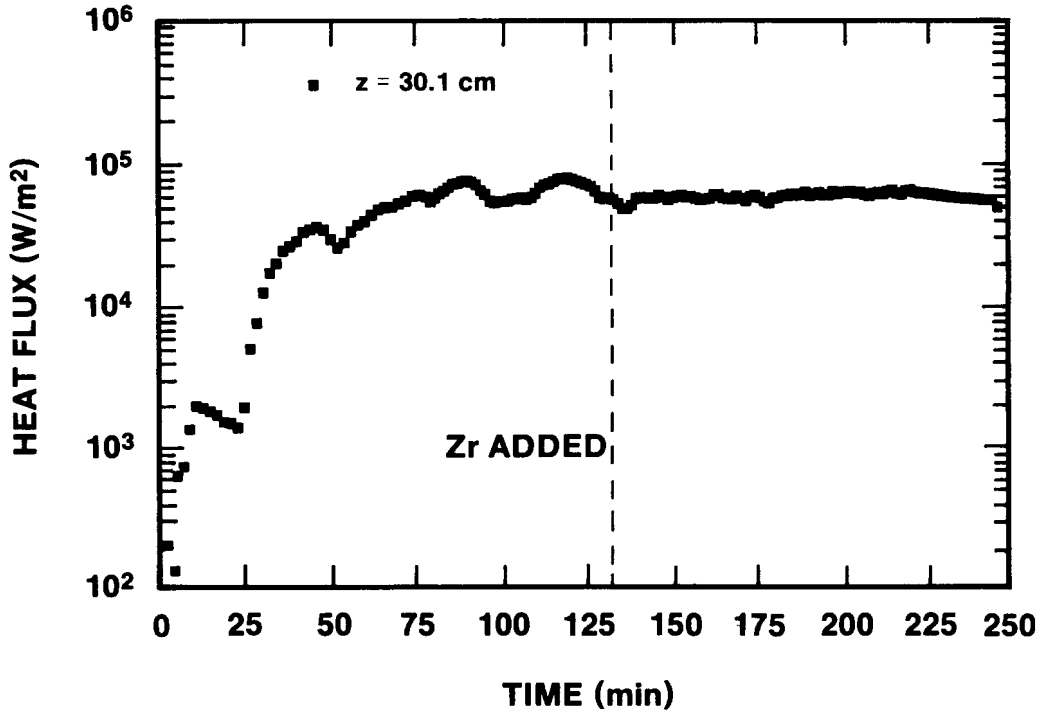

Figure H-32. MgO Sidewall Heat Flux Calculated From Thermocouple Data for the Array Located at z = -30.1 cm, SURC-3

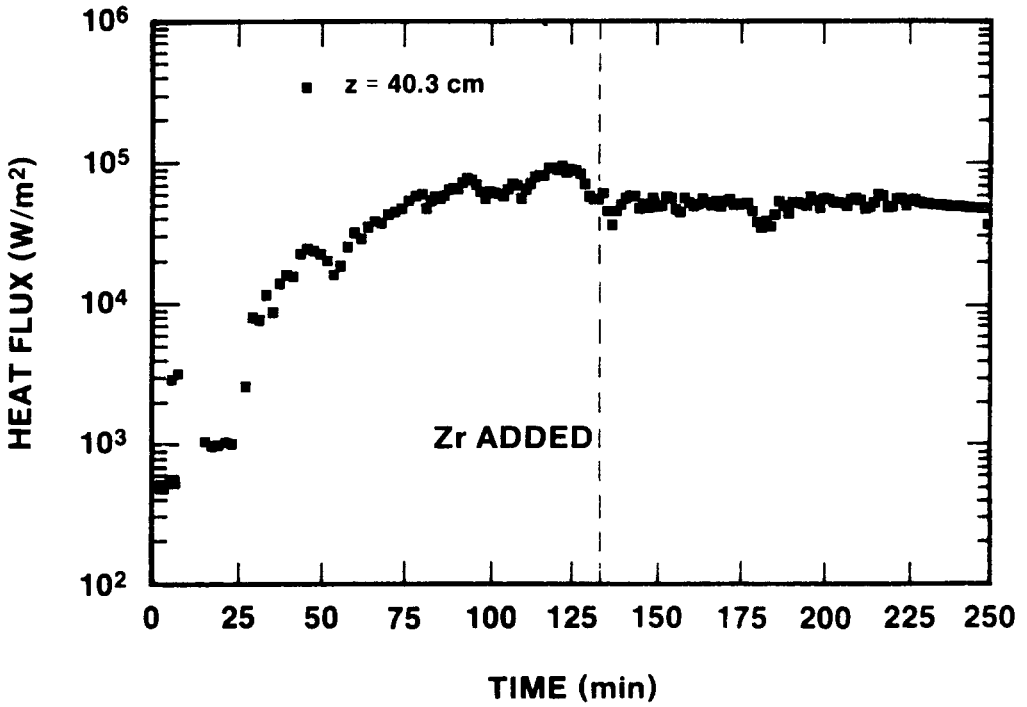

Figure H-33. MgO Sidewall Heat Flux Calculated From Thermocouple Data for the Array Located at z = -40.3 cm, SURC-3

APPENDIX I

Thermocouple Data from Test SURC-3 and SURC-3A

I.1 - Temperatures Indicated by Thermocouples Cast Into the Concrete Slug, TEST SURC-3A

Temperature data obtained with thermocouples embedded in the concrete slug used in the SURC-3A test are shown in Figures I-1 through I-8. The locations and the labels for these thermocouples can be found in Table 2.4.2 of the text.

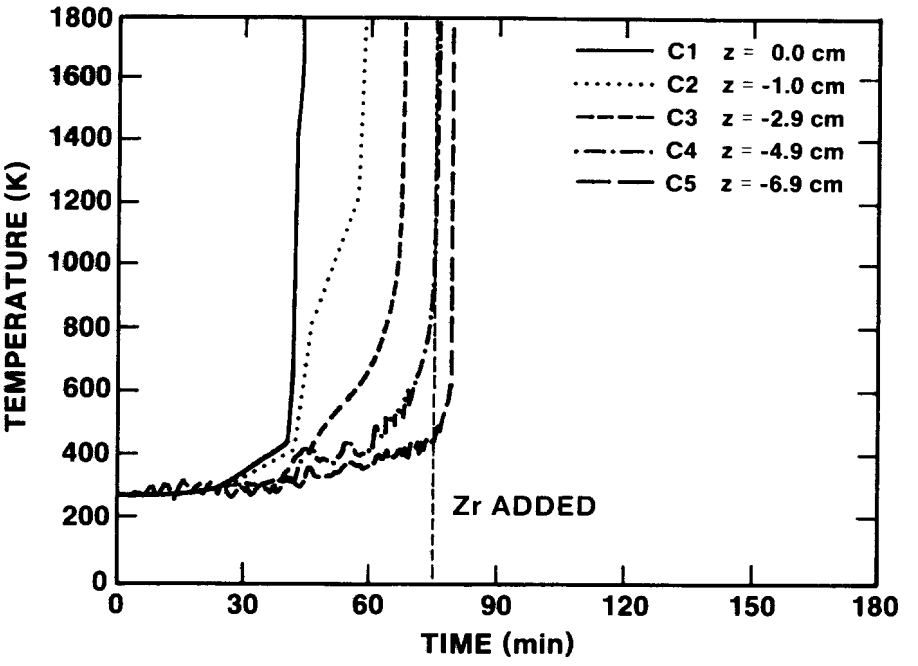

Figure I-1. Concrete Temperature Data Measured by Thermocouples Located on the Axial Centerline at z = -0.0, -1.0, -2.9, -4.9 and -6.9 cm, SURC-3A

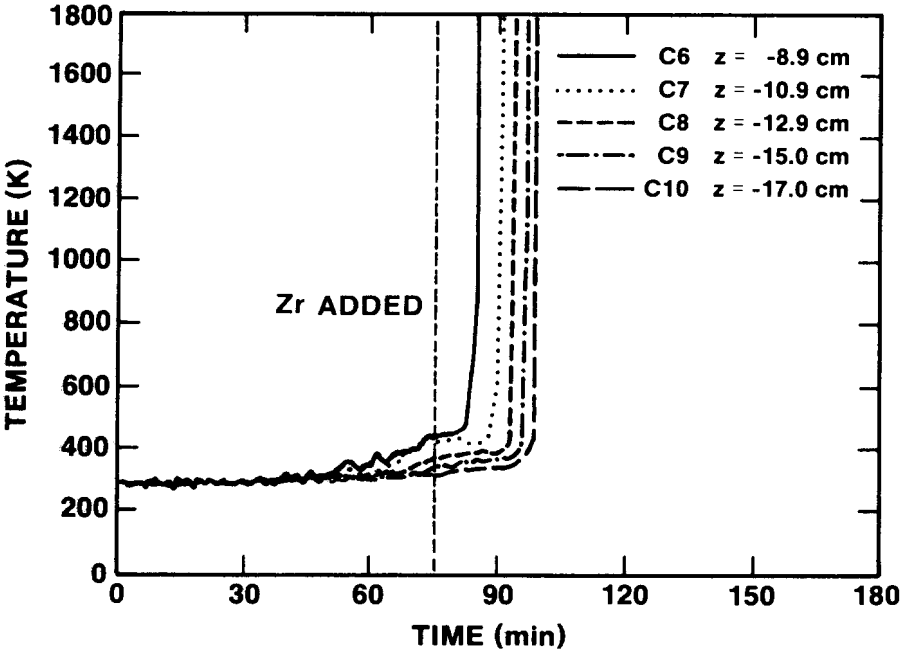

Figure I-2. Concrete Temperature Data Measured by Thermocouples Located on the Axial Centerline at z = -8.9, -10.9, -12.9, -15.9 and -17.0 cm, SURC-3A

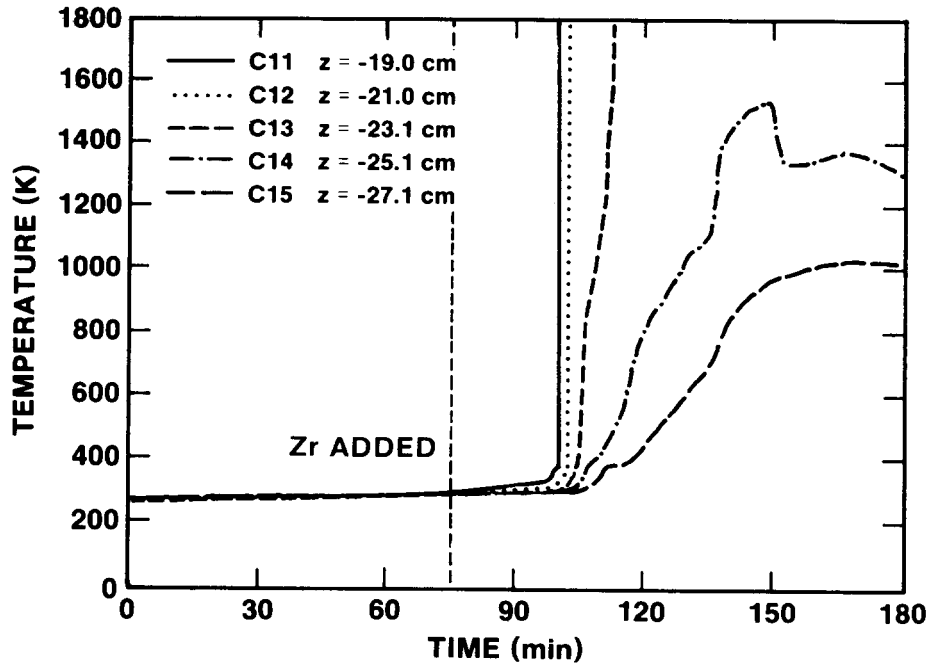

Figure I-3. Concrete Temperature Data Measured by Thermo-couples Located on the Axial Centerline at z = -19.0, -21.0, -23.1, -25.1 and -27.1 cm, SURC-3A

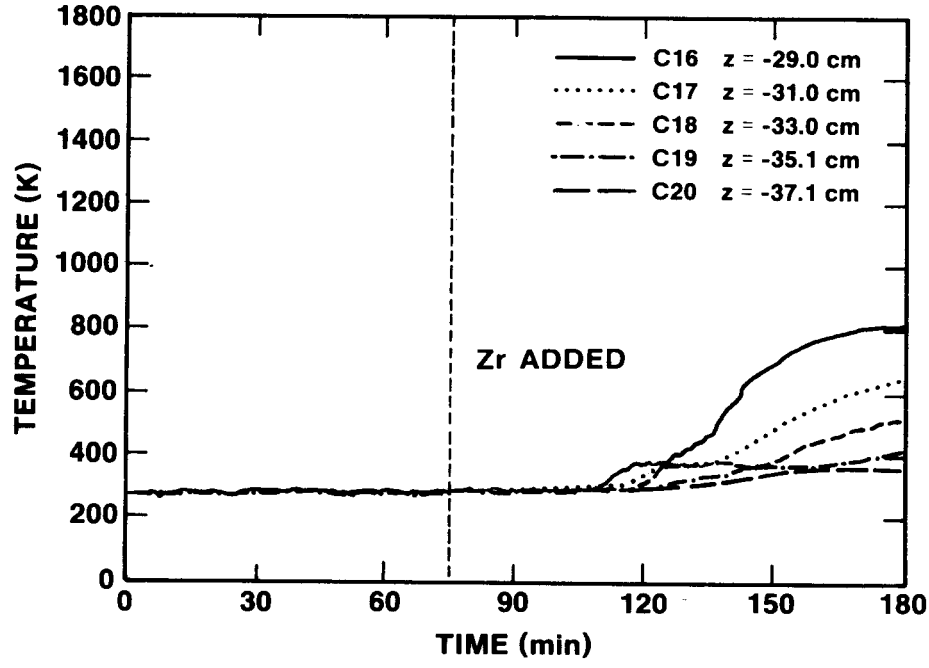

Figure I-4. Concrete Temperature Data Measured by Thermo-couples Located on the Axial Centerline at z = -29.0, -31.0, -33.0, -35.1 and -37.1 cm, SURC-3A

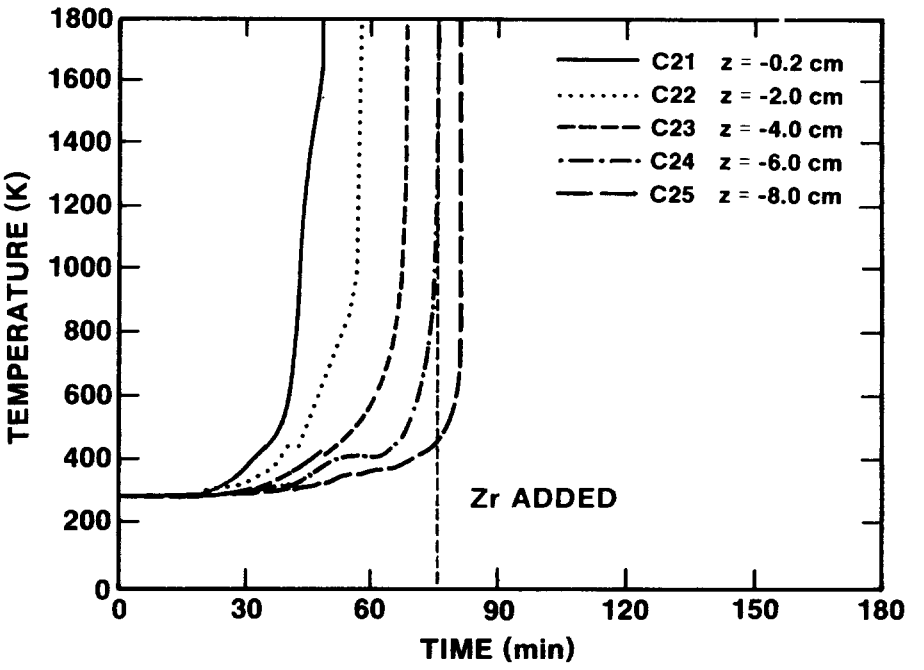

Figure I-5. Concrete Temperature Data Measured by Thermocouples Located on the Axial Centerline at z = -0.2, -2.0, -4.0, -6.0 and -8.0 cm, SURC-3A

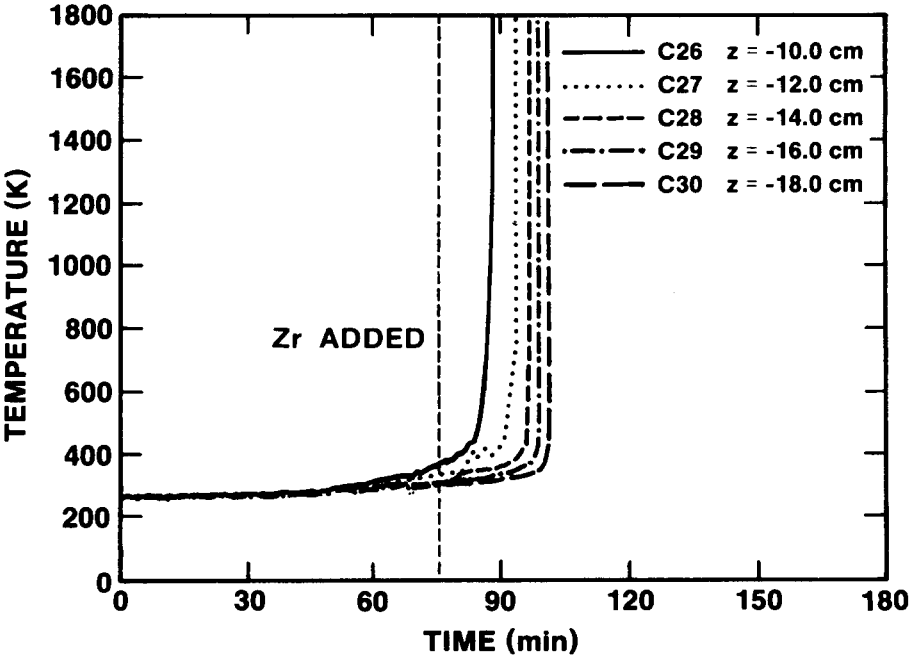

Figure I-6. Concrete Temperature Data Measured by Thermocouples Located on the Axial Centerline at z = -10.0, -12.0, -14.0, -16.0 and -18.0 cm, SURC-3A

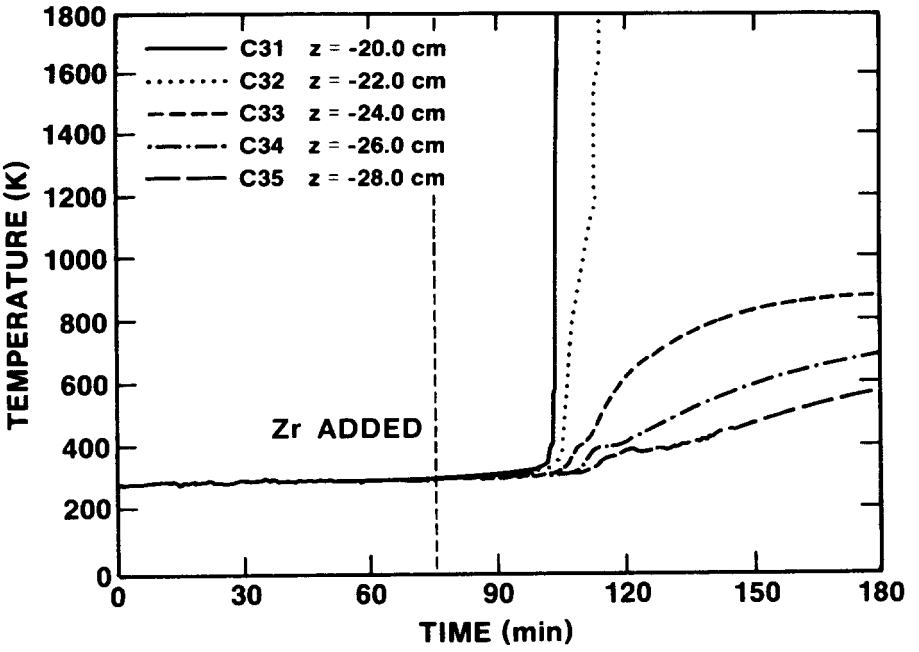

Figure I-7. Concrete Temperature Data Measured by Thermocouples Located on the Axial Centerline at z = -20.0, -22.0, -24.0, -26.0 and -28.0 cm, SURC-3A

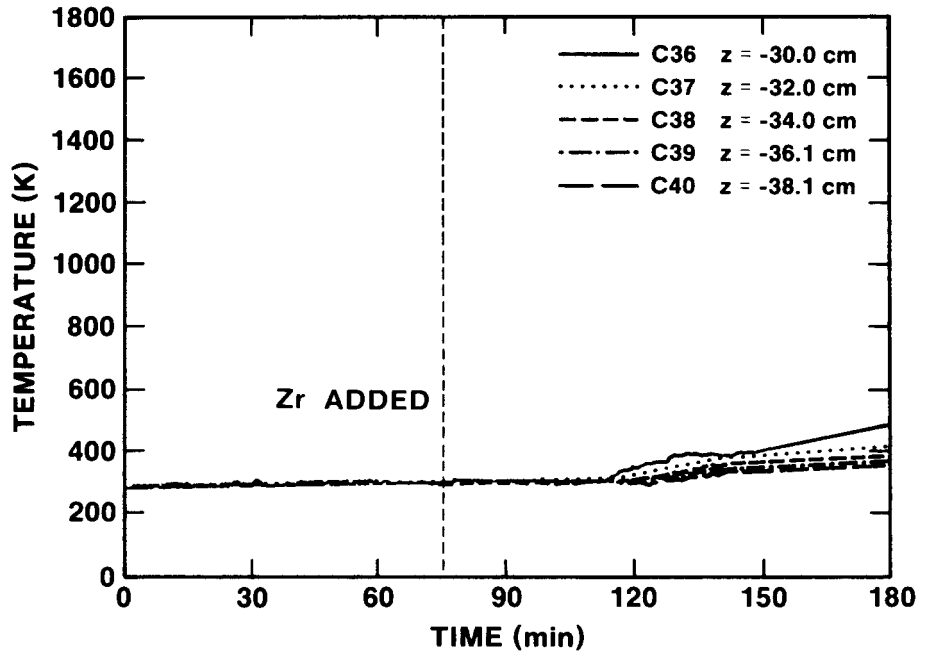

Figure I-8. Concrete Temperature Data Measured by Thermocouples Located on the Axial Centerline at z = -30.0, -32.0, -34.0, -36.1 and -38.1 cm, SURC-3A

I.2 - Temperatures Indicated by C and S Type Thermocouples Installed in Alumina Tubes and Cast Into the Concrete Slug, Test SURC-3A

Several type C and S thermocouples were installed into alumina tubes and cast into the concrete slug to measure melt temperature. Temperatures indicated by these thermocouples are shown as a function of time in Figures I-9 through I-11. The locations and labels for these thermocouples can be found in Table 2.4.3 in the text. The sheath of thermocouple A1-3 located at z = -15.0 cm was destroyed during assembly and is, therefore, not included in the plots.

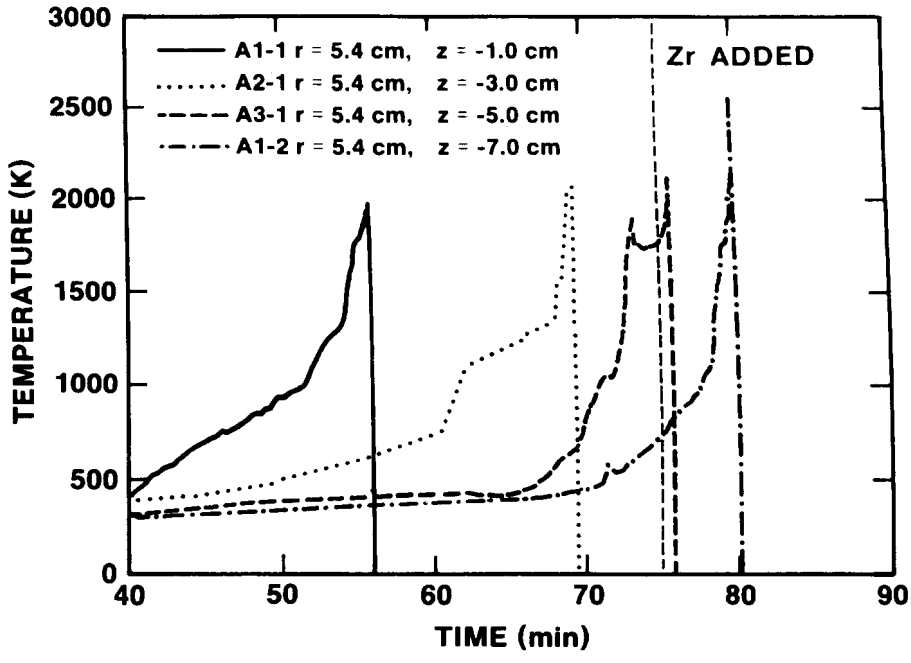

Figure I-9. Melt Temperature Data Measured by Thermocouples Cast Into the Concrete Slug at z = -1.0, 3.0, -5.0, and -7.0 cm, SURC-3A

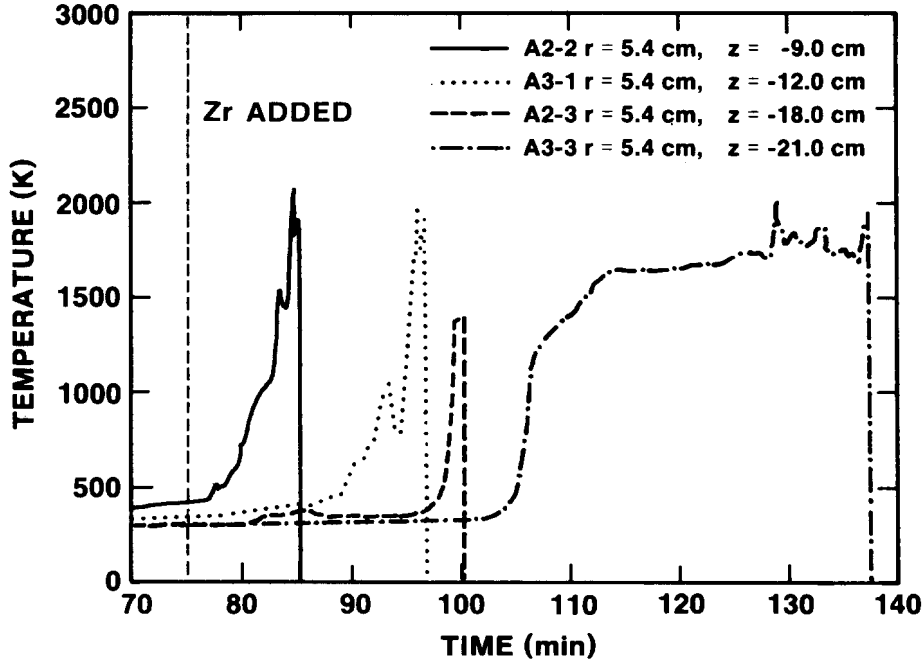

Figure I-10. Melt Temperature Data Measured by Thermocouples Cast Into the Concrete Slug at z = -9.0, 12.0, -18.0, and -21.0 cm, SURC-3A

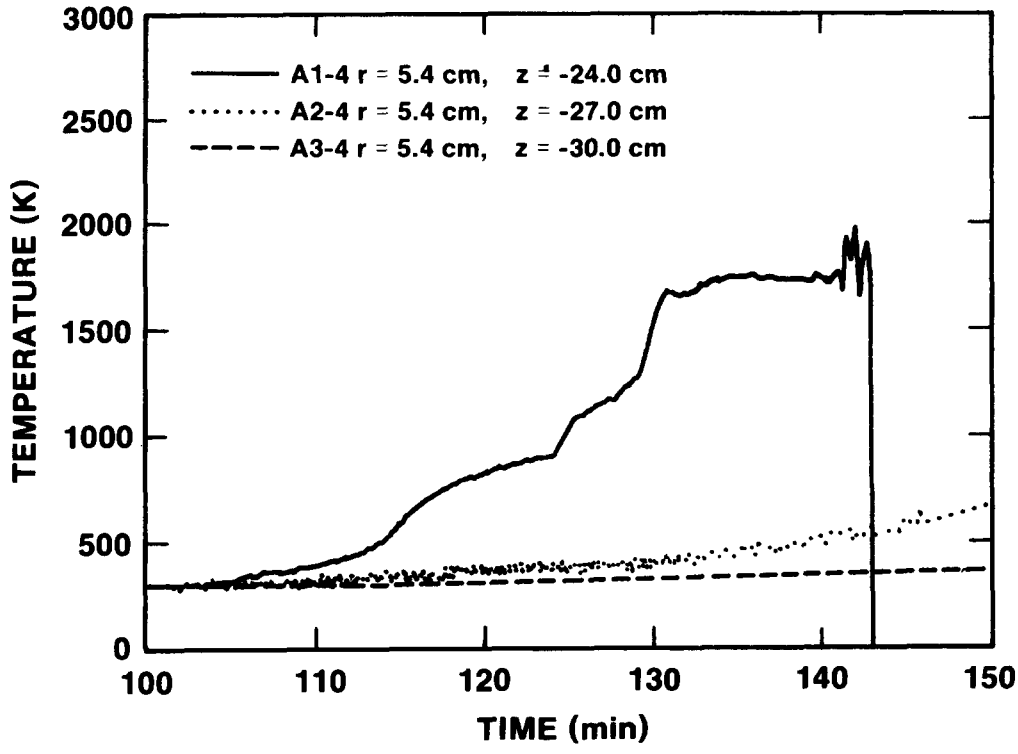

Figure I-11. Melt Temperature Data Measured by Thermocouples Cast Into the Concrete Slug at z = -24.0, 27.0, and -30.0 cm, SURC-3A

I.3 - Temperatures Indicated by Thermocouples Cast Into the Concrete Sidewall, Test SURC-3A

The temperature obtained with thermocouples cast into the limestone concrete annulus of the SURC-3A crucible are shown in Figures I-12 through I-22. The locations and labels for the thermocouples are described in Table 2.4.4 in the text.

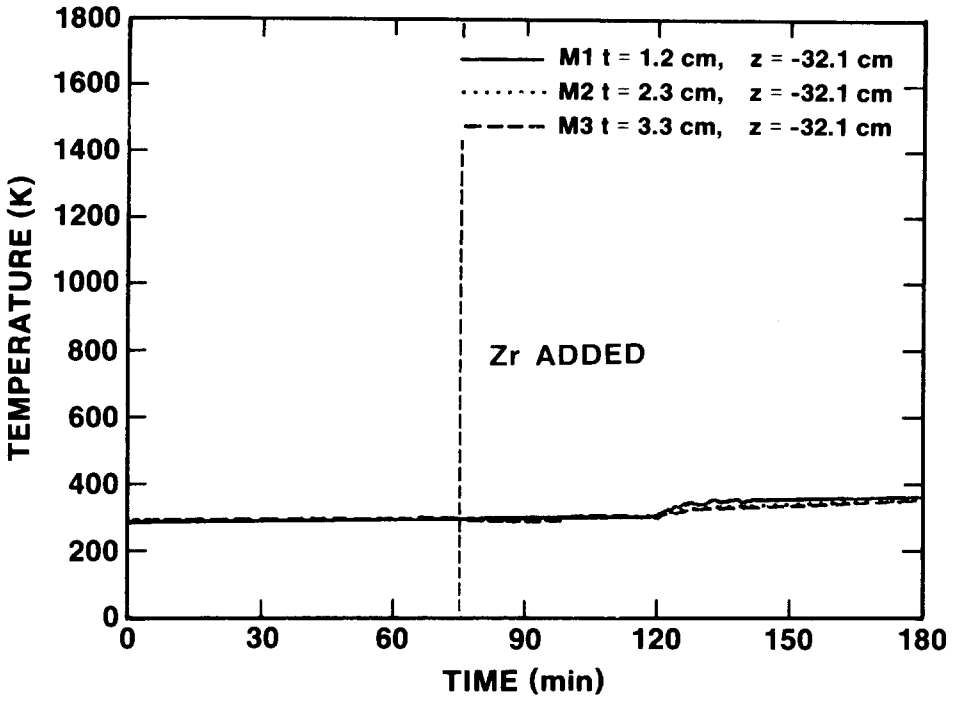

Figure I-12. Concrete Sidewall Temperature Data Measured by Thermocouples in the Array Located at z = -32.1 cm, SURC-3A

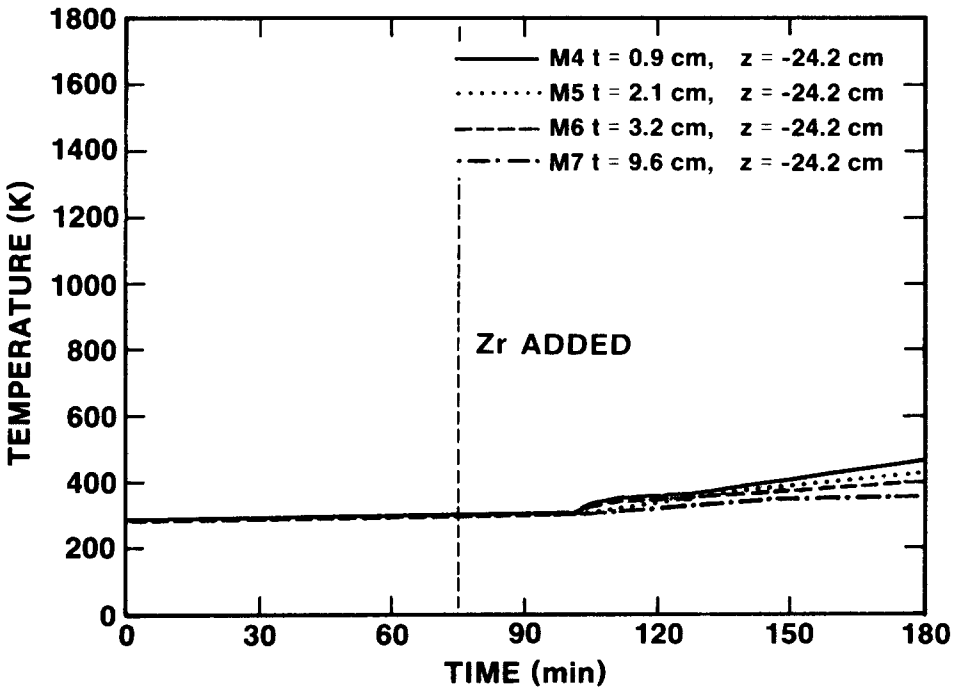

Figure I-13. Concrete Sidewall Temperature Data Measured by Thermocouples in the Array Located at z = -24.2 cm, SURC-3A

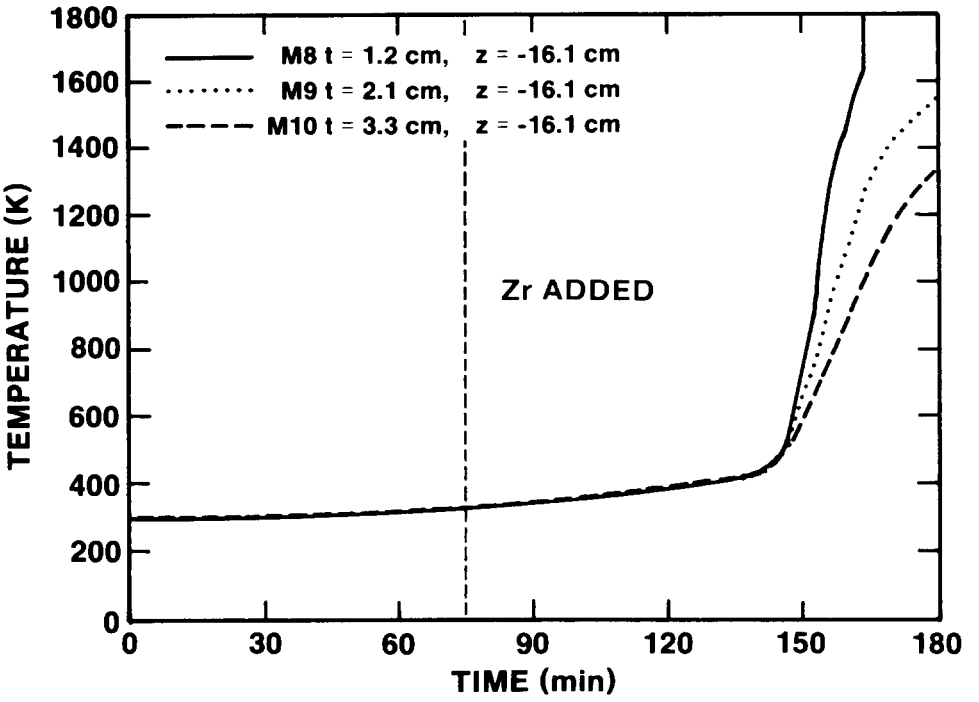

Figure I-14. Concrete Sidewall Temperature Data Measured by Thermocouples in the Array Located at z = -16.1 cm, SURC-3A

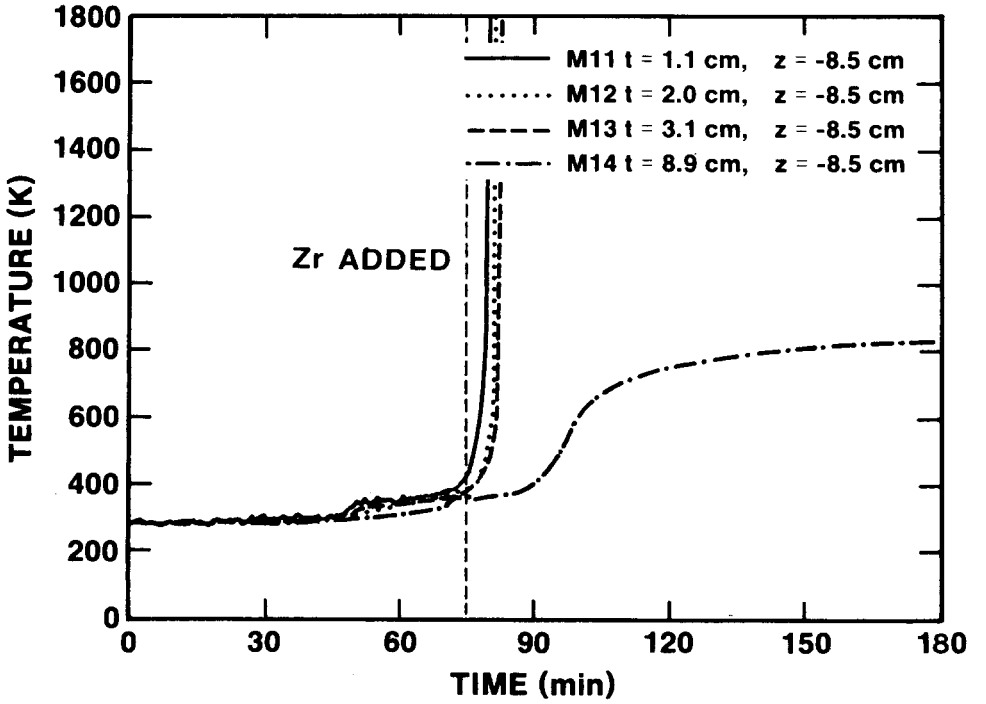

Figure I-15. Concrete Sidewall Temperature Data Measured by Thermocouples in the Array Located at z = -8.5 cm, SURC-3A

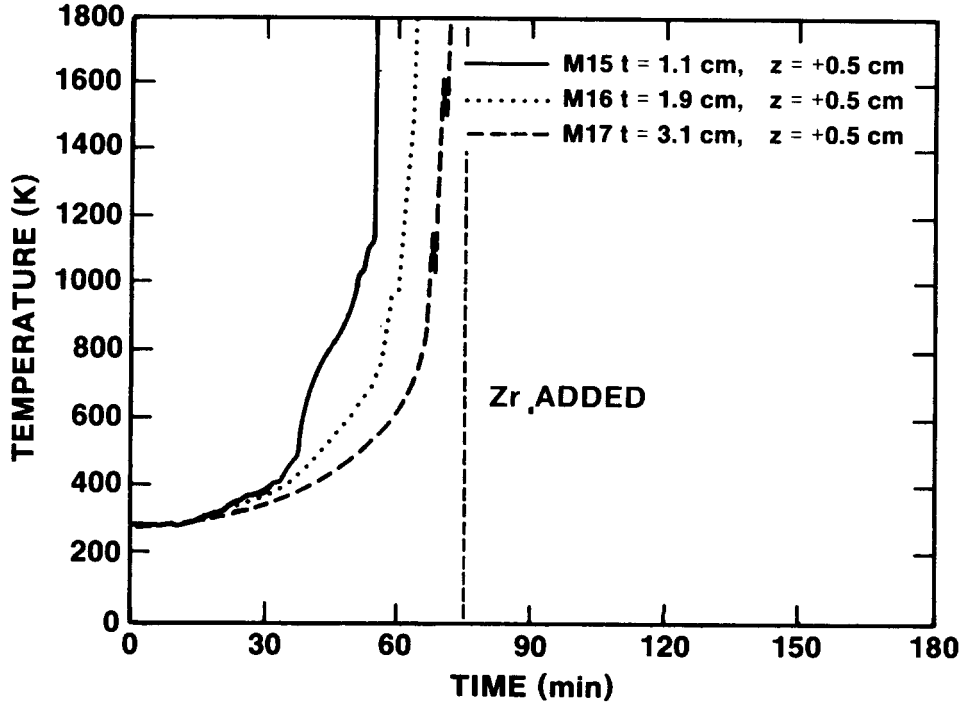

Figure I-16. Concrete Sidewall Temperature Data Measured by Thermocouples in the Array Located at z = -0.5 cm, SURC-3A

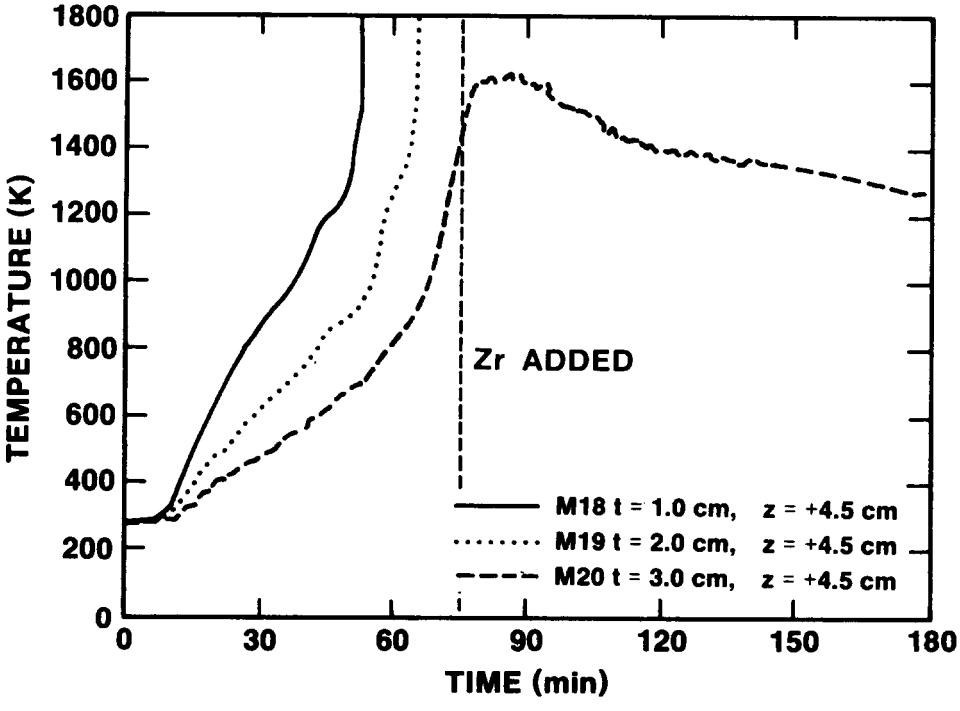

Figure I-17. Concrete Sidewall Temperature Data Measured by Thermocouples in the Array Located at z = -4.5 cm, SURC-3A

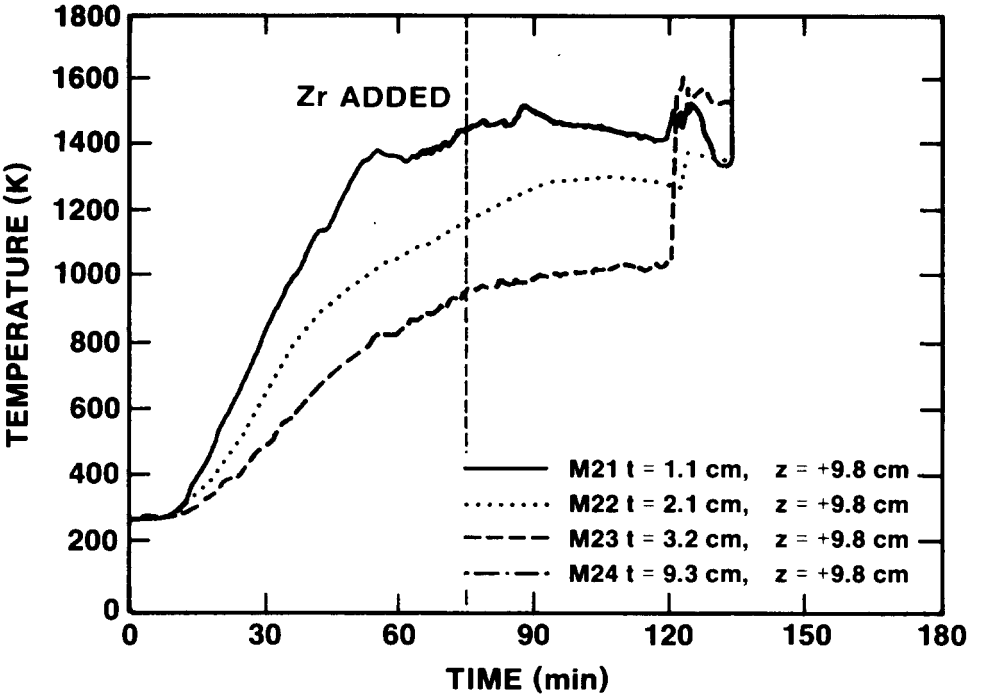

Figure I-18. Concrete Sidewall Temperature Data Measured by Thermocouples in the Array Located at z = -9.8 cm, SURC-3A

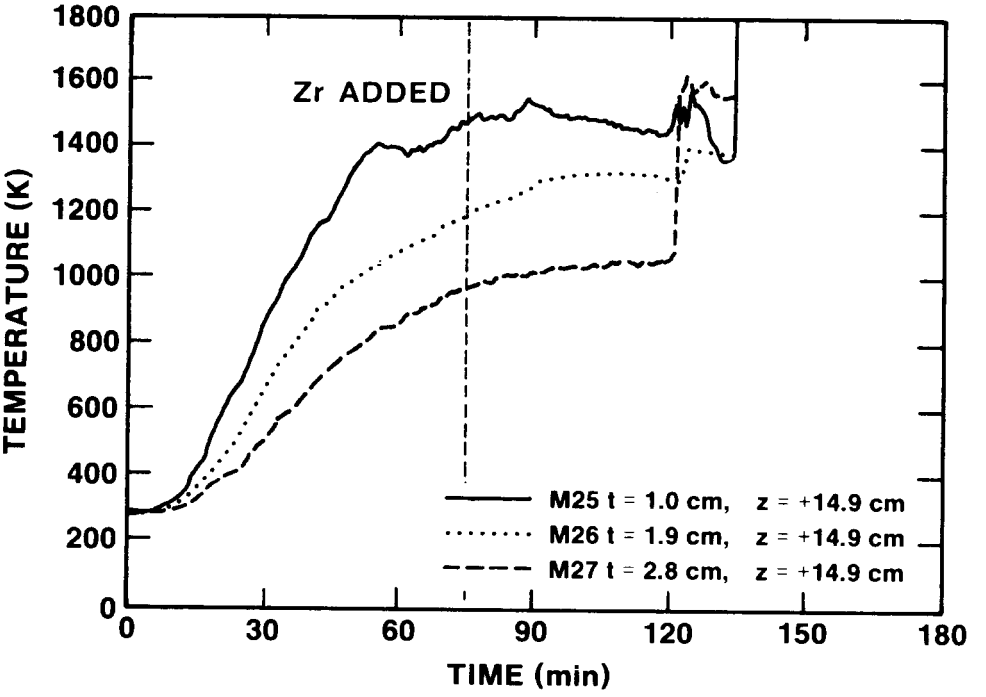

Figure I-19. Concrete Sidewall Temperature Data Measured by Thermocouples in the Array Located at z = -14.9 cm, SURC-3A

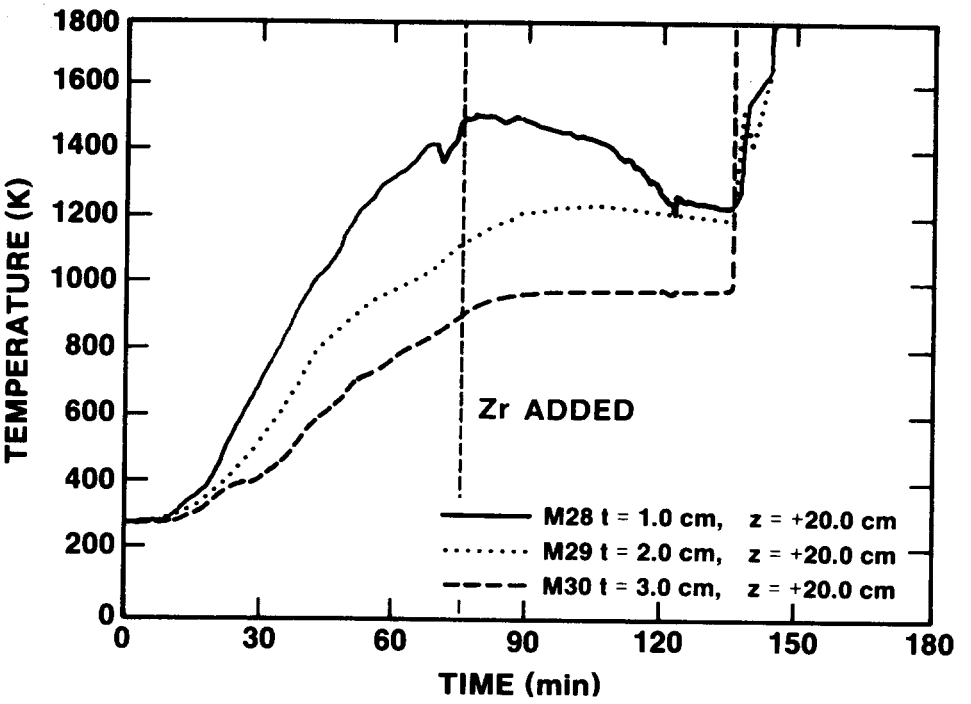

Figure I-20. Concrete Sidewall Temperature Data Measured by Thermocouples in the Array Located at z = -20.0 cm, SURC-3A

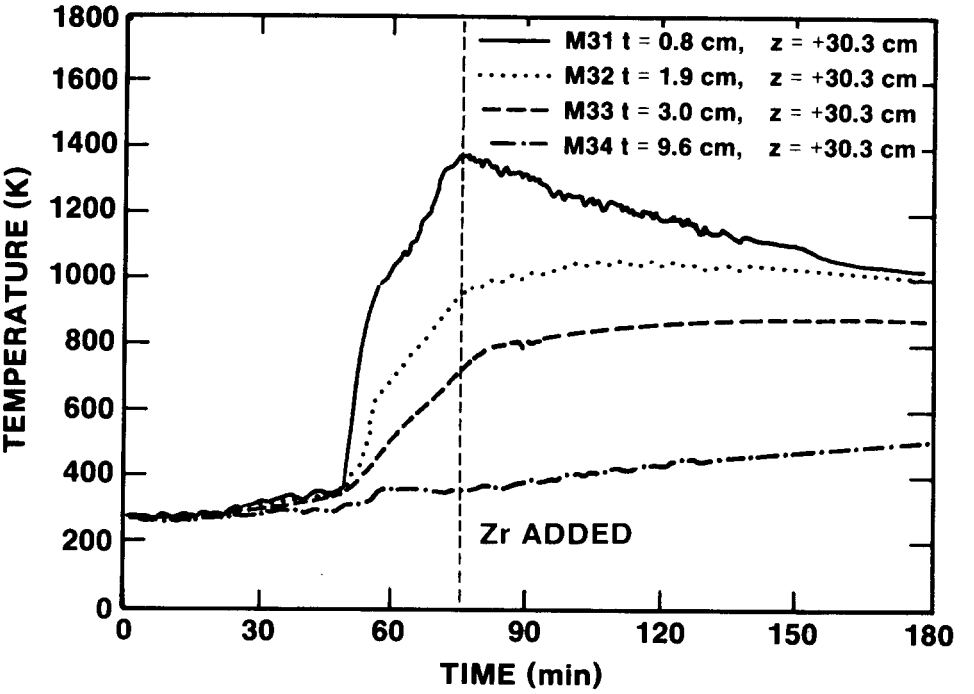

Figure I-21. Concrete Sidewall Temperature Data Measured by Thermocouples in the Array Located at z = -30.3 cm, SURC-3A

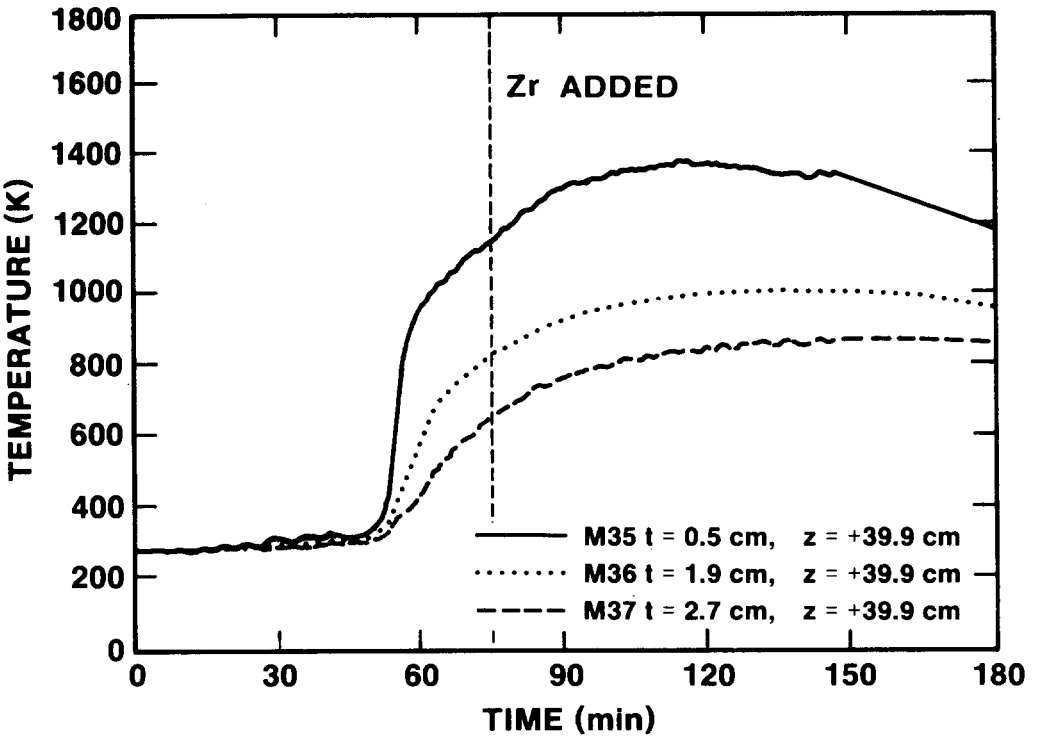

Figure I-22. Concrete Sidewall Temperature Data Measured by Thermocouples in the Array Located at z = -39.9 cm, SURC-3A

APPENDIX J

Thermocouple Calibration Results, SURC-3 and 3A Experiments

Three types of thermocouples were used in the SURC-3 and 3A experiments. Specifically, these were type K (chromal vs alumel), C (tungsten - 5% rhenium vs tungsten - 26% rhenium) and S (platinum vs platinum - 10% rhodium). The type K thermocouples were manufactured by Thermoelectric, the type C thermocouples were manufactured by Conax Corporation and the type S thermocouples were manufactured by ARi Industries Incorporated. Complete descriptions of the thermocouples are shown in Table J-1. The thermocouples were calibrated over a temperature range between 23 and 1186°C. Two temperature standards traceable to the National Bureau of Standards (NBS) were used. For temperatures to 500°C a Rosemount Model 162C, S/N 759, Platinum Resistance Thermometer (PRT) was used as the calibration standard. For temperatures above 500°C a calibrated type S thermocouple was used as a calibration standard.

TABLE J-1

Thermocouple Description Pretest Calibration, SURC-3 and 3A

Thermocouple Type	Identification Number	Sheath Material	Sheath Diameter	Junction Gnd/Ungnd
K	K1	304 Stainless	1.6 mm	Ungnd
K	K2	304 Stainless	1.6 mm	Ungnd
C	C8	Tantalum	1.6 mm	Ungnd
C	C12	Tantalum	1.6 mm	Ungnd
S	S13	Tantalum	1.6 mm	Ungnd
S	S14	Tantalum	1.6 mm	Ungnd

The six thermocouples were placed in the oven with the primary standards and instrumented to measure voltage. The oven was purged with argon to minimize oxidation of the sheaths at high temperatures. The temperature of the oven was increased from ambient 23 to 1186°C. Voltage measurements for the six thermocouples were taken at five temperatures spanning the calibration range at 23, 102, 492, 706 and 1186°C. The voltage measured for each thermocouple was converted to a temperature

equivalent based on the polynomial equation established for the particular junction. This temperature was then compared to the temperature measured by the calibration standard. The percent deviation of the thermocouple reading compared to the standard was calculated by

$$\% \text{ Deviation} = [(T^{out} - \text{Std})/\text{Std}] \times 100 \qquad \text{(J-1)}$$

where

% Deviation = temperature deviation from calibrated standard %

T^{out} = Indicated temperature of the thermocouple (C)

Std = Indicated temperature of the calibration standard (C)

The percent deviations plotted as functions of temperature for the K, C, and S thermocouples are shown in Figures J-1, J-2 and J-3, respectively.

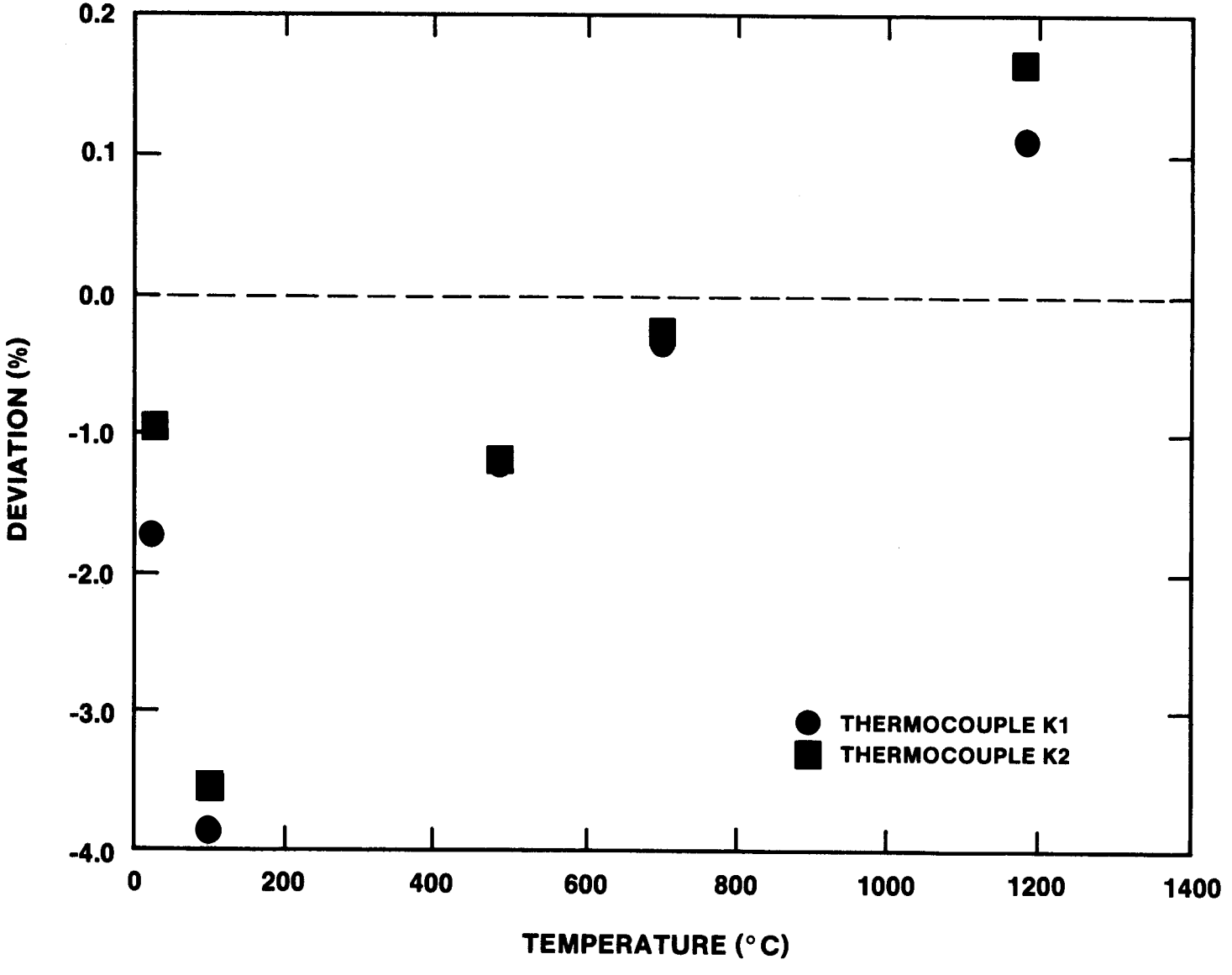

Figure J-1. Type K Thermocouple Calibration Data, SURC-3 and 3A

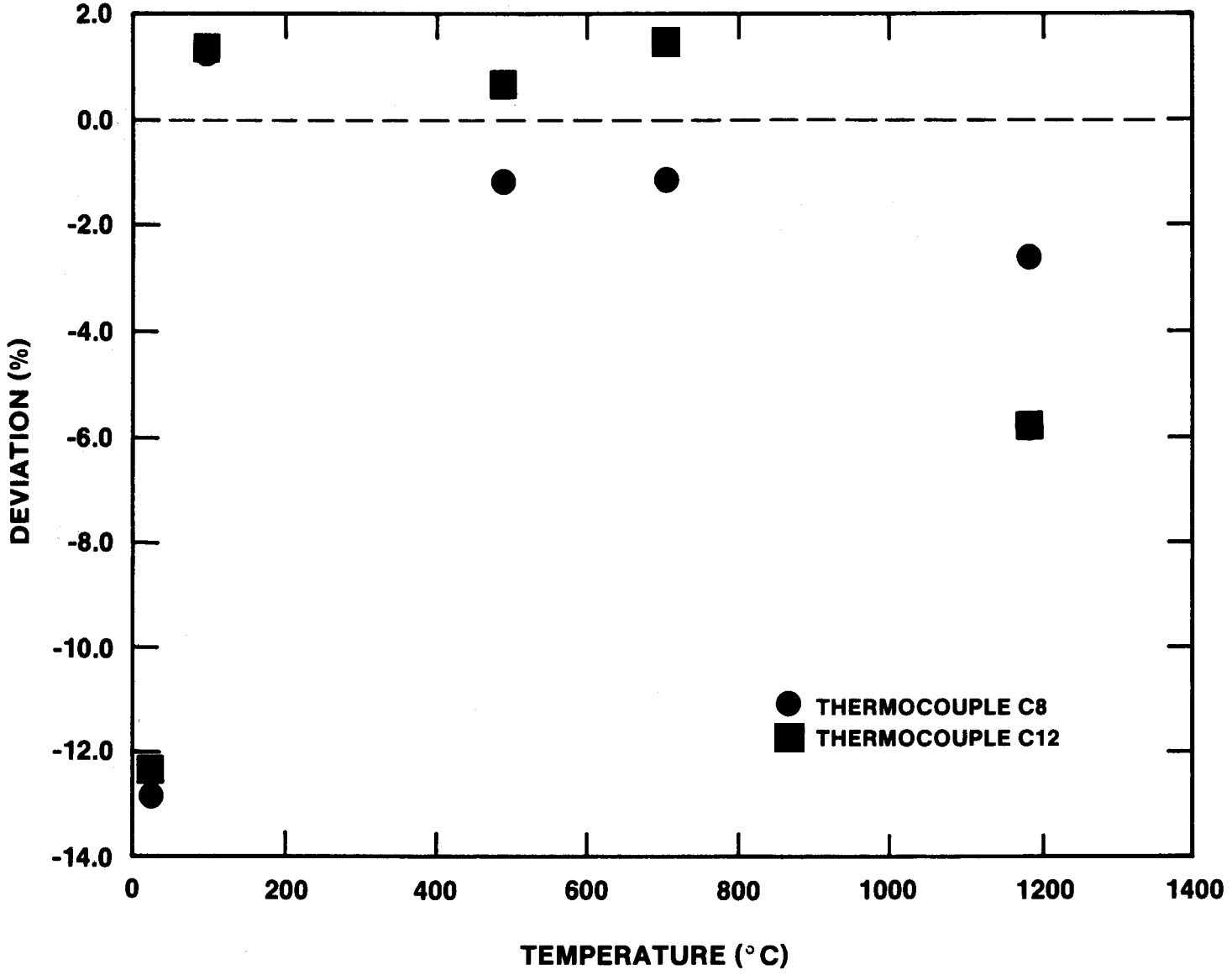

Figure J-2. Type C Thermocouple Calibration Data, SURC-3 and 3A

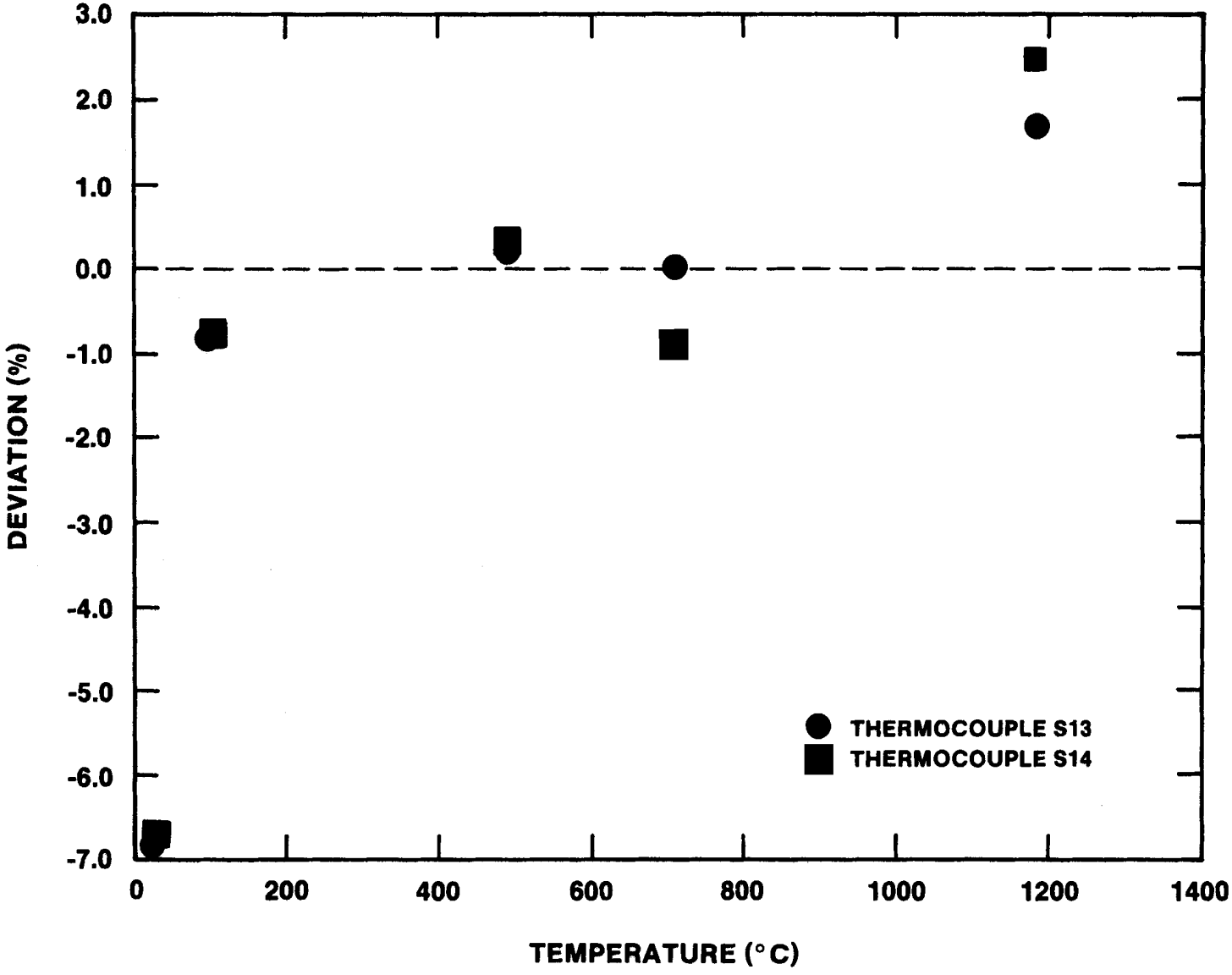

Figure J-3. Type S Thermocouple Calibration Data, SURC-3 and 3A

REFERENCES

Baker, W. C. and Pouchot, J. F. (1983), "The Measurement of Gas Flow," Control Technology News, Vol. 33, No. 1

Beck, J. V., Blackwell, B., and St. Clair, Jr., C. R. (1985), Inverse Heat Conduction, Wiley Interscience, New York, NY.

Berglund, R. N. and Liu, B. Y. H. (1973), "Generation of Monodisperse Aerosol Standards," Environmental Science Technology, 7, 147-153.

Blose, R. E., Gronager, J. E., Suo-Antilla, A. J., and Brockmann, J. E. (1987), SWISS: Sustained Heated Metallic Melt/Concrete Interactions with Overlying Water Pools, NUREG/CR-4727, SAND85-1546, Sandia National Laboratories, Albuquerque, NM.

Bradley, D. R. and Copus, E. R. (1986), Interaction of Hot Solid Core Debris with Concrete, NUREG/CR-4558, SAND85-1739, Sandia National Laboratories, Albuquerque, NM.

Brockmann, J. E. (1987), "Ex-Vessel Releases: Aerosol Source Terms in Reactor Accidents," Progress in Nuclear Energy, Vol. 19, 17-68.

Brockmann, J. E., Liu, B. Y. H., and McMurry, P. H. (1984), "A Sample Extraction Diluter for Ultra Fine Aerosol Sampling," Aerosol Science and Technology, Vol. 3, Number 4, pp 441-451.

Brockmann, J. E., Rader, D. J., and Lucero, D. A. (1987), "Experimental Determination of Dynamic Shape Factors," Paper presented at 1987 Annual Meeting of American Association for Aerosol Research, September 14-17, 1987, Seattle, WA.

Cole, R. K., Jr., Kelly, D. P., and Ellis, M. A. (1984), CORCON-MOD2: A Computer Program for Analysis of Molten-Core Concrete Interactions, NUREG/CR-3920, SAND84-1246, Sandia National Laboratories, Albuquerque, NM.

Cushing, K. E., Lacey, G. E., McCain, J. D. and Smith, W. B. (1976), Particulate Sizing Techniques for Control Device Evaluation: Cascade Impactor Calibrations, EPA-600/2-76-280, U. S. Environmental Protection Agency.

Davies, C. N. and Subari, M. (1982), "Aspiration Above Wind Velocity of Aerosols with Thin-Walled Nozzles Facing and at Right Angles to the Wind Direction," J. Aerosol Sci., Vol. 13, Number 1, pp 59-71.

Eckert, E. R. G. and Drake, R. M., Analysis of Heat and Mass Transfer (1972), McGraw-Hill, New York, p 415.

Gronager, J. E., Suo-Antilla, A. J., and Brockmann, J. E. (1986), TURC2 and 3: Large Scale $UO_2/ZrO_2/Zr$ Melt-Concrete Interaction Experiments and Analysis, NUREG/CR-4521, SAND86-0318, Sandia National Laboratories, Albuquerque, NM.

Gutfinger, C. and Tardos, G. I. (1979), Atmospheric Environment, Vol. 13, pp 853-876.

Holman, J. P. (1966), Experimental Methods for Engineers, McGraw-Hill, Inc., New York, NY.

Jayasekera, P. N. and Davies, C. N. (1980), "Aspiration Below Wind Velocity of Aerosols with Sharp Edged Nozzles Facing the Wind," J. Aerosol Sci., Vol. 11, pp 535-547.

Lee, K. W. (1981), Journal of Aerosol Science, Vol. 12, pp 79-87.

Marple, V. A. and Willeke, K. (1979), "Inertial Impactors in Aerosol Measurement," Lundgren, et al., editors, University Presses of Florida, Gainsville, FL, pp 90-107.

McFarland, A. R., Ortiz, C. A., and Bertch, R. W., Jr. (1978), "A High Capacity Preseparator for Collecting Large Particles," AIHA Paper No. 80, Texas A&M University, Civil Engineering Department, Air Quality Lab Publication 3718/04/78/ARM.

Powers, D. A., Brockmann, J. E., and Shiver, A. W. (1986) VANESA: A Mechanistic Model of Radionuclide Release and Aerosol Generation During Core Debris Interactions with Concrete, NUREG/CR-4308, SAND85-1370, Sandia National Laboratories, Albuquerque, NM.

Tardos, G. I., Yu, E., Pfeffer, R. E., and Squires, A. M. (1979), A Journal of Colloid and Interface Science, Vol. 71, No. 3, pp 616-621.

DISTRIBUTION:

U. S. Nuclear Regulatory Commission (17)
Office of Nuclear Regulatory Research
Attn: B. Sheron
C. N. Kelber
N. Costanzi
G. Marino
F. Eltawila
R. W. Wright
T. Walker
R. O. Meyer
J. Mitchell
C. Tinkler (5)
P. Worthington
S. B. Burson
M. Cunningham
Washington, D.C. 20555

U. S. Nuclear Regulatory Commission (4)
Office of Nuclear Reactor Regulation
Attn: P. Easky
J. Rosenthal
B. Hardin
R. Barrett
Washington, D.C. 20555

U. S. Nuclear Regulatory Commission (6)
NRC/RES
Attn: E. Beckjord
T. Lee
W. Lyon
Z. Rosztoczy
C. Ryder
T. Speis
Washington, D.C. 20555

U. S. Departrment of Energy (2)
Albuquerque Operations Office
Attn: C. E. Garcia, Director
For: C. B. Quinn
R. L. Holton
P. O. Box 5400
Albuquerque, NM 87185

Electric Power Research Institute (4)
Attn: F. Rahn
R. Ritzman
W. Lowenstein
R. Sehgal
3412 Hillview Avenue
Palo Alto, CA 94303

Brookhaven National Laboratory (6)
Attn: R. A. Bari
T. Pratt
G. Greene
T. Ginsberg
M. Lee
N. Tutu
130 BNL
Upton, NY 11973

Professor R. Seale
Department of Nuclear Engineering
University of Arizona
Tucson, AZ 85721

Oak Ridge National Laboratory (2)
Attn: T. Kress
A. Wright
P. O. Box Y
Oak Ridge, TN 37830

Argonne National Laboratory (8)
Attn: J. Rest
C. Johnson
L. Baker, Jr.
D. Cho
B. Spencer
K. Leong
J. Fink
V. Novick
9700 S. Cass Avenue
Argonne, IL 60439

Cathy Anderson
Nuclear Safety Oversight Commission
1133 15th Street, NW
Room 307
Washington, D.C. 20005

Battelle Columbus Laboratory (4)
Attn: C. Alexander
P. Cybulskis
R. Denning
J. Gieseke
505 King Avenue
Columbus, OH 43201

J. E. Antill
Berkeley Nuclear Laboratory
Berkeley GL 139PB
Gloucestershire, England
UNITED KINGDOM

W. G. Cunliffe
Bldg. 396
British Nuclear Fuels, Ltd.
Springfield Works
Salwick, Preston
Lancashire, England
UNITED KINGDOM

Professor Agustin Alonso
E.T.S. Ingenieros Industriales
Jost Gutierrez Abascal, 2
28006 Madrid
SPAIN

Dr. Alfonso Perez
Departmento de Seguridad Nuclear
Junta de Energia Nuclear
Avenida Complutense, 22
Madrid - 3
SPAIN

R. Sherry
JAYCOR
P. O. Box 85154
San Diego, CA 92138

Los Alamos National Laboratories
Attn: M. Stevenson
P.O. Box 1663
Los Alamos, NM 87545

UCLA (2)
Nuclear Energy Laboratory
Attn: I. Catton
D. Okrent
405 Hilgaard Avenue
Los Angeles, CA 90024

University of Wisconsin
Nuclear Engineering Department
Attn: M. L. Corradini
1500 Johnson Drive
Madison, WI 53706

EG&G Idaho
Willow Creek Building, W-3
Attn: R. Hobbins
P. O. Box 1625
Idaho Falls, ID 83415

Battelle Pacific Northwest Laboratory
Attn: M. Freshley
P. O. Box 999
Richland, WA 99352

W. Stratton
2 Acoma Lane
Los Alamos, NM 87544

Gesellschaft fur Reaktorsicherheit (GRS)
Postfach 101650
Glockengrasse 2
5000 Koeln 1
FEDERAL REPUBLIC of GERMANY

Kraftwerk Union
Attn: Dr. M. Peehs
Hammerbacher Strasse 1214
Postfach 3220
D-8520 Erlangen 2
FEDERAL REPUBLIC of GERMANY

UKAEA (8)
Attn: R. Potter 209/A32
A. Nicholas 102/A50
B. Bowsher 105A/A50
J. Mitchell 01/A50
B. Morris 216/A32
P. Smith 215/A32
S. Kinnersly 203/A32
D. Williams 210/A32
Winfrith, Dorchester
Dorset DT2 8DH
UNITED KINGDOM

Nucleare e della Protezione Sanitaria (DISP) (2)
Attn: Mr. Manilia
Mr. G. Petrangeli
Ente Nazionnle Energie Alternative (ENEA)
Viale Regina Margherita, 125
Casella Postale M. 2358
I-00100 Roma A. D.
ITALY

Dr. K. J. Brinkman
Reactor Centrum Nederland
1755 ZG Petten
THE NETHERLANDS

Dr. S. J. Niemczyk
1545 18th Street, NW
#112
Washington, D.C. 20036

Kernforschungszentrum Karlsruhe (2)
Attn: H. Alsmeyer
H. Rininsland
Postfach 3640
75 Karlsruhe
FEDERAL REPUBLIC of GERMANY

Mr. H. Bairiot, Chief
Department LWR Fuel
Belgonucleaire
Rue de Champde Mars. 25
B-1050 Brussels
BELGIUM

Japan Atomic Energy Research Institute
Attn: S. Saito
Tokai-Mura, Naka-Gun
Ibaraki-Ken 319-11
JAPAN

Wang Lu
TVA
400 Commerce, W9C157-CK
Knoxville, TN 37902

Peter Bieniarz
Risk Management Associates
2309 Dietz Farm Road, NW
Albuquerque, NM 87107

Dr. K. Soda
Fuel Reliability Laboratory
Department of Nuclear Fuel Safety
Japan Atomic Energy Resarch Institute
Tokai-Muri, Naku-Gun, Ibaraki-Ken
319-11
JAPAN

K. Sato, Director
Department of Reactor Safety Research
Japan Atomic Energy Research Institute
Tokai-Mura, Naka-Gun, Ibaraki-Ken
319-11
JAPAN

P. Fehrenback
Atomic Energy Canada, Ltd.
Chalk River, Ontario
CANADA KOJ IJO

UKAEA (2)
Attn: A. Taig
M. Haynes
Safety and Reliability Directorate
Wigshaw Lane
Culcheth
Warrington WA3 4NE
Chesire
UNITED KINGDOM

J. R. Mathews
Aere Harwell
Didcot
Oxfordshire OX11 ORA
UNITED KINGDOM

UKAEA Culham Laboratory (3)
Attn: N. J. Brealey E5.152
B. D. Turland E5.157
F. Briscoe
Abingdon
Oxfordshire OX14 3DB
UNITED KINGDOM

H. J. Teague (3)
UKAEA
Safety and Reliability Directorate
Wigshaw Lane
Culcheth
Warrington, WA3 4NE
UNITED KINGDOM

M. Jankowski
IAEA
Division of Nuclear Reactor Safety
Wagranesrstrasse 5
P. O. Box 100
A/1400 Vienna
AUSTRIA

Statens Karnkraftinspektion (2)
Attn: L. Hammer
W. Frid
P. O. Box 27106
S-10252 Stockholm
SWEDEN

Studvik Energiteknik AB
Attn: K. Johansson
S-611 82 Nykoping
SWEDEN

Atomic Energy Canada Ltd. (2)
Attn: H. Rosinger
D. Wren
Pinawa, Manitoba
CANADA ROE 1LO

Korea Adv Energy Research Inst
Attn: H. R. Jun
P. O. Box 7
Daeduk-Danji
Choong-Nam
KOREA

Institute of Nuclear Energy Research
Attn: Sen-I Chang
P. O. Box 3
Lungtan
Taiwan 325
REPUBLIC OF CHINA

Juan Bagues
Consejo de Seguridad Nuckan
SOR Angela de la Cruz No 3
Madrid 28056
SPAIN

U. S. Department of Energy
Office of Nuclear Safety Coordination
Attn: R. W. Barber
Washington, D.C. 20545

Department of Energy
Scientific and Tech. Info. Center
P. O. Box 62
Oak Ridge, TN 37831

Power Authority State of New York
Attn: R. Deem
10 Columbus Circle
New York, NY 10019

M. Fontana
Director, IDCOR Program
ENERGEX
575 Oak Ridge Turnpike
Oak Ridge, TN 37830

Fauske and Associates, Inc. (2)
Attn: R. Henry
M. Plys
16W070 West 83rd Street
Burr Ridge, IL 60952

UKAEA
Reactor Development Division
Attn: T. Butland
Winfrith, Dorchester
Dorset DT2 8DH
England
UNITED KINGDOM

3141 S. A. Landenberger (5)
3151 W. I. Klein
3202 R. D. Gomez
6321 B. D. Zak
6400 D. J. McCloskey
6410 D. A. Dahlgren
6412 A. L. Camp
6415 R. M. Cranwell
6418 R. K. Cole
6420 W. B. Gauster
6422 D. A. Powers (5)
6422 M. D. Allen
6422 F. E. Arellano
6422 R. Blose
6422 J. E. Brockmann
6422 R. M. Elrick
6422 E. R. Copus (15)
6422 D. A. Lucero
6422 D. Sweet
6422 M. Pilch
6423 K. O. Reil
6425 S. S. Dosanjh
6425 B. R. Bradley
6429 K. D. Bergeron
6429 F. Gelbard
6429 D. C. Williams
6454 G. L. Cano
6523 W. A. Von Riesemann
8524 J. A. Wackerly

NRC FORM 335 (2-89) NRCM 1102, 3201, 3202

U.S. NUCLEAR REGULATORY COMMISSION

BIBLIOGRAPHIC DATA SHEET

(See instructions on the reverse)

1. REPORT NUMBER (Assigned by NRC, Add Vol., Supp., Rev., and Addendum Numbers, If any.)

NUREG/CR-4794
SAND86-2638

2. TITLE AND SUBTITLE

EXPERIMENTAL RESULTS OF CORE-CONCRETE INTERACTIONS USING MOLTEN STEEL WITH ZIRCONIUM

3. DATE REPORT PUBLISHED

MONTH	YEAR
July	1990

4. FIN OR GRANT NUMBER

A1218

5. AUTHOR(S)

E. R. Copus, R. E. Blose, J. E. Brockmann, R. D. Gomez, D. A. Lucero

6. TYPE OF REPORT

7. PERIOD COVERED *(Inclusive Dates)*

8. PERFORMING ORGANIZATION – NAME AND ADDRESS *(If NRC, provide Division, Office or Region, U.S. Nuclear Regulatory Commission, and mailing address; if contractor, provide name and mailing address.)*

Sandia National Laboratories
Albuquerque, NM 87185

9. SPONSORING ORGANIZATION – NAME AND ADDRESS *(If NRC, type "Same as above"; if contractor, provide NRC Division, Office or Region, U.S. Nuclear Regulatory Commission, and mailing address.)*

Division of Systems Research
Office of Nuclear Regulatory Research
U. S. Nuclear Regulatory Commission
Washington, DC 20555

10. SUPPLEMENTARY NOTES

11. ABSTRACT *(200 words or less)*

Four experiments were performed in order to evaluate the additional effects of zirconium metal oxidation on core debris interactions with limestone concrete using molten stainless steel as the core debris simulant. The QT-D, QT-E, SURC-3 and SURC-3A experiments eroded between 10 and 33 cm of limestone concrete during sustained interactions which lasted 35 to 120 minutes. Melt pool temperatures during the tests ranged from 1900 K before zirconium addition to 2100 K during the zirconium-steel-concrete phase of the tests. Large increases in erosion rate, gas production and aerosol release were also measured shortly after Zr metal was added to the melt.

12. KEY WORDS/DESCRIPTORS *(List words or phrases that will assist researchers in locating the report.)*

molten core interactions, ex-vessel interactions, reactor containment safety studies, melt-concrete heat transfer, core debris-concrete interactions, ex-vessel aerosol source terms, zirconium oxidation.

13. AVAILABILITY STATEMENT

Unlimited

14. SECURITY CLASSIFICATION

(This Page) Unclassified

(This Report) Unclassified

15. NUMBER OF PAGES

16. PRICE